Probing the Photophysics of Organic Photovoltaics from an Electron Spin Perspective

Jack Palmer

A thesis submitted for the degree of
Doctor of Philosophy

Worcester College, University of Oxford

Trinity Term 2025

Abstract

The field of organic photovoltaics (OPVs) has undergone a renaissance driven by the advent of non-fullerene acceptor molecules that have propelled efficiencies beyond 20%. Despite this progress, the fundamental processes that drive the conversion of light to electricity remain under debate. Electron paramagnetic resonance (EPR) spectroscopy can help provide answers: by selectively probing electron spin, the key photoinduced states - charge-transfer (CT) states, separated charges, and triplet excitons - can be investigated. A series of donor:acceptor OPV blends were investigated to gain information on the properties and dynamics of the spin states involved in the photovoltaic mechanism.

Initially, the photoinduced separated charges within donor and acceptor domains were identified and characterised through multi-frequency pulse EPR under steady-state conditions. Overlapping spectral contributions were disentangled by exploiting couplings of electron spins to ^{14}N nuclei and leveraging differences in relaxation times. The obtained g-values were verified by quantum chemical calculations validated with electron-nuclear double resonance experiments, and provided the basis for interpreting the more complex spin-correlated CT state signals.

The evolution of CT states at the donor:acceptor interface was probed through time-resolved EPR. Interpretation of the observed spin polarisation, reflective of CT state formation and decay, as well as further separation to free charges, required the development of a purpose-built simulation framework to model the interplay of spin dynamics, kinetics and relaxation. The effects of laser intensity, temperature and film morphology were explored through time-resolved EPR, and extensive modelling revealed two channels of charge separation: a channel slow enough to enable spin-mixing in the CT state, observed for all OPV blends, and an ultrafast charge separation channel, exclusive to the highest-performing materials. This work presents the first observation of both channels for efficient non-fullerene acceptor blends. The observed evolution of spin polarisation additionally confirms the presence of a reversible equilibrium between the CT state and separated charges, previously suggested to explain improved efficiencies of non-fullerene acceptor blends.

A connection between the interfacial CT state and steady-state charges within donor and acceptor domains was established by time-resolved pulse EPR, through a range of pulse sequences aimed at separating contributions from different spin states. This allowed identification of additional efficiency-limiting pathways involving quenching of singlet excitons by trapped charges, underscoring the importance of managing trap density in device optimisation.

Acknowledgements

I would like to express my deepest gratitude to my supervisor, Dr. Claudia Tait, for her enduring support and guidance over the past four years. Choosing your first DPhil student is no small decision, and I am profoundly grateful that you welcomed me into your now-burgeoning research group. Your seemingly boundless knowledge and insight have been invaluable, and I have benefitted greatly from your ability to find clarity in even the most complex of questions. Thank you for granting me the freedom to pursue my research ambitions and for consistently pushing me to grow beyond my academic comfort zone. Beyond your intellectual mentorship, I am also deeply thankful for your humility and kindness. From the home-baked cakes celebrating birthdays and milestones to thoughtful check-ins during my many cuts and bruises, your generosity and care have left a lasting impact.

To the wider members of the Tait Research group, boy oh boy has it been fun! Lorenzo Catini: the yin to my yang, every computational chemist needs someone to mix solutions. It's been a pleasure being parked next to you in the office every day, and I will miss all the chatter and general rubbish we talk. Now that I'm gone, don't think I won't stop sending you recipes for ham, cream, and pea carbonara and other British-Italian fusion dishes. I've also had the great privilege of supervising two incredibly smart Part II students, Niall Curwen and Oliver Christie. Thank you for your patience, enthusiasm, and your bold (if misguided) belief that you can code better than me. To Dr Max Mayländer and his revolving door of German Master's students, Marco and Jonas, thank you for the camaraderie, the moral support during thesis writing (mainly in the form of shoving ice cream down my throat), and for reinforcing the importance of a good 'glug glug' on a Friday evening. And to the many other wonderful, if transient, members of the group, my good friend Daniele Panariti, social butterfly Dr Gabriel Moise, Jack, Luke, Ben and more who have graced the office, thank you for making this experience memorable.

I would also like to thank Prof. Stefan Stoll for providing me with an invaluable opportunity to expand my academic horizons during a research stay at the University of Washington, in Seattle. I thoroughly enjoyed our regular discussions that probed at the heart of spin fundamentals. I would also like to mention his group members

Dr Maxx Tessmer and Rachelle Stowell for their warm hospitality in showing a wide-eyed Brit the sights of Western America.

Beyond the EPR community, I am deeply grateful to the friends who have kept me grounded and supported throughout my time in Oxford. My house of spectroscopists, Sophie, Matt and Tom, the OUGC community - Karl, Josh, Niall (again), Emily, and many more; Alex and my home and undergraduate pals living in London and further afield.

And finally to my family, thank you for your unwavering belief in me.

Contents

Chapter 1

Introduction to Organic Photovoltaics

The 21st century faces an unprecedented energy challenge. As global populations grow and living standards improve in developing nations, energy demand continues to rise sharply. This escalating demand is still largely met through fossil fuels - coal, oil, and natural gas - which are finite, environmentally destructive, and primary drivers of anthropogenic climate change. The scientific consensus is clear: to minimise the most catastrophic effects of global warming, including extreme weather events, sea-level rise, and large-scale ecological disruption, a rapid transition to cleaner, more sustainable energy sources must be made.[1,2]

The case for renewable energy is not based on environmental urgency alone. Renewables have become central to addressing broader challenges such as energy security, economic resilience, and technological leadership. Recent global events have revealed critical vulnerabilities in fossil fuel supply chains, resulting in widespread price volatility and energy shortages. These disruptions have pushed millions worldwide into energy poverty and highlighted the risks associated with heavy reliance on imported fuels. Today, renewables are valuable not only for their environmental

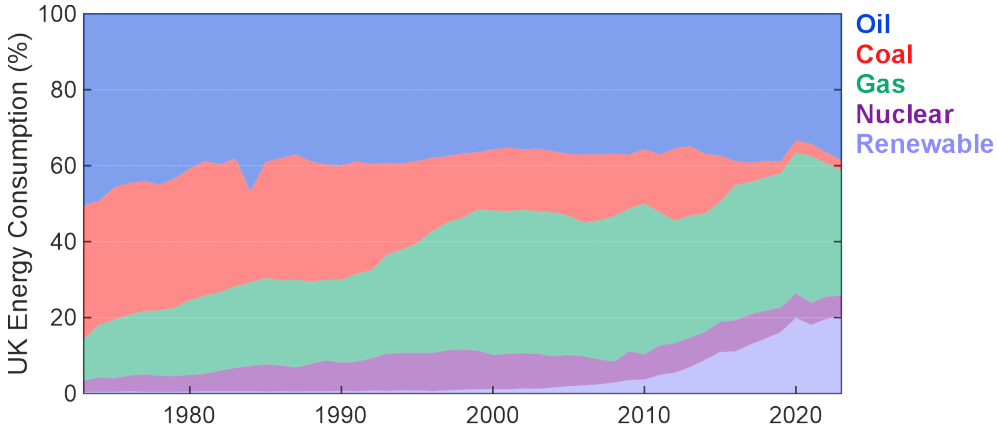

Figure 1.1: Energy consumption by source in the United Kingdom, over the last fifty years.[3]

benefits but also for their capacity to enhance energy independence, stabilise markets, and strengthen economic and geopolitical resilience over the long term.

These shifts are already visible in national energy landscapes. In the UK, for instance, the share of renewable energy has risen significantly over the last decade. As shown in Figure 1.1, the contribution of renewables to the national energy mix has grown from less than 5% in 2010 to around 20% in recent years. This increase has come largely at the expense of coal, while consumption of oil and natural gas has remained largely steady, highlighting that, while progress has been made towards cleaner sources, more work is still urgently needed.

The global shift to renewables also presents a profound economic opportunity. The clean energy sector is now generating millions of jobs across industries such as solar installation, wind turbine management, battery manufacturing, green construction, and hydrogen production. Technological progress continues to lower costs: solar power, for instance, is now the cheapest electricity source in history.[4] Renewable energy is no longer just a moral imperative; it is an economic inevitability.

1.1 The Case for Solar Renewable Energy

Among renewable energy technologies, solar power stands out as one of the most abundant and widely accessible.[5–7] Every hour, the Earth receives more energy from the sun than the entire human population consumes in a year. Capturing even a fraction of this energy could meet global energy needs while drastically reducing carbon emissions. Solar power offers additional strategic advantages: it is silent, modular, and can be deployed in remote or off-grid areas. This potential to decentralise energy production makes solar energy technology particularly appealing

for building sustainable, resilient infrastructure. Its modular nature allows for flexible deployment options, from small-scale residential rooftop installations to large utility-scale solar farms, making it accessible to diverse communities and markets. As solar technologies have matured, ongoing improvements in efficiency and manufacturing have made solar electricity increasingly competitive.

Silicon remains the dominant material in commercial solar technology. Its widespread success stems from abundant raw materials, high stability, and an optimised manufacturing process, enabling power conversion efficiencies (PCEs) approaching 27%,[8] close to the theoretical maximum of approximately $32-34\%$ for single-junction solar cells.[9] This limit, known as the Shockley-Queisser or detailed balance limit, is set by fundamental energy losses, including the inability to absorb all wavelengths of sunlight and the dissipation of excess photon energy as heat, which restrict how efficiently solar energy can be converted into electricity. Nonetheless, these attributes make silicon the cornerstone of utility-scale solar installations. Silicon-based solar cells, however, are not without drawbacks. Their fabrication requires high-temperature, energy-intensive processes, and large quantities of high-purity silicon that require environmental-damaging mining to obtain. The resulting devices are rigid and heavy, with typical modules weighing between 20 and $30\,\mathrm{kg\,m^{-2}}$.[10] This weight, combined with their rigid structure, limits their use in applications where flexibility, low weight, or surface conformity are essential, such as lightweight rooftops, curved surfaces, or portable devices.

Next-generation photovoltaic technologies aim to address these limitations by offering new materials with greater adaptability and novel physical properties.[12] The development in efficiency of some of these materials is illustrated in Figure 1.2.[11,13]

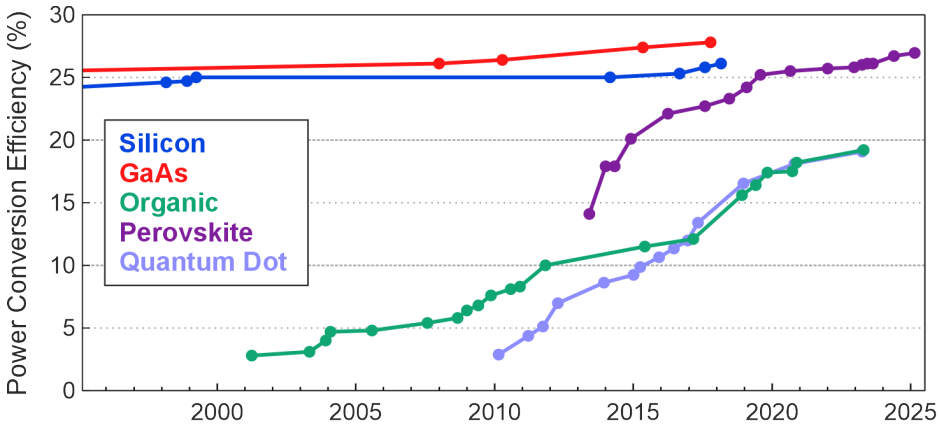

Figure 1.2: Improvements in certified power conversion efficiencies of various single-junction photovoltaic technologies over the past three decades, highlighting advances in silicon, gallium arsenide (GaAs), organic photovoltaics, perovskites, and quantum dot solar cells.[11]

Gallium arsenide (GaAs), for example, has achieved record PCEs of 28% and excels in high-performance applications like satellites, but its high cost restricts broader use. Metal halide perovskites, reaching over 26% efficiency in lab-built devices, offer impressive performance with simple processing, but suffer from long-term stability and toxicity of lead-based components. Quantum dot solar cells and other emerging technologies provide benefits such as infrared absorption, but are still under development.

Among emerging photovoltaic technologies, organic photovoltaics (OPVs), composed of carbon-based organic semiconductors, offer advantages in flexibility, lightweight design, low-temperature fabrication, and ease of modification.[14–16] OPV materials are solution-processable, enabling scalable fabrication methods like roll-to-roll processing. In addition, organic semiconductors have a high absorption coefficient of about $10^5\,\mathrm{cm}^{-1}$, around two orders of magnitude higher than crystalline silicon.[17,18] This high absorption allows for the creation of thin, flexible films with weights around $0.5\,\mathrm{kg\,m}^{-2}$, requiring far smaller material quantities and making OPVs over 40 times lighter than conventional silicon panels. A film thickness of only 100 nm is sufficient to absorb up to 90% of incident light. The mechanical adaptability of OPVs makes them suitable for applications where weight constraints and surface conformity is critical, such as in portable electronics and building façades. Electronic and optical properties can be tuned via molecular design, allowing optimisation to specific lighting conditions like diffuse sunlight or indoor illumination. Their degree of transparency can be engineered, enabling semi-transparent devices that can be integrated into windows, for both aesthetic purposes and harvesting of energy from previously unusable surfaces. From a sustainability perspective, organic semiconductors can be synthesised from petrochemicals, offering a route to repurpose fossil fuels.[19] Increasing research is directed towards the development of greener synthetic routes and more environmentally benign materials to improve the sustainability of the organic materials.[20]

OPVs are best seen as a complementary technology to silicon and other next-generation photovoltaics, extending photovoltaic applications to contexts where lightweight design, structural flexibility, or adjustable properties are required.[21] Although certified efficiencies and lifetimes remain lower than those of silicon, continued advances in materials and device design are closing the gap. A recent OPV device exceeded 20% PCE in the lab,[22] and with commercial products already emerging from start-ups, real-world deployment is steadily advancing.

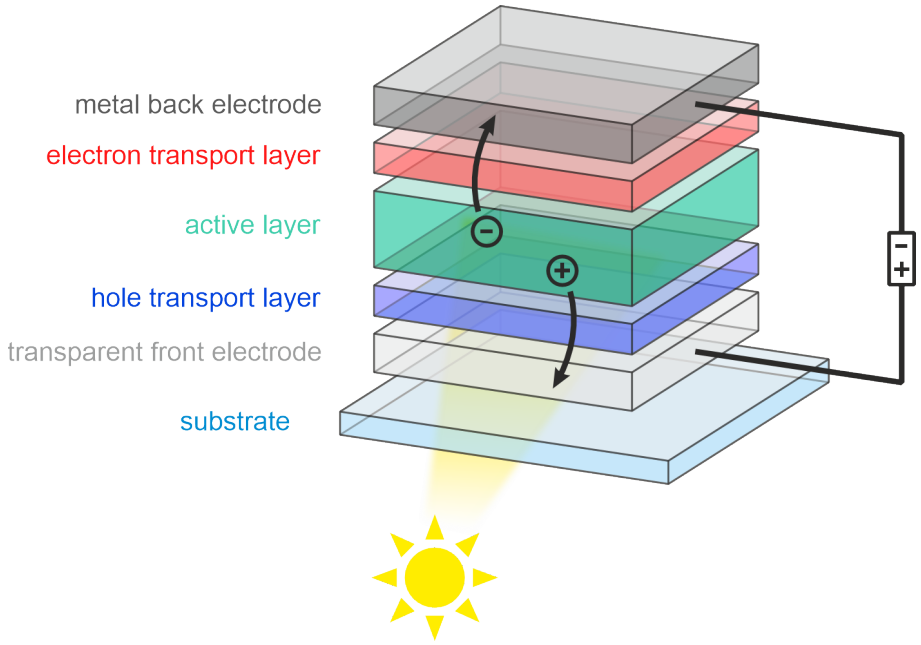

Figure 1.3: Schematic illustration of the typical structure of an organic photovoltaic device: the transparent front electrode, hole transport layer, active layer, electron transport layer, and metal back electrode, on top of a substrate.

1.2 Organic Photovoltaic Devices

OPV devices typically consist of five functional layers, displayed in Figure 1.3: a transparent front electrode, a hole transport layer, an active layer consisting of a blend of organic donor and acceptor molecules, an electron transport layer, and a metal back electrode. Sunlight is absorbed in the active layer and converted into electrical charges, which are then transported through the electron and hole transport layers to their respective electrodes for extraction and delivery to an external circuit.

The transparent front electrode, most commonly indium tin oxide, serves a dual role: it allows light to enter the device while efficiently conducting holes to the external circuit. To perform these roles effectively, it must exhibit both high optical transparency and excellent electrical conductivity. Above this lies the hole transport layer, which selectively transports holes towards the electrode while blocking electrons. Effective hole transport layers possess high hole mobility, suitable energy-level alignment with the donor material in the active layer, and morphological stability under operating conditions. Mirroring this on the opposite side of the device, the electron transport layer extracts and transports electrons to the electrode while blocking holes. Materials used in this layer must exhibit high electron mobility and appropriate energy level alignment with the acceptor material in the active layer. The back metal electrode, often silver or aluminium,

collects electrons and closes the circuit, providing a low-resistance, stable contact with the electron transport layer.

The active layer, positioned at the heart of the OPV device, is responsible for absorbing photons and generating charges. It consists of a blend of electron donor and electron acceptor organic semiconducting materials. When photons are absorbed by these materials, they create *excitons*: neutral excited states consisting of a bound electron-hole pair. In inorganic semiconductors, these excitons are weakly-bound: silicon excitons have a binding energy of around 15 meV,[23,24] which is less than the thermal energy at room temperature ($k_{\mathrm{B}}T \approx 26\,\mathrm{meV}$), allowing spontaneous dissociation of the electron-hole pair. In contrast, excitons in organic semiconductors are strongly-bound, with binding energies of $0.1 - 0.4\,\mathrm{eV}$,[25–27] due to the low dielectric constants of organic semiconducting materials, which screens the electrostatic Coulomb attraction poorly. As a result, excitons in organic materials do not readily dissociate on their own and must instead diffuse to a donor:acceptor interface, where dissociation via charge transfer becomes energetically favourable.[28]

Because exciton dissociation in organic semiconductors requires access to a donor:acceptor interface, early OPV devices were designed using the **planar heterojunction** architecture,[29] in which separate donor and acceptor layers are stacked to create a defined interface for charge separation. While this geometry ensures controlled interfacial charge transfer, the limited interface area is poorly matched to the short *exciton diffusion length*: the average distance an exciton can travel before decaying. In organic materials, exciton diffusion lengths are typically only $10 - 40\,\mathrm{nm}$,[30–32] compared to active layer thicknesses of around $100\,\mathrm{nm}$.[33,34] As a result, many excitons decay before reaching the interface, significantly limiting efficiency. To overcome this limitation, the **bulk heterojunction** (BHJ) architecture was introduced, in which donor and acceptor materials are blended into a nanoscale interpenetrating network, shown schematically in Figure 1.4.

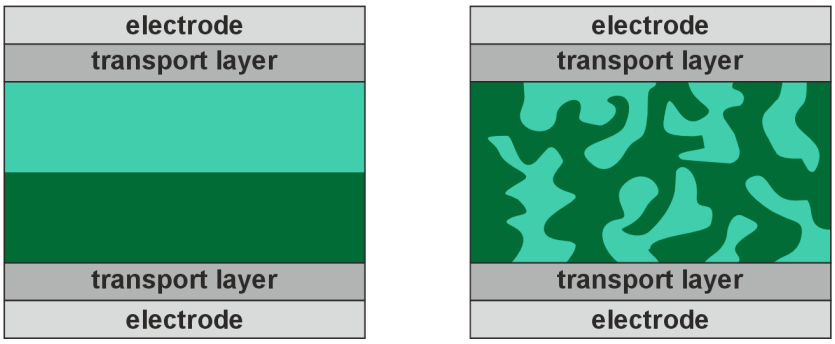

Figure 1.4: Active layer morphologies for a planar heterojunction (left) and a bulk heterojunction (right).

This increases the interfacial area throughout the film, improving the probability that excitons encounter an interface within their lifetime. However, this comes with a trade-off: while a high interfacial area promotes exciton dissociation, efficient charge transport requires relatively pure, phase-separated domains.[35] If domains are too small or overly mixed, charges may become trapped or recombine at interfaces; if too large, excitons may decay before reaching a donor:acceptor interface. As a result, optimal performance is achieved with domain sizes of around 20 nm in average diameter.[36]

More advanced architectures continue to explore ways of optimising the active layer composition. Strategies such as ternary blends (introducing a third component to control morphology, absorption, or charge transport)[37] and vertical composition gradients (varying the donor and acceptor concentration across the active layer)[38] aim to improve performance by manipulating the morphology and energetics of donor and acceptor materials within the active layer.

1.3 Donor and Acceptor Molecular Design

The performance of OPVs is fundamentally determined by the properties of the donor and acceptor materials that make up the active layer. These molecules must not only absorb light efficiently but also facilitate charge transfer and separation, support high charge mobility, and organise into a favourable morphology. Molecular design strategies are therefore essential, and involve the tuning of energy levels to optimise bandgaps and the engineering of side chains to control phase separation, molecular conjugation and bulk morphology.[36,39,40]

The current best-performing solution-processed OPVs typically employ polymer donors combined with small molecule acceptors. This combination leverages the distinct morphological tendencies of each component: polymer donors generally form continuous networks that facilitate hole transport and support the formation of an optimised bulk heterojunction,[41,42] while small molecule acceptors tend to crystallise into well-ordered domains that promote high electron mobility.[43] When optimally blended, these materials create an interpenetrating bulk heterojunction with balanced phase separation and abundant donor:acceptor interfaces for efficient exciton dissociation. Controlling the morphology of systems based entirely on polymers or small molecules is more challenging. All-polymer blends may phase-separate excessively or mix too intimately, while small molecule blends may crystallise too strongly or fail to form continuous transport networks.[44] However, ongoing advances continue to improve morphological control in these systems.[44,45] In this thesis, two polymer donors, PBDB-T and PM6, and three small-molecule

acceptors, PCBM, ITIC, and Y6, are studied, with molecular structures displayed in Figure 1.5.*

The first significant advances in OPV efficiency came from systems combining conjugated polymer donors with **fullerene acceptors**: a class of molecules featuring the characteristic C_{60} buckyball cage structure, like PCBM.[43,50] Through mainly optimisation of polymer donor design, power conversion efficiencies steadily increased from under 3% to over 10% over a decade, as shown in Figure 1.6. Initial polymers featured simple conjugated backbones, which was followed by the development of polymers incorporating alternating electron-rich and electron-poor units along the backbone, like in the structures of PBDB-T and PM6. This internal donor:acceptor architecture enhances intramolecular charge transfer and backbone planarity, promoting $\pi - \pi$ stacking: non-covalent interactions of aromatic rings on different polymer chains. These interactions facilitate self-assembly into ordered domains that support efficient charge transport.[39,51,52] Furthermore, the design of solubilising side chains helped tune polymer solubility, control nanoscale morphology, and optimise compatibility with fullerene acceptors, enabling well-controlled phase separation and morphology essential for efficient charge separation and transport. The deep HOMO (highest occupied molecular orbital) and LUMO (lowest unoccupied molecular orbital) levels of the fullerene acceptor provide a sufficient energetic offset from the polymer donor levels to drive exciton dissociation and charge transfer,[53] as illustrated in Figure 1.6. In addition, the spherical nature of the fullerene cage enables good miscibility with a variety of donor polymers,[50] resulting in nanoscale phase-separated blends with minimal structural constraints. Once solubilised via side-chain functionalisation, fullerene acceptors like PCBM can be easily processed from solution, helping to standardise device fabrication.

Despite their early success, fullerene acceptors exhibit inherent limitations that ultimately restricted further improvements in OPV performance. One major drawback is their poor absorption in the visible region, as shown in the absorption spectra in Figure 1.7. PCBM absorbs mainly in the ultraviolet range, where solar irradiance, after atmospheric filtering, is relatively low,[54] leaving most of the light harvesting to be performed by the donor polymer. The rigid fullerene core limits

*The nomenclature of donor and acceptor molecules in OPVs generally does not follow a strict convention; instead, abbreviated names or shorthand nicknames are typically used to highlight features of their chemical structures. For example, PBDB-T can be parsed as P = polymer, BDB = benzodithiophene backbone, and T = thiophene. PCBM corresponds to P = phenyl, C = C_{60} fullerene, B = butyric acid, and M = methyl ester. ITIC derives from I = indacenodithieno[3,2-b]thiophene (core unit), T = thiophene, and IC = indanone functionalised with cyano groups (end group). In contrast, PM6 and Y6 are not acronyms of their structures but designations assigned by the research group that developed them.[46] For instance, Y6 is part of a series of related molecules, with Y5 and Y7 differing only in the substitution of the fluorine atoms with hydrogen and chlorine, respectively.

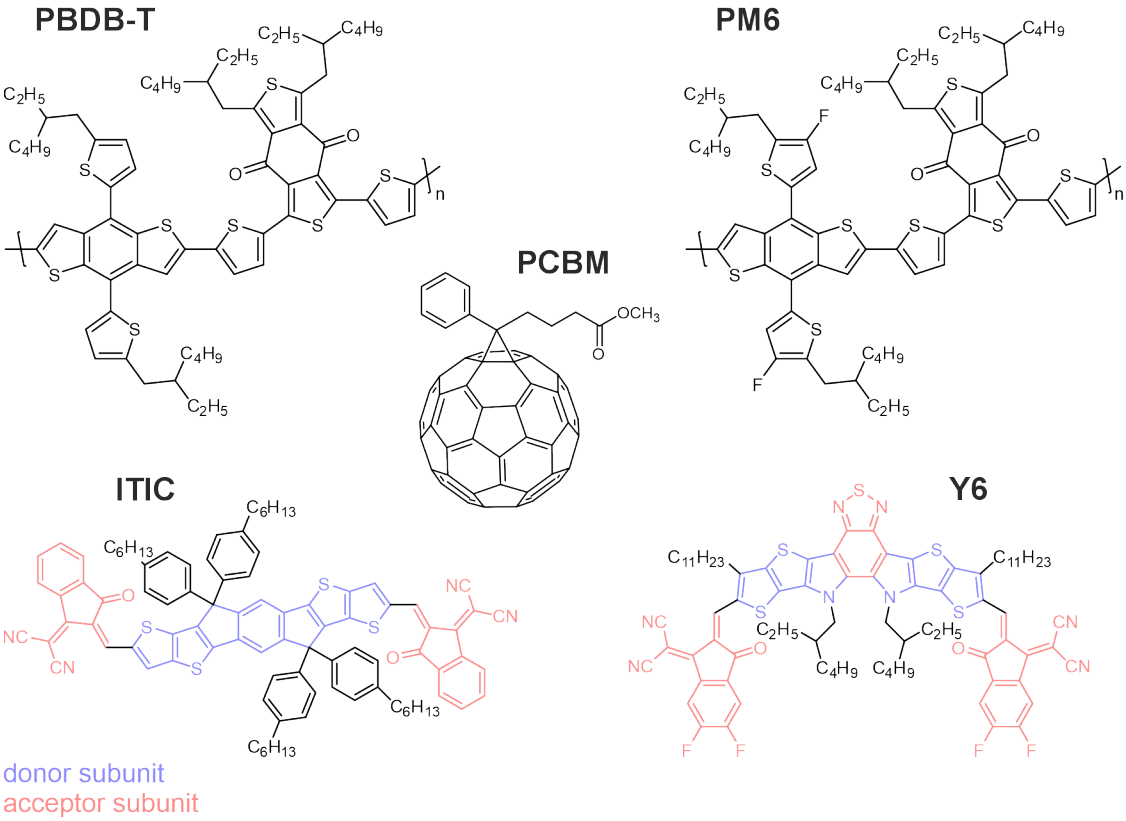

Figure 1.5: Structures of the donor and acceptor molecules examined in this thesis. Donor polymers PBDB-T and PM6, fullerene acceptor PCBM, and non-fullerene acceptors ITIC and Y6. For ITIC and Y6, donor and acceptor subunits are highlighted in blue and red, respectively.

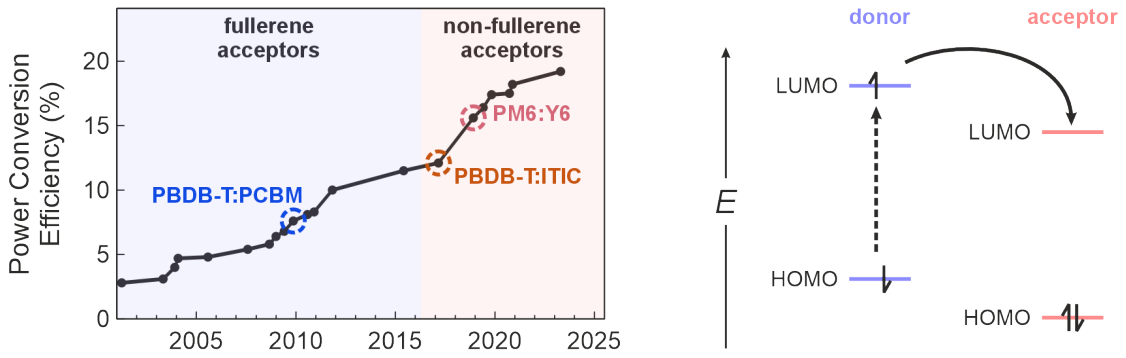

Figure 1.6: Left) Power conversion efficiency improvement of organic photovoltaics over the last 25 years. In the last decade, blends with non-fullerene acceptors have surpassed efficiencies of fullerene acceptor blends. Power conversion efficiencies of PBDB-T:PCBM,[47,48] PBDB-T:ITIC,[49] and PM6:Y6[46] are highlighted. Right) Schematic energy level alignment of donor and acceptor molecules, illustrating charge transfer at the donor:acceptor interface after photoexcitation. Excitation on the donor molecule, as shown, leads to electron transfer, while excitation of the acceptor molecule is followed by hole transfer.

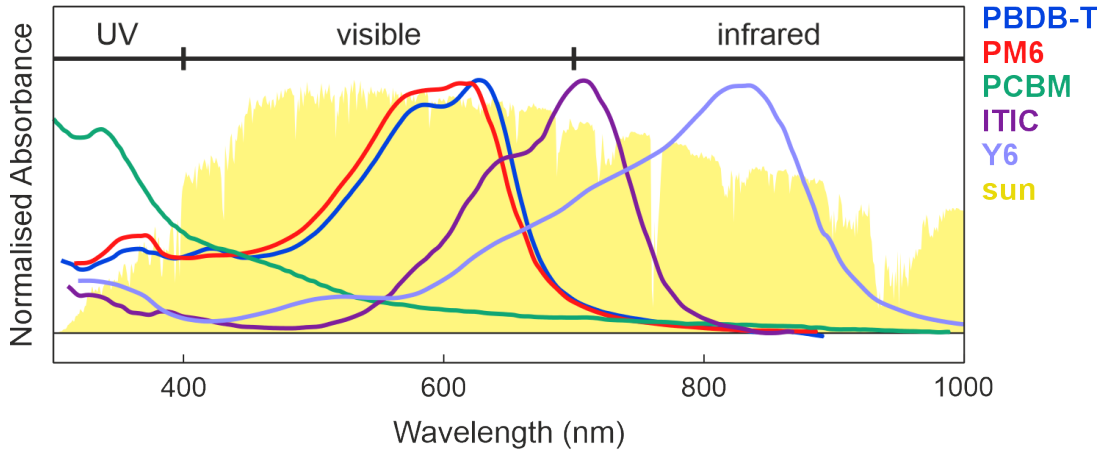

Figure 1.7: Absorption spectra of polymer donors PBDB-T and PM6, fullerene acceptor PCBM, and non-fullerene acceptors ITIC and Y6, compared with the solar spectrum (AM1.5 solar spectral irradiance taking into account the influence of the atmosphere).[46,54,57,58] While PCBM absorbs poorly across the visible range, for ITIC and Y6 absorption extends into the near-infrared, complementing the donor polymer absorption spectrum.

chemical modification, restricting the ability to tune the electronic properties and absorption profiles of these fullerene molecules. Additionally, fullerene acceptors tend to crystallise into relatively large domains,[55] which can disrupt the nanoscale bicontinuous morphology required for efficient exciton dissociation and charge transport.[56] These challenges have motivated the search for alternative electron acceptors capable of overcoming these fundamental limitations.

A major breakthrough in OPV performance came with the development of electron acceptors based on a planar, fused-ring backbone architecture. These molecules featured an acceptor-donor-acceptor (A-D-A) subunit motif, enabling strong intramolecular charge-transfer character, extended conjugation, and straightforward chemical tunability via modification of end groups and side chains.[55] Their architecture allows more precise control over energy levels, absorption profiles, and solid-state packing, marking a sharp departure from the limitations imposed by fullerene acceptors. As they did not share the characteristic fullerene cage structure, this new class became known as **non-fullerene acceptors**.

One of the earliest non-fullerene acceptors was ITIC, which exhibits strong absorption in the visible and near-infrared regions where polymer donors like PBDB-T absorb relatively weakly. This complementary absorption is illustrated in Figure 1.7, where ITIC fills spectral gaps left by PBDB-T, enhancing the light-harvesting capability of the blend.[58] The PBDB-T:ITIC blend was the first to surpass the efficiencies of fullerene-based OPVs, achieving power conversion efficiencies above 11%.[49]

Beyond enhanced absorption, non-fullerene acceptor blends demonstrate efficient charge generation with significantly smaller energetic offsets between the donor and acceptor energy levels. It had previously been believed that an offset of at least 0.3 eV was necessary to overcome exciton binding energy and enable charge separation in organic materials.[59] However, this offset corresponds to around $10-20\%$ of the HOMO-LUMO gap and represents energy that is unavoidably lost as heat. In contrast, non-fullerene acceptor blends such as PBDB-T:ITIC demonstrated that efficient exciton dissociation was still possible at lower energetic offsets, provided the non-fullerene acceptor excitons had sufficiently long lifetimes enabling diffusion lengths on the order of $25-35$ nm, compared to just 10 nm for polymer donors and fullerene acceptors.[30–32] Longer diffusion lengths increase the likelihood that excitons will reach a donor:acceptor interface before recombining, thereby compensating for the reduced energetic driving force for exciton dissociation

This principle of minimising energetic losses reached its peak with the development of the Y-series non-fullerene acceptors, exemplified by the prototypical Y6 molecule. Despite a remarkably small HOMO-HOMO offset of just 0.09 eV with the polymer donor PM6 (a fluorinated derivative of PBDB-T), power conversion efficiencies exceeding 17% were achieved.[46] The Y6 absorption spectrum is shifted strongly into the near-infrared, complementing the PM6 absorption spectrum and enabling broader light harvesting, while fluorination of PM6 improved energy level alignment with Y6, minimising energy loss. Y6 extends the internal A-D-A structure of ITIC to an A-D-A-D-A motif, enabling improved control over molecular planarity and aggregation, and supporting $\pi-\pi$ stacking and ordered packing.[39,52] The resulting blend morphology supports long-range exciton diffusion and optimal phase separation, enabling efficient charge generation even in the absence of a large energetic offset.

This evolution, from early fullerene acceptor blends to high-performance non-fullerene acceptor blends, has shaped the OPV landscape. Although device efficiencies continue to improve, detailed insights into the photophysical processes that govern efficient charge generation and extraction often lag behind material innovations.[60] In particular, non-fullerene acceptor blends operate via mechanisms that differ in subtle yet significant ways from those of fullerene acceptor blend, challenging established concepts of energy alignment and charge dynamics. Developing a deeper mechanistic understanding is essential for guiding further performance improvements.

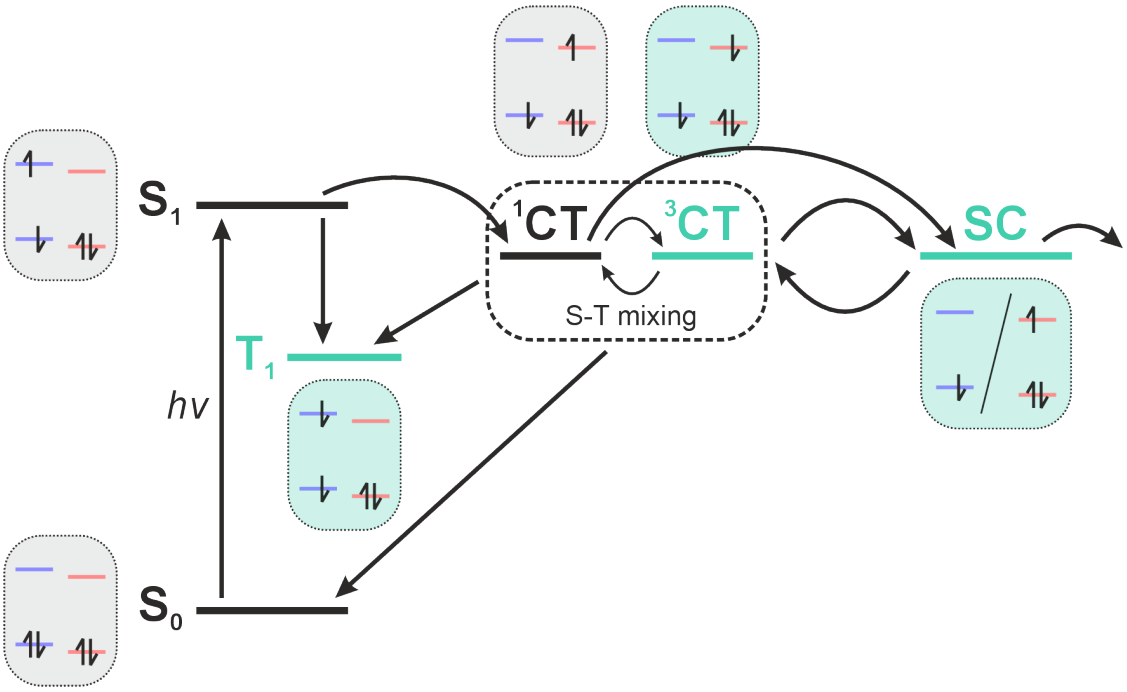

Figure 1.8: Schematic diagram of the photophysical mechanism of light to charge conversion in the active layer of organic photovoltaic devices, as described in the text. Electronic configurations are shown alongside each state, assuming photoexcitation of the donor molecule followed by electron transfer. Photoexcitation of the acceptor followed by hole transfer or energy transfer followed by charge transfer are also possible. The charge-transfer (CT) state, separated charges (SCs) and triplet state (T_1), highlighted in green, all contain unpaired electrons, and so can be selectively probed by electron paramagnetic resonance (EPR) spectroscopy.

1.4 Conversion of Light to Electricity

The conversion of absorbed photons into extractable electrical current in OPVs involves a sequence of photophysical processes occurring within the active layer. These include the generation of singlet excitons (S_1) from the ground state (S_0), formation of charge-transfer (CT) states, dissociation into separated charges (SCs), and charge transport to the electrodes. Several loss pathways can compete with efficient charge extraction, including a variety of recombination mechanisms and formation of lower-energy triplet excitons (T_1). A schematic overview of these steps is provided in Figure 1.8, which serves as a roadmap for the detailed discussion that follows.

Many of the states central to OPV function, namely the CT state, SCs, and T_1, are paramagnetic, meaning they contain unpaired electrons. These spin-bearing species can be selectively probed by electron paramagnetic resonance (EPR) spectroscopy, a technique that provides molecular-level information on the properties, molecular environment, and dynamics of paramagnetic states. While a

more thorough treatment of spin physics in the context of EPR characterisation of OPVs will be presented in the next chapter, it is helpful here to note that spin conservation rules influence many of the photophysical transitions relevant to OPVs. The paramagnetic states involved in the photovoltaic mechanism that can be characterised by EPR are highlighted in green in Figure 1.8.

Each stage of the charge generation sequence plays a critical role in determining photovoltaic performance (with typical timescales for the different processes at room temperature):[61]

1. $S_0 \rightarrow S_1$: Absorption of photons generates singlet excitons on the donor or acceptor molecules (femtoseconds).
2. $S_1 \rightarrow {}^1CT$: Electron or hole transfer at donor:acceptor interfaces forms CT states initially in a singlet spin configuration (picoseconds).
3. ${}^1CT \leftrightarrow {}^3CT$: Spin mixing converts singlet CT states into triplet CT states (nanoseconds to microseconds).
4. ${}^1CT, {}^3CT \rightarrow SC$: Charge separation from the CT state produces SCs, to be extracted at the electrodes (picoseconds to microseconds).

Efficiency-limiting loss pathways include:

- $CT \rightarrow S_0, T_1$: direct recombination of CT states before charge separation, referred to as geminate recombination (picoseconds to nanoseconds).
- $SC \rightarrow CT \rightarrow S_0, T_1$: free charges re-encounter to form CT states, which then decay, referred to as non-geminate recombination (microseconds).
- $S_1 \rightarrow T_1$: Intersystem crossing - conversion of singlet excitons to long-lived triplet excitons, which act as energetic traps (nanoseconds to microseconds).

1.4.1 Exciton Formation

The first stage of the photovoltaic process in any OPV device is the absorption of light by molecules in the active layer, where photons with energies equal to or greater than the HOMO-LUMO gap excite an electron from the HOMO to the LUMO, creating an exciton. Excitation can occur either in the donor or acceptor, depending on the absorbed wavelength. Both the ground state (S_0) and the exciton (S_1) are in a singlet spin configuration, meaning the two electron spins are antiparallel to one another. The electron and hole on the exciton are strongly-bound, due to the poor screening of their Coulomb attraction by organic materials of low dielectric constants. As a result, exciton binding energies are large, between 0.1 and 0.4 eV.[25–27]

The high binding energy constrains exciton lifetime and diffusion length since excitons can rapidly decay radiatively or non-radiatively if they are unable to

dissociate. Consequently, exciton diffusion lengths are generally short, around 10 nm in fullerene acceptor blends. This short diffusion length imposes an upper bound on the donor and acceptor domain sizes, typically limiting fullerene-based domains to no larger than 20 nm in diameter, to ensure excitons reach an interface before decaying.[31]

In fullerene blends, the energetic driving force for charge transfer, the energy difference between the S_1 and the CT state, is relatively large. This results in ultrafast exciton dissociation at the donor:acceptor interface, occurring on sub-picosecond timescales, which compensates for the limited exciton diffusion length.[60] Non-fullerene acceptor blends differ significantly. The S_1-CT state energy difference is smaller, with charge transfer occurring over $10-1000$ ps.[60] To maintain efficient charge generation despite this slower dissociation, non-fullerene acceptor blends exhibit longer exciton lifetimes, and consequently, longer diffusion lengths. This extended diffusion allows excitons to travel further to reach interfaces, allowing the morphologies of larger, purer domains, up to 50 nm in size, within the blend.[31] These larger domains exhibit superior exciton transport properties, including faster diffusion rates and efficient long-range energy transfer.[62]

1.4.2 Interfacial Charge Transfer

Once an exciton reaches the donor:acceptor interface, charge transfer occurs via electron movement across the interface. If the exciton originates in the donor, the electron is transferred from the donor LUMO to the acceptor LUMO, referred to as **electron transfer**. If the exciton originates in the acceptor, the electron is transferred from the donor HOMO to fill the hole in the acceptor HOMO, described as **hole transfer**. In both cases, an electron is transferred, but the terminology reflects the location of the initial excitation, and the result is the formation of a *charge-transfer (CT) state*: a weakly-bound electron-hole pair with charges localised on separate molecules. The CT state initially forms in a singlet spin configuration because the exciton was a singlet, and during the charge transfer, spin angular momentum is conserved. However, the CT state may undergo spin mixing, interconverting between CT states of singlet and triplet spin configurations, a process discussed in more detail in Section 2.4.2 of the following chapter. This spin mixing influences recombination pathways: singlet CT states recombine directly to the electronic ground state (S_0), whereas triplet CT states recombine to form triplet excitons (T_1).

In fullerene acceptor blends, the polymer donor typically dominates light absorption (see the absorption spectrum in Figure 1.7). As a result, charge transfer at the interface primarily proceeds via electron transfer from the donor to the fullerene

acceptor. This process is driven by a relatively large LUMO-LUMO energetic offset, and therefore a large $S_1 \rightarrow$ CT energy difference.[43] While this offset enables ultrafast charge transfer, it also causes substantial energy loss, dissipated as heat.[63]

Non-fullerene acceptor blends, in contrast, absorb light on both donor and acceptor molecules due to their complementary absorption profiles. When the acceptor absorbs light (typically in the near-infrared), the resulting exciton dissociates via hole transfer to the donor. Alternatively, when the donor absorbs light (in the visible range), exciton dissociation often occurs via an intermediate step: Förster resonance energy transfer (FRET).[64,65] FRET is a long-range, non-radiative process, where energy is transferred from an excited donor to an acceptor, generating a new exciton on the acceptor (illustrated in Figure 1.9). Because FRET can occur over distances of up to 10 nm,[65] it effectively extends the exciton diffusion length by funnelling excitons from donor domains towards the donor:acceptor interface, increasing the probability of successful charge transfer. A key requirement for FRET is spectral overlap between the donor's emission and the acceptor's absorption spectra (see Figure 1.7). This overlap in non-fullerene acceptor blends is enabled by the Stokes shift, which arises because emission occurs from the lowest vibrational level of S_1 to higher vibrational levels of S_0, while absorption starts from the lowest vibrational level of S_0 to higher vibrational levels of S_1. As a result, the emitted photon has lower energy (longer wavelength) than the absorbed one, causing a red-shift in the emission spectrum. This red-shift creates the necessary spectral overlap that enables efficient FRET between the polymer donor and non-fullerene acceptor. In non-fullerene acceptor blends, the HOMO-HOMO offset (the driving force for hole transfer) is considerably narrower than the LUMO-LUMO offset (the driving force for electron transfer).[66,67] As hole transfer in the non-fullerene acceptors dominates,

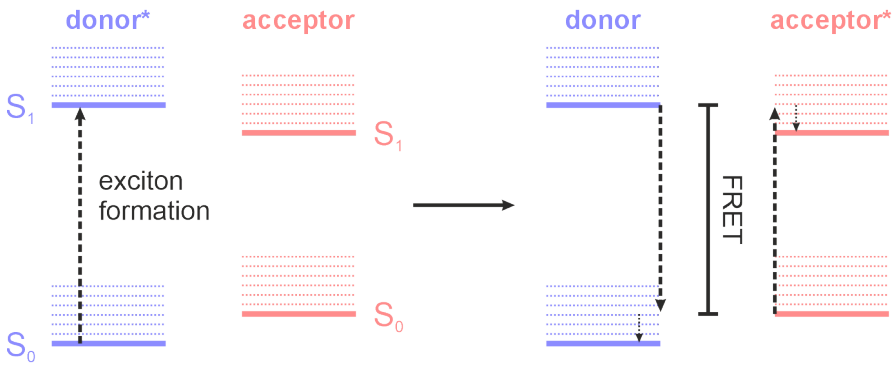

Figure 1.9: Schematic of the Förster Resonance Energy Transfer (FRET) mechanism. After exciton formation, energy may be transferred from the higher energy donor exciton to the lower energy acceptor exciton, provided that there is overlap of the donor emission and acceptor absorption spectra. Upon FRET, the system will often be in higher vibrational levels (shown as dotted lines); this will be followed by ultrafast vibrational relaxation.

the smaller energetic offset reduces energy loss during charge generation.[68,69] By contrast, fullerene acceptors like PCBM exhibit low oscillator strengths, meaning they absorb and emit light weakly, limiting the efficiency of FRET in those systems.[68]

1.4.3 Charge Separation and Transport

Once charge transfer has occurred at the donor:acceptor interface, forming a Coulombically bound CT state, the next key step is the separation of this electron-hole pair into free charges that can be collected at the electrodes. This process must overcome the residual attraction that still exists between the electron and hole.[70,71] For typical relative dielectric constants of $2-4$ for organic semiconducting materials,[72] the Coulomb attraction between an electron and a hole remains stronger than the thermal energy at room temperature up to separations of $14-28\,\mathrm{nm}$. Efficient charge separation is essential to prevent recombination of the CT state and enable long-range charge transport. Once free, charges must traverse the donor and acceptor domains towards their respective electrodes, a journey that is strongly influenced by the local morphology, energetic landscape, and material properties.

In fullerene acceptor blends, interfacial CT state binding energies have been measured in the range of $0.2-0.3\,\mathrm{eV}$,[73] far exceeding room temperature thermal energy ($26\,\mathrm{meV}$). Consequently, charge separation in these blends is assumed to proceed predominantly via a thermally-activated pathway. The efficiency of charge separation increases steeply with temperature, indicating the presence of a substantial activation barrier to free-charge formation.[74,75]

Non-fullerene acceptor blends such as PM6:Y6, meanwhile, exhibit CT state binding energies around $0.1\,\mathrm{eV}$,[76] still larger than the thermal energy, yet demonstrate near barrier-less, ultrafast charge separation that is largely independent of excitation energy or temperature.[77] To rationalise this discrepancy, several mechanisms have been proposed in the literature, although none have been definitively established. Non-fullerene acceptors possess large quadrupole moments: non-uniform, often axial, charge distributions that generate an internal electrostatic potential. If these quadrupoles are aligned along the $\pi-\pi$ stacking direction, they can generate an internal electrostatic potential that stabilises the LUMO (and HOMO) acceptor energies of the bulk relative to the interface.[78–80] The result, illustrated in Figure 1.10, would be a cascaded electrostatic landscape that creates an energetic funnel driving electrons away from the interface, thereby reducing the effective Coulomb barrier to separation.

Charge separation may also be facilitated by morphological disorder of the non-fullerene acceptor domains close to the interface, providing an entropic driving force for charge separation. It has been proposed that there is a low density of well-ordered

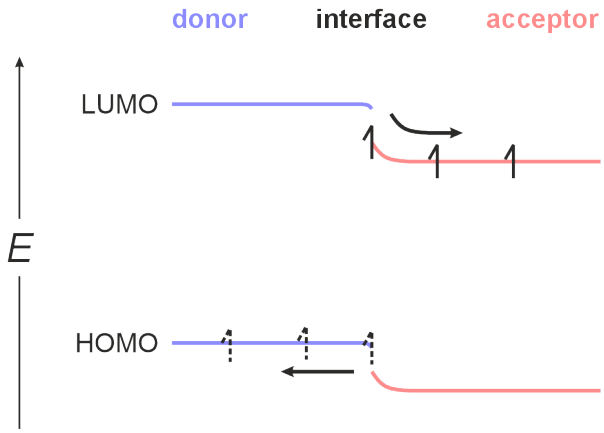

Figure 1.10: Schematic representation of the energetic landscape at the donor:acceptor interface in a non-fullerene acceptor blend. The large quadrupole moment of non-fullerene acceptors induces significant band-bending by lowering the HOMO and LUMO energies within the acceptor domain relative to the interface. This creates an energetic cascade that facilitates spontaneous separation of electrons.[78–80] Band-bending is less pronounced for the polymer donor, which has a much smaller quadrupole moment. Electrons are illustrated as solid arrows, and holes as dashed arrows.

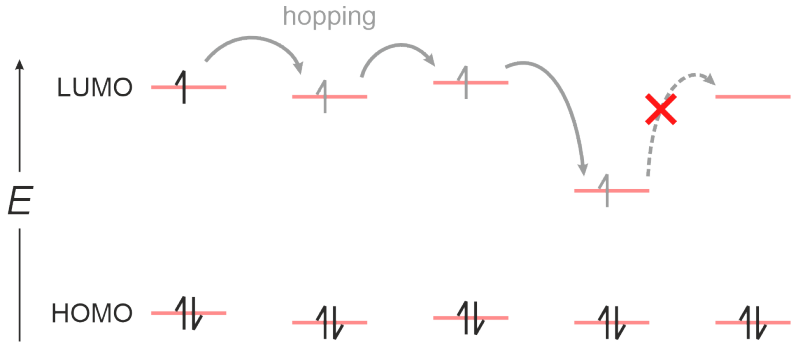

Figure 1.11: Trapping of free charges during charge transport, due to low-lying localised trap sites. Thermal energy is required for charges to escape the trap site and rejoin the transport pathway. Electron trapping in acceptor molecules is shown here, an equivalent mechanism would occur in the HOMOs for hole trapping in donor molecules.

CT states,[81] and upon separation, the many more possible free charge configurations corresponds to an entropy gain. This gain in configurational entropy could help offset any residual binding energy (predicted to be in the range $10 - 20\,\text{meV}$).[82] Charge delocalisation has also been widely suggested as a pathway to overcoming the CT state binding energy.[70,83–87] Spreading the electron or hole wavefunction over multiple molecules increases the average electron-hole separation, lowering the Coulomb attraction. Studies of Y6 aggregates suggest that $\pi - \pi$ stacking supports delocalisation across multiple acceptor molecules, further weakening interfacial Coulomb binding.[86,88] Developing a unified model that reconciles these proposals with experimental observations remains an open challenge in OPV research.

Once separated, charges must migrate through their respective domains to reach the electrodes. Charge transport in organic semiconductors primarily occurs via a series of thermally-activated hops through a density of states whose energetic distribution reflects the varied local molecular environments.[89] Electrons hop between LUMOs (the electron transport level) and holes between HOMOs (the hole transport level) of different molecules. This energetic disorder gives rise to *trap sites*: localised transport energy levels, created by structural inhomogeneities or chemical defects,[90,91] which can temporarily or indefinitely capture a free charge and impede its progress until thermal energy liberates it, as illustrated in Figure 1.11. The hopping rate between any two sites depends intrinsically on the electronic coupling (wavefunction overlap) of adjacent molecules,[92] so tight $\pi - \pi$ stacking can enhance transport by maximising intermolecular orbital overlap.[93] Domain purity and well-connected transport networks are equally crucial: purer domains reduce the density of trap sites, while crystalline regions promote long-range charge mobility.[94,95]

1.4.4 Charge Recombination

While thermally-activated hopping sustains charge transport, electrons and holes can still encounter one another before extraction. When they reunite, usually at a donor:acceptor interface, they reform a bound CT state that can recombine and relax back to the ground state, dissipating useful energy as heat or radiation. This charge recombination directly reduces photocurrent and device efficiency, so minimising it is paramount. Recombination proceeds via two principal routes:[96]

- **Geminate recombination**: A CT state formed from a singlet exciton fails to fully separate and the pair instead recombines.
- **Non-geminate recombination**: Electrons and holes generated from different CT states meet by diffusion or drift and form a CT state before recombining. Non-geminate recombination can proceed via two primary pathways, shown in Figure 1.12:
  - Langevin (bimolecular) recombination, in which two mobile charges of opposite sign directly recombine via CT state formation.
  - Trap-assisted (monomolecular) recombination, where a free charge is first captured by a localised defect and subsequently recombines with a charge of opposite sign.

In geminate recombination, an electron-hole pair recombines from the interfacial CT state before full separation occurs. Since the charges originate from the same exciton, they remain correlated and are more likely to recombine if the CT state does not rapidly dissociate. While this process can result in non-radiative decay to

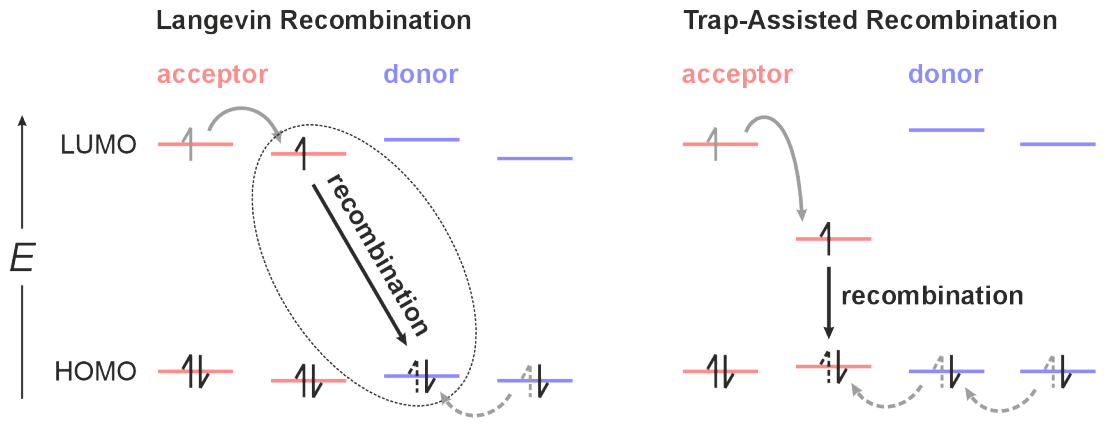

Figure 1.12: Schematic of the non-geminate recombination pathways: Langevin recombination and trap-assisted recombination. Langevin recombination reforms a charge-transfer state before decay to the ground state, while trap-assisted recombination involves a mobile charge encountering a charge in a trap site.

the ground state S_0, in high-efficiency blends like PM6:Y6, geminate recombination is typically minimal due to the rapid and efficient separation of CT states.[39]

In Langevin recombination, free electrons and holes hop through their respective donor and acceptor domains until they meet and recombine, via the reformation of a CT state. This CT state can then relax radiatively or non-radiatively to the ground state, resulting in energy loss.[39] The rate of Langevin recombination is proportional to the product of the charge mobilities and concentrations, and is therefore sensitive to molecular design and morphology. Yet, OPV materials almost always show recombination rates far below this prediction.[97,98] This suppression, referred to as reduced Langevin recombination, is particularly pronounced in non-fullerene acceptor blends and has previously been attributed to an equilibrium among three photoexcited states: the singlet exciton, the CT state, and mobile charges.[99–102] The small energetic offsets permit back-transfer of electrons returning to the singlet exciton from the CT state, enabling exciton regeneration rather than direct decay to S_0.[81] Moreover, theoretical studies have proposed a reversible equilibrium between CT states and separated charges.[99] If the rate of charge separation from the CT state outcompetes the rate of re-encounter of mobile charges, then the steady-state CT state population is lowered, slowing recombination to the ground state.[100] The slower rate of charge re-encounter may be facilitated by the large quadrupole moments of the non-fullerene acceptors.[62] As discussed before, the band-bending effect reduces the electron density near the donor:acceptor interface, decreasing the probability of interfacial charge re-encounter.[103]

In trap-assisted recombination, one charge, immobilised in a trap site, acts as a recombination partner for an opposite mobile charge. The presence of trap states therefore not only hinders charge transport by capturing free charges, but also

increases the likelihood of recombination by extending the charge lifetime and thus the probability of charge encounter. The rate of trap-assisted recombination is strongly dependent on defect density and the degree of energetic disorder within the active layer.[52,104,105]

1.4.5 Intersystem Crossing

Beyond recombination losses, intersystem crossing (ISC) into triplet excitons constitutes another efficiency bottleneck. In ISC, a photogenerated singlet exciton (S_1) is converted into a lower-energy triplet exciton (T_1).[106] Although formally spin-forbidden and typically slow, transitions between states of different spin configuration, like S_1 and T_1, can be facilitated by direct spin-orbit coupling or spin-orbit coupling introduced by mixing of electronic wavefunctions due to molecular vibrations,[107] explained in more detail in Section 2.4.3 of Chapter 2, allowing ISC to proceed on timescales of nanoseconds to microseconds.[108] ISC can compete with exciton dissociation if the photoexcited molecule is far from an interface.

Once formed, triplet excitons are typically long-lived: T_1 lies lower than S_1 and is energetically trapped. In organic semiconductors, this singlet-triplet energy gap can be large, often several hundred meV,[109] making the back-conversion from T_1 to S_1 (reverse intersystem crossing) unlikely. Triplet formation becomes particularly detrimental in donor:acceptor blends where T_1 lies below the CT state. In such cases, the CT state may recombine, in a geminate or non-geminate fashion, to T_1 instead of dissociating into free charges, especially when the driving force for separation is small. To mitigate triplet-related losses, materials design often aims to minimise the $S_1 - T_1$ gap, reduce ISC rates, or ensure that the CT state lies energetically below T_1, making triplet formation unfavourable.[110,111] In high-performance non-fullerene acceptor blends, triplet losses are generally suppressed due to favourable energy level alignment and fast and efficient CT dissociation.[112]

1.5 Current Challenges

Despite significant advances over the past decade, driven largely by the emergence of non-fullerene acceptors, OPVs still fall short of their theoretical Shockley-Queisser efficiency limit and remain less efficient and stable than conventional technologies such as silicon. For OPVs to contribute meaningfully to a low-carbon energy future, this performance gap must be closed. Achieving this will require more than incremental improvements in materials or device engineering; it demands a deeper, molecular-level understanding of the fundamental photophysical processes that govern device operation.

Several critical aspects remain poorly understood. These include the efficiency of exciton dissociation and charge separation, the formation and decay pathways of CT states, the influence of trap states and energetic disorder, and the role of spin-dependent losses such as triplet excitons and CT state recombination. Electron paramagnetic resonance (EPR) spectroscopy offers a powerful way to address these challenges. By directly detecting species with unpaired electron spins, such as CT states, separated charges, and triplet excitons, EPR can selectively probe the intermediates most relevant to charge generation and loss. Each of these states exhibits a distinct spectral signature, allowing them to be clearly identified and characterised.[113] EPR can reveal the extent of charge delocalisation, quantify coupling and intermolecular separation in CT states, identify the role of trap sites, and distinguish between competing recombination pathways. The next chapter introduces the principles of EPR spectroscopy and outlines how this technique enables molecular-level insight into the mechanisms that determine OPV performance.

Chapter 2

Fundamentals of Electron Paramagnetic Resonance

Interactions at the nanoscale between donor and acceptor OPV materials influence how excitons split, charges separate, and ultimately how current is generated. While conventional optical and electrical methods have been instrumental in probing these processes, electron paramagnetic resonance (EPR) spectroscopy can provide a powerful complementary approach, offering molecular-level insight through its unique ability to directly probe one of the most fundamental quantum properties of matter: **spin**.

Electron spin is intrinsically linked to charge: when a neutral, closed-shell molecule either loses or gains an electron, the resulting charged species will contain an unpaired electron spin. The photophysical processes that define the light-to-electricity conversion in OPVs are characterised by a number of states with unpaired electrons: charge-transfer states, separated charges, and triplets. The inherent connection of charge and spin enables EPR to sensitively monitor the generation, separation, and recombination of charged states. By probing the magnetic moment of the electron spin and its interactions with external magnetic fields and nearby electron and nuclear spins, EPR spectra can access information about the electronic structure, molecular dynamics, and local environment of paramagnetic species.

Since its inception in the 1940s, EPR has evolved from a specialised technique into a versatile spectroscopic tool used across chemistry, physics, biology, and materials science. Advances in instrumentation and pulse techniques have expanded the reach of EPR to include flexible macromolecules, disordered solids, and functional materials such as those employed in OPVs.[114] Today, EPR offers both continuous-wave and pulsed methods that enable the study of spin dynamics, spatial distribution of paramagnetic centres, and interactions of electron spins. For OPVs, where device efficiency is influenced by subtle morphological and electronic factors, EPR provides a unique window into the fundamental processes governing device operation.

Understanding how spin behaves in a magnetic field, how it interacts with its environment, and how these interactions are detected spectroscopically is essential to interpreting EPR data. A foundation for understanding EPR spectroscopy in organic materials is provided in this chapter. The fundamental concept of electron spin and its quantum mechanical properties are first introduced, establishing the basis for interpreting magnetic resonance phenomena. The spin Hamiltonian formalism, which describes the interactions between electrons, nuclei, and magnetic fields, is then detailed. Subsequently, the generation of spin-polarised states, such as charge-transfer states, triplet excitons, and separated charges, following photoexcitation in donor:acceptor OPVs is examined. The latter sections focus on the principles of continuous-wave and pulse EPR, with details on the time-resolved and electron-nuclear hyperfine EPR experiments used in this thesis.

2.1 Electron Spin

The concept of electron spin was introduced in the early 20th century as physicists grappled with unexplained features in atomic spectra. In 1925, George Uhlenbeck and Samuel Goudsmit proposed that the electron possesses an intrinsic angular momentum, independent of its orbital motion, which they termed *spin*.* This revolutionary idea helped explain the fine structure observed in atomic spectra and was supported experimentally by the Stern-Gerlach experiment, which demonstrated the quantised deflection of silver atoms in a magnetic field. Although initially met with scepticism, the concept of spin gained widespread acceptance following the development of Dirac's relativistic quantum mechanics, which provided a rigorous theoretical foundation. Spin is now understood as a fundamental and experimentally verified property of all elementary particles.

The total spin angular momentum is defined by the operator $\hat{\boldsymbol{S}}$, with a quantum number $S = \frac{1}{2}$ for a single electron. The projection of that angular momentum along an arbitrarily chosen axis, conventionally the z-axis, is represented by the spin operator, $\hat{S}_z$. The associated eigenstates, denoted $|\alpha\rangle$ and $|\beta\rangle$, correspond to spin 'up' and spin 'down' orientations with magnetic quantum numbers $m_S = +\frac{1}{2}$ and $m_S = -\frac{1}{2}$, respectively. $\hat{S}_z$ commutes with the square of the total spin angular momentum $\hat{S}^2$, sharing the same $|\alpha\rangle$ and $|\beta\rangle$ eigenstates:

$$\begin{aligned} \hat{S}^2 |S, m_S\rangle &= \hbar^2 S(S+1) |S, m_S\rangle & |\alpha\rangle &= |\tfrac{1}{2}, +\tfrac{1}{2}\rangle \\ \hat{S}_z |S, m_S\rangle &= \hbar m_S |S, m_S\rangle & |\beta\rangle &= |\tfrac{1}{2}, -\tfrac{1}{2}\rangle \end{aligned} \tag{2.1}$$

In the absence of a magnetic field, the $|\alpha\rangle$ and $|\beta\rangle$ spin states are degenerate. Applying an external magnetic field lifts this degeneracy, owing to the magnetic moment associated with the electron spin. This magnetic moment, $\hat{\boldsymbol{\mu}}_\mathrm{e}$, arises from the intrinsic spin angular momentum, and is given by:

$$\hat{\boldsymbol{\mu}}_\mathrm{e} = -g_\mathrm{e} \frac{e}{2m_\mathrm{e}} \hat{\boldsymbol{S}} = -\frac{g_\mathrm{e}\mu_\mathrm{B}}{\hbar} \hat{\boldsymbol{S}} \tag{2.2}$$

where e is the elementary charge, m_e is the electron mass, μ_B is the Bohr magneton, and g_e is the g-value of the free electron ($g_\mathrm{e} = 2.002319$).[115] The z-component of the magnetic moment is:

$$\mu_z = -g_\mathrm{e}\mu_\mathrm{B} m_S \tag{2.3}$$

and depends on the spin state ($|\alpha\rangle$ or $|\beta\rangle$). A similar expression can be derived for nuclear spins; however, due to their greater mass, nuclear magnetic moments are considerably smaller than electron magnetic moments: for ^{1}H, a factor of 660.

*Despite the term 'spin', the electron is not physically spinning in a classical sense; rather, it possesses an intrinsic angular momentum that has no classical analogue.

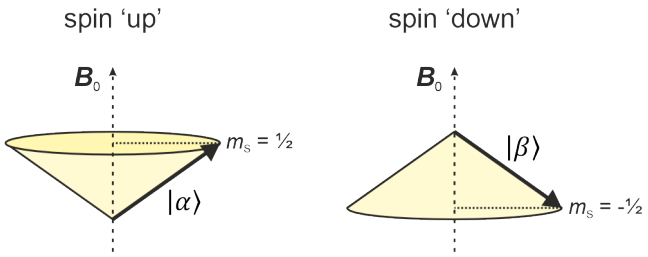

Figure 2.1: Vector model representation of $|\alpha\rangle$ and $|\beta\rangle$ spin states in a magnetic field.

As a visual aide, the spin magnetic moment can be represented using the vector model representation shown in Figure 2.1. In the presence of an external magnetic field $\boldsymbol{B}_0$ aligned along the z-axis, the spin magnetic moment undergoes *Larmor precession*: circular motion around the field direction caused by the torque exerted by $\boldsymbol{B}_0$, with a characteristic frequency:

$$\omega_0 = \frac{g_e \mu_\mathrm{B} B_0}{\hbar} \tag{2.4}$$

This precession traces out a cone around the magnetic field axis at a fixed angle. The cone illustrates not only the continuous precession of the magnetic moment around $\boldsymbol{B}_0$, but also the uncertainty in the direction of the magnetic moment perpendicular to $\boldsymbol{B}_0$. This restriction arises because the spin angular momentum components along different axes do not commute, which restricts the simultaneous exact determination of these spin components. As a result, only the magnitude and projection along one axis is well-defined, and for an electron, this projection is quantised to $\pm\frac{1}{2} g_\mathrm{e} \mu_\mathrm{B}$.

2.2 The Spin Hamiltonian

To fully describe the behaviour of electron spins in an external magnetic field, particularly in systems containing multiple magnetic nuclei and electrons, the spin Hamiltonian formalism is essential. While the classical picture of the magnetic moment provides a conceptual understanding of the interaction between spins and magnetic fields, the spin Hamiltonian offers a rigorous quantum mechanical framework that incorporates all relevant magnetic interactions involving both electron and nuclear spins.

These interactions are typically categorised into two groups: spin-field interactions, which describe how spins couple to external magnetic fields, and spin-spin interactions, which account for couplings of electron and nuclear spins with

other electron or nuclear spins within the system.[116–119] The full spin Hamiltonian is expressed as:

$$\hat{\mathcal{H}} = \hat{\mathcal{H}}_{\mathrm{eZ}} + \hat{\mathcal{H}}_{\mathrm{nZ}} + \hat{\mathcal{H}}_{\mathrm{zf}} + \hat{\mathcal{H}}_{\mathrm{dip}} + \hat{\mathcal{H}}_{\mathrm{ex}} + \hat{\mathcal{H}}_{\mathrm{hf}} + \hat{\mathcal{H}}_{\mathrm{nq}} + \hat{\mathcal{H}}_{\mathrm{nn}} \tag{2.5}$$

where the individual contributions are:

- **spin-field interactions**
  - the electron Zeeman interaction $\hat{\mathcal{H}}_{\mathrm{eZ}}$
  - the nuclear Zeeman interaction $\hat{\mathcal{H}}_{\mathrm{nZ}}$
- **electron-electron interactions**
  - the zero-field interaction $\hat{\mathcal{H}}_{\mathrm{zf}}$
  - the dipolar interaction $\hat{\mathcal{H}}_{\mathrm{dip}}$
  - the exchange interaction $\hat{\mathcal{H}}_{\mathrm{ex}}$
- **electron-nuclear interactions**
  - the electron-nuclear hyperfine interaction $\hat{\mathcal{H}}_{\mathrm{hf}}$
- **additional nuclear spin interactions**
  - the nuclear quadrupole interaction $\hat{\mathcal{H}}_{\mathrm{nq}}$
  - the nuclear-nuclear interaction $\hat{\mathcal{H}}_{\mathrm{nn}}$

Each of these terms will be described in detail in the sections that follow.

2.2.1 Electron Zeeman Interaction

The interaction of an electron spin with an external magnetic field, $\boldsymbol{B}_0$, is governed by the electron Zeeman Hamiltonian. For a free electron in vacuum, the interaction is described by:

$$\hat{\mathcal{H}}_{\mathrm{eZ}} = -\boldsymbol{B}_0 \cdot \hat{\boldsymbol{\mu}} = \frac{g_{\mathrm{e}}\mu_{\mathrm{B}}}{\hbar}\boldsymbol{B}_0 \cdot \hat{\boldsymbol{S}} \tag{2.6}$$

More generally, the g-value can be orientation-dependent, reflecting the directional dependence of the electron's magnetic response, and is defined as a matrix or tensor,[†] with the Zeeman interaction expressed as:

$$\hat{\mathcal{H}}_{\mathrm{eZ}} = \frac{\mu_{\mathrm{B}}}{\hbar}\boldsymbol{B}_0 \cdot \boldsymbol{g} \cdot \hat{\boldsymbol{S}} \tag{2.7}$$

[†]The $\boldsymbol{g}$-matrix is commonly called a tensor in the literature, though it is not a true tensor in the strict mathematical sense, as it connects the external magnetic field vector in real (laboratory) space with the electron spin operator in spin space, whereas a tensor formally transforms within a single coordinate frame.[120] Despite this, the term 'tensor' is widely used for convenience when describing anisotropic interactions.

where $\boldsymbol{g}$ is described by a second-rank[‡] tensor (represented by a 3×3 real, symmetric matrix) that captures the directional dependence of the electron's magnetic response. The $\boldsymbol{g}$-tensor is typically defined in the laboratory frame, the coordinate system in which $\boldsymbol{B}_0$ lies along the z-axis. $\boldsymbol{g}$ can be diagonalised by an orthogonal transformation:

$$\boldsymbol{g} = \begin{pmatrix} g_{xx} & g_{xy} & g_{xz} \\ g_{yx} & g_{yy} & g_{yz} \\ g_{zx} & g_{zy} & g_{zz} \end{pmatrix} \xrightarrow{\boldsymbol{U}_g^{\mathrm{T}} \boldsymbol{g} \boldsymbol{U}_g} \begin{pmatrix} g_x & 0 & 0 \\ 0 & g_y & 0 \\ 0 & 0 & g_z \end{pmatrix} \tag{2.8}$$

where $\boldsymbol{U}_g$ is the matrix that transforms $\boldsymbol{g}$ into diagonal form, 'rotating' $\boldsymbol{g}$ from the laboratory frame into the g-frame. This rotation is parametrised by the Euler angles α, β, and γ:

$$\boldsymbol{U}_g = \begin{pmatrix} c\gamma\, c\beta\, c\alpha - s\gamma\, s\alpha & c\gamma\, c\beta\, s\alpha + s\gamma\, c\alpha & -c\gamma\, s\beta \\ -s\gamma\, c\beta\, c\alpha - c\gamma\, s\alpha & -s\gamma\, c\beta\, s\alpha + c\gamma\, c\alpha & s\gamma\, s\beta \\ s\beta\, c\alpha & s\beta\, s\alpha & c\beta \end{pmatrix} \tag{2.9}$$

with $s\alpha = \sin\alpha$ and $c\alpha = \cos\alpha$.

[‡]A mathematical object that can be represented as a matrix and transforms vectors linearly.

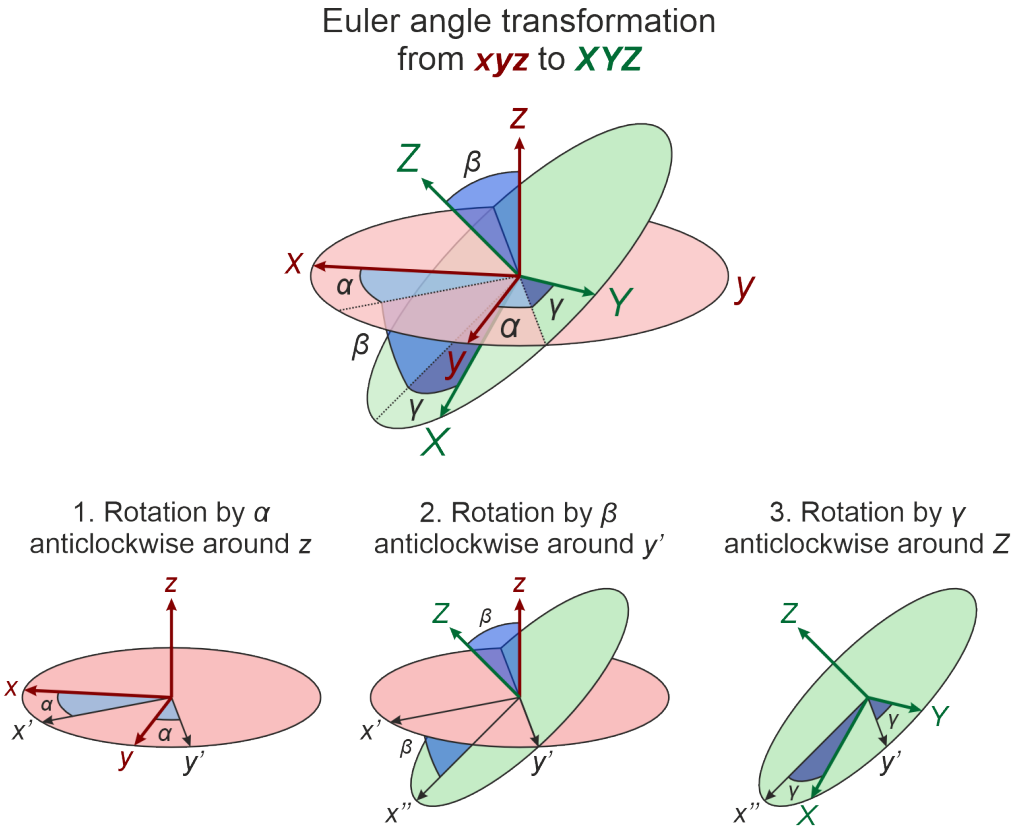

Figure 2.2: Transformation of one co-ordinate system, xyz, to another, XYZ. The transformation is defined by three Euler angles, α, β, and γ, using the ZYZ convention.[121]

The diagonalised matrix defines the principal g-values: g_x, g_y, and g_z, which describe the magnetic response along the principal axes of the g-frame. The transformation from the molecular reference frame to the g-frame is illustrated in Figure 2.2 and follows the standard EPR ZYZ convention:[121] 1. Anticlockwise rotation by angle α about the z-axis, 2. Anticlockwise rotation by angle β about the new y'-axis, 3. Anticlockwise rotation by angle γ about the new Z-axis.

For the external magnetic field, $\boldsymbol{B}_0$, applied along the z-axis of the laboratory frame, and in the case of an isotropic g-value, $g_{\text{iso}} = g_x = g_y = g_z$, the electron Zeeman spin Hamiltonian simplifies to:

$$\hat{\mathcal{H}}_{\text{eZ}} = \frac{g_{\text{iso}}\mu_{\text{B}}B_0}{\hbar}\hat{S}_z \tag{2.10}$$

giving energy levels of the spin states and a transition energy of:

$$\begin{aligned} E_\alpha &= +\tfrac{1}{2}g_{\text{iso}}\mu_{\text{B}}B_0 & \Delta E_{\alpha\leftrightarrow\beta} &= E_\alpha - E_\beta \\ E_\beta &= -\tfrac{1}{2}g_{\text{iso}}\mu_{\text{B}}B_0 & &= g_{\text{iso}}\mu_{\text{B}}B_0 \end{aligned} \tag{2.11}$$

The transition $|\alpha\rangle \leftrightarrow |\beta\rangle$ is governed by the selection rule $\Delta m_S = \pm 1$. This rule arises from conservation of angular momentum: since a photon carries one quantum of angular momentum, the spin system can only absorb or emit a single photon when its spin projection changes by one unit.

The electron Zeeman interaction in real systems deviates from that of a free electron due to the influence of *spin-orbit coupling* (SOC), which mixes orbital angular momentum from excited states into the ground state.[122] The electron Zeeman Hamiltonian from Equation 2.6 becomes:

$$\hat{\mathcal{H}}_{\text{eZ}} + \hat{\mathcal{H}}_{\text{soc}} = \frac{\mu_{\text{B}}}{\hbar}\boldsymbol{B}_0 \cdot \left(g_{\text{e}}\hat{\boldsymbol{S}} + \hat{\boldsymbol{L}}\right) + \lambda\hat{\boldsymbol{L}} \cdot \hat{\boldsymbol{S}} \tag{2.12}$$

where $\hat{\boldsymbol{L}}$ is the orbital angular momentum operator and λ is the spin-orbit coupling constant, which, for a single electron, correlates strongly with the effective nuclear charge Z_{eff}: $\lambda \propto Z_{\text{eff}}^4$. The first term accounts for the orbital and spin contributions to the magnetic moment, while the second term represents the spin-orbit interaction.

In systems with a non-degenerate ground state, orbital angular momentum is quenched, but SOC introduces second-order contributions from excited states.[117] Under this approximation, the $\boldsymbol{g}$-tensor becomes:

$$\boldsymbol{g} = g_{\text{e}}\mathbf{1} + 2\lambda\boldsymbol{\Lambda} \tag{2.13}$$

where $\mathbf{1}$ is the identity matrix and the elements of $\boldsymbol{\Lambda}$ are given by:

$$\Lambda_{ij} = \sum_{n\neq 0} \frac{\langle\psi_0|\,\hat{L}_i\,|\psi_n\rangle\,\langle\psi_n|\,\hat{L}_j\,|\psi_0\rangle}{E_n - E_0} \tag{2.14}$$

ψ_0 and ψ_n are the ground and excited state wavefunctions with energies E_0 and E_n, respectively. The anisotropy of the $\boldsymbol{g}$-tensor originates from the coupling between the ground and excited states via their orbital angular momentum, modulated by the spin-orbit coupling strength. Physically, this means the electron experiences an effective local magnetic field different from the external field $\boldsymbol{B}_0$, leading to an anisotropic magnetic response. The degree of deviation from g_e depends on both the magnitude of λ and the energy separation between the ground and excited states: smaller energy gaps and stronger spin-orbit coupling cause larger deviations from g_e.

Organic molecules typically exhibit g-values that deviate only slightly from g_e: the lack of heavy atoms reduces the strength of spin-orbit coupling, while the excited states are generally high in energy and less accessible for mixing of orbital angular momentum. Typical organic radicals have g-values in the range $1.99 - 2.01$, while molecules containing transition metal ions can exhibit much broader ranges, with g-values reported from $g < 0.1$ to $g > 10$.[123,124] Large magnetic fields are therefore typically required to resolve the small g-anisotropy in organic molecules.

For an isotropic g-value, the EPR spectrum exhibits a single sharp peak, centred at the magnetic field strength B_0 that satisfies the resonance condition:

$$\hbar\omega = h\nu = \Delta E_{\alpha\leftrightarrow\beta} = g_\mathrm{iso}\mu_\mathrm{B}B_0 \tag{2.15}$$

where ω and ν are the angular and linear frequencies of the radiation applied to induce transitions between spin states.

In EPR spectroscopy, transitions are driven by the application of microwave radiation. When the photon energy matches the energy separation between spin levels, energy absorption occurs, resulting in an EPR signal. The intensity of a transition between two states $|i\rangle$ and $|j\rangle$ depends on two factors: the population difference between those states and the transition probability. Under thermal equilibrium, the population difference is determined by the Boltzmann distribution, which favours lower-energy spin states.

The transition probability may be derived from time-dependent perturbation theory. According to Fermi's Golden Rule, the transition rate $W_{i\to j}$ is proportional to the square of the matrix element of the perturbing Hamiltonian $\hat{\mathcal{H}}_1$:

$$W_{i\to j} \propto \left|\langle j|\,\hat{\mathcal{H}}_1\,|i\rangle\right|^2 \tag{2.16}$$

In the case of EPR, the perturbation is introduced by an oscillating microwave magnetic field $\boldsymbol{B}_1$, which is applied perpendicular to the static magnetic field $\boldsymbol{B}_0$, and is conventionally defined along the x-axis of the laboratory frame. The

interaction of $\boldsymbol{B}_1$ with the electron magnetic moment is described by the perturbing spin Hamiltonian:

$$\hat{\mathcal{H}}_1 = \frac{g_{\text{iso}}\mu_{\text{B}}B_1(t)}{\hbar}\hat{S}_x \tag{2.17}$$

In systems with lower symmetry, the principal g-values may differ: for axial symmetry, $g_x = g_y \neq g_z$, while for orthorhombic symmetry, $g_x \neq g_y \neq g_z$. For a single crystal with a specific orientation with respect to the magnetic field vector, the magnetic field position for the EPR transition will be determined by the projection of the $\boldsymbol{g}$-tensor along the magnetic field direction. For powder samples, there is a uniform distribution of molecular orientations with respect to the applied magnetic field. Each orientation will contribute a resonance peak, and the sum of all these peaks will give a broadened EPR spectrum covering the full range of g-values, with turning points corresponding to the field positions of the principal g-values.

EPR spectra for different g-value symmetries are shown in Figure 2.3, assuming no other contributions to the spin Hamiltonian. The principal values of the $\boldsymbol{g}$-tensor reflect the underlying electronic structure and spatial symmetry of the paramagnetic centre, providing a unique spectroscopic signature that can distinguish between different paramagnetic species. Instead of sharp lines, the spectra exhibit broader peaks due to a number of line broadening effects, discussed in Section 2.3.

In this thesis, organic molecules are studied as solid samples, where the anisotropy of the $\boldsymbol{g}$-tensor is preserved and clearly observable in the EPR spectra. In contrast, if the samples were measured in solution, rapid molecular tumbling would average out the anisotropy. This motional averaging leads to a single, sharp resonance peak, determined by the isotropic g-value, $g_{\text{iso}} = \frac{1}{3}(g_x + g_y + g_z)$, despite the underlying g-anisotropy. A similar averaging effect can also occur in solids if the unpaired electrons are highly mobile.

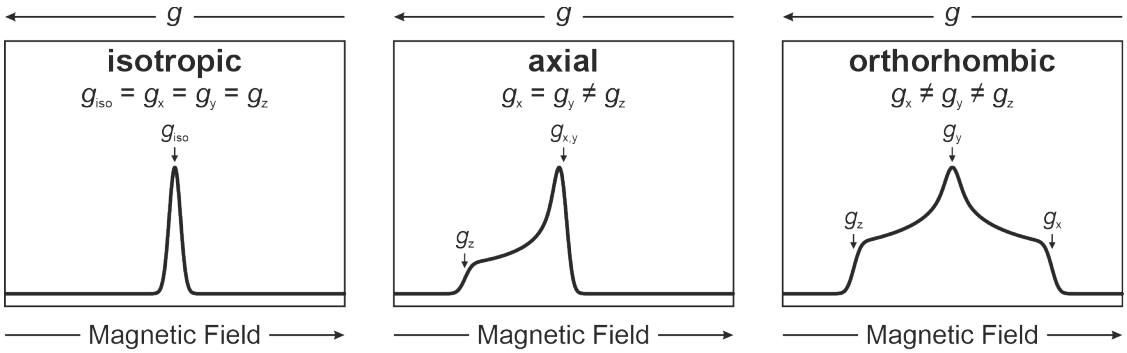

Figure 2.3: Simulated EPR spectra for g-values of isotropic, axial, and orthorhombic symmetry. A convolutional line broadening was also included.

2.2.2 Nuclear Zeeman Interaction

In the same fashion, the spin Hamiltonian describing the Zeeman interaction for a nuclear spin can be constructed:

$$\hat{\mathcal{H}}_{\mathrm{nZ}} = -\frac{g_{\mathrm{n}}\mu_{\mathrm{N}}}{\hbar}\boldsymbol{B}_0 \cdot \hat{\boldsymbol{I}} \tag{2.18}$$

with $\hat{\boldsymbol{I}}$ the nuclear spin angular momentum operator, μ_{N} the nuclear Bohr magneton and g_{n} the nuclear g-value. The much smaller nuclear magnetic moment leads to Zeeman energies orders of magnitude weaker.

2.2.3 Electron-Electron Interactions

In systems with more than one electron spin, the total spin state of the system is determined by the joint configuration of the individual spins. These spin states can be expressed as products of single-spin states, $\{|\alpha_1\alpha_2\rangle, |\alpha_1\beta_2\rangle, |\beta_1\alpha_2\rangle, |\beta_1\beta_2\rangle\}$, where each spin is described independently. This forms the **uncoupled basis**, in which states are written as $|m_{S_1}, m_{S_2}\rangle$. This basis is especially convenient when the interaction between spins is weak compared to the electron Zeeman interaction, such that each spin responds to the external magnetic field approximately independently.

When there is a significant interaction between the electron spins, however, the energy levels of the system are more suitably described in terms of the total spin angular momentum: $\hat{\boldsymbol{S}} = \hat{S}_1 + \hat{S}_2$. In this case, the **coupled basis** is more appropriate, with eigenstates labelled by the total spin quantum numbers S and M_S. For a pair of electron spins, this gives rise to a singlet state ($S = 0, M_S = 0$) and three triplet states ($S = 1, M_S = 0, \pm 1$), which are linear combinations of the uncoupled basis states:

$$\begin{aligned} |\mathrm{S}\rangle &= |0,0\rangle = \tfrac{1}{\sqrt{2}}(|\alpha_1\beta_2\rangle - |\beta_1\alpha_2\rangle) \\ |\mathrm{T}_+\rangle &= |1,+1\rangle = |\alpha_1\alpha_2\rangle \\ |\mathrm{T}_0\rangle &= |1,0\rangle = \tfrac{1}{\sqrt{2}}(|\alpha_1\beta_2\rangle + |\beta_1\alpha_2\rangle) \\ |\mathrm{T}_-\rangle &= |1,-1\rangle = |\beta_1\beta_2\rangle \end{aligned} \tag{2.19}$$

In the same fashion as the representation of $|\alpha\rangle$ and $|\beta\rangle$ in Figure 2.1, the vector model can provide an intuitive way to understand the spin states of the two electrons in the coupled spin basis. In this framework, shown in Figure 2.4, the spins can align to form a resultant triplet vector with magnitude $\sqrt{2}g_{\mathrm{e}}\mu_{\mathrm{B}}$, or cancel to form a singlet vector of zero magnitude. The projection of the spin states onto $\boldsymbol{B}_0$ distinguishes $|\mathrm{T}_+\rangle$, $|\mathrm{T}_0\rangle$ and $|\mathrm{T}_-\rangle$.[§]

[§]The vector model representation for spins is often depicted inaccurately in the literature. The cone angle for a single spin is always fixed at 54.7° relative to $\boldsymbol{B}_0$. For the $|\mathrm{T}_+\rangle$ and $|\mathrm{T}_-\rangle$ spin states, the two individual spins are separated by 70.5°, corresponding to an azimuthal phase shift of 90°, provided the two spins have the same Larmor frequency. These angles can be derived trigonometrically from the eigenvalues of $\hat{S}^2$ and $\hat{S}_z$ for the single spin and total spin states.

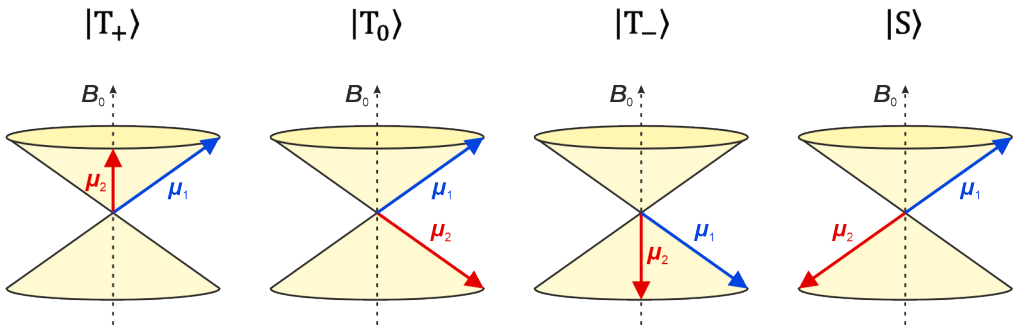

Figure 2.4: Vector model representation of the spin states for two coupled electrons in the coupled spin basis.

Electron-electron interactions between two spins arise from two sources: the exchange interaction, resulting from electron wavefunction overlap, and the dipolar interaction, from interaction of the two spin magnetic moments. The appropriate spin basis and description depend on the strength of interaction between the two spins.

When the two spins reside on the same molecule, as in an exciton, the exchange interaction is typically strong, resulting in a large energy gap between singlet and triplet states. In this strongly-coupled regime, the coupled spin basis is most suitable. Only spin states with non-zero total spin angular momentum ($S > 0$) have a net magnetic moment and are thus relevant for EPR. The dipolar coupling within the triplet manifold leads to a splitting of the triplet sublevels even in the absence of an external magnetic field, known as zero-field splitting (ZFS):

$$\hat{\mathcal{H}}_{\text{ee}} = \hat{\mathcal{H}}_{\text{zf}} \tag{2.20}$$

In contrast, when the spins are located on different molecules, as in a charge-transfer state, the exchange interaction is much weaker and often comparable to the dipolar coupling. In this weakly-coupled regime, describing the system in terms of total spin S becomes less appropriate, and the uncoupled spin basis provides a more accurate representation. The total electron-electron interaction Hamiltonian explicitly includes both dipolar and exchange terms:

$$\hat{\mathcal{H}}_{\text{ee}} = \hat{\mathcal{H}}_{\text{dip}} + \hat{\mathcal{H}}_{\text{ex}} \tag{2.21}$$

Zero-Field Interaction

Dipolar coupling between two electron spins can be expressed using a symmetric, traceless tensor $\boldsymbol{D}$. In the strong exchange regime, when the two electron spins are

no longer distinguishable and behave as a single $S = 1$ triplet, this interaction is described as the zero-field interaction, given by the spin Hamiltonian:

$$\hat{\mathcal{H}}_{\mathrm{zf}} = \hat{\boldsymbol{S}} \cdot \boldsymbol{D} \cdot \hat{\boldsymbol{S}} \tag{2.22}$$

$\boldsymbol{D}$ can be diagonalised by transformation into its principal axis D-frame:

$$\boldsymbol{D} = \begin{pmatrix} D_{XX} & D_{XY} & D_{XZ} \\ D_{YX} & D_{YY} & D_{YZ} \\ D_{ZX} & D_{ZY} & D_{ZZ} \end{pmatrix} \xrightarrow{\boldsymbol{U}_D^{\mathrm{T}} \boldsymbol{D} \boldsymbol{U}_D} \begin{pmatrix} D_X & 0 & 0 \\ 0 & D_Y & 0 \\ 0 & 0 & D_Z \end{pmatrix} \tag{2.23}$$

where $\boldsymbol{U}_D$ is a rotation matrix with Euler angles $\alpha_D, \beta_D, \gamma_D$.

Because $\boldsymbol{D}$ has zero trace, its three principal values can be expressed in terms of two scalar parameters:

$$D = \frac{3}{2} D_Z \qquad E = \frac{1}{2}(D_X - D_Y) \tag{2.24}$$

By convention, the ordering $|D_Z| \geq |D_X| \geq |D_Y|$ ensures that D and E have opposite signs and that the rhombicity ratio $\frac{E}{D}$ is bounded between $-\frac{1}{3}$ and 0.[125] The spin Hamiltonian, in terms of D and E, from Equation 2.22 becomes:

$$\hat{\mathcal{H}}_{\mathrm{zf}} = D\left(\hat{S}_z^2 - \tfrac{1}{3}\hat{S}^2\right) + E\left(\hat{S}_x^2 - \hat{S}_y^2\right) \tag{2.25}$$

For a triplet state, the eigenvalues of this Hamiltonian yield the following spin sublevel energies:

$$\begin{aligned} E_x &= -D_X = \tfrac{1}{3}D - E \\ E_y &= -D_Y = \tfrac{1}{3}D + E \\ E_z &= -D_Z = -\tfrac{2}{3}D \end{aligned} \tag{2.26}$$

with the relative ordering of these levels dependent on the signs of D and E.

The zero-field interaction has two main contributions. The first is magnetic dipole-dipole coupling between unpaired electron spins, which depends on their spatial separation and relative orientation. The second contribution arises from spin-orbit coupling, which is generally weak in organic molecules due to small spin-orbit coupling constants and large energy gaps to excited states.[126] The ZFS Hamiltonian can therefore be approximated as a dipole-dipole Hamiltonian, which leads to expressions for D and E of:

$$\begin{aligned} D &= \frac{3}{16}\frac{\mu_0}{\pi\hbar}(g_{\mathrm{e}}\mu_{\mathrm{B}})^2 \left\langle \frac{r^2 - 3z^2}{r^5} \right\rangle \\ &= \frac{3}{16}\frac{\mu_0}{\pi\hbar}(g_{\mathrm{e}}\mu_{\mathrm{B}})^2 \left\langle \frac{1 - 3\cos^2\theta}{r^3} \right\rangle \\ E &= \frac{3}{16}\frac{\mu_0}{\pi\hbar}(g_{\mathrm{e}}\mu_{\mathrm{B}})^2 \left\langle \frac{y^2 - x^2}{r^5} \right\rangle \end{aligned} \tag{2.27}$$

with μ_0 the vacuum permeability, r the distance between the two spins, and θ the angle between the interspin vector $\boldsymbol{r}$ and the principal z-axis of the ZFS tensor. The angular brackets represent the average value over the spin density distribution.

The magnitude of D reflects the average distance between the two unpaired electron spins. A larger $|D|$ corresponds to a smaller spin-spin separation and a stronger dipolar interaction. The parameter E quantifies the deviation from axial symmetry; when $E = 0$, the $\boldsymbol{D}$ tensor is axially symmetric. The sign of D provides insight into the shape of the spin density distribution. From the angular dependence in Equation 2.27, when $\theta = 90°$ ($\boldsymbol{r}$ lies in the plane perpendicular to the axis of the largest principal D-value D_Z), $D > 0$ and the spin density distribution is oblate (disk-like). Conversely, when $\theta = 0°$ ($\boldsymbol{r}$ aligned with the axis of D_Z), $D < 0$ and the spin density is prolate (rod-like), with the D_Z principal axis oriented along the long-axis.

Dipolar Interaction

For weakly-coupled spins, the dipolar interaction is often treated using the *point-dipole approximation*, which models each electron spin as a magnetic point dipole. This approach is valid when the spatial extent of the electron spin density is small compared to the separation between the two spins. Under this approximation, the dipolar coupling Hamiltonian takes the form:

$$\hat{\mathcal{H}}_{\text{dip}} = \hat{\boldsymbol{S}}_1 \cdot \boldsymbol{D} \cdot \hat{\boldsymbol{S}}_2 = \frac{\mu_0}{4\pi\hbar} g_1 g_2 \mu_{\text{B}}^2 \frac{1}{r^3} \left(\hat{\boldsymbol{S}}_1 \cdot \hat{\boldsymbol{S}}_2 - \frac{3}{r^2} (\hat{\boldsymbol{S}}_1 \cdot \boldsymbol{r})(\hat{\boldsymbol{S}}_2 \cdot \boldsymbol{r}) \right) \tag{2.28}$$

The dipolar Hamiltonian in Equation 2.28 can be decomposed into three types of terms: secular, pseudo-secular, and non-secular.[¶] At the magnetic field strengths typically used in EPR experiments, the non-secular terms are often neglected,[127] reducing the dipolar Hamiltonian to only secular and pseudo-secular contributions.

For an axial dipolar coupling tensor, expressed in its principal axis system as:

$$\boldsymbol{D} = \begin{pmatrix} d & 0 & 0 \\ 0 & d & 0 \\ 0 & 0 & -2d \end{pmatrix} \tag{2.29}$$

the dipolar Hamiltonian, neglecting non-secular terms, becomes:

$$\hat{\mathcal{H}}_{\text{dip}} = \frac{D}{2} \left(3\hat{S}_{1z}\hat{S}_{2z} - \hat{\boldsymbol{S}}_1 \cdot \hat{\boldsymbol{S}}_2 \right) \tag{2.30}$$

[¶]In the context of dipolar coupling, **secular** terms commute with the Zeeman Hamiltonian and cause energy level shifts; **pseudo-secular** terms do not commute with the Zeeman Hamiltonian but induce weak mixing between spin states; **non-secular** terms also do not commute but oscillate rapidly in time at frequencies set by the large Zeeman splitting.[117] These rapid oscillations average out over typical experimental timescales, and so do not cause meaningful energy shifts or spin state mixing.[127]

with

$$D = d\left\langle 1 - 3\cos^2\theta \right\rangle = \frac{\mu_0}{4\pi\hbar} g_1 g_2 \mu_\mathrm{B}^2 \left\langle \frac{1 - 3\cos^2\theta}{r^3} \right\rangle \tag{2.31}$$

When $\theta = 0°$ with $\boldsymbol{B}_0$ parallel to $\boldsymbol{r}$, the dipolar interaction reaches its maximum, corresponding to the principal value $D_z = -2d$. When $\theta = 90°$, the interaction is minimised, corresponding to the smallest principal values $D_x = D_y = d$.

Exchange Interaction

Unlike the dipolar coupling, which can be approximated as a classical interaction between magnetic moments, the exchange interaction is a purely quantum effect arising from the antisymmetry of the total two-electron wavefunction under fermion exchange, as required by the Pauli principle:[128]

$$\Psi_\mathrm{total}(\boldsymbol{r}_2, \boldsymbol{r}_1, \sigma_2, \sigma_1) = -\Psi_\mathrm{total}(\boldsymbol{r}_1, \boldsymbol{r}_2, \sigma_1, \sigma_2) \tag{2.32}$$

with $\boldsymbol{r}_i$ and σ_i representing the spatial and spin coordinates of electron i, respectively. The total wavefunction is separable into spatial and spin parts:

$$\Psi_\mathrm{total}(\boldsymbol{r}_1, \boldsymbol{r}_2, \sigma_1, \sigma_2) = \psi(\boldsymbol{r}_1, \boldsymbol{r}_2)\,\chi(\sigma_1, \sigma_2) \tag{2.33}$$

In the singlet state, the spin wavefunction (Equation 2.19) is antisymmetric with respect to electron exchange. Thus, the spatial part of the wavefunction must be symmetric:

$$\psi(\boldsymbol{r}_2, \boldsymbol{r}_1) = \psi(\boldsymbol{r}_1, \boldsymbol{r}_2) \tag{2.34}$$

Conversely, for the triplet state, the spin wavefunctions are symmetric. Therefore, the spatial wavefunction must be antisymmetric:

$$\psi(\boldsymbol{r}_2, \boldsymbol{r}_1) = -\psi(\boldsymbol{r}_1, \boldsymbol{r}_2) \tag{2.35}$$

The symmetric spatial wavefunction of the singlet state results in a higher probability of the two electrons being found close together, whereas the antisymmetric spatial wavefunction of the triplet state ensures that both electrons cannot occupy the same region of space. This difference in spatial distribution reduces electron-electron repulsion in the triplet state, stabilising its energy relative to the singlet state. This difference in electrostatic energy is the origin of the exchange interaction. In rare cases, the singlet state may be stabilised relative to the triplet state through additional singlet-stabilising contributions like low-lying, accessible singlet excited states.[129] The exchange interaction can be described by the following Hamiltonian:

$$\hat{\mathcal{H}}_\mathrm{ex} = J\hat{\boldsymbol{S}}_1 \cdot \hat{\boldsymbol{S}}_2 \tag{2.36}$$

where J is the isotropic exchange coupling constant.[‖] While in principle, J can be anisotropic; for organic materials, this contribution, controlled by spin-orbit coupling, is minimal and can be ignored. The sign of J determines the relative energies of the singlet and triplet states: if $J < 0$, the triplet state is lower in energy, while if $J > 0$, the singlet state is energetically favourable. The energy gap between the singlet and triplet states is equal to the magnitude of J.

The strength of the exchange interaction depends critically on the spatial overlap of the unpaired electron wavefunctions. Because exchange arises from the requirement that the total wavefunction be antisymmetric with respect to particle exchange, any interaction energy difference between the singlet and triplet states can only emerge if the electrons are close enough for their wavefunctions to overlap significantly. Without such overlap, the electrons are effectively independent, and no exchange interaction arises. As a result, the exchange interaction is highly sensitive to inter-spin distance. This distance dependence can be approximated by an exponential decay:[131,132]

$$J(r) = J_0 e^{-\beta r} \tag{2.38}$$

J_0 represents the maximum exchange interaction strength at very short spin-spin separations, where the spatial overlap of the electron wavefunctions is largest, and β controls how rapidly the interaction diminishes with increasing distance r and depends on the extent of orbital overlap and electron delocalisation. In general, exchange dominates at short distances, while the dipolar interaction, which falls off more slowly with $1/r^3$, becomes more important at larger separations.

2.2.4 Electron-Nuclear Hyperfine Interaction

The electron-nuclear hyperfine interaction describes the magnetic interaction between an electron spin and a nearby nuclear spin:

$$\begin{aligned} \hat{\mathcal{H}}_{\mathrm{hf}} &= \hat{\boldsymbol{S}} \cdot \boldsymbol{A} \cdot \hat{\boldsymbol{I}} \\ &= a_{\mathrm{iso}} \hat{\boldsymbol{S}} \cdot \hat{\boldsymbol{I}} + \hat{\boldsymbol{S}} \cdot \boldsymbol{A}_{\mathrm{dip}} \cdot \hat{\boldsymbol{I}} \end{aligned} \tag{2.39}$$

The first term is the Fermi contact interaction and arises from electron spin density at the nucleus; it is typically associated with s-orbital character, but

[‖]There are various conventions in the literature for defining $\hat{\mathcal{H}}_{\mathrm{ex}}$, such as:

$$+J\hat{\boldsymbol{S}}_1 \cdot \hat{\boldsymbol{S}}_2 \qquad +2J\hat{\boldsymbol{S}}_1 \cdot \hat{\boldsymbol{S}}_2 \qquad -J\hat{\boldsymbol{S}}_1 \cdot \hat{\boldsymbol{S}}_2 \qquad -2J\hat{\boldsymbol{S}}_1 \cdot \hat{\boldsymbol{S}}_2 \tag{2.37}$$

and so care must be taken when comparing J-values from literature. J-values defined in this thesis adopt the $+J$ convention, like in the EPR simulation package EasySpin.[130]

significant isotropic hyperfine coupling can also occur in systems with π-electrons through spin polarisation effects, as is the case in organic radicals.[116] The anisotropic component, $\hat{\boldsymbol{S}} \cdot \boldsymbol{A}_{\text{dip}} \cdot \hat{\boldsymbol{I}}$, reflects a through-space dipole-dipole interaction that outweighs a_{iso} at longer electron-nuclear distances.

In organic molecules, there are many magnetic nuclei present in the molecular structure and the hyperfine Hamiltonian is a sum of the interaction of the electron spin with each magnetic nucleus:

$$\hat{\mathcal{H}}_{\text{hf}} = \sum_{i=1}^{n} \hat{\boldsymbol{S}} \cdot \boldsymbol{A}_i \cdot \hat{\boldsymbol{I}}_i \tag{2.40}$$

Similar to $\boldsymbol{g}$ and $\boldsymbol{D}$, $\boldsymbol{A}$ can be diagonalised by an appropriate transformation into its principal axis system ($\boldsymbol{U}_A^{\text{T}} \boldsymbol{A} \boldsymbol{U}_A$); importantly, the $\boldsymbol{g}$, $\boldsymbol{D}$, and $\boldsymbol{A}$ principal axes are not necessarily the same. The $\boldsymbol{A}_{\text{dip}}$ part of the $\boldsymbol{A}$-tensor is traceless, and so its principal values can be expressed in terms of a dipolar coupling constant, T, and a rhombicity parameter, η, bounded between 0 and 1:

$$\boldsymbol{A} = \begin{pmatrix} A_x & 0 & 0 \\ 0 & A_y & 0 \\ 0 & 0 & A_z \end{pmatrix} = \begin{pmatrix} a_{\text{iso}} - T(1-\eta) & 0 & 0 \\ 0 & a_{\text{iso}} - T(1+\eta) & 0 \\ 0 & 0 & a_{\text{iso}} + 2T \end{pmatrix} \tag{2.41}$$

with T, within the point-dipole approximation, equal to

$$T = \frac{\mu_0}{4\pi\hbar} g_{\text{e}} \mu_{\text{B}} g_{\text{n}} \mu_{\text{N}} \left\langle \frac{1}{r^3} \right\rangle \tag{2.42}$$

In organic molecules, delocalisation of electron spin density across the π-system results in many small hyperfine couplings. This typically causes the hyperfine structure to be unresolved in EPR spectra, contributing primarily to line broadening. The strength of the hyperfine interaction, however, does provide useful information on the extent of spin delocalisation, and can be studied using pulse EPR techniques, discussed in Section 2.8.

2.2.5 Nuclear Quadrupole Interaction

For nuclei with spin quantum number $I \geq 1$, an additional contribution to the spin Hamiltonian arises from the nuclear quadrupole interaction. This interaction is analogous in form to the zero-field interaction, but it originates from a different physical mechanism.

Specifically, the nuclear quadrupole interaction stems from the electrostatic interaction between the non-spherical nuclear charge distribution, characteristic of nuclei with quadrupole moments, and the electric field gradient produced by

an asymmetric distribution of surrounding electron density. Molecular asymmetry, nearby electronegative atoms, or local bonding geometries can result in uneven electron charge distributions that give rise to measurable electric field gradients at the nucleus.[133] The spin Hamiltonian due to the quadrupole interaction is given by:

$$\hat{\mathcal{H}}_{\mathrm{nq}} = \hat{\boldsymbol{I}} \cdot \boldsymbol{Q} \cdot \hat{\boldsymbol{I}} \tag{2.43}$$

with $\boldsymbol{Q}$ the quadrupole tensor, which depends both on the nuclear quadrupole moment and the electric field gradient at the nucleus. This tensor captures the effect of deviations from spherical symmetry in the nuclear charge distribution. The magnitude of the nuclear quadrupole interaction is generally small compared to other spin interactions.

2.2.6 Nuclear-Nuclear Interaction

Nuclear spins may also interact with other nuclear spins in their vicinity, of which there are plenty in organic molecules. The interaction is isomorphic to the electron-electron and electron-nuclear interactions and the Hamiltonian can be expressed in a similar form as the dipolar and exchange interactions in Equations 2.28 and 2.36:

$$\begin{aligned}\hat{\mathcal{H}}_{\mathrm{nn}} &= \hat{\boldsymbol{I}}_1 \cdot \boldsymbol{D}_{\mathrm{nn}} \cdot \hat{\boldsymbol{I}}_2 \\ &= d_{\mathrm{nn,iso}} \hat{\boldsymbol{I}}_1 \cdot \hat{\boldsymbol{I}}_2 + \frac{\mu_0}{4\pi\hbar} (g_{\mathrm{n}}\mu_{\mathrm{N}})^2 \frac{1}{r^3} \left(\hat{\boldsymbol{I}}_1 \cdot \hat{\boldsymbol{I}}_2 - \frac{3}{r^2} (\hat{\boldsymbol{I}}_1 \cdot \boldsymbol{r})(\hat{\boldsymbol{I}}_2 \cdot \boldsymbol{r}) \right)\end{aligned} \tag{2.44}$$

The far weaker magnetic moment associated with nuclei often renders the contribution of $\hat{\mathcal{H}}_{\mathrm{nn}}$ to the overall spin Hamiltonian negligible, although, in a few cases, it can impact the signal shape in pulse EPR hyperfine experiments.[134,135]

2.3 Line Broadening Mechanisms

EPR spectra are typically not composed of perfectly sharp, discrete lines; rather, the observed spectral lines are broadened by several effects. At a fundamental level, any excited state with a finite lifetime is subject to lifetime broadening, as described by the uncertainty principle:

$$\tau \, \Delta E \geq \frac{\hbar}{2} \tag{2.45}$$

where τ is the lifetime of the state and ΔE the uncertainty in its energy. A shorter lifetime increases the energy uncertainty, leading to a wider distribution of resonance frequencies and thus broadening the idealised 'stick' spectrum.

Broadening mechanisms in EPR are typically categorised as homogeneous or inhomogeneous. **Homogeneous broadening**, like lifetime broadening, arises from dynamic processes that uniformly affect all spins with the same resonance frequencies, such as fluctuating local fields arising from random spin flips in the environment. In contrast, **inhomogeneous broadening** results from static variations in the local spin environments across the sample. These include distributions in spin Hamiltonian parameters ($\boldsymbol{g}, \boldsymbol{D}, \boldsymbol{A}$), unresolved hyperfine splittings, and local magnetic field inhomogeneities. These effects cause each spin to resonate at slightly different field values with the overall EPR line a convolution of many shifted resonances, producing a broadened line shape that typically follows a Gaussian distribution.

Disorder in the molecular environment leads to variations in local structure, which manifest as small shifts in the spin Hamiltonian tensor components. This distribution in parameter values is termed *strain*, and contributes to inhomogeneous broadening of the EPR signal. Strain is generally anisotropic, with different degrees of spread along g_x, g_y, and g_z, and can be modelled as a Gaussian distribution about the principal g-values (and similarly for $\boldsymbol{D}$ and $\boldsymbol{A}$). The effect of strain is exemplified in Figure 2.5. In the case shown, along with a homogeneous line broadening, strain is also modelled, impacting only g_x. As g_x-strain, defined as the full-width half-maximum of the Gaussian distribution of g_x-values, increases, the linewidth broadens around the field position of g_x.

Importantly, while inhomogeneous broadening contributions from anisotropic spin-field interactions, like the electron Zeeman interaction, increase with the magnetic field strength, others such as unresolved hyperfine or dipolar couplings are independent of the magnetic field, and their broadening on the spectrum can be mitigated by measurements at higher microwave frequencies, resolving anisotropy and overlapping features more clearly.

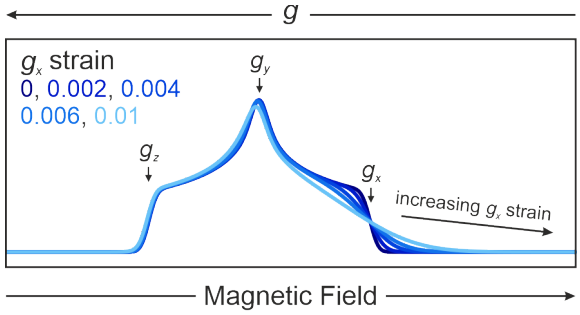

Figure 2.5: Simulated EPR spectra for an electron spin system with orthorhombic g-values, $[g_x, g_y, g_z] = [1.99, 2.00, 2.01]$, with different amounts of g_x-strain. The g-strain value is defined as the full-width half maximum of the Gaussian distribution of g-values; as the g_x-strain increases, the broadening around the g_x field position increases.

2.4 Spin-Polarised Photoinduced States

In systems with unpaired electron spins, the spin Hamiltonian determines the energy levels and character of the spin states. These energy levels, in turn, govern how the population of spins is distributed among the available spin states under thermal equilibrium. *Spin polarisation* refers to any deviation from equal spin populations, and it directly influences the observable EPR signal and the dynamics of the system.

At thermal equilibrium, spin polarisation is described by the Boltzmann distribution, with lower-energy states more populated than higher-energy ones. The probability, p_i, of the system being in spin state $|i\rangle$ is a function of the state's energy, E_i, and the available thermal energy:

$$p_i = \frac{\mathrm{e}^{-\frac{E_i}{k_\mathrm{B}T}}}{\sum_{j=1}^{n} \mathrm{e}^{-\frac{E_j}{k_\mathrm{B}T}}} = \frac{1}{N}\mathrm{e}^{-\frac{E_i}{k_\mathrm{B}T}} \tag{2.46}$$

where k_B is the Boltzmann constant, N is a normalisation constant, and there are n possible spin states. For a single electron in a magnetic field, the population of the two spin states, $|\alpha\rangle$ and $|\beta\rangle$, can be calculated from their probabilities, which can then be used to define the spin polarisation P:

$$\begin{aligned} N_\alpha &= N_0 p_\alpha = \frac{N_0}{N}\mathrm{e}^{-\frac{g\mu_\mathrm{B}B_0}{2k_\mathrm{B}T}} \\ N_\beta &= N_0 p_\beta = \frac{N_0}{N}\mathrm{e}^{\frac{g\mu_\mathrm{B}B_0}{2k_\mathrm{B}T}} \end{aligned} \qquad P = \frac{N_\beta - N_\alpha}{N_\beta + N_\alpha} \tag{2.47}$$

with N_0 the total number of spins. By making use of a Taylor series approximation ($\mathrm{e}^x = 1 + x + \ldots$), relying on the assumption that $k_\mathrm{B}T \gg g\mu_\mathrm{B}B_0$, which is true for typical magnetic field strengths and temperatures used in EPR, the spin polarisation can be simplified to:

$$\begin{aligned} P = \frac{\mathrm{e}^{\frac{g\mu_\mathrm{B}B_0}{2k_\mathrm{B}T}} - \mathrm{e}^{-\frac{g\mu_\mathrm{B}B_0}{2k_\mathrm{B}T}}}{\mathrm{e}^{\frac{g\mu_\mathrm{B}B_0}{2k_\mathrm{B}T}} + \mathrm{e}^{-\frac{g\mu_\mathrm{B}B_0}{2k_\mathrm{B}T}}} &= \frac{\left(1 + \frac{g\mu_\mathrm{B}B_0}{2k_\mathrm{B}T} + \ldots\right) - \left(1 - \frac{g\mu_\mathrm{B}B_0}{2k_\mathrm{B}T} + \ldots\right)}{\left(1 + \frac{g\mu_\mathrm{B}B_0}{2k_\mathrm{B}T} + \ldots\right) + \left(1 - \frac{g\mu_\mathrm{B}B_0}{2k_\mathrm{B}T} + \ldots\right)} \\ &\approx \frac{g\mu_\mathrm{B}B_0}{2k_\mathrm{B}T} \end{aligned} \tag{2.48}$$

At room temperature and X-band microwave frequency ($\nu = 9.8\,\mathrm{GHz}$, $B_0 = 350\,\mathrm{mT}$), the spin polarisation is 0.08%. EPR experiments are generally performed at cryogenic temperatures and high magnetic fields in order to maximise the spin polarisation and improve the signal-to-noise ratio.

However, many systems, particularly paramagnetic states generated following photoexcitation, exhibit non-equilibrium spin polarisation, where population differences arise from spin-selective generation and decay pathways rather than thermal

energy. These polarisations are often much larger in magnitude than Boltzmann polarisation and carry detailed information about the underlying spin physics.[136–138] In the following section, the spin polarisations and underlying spin interactions of the key photoinduced paramagnetic states in donor:acceptor OPV blends are examined. These are the charge-transfer states and separated charges that play critical roles in efficient charge generation, as well as the triplet states that are detrimental to OPV performance.

2.4.1 Separated Charges

The spin Hamiltonian for two spatially separated charges on the donor and acceptor molecules in an OPV blend includes the electron Zeeman interactions and hyperfine couplings to nearby nuclear spins:

$$\begin{aligned}\hat{\mathcal{H}}_{\mathrm{SC}} &= \hat{\mathcal{H}}_{\mathrm{eZ,D}} + \hat{\mathcal{H}}_{\mathrm{eZ,A}} + \hat{\mathcal{H}}_{\mathrm{hf,D}} + \hat{\mathcal{H}}_{\mathrm{hf,A}} \\ &= \frac{\mu_{\mathrm{B}}}{\hbar}\boldsymbol{B}_0 \cdot \boldsymbol{g}_{\mathrm{D}} \cdot \hat{\boldsymbol{S}}_{\mathrm{D}} + \frac{\mu_{\mathrm{B}}}{\hbar}\boldsymbol{B}_0 \cdot \boldsymbol{g}_{\mathrm{A}} \cdot \hat{\boldsymbol{S}}_{\mathrm{A}} + \sum_{i=1}^{n} \hat{\boldsymbol{S}}_{\mathrm{D}} \cdot \boldsymbol{A}_{\mathrm{D},i} \cdot \hat{\boldsymbol{I}}_i + \sum_{j=1}^{m} \hat{\boldsymbol{S}}_{\mathrm{A}} \cdot \boldsymbol{A}_{\mathrm{A},j} \cdot \hat{\boldsymbol{I}}_j \\ &\approx \frac{\mu_{\mathrm{B}}}{\hbar}\boldsymbol{B}_0 \cdot \boldsymbol{g}_{\mathrm{D}} \cdot \hat{\boldsymbol{S}}_{\mathrm{D}} + \frac{\mu_{\mathrm{B}}}{\hbar}\boldsymbol{B}_0 \cdot \boldsymbol{g}_{\mathrm{A}} \cdot \hat{\boldsymbol{S}}_{\mathrm{A}}\end{aligned} \tag{2.49}$$

where the subscripts D and A denote the donor and acceptor molecules, respectively. The first two terms describe the electron Zeeman interaction for each spin. The subsequent terms represent hyperfine couplings between each electron spin and nearby magnetic nuclei.

In OPV materials, these hyperfine interactions are generally too weak to be spectrally resolved and can usually be neglected in the spin Hamiltonian, instead contributing as line broadening, particularly at high microwave frequencies such as Q-band ($\nu = 33.9\,\mathrm{GHz}$) and above. Even at X-band, only nuclei with relatively large couplings (greater than 10 MHz) tend to produce resolved hyperfine structure.

For a single molecular orientation and in the absence of resolved hyperfine structure, each separated charge (donor or acceptor) contributes a single EPR transition at a field determined by its g-value. In disordered OPV samples, where molecules adopt many random orientations, this leads to a powder pattern, a broadened EPR signal shaped by the anisotropy of the g-values. If the donor and acceptor have sufficiently different g-values, their signals appear as two distinct features in the spectrum, as shown in Figure 2.6. When the g-values are similar, the signals overlap, giving a single broadened peak. The separated charges in OPV blends are typically long-lived under steady-state illumination and relax to thermal equilibrium, resulting in spin populations that follow a Boltzmann distribution. Consequently, their EPR spectrum exhibits a purely absorptive lineshape.

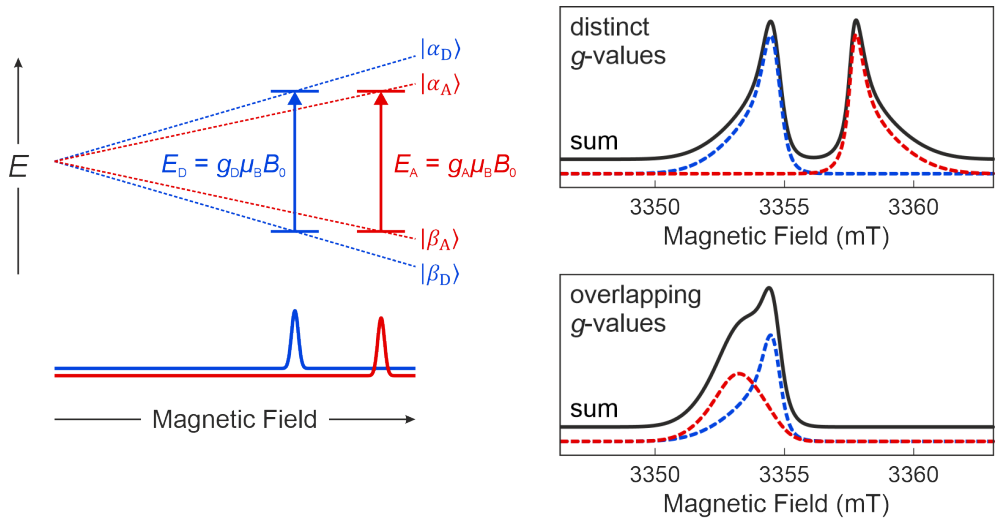

Figure 2.6: Left) Energy level spitting of the spins of the charged states on the donor and acceptor molecules due to the electron Zeeman interaction, for a single molecular orientation. Right) W-band ($\nu = 94\,\text{GHz}$) powder spectrum of the charged states (black), with donor (blue) and acceptor (red) signal contributions offset, using g-values and linewidths of OPV blends with distinct g-values (PM6:PCBM) and overlapping g-values (PM6:Y6), determined from EPR spectra in Chapter 3 (Tables 3.1 and 3.4 in Section 3.3.1).

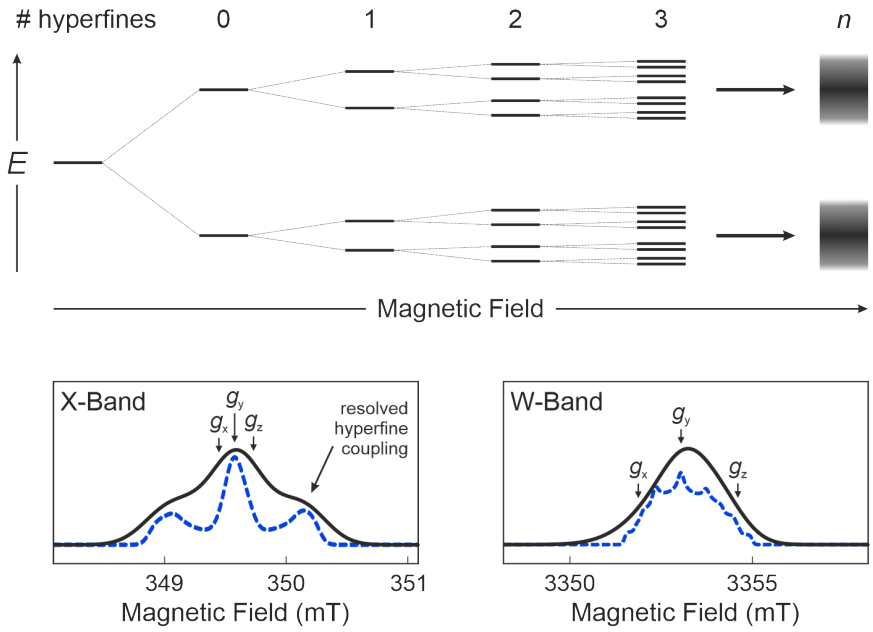

Figure 2.7: Top) Energy level splitting for an electron in the presence of many $I = \frac{1}{2}$ nuclei; as the number of hyperfine interactions increases, the energy level splittings tend to a broad distribution of levels, where the many possible EPR transitions occur at similar resonance positions, and are no longer individually resolved. Bottom) Simulated EPR spectrum of $Y6^{\bullet-}$, using parameters from Chapter 3 (Table 3.4 in Section 3.3.3), at X-band and W-band. The pair of hyperfine interactions ($A_{\text{max}} = 20\,\text{MHz}$) are resolvable at X-band, but not W-band. Simulations with reduced homogeneous line broadening (blue dashed lines) reveal the effect of the hyperfine splittings more clearly.

While the spectra in Figure 2.6 were simulated without considering hyperfine interactions, these interactions can still alter the spin energy levels and EPR lineshape, as illustrated in Figure 2.7. The coupling to a nucleus of spin I splits each electron spin level into $2I+1$ components, with the energy splitting determined by the hyperfine interaction strength and, to a lesser extent, the nuclear Zeeman interaction. This splitting is much smaller than the electron Zeeman interaction and the energy level diagram becomes more complex as additional, non-equivalent nuclei are included. In systems with many weakly-coupled nuclei, the resulting spin energy levels form a dense manifold. This leads to a large number of closely spaced transitions, which overlap in frequency and give rise to a broadened EPR spectrum with unresolved hyperfine structure.

The hyperfine resolution, particularly at higher microwave frequencies, is demonstrated through simulations of the EPR spectrum of the non-fullerene acceptor $Y6^{\bullet-}$, using parameters from Chapter 3 (Table 3.4 in Section 3.3.1). The simulation includes two orthorhombic proton hyperfine interactions, each with a largest principal value of approximately 20 MHz, corresponding to a splitting of about 0.7 mT. At X-band, this interaction is comparable to the intrinsic linewidth and gives rise to subtle features such as shoulders or asymmetric broadening. Simulations with reduced homogeneous broadening (blue dashed lines) reveal the expected $1:2:1$ splitting for a pair of hyperfine interactions more clearly.

At higher microwave frequencies such as W-band ($\nu = 94$ GHz), spectral broadening due to g-strain caused by the distribution of molecular environments becomes the dominant effect. Since hyperfine couplings do not scale with microwave frequency, the relative impact of g-strain on the overall linewidth increases at higher magnetic fields, effectively masking the smaller hyperfine splittings. Consequently, in these disordered OPV materials, the W-band spectrum appears as a single broad peak without any resolved hyperfine structure.

2.4.2 Charge-Transfer States

Charge-transfer (CT) states, also referred to as spin-correlated radical pairs, consist of weakly-coupled spins located on the donor and acceptor molecules. These species form immediately following photoinduced electron transfer at the donor:acceptor interface. Unlike fully separated charges, the electron and hole in a CT state remain electrostatically bound by the Coulomb interaction, with partial wavefunction overlap that depends on the donor:acceptor geometry and spatial extent of the molecular orbitals. This proximity leads to spin-spin interactions between the two unpaired electrons, which must be accounted for in the spin Hamiltonian. The spin Hamiltonian for a CT state includes contributions from

the electron Zeeman interaction, electron-electron exchange and dipolar couplings, and electron-nuclear hyperfine interactions:

$$\hat{\mathcal{H}}_{\mathrm{CT}} = \hat{\mathcal{H}}_{\mathrm{eZ,D}} + \hat{\mathcal{H}}_{\mathrm{eZ,A}} + \hat{\mathcal{H}}_{\mathrm{hf,D}} + \hat{\mathcal{H}}_{\mathrm{hf,A}} + \hat{\mathcal{H}}_{\mathrm{ex}} + \hat{\mathcal{H}}_{\mathrm{dip}} \tag{2.50}$$

A simple case of isotropic g-values for donor and acceptor molecules, axial dipolar coupling, and no resolved hyperfine couplings is considered, and the spin Hamiltonian reduces to:

$$\hat{\mathcal{H}}_{\mathrm{CT}} = \frac{\mu_{\mathrm{B}}}{\hbar} B_0 g_{\mathrm{D}} \hat{S}_{\mathrm{D},z} + \frac{\mu_{\mathrm{B}}}{\hbar} B_0 g_{\mathrm{A}} \hat{S}_{\mathrm{A},z} + J\, \hat{\boldsymbol{S}}_{\mathrm{D}} \cdot \hat{\boldsymbol{S}}_{\mathrm{A}} + \frac{D}{2}\left(3\hat{S}_{\mathrm{D},z}\hat{S}_{\mathrm{A},z} - \hat{\boldsymbol{S}}_{\mathrm{D}} \cdot \hat{\boldsymbol{S}}_{\mathrm{A}}\right) \tag{2.51}$$

This spin Hamiltonian may be represented in matrix form in either the coupled or uncoupled basis. The matrix element $\mathcal{H}_{ij}$ corresponds to $\langle i|\, \hat{\mathcal{H}}_{\mathrm{CT}}\, |j\rangle$, with i/j referring to the spin states i and j in that basis representation. In the coupled basis $\{|\mathrm{T}_+\rangle, |\mathrm{T}_0\rangle, |\mathrm{S}\rangle, |\mathrm{T}_-\rangle\}$, the spin Hamiltonian becomes:

$$\hat{\mathcal{H}}_{\mathrm{CT}} = \begin{pmatrix} \omega + \frac{1}{4}(J+D) & 0 & 0 & 0 \\ 0 & \frac{1}{4}(J-2D) & \delta\omega & 0 \\ 0 & \delta\omega & -\frac{3}{4}J & 0 \\ 0 & 0 & 0 & -\omega + \frac{1}{4}(J+D) \end{pmatrix} \tag{2.52}$$

with

$$\omega = \frac{\mu_{\mathrm{B}} B_0}{2\hbar}(g_{\mathrm{D}} + g_{\mathrm{A}}) \qquad \delta\omega = \frac{\mu_{\mathrm{B}} B_0}{2\hbar}(g_{\mathrm{D}} - g_{\mathrm{A}}) \tag{2.53}$$

Alternatively, in the uncoupled basis $\{|\alpha_{\mathrm{D}}\alpha_{\mathrm{A}}\rangle, |\alpha_{\mathrm{D}}\beta_{\mathrm{A}}\rangle, |\beta_{\mathrm{D}}\alpha_{\mathrm{A}}\rangle, |\beta_{\mathrm{D}}\beta_{\mathrm{A}}\rangle\}$, the spin Hamiltonian is:

$$\hat{\mathcal{H}}_{\mathrm{CT}} = \begin{pmatrix} \omega + \frac{1}{4}(J+D) & 0 & 0 & 0 \\ 0 & \delta\omega - \frac{1}{4}(J+D) & \frac{1}{4}(2J-D) & 0 \\ 0 & \frac{1}{4}(2J-D) & -\delta\omega - \frac{1}{4}(J+D) & 0 \\ 0 & 0 & 0 & -\omega + \frac{1}{4}(J+D) \end{pmatrix} \tag{2.54}$$

In both representations, the spin Hamiltonian is block-diagonal. A fully-diagonal Hamiltonian would indicate that all basis states are eigenstates of the system; however, the presence of non-zero off-diagonal terms shows that neither the uncoupled or coupled spin bases fully diagonalise the Hamiltonian and are eigenbases.

Inspection of Equations 2.52 and 2.54 shows that the states $|\mathrm{T}_+\rangle \equiv |\alpha_{\mathrm{D}}\alpha_{\mathrm{A}}\rangle$ and $|\mathrm{T}_-\rangle \equiv |\beta_{\mathrm{D}}\beta_{\mathrm{A}}\rangle$ are eigenstates of the spin Hamiltonian with well-defined energies:

$$E_{\pm} = \pm\omega + \frac{1}{4}(J+D) \tag{2.55}$$

The remaining two eigenstates are formed from linear combination of $|\mathrm{S}\rangle$ and $|\mathrm{T}_0\rangle$ in the coupled basis, or equivalently, $|\alpha_\mathrm{D}\beta_\mathrm{A}\rangle$ and $|\beta_\mathrm{D}\alpha_\mathrm{A}\rangle$ in the uncoupled basis. These pairs of states are related through the transformation defined in Equation 2.19, where $|\mathrm{S}\rangle$ and $|\mathrm{T}_0\rangle$ are the antisymmetric and symmetric combinations, respectively, of $|\alpha_\mathrm{D}\beta_\mathrm{A}\rangle$ and $|\beta_\mathrm{D}\alpha_\mathrm{A}\rangle$.

In the **strong coupling** regime, where the spin-spin interactions dominate over the difference in spin resonance frequencies $\left(\frac{1}{4}\left|2J-D\right| \gg \delta\omega\right)$, the off-diagonal elements ($\delta\omega$) in the coupled basis become negligible. In this limit, $|\mathrm{S}\rangle$ and $|\mathrm{T}_0\rangle$ approximate the true eigenstates of the spin system, making the coupled basis the most appropriate representation.

In the **weak coupling** regime, where the difference in spin resonance frequencies outweighs the spin-spin interactions $\left(\frac{1}{4}\left|2J-D\right| \ll \delta\omega\right)$, the off-diagonal elements $\left(\frac{1}{4}\left(2J-D\right)\right)$ in the uncoupled basis become negligible. The uncoupled basis therefore provides a more accurate description, with $|\alpha_\mathrm{D}\beta_\mathrm{A}\rangle$ and $|\beta_\mathrm{D}\alpha_\mathrm{A}\rangle$ serving as better approximations to the eigenstates.

Outside these limiting regimes, the true eigenstates arise from mixing of these basis states. In the coupled basis, $|\mathrm{S}\rangle - |\mathrm{T}_0\rangle$ mixing is driven by the difference in spin resonance frequencies $\delta\omega$. In the uncoupled basis, it is the spin-spin interactions, J and D, that mix the uncoupled basis states $|\alpha_\mathrm{D}\beta_\mathrm{A}\rangle$ and $|\beta_\mathrm{D}\alpha_\mathrm{A}\rangle$.

The eigenstates and energies of the CT spin states are obtained by diagonalisation of the spin Hamiltonian:

$$\begin{aligned}
|1\rangle &= |\mathrm{T}_-\rangle && = |\beta_\mathrm{D}\beta_\mathrm{A}\rangle \\
|2\rangle &= \cos\phi\ |\mathrm{T}_0\rangle - \sin\phi\ |\mathrm{S}\rangle && = \sin\left(\phi+\tfrac{\pi}{4}\right)|\alpha_\mathrm{D}\beta_\mathrm{A}\rangle + \cos\left(\phi+\tfrac{\pi}{4}\right)|\beta_\mathrm{D}\alpha_\mathrm{A}\rangle \\
|3\rangle &= \sin\phi\ |\mathrm{T}_0\rangle + \cos\phi\ |\mathrm{S}\rangle && = \cos\left(\phi+\tfrac{\pi}{4}\right)|\alpha_\mathrm{D}\beta_\mathrm{A}\rangle - \sin\left(\phi+\tfrac{\pi}{4}\right)|\beta_\mathrm{D}\alpha_\mathrm{A}\rangle \\
|4\rangle &= |\mathrm{T}_+\rangle && = |\alpha_\mathrm{D}\alpha_\mathrm{A}\rangle
\end{aligned} \tag{2.56}$$

and

$$\begin{aligned}
E_1 &= -\omega + \tfrac{1}{4}(J+D) \\
E_2 &= -\Omega - \tfrac{1}{4}(J+D) \\
E_3 &= +\Omega - \tfrac{1}{4}(J+D) \\
E_4 &= +\omega + \tfrac{1}{4}(J+D)
\end{aligned} \tag{2.57}$$

with

$$\phi = \frac{1}{2}\arctan\left(\frac{\delta\omega}{\frac{1}{4}(2J-D)}\right) \qquad \Omega = \sqrt{\delta\omega^2 + \left(\tfrac{1}{4}(2J-D)\right)^2} \tag{2.58}$$

The angle ϕ describes the extent of coupling. When $\frac{1}{4}\left|2J-D\right| \ll \delta\omega$ ($\phi = 0$), the coupled basis states become the eigenstates, while for $\phi = \frac{\pi}{4}$, the eigenstates are the uncoupled basis states.

The observable EPR transitions between eigenstates of a weakly-coupled CT state occur at the following frequencies:

$$\begin{aligned} |3\rangle \leftrightarrow |4\rangle \qquad & \omega_{34} = \omega - \Omega + \frac{1}{2}(J + D) \\ |1\rangle \leftrightarrow |2\rangle \qquad & \omega_{12} = \omega - \Omega - \frac{1}{2}(J + D) \\ |2\rangle \leftrightarrow |4\rangle \qquad & \omega_{24} = \omega + \Omega + \frac{1}{2}(J + D) \\ |1\rangle \leftrightarrow |3\rangle \qquad & \omega_{13} = \omega + \Omega - \frac{1}{2}(J + D) \end{aligned} \tag{2.59}$$

These transitions are ordered by increasing energy under the assumptions that $\Omega > |J|, |D|$, with $J < 0$ and the dipolar vector $\boldsymbol{r}$ aligned with $\boldsymbol{B}_0$ ($\theta = 0°$), giving $D = -2d < 0$ from Equation 2.31.

In the frequency domain, the four transitions are centred at their linear frequencies $\nu_{ij} = \omega_{ij}/2\pi$, as illustrated in Figure 2.8. The spectrum is centred at $\nu = \omega/2\pi$ and exhibits a doublet-doublet structure: the overall splitting between the doublets is set by Ω, while the further splitting within each doublet arise from the spin-spin coupling term $|J + D|$, which for the case of $\theta = 0°$ is $|J - 2d|$. Under thermal equilibrium, eigenstate populations are determined by the Boltzmann distribution, and all transitions appear as absorptions. For simplicity, all transition intensities are assumed to be equal, with roofing effects neglected.

In EPR spectroscopy, spectra are typically recorded by varying the external magnetic field strength B_0, rather than the microwave frequency ν. As B_0 is varied, the spin Hamiltonian changes accordingly, and resonance conditions shift. While

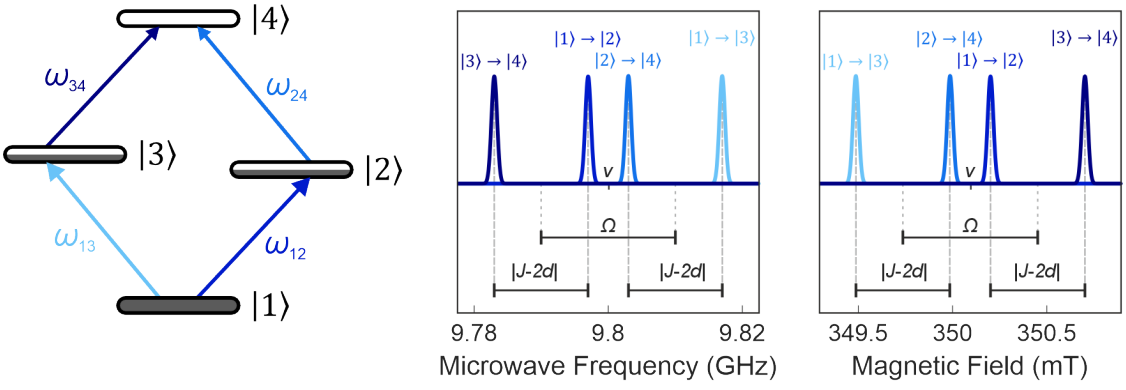

Figure 2.8: Left) Energy level diagram for a charge-transfer state under thermal equilibrium, showing four absorptive transitions. Sublevel populations are illustrated by the shaded area of the sublevel. Right) Simulated frequency-swept and field-swept EPR stick spectra, with roofing effects omitted. Simulation parameters: $g_{\mathrm{D}} = 1.998$, $g_{\mathrm{A}} = 2.008$, $J = -2\,\mathrm{MHz}$, $d = 6\,\mathrm{MHz}$, and $\theta = 0°$, giving $D = -2d$ via Equation 2.31.

transition frequencies are straightforwardly obtained from differences in energy eigenvalues, resonance field positions are not as easily accessible analytically.[130]

To determine the resonance fields, the microwave frequency ω_{mw} is fixed, such that:

$$\omega_{\mathrm{mw}} = \omega_{ij}(B_0) \tag{2.60}$$

for each transition. Inserting the expressions for ω and Ω in terms of B_0, from Equations 2.53 and 2.58, the resonance condition for, e.g., the $|3\rangle \leftrightarrow |4\rangle$ transition becomes:

$$\omega_{34} = \frac{\mu_{\mathrm{B}} B_0}{2\hbar}(g_{\mathrm{D}} + g_{\mathrm{A}}) - \sqrt{\left(\frac{\mu_{\mathrm{B}} B_0}{2\hbar}(g_{\mathrm{D}} - g_{\mathrm{A}})\right)^2 + \left(\frac{1}{4}(2J - D)\right)^2} + \frac{1}{2}(J + D) \tag{2.61}$$

This is function of B_0 that, along with analogous ones for the remaining transitions, must be solved analytically or numerically to obtain the corresponding resonance fields.[139] Higher-energy transitions require lower fields to match a fixed microwave frequency, and so the order of the transitions is reversed in a field-swept spectrum. For instance, the $|1\rangle \rightarrow |3\rangle$ transition, being the highest in energy, appears at the lowest magnetic field. Thus, the shape of the field-swept spectrum appears as a mirror image of the frequency-swept spectrum. From the observed field separations, both Ω and $J - 2d$ can be extracted in magnetic field units.

The previous expressions consider a single crystal in which all CT states are identically aligned with respect to the external magnetic field, specifically with the dipolar vector $\boldsymbol{r}$ parallel to $\boldsymbol{B}_0$ ($\theta = 0°$). In this orientation, the angular term $(1 - 3\cos^2\theta)$ evaluates to -2, resulting in a dipolar coupling of $D = -2d$.

At the opposite extreme, for a single crystal in which $\boldsymbol{r}$ is perpendicular to $\boldsymbol{B}_0$ ($\theta = 90°$), the angular term becomes $+1$, giving $D = +d$. This reversal in sign has a significant effect on the CT energy levels. In particular, when $|d| > |J|$, the reordering of state energies causes a reversal in the field positions of certain transitions. At $\theta = 0°$, the $|1\rangle \rightarrow |3\rangle$ transition occurs at the lowest magnetic field, whereas for $\theta = 90°$, it is the $|2\rangle \rightarrow |4\rangle$ transition that shifts to the lowest field. These two limiting cases are highlighted in dark and light green in Figure 2.9.

In a powder sample, the molecular orientations are distributed uniformly with respect to the magnetic field. The angle θ between $\boldsymbol{r}$ and $\boldsymbol{B}_0$ can take any value between 0° and 90°, producing a continuous range of dipolar couplings from $D = -2d$ to $D = +d$. As a result, each transition is broadened into a feature that spans this entire range.

The contribution of each orientation corresponds to a discrete 'stick' spectrum, and the total EPR signal is the sum over all orientations. The powder spectrum for each transition shows two turning points, corresponding to the limiting values of D,

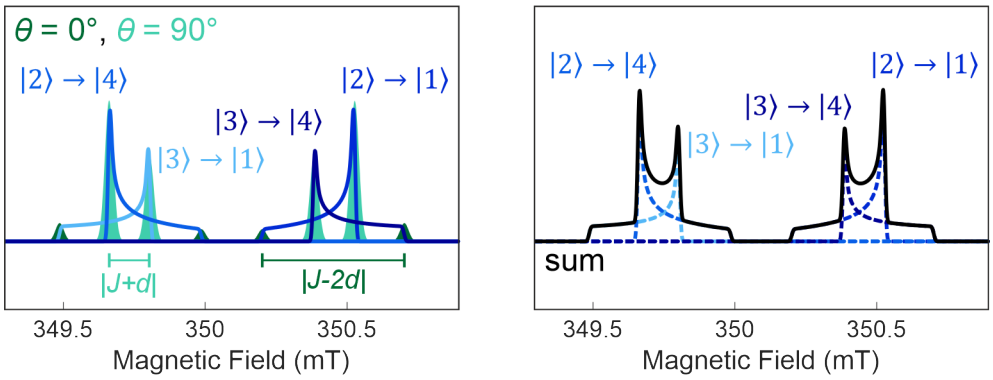

Figure 2.9: Left) Powder patterns for the four CT state transitions. Single crystal spectra are also shown, for the dipolar vector parallel ($\theta = 0°$ - dark green) and perpendicular to the magnetic field ($\theta = 90°$ - light green). Simulation parameters: $g_D = 1.998$, $g_A = 2.002$, $J = -2\,\text{MHz}$, and $d = 6\,\text{MHz}$, giving $D = -2d$ when $\theta = 0°$, and $D = +d$ when $\theta = 90°$ as per Equation 2.31. Right) Total EPR spectrum obtained as a sum of the four CT state sublevel transitions (shown as dashed lines).

with increased intensity near the turning point for $\theta = 90°$. For an axial dipolar interaction, more molecules lie near $\theta = 90°$, where the density of orientations is greatest. This characteristic line shape is known as a *Pake pattern*, as shown in Figure 2.9. The left panel shows the powder patterns for the four CT state transitions, alongside the limiting single-crystal cases at 0° and 90°. The right panel shows the total EPR spectrum obtained by summing the individual transitions. The resulting lineshape exhibits sharp inner features and broad outer wings for each transition pair, directly reflecting the underlying angular dependence of the dipolar coupling.

Singlet-born Charge-Transfer State

When a CT state forms at a donor:acceptor interface from dissociation of a singlet exciton, the CT state inherits the spin configuration of the singlet exciton, due to conservation of spin angular momentum during the electron transfer process. Initially only CT eigenstates with singlet character will be populated. Based on the eigenstates derived earlier (Equation 2.56), this corresponds to $|2\rangle$ and $|3\rangle$. The pure triplet eigenstates, $|1\rangle$ and $|4\rangle$, remain unpopulated at the moment of CT state formation.

While this provides an intuitive picture of the initial spin configuration, a more general and quantitative framework is required to describe a range of population mechanisms and the subsequent time evolution of the spin states. This is provided by the *density matrix formalism*, which describes both populations of the eigenstates and coherences between them and their evolution in time. The density matrix $\hat{\rho}$ provides a complete statistical description of a quantum system.

The starting point is the definition of a quantum state. A pure quantum state is represented by a state vector $|\psi\rangle$ in a chosen basis $|i\rangle$:

$$|\psi_k\rangle = \sum_i c_i^{(k)} |i\rangle \tag{2.62}$$

with c_i the coefficient of the basis state $|i\rangle$ in the total state $|\psi_k\rangle$.

In a more general case, an ensemble of such systems may occupy a mixture of pure states $|\psi_k\rangle$, each with an associated probability p_k. Such a statistical mixture is referred to as a mixed state, and is described by the density matrix:

$$\hat{\rho} = \sum_k p_k |\psi_k\rangle \langle\psi_k| \tag{2.63}$$

where $|\psi_k\rangle \langle\psi_k|$ is the projection operator corresponding to the pure state $|\psi_k\rangle$, and the probabilities satisfy $\sum_k p_k = 1$. In matrix notation, the projection operator $|\psi_k\rangle \langle\psi_k|$ corresponds to the outer product $\boldsymbol{\psi}_k \boldsymbol{\psi}_k^\dagger$, where $\boldsymbol{\psi}_k$ is a column vector of coefficients and $\boldsymbol{\psi}_k^\dagger$ is its conjugate transpose. $\hat{\rho}$ is an $n \times n$ Hermitian matrix, where n is the number of basis states ($n = 4$ for a CT state with no hyperfine interactions).

The matrix elements of $\hat{\rho}$ in this basis are:

$$\rho_{ij} = \langle i| \hat{\rho} |j\rangle = \sum_k p_k \langle i|\psi_k\rangle \langle\psi_k|j\rangle = \sum_k p_k c_i^{(k)} c_j^{(k)*} \tag{2.64}$$

where $c_i^{(k)}$ is the coefficient of basis state $|i\rangle$ in the pure state $|\psi_k\rangle$. The diagonal elements ρ_{ii} represent the populations of basis states $|i\rangle$, while the off-diagonal elements ρ_{ij} encode the quantum coherences between states $|i\rangle$ and $|j\rangle$, in the eigenbasis of the spin Hamiltonian.

In the case of a singlet-born CT state, the system begins in a pure quantum state, specifically the spin singlet:

$$|\psi\rangle = |\mathrm{S}\rangle \tag{2.65}$$

Expressed in the CT eigenbasis $|1\rangle, |2\rangle, |3\rangle, |4\rangle$ (in ascending energy order), this singlet state takes the form (as derived in Equation 2.56):

$$|\mathrm{S}\rangle = \begin{pmatrix} 0 \\ -\sin\phi \\ \cos\phi \\ 0 \end{pmatrix} \tag{2.66}$$

indicating that the initial state is a coherent superposition of the eigenstates $|2\rangle$ and $|3\rangle$. The corresponding density matrix at $t = 0$ is:

$$\hat{\rho}(t=0) = |\mathrm{S}\rangle \langle\mathrm{S}| = \begin{pmatrix} 0 & 0 & 0 & 0 \\ 0 & \sin^2\phi & -\frac{1}{2}\sin 2\phi & 0 \\ 0 & -\frac{1}{2}\sin 2\phi & \cos^2\phi & 0 \\ 0 & 0 & 0 & 0 \end{pmatrix} \tag{2.67}$$

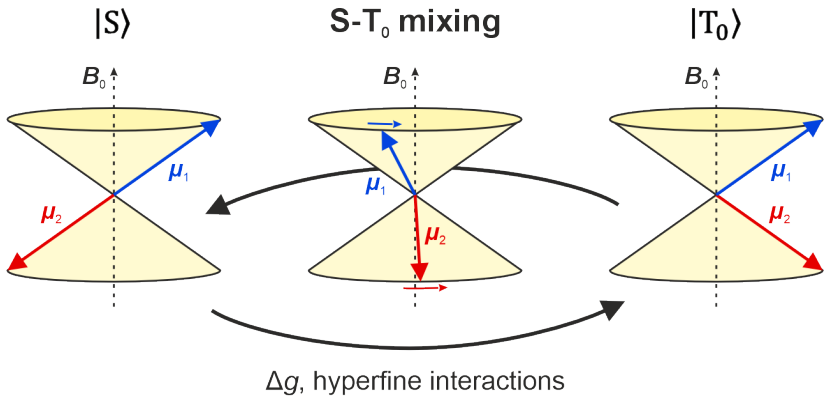

Figure 2.10: Mechanism of singlet-triplet mixing, due to differences in precession frequencies of the two electron spins.

clearly showing that population is initially confined to eigenstates $|2\rangle$ and $|3\rangle$:

$$p_1 = 0 \qquad p_2 = \sin^2\phi \qquad p_3 = \cos^2\phi \qquad p_4 = 0 \tag{2.68}$$

The presence of non-zero off-diagonal elements $\rho_{23} = \rho_{32} = -\frac{1}{2}\sin 2\phi$ reflects quantum coherence between $|2\rangle$ and $|3\rangle$, allowing for coherent oscillations between these eigenstates. In the coupled basis, this corresponds to mixing between $|\mathrm{S}\rangle$ and $|\mathrm{T}_0\rangle$.[140]

The physical origin of $|\mathrm{S}\rangle - |\mathrm{T}_0\rangle$ mixing can be intuitively understood using the vector model illustration in Figure 2.10. The magnetic moments associated with the unpaired electrons on the donor and acceptor precess around the external magnetic field with Larmor frequencies determined by their respective g-values. If $g_\mathrm{D} \neq g_\mathrm{A}$, the resulting difference in precession frequencies, $\delta\omega$, causes the spin configuration to evolve over time, periodically interconverting $|\mathrm{S}\rangle$ and $|\mathrm{T}_0\rangle$. Hyperfine interactions can also drive singlet-triplet mixing, particularly at low magnetic fields where $\delta\omega$ is small.

The oscillating microwave field $\boldsymbol{B}_1$ induces transitions between spin states by perturbing the coupled electron spins of the CT state. The resulting interaction is described by the perturbation Hamiltonian:

$$\hat{\mathcal{H}}_1(t) = \frac{\mu_\mathrm{B} B_1(t)}{\hbar} g_\mathrm{D} \hat{S}_{\mathrm{D},x} + \frac{\mu_\mathrm{B} B_1(t)}{\hbar} g_\mathrm{A} \hat{S}_{\mathrm{A},x} \tag{2.69}$$

The probability amplitude for a transition between eigenstates $|i\rangle$ and $|j\rangle$, by using Fermi's Golden Rule from Equation 2.16, is governed by the matrix element:

$$P_{ij} \propto \left| \langle i | \, \hat{S}_{\mathrm{D},x} + \hat{S}_{\mathrm{A},x} \, | j \rangle \right|^2 \tag{2.70}$$

The resulting EPR signal intensity depends on both the transition matrix element and the population difference between the two states:

$$I_{ij} \propto (p_i - p_j) P_{ij} \tag{2.71}$$

The sign of the population difference $p_i - p_j$ determines whether the transition will be in absorption ($p_i > p_j$) or in emission ($p_i < p_j$). For the four allowed transitions (see Equation 2.59), the transition probabilities are:

$$P_{12} = P_{24} = \frac{1}{2}\cos^2\phi \qquad P_{13} = P_{34} = \frac{1}{2}\sin^2\phi \tag{2.72}$$

The population differences between the states involved in the four transitions can be calculated from the previously determined eigenstate populations in Equation 2.68:

$$\begin{aligned} \Delta p_{12} &= p_1 - p_2 = -\sin^2\phi & \Delta p_{13} &= p_1 - p_3 = -\cos^2\phi \\ \Delta p_{24} &= p_2 - p_4 = +\sin^2\phi & \Delta p_{34} &= p_3 - p_4 = +\cos^2\phi \end{aligned} \tag{2.73}$$

which, using Equation 2.71, leads to the following four transition intensities, with corresponding transition frequencies:

$$\begin{aligned} I_{34} &\propto -\frac{1}{2}\sin^2\phi\cos^2\phi & \omega_{34} &= \omega - \Omega + \frac{1}{2}(J + D) \\ I_{12} &\propto +\frac{1}{2}\sin^2\phi\cos^2\phi & \omega_{12} &= \omega - \Omega - \frac{1}{2}(J + D) \\ I_{24} &\propto -\frac{1}{2}\sin^2\phi\cos^2\phi & \omega_{24} &= \omega + \Omega + \frac{1}{2}(J + D) \\ I_{13} &\propto +\frac{1}{2}\sin^2\phi\cos^2\phi & \omega_{13} &= \omega + \Omega - \frac{1}{2}(J + D) \end{aligned} \tag{2.74}$$

with all transitions having the same magnitude, regardless of the strength of the coupling, and alternating signs.

A model spectrum is constructed for the EPR signal of a singlet-born CT state, displayed in Figure 2.11. The spin parameters (g_{D}, g_{A}, J, and d) are the same as in the thermal equilibrium case in Figure 2.9, but the populations now reflect generation from a singlet precursor rather than thermal equilibrium. As before, a Pake pattern is observed for each of the four transitions, but in contrast to thermal equilibrium, two of the four transitions are now emissive. The overall EPR signal, resulting from the sum of the four transitions, arises from partial cancellation of these overlapping, oppositely-polarised transitions.

The examples discussed so far employ well-separated donor and acceptor g-values to clearly illustrate the influence of the spin-spin interactions J and d on the EPR spectrum. However, in OPV blends, the difference in g-values is smaller, typically

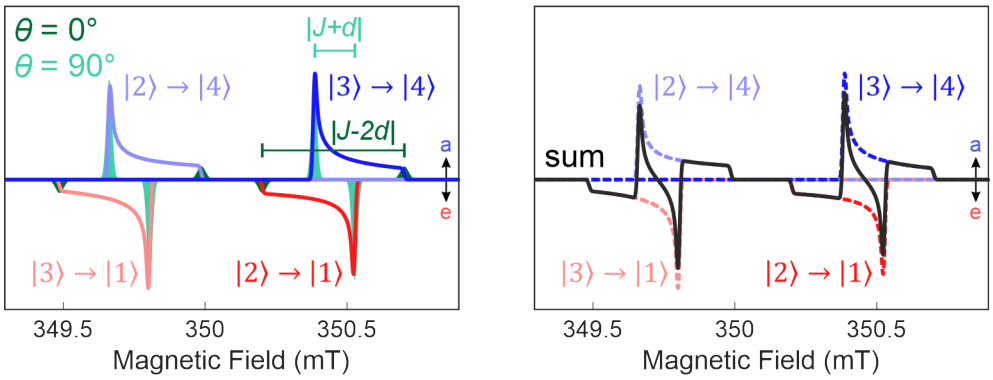

Figure 2.11: Left) Powder patterns for the four singlet-born CT state transitions. Single crystal spectra are also shown, for the dipolar vector parallel ($\theta = 0°$ - dark green) and perpendicular to the magnetic field ($\theta = 90°$ - light green). The same simulation parameters as Figure 2.9 are used. Right) Total EPR spectrum obtained as a sum of the four singlet-born CT state sublevel transitions (shown as dashed lines).

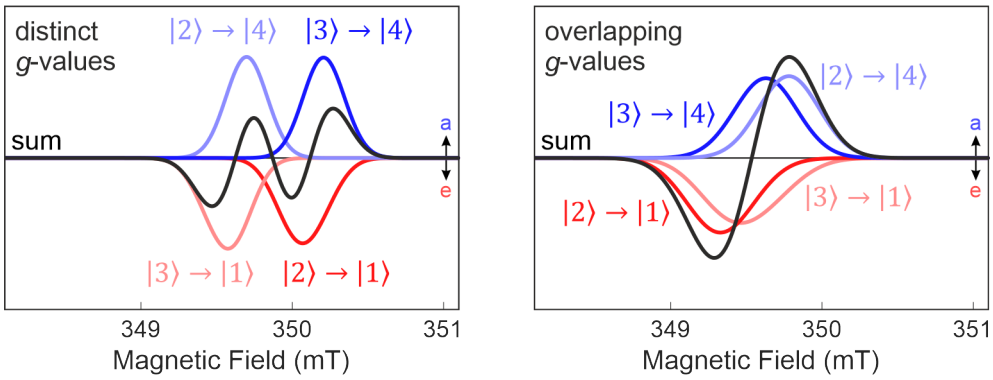

Figure 2.12: Simulated powder EPR spectra of a singlet-born CT state for an OPV blend with distinct g-values (PBDB-T:PCBM) and overlapping g-values (PBDB-T:ITIC), using spin system parameters from Chapter 5 (Table 5.3 in Section 5.3.3).

within the range 1.99 to 2.01. In such spin systems, the four CT state transitions occur at similar resonance field positions, leading to extensive spectral overlap and near-cancellation of absorptive and emissive components. As a consequence, the EPR spectra of singlet-born CT states in OPVs are exquisitely sensitive to the magnitude and relative signs of J and d, as well as the relative orientations of the $\boldsymbol{g}$-tensor and the dipolar coupling vector.

Simulated powder spectra of two donor:acceptor OPV blends, PBDB-T:PCBM and PBDB-T:ITIC, are shown in Figure 2.12, using the spin Hamiltonian parameters determined in Chapter 5, listed in Table 5.3 of Section 5.3.3. In both cases, line broadening due to g-strain, reflecting the distribution of local molecular environments, smooths out spectral structure. While this broadening reduces the visibility of sharp turning points associated with the dipolar coupling constant d, a distinctive polarisation pattern remains discernible: an *eaea*-polarised signal. For CT states in

systems with distinct donor and acceptor g-values, such as PBDB-T:PCBM, the four transitions are sufficiently separated to retain the alternating *eaea* polarisation characteristic of a singlet-born CT state. In contrast, for systems where the donor and acceptor EPR spectra have significant spectral overlap, such as PBDB-T:ITIC, the emissive and absorptive transitions coincide spectrally, and the resulting signal coalesces into an effective *ea* polarisation. Despite this collapse of the full *eaea* signature, the residual *ea* polarisation remains indicative of a singlet-born CT state.

The simulations of the CT state in PBDB-T:PCBM and PBDB-T:ITIC assume a negative exchange interaction ($J < 0$), consistent with experimental findings for OPV materials.[141] If, in contrast, the exchange coupling were positive, the ordering of energy levels would change, and an *aeae*-polarised signal would emerge instead.[142]

Triplet-born Charge-Transfer State

The CT state may originate not only from a singlet precursor, but alternatively from a triplet precursor.[138] In this case, the initial density matrix, $\hat{\rho}$, is expressed as a statistical mixture of the triplet sublevels:

$$\hat{\rho}(t=0) = p_+ \left|\mathrm{T}_+\right\rangle \left\langle\mathrm{T}_+\right| + p_0 \left|\mathrm{T}_0\right\rangle \left\langle\mathrm{T}_0\right| + p_- \left|\mathrm{T}_-\right\rangle \left\langle\mathrm{T}_-\right| \tag{2.75}$$

where the coefficients p_+, p_0, and p_- reflect the population distribution across the triplet basis states. These populations depend on the spin polarisation of the precursor triplet exciton and are governed by formation mechanisms discussed later in Section 2.4.3.

The initial triplet precursor can exhibit non-uniform spin sublevel populations, which will be preserved during CT state formation,[143] resulting in unequal populations across the CT sublevels. Overpopulation of the $|\mathrm{T}_+\rangle$ and $|\mathrm{T}_0\rangle$ states has been observed experimentally in CT states DNA hairpins that originate from an intersystem crossing triplet.[144]

In the case of a thermalised triplet, the density matrix approximates to:

$$\hat{\rho}(t=0) = \left|\mathrm{T}\right\rangle \left\langle\mathrm{T}\right| = \frac{1}{3}(\left|\mathrm{T}_+\right\rangle \left\langle\mathrm{T}_+\right| + \left|\mathrm{T}_0\right\rangle \left\langle\mathrm{T}_0\right| + \left|\mathrm{T}_-\right\rangle \left\langle\mathrm{T}_-\right|) \tag{2.76}$$

The initial populations can be calculated similarly to the singlet-born case (Equation 2.67), yielding:

$$p_1 = \tfrac{1}{3}, \quad p_2 = \tfrac{1}{3}\cos^2\phi, \quad p_3 = \tfrac{1}{3}\sin^2\phi, \quad p_4 = \tfrac{1}{3} \tag{2.77}$$

and population differences for the four transitions of:

$$\begin{aligned} \Delta p_{12} &= p_1 - p_2 = +\frac{1}{3}\left(1 - \cos^2\phi\right) & \Delta p_{13} &= p_1 - p_3 = +\frac{1}{3}\left(1 - \sin^2\phi\right) \\ \Delta p_{24} &= p_2 - p_4 = -\frac{1}{3}\left(1 - \cos^2\phi\right) & \Delta p_{34} &= p_3 - p_4 = -\frac{1}{3}\left(1 - \sin^2\phi\right) \end{aligned} \tag{2.78}$$

The transition matrix elements P_{ij} remain unchanged from the singlet-born case (Equation 2.72), resulting in the following transition intensities, occurring at the same transition frequencies as for the singlet-born CT state:

$$\begin{aligned} I_{34} &\propto +\frac{1}{6}\sin^2\phi\cos^2\phi & \omega_{34} &= \omega - \Omega + \frac{1}{2}(J+D) \\ I_{12} &\propto -\frac{1}{6}\sin^2\phi\cos^2\phi & \omega_{12} &= \omega - \Omega - \frac{1}{2}(J+D) \\ I_{24} &\propto +\frac{1}{6}\sin^2\phi\cos^2\phi & \omega_{24} &= \omega + \Omega + \frac{1}{2}(J+D) \\ I_{13} &\propto -\frac{1}{6}\sin^2\phi\cos^2\phi & \omega_{13} &= \omega + \Omega - \frac{1}{2}(J+D) \end{aligned} \tag{2.79}$$

Compared to the singlet-born case, the signs of the transition intensities are inverted, producing an *aeae*-polarised signal instead of *eaea*, as shown in Figure 2.13. Furthermore, the overall intensity is reduced by a factor of three, since all four eigenstates contain some triplet character and are partially populated in the thermalised case.

Thermally-populated Charge-Transfer State

At long times after photoexcitation, the CT sublevel populations tend to thermal equilibrium, described by the Boltzmann population distribution. The four sublevel populations can be calculated by considering the Boltzmann distribution formula in Equation 2.46. The Taylor series $e^{-x} \approx 1 - x$, with the approximation that the thermal energy exceeds the sublevel energy, gives:

$$p_i = \frac{e^{-\frac{E_i}{k_B T}}}{N} \approx \frac{1}{N}\left(1 - \frac{E_i}{k_B T}\right) \tag{2.80}$$

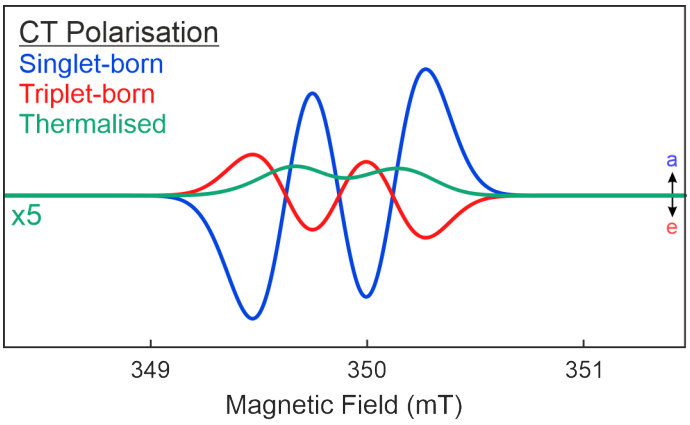

Figure 2.13: Example EPR spectra for a CT state, originating from a singlet precursor, a thermalised triplet precursor, and with fully thermalised populations. The thermalised spin polarisation is very small; hence, the EPR signal is shown multiplied by a factor of 5.

where $N = \sum_j \mathrm{e}^{-\frac{E_j}{k_\mathrm{B}T}}$ is a normalisation constant.

Using the four spin sublevel energies of the CT state from Equation 2.57, and the approximation $\omega \gg |\Omega|, |J|, |d|$, the thermalised eigenstate populations are:

$$\begin{aligned}
p_1 &= \frac{1}{N}\left(1 - \frac{\hbar\left(-\omega + \frac{1}{4}(J+d)\right)}{k_\mathrm{B}T}\right) \approx \frac{1}{4}(1+\Delta) \\
p_2 &= \frac{1}{N}\left(1 - \frac{\hbar\left(-\Omega - \frac{1}{4}(J+d)\right)}{k_\mathrm{B}T}\right) \approx \frac{1}{4} \\
p_3 &= \frac{1}{N}\left(1 - \frac{\hbar\left(+\Omega - \frac{1}{4}(J+d)\right)}{k_\mathrm{B}T}\right) \approx \frac{1}{4} \\
p_4 &= \frac{1}{N}\left(1 - \frac{\hbar\left(-\omega + \frac{1}{4}(J+d)\right)}{k_\mathrm{B}T}\right) \approx \frac{1}{4}(1-\Delta)
\end{aligned} \tag{2.81}$$

where

$$\Delta = \frac{\hbar\omega}{k_\mathrm{B}T} \tag{2.82}$$

Lower energy sublevels are populated more than higher energy levels, and each allowed transition is absorptive with a population difference of $\Delta/4$. At X-band microwave frequency (9.8 GHz) and $T = 20\,\mathrm{K}$, $\Delta = 1\%$. Spin polarisation for a thermalised CT state is far lower than those seen for the singlet- or triplet-born cases, as demonstrated in Figure 2.13. The difference in signal intensity is apparent: the thermalised CT state is shown $\times 5$ magnitude and yet is still a weaker signal than those of the spin-selective mechanisms.

2.4.3 Triplet States

The EPR spectrum of triplet states is dominated by the zero-field interaction, as discussed in Section 2.2.3, because the two electron spins reside on the same molecule. The spin Hamiltonian for a triplet state is given by the zero-field and electron Zeeman interactions:

$$\hat{\mathcal{H}}_\mathrm{T} = \hat{\mathcal{H}}_\mathrm{eZ} + \hat{\mathcal{H}}_\mathrm{zf} \tag{2.83}$$

At low fields, $\hat{\mathcal{H}}_\mathrm{T} \approx \hat{\mathcal{H}}_\mathrm{zf}$ and the energies can be approximated by the zero-field energies given in Equation 2.26, governed by the zero-field splitting parameters D and E. At high fields, the energies of the spin sublevels will be additionally affected by the electron Zeeman interaction, with a dependence on the alignment of the $\boldsymbol{D}$-tensor relative to the magnetic field $\boldsymbol{B}_0$. If one of the principal axis of $\boldsymbol{D}$ is aligned with $\boldsymbol{B}_0$, the energy of its spin sublevel will remain unchanged as

a function of a field (denoted T_0, with $M_S = 0$), while the remaining two spin sublevels will split into the lower ($M_S = -1$) and higher ($M_S = +1$) energy spin states. This behaviour arises because the high-field states $|T_+\rangle, |T_0\rangle, |T_-\rangle$ are linear combinations of the zero-field states $|T_X\rangle, |T_Y\rangle, |T_Z\rangle$, with the magnetic field direction selecting which zero-field component maps onto $|T_0\rangle$.

In OPV blends with small g-value anisotropy, $\boldsymbol{g}$ can often be approximated as g_{iso} when measuring at X-band. For the case where the z-axis of $\boldsymbol{D}$ is aligned along $\boldsymbol{B}_0$:

$$\begin{aligned} E_+ &= \frac{1}{3}D + \sqrt{E^2 + \left(\frac{g_{\text{iso}}\mu_{\text{B}}B_0}{\hbar}\right)^2} \\ E_0 &= E_z = -\frac{2}{3}D \\ E_- &= \frac{1}{3}D - \sqrt{E^2 + \left(\frac{g_{\text{iso}}\mu_{\text{B}}B_0}{\hbar}\right)^2} \end{aligned} \tag{2.84}$$

The triplet selection rules apply here ($\Delta S = 0$, $\Delta M_S = \pm 1$) and the transitions observed are:

$$|T_-\rangle \leftrightarrow |T_0\rangle \qquad\qquad |T_0\rangle \leftrightarrow |T_+\rangle \tag{2.85}$$

In some cases, the formally forbidden $\Delta M_S = \pm 2$ *half-field* transition ($|T_-\rangle \leftrightarrow |T_+\rangle$) can also be detected at approximately half the resonance field of the allowed $\Delta M_S = \pm 1$ transitions, although it is typically much weaker in intensity.[145]

In a powder sample, every molecular orientation contributes two such transitions, with resonance fields determined by the alignment of the $\boldsymbol{D}$-tensor principal axes relative to $\boldsymbol{B}_0$. The three *canonical* orientations (principal axis of the $\boldsymbol{D}$-tensor) produce six characteristic transitions, denoted $X_\pm$, $Y_\pm$, and $Z_\pm$, which manifest as turning points in the triplet EPR spectrum.

When these turning points are well-resolved, the zero-field splitting parameters D and E can be extracted directly: the separation between the Z_+ and Z_- transitions equals $2D$, while E is determined from the relative positions of the X and Y turning points, as illustrated in Figure 2.14. The spectral shape is insensitive to the sign of D and E, and the sign of D requires advanced spectroscopic methods to resolve, such as optically detected magnetic resonance or magnetophotoselection experiments.[146] The spin polarisation pattern also depends on the populations of the triplet sublevels, which in turn are governed by the mechanism of triplet formation.

Intersystem Crossing Triplet

In both pristine donor and acceptor molecules, as well as blended donor:acceptor OPVs, the singlet exciton generated by photoexcitation can, instead of dissociating into a CT state, undergo conversion to a triplet exciton via intersystem crossing (ISC). Although ISC from S_1 to T_1 involves a change in spin angular momentum that formally violates the $\Delta S = 0$ selection rule, spin-orbit coupling relaxes this restriction by conserving angular momentum even if the spin angular momentum changes. In organic molecules comprised of light atoms, direct spin-orbit coupling is typically weak and insufficient to drive ISC efficiently. Instead, ISC predominantly occurs through a spin-vibronic mechanism, where vibrations simultaneously modulate electronic states and facilitate spin-orbit coupling-mediated mixing between S_1 and T_1.[107]

In aromatic π-conjugated systems, such as the polymer donors and non-fullerene acceptors, the efficiency of ISC depends on the type of orbital mixing involved. When both the S_1 and T_1 states are predominantly $\pi - \pi^*$ in nature, ISC is typically weak. However, vibrational modes, strongest in the molecular plane, can enhance ISC by introducing σ-orbital character, which increases spin-orbit coupling.[147] As a result, the populations of the triplet sublevels are selectively distributed within the molecular frame, leading to unequal zero-field populations ($p_X : p_Y : p_Z$) along the molecular axes.

When one of the principal axes of $\boldsymbol{D}$ is aligned with $\boldsymbol{B}_0$, the triplet sublevel populations in the high-field basis are related to the zero-field populations by:

$$\boldsymbol{B}_0 \,||\, i \quad (i,j,k = X,Y,Z) \qquad\qquad p_0 = p_i \qquad p_\pm = \frac{1}{2}(p_j + p_k) \tag{2.86}$$

The polarisation of the overall EPR signal will then depend on the population differences, determining whether each of the six canonical transitions will be absorptive or emissive. Each canonical orientation will give one absorption and one emission. For a triplet where ISC predominantly populates the X and Y sublevels, an *eeeaaa* signal polarisation, as shown in Figure 2.14, would be obtained.

The relative populations of the triplet sublevels determine the observed signal polarisation. Spin-polarised triplet states formed via ISC exhibit a variety of polarisation patterns, which can be broadly categorised into six distinct types:[146] *eeaeaa*, *aaeaee*, *eaeaea*, *aeaeae*, *aaaeee*, and *eeeaaa*, as displayed in Figure 2.16.

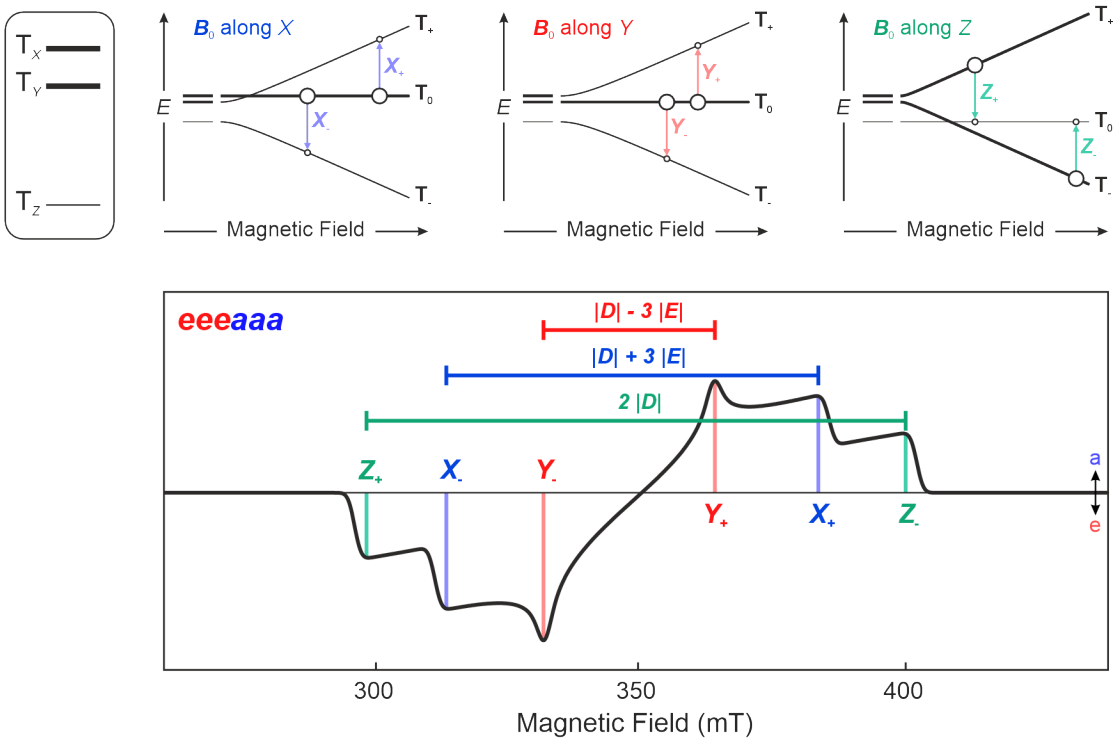

Figure 2.14: Top) Energies of the triplet sublevels as a function of magnetic field for alignment with the canonical orientations X, Y, and Z of the $\boldsymbol{D}$-tensor. A transition is observed when the microwave energy matches the energy gap of an allowed transition: $|\mathrm{T}_-\rangle \leftrightarrow |\mathrm{T}_0\rangle$ or $|\mathrm{T}_0\rangle \leftrightarrow |\mathrm{T}_+\rangle$. Each canonical orientation gives one absorption and one emission, with sublevel populations illustrated by the size of the circles. Bottom) For the case of $p_X = p_Y > p_Z$, and $D > 0$, $E < 0$, an *eeeaaa* polarisation is observed for the ISC triplet. The zero-field splitting parameters can be determined from the resonance positions of the canonical transitions.

Geminate Recombination Triplet

Intersystem crossing is not the only way to form a triplet in a donor:acceptor OPV blend. After formation of the CT state at the donor:acceptor interface, the spins may recombine to form a triplet exciton instead of dissociating into separated charges. This process is called geminate recombination: geminate referring to the triplet spins arising from the same CT state without separating. The spins remain correlated, maintaining the spin configuration of the precursor state.[148]

Formation of the CT state from a singlet precursor will preserve singlet spin character, populating only the CT eigenstates with singlet character: $|2\rangle = \cos\phi\ |\mathrm{T}_0\rangle - \sin\phi\ |\mathrm{S}\rangle$ and $|3\rangle = \sin\phi\ |\mathrm{T}_0\rangle + \cos\phi\ |\mathrm{S}\rangle$. States $|2\rangle$ and $|3\rangle$ contain only $|\mathrm{S}\rangle$ and $|\mathrm{T}_0\rangle$ spin character, and so, following recombination to a triplet state, the $|\mathrm{T}_0\rangle$ triplet eigenstate will be preferentially populated over the $|\mathrm{T}_+\rangle$ and $|\mathrm{T}_-\rangle$ spin states:

$$\hat{\rho}(t=0) = |\mathrm{T}_0\rangle\langle\mathrm{T}_0| \tag{2.87}$$

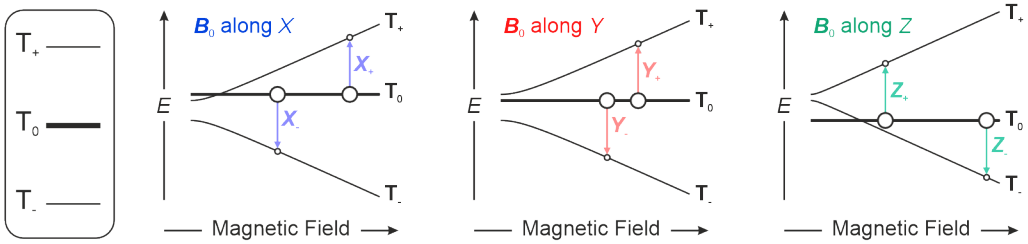

Figure 2.15: Triplet sublevel energies as a function of magnetic field for a triplet formed by geminate recombination. Only the T_0 sublevel is populated, independent of orientation, resulting in an *aeeaae*-polarised EPR signal (see Figure 2.16), unachievable through the ISC mechanism.

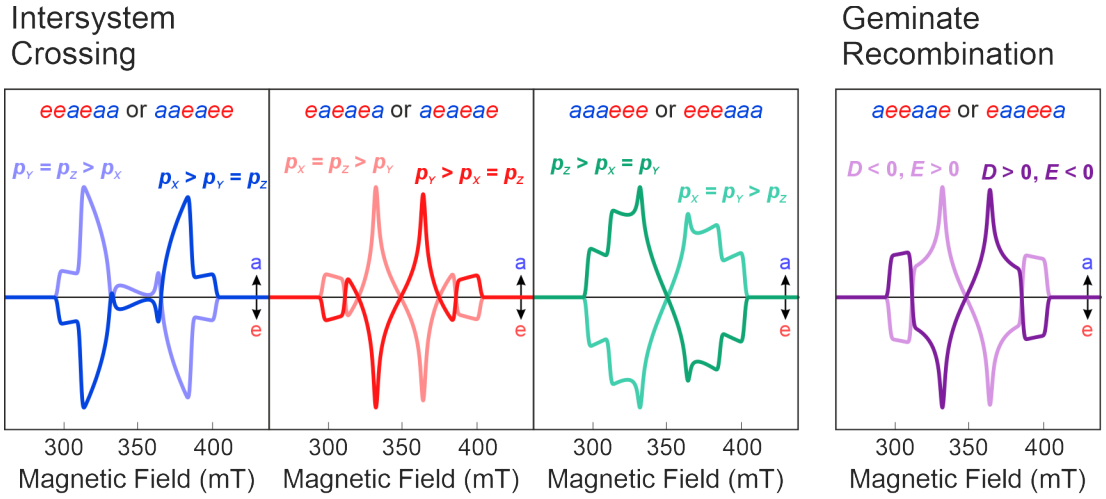

Figure 2.16: Possible spin polarisation patterns for the EPR spectrum of an intersystem crossing triplet and a geminate recombination triplet.

Preferential population of the $|T_0\rangle$ sublevel is independent of molecular orientation, as demonstrated in Figure 2.15, in contrast to ISC-generated triplets, where zero-field populations along the molecular axes $\{|T_X\rangle, |T_Y\rangle, |T_Z\rangle\}$ determine the orientation-dependent, high-field populations.[146] In a triplet formed from geminate recombination, the selective $|T_0\rangle$ population results in one of two possible spin polarisation patterns: *aeeaae* for $D > 0$, $E < 0$, or *eaaeea* for $D < 0$, $E > 0$, with no other patterns observed.

This contrast in population selectivity means that spin polarisations arising from geminate recombination differ from those produced by ISC triplets. As a result, EPR spectroscopy can reliably distinguish between these two triplet formation mechanisms, visualised in Figure 2.16.

Non-Geminate Recombination Triplet

There is a third mechanism for triplet formation in OPV blends: non-geminate recombination. Separated charges, formed after dissociation of the CT state, can re-encounter to reform a CT state that then recombines to form a triplet exciton.[96] Because the spins have undergone charge separation, they have lost their initial spin correlation.[112] As a result, upon recombination, all spin eigenstates are populated equally. Formally:

$$\hat{\rho}(t=0) = \frac{1}{3}\left(|\mathrm{T}_+\rangle\langle\mathrm{T}_+| + |\mathrm{T}_0\rangle\langle\mathrm{T}_0| + |\mathrm{T}_-\rangle\langle\mathrm{T}_-|\right) \tag{2.88}$$

With equal populations in each triplet eigenstate, all transitions have zero net intensity initially. Over time, the spin populations relax towards Boltzmann equilibrium, resulting in a weak, purely absorptive EPR signal. Since the thermal energy greatly exceeds the triplet sublevel energy splittings, the resulting spin polarisation is minimal, and the EPR signal is significantly weaker than those arising from either intersystem crossing or geminate recombination triplets.[106]

2.5 EPR Instrumentation

With the theoretical foundation of electron spins and their interactions established, attention is now turned to how these properties are accessed experimentally. In EPR spectroscopy, spin transitions are induced by microwave excitation, applied either continuously or in pulses. The system's response is detected either through the absorption of microwave power or through the detection of time-dependent magnetisation resulting from the precession of spin ensembles. From these measurements, spectra are obtained that reflect the spin Hamiltonian and thus provide detailed information about the electronic environment, molecular structure, and spin dynamics.

In continuous-wave EPR, a constant microwave field is applied while the magnetic field is swept; in pulse EPR, short bursts of microwave power are used to manipulate spin populations and coherences. Each approach offers distinct advantages, with continuous-wave EPR suited to routine spectral acquisition and pulse EPR enabling precise measurements of spin interactions and dynamics.

The most common commercial systems operate at microwave frequency bands of X-band (9.8 GHz, 0.35 T), Q-band (33.9 GHz, 1.2 T), and W-band (94 GHz, 3.4 T). Higher microwave frequencies offer increased sensitivity, enhanced spectral resolution, and greater ability to resolve anisotropic interactions and overlapping features. However, these benefits come at the cost of increased complexity and

stricter limitations on sample size. This section briefly describes the core components of EPR spectrometers; the architecture and function of spectrometers for time-resolved and pulse EPR is described in more detail in several textbooks, including those by Hemminga,[149] Schweiger and Jeschke,[117] Stoll and Goldfarb,[119] and Weil and Bolton.[118]

An EPR spectrometer consists of three primary components: a magnet, a microwave bridge, and a resonator. For light-induced EPR experiments, a pulsed laser is also required to generate spin-polarised states, synchronised precisely with data acquisition.

The magnet generates the static magnetic field $\boldsymbol{B}_0$ that induces Zeeman splitting of the spin energy levels. To ensure reliable and high-resolution measurements, the field must be highly stable and homogeneous across the sample volume. X-band and Q-band spectrometers typically use electromagnets, while the higher magnetic fields required for W-band operation are achieved using superconducting magnets.

The microwave bridge generates, monitors, and detects the microwave radiation used to manipulate electron spins. It houses a stable microwave source that produces microwaves at a specified frequency, which are directed to the resonator holding the sample. When the resonance condition is met, the microwave magnetic field $\boldsymbol{B}_1$ induces transitions between electron spin states. The absorption of microwaves affects the intensity of the reflected microwaves, which is detected in the bridge and forms the basis of the EPR signal. The exact detection method depends on the type of experiment, continuous-wave or pulsed, and determines how the signal is processed.

The resonator is a critical component of the spectrometer, essential for enhancing sensitivity given the low spin polarisations in EPR spectroscopy. It confines the microwave energy into a small cavity by creating a standing wave within the resonator, maximising the magnetic field component ($\boldsymbol{B}_1$) that drives spin transitions at the position of the sample, while minimising the electric field component to reduce dielectric losses, sample heating, and background artefacts. This is especially important for samples in high-dielectric solvents, like water, which strongly absorb microwaves through their electric field. The sample, contained in an EPR tube, is positioned at the resonator's centre where the microwave field is strongest. EPR sample volumes are determined by the microwave frequency and the type of resonator, with typical outer diameters of 4 mm for X-band down to 0.9 mm for W-band.

The quality factor, Q, of the resonator, defined as:

$$Q = \frac{\nu_0}{\Delta\nu} \tag{2.89}$$

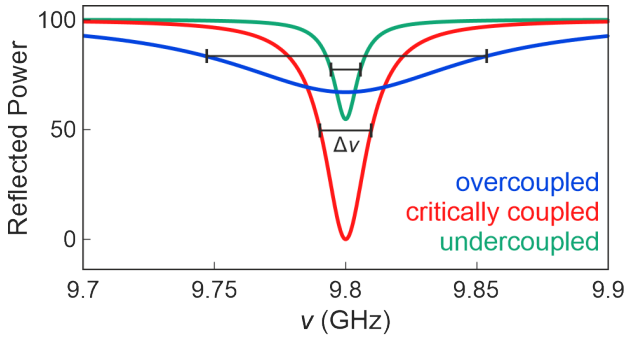

Figure 2.17: Microwave power reflected back to the microwave bridge as a function of a microwave frequency, shown for different coupling of the resonator to the microwave bridge. The resonator bandwidth is determined by the full-width half-maximum of the resonator coupling profile.

characterises how efficiently microwave power is stored in the resonator and transferred to the sample. ν_0 is the resonator's central frequency and $\Delta\nu$ its bandwidth. The interaction between the microwave source and the resonator can be characterised into three distinct coupling regimes, displayed in Figure 2.17.

In the **undercoupled regime**, much of the microwave power is reflected back towards the source, resulting in weak interaction with the sample and a high Q-factor, but poor signal strength; this is generally undesirable in EPR. In the **critical coupling regime**, power transfer is maximised with minimal reflection; under these conditions, the resonator efficiently stores energy and is most sensitive to changes in reflection caused by microwave absorption on resonance. When in the **overcoupled regime**, the resonator loses the ability to store energy efficiently, lowering the Q-factor and broadening the bandwidth, which reduces sensitivity but allows excitation of a broader range of spins of different resonance conditions.

Charge-transfer and triplet states in OPV blends often exhibit short lifetimes and rapid spin relaxation at room temperature, limiting both the detectability and sensitivity of EPR signals. To overcome this, measurements are performed at cryogenic temperatures, where kinetics is slowed and relaxation extended. These conditions are achieved using a cryostat: the sample, and sometimes also the resonator, is placed in a vacuum-insulated chamber cooled with liquid helium or nitrogen and stabilised via active temperature control.

Field Calibration

Accurate determination of g-values is essential in EPR spectroscopy, as it provides a unique fingerprint for identifying and characterising paramagnetic species. Calculating the g-value using the resonance condition in Equation 2.15 requires precise measurement of both the magnetic field and microwave frequency. Typically,

the magnetic field is set by adjusting the current in the magnet until the field measured by a Hall probe reaches the desired value. However, because the Hall probe is positioned differently from the sample, there is often an offset between the measured field and the actual field experienced by the sample. To correct for this, calibration is performed using a standard sample with a well-known g-value, such as N@C_{60}.[150] A detailed description of the calibration procedure is provided in Appendix A.

2.6 Time-Resolved EPR

Time-resolved EPR is a variant of continuous-wave EPR where the signal is monitored as a function of time following a short laser pulse that both generates the paramagnetic species and triggers data acquisition. The measurement is performed at a fixed magnetic field, detecting changes in the microwaves reflected from the resonator caused by the absorption or emission of the applied microwave field by the spins. After averaging multiple time profiles (transients) to improve the signal-to-noise ratio, the magnetic field is incremented in small field steps and the process is repeated. This yields a two-dimensional dataset, illustrated in Figure 2.18, where the EPR intensity is recorded as a function of both time and magnetic field: $I_{\mathrm{EPR}} = f(t, B)$. Time-resolved EPR is especially effective for detecting species exhibiting large non-Boltzmann spin polarisations.

Maximising signal-to-noise ratio is essential in time-resolved EPR and is achieved through critical coupling of the resonator. This condition optimises microwave power transfer, minimises reflection losses, and maximises the quality factor Q, thereby enhancing the resonator's sensitivity. However, a narrower bandwidth also increases the resonator's response time, or rise time, because the resonator stores energy for longer and responds more slowly. This instrumental time response dampens fast transient features in the signal. Consequently, excessively high Q-values can obscure short-lived spin polarisations, limiting the detection of rapid dynamics.[138]

The laser repetition rate, typically between 10 and 50 Hz and limited by the laser's capabilities, is chosen to allow complete relaxation of photoexcited states before the next laser pulse. Excitation is delivered either through an optical window in the resonator or via optical fibres inserted into the sample tube, depending on the spectrometer design.

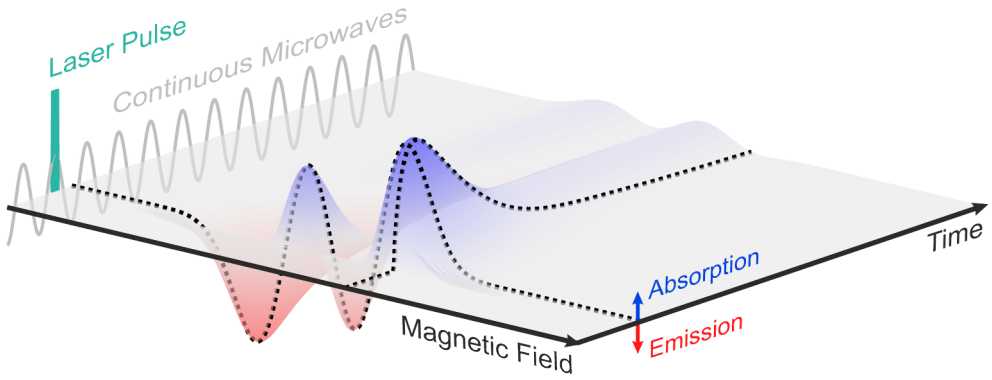

Figure 2.18: Schematic of a time-resolved EPR spectrum showing the evolution of signal intensity as a function of magnetic field and time after laser excitation. Both absorptive (blue) and emissive (red) features are observed, arising from non-Boltzmann spin polarisation. Slices through the surface at specific fields or times allow interpretation of either the spin dynamics at a fixed field or the spectrum and spin polarisation at a fixed delay after excitation.

2.7 Pulse EPR

Pulse EPR involves applying short, high-power microwave pulses while varying parameters such as magnetic field strength, pulse lengths, time delays, and frequencies. This approach not only enables selective excitation of specific spin transitions but also permits the design of advanced pulse sequences that isolate and precisely measure different spin interactions, beyond what continuous-wave methods can achieve.

A critical consideration in pulse EPR is the need for broad excitation bandwidths to uniformly excite spins across a wide spectral range. To accomplish this, the resonator is operated in the overcoupled regime, which lowers the quality factor Q and consequently increases the resonator bandwidth. While a high Q-factor enhances sensitivity by efficiently storing microwave energy, it restricts the bandwidth and thus limits the range of spins that can be excited by short pulses. Operating with a reduced Q therefore represents a trade-off to achieve sufficient bandwidth for these intense pulses.

To generate these pulses, the microwave bridge is equipped with fast switches, or more recently, arbitrary waveform generators for the generation of arbitrary pulse shapes through digital to analogue conversion, and high-power amplifiers, enabling the delivery of short, intense microwave bursts. These pulses simultaneously excite many spin transitions or broad distributions of spins. Immediately following each pulse, the spectrometer experiences a brief period known as *dead time*, during which signal detection is suspended. This is necessary because the resonator and detection system undergo *ringing*: prolonged oscillations of residual microwave

energy at the operating frequency after the pulse. This lingering energy obscures the much weaker spin signals and can damage sensitive components such as the detector. By suspending detection during this dead time, the system protects itself and allows the ringing to decay.

Once the dead time has elapsed, the system can resume detection. The detected signal is routed through a pulse detection unit and recorded using quadrature detection, which separates the signal into real and imaginary components. This allows full characterisation of the spin magnetisation's amplitude and phase.

More specialised pulse EPR techniques require additional hardware. For example, ENDOR combines electron and nuclear spin transitions, necessitating a radiofrequency pulse generator and amplifier alongside the microwave components.

To understand pulse EPR experiments, it is instructive to consider the collective behaviour of an ensemble of electron spins, each possessing a magnetic moment. When placed in an external static magnetic field $\boldsymbol{B}_0$, these magnetic moments partially align with or against the field, corresponding to the spin states $|\alpha\rangle$ and $|\beta\rangle$, respectively. Due to the slight energy difference between these states at thermal equilibrium, there is a small excess population in the lower-energy $|\beta\rangle$ state. The net result is a macroscopic magnetisation vector, $\boldsymbol{M}$, which represents the vector sum of all individual spin magnetic moments in the ensemble. This net magnetisation aligns along the $+z$-axis, parallel to $\boldsymbol{B}_0$.

2.7.1 The Effect of a Pulse

To manipulate the net magnetisation vector $\boldsymbol{M}$, a short pulse of linearly polarised microwave radiation is applied perpendicular to the external magnetic field $\boldsymbol{B}_0$. The microwave field, $\boldsymbol{B}_1$, oscillates along the x-axis at a frequency $\omega_{\text{mw}} \approx \omega_0$, where ω_0 is the Larmor precession frequency of spins around $\boldsymbol{B}_0$, and is much weaker in magnitude than $\boldsymbol{B}_0$. This time-dependent field causes $\boldsymbol{M}$ to precess around the instantaneous effective magnetic field given by the vector sum of $\boldsymbol{B}_0$ and $\boldsymbol{B}_1$. In the laboratory frame, this precession is complicated by the oscillatory nature of $\boldsymbol{B}_1$.

To simplify the analysis, it is convenient to express the linearly-polarised field as a superposition of two circularly-polarised components rotating at $+\omega_{\text{mw}}$ and $-\omega_{\text{mw}}$ around $\boldsymbol{B}_0$. By transforming into a rotating reference frame that rotates at the same frequency as one of the two components ($\omega_{\text{rot}} = +\omega_{\text{mw}}$), this component of $\boldsymbol{B}_1$ becomes static. The counter-rotating component will then precess at twice ω_{mw} and its frequency will be too dissimilar to ω_0 to affect the spins in a significant way, and so can typically be neglected. In this rotating frame, the static external field $\boldsymbol{B}_0$ transforms into an effective field $\Delta\boldsymbol{B}$ aligned along z. Thus, in the rotating

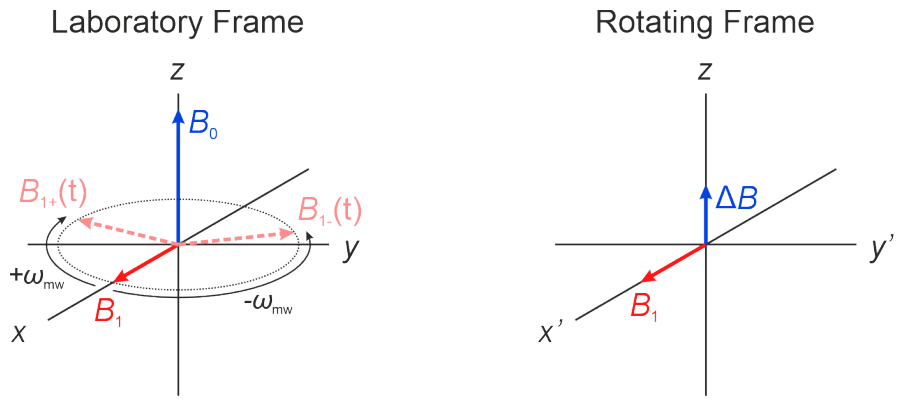

Figure 2.19: Visualisation of the laboratory and rotating frame. In the laboratory frame, $\boldsymbol{B}_1$ linearly oscillates along x with frequency ω_{mw}, which can be decomposed into two components rotating around $\boldsymbol{B}_0$ with frequencies $+\omega_{\mathrm{mw}}$ and $-\omega_{\mathrm{mw}}$. The rotating frame, rotating around $\boldsymbol{B}_0$ with frequency $+\omega_{\mathrm{mw}}$, simplifies interpretation of the effect of a pulse by removing the time dependence of $\boldsymbol{B}_1$. In this frame, $\boldsymbol{B}_1$ is static, while $\boldsymbol{B}_0$ becomes $\Delta\boldsymbol{B}$, where an electron spin will precess around this effective $\Delta\boldsymbol{B}$ field with offset frequency $\Delta\omega = \omega_0 - \omega_{\mathrm{mw}}$. The magnetisation vectors are not to scale: $B_0 \gg B_1 \gg \Delta B$.

frame, the magnetisation $\boldsymbol{M}$ precesses about an effective static field composed of $\boldsymbol{B}_1$ in the transverse plane and $\Delta\boldsymbol{B}$ along z. The laboratory and rotating frame representations are visualised in Figure 2.19.

In the rotating frame, when the microwave pulse is on resonance ($\Delta\omega = \omega_0 - \omega_{\mathrm{mw}} = 0$ and so the effective field strength $\Delta B = 0$) and applied along x, $\boldsymbol{M}$ is rotated from the z-axis towards the transverse plane. For a pulse with a flip angle of $\beta = \frac{\pi}{2}$, the magnetisation is rotated entirely into the xy-plane, pointing along the negative y-axis. This evolution can be described as:

$$\boldsymbol{M} = \begin{pmatrix} M_x \\ M_y \\ M_z \end{pmatrix} = \begin{pmatrix} 0 \\ 0 \\ M_0 \end{pmatrix} \xrightarrow{(\beta)_x} \boldsymbol{M} = \begin{pmatrix} 0 \\ -M_0 \sin\beta \\ M_0 \cos\beta \end{pmatrix} \tag{2.90}$$

where the flip angle β is defined by:

$$\beta = \omega_1 t_{\mathrm{p}} \qquad \omega_1 = \frac{g_{\mathrm{e}} \mu_{\mathrm{B}} B_1}{\hbar} \tag{2.91}$$

with ω_1 as the amplitude of the oscillating microwave field $\boldsymbol{B}_1$, and t_{p} as the duration of the pulse. A larger flip angle can thus be achieved by increasing either the pulse amplitude ω_1 or its duration t_{p}. ω_1 is the precession frequency of spins about $\boldsymbol{B}_1$ in the rotating frame, known as the Rabi frequency, which is much slower than precession around $\boldsymbol{B}_0$, as $B_1 \ll B_0$.

If $\Delta B = 0$, the magnetisation remains stationary in the rotating frame after the pulse, as $\boldsymbol{B}_1$ is no longer applied and there is no field for the magnetisation to precess around. Off-resonance ($\Delta B \neq 0$), the magnetisation vector precesses

about $\boldsymbol{\Delta B}$ with offset frequency $\Delta\omega$. After a $\left(\frac{\pi}{2}\right)_x$-pulse, this precession occurs in the transverse plane:

$$\boldsymbol{M}(t) = \begin{pmatrix} M_0 \sin(\Delta\omega\, t) \\ -M_0 \cos(\Delta\omega\, t) \\ 0 \end{pmatrix} \tag{2.92}$$

The transverse components $M_x(t)$ and $M_y(t)$ correspond to the imaginary and real coefficients, respectively, of the complex signal recorded via quadrature detection:

$$I(t) = -M_0 \mathrm{e}^{-\mathrm{i}\Delta\omega t} \tag{2.93}$$

In reality, relaxation processes must also be accounted for. Following a $\frac{\pi}{2}$-pulse, the longitudinal component M_z returns to equilibrium magnetisation M_0 with a time constant T_1 (longitudinal relaxation), while the transverse components M_x and M_y decay with a time constant T_2 (transverse relaxation), as illustrated in Figure 2.20. Including these effects, the evolution in the rotating frame becomes:

$$\boldsymbol{M}(t) = \begin{pmatrix} M_0 \sin(\Delta\omega\, t)\, \mathrm{e}^{\frac{-t}{T_2}} \\ -M_0 \cos(\Delta\omega\, t)\, \mathrm{e}^{\frac{-t}{T_2}} \\ M_0 \left(1 - \mathrm{e}^{\frac{-t}{T_1}}\right) \end{pmatrix} \tag{2.94}$$

where the time-dependent behaviour of $\boldsymbol{M}(t)$ is derived from solution of the Bloch equations,[151] a set of first-order differential equations that describes the rate of change of the magnetisation with time in the rotating frame:

$$\begin{aligned} \frac{dM_x}{dt} &= -\Delta\omega\, M_y - \frac{M_x}{T_2} \\ \frac{dM_y}{dt} &= \Delta\omega\, M_x - \frac{M_y}{T_2} \\ \frac{dM_z}{dt} &= -\frac{M_z - M_0}{T_1} \end{aligned} \tag{2.95}$$

The transverse components $M_x(t)$ and $M_y(t)$, which precess and decay following the pulse, give rise to a time-domain signal known as the free induction decay (FID).

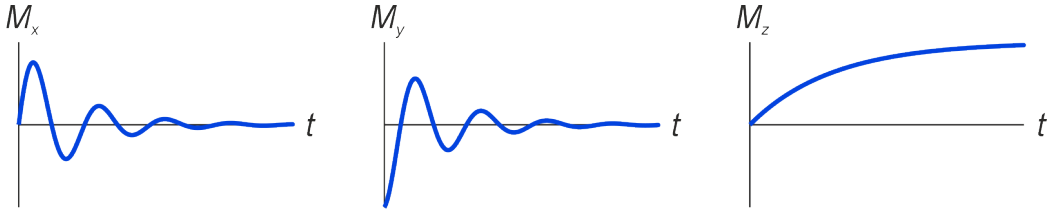

Figure 2.20: Time-dependence of the components of the magnetisation vector in the rotating frame following an off-resonant $(\frac{\pi}{2})_x$ pulse, as described by Equation 2.94.

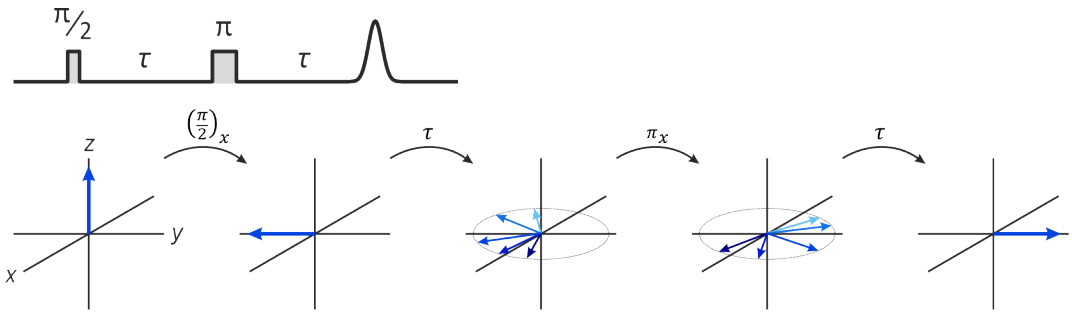

Figure 2.21: Evolution of the magnetisation during the Hahn echo pulse sequence. During the first delay τ, the net magnetisation (blue vector) fans out due to variations in Larmor frequencies across different spin packets. After an inversion π_x-pulse and another delay τ, the spin packets refocus, and the net magnetisation can be measured along $+y$.

This signal reflects the coherent transverse magnetisation and contains information about the offset frequency $\Delta\omega$, which depends on the g-value, and the relaxation time T_2. In practice, however, the FID decays rapidly, usually within the instrument dead time, making direct detection challenging.

To overcome this, a signal can instead be obtained using the two-pulse Hahn echo sequence displayed in Figure 2.21.** First, a $\left(\frac{\pi}{2}\right)_x$-pulse brings the magnetisation into the transverse plane, followed by a delay τ. Because the ensemble of spins will have a distribution of Larmor frequencies ω_0, not all the spins in the ensemble $\boldsymbol{M}$ will be on resonance. $\boldsymbol{M}$ can be considered as a group of spin sub-ensembles (*spin packets*), where all spins in a given packet have the same ω_0 and, therefore, offset frequency $\Delta\omega$ in the rotating frame. Each spin packet's precession during the delay τ is governed by the expression for $\boldsymbol{M}(t)$ from Equation 2.92; relaxation effects can be neglected if τ is short. If the spin packet is on resonance, it will remain stationary during the delay τ. All off-resonant packets will precess either clockwise ($\omega_0 > \omega_{\mathrm{mw}}$) or anticlockwise ($\omega_0 < \omega_{\mathrm{mw}}$) around $\boldsymbol{\Delta B}$. This 'fanning out' of the contributions of different spin packets to the overall magnetisation, or dephasing, reduces the M_x and M_y components of the net magnetisation $\boldsymbol{M}$.

A second microwave π_x-pulse rotates the spin packets by 180° around the x-axis and the packets continue to precess in the same direction and at the same frequency as before. After another delay of τ, all the spin packets are refocused, and point along $+y$. The magnetisation $\boldsymbol{M}$ can be measured as a spin echo at 2τ after the initial pulse with no concern about spectrometer dead time, as τ is chosen to be longer than the dead time to ensure the echo is detectable. As τ lengthens, spin relaxation can no longer be neglected and the evolution of the magnetisation

**Although commonly referred to as the Hahn echo sequence after American physicist Erwin Hahn, his original experiment employed a $\frac{\pi}{2} - \frac{\pi}{2}$ pulse sequence.[152] This was later extended by Carr and Purcell to the now-standard $\frac{\pi}{2} - \pi$ sequence.[153]

vectors of different spin packets are better represented by the form of $\boldsymbol{M}(t)$ in Equation 2.94. Relaxation leads to irreversible dephasing, reducing the number of spins that rephase at 2τ, thus diminishing the echo intensity.

In addition to generating the desired echo, the Hahn echo sequence also produces FIDs immediately following each microwave pulse. Although these FIDs begin at different times than the spin echo, their residual signal can extend into the time window where the echo is detected, leading to temporal overlap and distortion of the echo shape. As pulse sequences become more complex and incorporate additional pulses, further unwanted signals, including additional FIDs and overlapping, stimulated or refocused echoes, can arise and may interfere with the measurement of the intended signal. To minimise these effects, phase cycling is employed. This technique involves systematically varying the phases of the microwave pulses across repeated executions of the sequence. A $\left(\frac{\pi}{2}\right)_x$-pulse transfers magnetisation from the z-axis to the $-y$-axis, while a pulse of the opposite phase, $(\frac{\pi}{2})_{-x}$, rotates it into the $+y$ direction. By carefully selecting and combining sequences with different pulse phase configurations, phase cycling selectively enhances the desired spin echo while effectively cancelling unwanted signal contributions.[117,154]

The preceding discussion assumed that all spins are uniformly excited by the microwave pulse, resulting in a net magnetisation vector aligned along the x-axis of the rotating frame for all spin packets after the pulse. In practice, however, spins with different resonance frequencies experience different excitation due to the limited spectral bandwidth of the pulse. For a rectangular pulse, the excitation profile follows a sinc function $\left(\mathrm{sinc}(\Delta\nu) = \frac{\sin(\Delta\nu)}{\Delta\nu}\right)$, with the excitation bandwidth $\Delta\nu$ approximated as:[117]

$$\Delta\nu \approx \frac{1}{t_\mathrm{p}} \tag{2.96}$$

This means short pulses have wide bandwidths and can excite a broader portion of the EPR spectrum (non-selective excitation), whereas longer pulses have narrow bandwidths and selectively excite spins within a limited frequency window. A 20 ns rectangular pulse corresponds to an excitation bandwidth of 50 MHz or roughly 1.8 mT, while a 200 ns pulse narrows the bandwidth to 5 MHz or around 0.18 mT.

Non-selective and selective pulses serve different purposes in pulse EPR. **Non-selective pulses** aim to excite as broad a portion of the spin ensemble as possible, which is useful in experiments that require detecting ensemble behaviour, for instance measuring relaxation times. **Selective pulses** are employed to isolate specific subsets of spins in systems where spectral features overlap. This selective

excitation is particularly helpful in orientation-selective experiments, where spins with certain orientations relative to the magnetic field are probed.

For systems exhibiting anisotropic g-values, the resonance field position depends on the molecular orientation relative to $\boldsymbol{B}_0$. Excitation at the g_x (or g_y or g_z) field position, with a pulse of very narrow bandwidth, corresponds to selecting molecules whose molecular g_x-axis is approximately aligned with $\boldsymbol{B}_0$ ($g_{\text{eff}} \approx g_x$). This phenomenon, known as *orientation selection*, allows experiments to probe spin packets corresponding to defined molecular orientations, and infer detailed information about the relative orientations of other anisotropic interaction tensors, like $\boldsymbol{D}$ and $\boldsymbol{A}$.

An illustration of orientation selection is shown in Figure 2.22. The EPR spectrum uses the simulation of one of the electron acceptor molecules ITIC$^{\bullet-}$ from Chapter 3 (Figure 3.11 in Section 3.3.3), a system with orthorhombic g-values ($g_x = 2.0021$, $g_y = 2.0030$, and $g_z = 2.0038$). A π-pulse of duration 100 ns, with a bandwidth of 1 MHz or 0.36 mT, is applied at the resonance field position corresponding to the g_x, g_y, or g_z principal values (shown in blue, red, and green). This pulse selectively excites spin packets whose g-values match the resonance condition.

At X-band, the spectral separation between g_x, g_y, and g_z is small relative to the pulse bandwidth. As a result, the excitation profile (shown in colour) overlaps with

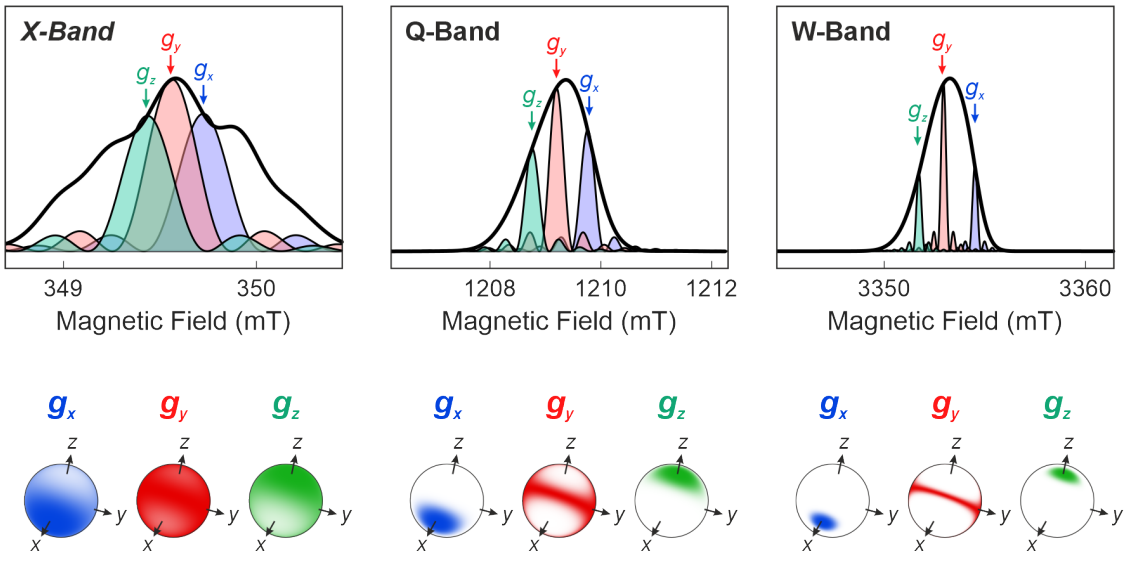

Figure 2.22: Excitation bandwidth and orientation selection effects of a $\pi = 100$ ns pulse, at X-, Q-, and W-band, using the simulated spectra and g-values of the non-fullerene acceptor ITIC$^{\bullet-}$ from Chapter 3 (Figure 3.11 in Section 2.8.2). Simulated spectra are shown in black, with excitation profiles of the pulse displayed in colour. The subset of spins excited by the pulse is illustrated by the shaded regions on the spheres, with greater orientation selection achieved at higher microwave frequencies.

the resonance positions of spin packets corresponding to other orientations as well. Consequently, a pulse at the g_x resonance position excites not only molecules with the g_x-axis aligned with the field, but also a substantial fraction with orientations closer to the g_y- and g_z-axes.

At higher microwave frequencies (e.g., Q- and W-band), the separation in resonance fields between the principal g-values increases, since the electron Zeeman interaction scales with the external magnetic field strength B_0. The field separation between the g_x and g_z resonance positions for ITIC$^{\bullet-}$ is 2.8 mT at W-band, compared to only 0.29 mT at X-band. The same 100 ns pulse, of bandwidth 0.36 mT, thus excites a much narrower subset of orientations at W-band, enabling significantly improved orientation selection.

This trend is illustrated in Figure 2.22, where shaded regions on the surface of a sphere represent the range of molecular orientations (orientations of $\boldsymbol{B}_0$ relative to the molecular g-frame) that are excited by the pulse. In the sphere with selected orientations in blue, where excitation occurs at the g_x resonance position, orientation selection at W-band is evident from the tight shading near the g_x-axis direction: only molecules with their g_x-axis approximately aligned with $\boldsymbol{B}_0$ are excited. At X-band, the shaded area is much broader: molecules with their g_y- and even g_z-axes partially aligned with $\boldsymbol{B}_0$ also fall within the pulse bandwidth, resulting in minimal orientation selection.

This orientation selection is especially advantageous in EPR spectroscopy techniques that probe electron-nuclear hyperfine interactions. Each field position in the EPR spectrum corresponds to a specific orientation of the molecular g-frame relative to the external field, allowing for orientation-resolved measurements of hyperfine interactions. By selectively probing distinct orientations, it becomes possible to extract individual components of the hyperfine tensor along defined molecular axes. At high microwave frequencies, this enhanced selectivity improves spectral resolution, reduces overlap of peaks from different nuclei or tensor orientations, and enables more precise determination of spin-density distributions and the geometric configuration of nearby nuclei.

2.7.2 Spin Relaxation

Relaxation in EPR experiments arises from the interaction of electron spins with other spins and their environment, driving the system back towards thermal equilibrium after perturbation by microwave pulses. There are two primary mechanisms: **longitudinal relaxation** (T_1) and **transverse relaxation** (T_2). Longitudinal relaxation involves the transfer of energy between the spin system and its surroundings, re-establishing the Boltzmann population difference between spin

states and restoring the longitudinal (z-axis) magnetisation. Transverse relaxation, in contrast, refers to the loss of phase coherence among spins in the transverse plane. Relaxation processes cannot be fully understood using classical models like the vector picture of $\boldsymbol{M}$, as they fundamentally involve quantum mechanical events, such as discrete spin flips ($|\alpha\rangle \leftrightarrow |\beta\rangle$) and transitions between quantised energy levels.

Longitudinal Relaxation

The mechanisms driving longitudinal relaxation differ depending on the type of sample. In liquids, rapid molecular motion modulates anisotropic spin interactions ($\boldsymbol{g}$, $\boldsymbol{D}$, and $\boldsymbol{A}$), creating fluctuating local magnetic fields that induce spin flips. Collisions with other paramagnetic species, notably molecular oxygen, also contribute. In solids, like OPV films, where molecular motion is restricted, relaxation occurs via interactions with phonons, quantised vibrational modes of the surrounding environment that behave like quasi-particles and serve as carriers of thermal energy. Spin flips, transitions between $|\alpha\rangle$ and $|\beta\rangle$, are accompanied by an absorption or an emission of a phonon, enabling exchange of energy between the spins and the environment.

Lattice vibrations allow the spin system to exchange energy with its surroundings through three key mechanisms.[155] The **direct process** involves the absorption or emission of a single phonon whose energy matches the separation between spin energy levels. This process dominates at low temperatures and high magnetic fields, and its relaxation rate scales roughly linearly with temperature due to the thermal availability of low-energy phonons.

At higher temperatures, two-phonon relaxation mechanisms become dominant. The **Raman process** involves a virtual intermediate state where the electron spin interacts with two phonons, absorbing one and emitting another, allowing relaxation without accessing a real excited spin state. This process follows a steep temperature dependence, typically scaling as T^7 to T^9. In contrast, the **Orbach process** proceeds via a real, thermally-accessible excited spin state: a phonon excites the electron to this state, from which it relaxes back to the ground state by emitting a second phonon. This leads to an Arrhenius-type temperature dependence and becomes significant when the thermal energy is comparable to the energy gap between the ground and excited states. Given the number of competing relaxation processes, it is generally difficult to assign a measured relaxation rate to a specific process.

T_1 is commonly measured using the inversion recovery pulse sequence in Figure 2.23, which directly monitors the recovery of magnetisation along the z-axis after inversion. An initial π_x-pulse inverts the magnetisation from $+z$ to $-z$. Over a variable delay time T, the magnetisation begins to return towards equilibrium

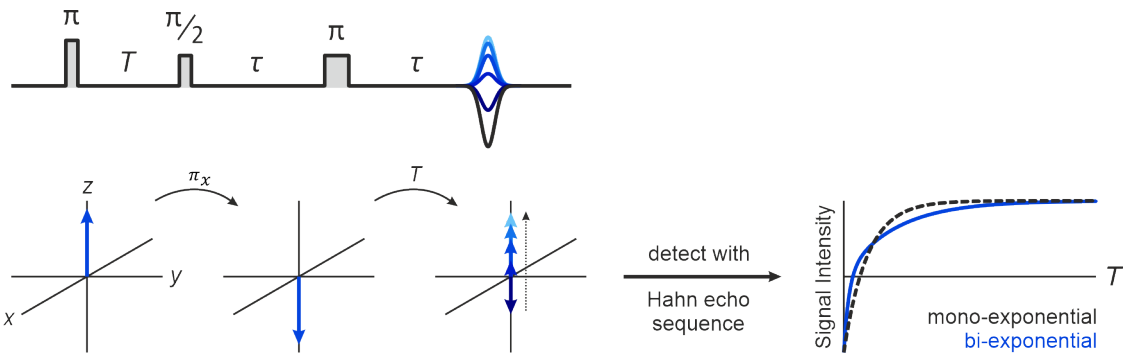

Figure 2.23: Vector model representation and pulse sequence of the inversion recovery experiment and a typical inversion recovery curve used to determine T_1.

due to energy exchange with the surroundings. A subsequent Hahn echo sequence, $(\frac{\pi}{2})_x - \tau - \pi_x - \tau$, probes the magnetisation that has returned along the z-axis as a function of the inversion recovery delay. Repeating the experiment over a series of delays yields an inversion recovery trace from which T_1 can be extracted. The echo intensity follows the equation:

$$I(T) = I_0 \left(1 - 2\mathrm{e}^{\frac{-T}{T_1}}\right) \tag{2.97}$$

with I_0 the intensity at $T = 0$.

In most samples, the recovery of longitudinal magnetisation following an inversion pulse is better described by a multi-exponential rather than a mono-exponential decay. This can arise from a distribution of intrinsic longitudinal relaxation times across different environments within the sample, each contributing to the overall signal. Extracted time constants only represent effective values of the distribution of T_1 values, and must be interpreted with caution.

The inversion recovery is also affected by **spectral diffusion**: time-dependent shifts in a spin's resonance frequency caused by changes in its magnetic surroundings, for example, spin flips of nearby nuclei or other electrons.[117,154] These shifts can move spins in or out of the frequency range detected by the microwave pulses, especially in systems with broad EPR lines or at high frequencies where the excitation bandwidth is narrow compared to the spectral width. This produces apparent changes in magnetisation that resemble relaxation, even though no true energy exchange with the environment has occurred. Using pulses with broader excitation bandwidth can reduce the influence of spectral diffusion. This pseudo-relaxation process occurs relatively quickly compared to genuine longitudinal relaxation, so it may appear as a fast decay component in the inversion recovery curve.[156] In such cases, the slower T_1 component of a bi-exponential fit is usually more representative of the true longitudinal relaxation time.

Transverse Relaxation

Transverse relaxation describes the decay of transverse magnetisation due to loss of phase coherence among an ensemble of spins. Unlike longitudinal relaxation, it does not involve net energy exchange with the environment but requires interactions that disrupt coherent spin dynamics.[117,157] A key mechanism is spin-spin relaxation, which includes energy-conserving flip-flop processes where two neighbouring spins simultaneously exchange their spin states: $|\alpha_1\rangle \rightarrow |\beta_1\rangle$ and $|\beta_2\rangle \rightarrow |\alpha_2\rangle$. These flip-flops preserve the overall spin population but cause phase coherence to decay, leading to dephasing of the transverse magnetisation. For organic radicals, decoherence is predominantly driven by interactions with nearby nuclear spins.[158]

Phase coherence is also diminished by longitudinal relaxation through single-spin flips; however, this process is roughly half as effective at destroying coherence as the flip-flop transitions that involve two spins. The total transverse relaxation rate is given by:

$$\frac{1}{T_2} = \frac{1}{T_2'} + \frac{1}{2T_1} \tag{2.98}$$

where T_2' denotes the pure spin-spin dephasing time (excluding longitudinal effects), and T_1 is the longitudinal relaxation time. From Equation 2.98, it follows that $T_2 \leq 2T_1$; there is no phase coherence at equilibrium. In liquids, $T_2' \leq 2T_1$ and therefore $T_2 \leq T_1$.[117]

In practice, transverse relaxation is measured via the phase memory time, T_m, which describes the decay of spin echo intensity as the inter-pulse delay τ of the Hahn echo pulse sequence increases. Unlike the intrinsic transverse relaxation time T_2, T_m encompasses additional dynamic processes that cause changes in the local magnetic environment, shifting electron spin resonance frequencies and preventing perfect refocusing. Because of these extra contributions, T_m represents a lower bound on T_2. The main additional contribution to T_m decay is spin diffusion, which includes spectral diffusion, instantaneous diffusion, and nuclear spin diffusion.[157] Molecular motions of the spin centre on the timescale of the echo experiment, including rotations and librations, additionally contribute to T_m by modulating the spin's magnetic environment but this contribution can often be suppressed by performing measurements at low temperatures.

Instantaneous diffusion occurs when a microwave pulse flips electron spins that are dipole-coupled to nearby electron spins. Flipping a neighbouring spin reverses its magnetic moment, abruptly altering the local magnetic field experienced by the observed spin. This shift changes the observed spin's resonance frequency, causing it to precess at a different rate during the second delay period τ and thus

reducing the effectiveness of refocusing. The magnitude of instantaneous diffusion increases with pulse bandwidth, as broader pulses excite more spins simultaneously, but can be reduced by using longer pulses with narrower bandwidths. Additionally, lowering the electron spin concentration reduces the number of coupled spins, further diminishing instantaneous diffusion effects.

At sufficiently low temperatures and low electron spin concentrations, decoherence is driven by **nuclear spin diffusion**.[159,160] This process arises from energy-conserving flip-flop transitions among nuclear spins that are hyperfine-coupled to the observed electron spins. These nuclear spin flips reverse their magnetic moment, causing fluctuations in the local magnetic field experienced by electron spins. These fluctuations shift electron spin resonance frequencies over time, reducing phase coherence and shortening the phase memory time, T_m. Although usually described semi-classically as a random process of nuclear spin flip-flops, nuclear spin diffusion can also be understood quantum mechanically as the result of a coherent, deterministic evolution of the coupled electron-nuclear spin system, through which decoherence is produced by complex many-body interactions.[158] In organic systems, protons are the main nuclear spins involved; substituting them with deuterons, which have smaller magnetic moments, weakens hyperfine couplings and extends T_m.

The echo decay experiment that quantifies T_m is based on the Hahn echo pulse sequence, with the detected echo measured as a function of the inter-pulse delay τ, as shown in Figure 2.24. The relaxation processes described above introduce random

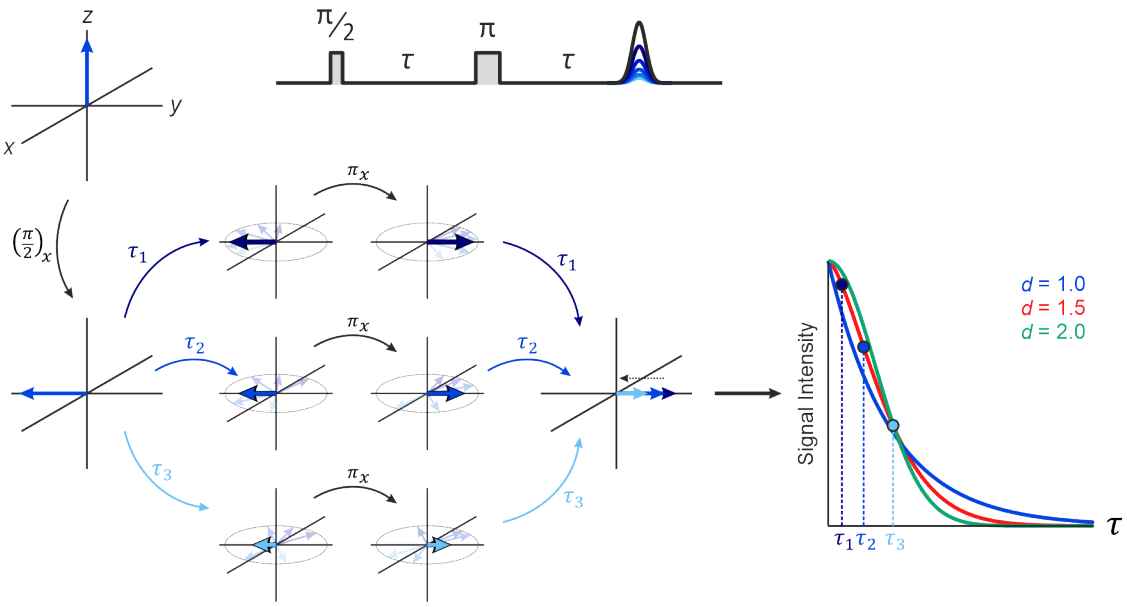

Figure 2.24: Vector model representation and pulse sequence of the echo decay experiment and typical echo decay traces with different stretched exponential factors d.

shifts in spin packet precession frequencies between the two τ periods, causing irreversible decay of the spin echo, which is modelled by a stretched exponential:

$$I(\tau) = I_0 \mathrm{e}^{-\left(\frac{2\tau}{T_\mathrm{m}}\right)^d} \tag{2.99}$$

with d a stretch factor that can provide insight on the dominant dephasing mechanism. A value of $d = 1$ suggests an echo decay driven purely by random spin flips or additional presence of instantaneous diffusion, while $d > 2$ indicates a contribution from nuclear spin diffusion.[155,161] The vector model description of the echo decay experiment is also shown in Figure 2.24, along with echo decay curves for different d-values.

From a practical standpoint, T_1 determines the rate at which the spin system returns to thermal equilibrium following excitation, thereby setting the minimum repetition time between pulse sequences. To avoid signal saturation and ensure full relaxation, the repetition time is typically chosen to be at least five times T_1.[154] At cryogenic temperatures, T_1 increases, allowing non-Boltzmann spin polarisation to persist longer and improving spectral resolution, though this reduces acquisition speed by lengthening the repetition time. In contrast, T_m defines how long transverse spin coherence is maintained, thereby limiting the maximum inter-pulse delay τ and the total duration of multi-pulse experiments involving coherent spin evolution.[119]

2.8 Electron-Nuclear Hyperfine Spectroscopy

For OPV materials, EPR spectra from field-swept Hahn echo experiments are predominantly governed by the electron Zeeman interaction, which is typically orders of magnitude stronger than hyperfine couplings at the microwave frequencies used in EPR experiments. As a result, fine spectral details arising from interactions with nearby nuclear spins are often masked. Hyperfine couplings of small magnitude lead only to unresolved splittings that contribute to broadening of the echo-detected field-swept spectrum, making direct measurement of these couplings from standard field-swept spectra challenging, if not impossible. Yet, the hyperfine interaction carries rich structural and electronic information. Both isotropic and anisotropic contributions to the hyperfine coupling provide insight into the spin density distribution and the spatial relationship between electron and nuclear spins. The dipolar component, in particular, is sensitive to the electron-nuclear separation, offering a means to estimate distances and orientations within the molecular structure. Furthermore, when orientation selection is exploited, the principal axes of the hyperfine tensor can be correlated with those of other interaction tensors, such as the $\boldsymbol{g}$- or $\boldsymbol{D}$-tensor, providing detailed insight into molecular geometry and spin density distributions.

To overcome the resolution limitations of field-swept experiments and to access this valuable hyperfine information, specialised pulse EPR techniques have been developed. Among these are:

- **ENDOR**: **E**lectron **N**uclear **DO**uble **R**esonance
- **EDNMR**: **E**LDOR[††]-**D**etected **N**uclear **M**agnetic **R**esonance

Both methods enable direct measurement of hyperfine couplings by monitoring how changes in nuclear spin populations influence the intensity of the electron spin echo. The main difference is in how the population differences are created: ENDOR uses separate excitation of electron and nuclear spins, while EDNMR achieves the same effect by exciting a single, forbidden electron spin transition that involves both electron and nuclear spins simultaneously. Although the excitation approaches differ, they ultimately produce similar nuclear spin population distributions that are detected through their influence on the electron spin echo.

The ENDOR and EDNMR experiments can be conceptually understood by considering the simple case of an electron spin ($S = \frac{1}{2}$) coupled to a nuclear spin ($I = \frac{1}{2}$). The overall spin Hamiltonian, neglecting anisotropy and non-secular contributions to the hyperfine coupling,[117] is:

$$\begin{aligned}\hat{\mathcal{H}} &= \hat{\mathcal{H}}_{\mathrm{eZ}} + \hat{\mathcal{H}}_{\mathrm{nZ}} + \hat{\mathcal{H}}_{\mathrm{hf}} \\ &= \frac{g_{\mathrm{e}}\mu_{\mathrm{B}}}{\hbar} B_0 \hat{S}_z + \frac{g_{\mathrm{n}}\mu_{\mathrm{N}}}{\hbar} B_0 \hat{I}_z + a \hat{S}_z \hat{I}_z \\ &= \omega_{\mathrm{e}} \hat{S}_z + \omega_{\mathrm{n}} \hat{I}_z + a \hat{S}_z \hat{I}_z\end{aligned} \tag{2.100}$$

The hyperfine coupling interaction is weaker than the electron Zeeman interaction and so the four eigenstates of the electron-nuclear spin Hamiltonian, under the secular approximation, are given by the uncoupled basis states, with energies:

$$\begin{aligned} |1\rangle &= |\beta_S \alpha_I\rangle & E_1 &= \frac{1}{2}(-\omega_{\mathrm{e}} + \omega_{\mathrm{n}}) - \frac{1}{4}a \\ |2\rangle &= |\beta_S \beta_I\rangle & E_2 &= \frac{1}{2}(-\omega_{\mathrm{e}} - \omega_{\mathrm{n}}) + \frac{1}{4}a \\ |3\rangle &= |\alpha_S \alpha_I\rangle & E_3 &= \frac{1}{2}(+\omega_{\mathrm{e}} + \omega_{\mathrm{n}}) + \frac{1}{4}a \\ |4\rangle &= |\alpha_S \beta_I\rangle & E_4 &= \frac{1}{2}(+\omega_{\mathrm{e}} - \omega_{\mathrm{n}}) - \frac{1}{4}a \end{aligned} \tag{2.101}$$

For nuclear spins with a positive gyromagnetic ratio, such as protons, the $|\alpha\rangle$ state is stabilised relative to $|\beta\rangle$, in contrast to electron spins. The energy level diagram of the $S = \frac{1}{2}$, $I = \frac{1}{2}$ system is depicted in Figure 2.25. At thermal equilibrium, the two eigenstates with $|\beta_S\rangle$ character are preferentially populated,

[††]ELDOR: **EL**ectron **DO**uble **R**esonance

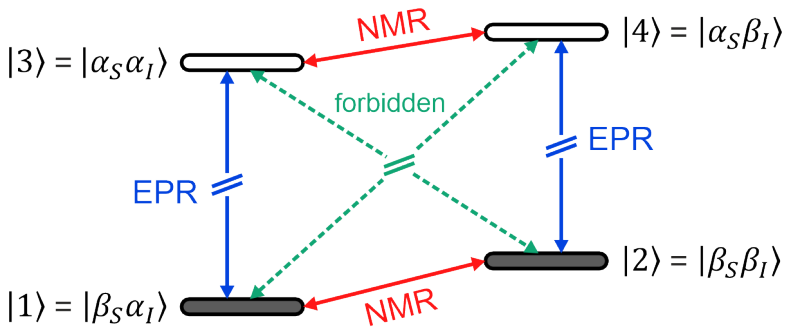

Figure 2.25: Energy level diagram for $S = \frac{1}{2}$, $I = \frac{1}{2}$ in the weak-coupling regime. The diagram is not to scale; the EPR transition energies are orders of magnitude larger than the NMR transition energies.

as the electron Zeeman splitting is far greater than the nuclear Zeeman splitting ($|\omega_e| \gg |\omega_n|$), although overall polarisation remains small as the thermal energy far exceeds all Zeeman splitting. Transitions observed in EPR involve an electron spin flip ($|\alpha_S\rangle \leftrightarrow |\beta_S\rangle$), while NMR transitions correspond to nuclear spin flips ($|\alpha_I\rangle \leftrightarrow |\beta_I\rangle$). Transitions that flip both spin states are formally forbidden.

The EPR transitions and transition energies are:

$$\begin{aligned} |1\rangle \leftrightarrow |3\rangle \qquad & |\beta_S\alpha_I\rangle \leftrightarrow |\alpha_S\alpha_I\rangle \qquad & \Delta E_{13} = \omega_e + \frac{1}{2}a \\ |2\rangle \leftrightarrow |4\rangle \qquad & |\beta_S\beta_I\rangle \leftrightarrow |\alpha_S\beta_I\rangle \qquad & \Delta E_{24} = \omega_e - \frac{1}{2}a \end{aligned} \tag{2.102}$$

and for the NMR transitions:

$$\begin{aligned} |1\rangle \leftrightarrow |2\rangle \qquad & |\beta_S\alpha_I\rangle \leftrightarrow |\beta_S\beta_I\rangle \qquad & \Delta E_{12} = \omega_n - \frac{1}{2}a \\ |3\rangle \leftrightarrow |4\rangle \qquad & |\alpha_S\alpha_I\rangle \leftrightarrow |\alpha_S\beta_I\rangle \qquad & \Delta E_{34} = \omega_n + \frac{1}{2}a \end{aligned} \tag{2.103}$$

The EPR transitions occur at much larger transition energies than the NMR transitions, requiring microwaves to induce transitions, whereas NMR transitions are induced by radiofrequency pulses.

2.8.1 Electron Nuclear Double Resonance (ENDOR)

ENDOR is a well-established technique for resolving hyperfine interactions between unpaired electron spins and nearby nuclear spins. By combining microwave and radiofrequency excitation, ENDOR can detect weak nuclear signals through the more sensitive electron spin, greatly improving the sensitivity compared to direct nuclear detection. ENDOR enables the measurement of hyperfine anisotropy, yielding information about the distribution of electron spin density across the

nuclear framework of the molecule. This is crucial for constructing detailed models of spin density distributions and understanding the local electronic structure in complex molecular systems.

The two principal pulsed ENDOR techniques are Davies and Mims ENDOR, each suited to different coupling regimes.[117,118,134] Mims ENDOR uses non-selective excitation, enhancing sensitivity by addressing a broad range of spin packets, but suffers from periodic blind spots that suppress signals at certain hyperfine couplings. These blind spots cause distortions in the ENDOR lineshape, complicating accurate determination of anisotropic hyperfine couplings, which are crucial for understanding spin delocalisation in OPVs. Although generally less sensitive, Davies ENDOR avoids this lineshape distortion by eliminating blind spots, making it the preferred method for resolving hyperfine interactions in OPV blends.

The Davies ENDOR pulse sequence and its effect on the sublevel populations are laid out in Figure 2.26. The experiment begins with a selective microwave π-pulse, typically inverting the population across one of the EPR transitions, without affecting the other transition; in the case shown, $|1\rangle \leftrightarrow |3\rangle$. Within the delay T, a radiofrequency π-pulse is applied. If the radiofrequency pulse is off-resonance, the populations remain unchanged, and a Hahn echo detection sequence measures an inverted echo corresponding to the $|3\rangle \rightarrow |1\rangle$ transition. If, however, the radiofrequency pulse is on-resonance with an NMR transition ($|3\rangle \leftrightarrow |4\rangle$ or $|1\rangle \leftrightarrow |2\rangle$), population is transferred between these states, thereby reducing the population difference across the detected EPR transition. This results in a reduced intensity of the inverted echo.

The ENDOR spectrum is acquired by monitoring the echo intensity as a function of radiofrequency. In the weak coupling regime, where the nuclear Larmor frequency dominates over the hyperfine interaction, the spectrum is centred at $\omega_{\mathrm{rf}} - \omega_{\mathrm{n}}$, and two peaks appear, split by the hyperfine coupling constant a. Experimentally, the measured quantity is the linear frequency ν, related to the angular frequency by:

$$\nu = \frac{\omega}{2\pi} \tag{2.104}$$

and a characteristic powder pattern is observed, with turning points corresponding to the principal values of A (A_x, A_y, and A_z), as shown in Figure 2.27. The ENDOR spectra are plotted on an axis given by $\nu_{\mathrm{rf}} - \nu_{\mathrm{n}}$, where the nucleus of interest is ^{1}H.

The duration of the radiofrequency π-pulse in ENDOR experiments is typically on the order of tens of microseconds.[134] During this time, partial relaxation of the electron spin system can occur, reducing the population difference between spin states ($|3\rangle \rightarrow |1\rangle$) and lowering the signal-to-noise ratio. While shorter radiofrequency pulses would reduce relaxation losses, they require higher power to

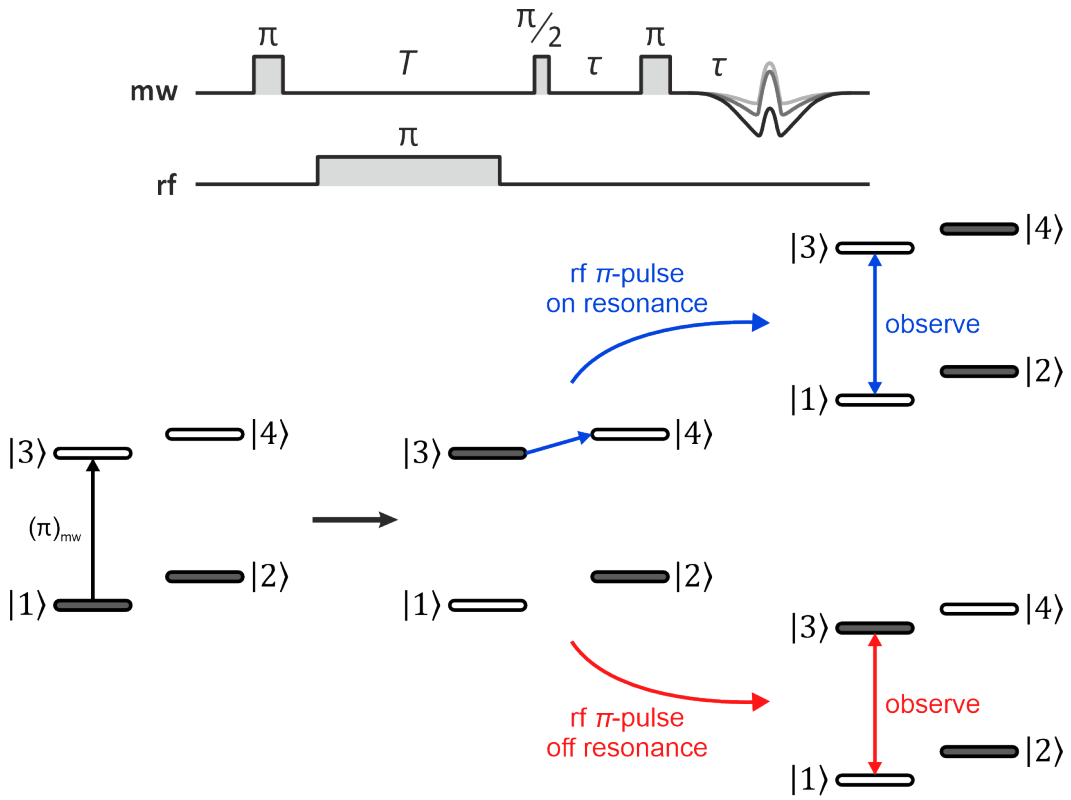

Figure 2.26: Pulse sequence and its effect on the sublevel populations for a Davies ENDOR experiment. The spin states correspond to a coupled $S = \frac{1}{2}$, $I = \frac{1}{2}$ system. The radiofrequency π-pulse inverts the population across an NMR transition, if on-resonance.

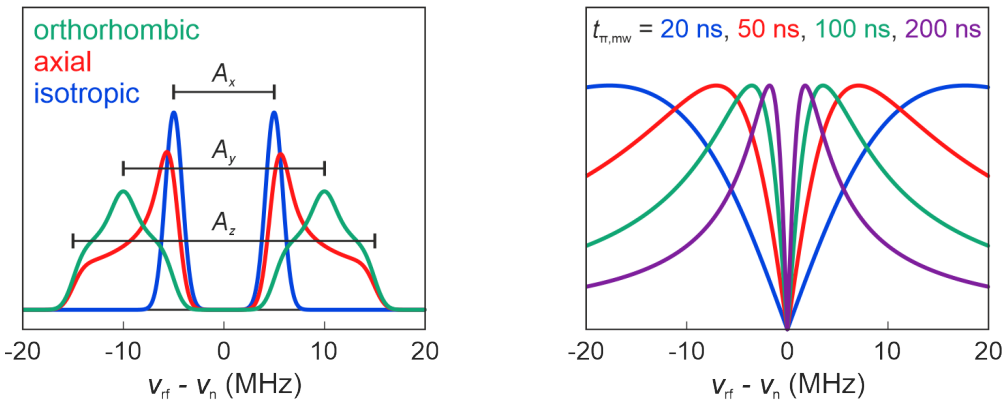

Figure 2.27: Left) Simulated ENDOR spectra for electron-nuclear hyperfine interactions of isotropic, axial, and orthorhombic symmetry. Right) Intensity function for the Davies ENDOR experiment for different microwave inversion pulse durations.

achieve a flip angle of π. However, excessively short, high-power pulses broaden the excitation bandwidth, known as power broadening, reducing spectral resolution.[119] A balance is therefore required: the pulse must be long enough to maintain resolution, yet short enough to minimise signal loss from electron spin relaxation.

To generate an ENDOR signal in the Davies sequence, the initial microwave π-pulse must selectively invert only one of the two electron spin transitions associated with each nucleus. If both transitions are excited simultaneously, their population differences become equalised, and subsequent radiofrequency-driven nuclear transitions produce no net change in electron spin echo intensity, eliminating the ENDOR effect. In spin systems with multiple hyperfine couplings, this selectivity governs which nuclei contribute to the observed spectrum. Strongly-coupled nuclei, whose associated EPR transitions are well separated, are more readily excited selectively. In contrast, weakly-coupled nuclei, with closely spaced EPR transitions, are more susceptible to simultaneous excitation and thus reduced ENDOR visibility.

This selectivity is determined by the bandwidth of the microwave π-pulse, which is inversely proportional to its duration (see Equation 2.96). To resolve a specific hyperfine coupling a, the pulse duration $t_{\pi,\mathrm{mw}}$ must be long enough that its excitation bandwidth is narrower than a.

The absolute Davies ENDOR intensity can be described by the intensity function V:[117]

$$V = V_{\max} \frac{\sqrt{2}\,\eta_\mathrm{s}}{\eta_\mathrm{s}^2 + \frac{1}{2}} \tag{2.105}$$

where $V_{\max}$ is the maximum ENDOR signal, achieved when the selectivity parameter $\eta_\mathrm{s} = \eta_{\mathrm{s,max}} = \frac{\sqrt{2}}{2}$. This parameter depends on the pulse length and the hyperfine coupling a:

$$\eta_\mathrm{s} \propto \frac{a}{2}\, t_\pi \tag{2.106}$$

The resulting Davies ENDOR intensity function is shown in Figure 2.27. At short pulse lengths, the excitation bandwidth is wide, allowing detection of nuclei with large hyperfine couplings but suppressing weakly-coupled nuclei due to insufficient selectivity. Conversely, longer pulses improve sensitivity to small couplings by narrowing the excitation bandwidth but reducing sensitivity to large ones.

A blind spot, where the ENDOR signal vanishes, occurs at the nuclear Larmor frequency ($\nu_\mathrm{rf} = \nu_\mathrm{n}$) when $\eta_\mathrm{s} = 0$. The width of this blind spot increases for shorter pulses, making it particularly problematic when attempting to measure weak couplings. Therefore, the microwave pulse length must be chosen to balance a number of factors: selectivity between hyperfine-split transitions, signal intensity,

and blind spot effects. As a rule of thumb, the optimal pulse duration for detection of a hyperfine coupling a is:[162]

$$t_{\pi,\mathrm{mw}} = \frac{\eta_{\mathrm{s,max}}}{a} \tag{2.107}$$

Experimental spectra often still show residual intensity at the central blind spot, attributed to contributions from a large number of weakly-coupled nuclear spins, typically outside the molecule of interest, such as distant protons on other molecules.[163]

If the hyperfine tensor is anisotropic, orientation-selective ENDOR can be used to correlate A-frames with g- or D-frames by recording spectra at a series of external magnetic field positions, as illustrated in Figure 2.28. In the example shown, the spin system possesses orthorhombic electron Zeeman and hyperfine tensors, $\boldsymbol{g}$ and $\boldsymbol{A}$, which are assumed to be aligned in the molecular frame. When the microwave π-pulse is applied at a magnetic field corresponding to g_x, spin packets are selectively excited in which $g \approx g_x$ and the molecular x-axis is aligned with the external magnetic field. Since the observed hyperfine splitting depends on the projection of the $\boldsymbol{A}$-tensor along the magnetic field direction, the resulting ENDOR spectrum reflects the A_x component of the hyperfine interaction. Similar measurements at the g_y and g_z field positions excite spin packets with the y- and z-axis aligned with the field, yielding the A_y and A_z components, respectively. At the g_x and g_z field positions, the ENDOR spectra closely resemble single-crystal patterns, while at g_y, the spectra include additional contributions from spin packets with orientations between the x- and z-axes.

It is generally not true that the $\boldsymbol{g}$- and $\boldsymbol{A}$-tensors are aligned. If the orientation of the $\boldsymbol{g}$-tensor is already known, however, then the relative orientation of the hyperfine tensor $\boldsymbol{A}$ can be determined, or vice-versa, from the change in hyperfine coupling across the set of orientation-selective ENDOR spectra.

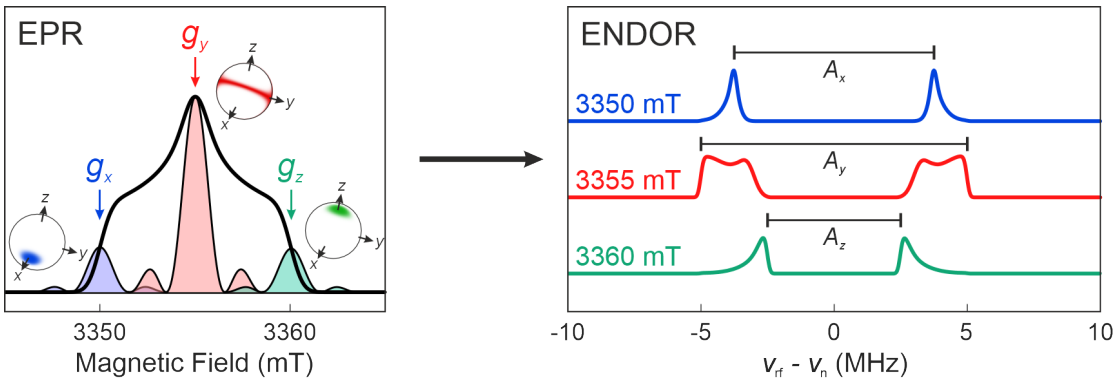

Figure 2.28: Orientation selection in ENDOR experiments. The microwave pulse excites a subset of electron spins satisfying the resonance condition at the selected field position. The ENDOR spectrum will then be dominated by the component of the hyperfine interaction aligned with the principal g-value being excited.

2.8.2 ELDOR-detected NMR (EDNMR)

EDNMR is especially powerful for detecting nuclei with small gyromagnetic ratios, because such nuclei respond weakly to radiofrequency pulses, requiring long or intense radiofrequency excitation that can be difficult to achieve experimentally. EDNMR bypasses direct nuclear excitation and instead uses microwave pulses to drive forbidden electron-nuclear transitions, enabling sensitive detection without relying on the nucleus's weak radiofrequency response.

An illustration of the EDNMR pulse sequence, and its corresponding effect on the sublevel populations, is shown in Figure 2.29. The experiment begins by applying a high-turning angle (HTA) microwave pulse at frequency ω_{mw_1}. This HTA pulse is designed to excite formally forbidden transitions, such as double quantum transitions involving simultaneous flips of electron and nuclear spins, that are not accessible by standard pulses. As a result, it requires far longer pulse durations than usual microwave pulses. Following the HTA pulse, a standard Hahn echo detection sequence is performed at a fixed frequency ω_{mw_0}. The electron spin echo intensity is monitored while sweeping the HTA pulse frequency, and the resulting spectrum is plotted as a function of $\nu_{\mathrm{mw}_1} - \nu_{\mathrm{mw}_0}$, with ν the linear frequency form of ω as before.

In Figure 2.29, the Hahn echo detection pulse sequence is fixed at a frequency corresponding to the $|1\rangle \leftrightarrow |3\rangle$ EPR transition, and any changes in the population difference between these two states will be detected. When the HTA pulse is resonant with a forbidden transition ($|1\rangle \rightarrow |4\rangle$ or $|2\rangle \rightarrow |3\rangle$), population is redistributed

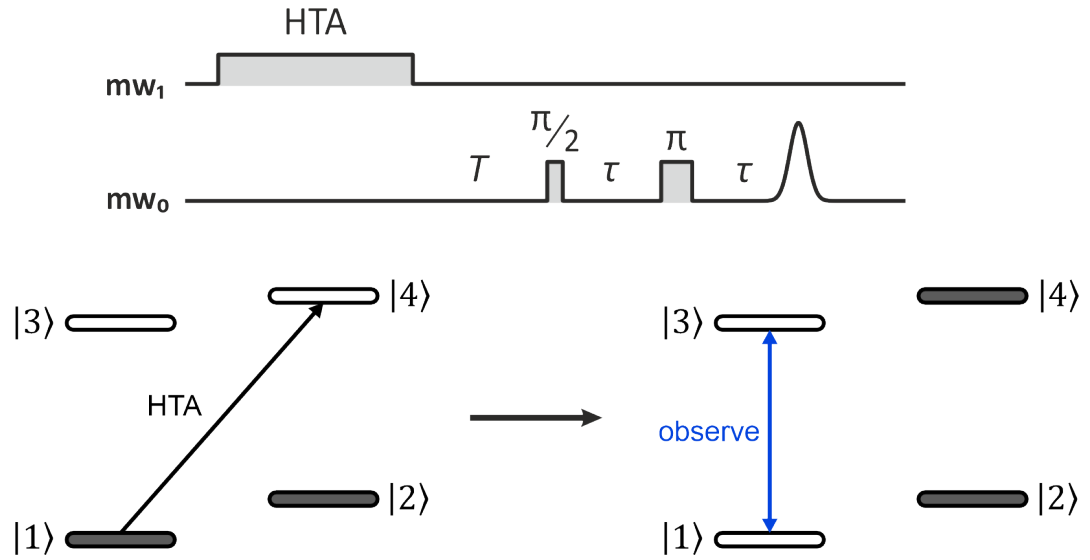

Figure 2.29: Pulse sequence and its effect on the sublevel populations for an EDNMR experiment. The four spin states correspond to a coupled $S = \frac{1}{2}$, $I = \frac{1}{2}$ system.

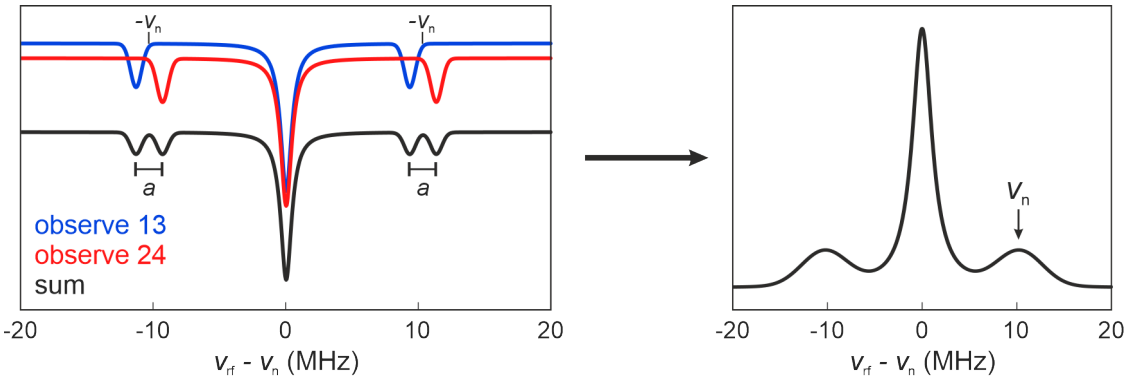

Figure 2.30: Left) Simulated EDNMR spectrum for an $S = \frac{1}{2}$, $I = \frac{1}{2}$ system with isotropic hyperfine coupling $a = 2\,\text{MHz}$ and a nuclear spin with $\nu_n = 10.3\,\text{MHz}$ (^{14}N Larmor frequency at W-band), Right) Simulated EDNMR spectrum for a broadened powder sample of an electron spin interacting with many ^{14}N nuclei with a becoming unresolved. By convention, the change in intensity of the EDNMR spectrum is made positive.

between these states. This reduces the population difference across the $|1\rangle \leftrightarrow |3\rangle$ EPR transition, leading to a reduction in echo intensity at the two frequencies:

$$\begin{aligned} \omega_{\text{mw}_1} &= \omega_{2\leftrightarrow 3} = \omega_\text{e} - \omega_\text{n} & \Delta\omega &= \omega_{2\leftrightarrow 3} - \omega_{1\leftrightarrow 3} = -\omega_\text{n} - \frac{1}{2}a \\ \omega_{\text{mw}_1} &= \omega_{1\leftrightarrow 4} = \omega_\text{e} + \omega_\text{n} & \Delta\omega &= \omega_{1\leftrightarrow 4} - \omega_{1\leftrightarrow 3} = +\omega_\text{n} - \frac{1}{2}a \end{aligned} \tag{2.108}$$

When the HTA pulse is resonant with the allowed $|1\rangle \leftrightarrow |3\rangle$ EPR transition ($\nu_{\text{mw}_1} = \nu_{\text{mw}_0}$), it equalises the populations between these states, saturating the transition and causing a significant reduction in echo intensity seen as a central hole. This central hole is undesired, and may obscure peaks corresponding to forbidden transitions. The sensitivity of EDNMR increases at higher magnetic fields, where nuclear Larmor frequencies have greater separation from the central hole.[135] If instead the HTA pulse excites the other EPR transition ($|2\rangle \leftrightarrow |4\rangle$), no change in echo intensity occurs because the Hahn echo sequence probes only the $|1\rangle \leftrightarrow |3\rangle$ transition.

The resulting EDNMR spectrum is shown in blue in Figure 2.30. Peaks due to the forbidden transitions appear at $\pm\omega_\text{n} - \frac{1}{2}a$. If every electron and nuclear spin was in the same environment, or the HTA pulse was extremely selective (very narrow bandwidth), then this EDNMR spectrum would be the overall spectrum. However, because there will be a distribution of spins in a powder sample, for another spin packet, ω_e and ω_n will take different values. There will be a spin packet where the fixed microwave frequency ω_{mw_0} now matches the other EPR transition: $|2\rangle \leftrightarrow |4\rangle$. When the HTA pulse matches the two forbidden transitions,

the frequencies of the reduction in echo intensity are now:

$$\begin{aligned} \omega_{\mathrm{mw}_1} &= \omega_{2\leftrightarrow 3} = \omega_\mathrm{e} - \omega_\mathrm{n} & \Delta\omega &= \omega_{2\leftrightarrow 3} - \omega_{2\leftrightarrow 4} = -\omega_\mathrm{n} + \frac{1}{2}a \\ \omega_{\mathrm{mw}_1} &= \omega_{1\leftrightarrow 4} = \omega_\mathrm{e} + \omega_\mathrm{n} & \Delta\omega &= \omega_{1\leftrightarrow 4} - \omega_{2\leftrightarrow 4} = +\omega_\mathrm{n} + \frac{1}{2}a \end{aligned} \tag{2.109}$$

The two peaks, in this case, appear at $\pm\omega_\mathrm{n} + \frac{1}{2}a$, as shown in red. The total EDNMR spectrum is therefore a sum of the EDNMR of each spin packet. The two peaks appear as doublets in the overall spectrum, centred at $\pm\omega_\mathrm{n}$ and split by a, as equivalently observed in ENDOR. Spin packets where ω_{mw_0} does not match either ω_{13} or ω_{24} do not reduce the echo intensity and contribute to the baseline signal. For an electron spin with many inequivalent nuclei, the hyperfine splitting will be unresolved.

Chapter 3

Charged States and Spin Delocalisation

3.1 Introduction

For successful charge generation in OPVs, charge transfer must occur at the donor:acceptor interface, followed by separation of the interfacial charge-transfer state into separated charges (SCs), also known as polarons, that then travel through the pure domains. One major challenge in OPV efficiency is to provide a pathway for charge separation from the Coulomb interaction that binds the charge-transfer state.[81,164–167]

Charge delocalisation has been proposed as an essential factor for promoting charge separation,[70,84–88,168] and understanding of the local electronic and molecular structure can inform interpretation of the different steps in the photovoltaic mechanism. A number of theoretical studies have been carried out to predict the effect of delocalisation on charge transport,[87,169–174] however, there are few

studies using a combined experimental and computational approach. The selectivity of EPR spectroscopy to electron spins lends its usefulness to characterisation of spin, and therefore charge, delocalisation: donor and acceptor SCs can be individually distinguished by EPR. Knowledge of the spin interactions that define the EPR spectrum, as well as the distribution of these parameters, can give insight into the electronic structure and charge delocalisation of organic materials. Classification of the g-values and their distribution is critical for meaningful interpretation of the charge-transfer state and its associated kinetics, which is later measured by time-resolved EPR in Chapter 5.[139,175–177]

A series of pulse EPR measurements were carried out at X-, Q- and W-band microwave frequencies in order to investigate charge behaviour in two high-performing non-fullerene acceptor blends, PBDB-T:ITIC and PM6:Y6. Their analogous fullerene acceptor blends, PBDB-T:PCBM and PM6:PCBM, were also probed. Characterisation of the echo-detected EPR signals was straightforward for the PCBM blends; the principal g-values of $PCBM^{\bullet-}$ are distinct from those of the polymer donor SCs at the microwave frequencies used in this work, such that the spectra are separated.[88,168,177,178] The non-fullerene acceptors, however, share similar molecular building blocks with the polymer donors, resulting in similar spin environments and considerable overlap of the EPR spectra.[177,178]

Accurate disentanglement required more complicated pulse EPR techniques, and a more sophisticated approach was adopted. Differences in longitudinal relaxation times of donor and acceptor SCs can be utilised to design a pulse sequence that minimises one of the two contributions to the EPR signal, a relaxation-filtering approach first proposed by Maly et al.[179,180] Alternatively, spin-active nuclei that appear in only one of the two molecular structures can be exploited to isolate its EPR contribution; ^{14}N nuclei are present in the non-fullerene acceptor molecules but not the polymer donors. Coupling of these nuclei to the electron spin can be capitalised on in an ELDOR-detected NMR (EDNMR)-induced EPR experiment.[178,181]

EPR characterisation of the donor and acceptor charges is complemented by DFT calculations that model charge delocalisation, with the DFT models corroborated by Electron-Nuclear Double Resonance (ENDOR) spectroscopy. ENDOR provides information about the strength of the electron-nuclear hyperfine interactions, which directly relate to the extent of charge delocalisation - a more delocalised electron spin density reduces the strength of the interaction of the electron spin with each spin-active nucleus.[88,168,177,182–185] The DFT spin density distributions provide a detailed insight into the local electronic structure of the charges, which will determine the efficiency of charge separation and transport, and more broadly, power conversion efficiency for a given OPV blend.

3.2 Experimental Methods

3.2.1 Sample Preparation

The donor polymers PBDB-T and PM6 and acceptor molecules ITIC and Y6 were purchased from 1-Material and the PCBM acceptor was purchased from Ossila. The sample preparation was performed in a glovebox under nitrogen atmosphere. Solutions were prepared in chlorobenzene (anhydrous, purity 99.8%, Sigma-Aldrich) for the PBDB-T blends and in chloroform (anhydrous, purity $\geq$ 99%, Sigma-Aldrich) for the PM6 blends. Initially, 20 mg mL^{-1} stock solutions were prepared for each material and stirred at 40 °C and 500 rpm for about three hours. Blend solutions were then prepared by mixing donor and acceptor solutions in a ratio of 1 : 1.5 for PBDB-T:PCBM,[47,48] 1 : 1 for PBDBT:ITIC,[186] 1 : 1.2 for PM6:PCBM,[187] and 1 : 1.2 for PM6:Y6,[46] and stirred overnight at room temperature.

For the X- and Q-band EPR measurements, samples were prepared by transferring 30 µL of the blend solutions, diluted to 10 mg mL^{-1}, into 2.0 mm ID, 2.9 mm OD quartz EPR tubes, evaporating the solvent under vacuum to create a film on the inside of the EPR tube and flame-sealing the tube after back-filling with helium to 500 mbar. For the W-band EPR measurements, powder samples were prepared from drop-cast films by scratching fragments of the films off a glass substrate with a scalpel and transferring them into 0.70 mm ID, 0.87 mm OD quartz EPR tubes up to a fill height of about 2 mm. The quality of the powder samples was verified by observing no change in EPR signal at different angles to the external magnetic field.

3.2.2 EPR Experiments

X-band pulse EPR measurements were performed on a Bruker ElexSys E680 spectrometer with a Bruker EN 4118X-MD4(-W1) resonator and 1 kW Applied Systems Engineering TWT amplifier. Q-band pulse EPR measurements were performed on a Bruker ElexSys E580 spectrometer with a TE011 cylindrical cavity Q-band resonator with large sample access and optical window,[188] built by the mechanical engineering workshop of the Physics department at the FU Berlin, and a 150 W TWT amplifier. W-band pulse EPR measurements were performed on a Bruker ElexSys E680 spectrometer with a Bruker Teraflex EN600-1021H resonator; all W-band pulse EPR measurements were carried out by Oliver Christie, a Master's student in the research group, at the FU Berlin. All spectrometers were equipped with Oxford Instruments helium-flow cryostats and temperature control systems and all experiments were performed at a temperature of 20 K. A field calibration using the known N@C_{60} g-value[150] was performed before the EPR measurements at all frequency bands.

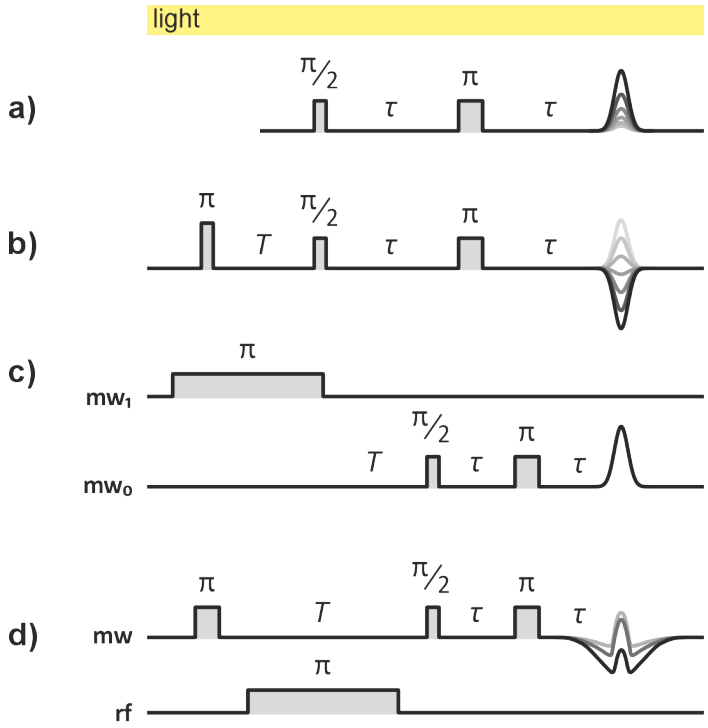

Figure 3.1: Pulse sequences used for the EPR experiments described in this chapter. a) Echo-detected EPR and Echo Decay b) Inversion Recovery and Relaxation Filtered EPR c) Electron-Electron Double Resonance Detected NMR (EDNMR) d) Electron Nuclear Double Resonance (ENDOR). All experiments were carried out with the sample under continuous illumination.

At X- and Q-band, the samples were illuminated through the optical window of the cryostat with depolarised light from an EKSPLA NT230 tuneable diode-pumped laser system set to 532 nm and $0.25-1$ mJ at 50 Hz. To achieve steady-state measurements, the laser and spectrometer were not synchronised. Some of the Q-band measurements were also performed using constant white-light illumination with a Schott DCR III 150 W halogen light source, giving equivalent spectra to non-synchronised laser excitation. At W-band, the samples were illuminated using a continuous-wave 532 nm diode-pumped solid state laser (Thorlabs DJ532-10) with an optical output power of 10 mW. The light was focused into an optical fibre fed through the sample holder and inserted into the W-band EPR tube with the tip of the fibre at a distance of about 1 cm from the bottom of the tube. Reference measurements without illumination were performed immediately after inserting the samples into the cryostat (with the optical window covered at X- and Q-band) before illumination.

Pulse EPR spectra were recorded as echo-detected field sweeps, using the pulse sequence depicted in Figure 3.1a. In order to obtain EPR spectra with undistorted lineshapes, selective pulses and broad integration windows were used. At X-band, $t_{\pi/2} = 50$ ns, $t_\pi = 100$ ns and $\tau = 300$ ns. At Q-band, $t_{\pi/2} = 60$ ns, $t_\pi = 120$ ns and

$\tau = 400\,\text{ns}$. At W-band, $t_{\pi/2} = 60\,\text{ns}$, $t_\pi = 120\,\text{ns}$ and $\tau = 400\,\text{ns}$. Echo decay measurements were performed using the same pulse sequence as the echo-detected field sweeps ($t_{\pi/2} = 60\,\text{ns}$, $t_\pi = 120\,\text{ns}$), recording the integrated echo and varying τ. A two-step phase cycle on the first pulse was used in all cases.

Inversion recovery measurements were performed with the pulse sequence described in Figure 3.1b, with an initial inversion pulse of $t_\pi = 60\,\text{ns}$ and an echo detection sequence with $t_{\pi/2} = 60\,\text{ns}$, $t_\pi = 120\,\text{ns}$, $\tau = 400\,\text{ns}$ with a four-step phase cycle on the first pulse.[154] The inter-pulse delay T was varied and the integrated echo was recorded. At W-band, the inversion recovery experiments were performed as a function of magnetic field.

ELDOR-detected NMR experiments were performed at W-band with the pulse sequence in Figure 3.1c: a high-turning angle (HTA) pulse of 40 µs (on the spectrometer's ELDOR channel (mw_1)), $T = 4\,\mu\text{s}$ and an echo detection sequence with $t_{\pi/2} = 120\,\text{ns}$, $t_\pi = 240\,\text{ns}$ and $\tau = 500\,\text{ns}$, with a two-step phase cycle. The length and intensity of the HTA pulse were tuned to minimise the central Lorentzian hole and maximise the intensity of the peaks centred at the ^{14}N Larmor frequency. The frequency of the HTA pulse was swept over 50 MHz around the frequency of the detection sequence. ELDOR-detected NMR experiments were performed both as a function of magnetic field and additionally at selected magnetic field positions. EDNMR-induced EPR experiments were performed by setting the HTA pulse frequency on- ($\Delta\nu = 10\,\text{MHz}$) and off-resonance ($\Delta\nu = 20\,\text{MHz}$) and sweeping the magnetic field.

Davies ENDOR measurements were performed using the pulse sequence in Figure 3.1d. At X-band, for the pulses at microwave frequencies: $t_\pi = 140\,\text{ns}$, $t_{\pi/2} = 70\,\text{ns}$ and $\tau = 600\,\text{ns}$; for the radiofrequency pulses: $t_{\pi,\text{rf}} = 12\,\mu\text{s}$, with delays of 2 µs between the radiofrequency and microwave pulses ($T = 16\,\mu\text{s}$). At Q-band, $t_\pi = 120\,\text{ns}$, $t_{\pi/2} = 60\,\text{ns}$, $\tau = 350\,\text{ns}$, $t_{\pi,\text{rf}} = 28\,\mu\text{s}$ and $T = 32\,\mu\text{s}$. At W-band, $t_\pi = 120\,\text{ns}$, $t_{\pi/2} = 60\,\text{ns}$, $\tau = 280\,\text{ns}$, $t_{\pi,\text{rf}} = 40\,\mu\text{s}$ and $T = 44\,\mu\text{s}$. For the W-band ENDOR experiments, an Amplifier Research 150 W RF amplifier was used, while a Bruker 150 W RF amplifier was used for the X- and Q-band ENDOR measurements. The radiofrequency pulse length was adjusted for ^{1}H using a Rabi nutation experiment. The frequency of the radiofrequency pulse was varied stochastically.

Simulation of the echo-detected EPR, relaxation-filtered and EDNMR-induced EPR spectra was carried out using the *pepper* function of the software package EasySpin[130] (Version 6.0), in MATLAB.

3.2.3 Density Functional Theory

DFT calculations were carried out by Oliver Christie, as part of a Master's project. All DFT calculations were performed with the ORCA program system[189–194] (version 5.0.4). Geometry optimisations were performed first for the ground state and then for the radical cation state for the donors and the radical anion state for the acceptors using either the BP86 or the range-separated hybrid ωB97X-D4[195,196] functional and the def2-SVP basis set, including a dispersion correction.[197–203] Calculations were performed for both the default range-separation parameter $\omega = 0.25\,{a_0}^{-1}$ as well as an ω value individually tuned for each of the investigated molecules based on matching the HOMO eigenvalue with the ionisation potential for donor radical cations or the LUMO eigenvalue with the electron affinity for acceptor radical anions following procedures described in the literature.[204–206] The optimised values of $\omega_{\text{opt}} = 0.11 - 0.12\,{a_0}^{-1}$ are in agreement with ranges previously determined for other organic semiconducting donor polymers.[207] In all calculations, a conductor-like polarisable continuum model with a dielectric constant of $\epsilon = 3.5$ was chosen to model effects of the environment in an organic semiconductor film.[70,178,208]

g-values, hyperfine and nuclear quadrupole couplings[209–212] were calculated for the optimised radical cation or radical anion geometries using either the hybrid PBE0 functional or the range-separated hybrid ωB97X-D4[195,196] functional and the EPR-II basis set for H, C, N, O and F and the IGLO-II basis set for S.[213–216]

3.3 Results and Discussion

3.3.1 Multi-Frequency Pulse EPR of Separated Charges

Echo-detected EPR spectra of PBDB-T:PCBM, PM6:PCBM, PBDB-T:ITIC, and PM6:Y6 are shown in Figure 3.2, measured at X-, Q-, and W-band microwave frequencies. All experimental spectra have been adjusted to a common microwave frequency for each band: 9.8 GHz (X-band), 33.9 GHz (Q-band), and 94 GHz (W-band). Unless otherwise stated, all EPR measurements were conducted at 20 K. The donor:acceptor blends were measured with and without continuous illumination. The difference between the two signals gives the EPR spectrum of the separated charges generated by light excitation. The dark signals represent a minor contribution and may be present for a number of reasons, including stable radicals in the instrument set-up, charged states formed from prior illumination, and residual charged states from unintentional dopants.

Background signals unrelated to the sample, due to contamination of the resonator, can be removed by measuring the EPR signal of an empty tube and

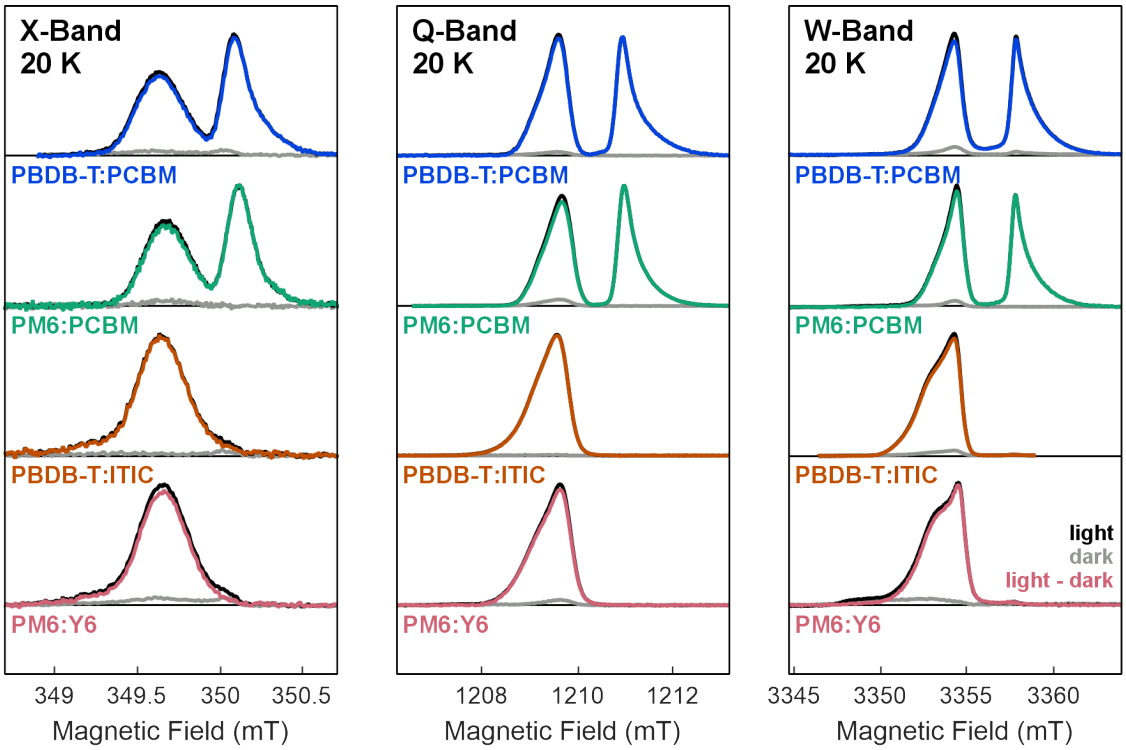

Figure 3.2: Experimental echo-detected EPR spectra of PBDB-T:PCBM, PM6:PCBM, PBDB-T:ITIC, and PM6:Y6, measured at three microwave frequencies: X-, Q- and W-band. Spectra were measured with and without light excitation, plotted in black and grey, with the difference, the light-induced contribution, shown in blue, green, orange or pink, depending on the donor:acceptor blend. This colour scheme will be used consistently throughout the thesis.

subtracting its signal from the experimental spectra; this was carried out at W-band, where the resonator had a significant background signal. Charges due to intrinsic defects or formed from unintentional doping are typically unavoidable and are the main contributor to the small dark signal observed in the blends, primarily due to the polymer donor.

The light-induced signal for the fullerene acceptor blends shows two well-resolved peaks, whilst the blends with non-fullerene acceptors show a broader single peak. At X-band, the PBDB-T$^{\bullet+}$/ PM6$^{\bullet+}$ and PCBM$^{\bullet-}$ contributions are mostly, but not fully, resolved - higher frequency measurements can fully separate the two peaks. PCBM$^{\bullet-}$ has been characterised extensively in the literature[139,168,177,178,217–226] and the peak at high-field can be assigned to a negative charge on the PCBM molecule. The conspicuous absence of this peak in the non-fullerene acceptor blend EPR spectra confirms this assignment. The low-field peak can therefore be assigned to a positive charge on the electron donor molecule: PBDB-T$^{\bullet+}$ and PM6$^{\bullet+}$. The shape of the PCBM$^{\bullet-}$ peak is consistent between PBDB-T:PCBM and PM6:PCBM, and generally holds the same shape as the microwave frequency increases, with a long broad tail extending into the high-field region.

While the PBDB-T$^{\bullet+}$ and PM6$^{\bullet+}$ peaks at X-band appear symmetrical, at higher microwave frequencies, asymmetry in the polymer donor EPR signal becomes visible. The lack of signal asymmetry in the X-band data of PBDB-T$^{\bullet+}$ and PM6$^{\bullet+}$ can be explained by the large number of spin-active ^{1}H nuclei present in the molecular structures of the polymers, which interact with the electron spin. These electron-nuclear hyperfine interactions do not depend on the external magnetic field, meaning line broadening from unresolved hyperfine couplings does not scale with microwave frequency. The field-dependent contributions to the linewidth may be asymmetric and will become more apparent at higher microwave frequencies. Asymmetry in the donor and acceptor peaks is caused by the orientation dependence of the g-value with the external magnetic field, known as g-anisotropy. In the cases of PBDB-T$^{\bullet+}$, PM6$^{\bullet+}$ and PCBM$^{\bullet-}$, the shapes of the signals are consistent with an axial, or near-axial, g-anisotropy; the shoulders on the low-field (PBDB-T$^{\bullet+}$, PM6$^{\bullet+}$) or high-field (PCBM$^{\bullet-}$) side of the peak are caused by one of the three principal g-values being distinct from the other two g-values. Recording EPR spectra at multiple frequencies also constrains the reasonable range of parameters that can fit the signal shape, improving spectral interpretation.

For non-fullerene acceptor blends, a single peak is observed, appearing at similar resonance frequencies as the polymer peak in the fullerene acceptor blends. At X-band, the spectral shape is similar to the polymer shape in the fullerene acceptor blend spectrum, with an additional broadening at the wings, particularly on the low-field side of the peak (349.2 mT). The fact that this feature appears only at X-band suggests it is likely related to hyperfine interactions. Single molecule acceptors, such as ITIC$^{\bullet-}$ and Y6$^{\bullet-}$, generally have more localised spin density distributions than charges on polymer donors with extensive conjugated π-systems.[178,227–231] This localisation increases the strength of the interactions with nearby nuclei, leading to larger hyperfine interactions that each split the signal. Due to the distribution of hyperfine couplings, these splittings manifest as an additional broadening.

At higher microwave frequencies, the non-fullerene acceptor contribution becomes more noticeable. At W-band, a clear shoulder is observed at lower magnetic fields than the main spectral peak for both PBDB-T:ITIC and PM6:Y6 ($3350-3353$ mT). This feature can be attributed to the non-fullerene acceptor. However, even at W-band, the donor and acceptor contributions overlap considerably. If the set of principal g-values of the donor and acceptor are too similar, then their contributions cannot be separated by increasing microwave frequency alone. In such cases, additional experimental methods are required for accurate spectral disentanglement.

With the donor and acceptor signals fully separated at Q- and W-band, the EPR spectra of the fullerene acceptor blends were simulated, fitting the experimental data globally. The resulting simulations are shown in Figure 3.3, with the corresponding

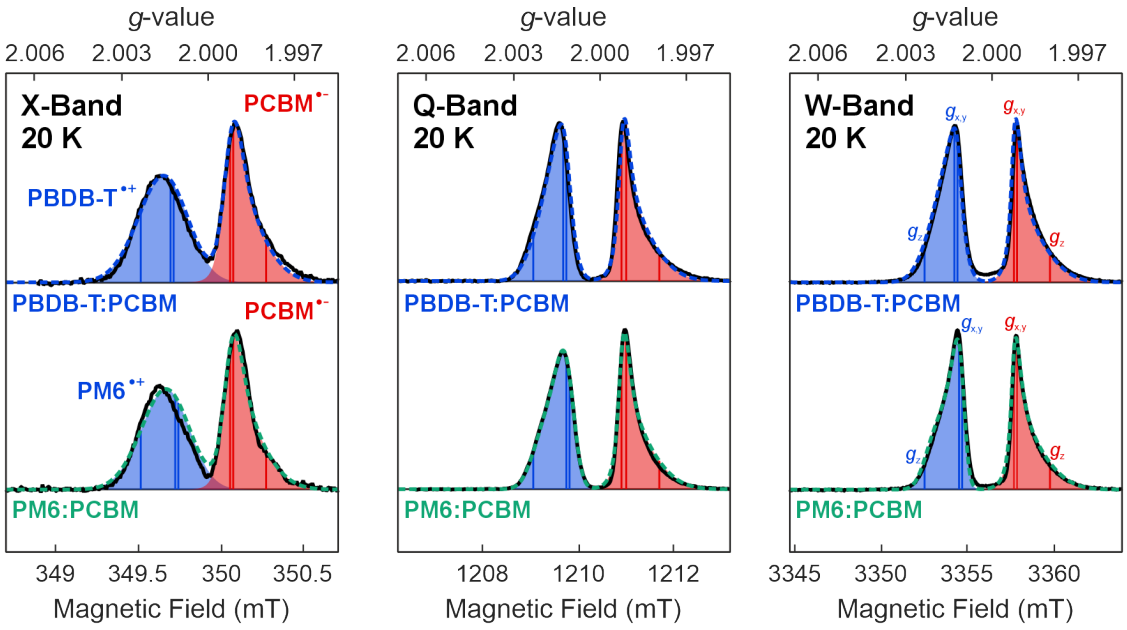

Figure 3.3: Simulation of the light-induced EPR spectra of PBDB-T:PCBM (top) and PM6:PCBM (bottom) at X-, Q- and W-band. The experimental spectrum is black, the simulated charged state on the donor is blue, the simulated charged state on the acceptor is red, and the sum of the two simulations is dashed over the experimental spectrum. The blue and red lines correspond to the three principal g-values. Full simulation parameters can be found in Table 3.1.

Material	g-value			g-strain	Linewidth (mT)		
	g_x	g_y	g_z	z	X	Q	W
PBDB-T$^{\bullet+}$	2.0022	2.0023	2.0033	0.0008	0.26	0.34	0.86
PM6$^{\bullet+}$	2.0020	2.0021	2.0033	0.0004	0.23	0.31	0.61
PCBM$^{\bullet-}$	2.0002	2.0001	1.9990	0.0019	0.10	0.16	0.32

Table 3.1: Simulation parameters of light-induced echo-detected EPR spectra for PBDB-T$^{\bullet+}$, PM6$^{\bullet+}$ and PCBM$^{\bullet-}$. The parameters were obtained by global fitting of the experimental spectra at X-, Q- and W-band The donor:acceptor weights were: 1 : 0.86 (PBDB-T:PCBM) and 1 : 0.92 (PM6:PCBM). Estimated fitting errors are 0.0001 for g-values and g-strains, and 0.02 mT for linewidths. Fitting errors are obtained from the Jacobian matrix, the matrix of partial derivatives of the model with respect to each fitted parameter.

simulation parameters provided in Table 3.1. The donor and acceptor contributions are depicted in blue and red, respectively, with the superimposed blue and red lines indicating the principal g-values of each species. The principal g-value with the greatest deviation from the free electron g-value ($g_e = 2.0023$) is denoted g_z, the g-value with the least deviation is g_x, and the remaining g-value, g_y lies in-between. The dashed line represents the sum of the simulated donor and acceptor contributions. All three plots share a common g-value axis (top x-axis), highlighting the improved resolution of g-anisotropy with increasing microwave frequency. Global simulation of the X-, Q-, and W-band data ensures an accurate and consistent set of EPR parameters for the donor and acceptor SCs.

Beyond determining the principal g-values, the simulations incorporated two forms of line broadening. The first, an isotropic convolutional Gaussian linewidth accounts for unresolved hyperfine splittings.* The second arises from a distribution of g-values due to variations in the molecular environment, known as g-strain. The effect of g-strain on the spectrum increases linearly with microwave frequency and is orientation-dependent; like g, there are three principal values. The value of the g_i-strain corresponds to the full-width half maximum of the distribution of the principal g_i-value. Finally, a donor:acceptor weighting factor was fitted to match the relative intensities of the two peaks. If the donor and acceptor signals are completely separated, their relative weights can be determined by integrating each peak. Although a 1 : 1 donor:acceptor ratio might be expected - every positive charge formed must be accompanied by formation of a negative charge - deviation from unity ratio can occur, due to differences in recombination rates of the two SCs.[34,36,232] In some cases, when the molecule has both donor and acceptor subunits, such as in PBDB-T, PM6, ITIC and Y6, intramolecular charge-transfer and charge generation can occur without the need for a donor:acceptor interface; different rates of formation for charged states on donor and acceptor molecules via this process will also alter the 1 : 1 ratio.[36,233–235]

In order to minimise the number of fitting parameters, only g_z-strain was included, which was observed experimentally to be the largest of the g-value distributions. That does not mean that there is no distribution in the g-values of g_x and g_y, merely that the g_x- and g_y-strains are accounted for in the convolutional linewidth fitted at each microwave frequency. The 'true' g_z-strain, therefore, is a combination of the g_z-strain and some part of the convolutional linewidth at each frequency. For $PCBM^{\bullet-}$, a significant g_z-strain was required to accurately reproduce the high-field tail observed in the experimental EPR spectrum, which is consistent with the

*The EPR convolutional linewidth is defined as the peak-to-peak linewidth: the horizontal distance between the maximum and minimum of the first-derivative lineshape. For a Gaussian lineshape, the peak-to-peak linewidth is $\frac{1}{\sqrt{2\ln 2}}\times$ the full width at half maximum.

literature.[139,224] The simulated $PCBM^{\bullet-}$ contribution in both PBDB-T:PCBM and PM6:PCBM employed the same EPR parameters.

The simulations confirm the near-axial symmetry of the g-values observed experimentally for $PBDB\text{-}T^{\bullet+}$, $PM6^{\bullet+}$, and $PCBM^{\bullet-}$; previous studies on $PBDB\text{-}T^{\bullet+}$ have also shown the same principal g-value symmetry.[178,226] The closely-related EPR parameters of $PBDB\text{-}T^{\bullet+}$ and $PM6^{\bullet+}$ are unsurprising, they have identical molecular backbones and differ only by two fluorines on the thiophene side chains.

For the overlapping non-fullerene acceptor blends, precise determination of the principal g-values from the echo-detected EPR spectra is challenging. One might assume that the molecular environment of the polymer remains unchanged in the presence of a non-fullerene acceptor and so the non-fullerene acceptor SC can be simulated using the polymer parameters from the fullerene acceptor blend simulations. Attempts with this method resulted in good matches to experimental data with isotropic, axial, or orthorhombic g-values for the acceptor molecule. The signal is simply too broad and unresolved and there are too many unknowns ($3 \times g$-values, $1 \times g$-strain, $3\times$ linewidth, $1\times$ weight) for accurate determination. An assumption of a $1:1$ polymer:non-fullerene acceptor contribution is not necessarily valid either, as evidenced by the non-unity donor:acceptor ratios observed in the fullerene acceptor blends. To accurately characterise the $ITIC^{\bullet-}$ and $Y6^{\bullet-}$ contributions, EPR techniques capable of separating the polymer donor and non-fullerene acceptor signals were required, leveraging differences in relaxation times or the presence of EPR-active nuclei in one, but not the other, molecule. A similar approach to Van Landeghem et al.,[178,181] who successfully isolated $ITIC^{\bullet-}$ in PBDB-T:ITIC and 2,4-diCN-Ph-DTTzTz$^{\bullet-}$ in MDMO-PPV:2,4-diCN-Ph-DTTzTz, is adopted.

3.3.2 Relaxation-Filtered EPR

One technique to separate out overlapping spectral contributions, known as inversion recovery-filtered or T_1-filtered EPR, relies on differences in longitudinal relaxation times of the donor and acceptor.[178–180] The longitudinal relaxation times of PBDB-T:PCBM, PM6:PCBM, PBDB-T:ITIC, and PM6:Y6 were measured using the inversion recovery pulse sequence depicted in Figure 3.1b of Section 3.2.2. For the fullerene acceptor blends, the recovery of the net magnetisation was recorded at magnetic field positions corresponding to the donor and acceptor peaks, whilst for the non-fullerene acceptor blends, the field positions were chosen at various points across the spectrum (denoted as far left, left and centre), where the relative contributions of donor and acceptor may vary. The inversion recovery curves at W-band and 20 K are shown in Figure 3.4, with the light-induced echo-detected

EPR spectra and measured field positions of the inversion recovery curves shown in the inset. The data were fitted with a bi-exponential, with the slower T_1 component assumed to be representative of the longitudinal relaxation time. As explained in Chapter 2 (Section 2.7.2), the inversion recovery curves are also affected by spectral diffusion: shifts in the resonance frequency of the measured spin due to changes in the surrounding spin environment, such as flips of nearby electron or nuclear spins, which occur faster than true longitudinal relaxation. The extracted T_1 values are summarised in Table 3.2, along with T_1 values at other microwave frequencies and temperatures, determined from inversion recovery curves in Appendix B.

Measurement of PBDB-T$^{\bullet+}$ and PM6$^{\bullet+}$ in the PBDB-T:PCBM and PM6:PCBM blends at different field positions can determine whether there is any anisotropy in the T_1 values for the polymer donor. Using the same three magnetic field values as in the PBDB-T:ITIC and PM6:Y6 measurements, the measured T_1 for PBDB-T$^{\bullet+}$ and PM6$^{\bullet+}$ were found to have only a small amount of orientation dependence. T_1 increases from 10.5 ms to 13.2 ms for PBDB-T$^{\bullet+}$ and 11.6 ms to 14.4 ms for PM6$^{\bullet+}$ as the magnetic field is reduced and $g_{x/y} \rightarrow g_z$. The T_1 value of 13.2 ms for the pure PBDB-T$^{\bullet+}$ peak (in PCBM) at the low-field position, designated 'far-left', is about a third of the T_1 of 39.4 ms observed for the same field position in PBDB-T:ITIC. PM6$^{\bullet+}$ demonstrated the same behaviour (14.4 ms vs 42.2 ms). As a result, the change in T_1 as a function of magnetic field in PBDB-T:ITIC can be confidently attributed to a different relaxation time for the ITIC$^{\bullet-}$ component (and similarly for Y6$^{\bullet-}$ in PM6:Y6). PCBM$^{\bullet-}$ displays a slightly longer T_1 time than the polymers PBDB-T$^{\bullet+}$ and PM6$^{\bullet+}$ (approximately 20% longer).

The T_1 times obtained from the polymer peaks can be compared to the relaxation times of the non-fullerene acceptor blends at different points across the signal. At the peak of the EPR signal (designated as 'centre'), the T_1 time obtained for PBDB-T:ITIC and PM6:Y6 is very similar to the T_1 obtained for PBDB-T$^{\bullet+}$ and PM6$^{\bullet+}$ in their PCBM blends, indicating that at this field position, the polymer is the predominant contribution to the EPR signal. As the field position is decreased, T_1 lengthens substantially, implying that the relative contribution of ITIC$^{\bullet-}$/ Y6$^{\bullet-}$ to the EPR signal increases at lower field positions, with the knowledge that there is limited anisotropy in the polymer T_1, and T_1 is longer for the non-fullerene acceptors (than the polymers).

The specific mechanisms of relaxation are not of particular importance for this work and will not be discussed in any great detail, more important is that significant differences in relaxation time between polymer donors and non-fullerene acceptors are indeed observed. Explanation of the change in T_1 as the microwave frequency is increased is made difficult by the number of contributing processes to relaxation;[117]

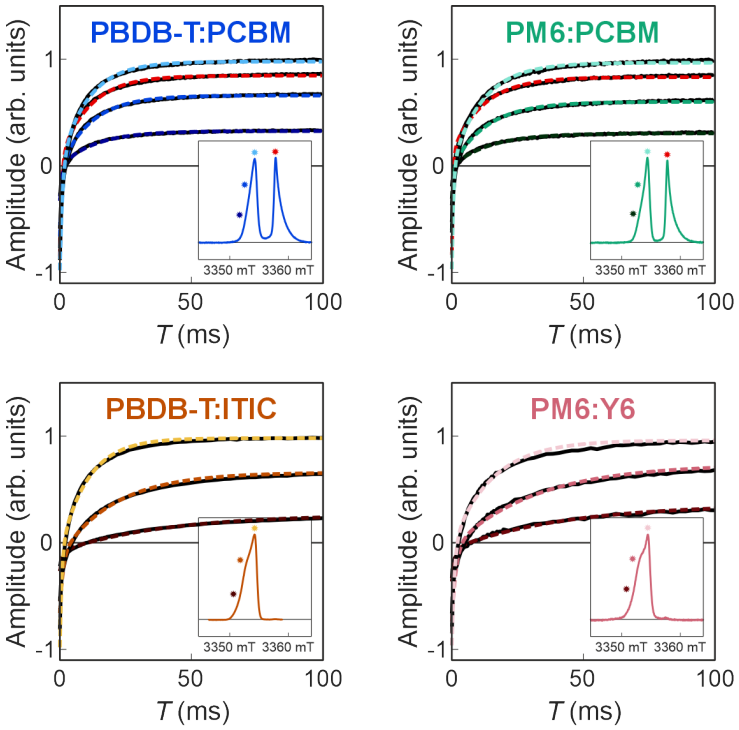

Figure 3.4: Inversion recovery curves for PBDB-T:PCBM, PM6:PCBM, PBDB-T:ITIC, and PM6:Y6, measured at 20 K and W-band. Simulations of the curves (dashed lines) are modelled by a bi-exponential, with the longer decay time considered to be representative of T_1. Simulation parameters are given in Table 3.2.

Material	Charge	Position	T_1 (ms) X 20 K	X 80 K	Q 20 K	W 20 K
PBDB-T:PCBM	PBDB-T$^{\bullet+}$	far-left				13.2
	PBDB-T$^{\bullet+}$	left				11.8
	PBDB-T$^{\bullet+}$	centre	3.5	0.1	4.6	10.5
	PCBM$^{\bullet-}$		4.4	0.1	7.6	11.1
PM6:PCBM	PM6$^{\bullet+}$	far-left				14.4
	PM6$^{\bullet+}$	left				13.1
	PM6$^{\bullet+}$	centre	5.0	0.2	5.8	11.6
	PCBM$^{\bullet-}$		5.6	0.2	6.9	11.8
PBDB-T:ITIC		far-left			11.0	39.4
		left			7.2	20.5
		centre	5.0	0.2	5.0	10.3
PM6:Y6		far-left			8.0	42.2
		left			5.8	31.3
		centre	3.1	0.1	4.9	15.0

Table 3.2: T_1 parameters obtained from simulation of inversion recovery curves in Figure 3.4 and Appendix B at a range of temperatures and frequencies. Far-left, left and centre refer to low- to high-field positions of the polymer and fullerene acceptor peaks. Estimated fitting errors are 0.1, 0.03, 0.1, and 0.5 ms for the four respective conditions.

however, it does inform us of the desirability of operating at W-band microwave frequency when isolating signal contributions in these OPV blends by their T_1 time.

Inversion recovery experiments at increased temperatures (see Appendix B) were carried out and values for T_1 at 80 K (at X-band) are displayed in Table 3.2. Evidently, in all cases, the T_1 time decreases considerably as temperature increases, by over an order of magnitude. T_1 is known to shorten with increasing temperature, with the empirical relationship of T_1 and temperature depending on the dominant relaxation mechanism.[117,118,156,236]

Using the differences in T_1 of the polymer donor and non-fullerene acceptor, a relaxation-filtered EPR experiment was carried out to exploit these differences and separate the two contributions. The strongest deviations in the T_1 values were observed at W-band, where spectral separation is strongest, and the relaxation filtering was done at this microwave frequency. First, echo-detected EPR spectra were measured at W-band for PBDB-T:ITIC and PM6:Y6 (Figure 3.5), varying only the shot repetition time. The shot repetition time is the time interval between successive pulse sequences applied to the sample and determines how much time the spins have to return to equilibrium before the next measurement cycle begins. If the shot repetition time is too short, then spins with longer T_1 values will not have sufficient time to fully relax before the next pulse sequence and the signal intensity of their contribution will be reduced. The EPR spectra shown are normalised by maximum intensity - the longer shot repetition time will always return an EPR spectrum of greater (or equal) intensity - and clear differences in signal shape are noticeable on the low magnetic field side. The increase in relative intensity of the low-field shoulder for longer shot repetition times must be attributed to a slower-relaxing species, known to be the non-fullerene acceptor from the simulated results of the inversion recovery curves in Figure 3.4.

With the knowledge that the slower-relaxing species is on the low-field side and is the non-fullerene acceptor, the inversion recovery pulse sequence can be optimised to minimise either the donor or the acceptor contributions to the spectrum. An initial π-pulse is applied, inverting the spins, and after a time delay, T, the magnetisation is recorded with an echo-detection pulse sequence ($\pi/2 - \tau - \pi - \tau$). T can be modified to match where one of the two inversion recovery trace crosses zero, and therefore, the donor and/or acceptor contributions at that magnetic field are minimised. The inversion recovery traces and their zero-crossing points for low- and high-field positions, where the non-fullerene acceptor contribution is minimised and maximised, respectively, are shown in Figure 3.5. The zero-crossing points determined from the traces were: $T_0^{\text{PBDB-T}^{\bullet+}} = 1.8\,\text{ms}$, $T_0^{\text{ITIC}^{\bullet-}} = 10.6\,\text{ms}$, $T_0^{\text{PM6}^{\bullet+}} = 2.2\,\text{ms}$ and $T_0^{\text{Y6}^{\bullet-}} = 6.5\,\text{ms}$.

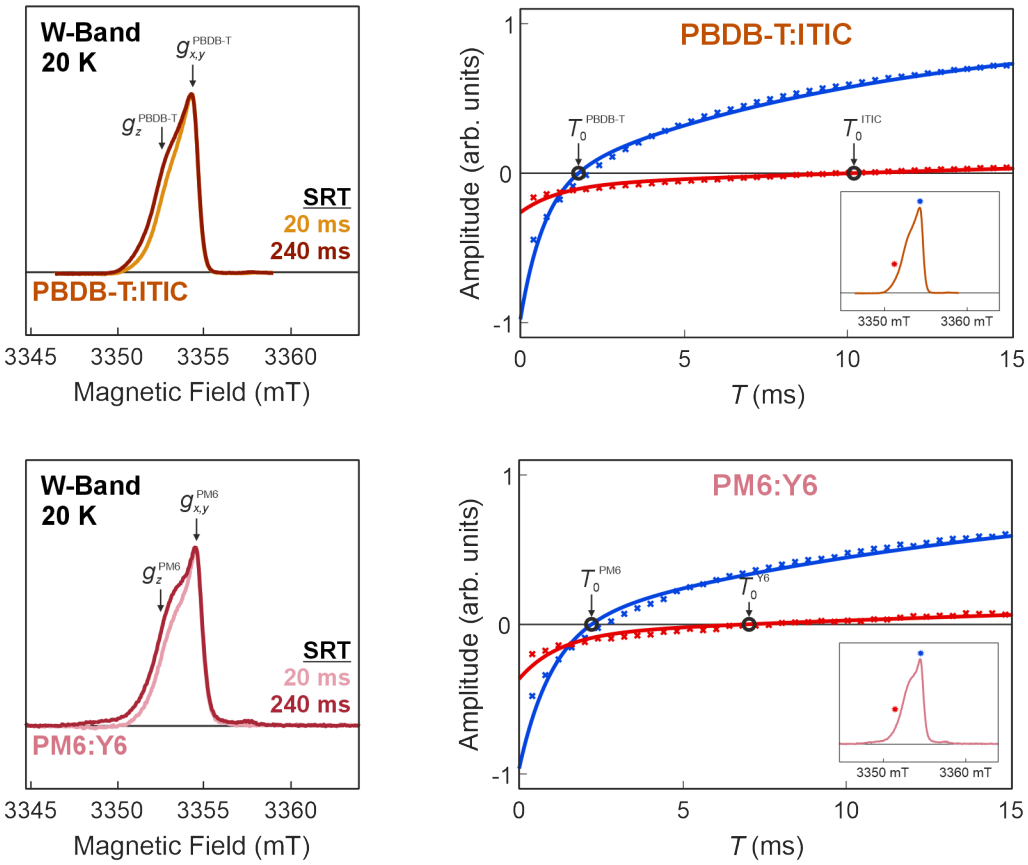

Figure 3.5: Left) Echo-detected EPR spectra for PBDB-T:ITIC and PM6:Y6, measured using shot repetition times (SRTs) of 20 ms and 240 ms. The principal g-values of PBDB-T$^{\bullet+}$ and PM6$^{\bullet+}$ are also plotted. Right) Inversion recovery traces under the same conditions, measured at the indicated field positions. The zero-crossing points indicate the pulse delay times at which the contributions at that given field positions would generate no echo-detected EPR signal.

The zero-crossing points may not be the best values for T_0. For instance, $T_0^{\text{PBDB-T}^{\bullet+}} = 1.8$ ms is determined from the field position where the majority of the signal is from PBDB-T$^{\bullet+}$, however, some ITIC$^{\bullet-}$ will also contribute to the inversion recovery trace, altering T_0. In addition, small amounts of T_1 anisotropy, observed in the relaxation measurements for PBDB-T$^{\bullet+}$ and PM6$^{\bullet+}$, will lead to a distribution of T_1 values, and therefore, T_0 crossing-points, and so the other signal contribution will never be fully suppressed. One could use the zero-crossing points obtained for PBDB-T$^{\bullet+}$ and PM6$^{\bullet+}$ in their PCBM blends ($T_0^{\text{PBDB-T}^{\bullet+}} = 1.8$ ms and $T_0^{\text{PM6}^{\bullet+}} = 1.4$ ms) to guide the choice of T_0, although this relies on the assumption that there is no change in the donor molecular environment with different acceptor molecules.

Instead, the EPR signal was recorded both as a function of magnetic field and filtering time, T_0, shown on the left in Figure 3.6. $T_0^{\text{ITIC/Y6}^{\bullet-}}$, which minimises the ITIC/Y6$^{\bullet-}$ signal and maximises the PBDB-T/PM6$^{\bullet+}$ signal, was optimised by comparing the extracted signal shape at that given T_0 to the simulation of

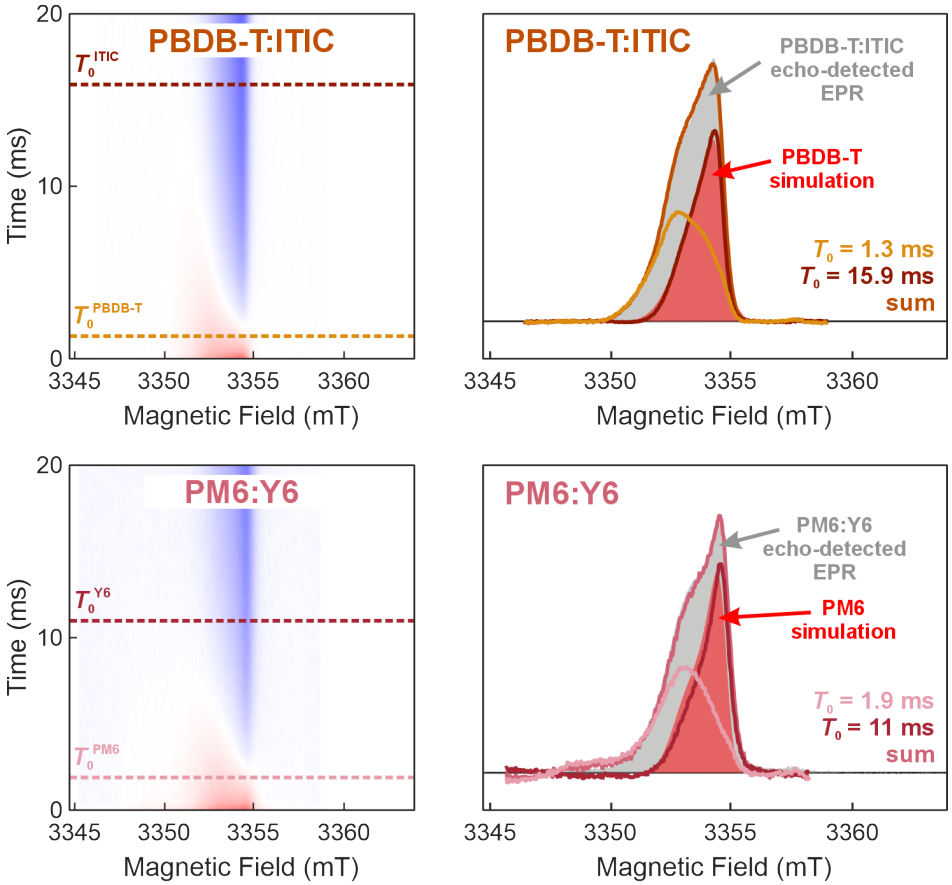

Figure 3.6: Echo-detected EPR spectra using the inversion recovery filtering method for PBDB-T:ITIC and PM6:Y6. Left) EPR signal as a function of magnetic field and filtering time, T_0. Dotted lines indicate the chosen T_0 times to minimise either the PBDB-T$^{\bullet+}$/ PM6$^{\bullet+}$ or ITIC$^{\bullet-}$/ Y6$^{\bullet-}$ contributions. Right) The filtered EPR spectra that isolate the polymer contribution are shown in comparison to the polymer SC simulations from Figure 3.3 (red), whilst the sum of the two filtered spectra is compared to the echo-detected EPR spectra from Figure 3.2 (grey).

PBDB-T/PM6$^{\bullet+}$ extracted from the echo-detected EPR spectra of PBDB-T:PCBM/ PM6:PCBM. This relies on the assumption that the polymer SC signal does not vary substantially between fullerene and non-fullerene acceptor blends. $T_0^{\text{PBDB-T/PM6}^{\bullet+}}$, which maximises the ITIC/Y6$^{\bullet-}$ signal, is optimised by summing the signal shape at the given T_0 with the PBDB-T/PM6$^{\bullet+}$ relaxation-filtered contribution and comparing it to the shape of the echo-detected EPR spectrum of the blend PBDB-T:ITIC, although this assumes a 1 : 1 ratio of donor to acceptor charges. The optimised T_0 values were $T_0^{\text{PBDB-T}^{\bullet+}} = 1.3\,\text{ms}$, $T_0^{\text{ITIC}^{\bullet-}} = 15.9\,\text{ms}$, $T_0^{\text{PM6}^{\bullet+}} = 1.9\,\text{ms}$ and $T_0^{\text{Y6}^{\bullet-}} = 11.0\,\text{ms}$.

The isolated polymer donor and non-fullerene acceptor contributions are displayed on the right in Figure 3.6. The figure also shows the PBDB-T$^{\bullet+}$ and PM6$^{\bullet+}$ simulations from the echo-detected EPR spectra, shaded red, as well as the sum

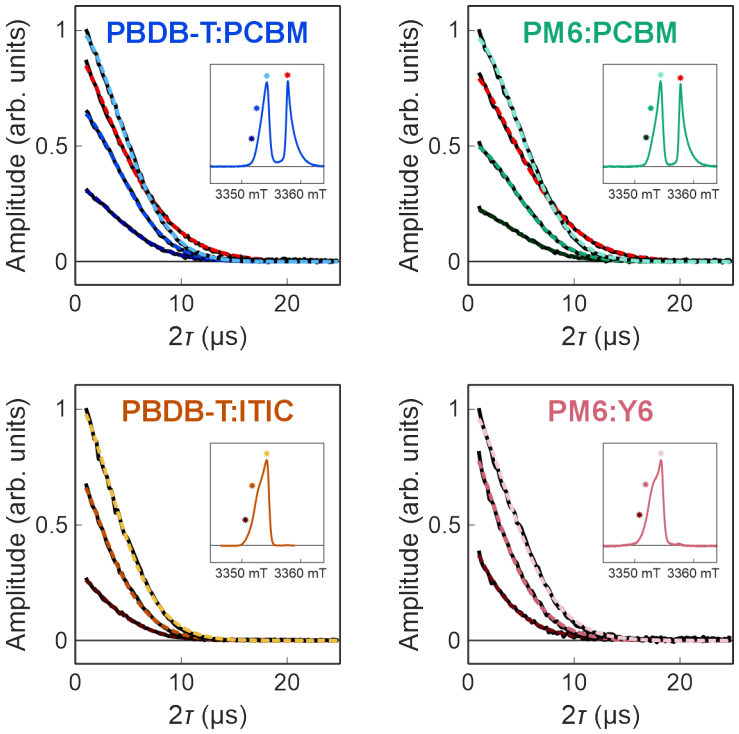

Figure 3.7: Decay of the echo-detected EPR signal for PBDB-T:PCBM, PM6:PCBM, PBDB-T:ITIC, and PM6:Y6, measured at 20 K and W-band. Simulations of the decays (dashed lines) are modelled by a stretched exponential, with simulation parameters given in Table 3.3.

Material	Charge	Position	T_m (μs)				d			
			X		Q	W	X		Q	W
			20 K	80 K	20 K	20 K	20 K	80 K	20 K	20 K
PBDB-T:PCBM	PBDB-T$^{\bullet+}$	far-left				5.8				1.6
	PBDB-T$^{\bullet+}$	left				6.0				1.8
	PBDB-T$^{\bullet+}$	centre	3.7	3.2	4.9	6.1	1.3	1.2	1.6	1.8
	PCBM$^{\bullet-}$		3.7	2.9	4.8	6.3	1.2	1.0	1.2	1.5
PM6:PCBM	PM6$^{\bullet+}$	far-left				6.1				1.7
	PM6$^{\bullet+}$	left				6.3				1.9
	PM6$^{\bullet+}$	centre	3.3	3.8	5.8	6.6	1.1	1.4	1.7	1.9
	PCBM$^{\bullet-}$		3.5	3.6	6.9	7.0	0.8	1.0	1.5	1.6
PBDB-T:ITIC		far-left			4.9	4.6			1.6	1.4
		left			5.0	4.6			1.6	1.5
		centre	2.8	3.3	5.4	5.3	1.2	1.2	1.7	1.7
PM6:Y6		far-left			4.5	3.7			1.7	1.1
		left			4.5	4.6			1.6	1.4
		centre	2.8	3.4	4.8	5.8	1.2	1.4	1.6	1.6

Table 3.3: T_m and d parameters obtained from simulation of echo decays in Figure 3.7 and Appendix B at a range of temperatures and frequencies. Estimated fitting errors are 0.1 μs at 20 K and 0.5 μs at 80 K for T_m and 0.1 for d.

of the two relaxation-filtered EPR contributions, compared to the echo-detected EPR spectra of the non-fullerene acceptor blend. The sum of the polymer donor and non-fullerene acceptor components shows excellent agreement with the echo-detected EPR signal for the non-fullerene acceptor blend. While good agreement may imply effective separation of the two contributions, one cannot exclude that any unsuppressed polymer signal in the non-fullerene acceptor spectrum is matched by an equivalent amount of non-fullerene acceptor signal in the polymer. Upon addition, these two unsuppressed signals will cancel.

The ITIC$^{\bullet-}$ and Y6$^{\bullet-}$ anion spectra match the left shoulder of the echo-detected EPR signal closely, confirming that, at the low-field spectral positions, the spectra are dominated by ITIC$^{\bullet-}$/ Y6$^{\bullet-}$. At the peak of the non-fullerene acceptor blend spectrum, there is considerable overlap of the donor and acceptor contributions. For PM6$^{\bullet+}$, there are small differences in line broadening; the isolated PM6$^{\bullet+}$ appears to be shifted to slightly higher magnetic field positions than the field sweep simulation and with a reduced shoulder on the low-field side - this would point to some minor morphological changes in PM6.

Echo decay experiments were performed to determine the phase-memory time T_{m}. The echo decays were recorded at the field positions denoted in the inset, the same field positions used for the inversion recovery experiments (Figure 3.4). The echo decays were fitted with a stretched exponential, a common fitting function for echo decays - see Equation 2.99 in Section 2.7.2 of Chapter 2,[156] and values of $1-2$ for the stretch factor (d) were obtained for all decay traces. The extracted decay times T_{m} and stretch factors d are given in Table 3.3, along with T_{m} values at other temperatures and microwave frequencies, shown in Appendix B.

Phase-memory times are similar in magnitude across all blends and show little dependence on temperature within the investigated range. Even if there were significant differences in T_{m}, it would be hard to exploit them in the same way as the T_1 filtering experiment, as there is no equivalent zero-crossing point where one signal contribution is suppressed. However, knowing the value of phase-memory time is useful for experimental set-up, as T_{m} affects the signal intensity and determines the longest pulse sequence that can be used.

3.3.3 EDNMR-Induced EPR

The presence of ^{14}N nuclei in ITIC and Y6, but not PBDB-T and PM6 (see molecular structures in Chapter 1 - Figure 1.5 of Section 1.3), can also be exploited to separate out the donor and acceptor contributions to the EPR spectrum. The ELDOR-detected NMR (EDNMR) spectra of PBDB-T:ITIC and PM6:Y6 are displayed in Figure 3.8. On the left, the EDNMR signal is shown at three different

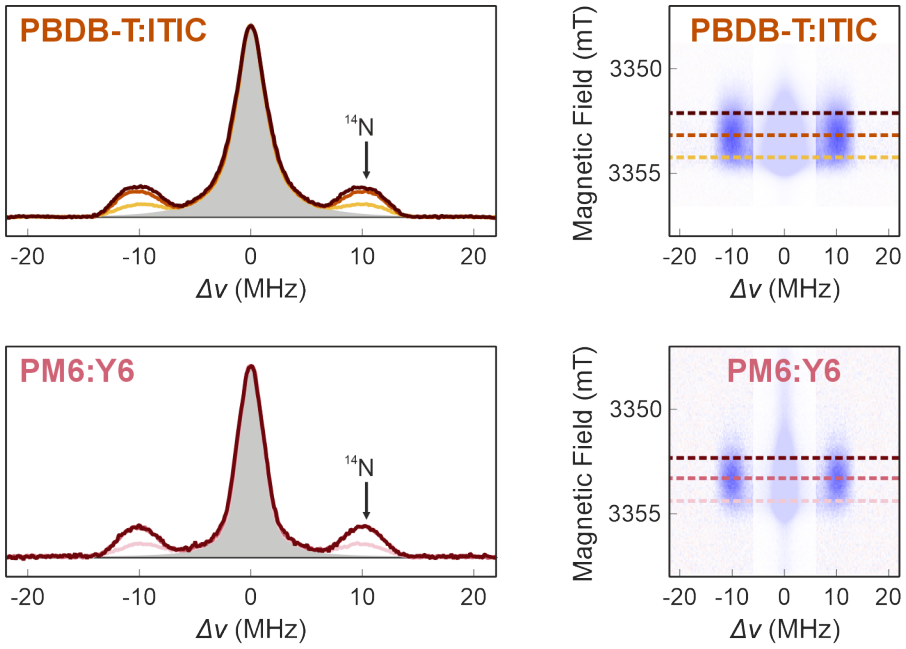

Figure 3.8: Left) EDNMR spectra extracted at given magnetic fields, shown by the dashed lines on the two-dimensional EDNMR spectra. The peak at $\Delta\nu = 0\,\mathrm{MHz}$ has been fitted with a Lorentzian lineshape (grey). Right) W-band EDNMR spectra of PBDB-T:ITIC and PM6:Y6, measured as a function of magnetic field and change in microwave frequency. The central region around $\Delta\nu = 0\,\mathrm{MHz}$ is partially covered in order to emphasise the wing features.

magnetic field positions, the same field positions used for the relaxation-filtered EPR experiments, and are normalised and plotted on top of one another. The EDNMR signal can also be measured as both a function of frequency and magnetic field, shown on the right of the figure, with the dashed lines corresponding to the field positions of the displayed EDNMR spectra on the left. The large central peak ($-5\,\mathrm{MHz} < \Delta\nu < 5\,\mathrm{MHz}$) is due to saturation of the EPR transition by the high-turning angle pulse and is often noted as the central blind spot. This central blind spot can obscure signals from weakly-coupled nuclei and so frequencies of W-band or higher are required. The central blind spot was fitted with a Lorentzian (coloured in grey), which has negligible intensity at the microwave frequencies where the additional signal contributions are observed.

For species with spin-active nuclei, the EDNMR spectrum will show side peaks to the central blind spot, centred at the Larmor frequency of that particular nucleus. For both PBDB-T:ITIC and PM6:Y6, there are side peaks centred at $\pm 10\,\mathrm{MHz}$ for all the magnetic field positions probed. At W-band, the ^{14}N nuclei has a Larmor frequency of 10.3 MHz, and so these side peaks can be assigned to hyperfine couplings between electron spins and ^{14}N nuclei in ITIC$^{\bullet-}$ and Y6$^{\bullet-}$. In theory, the ^{14}N side peaks will be split by hyperfine and nuclear quadrupole interactions. The

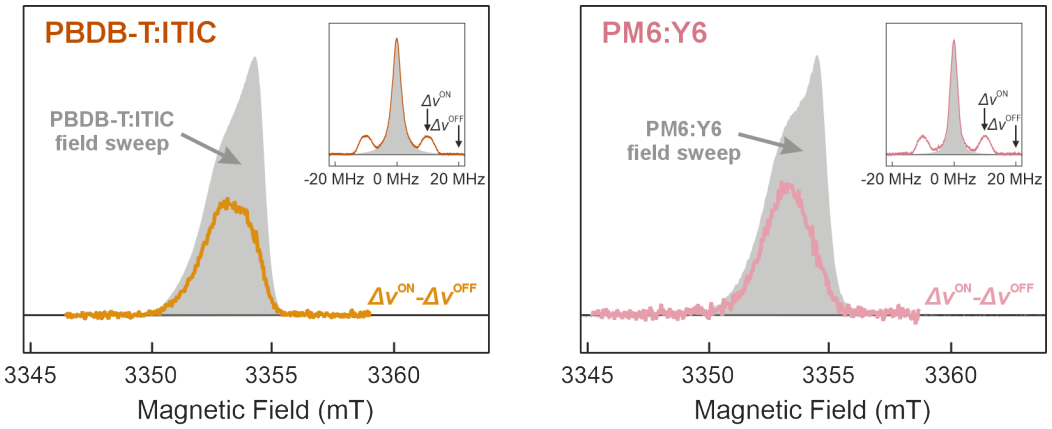

Figure 3.9: Echo-detected EPR spectra of PBDB-T:ITIC and PM6:Y6, at 20 K and at W-band, obtained by taking the difference between EPR spectra measured with HTA pulse frequency offsets of $\Delta\nu = 10$ MHz and $\Delta\nu = 20$ MHz as illustrated in the inset, isolating the non-fullerene acceptor contribution. The overall donor:acceptor blend spectrum (grey) is also shown.

number of hyperfine interactions and the distribution of these interactions means the peak splitting is unresolved and contributes as a line broadening effect. The nuclear quadrupole interaction is also unresolved as a result of the distribution of the ^{14}N nuclear environments.[117]

The EDNMR spectrum does not change significantly across the acceptor spectrum; for instance, there are no significant differences in relative signal shape for the EDNMR-induced EPR signals at $\Delta\nu = 9$ MHz vs $\Delta\nu = 11$ MHz. This indicates there is negligible orientation selection and accurate extraction of the non-fullerene acceptor EPR signal is possible. The relative intensity of the side peaks depends on the proportion of contributing electron spins that are coupled to ^{14}N nuclei. In both PBDB-T:ITIC and PM6:Y6, the low-field position showed the strongest contribution of ^{14}N-containing molecules. In agreement with the findings from the relaxation-filtering approach, a ^{14}N peak was also observed at 3354 mT, confirming that there is significant overlap of donor and acceptor at the high-field position, which corresponds to the peak of the non-fullerene acceptor blend spectra.

Knowing that the ^{14}N peak is caused by the non-fullerene acceptor contribution only, the EPR spectrum of ITIC$^{\bullet-}$/ Y6$^{\bullet-}$ can be extracted by taking the 2D EPR signal from Figure 3.8 at fixed values of $\Delta\nu$. The obtained EPR spectrum of ITIC$^{\bullet-}$/ Y6$^{\bullet-}$ is given by taking the difference of the EPR signals on- (10 MHz) and off-resonance (20 MHz). The resulting EDNMR-induced EPR spectra are shown in Figure 3.9, with the inset highlighting the on- and off-resonance positions used to extract the spectral contribution.

A comparison of the spectral shapes obtained for ITIC$^{\bullet-}$ and Y6$^{\bullet-}$ with the EDNMR-induced and relaxation-filtered separation methods is shown in Figure 3.10,

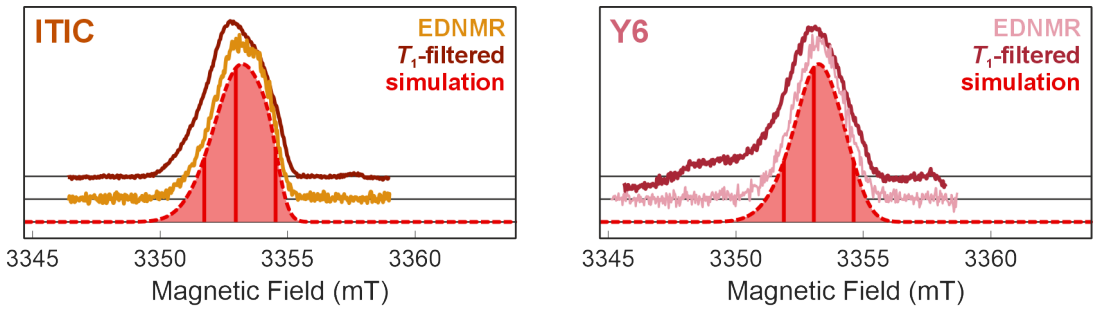

Figure 3.10: Comparison of the spectral filtering methods for the non-fullerene acceptors ITIC$^{\bullet-}$ and Y6$^{\bullet-}$ and their corresponding simulations.

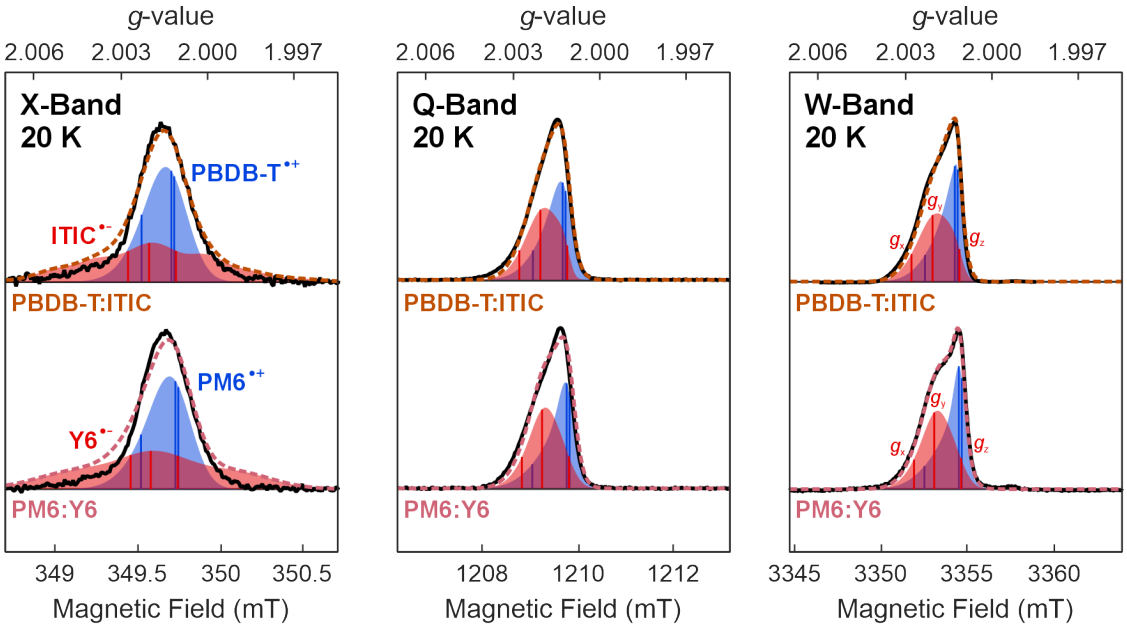

Figure 3.11: Simulation of the light-induced EPR spectra (dashed lines) of PBDB-T:ITIC (top) and PM6:Y6 (bottom) at X-, Q- and W-band, along with the individual simulations of the donor and acceptor SC contributions. The principal g-values of the polymer SC are the same as the values used in the fullerene acceptor blend simulations, but the g-strains and linewidths were allowed to vary. Full simulation parameters are given in Table 3.4.

Material	g-value			g-strain			Linewidth (mT)		
	g_x	g_y	g_z	x	y	z	X	Q	W
PBDB-T$^{\bullet+}$	2.0022	2.0023	2.0033	0	0	0.0018	0.19	0.32	0.54
PM6$^{\bullet+}$	2.0020	2.0021	2.0033	0	0	0.0018	0.19	0.27	0.48
ITIC$^{\bullet-}$	2.0021	2.0030	2.0038	0	0.0008	0.0013	0.19	0.18	0.63
Y6$^{\bullet-}$	2.0021	2.0030	2.0037	0	0	0.0011	0.22	0.39	1.10

Table 3.4: Simulation parameters of light-induced echo-detected EPR spectra for PBDB-T$^{\bullet+}$, PM6$^{\bullet+}$, ITIC$^{\bullet-}$ and Y6$^{\bullet-}$. The parameters were obtained by global fitting the experimental spectra at X-, Q- and W-band simultaneously, with g-values and g-strains consistent across microwave frequency. The relative weights of donor and acceptor were: 1 : 0.93 (PBDB-T:ITIC) and 1 : 0.99 (PM6:Y6). Estimated fitting errors are 0.0001 for g-values and g-strains, and 0.02 mT for linewidths.

along with a simulation of the signal from global fitting of the echo-detected, relaxation-filtered and EDNMR-induced EPR spectra. The high-field shoulder (3354 mT) in both ITIC$^{\bullet-}$ and Y6$^{\bullet-}$ from each method matches particularly well. In principle, EDNMR-induced EPR is generally the more accurate technique, but it is only suitable for donor:acceptor blends that have spin-active nuclei present in just one of the two molecules, and so it not as widely applicable. One potential issue of relaxation-filtered EPR would be the presence of any T_1 anisotropy in the donor molecule and, for strongly overlapping regions where the donor contribution is more intense than the acceptor, like at the high field shoulder, true suppression of the donor contribution would be difficult (and similarly for the acceptor). It seems from the experimental results that this is not the case here. The low-field shoulder (3352 mT) is marginally shifted to slightly higher magnetic fields for the EDNMR-induced signal and does not match the low-field shoulder of the non-fullerene acceptor blend echo-detected EPR signal (in grey in Figure 3.9). This would imply that the donor signal may contribute to the EPR signal at low magnetic fields.

With the additional EPR results for ITIC$^{\bullet-}$ and Y6$^{\bullet-}$, the donor and acceptor contributions to the PBDB-T:ITIC and PM6:Y6 echo-detected EPR spectra were modelled using a similar approach to the fullerene acceptor blend spectra. The X-, Q- and W-band echo-detected EPR spectra, relaxation-filtered EPR and EDNMR-induced EPR were all fitted simultaneously. For the polymer donor contributions, the same g-values from simulation of the fullerene acceptor blends were used and not fitted, while the factors affecting linewidth (convolutional line broadening and g-strain) were allowed to vary. Simulations of the echo-detected EPR spectra of PBDB-T:ITIC and PM6:Y6 are shown in Figure 3.11, with simulation parameters given in Table 3.4.

The simulations match very closely to the experimental EPR spectra, and capture the low-field shoulder at W-band - the position of this shoulder corresponds to the central principal g-value (g_y) of ITIC$^{\bullet-}$ and Y6$^{\bullet-}$. For both ITIC$^{\bullet-}$ and Y6$^{\bullet-}$, the g-values are orthorhombic and very similar; previous characterisation of ITIC$^{\bullet-}$ has also found similar absolute values and symmetry of the g-values.[178] At X-band, the broad wings seen on both the low- and high-field sides of the EPR spectrum could not be modelled without including explicit hyperfine interactions. The simulations shown include hyperfine interactions calculated from DFT, using the basis set and functional described in Section 3.2.3; given the large number of calculated hyperfine interactions (one for every proton), only those over 10 MHz were included. For ITIC$^{\bullet-}$, the largest predicted hyperfine interaction was 18 MHz; for Y6$^{\bullet-}$, it was 20 MHz. The width of the EPR signal was captured well by including these contributions, but the relative intensity of the wings was overestimated. For PBDB-T$^{\bullet+}$, PM6$^{\bullet+}$ and Y6$^{\bullet-}$, an additional g_z-strain was required to capture the

behaviour of the shoulder on the low-field side; for ITIC$^{\bullet-}$, some additional g_y-strain was also needed. The isotropic distribution of the g-values is contained with the linewidth and is the primary cause for the observed increase in linewidth (in mT) as a function of microwave frequency. The relative weights of donor and acceptor were 1 : 0.93 (PBDB-T:ITIC) and 1 : 0.99 (PM6:Y6).

3.3.4 Interpretation of Spin System Parameters

g-values obtained from EPR spectra do not directly provide structural information about the molecules probed, but in combination with DFT calculations, interpretation of the electronic structure becomes possible. Quantum calculations of the EPR parameters were carried out and aided interpretation of the set of principal g-values extracted from the experimental EPR spectra. The molecular structures and predicted orientations of the principal g-values for the polymer, fullerene and non-fullerene acceptor SCs are displayed in Figure 3.12. For PBDB-T$^{\bullet+}$ and PM6$^{\bullet+}$, g_y lies along the long-axis of the polymer backbone (the aromatic rings), g_z lies along the short-axis of the backbone and g_x is perpendicular to the backbone. For ITIC$^{\bullet-}$ and Y6$^{\bullet-}$, g_z lies along the long-axis of the molecular backbone, with g_y along the short-axis, and g_x again perpendicular. For PCBM$^{\bullet-}$, g_x lies along the unique axis (containing the functional group), g_z is perpendicular to the functional group and g_y is parallel to the functional group.

For aromatic radicals with extensive π-systems, it has been observed that the g-value pointing out of the plane of the π-system is least affected by the spin density and lies closest to the g-value of the free electron: 2.0023.[116,168,237] For the molecules with orthorhombic g-values (ITIC$^{\bullet-}$ and Y6$^{\bullet-}$), the experimentally-determined g-value closest to g_e is g_x, (see Table 3.4) agreeing with DFT that predicts g_x lying

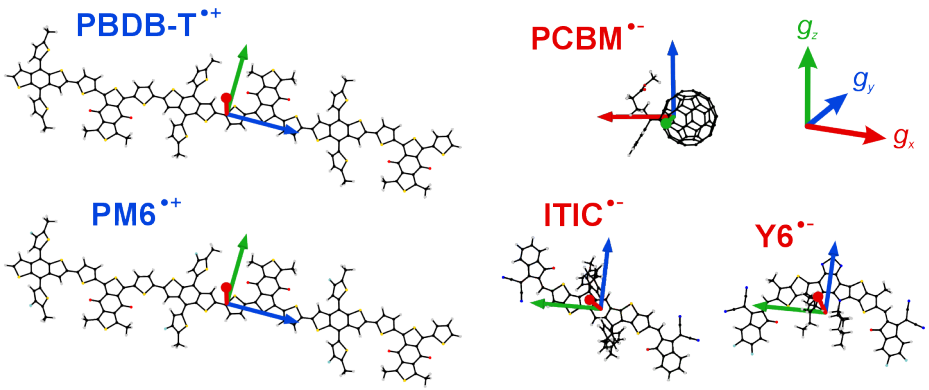

Figure 3.12: Molecular structures of PBDB-T$^{\bullet+}$, PM6$^{\bullet+}$, PCBM$^{\bullet-}$, ITIC$^{\bullet-}$ and Y6$^{\bullet-}$, and the orientation of their principal g-values calculated from DFT. Three monomer units are displayed for the polymer donors. The carbon, hydrogen, oxygen, sulfur, nitrogen and fluorine atoms are coloured black, grey, red, yellow, dark blue and light blue, respectively.

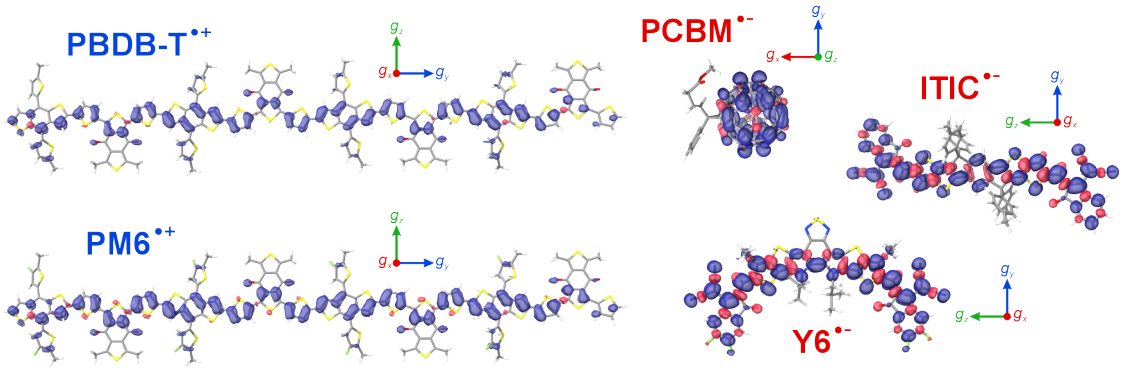

Figure 3.13: Spin density distributions of PBDB-T$^{\bullet+}$, PM6$^{\bullet+}$, PCBM$^{\bullet-}$, ITIC$^{\bullet-}$ and Y6$^{\bullet-}$ calculated from DFT. Four monomer units are displayed for the polymer donors. The $\boldsymbol{g}$-tensor orientations, from Figure 3.12, are also shown.

out of the plane of the polymer backbone. For PBDB-T$^{\bullet+}$ and PM6$^{\bullet+}$, the g-values have near axial symmetry (see Table 3.1), and so either one of g_x or g_y lying out of plane to the polymer backbone would be in agreement; in this case, DFT predicts g_x out-of-plane. The g_x and g_y, but never g_z, orientations flipped depending on the polymer model chosen for the DFT calculations.

The predicted g-values derive from spin-density distributions calculated by DFT; these distributions also provide insight into the absolute values and symmetry of the principal g-values. The spin density distributions of PBDB-T$^{\bullet+}$, PM6$^{\bullet+}$, PCBM$^{\bullet-}$, ITIC$^{\bullet-}$, and Y6$^{\bullet-}$ are given in Figure 3.13. Positive spin density is represented in blue, and negative spin density in red. The polymers, modelled as tetramers, showed that the spin density extended across the whole polymer backbone. Very little spin density resides on the thiophene sulfurs of the conjugated backbone (sulfur atoms in yellow) for either PBDB-T$^{\bullet+}$ or PM6$^{\bullet+}$. It has been shown that, for an unpaired electron localised on a sulfur within extended organic π-systems, the g-value will increase to 2.020.[238] The g-values of PBDB-T$^{\bullet+}$ and PM6$^{\bullet+}$ that lie in the plane of the π-system, $g_y = 2.0021 - 2.0023$ and $g_z = 2.0033$, show a much smaller deviation from g_e than the predicted 2.020, consistent with a lack of spin density on the sulfur atoms. The same work also theorised that non-compensated orbital angular momentum within the plane of the backbone induces an additional magnetic field, leading to g-anisotropy along the short and long axis of the π-system. For both PBDB-T$^{\bullet+}$ and PM6$^{\bullet+}$, the distinct principal g-value, g_z, resides in the plane of the π-system, as expected. ITIC$^{\bullet-}$ and Y6$^{\bullet-}$, on the other hand, delocalise some spin density onto their sulfur atoms, causing a larger deviation of their in-plane g-values from g_e. $g_y = 2.0030$ and $g_z = 2.0037 - 2.0038$, compared to $g_y = 2.0021 - 2.0023$ and $g_z = 2.0033$ for PBDB-T$^{\bullet+}$ and PM6$^{\bullet+}$.

PCBM$^{\bullet-}$ has a near-axial symmetry of its principal g-values (see Table 3.1), with the distinct g-value, $g_z = 1.9990$, positioned perpendicular to the aromatic

ester functional group. The spin density has a belt-like structure, encompassing the plane of g_y and g_z; the nodal poles of the spin 'belt' lie along g_x, the unique axis of the molecule. The region of negative spin density, lying in the centre of the fullerene (in red) and facing the reader according to the view in Figure 3.13, points along g_z, and is the cause of the difference in g-values for g_y and g_z. In the films studied, $PCBM^{\bullet-}$ is surrounded by a cage of other PCBM molecules. The cage can distort the fullerene structure along low-frequency vibrational modes, which stretch and squeeze the molecule. These distortions occur as full-body breathing motions, lengthening and shortening the fullerene along the g_x-axis.[224,225] As a result, the distribution of g-values (perpendicular to the vibrational axis, g_x) broadens, as observed in the larger g_z-strain from simulations of the EPR data. g_y-strain should also be larger than g_x-strain, but given that g_x and g_y of $PCBM^{\bullet-}$ are near-identical, their strains are not distinguishable from one another.

3.3.5 Determination of Spin Delocalisation by ENDOR

The spin density distribution does not only affect the g-values of the charged states on donor and acceptor molecules, but also the hyperfine interactions with nearby nuclei; for a more delocalised spin density, the strength of each electron-nuclear hyperfine interaction will be reduced. Hyperfine couplings can be measured directly by Electron Nuclear Double Resonance (ENDOR) spectroscopy, even if the hyperfine couplings are unresolved in the echo-detected EPR spectra. ENDOR measurements can validate the spin density distributions determined from DFT, and characterise the extent of charge delocalisation, as well as the relative orientations of the g-values and the principal axes of the hyperfine interactions.

Davies ENDOR spectra were recorded for the OPV blends PBDB-T:PCBM, PM6:PCBM, PBDB-T:ITIC, and PM6:Y6, at multiple microwave frequencies, shown in Figures 3.14 to 3.17. ENDOR spectra were recorded at different magnetic field positions across the donor and acceptor peaks to investigate any effects of orientation selection, and these field positions are indicated by the asterisks on the echo-detected EPR spectra displayed above the ENDOR plots. The blue and red lines correspond to the principal g-values. ENDOR spectra are plotted on top of each other (bottom of figure) to identify any noticeable changes in signal shape.

The ENDOR spectra for PBDB-T:PCBM at X- and W-band are shown in Figure 3.14. At X-band, the ENDOR peaks are symmetrical about the proton Larmor frequency ($\Delta\nu = \nu_{\mathrm{rf}} - \nu_{^1\mathrm{H}} = 0$), with a total spectral width of 5 MHz. The lack of distinctive features means hyperfine couplings cannot be attributed to individual protons and instead indicate a distribution of many hyperfine interactions. The characteristic two shoulder shape to the ENDOR signal is a result of the blind

spot intrinsic to the Davies ENDOR experiment. Small hyperfine couplings, which generate small splittings about $\Delta\nu = 0$, are suppressed by the central blind spot, creating the appearance of two shoulders; this is the usual ENDOR shape for a broad distribution of many nuclei. A sharp peak still remains at $\Delta\nu = 0$, due to the contributions of large numbers of distant protons on other molecules surrounding the probed molecule.[163] The Mims ENDOR technique is more sensitive for probing small hyperfine interactions,[177,239] but for the purposes of determining charge delocalisation, the largest hyperfine interaction is of more importance, and Davies ENDOR is the more suitable technique. Tentative assignment of 5 MHz for an approximate upper limit of the electron-nuclear hyperfine coupling can be made from the spectral width.

At X-band, there is no change in spectral width as a function of magnetic field, while there is a small amount of asymmetry in the 349.4 mT ENDOR spectrum (darkest blue). Under strong polarisation conditions, ENDOR spectral asymmetry can reveal the sign of the hyperfine interactions,[240] but at the temperature and magnetic fields measured here, the asymmetry is likely due to experimental imperfections, relaxation or polarisation effects.[117,241,242] The similarity of the ENDOR signal shapes at different magnetic fields at X-band is due to the bandwidth of the microwave pulse used to measure the spins. A π-pulse with $t_\pi = 140$ ns has an excitation profile of width 0.4 mT, meaning that if the π-pulse is applied at a magnetic field of 349.6 mT, it will probe all spins with resonance frequencies of 349.4 − 349.8 mT. The difference between the largest and smallest g-values at X-band, $g_x - g_z$, is 0.2 mT and so the microwave pulse is not selective enough - spins with a range of different orientations relative to the static magnetic field will be excited, regardless of where the magnetic field is applied across the PBDB-T$^{\bullet+}$ peak. In order to observe orientation selection, only a subset of spins must be excited, not the whole ensemble. This is possible at higher microwave frequencies, where the distance between field positions corresponding to the principal g-values is increased: at W-band, the g-value separation is 1.9 mT. Higher microwave frequencies also increase the energy gap between the two spin sublevels involved in the EPR transition, which, by the Boltzmann distribution, lead to a greater population difference, and therefore signal intensity. The W-band ENDOR spectra show a similar spectral width of 5 MHz to the X-band spectra, although differences between ENDOR spectra with magnetic field are now noticeable. As the magnetic field decreases (darker blue) and $g_{x/y} \rightarrow g_z$, the ENDOR shoulders move slightly closer together. While these are only small changes, conclusions can still be made. The maximum hyperfine coupling is capped by the width of the ENDOR spectrum and so cannot be any larger than 5 MHz. The PBDB-T$^{\bullet+}$ principal g-value at lower magnetic fields is g_z, which, from the DFT predictions in Section 3.3.4 (Figure 3.12), points along the short axis of the polymer backbone. The shift of the main ENDOR

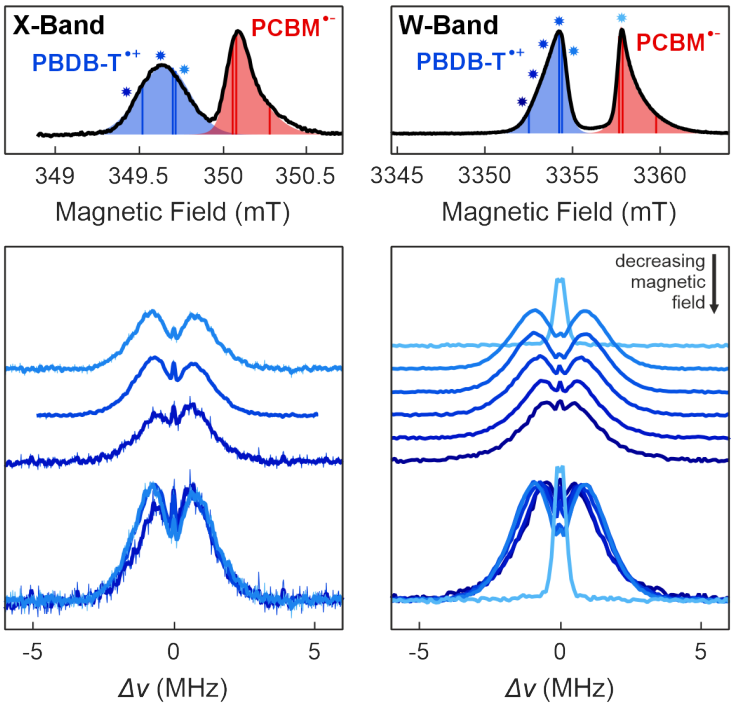

Figure 3.14: Davies ^{1}H ENDOR spectra of PBDB-T:PCBM, measured at X- and W-band, recorded at a number of field positions, with corresponding echo-detected EPR spectra.

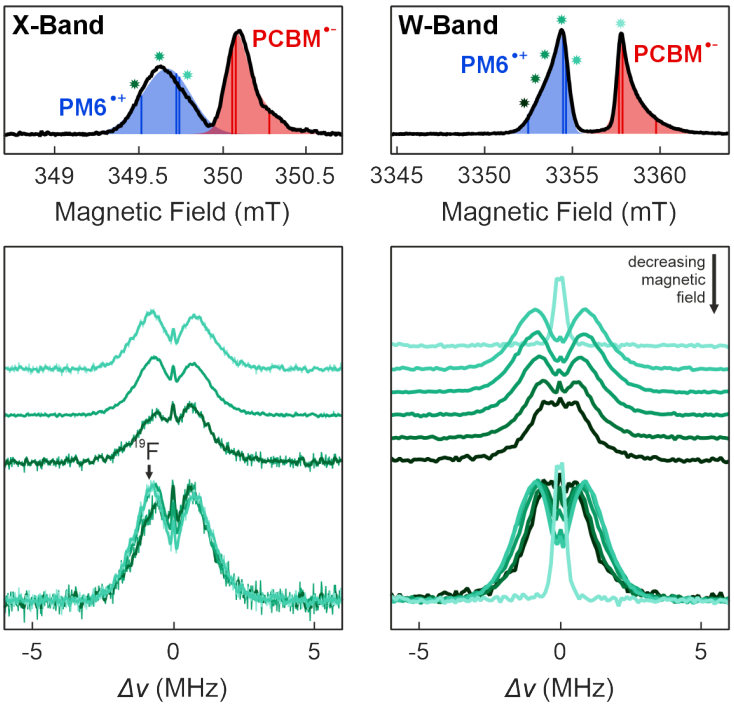

Figure 3.15: Davies ^{1}H ENDOR spectra of PM6:PCBM, measured at X- and W-band, recorded at a number of field positions, with corresponding echo-detected EPR spectra. The Larmor frequency of ^{19}F, present in PM6$^{\bullet+}$, is also shown. At W-band, it is outside the range of $\Delta\nu$.

shoulders can be linked to the orientation of the hyperfine tensor of the backbone protons, which must have larger principal hyperfine values in the plane of g_x and g_y.

The ENDOR spectrum at the $PCBM^{\bullet-}$ field position (lightest blue) shows a very narrow peak of width 1 MHz. The belt of spin density is contained on the proton-free fullerene core and does not extend onto the aromatic ester functional group. The narrow peak is caused by very small hyperfine interactions that originate from distant weakly-coupled protons, either on the functional group or on neighbouring molecules.

The ENDOR spectra of PM6:PCBM (Figure 3.15) at X- and W-band are very similar to the ENDOR spectra of PBDB-T:PCBM, confirming the analogous spin density distributions predicted from DFT calculations. The ^{19}F Larmor frequency is also plotted, which at X-band falls within the spectral width of the ENDOR signal. However, due to the large number of protons in the molecular structure, compared to the relatively few fluorines (2 : 76 F:H ratio per monomer unit), all of which contribute to the ENDOR signal at X-band, there is no discernible impact of $e^- - {}^{19}F$ hyperfine interactions on the spectra. The fluorines are also all bonded to side-chain thiophenes and so have a weak interaction with the spin density that sits predominantly on the polymer backbone.

Figure 3.16 displays the ENDOR spectra of PBDB-T:ITIC at X-, Q- and W-band. At X-band, again, the ENDOR signal shapes at different magnetic field positions are very similar, as the pulse excitation bandwidth covers the width of the PBDB-T:ITIC EPR spectrum. The spectra have the same symmetric broad peak of width 5 MHz, which can be assigned to hyperfine interactions on $PBDB\text{-}T^{\bullet+}$. Although hard to see, broad but weak spectral wings are also present in the signal, extending to an overall width of 10 MHz, and these are not observed at the $PBDB\text{-}T^{\bullet+}$ field positions in the PBDB-T:PCBM ENDOR spectra. Larger hyperfine couplings of 10 MHz can be tentatively assigned to $ITIC^{\bullet-}$.

Measurements at Q- and W-band begin to reveal clear differences in signal shape as a function of magnetic field. At higher magnetic fields (lighter yellow), the ENDOR signal shape resembles the $PBDB\text{-}T^{\bullet+}$ signal shape in PBDB-T:PCBM, but also contains the weak spectral wings assigned to $ITIC^{\bullet-}$ that were seen at X-band. Importantly, this confirms the results of the relaxation-filtered and EDNMR-induced EPR that found that the $ITIC^{\bullet-}$ contribution extends on to the high-field side of the PBDB-T:ITIC signal. As the magnetic field is decreased and the contribution of $ITIC^{\bullet-}$ to the PBDB-T:ITIC spectrum is increased, these spectral wings grow in intensity. At the lowest magnetic field (darkest yellow - 3352.3 mT), the signal is dominated by the $ITIC^{\bullet-}$ contribution. The width of the spectrum is more easily obtainable from the Q- and W-band data, and the largest $ITIC^{\bullet-}$ hyperfine interaction must be no greater than 20 MHz. The broadness of the low field ENDOR peaks suggests a distribution of larger hyperfine couplings up to this maximum value.

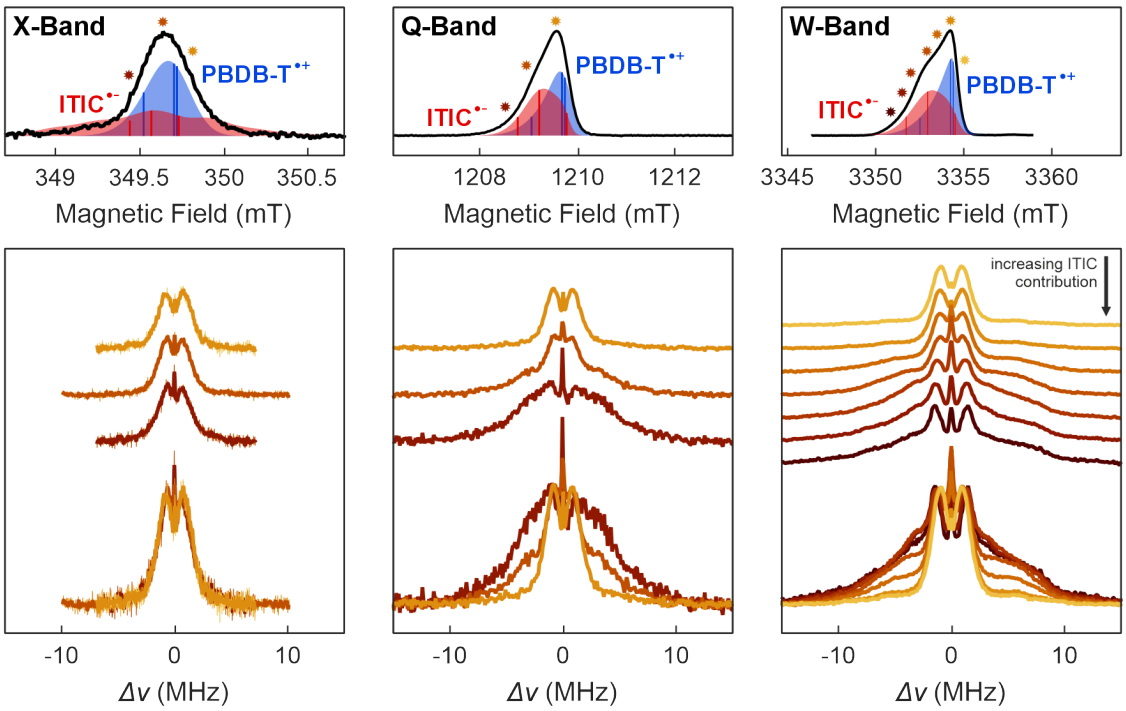

Figure 3.16: Davies ^{1}H ENDOR spectra of PBDB-T:ITIC, measured at X-, Q- and W-band, recorded at a number of field positions, with corresponding echo-detected EPR spectra.

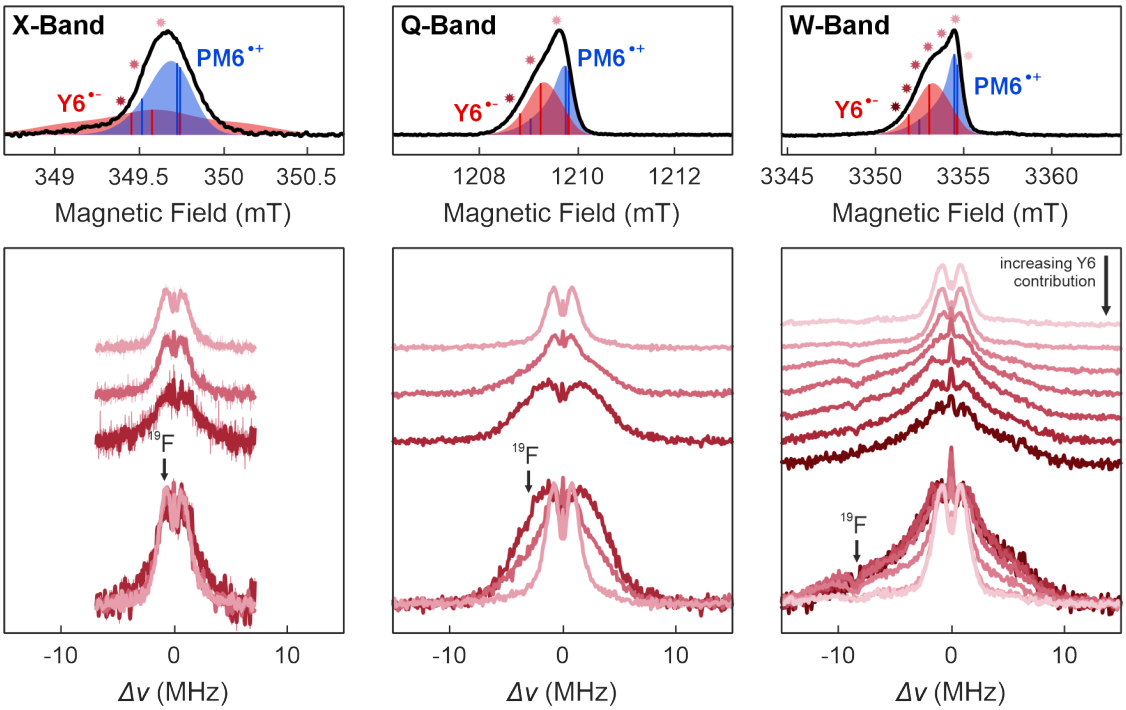

Figure 3.17: Davies ^{1}H ENDOR spectra of PM6:Y6, measured at X-, Q- and W-band, recorded at a number of field positions, with corresponding echo-detected EPR spectra. The position of the Larmor frequency of ^{19}F, nuclei present in both PM6$^{\bullet+}$ and Y6$^{\bullet-}$, is also shown.

PM6:Y6 shows similar behaviour in its ENDOR spectra as PBDB-T:ITIC (Figure 3.17). At X-band, the ENDOR signals are near-identical, with some slight broadening for the ENDOR spectrum at the low magnetic field position (darkest pink), which can be attributed to the increase in relative $Y6^{\bullet-}$ contribution. The width of the strong central signal matches the spectral width of $PM6^{\bullet+}$ in PM6:PCBM of 5 MHz. As the microwave frequency is increased, the ENDOR signal varies with magnetic field, with the spectra at lower magnetic fields, and greater $Y6^{\bullet-}$ contributions, having a broader distribution of larger hyperfine couplings, in a similar fashion to PBDB-T:ITIC. The spectral width is also 20 MHz, capping the largest hyperfine coupling at this value.

The presence of ^{19}F nuclei in the Y6 molecular structure also impacts the ENDOR signal shape. Looking at the ENDOR spectra with the largest $Y6^{\bullet-}$ contribution at W-band (darkest pink), a dip in signal intensity is observed at -8.3 MHz - this corresponds to the Larmor frequency of ^{19}F (relative to ^{1}H). There is also an additional broadening of the peak on the left hand side of the spectral shape that is not matched on the right hand side - the ENDOR signal extends to -15 MHz. This additional broadening is the result of hyperfine couplings to ^{19}F, while the dip in intensity at -8.3 MHz arises from the blind spot of the ENDOR experiment, analogous to the dip in signal at $\Delta\nu = 0$ MHz. At Q-band, the effect of the ^{19}F nuclei is much less apparent, although there is a very slight increase in broadening on the left hand side of the lowest magnetic field ENDOR signal.

A comparison of the ENDOR spectra of the PBDB-T and PM6 blends at each recorded field position is given in Figure 3.18. At the highest magnetic fields (3354.6 − 3354.8 mT), the spectral shapes are almost identical, confirming that the EPR signal at that field position is dominated by $PBDB\text{-}T^{\bullet+}$/ $PM6^{\bullet+}$. The presence of the weak side wings does confirm that there is still a small contribution of $ITIC^{\bullet-}$/ $Y6^{\bullet-}$ at high fields. As the magnetic field is decreased, the spectral wings grow in intensity, confirming a rise in contribution of the non-fullerene acceptor. The relative magnitudes of the signal components with width 5 MHz and 20 MHz also relates to the donor:acceptor ratio at the given magnetic field, matching the simulations from the EPR experiments.

The larger hyperfine interactions observed for $ITIC^{\bullet-}$ and $Y6^{\bullet-}$, compared to $PBDB\text{-}T^{\bullet+}$ and $PM6^{\bullet+}$, are consistent with the results of the DFT calculations. The spin density in the polymer donors is delocalised across multiple monomeric units; when $PBDB\text{-}T^{\bullet+}$ and $PM6^{\bullet+}$ were modelled as tetramers, the spin density delocalises across all four repeat units. As a result, the spin density that each proton interacts with, and therefore the magnitude of the hyperfine coupling, is reduced relative to the hyperfine interactions in the non-fullerene acceptors. Modelling the polymer donors as smaller repeat units (monomer, dimer, or trimer) predicts hyperfine

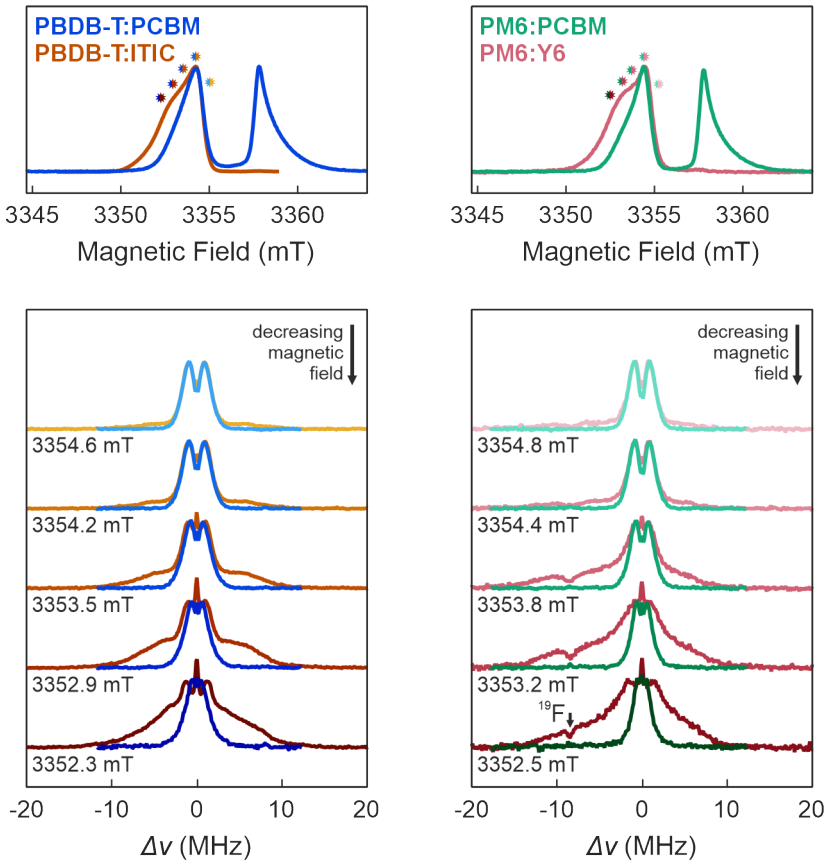

Figure 3.18: Comparison of the Davies ^{1}H ENDOR spectra of the PBDB-T and PM6 blends at the magnetic fields indicated in the echo-detected EPR spectra above - the Davies ^{1}H ENDOR spectra are plotted in lighter colours as the magnetic field is increased. Each Davies ^{1}H ENDOR spectrum is normalised to compare the effect on line shape of the acceptor molecule.

interaction strengths that are not supported by the width of the ENDOR spectra. In general, the ENDOR spectral width can be used as a probe to determine the degree and distribution of spin delocalisation in the polymer donor charged states.

X-band echo-detected EPR spectra of PBDB-T:ITIC and PM6:Y6 exhibited broad wings at low magnetic fields (349.2 mT) that were assigned to hyperfine interactions within ITIC$^{\bullet-}$ and Y6$^{\bullet-}$ (Section 3.3.1). A pair of orthorhombic hyperfine interactions that each have the same $A_{\max} \simeq 20$ MHz (18 MHz for ITIC$^{\bullet-}$ and 20 MHz for Y6$^{\bullet-}$) were required to accurately simulate these wings, and these values are in line with the predicted upper limit of the hyperfine interactions from the ENDOR results of PBDB-T:ITIC and PM6:Y6. Despite these relatively large hyperfine interaction strengths, the spin density distributions of ITIC$^{\bullet-}$ and Y6$^{\bullet-}$ (see Figure 3.13) are delocalised across the whole molecular structure, and this delocalisation may reduce the Coloumb attraction of charges at the donor-acceptor interface, allowing more efficient charge separation.

3.4 Conclusions

Characterisation of the separated charges for PBDB-T$^{\bullet+}$, PM6$^{\bullet+}$, PCBM$^{\bullet-}$, ITIC$^{\bullet-}$, and Y6$^{\bullet-}$ was accomplished through a series of EPR experiments. For PBDB-T$^{\bullet+}$, PM6$^{\bullet+}$, and PCBM$^{\bullet-}$, the principal g-values and their distributions, encoded in the g-strain, can be directly modelled from the echo-detected EPR spectrum, revealing an axial g-symmetry for all three charged states. Multiple microwave frequencies are required to resolve the g-anisotropy and determine the effect of hyperfine interactions on the signal, a problem at X-band. For classification of the ITIC$^{\bullet-}$ and Y6$^{\bullet-}$ parameters, more advanced EPR techniques were required. If there are differences in T_1 between donor and acceptor, then exploitation of the inversion recovery pulse sequence can filter out one of the two contributions, although this relies on no T_1 anisotropy and a limited distribution of spin environments and therefore relaxation times.

An alternative approach is to leverage the presence of any spin-active nuclei in only one of the two molecules and apply the EDNMR-induced EPR technique to measure EPR spectra at the Larmor frequency of that nucleus. In combination with multifrequency echo-detected EPR spectra, these two methods allowed isolation of the acceptor contribution, revealing an orthorhombic symmetry of the principal g-values for ITIC$^{\bullet-}$ and Y6$^{\bullet-}$. Prior characterisation of the PBDB-T$^{\bullet+}$ and PM6$^{\bullet+}$ components from PBDB-T:PCBM and PM6:PCBM greatly aids the accurate simulation of the acceptor contributions. These separation methods can be applied to any OPV system with overlapping donor and acceptor contributions.

The extracted g-values and strains were rationalised with quantum mechanical DFT calculations, providing justification of the symmetry of the g-values, as well as deviations away from the free-electron g-value. The DFT results were verified by ENDOR experiments at various field positions across the EPR spectrum. ITIC$^{\bullet-}$ and Y6$^{\bullet-}$ showed far larger hyperfine couplings than PBDB-T$^{\bullet+}$ and PM6$^{\bullet+}$, consistent with an increase in localisation of the spin density. This in-depth characterisation of the properties of charged states on donor and acceptor molecules in the investigated OPV blends forms the basis for further measurements aimed at gaining insights into the photovoltaic mechanism and the role of different spin states.

Chapter 4

Modelling the Evolution of Spin Polarisation

4.1 Introduction

While the previous chapter focused on steady-state EPR to probe the EPR spectral signatures and charge delocalisation of long-lived photoinduced separated charges (SCs), this chapter shifts attention to the earlier steps in the photophysical mechanism. These involve short-lived photoexcited intermediates, the charge-transfer (CT) state and mobile SCs, that evolve on nanosecond to microsecond timescales and play a decisive role in determining the efficiency of charge generation.

These photoexcited intermediates are often formed via spin-selective processes, resulting in non-equilibrium spin polarisation of these states. The evolution of this polarisation, shaped by spin dynamics, reaction kinetics, and relaxation processes, encodes crucial mechanistic information, including reaction pathways, recombination rates, and spin coherence lifetimes.[113] Spin-polarised states are fundamental to a wide array of research fields, not only OPVs,[243] but also biological systems,[244–248] organic optoelectronics,[249,250] and quantum information science.[251,252] Time-resolved EPR spectroscopy provides a powerful means to probe the spin evolution of these intermediates in real time, offering insight into the fundamental photophysical processes that govern their spectral behaviour.

However, interpreting time-resolved EPR spectra of CT states and identifying contributions from SCs is particularly challenging due to overlapping spin transitions and the complex evolution of spin polarisation. Consequently, simulations have become an indispensable tool for extracting mechanistic insights from experimental time-resolved EPR data.[140,253–256] Accurate modelling enables the connection of spectral features to underlying physical parameters, exploration of proposed reaction schemes, and testing of mechanistic hypotheses.

This chapter describes the development and optimisation of code for simulating the evolution of spin-polarised CT states and SCs in a time-resolved EPR experiment. It begins by establishing the theoretical foundations: the Liouville-von Neumann formalism for time evolution of the density operator, and the incorporation of relaxation and kinetic processes in Liouville space. The next section presents the computational implementation of this theory in a purpose-built simulation package, designed for accuracy, speed, clarity, and ease of use. This includes a discussion of numerical optimisation strategies and validation by comparison to literature. Finally, a series of representative kinetic scenarios are modelled, each illustrating how different regimes of charge transfer and separation manifest in the time-resolved EPR signal.

4.2 Theoretical Foundations

4.2.1 Density Operator Formalism

Modelling of the evolution of spin polarisation requires a time-dependent quantum mechanical description. The time evolution of a pure quantum state $|\psi(t)\rangle$ is governed by the time-dependent Schrödinger equation. This evolution occurs under the influence of the system Hamiltonian $\hat{\mathcal{H}}$, expressed in units of angular frequency, encapsulating the interactions determining the energy of the spin system:

$$\frac{\mathrm{d}\,|\psi\rangle}{\mathrm{d}t} = -\mathrm{i}\hat{\mathcal{H}}\,|\psi\rangle \qquad\qquad \frac{\mathrm{d}\,\langle\psi|}{\mathrm{d}t} = +\mathrm{i}\,\langle\psi|\,\hat{\mathcal{H}} \tag{4.1}$$

To describe the evolution of both pure and mixed states, the density operator formalism from Chapter 2 is revisited (see Equation 2.63 in Section 2.4). Differentiating the density operator $\hat{\rho} = |\psi\rangle\langle\psi|$ with respect to time and applying the product rule yields

$$\frac{\mathrm{d}\hat{\rho}}{\mathrm{d}t} = \frac{\mathrm{d}\,|\psi\rangle}{\mathrm{d}t}\langle\psi| + |\psi\rangle\frac{\mathrm{d}\,\langle\psi|}{\mathrm{d}t} \tag{4.2}$$

Substituting the expressions from Equation 4.1 gives the Liouville-von Neumann equation:

$$\frac{\mathrm{d}\hat{\rho}}{\mathrm{d}t} = -\mathrm{i}\hat{\mathcal{H}}\,|\psi\rangle\langle\psi| + \mathrm{i}\,|\psi\rangle\langle\psi|\,\hat{\mathcal{H}} = -\mathrm{i}\left[\hat{\mathcal{H}},\hat{\rho}\right] \tag{4.3}$$

where $\left[\hat{\mathcal{H}},\hat{\rho}\right]$ is the commutator of $\hat{\mathcal{H}}$ and $\hat{\rho}$. This differential equation, for a time-independent Hamiltonian $\hat{\mathcal{H}}$, has the solution:

$$\hat{\rho}(t) = \mathrm{e}^{-\mathrm{i}\hat{\mathcal{H}}t}\hat{\rho}_0\mathrm{e}^{+\mathrm{i}\hat{\mathcal{H}}t} = \hat{U}(t)\hat{\rho}_0\hat{U}^{\dagger}(t) \tag{4.4}$$

This expression describes the time evolution of a closed system, one that does not exchange energy or matter with its environment. In such systems, the dynamics are governed by unitary evolution,* meaning the state evolves under a unitary time evolution operator $\hat{U}(t) = \mathrm{e}^{-\mathrm{i}\hat{\mathcal{H}}t}$.

In contrast, an open system interacts with its surroundings and non-unitary processes, such as spin relaxation and chemical kinetics, also influence its evolution. These processes reduce quantum coherence, redistribute populations among spin states, and can result in the formation or irreversible decay of spin states, changing the total number of spins in the system. In order to incorporate non-unitary dynamics, a transformation is made from Hilbert space to Liouville space. In Hilbert space, the density matrix is an $n \times n$ matrix, and operators act via matrix multiplication. In Liouville space, the density matrix becomes a column vector of size $n^2 \times 1$ through column-wise flattening:

$$\hat{\rho} = \begin{pmatrix} \rho_{11} & \rho_{12} & \cdots \\ \rho_{21} & \rho_{22} & \cdots \\ \vdots & \vdots & \ddots \end{pmatrix} \Rightarrow \begin{pmatrix} \rho_{11} \\ \rho_{21} \\ \vdots \\ \rho_{12} \\ \rho_{22} \\ \vdots \end{pmatrix} \tag{4.5}$$

*Unitary evolution ensures that the quantum state evolves in a way that preserves both total probability (the trace of $\hat{\rho}$ remains 1) and quantum coherence (relative phases between components of $|\psi\rangle$ are maintained). Mathematically, a unitary operator $\hat{U}$ satisfies $\hat{U}^{\dagger}\hat{U} = \hat{1}$, where $\hat{1}$ is the identity operator.

This conversion, known as vectorisation, allows the Liouville-von Neumann equation in Equation 4.3 to be rewritten as a first-order linear differential equation of the form:

$$\begin{aligned}\frac{\mathrm{d}\hat{\rho}}{\mathrm{d}t} &= \mathrm{i}\,\mathrm{vec}\left(\hat{\rho}\hat{\mathcal{H}}\right) - \mathrm{i}\,\mathrm{vec}\left(\hat{\mathcal{H}}\hat{\rho}\right) \\ &= \mathrm{i}\left(\hat{\mathcal{H}}^{\mathrm{T}} \otimes \hat{1}\right)\hat{\rho} - \mathrm{i}\left(\hat{1} \otimes \hat{\mathcal{H}}\right)\hat{\rho} \\ &= -\mathrm{i}\left(\hat{1} \otimes \hat{\mathcal{H}} - \hat{\mathcal{H}}^{\mathrm{T}} \otimes \hat{1}\right)\hat{\rho} \\ &= -\mathrm{i}\hat{\hat{\mathcal{H}}}\hat{\rho}\end{aligned} \tag{4.6}$$

which follows from the identity:

$$\mathrm{vec}(ABC) = \left(C^{\mathrm{T}} \otimes A\right)\,\mathrm{vec}(B) \tag{4.7}$$

with $\otimes$ the direct or Kronecker product and the Liouville space superoperator $\hat{\hat{\mathcal{H}}}$ defined as:

$$\hat{\hat{\mathcal{H}}} = \hat{1} \otimes \hat{\mathcal{H}} - \hat{\mathcal{H}}^{\mathrm{T}} \otimes \hat{1} \tag{4.8}$$

This formulation enables the treatment of density operator evolution as a matrix-vector product, which allows for more efficient numerical simulations.[†] The Liouville-von Neumann equation above describes the coherent evolution of the density operator, governed by the spin Hamiltonian. The equation can be expanded to include kinetics and relaxation, which yields the master equation:

$$\begin{aligned}\frac{\mathrm{d}\hat{\rho}}{\mathrm{d}t} &= -\mathrm{i}\hat{\hat{\mathcal{H}}}\hat{\rho} - \hat{\hat{K}}\hat{\rho} - \hat{\hat{\Gamma}}\left(\hat{\rho} - \hat{\rho}_{\mathrm{eq}}\right) \\ &= \left(-\mathrm{i}\hat{\hat{\mathcal{H}}} - \hat{\hat{K}} - \hat{\hat{\Gamma}}\right)\hat{\rho} + \hat{\hat{\Gamma}}\hat{\rho}_{\mathrm{eq}} \\ &= \hat{\hat{\mathcal{L}}}\hat{\rho} + \hat{\hat{\Gamma}}\hat{\rho}_{\mathrm{eq}}\end{aligned} \tag{4.9}$$

with each superoperator playing a distinct role:

- $\hat{\hat{\mathcal{H}}}$ governs the unitary spin dynamics.
- $\hat{\hat{K}}$ encodes kinetic recombination pathways.
- $\hat{\hat{\Gamma}}$ describes longitudinal and transverse relaxation driving the system towards equilibrium.

[†]From here on, $\hat{\rho}$ is the vectorised density operator in **Liouville space**: its space representation is inferred from the object that acts on the density operator: superoperators like $\hat{\hat{\mathcal{H}}}$ act on $\hat{\rho}$ in Liouville space, while operators like $\hat{\mathcal{H}}$ act on $\hat{\rho}$ in Hilbert space.

The total Liouvillian superoperator $\hat{\hat{\mathcal{L}}}$ thus includes all processes that modify the state of the system. The vector $\hat{\rho}_{\mathrm{eq}}$ is the density operator at thermal equilibrium, representing the equilibrium state with Boltzmann sublevel populations and no coherences. The master equation in Equation 4.9 is an inhomogeneous first-order linear differential equation. Under the assumption that the Liouvillian superoperator $\hat{\hat{\mathcal{L}}}$ is time-independent, its general solution comprises a homogeneous solution and a particular solution to the inhomogeneous term. The homogeneous part is given by:

$$\frac{\mathrm{d}\hat{\rho}}{\mathrm{d}t} - \hat{\hat{\mathcal{L}}}\hat{\rho} = 0 \qquad \Rightarrow \qquad \hat{\rho} = \mathrm{e}^{\hat{\hat{\mathcal{L}}}t}\hat{A} \tag{4.10}$$

where $\hat{A}$ is a time-independent operator to be determined from initial conditions. The particular solution to the inhomogeneous part is found using an integrating factor and gives:

$$\frac{\mathrm{d}\hat{\rho}}{\mathrm{d}t} - \hat{\hat{\mathcal{L}}}\hat{\rho} = \hat{\hat{\Gamma}}\hat{\rho}_{\mathrm{eq}} \qquad \Rightarrow \qquad \hat{\rho} = -\hat{\hat{\mathcal{L}}}^{-1}\hat{\hat{\Gamma}}\hat{\rho}_{\mathrm{eq}} \tag{4.11}$$

The general solution is the sum of the two solutions, and the initial condition of $\hat{\rho}(t = 0) = \hat{\rho}_0$ allows determination of A:

$$\hat{\rho} = -\hat{\hat{\mathcal{L}}}^{-1}\hat{\hat{\Gamma}}\hat{\rho}_{\mathrm{eq}} + \mathrm{e}^{\hat{\hat{\mathcal{L}}}t}\hat{A} \qquad\qquad \hat{A} = \hat{\rho}_0 + \hat{\hat{\mathcal{L}}}^{-1}\hat{\hat{\Gamma}}\hat{\rho}_{\mathrm{eq}} \tag{4.12}$$

which yields the full solution of the master equation:

$$\hat{\rho} = -\hat{\hat{\mathcal{L}}}^{-1}\hat{\hat{\Gamma}}\hat{\rho}_{\mathrm{eq}} + \mathrm{e}^{\hat{\hat{\mathcal{L}}}t}\left(\hat{\rho}_0 + \hat{\hat{\mathcal{L}}}^{-1}\hat{\hat{\Gamma}}\hat{\rho}_{\mathrm{eq}}\right) \tag{4.13}$$

The density operator at steady-state, $\hat{\rho}_{\mathrm{ss}}$, can be obtained by setting the time-derivative of the density operator to zero:

$$\frac{\mathrm{d}\hat{\rho}_{\mathrm{ss}}}{\mathrm{d}t} = 0 \qquad \Rightarrow \qquad \hat{\rho}_{\mathrm{ss}} = -\hat{\hat{\mathcal{L}}}^{-1}\hat{\hat{\Gamma}}\hat{\rho}_{\mathrm{eq}} \tag{4.14}$$

Substituting in the steady-state density operator into the full solution of the master equation simplifies the expression to:

$$\begin{aligned}\hat{\rho}(t) &= \hat{\rho}_{\mathrm{ss}} + \mathrm{e}^{\hat{\hat{\mathcal{L}}}t}\left(\hat{\rho}_0 - \hat{\rho}_{\mathrm{ss}}\right) \\ &= \hat{\rho}_{\mathrm{ss}} + \mathrm{e}^{\left(-\mathrm{i}\hat{\hat{\mathcal{H}}} - \hat{\hat{K}} - \hat{\hat{\Gamma}}\right)t}\left(\hat{\rho}_0 - \hat{\rho}_{\mathrm{ss}}\right)\end{aligned} \tag{4.15}$$

This solution describes the time evolution of the system from an initial state $\hat{\rho}_0$ towards its steady-state $\hat{\rho}_{\mathrm{ss}}$. At $t = 0$, the solution recovers the initial condition $\hat{\rho} = \hat{\rho}_0$, while in the limit $t \to \infty$, the exponential term vanishes and $\hat{\rho} \to \hat{\rho}_{\mathrm{ss}}$. Both the transient evolution and the steady state are governed by the form of the Liouvillian superoperator $\hat{\hat{\mathcal{L}}} = -\mathrm{i}\hat{\hat{\mathcal{H}}} - \hat{\hat{K}} - \hat{\hat{\Gamma}}$, which combines coherent Hamiltonian evolution,

and incoherent relaxation and population transfer. The competition between these terms determines how populations redistribute and how coherence decays over time.

Even if some terms in $\hat{\hat{\mathcal{L}}}$ are time-dependent, the propagation can be split into small time intervals over which the superoperator can be considered approximately time-independent. The propagation is done via a pre-computed time-step propagator, $\hat{\hat{O}}$, applied iteratively to obtain the density operator as a function of time:

$$\hat{\rho}(t + \mathrm{d}t) = \hat{\hat{O}}\,\hat{\rho}(t) \qquad \hat{\hat{O}} = \hat{\hat{O}}_{\mathrm{ss}} + \mathrm{e}^{\hat{\hat{\mathcal{L}}}\mathrm{d}t}\left(\hat{\hat{1}} - \hat{\hat{O}}_{\mathrm{ss}}\right) \tag{4.16}$$

where $\hat{\hat{1}}$ is the identity superoperator and $\hat{\hat{O}}_{\mathrm{ss}}$ is the projection superoperator that maps $\hat{\rho}(t)$ to $\hat{\rho}_{\mathrm{ss}}$. The derivation of $\hat{\hat{O}}$ from the form of $\hat{\rho}(t)$ in Equation 4.15 is given in Appendix C. This equation forms the computational basis for simulating the time evolution of spin polarisation and is central to modelling time-resolved EPR spectra. At each time point, the populations and coherences contained in $\hat{\rho}(t)$ determine the intensity of each EPR transition.

The forms of the superoperators in $\hat{\hat{\mathcal{L}}}$ depend on the specific spin system considered; the subsequent discussion focuses on those relevant to the simulation of photoinduced states in OPVs. The evolution of the spin polarisation in the charge-transfer state is initially examined in isolation, before extending the theoretical framework to incorporate the behaviour of separated charges.

4.2.2 Spin-Correlated Charge-Transfer States

Evolution of the spin polarisation of the CT state, during a time-resolved EPR experiment, is governed by the master equation in Equation 4.15, and requires explicit evaluation of each constituent superoperator.

The total spin Hamiltonian of the CT state can be written as the sum of two contributions:

$$\hat{\mathcal{H}}_{\mathrm{CT}}(t) = \hat{\mathcal{H}}_{0,\mathrm{CT}} + \hat{\mathcal{H}}_1(t) \tag{4.17}$$

where $\hat{\mathcal{H}}_{0,\mathrm{CT}}$ is the static spin Hamiltonian capturing the spin-spin and spin-field interactions of the CT state:

$$\hat{\mathcal{H}}_{0,\mathrm{CT}} = \frac{\mu_{\mathrm{B}}}{\hbar} B_0 g_{\mathrm{D}} \hat{S}_{\mathrm{D},z} + \frac{\mu_{\mathrm{B}}}{\hbar} B_0 g_{\mathrm{A}} \hat{S}_{\mathrm{A},z} + J\,\hat{S}_{\mathrm{D}}\hat{S}_{\mathrm{A}} + \frac{D}{2}\left(3\hat{S}_{\mathrm{D},z}\hat{S}_{\mathrm{A},z} - \hat{S}_{\mathrm{D}}\hat{S}_{\mathrm{A}}\right) \tag{4.18}$$

with the hyperfine interaction neglected for simplicity.

The second term, $\hat{\mathcal{H}}_1$, represents the time-dependent interaction with the oscillating microwave magnetic field $\boldsymbol{B}_1$, applied perpendicular to $\boldsymbol{B}_0$:

$$\hat{\mathcal{H}}_1 = \frac{\mu_{\mathrm{B}}}{\hbar} B_1(t) g_{\mathrm{D}} \hat{S}_{\mathrm{D},x} + \frac{\mu_{\mathrm{B}}}{\hbar} B_1(t) g_{\mathrm{A}} \hat{S}_{\mathrm{A},x} \tag{4.19}$$

where $B_1(t) = B_1 \cos(\omega_{\mathrm{mw}} t)$ is the time-dependent microwave field amplitude. In a time-resolved EPR experiment, $\boldsymbol{B}_1$ is applied continuously throughout the measurement window.

The spin dynamics are modelled in the rotating frame, a new reference frame that rotates around the static magnetic field axis, z, with angular frequency $+\omega_{\mathrm{mw}}$, and the spin Hamiltonian becomes:

$$\hat{\mathcal{H}}_{\mathrm{CT}} = \hat{\mathcal{H}}_{0,\mathrm{CT}} + \hat{\mathcal{H}}_1 - \omega_{\mathrm{mw}} \hat{S}_z \tag{4.20}$$

where the $\omega_{\mathrm{mw}} \hat{S}_z$ term accounts for the transformation to the rotating frame, removing the precession of on-resonance spins around $\boldsymbol{B}_0$, with $\hat{\mathcal{H}}_1$ now time-independent:

$$\hat{\mathcal{H}}_1 = \frac{\mu_{\mathrm{B}}}{2\hbar} B_1 g_{\mathrm{D}} \hat{S}_{\mathrm{D},x} + \frac{\mu_{\mathrm{B}}}{2\hbar} B_1 g_{\mathrm{A}} \hat{S}_{\mathrm{A},x} \tag{4.21}$$

A full derivation of the rotating frame transformation can be found in Appendix C. Finally, the spin Hamiltonian is converted into its superoperator form using the transformation in Equation 4.8.

Recombination of charges in the CT state, to either the ground state ($\mathrm{CT} \rightarrow \mathrm{S}_0$) or to the lower-lying triplet state ($\mathrm{CT} \rightarrow \mathrm{T}_1$), is incorporated via the kinetic superoperator $\hat{\hat{K}}_{\mathrm{CT}}$. Since S_0 contains no unpaired spins and the T_1 state gives rise to signals that are removed by baseline-correction within the magnetic field range of interest of the CT state, neither contributes to the time-resolved EPR spectrum of the CT state, and their spin dynamics are not modelled explicitly here. The spin polarisation of the T_1 state is investigated separately in Section 5.3.1 Chapter 5.

The superoperator $\hat{\hat{K}}_{\mathrm{CT}}$ thus captures the irreversible, spin-selective depletion of the CT state to undetected products, a non-unitary evolution, characterised by the phenomenological singlet and triplet recombination rate constants k_{S} and k_{T}. In Hilbert space, these processes are commonly described using the Haberkorn reaction operator:[257]

$$\begin{aligned} \hat{K}_{\mathrm{CT}} &= \frac{k_{\mathrm{S}}}{2} \hat{P}_{\mathrm{S}} + \frac{k_{\mathrm{T}}}{2} \hat{P}_{\mathrm{T}} \\ &= \frac{k_{\mathrm{S}}}{2} |\mathrm{S}\rangle \langle \mathrm{S}| + \frac{k_{\mathrm{T}}}{2} |\mathrm{T}\rangle \langle \mathrm{T}| \end{aligned} \tag{4.22}$$

where the total triplet projection operator is defined as:

$$\hat{P}_{\mathrm{T}} = |\mathrm{T}\rangle \langle \mathrm{T}| = \frac{1}{3} \left(|\mathrm{T}_+\rangle \langle \mathrm{T}_+| + |\mathrm{T}_0\rangle \langle \mathrm{T}_0| + |\mathrm{T}_-\rangle \langle \mathrm{T}_-| \right) \tag{4.23}$$

To include this kinetic term in the Liouville space formulation of the master equation, the projection operators, $\hat{P}_{\mathrm{S}}$ and $\hat{P}_{\mathrm{T}}$, are transformed into superoperator form via the anticommutator mapping:

$$\begin{aligned} \hat{\hat{P}}_{\mathrm{S}} &= \hat{1} \otimes \hat{P}_{\mathrm{S}} + \hat{P}_{\mathrm{S}}^{\mathrm{T}} \otimes \hat{1} \\ \hat{\hat{P}}_{\mathrm{T}} &= \hat{1} \otimes \hat{P}_{\mathrm{T}} + \hat{P}_{\mathrm{T}}^{\mathrm{T}} \otimes \hat{1} \end{aligned} \tag{4.24}$$

The spin-selective recombination of the CT state leads to the decay of population in each of the spin sublevels. These decays are captured by the diagonal elements of the density matrix $\hat{\rho}$, with the population of each CT eigenstate $|i\rangle$ evolving as:

$$\frac{\mathrm{d}\hat{\rho}_{ii}}{\mathrm{d}t} = -\left(k_{\mathrm{S}}|\langle i|\mathrm{S}\rangle|^2 + k_{\mathrm{T}}|\langle i|\mathrm{T}\rangle|^2\right)\,\hat{\rho}_{ii} \tag{4.25}$$

Using the CT eigenstate definitions provided in Chapter 2 (see Equation 2.56 in Section 2.4), the population decay equations for the four CT sublevels become:

$$\begin{aligned}
\frac{\mathrm{d}\rho_{11}}{\mathrm{d}t} &= -k_{\mathrm{T}}\rho_{11} \\
\frac{\mathrm{d}\rho_{22}}{\mathrm{d}t} &= -(k_{\mathrm{S}}\sin^2\phi + k_{\mathrm{T}}\cos^2\phi)\rho_{22} \\
\frac{\mathrm{d}\rho_{33}}{\mathrm{d}t} &= -(k_{\mathrm{S}}\cos^2\phi + k_{\mathrm{T}}\sin^2\phi)\rho_{33} \\
\frac{\mathrm{d}\rho_{44}}{\mathrm{d}t} &= -k_{\mathrm{T}}\rho_{44}
\end{aligned} \tag{4.26}$$

where ϕ defines the coupling regime: $\phi \approx 0$ for strongly-coupled spins, and $\phi \approx \frac{\pi}{4}$ for uncoupled spins.

To account for additional singlet-triplet dephasing, predicted from quantum measurements, a damping term is often appended:[258,259]

$$\hat{\hat{K}}_{\mathrm{CT}} = \frac{k_{\mathrm{S}}}{2}\hat{\hat{P}}_{\mathrm{S}} + \frac{k_{\mathrm{T}}}{2}\hat{\hat{P}}_{\mathrm{T}} + \frac{k_{\mathrm{S}}+k_{\mathrm{T}}}{2}\left(\hat{P}_{\mathrm{S}}\otimes\hat{P}_{\mathrm{T}} + \hat{P}_{\mathrm{T}}\otimes\hat{P}_{\mathrm{S}}\right) \tag{4.27}$$

where the final term selectively damps singlet-triplet coherences. Although this contribution is often small and hard to demonstrate unequivocally in experimental systems, it is retained here for completeness.

Relaxation processes are captured by the superoperator $\hat{\hat{\Gamma}}_{\mathrm{CT}}$, which describes how populations and coherences return to thermal equilibrium. These processes can be described by the phenomenological longitudinal (T_1) and transverse (T_2) relaxation times (see Section 2.7.2 in Chapter 2 for details), although more sophisticated treatments of spin relaxation also exist.[260] T_1 relaxation affects the diagonal elements of the density matrix, modelling redistribution of populations back to equilibrium. T_2 relaxation governs decay of coherence, represented by off-diagonal elements.

Unlike the other superoperators that act on the density operator $\hat{\rho}$, relaxation drives the system towards its thermal equilibrium state $\hat{\rho}_{\mathrm{eq}}$ and must therefore be formulated in terms of the deviation $\hat{\rho}-\hat{\rho}_{\mathrm{eq}}$. In some time-resolved EPR simulations, where the thermal polarisation is negligible, a simplified approach is adopted in which relaxation is treated as acting directly on $\hat{\rho}$ alone. This approximation renders the master equation homogeneous and computationally simpler. In doing

so, the modelled system relaxes towards equally-populated spin sublevels, rather than towards a thermally-populated distribution.[261]

The relaxation superoperator $\hat{\hat{\Gamma}}_{\mathrm{CT}}$ is constructed by approximating elements of the Redfield relaxation matrix with T_1 and T_2 values:[116,262,263]

$$\begin{aligned} \langle ii|\,\hat{\hat{\Gamma}}_{\mathrm{CT}}\,|jj\rangle &= -\frac{1}{nT_1} \quad \text{if } i \neq j \\ &= \sum_{i \neq j} \frac{1}{nT_1} \quad \text{if } i = j \end{aligned} \tag{4.28}$$

and

$$\begin{aligned} \langle ij|\,\hat{\hat{\Gamma}}_{\mathrm{CT}}\,|ij\rangle &= \frac{1}{T_2} \quad \text{if } i \neq j \\ &= 0 \quad \text{if } i = j \end{aligned} \tag{4.29}$$

with all other matrix elements zero and n the number of eigenstates. T_1 terms appear off-diagonal in the Liouville space relaxation superoperator and conserve total population, reflecting population shuffling within a closed system. T_2 terms lie along the diagonal and lead to a net loss of coherence.

4.2.3 Charge-Transfer States and Separated Charges

The spin dynamics described so far consider only the CT state. However, in principle, the CT state may evolve into spatially separated charges (SCs) through charge separation processes. A more complete model of the photophysics in OPVs must therefore incorporate both the CT state and SCs, along with the kinetic processes that govern their interconversion.

A convenient approach is to describe the CT state and SCs within a unified two-state framework. In this model, the total superoperator $\hat{\hat{\mathcal{L}}}$ is expanded to include both CT and SC subspaces.[264] Spins in SCs are uncorrelated and can be treated as two spins at infinite separation ($J = 0, D = 0$), resulting in four spin eigenstates: $\{|\alpha\alpha\rangle, |\alpha\beta\rangle, |\beta\alpha\rangle, |\beta\beta\rangle\}$. The corresponding density operator for SCs, $\hat{\rho}_{\mathrm{SC}}$, will then have the same dimensions ($n^2 \times 1$) as that of the CT state.

This leads to a composite Liouvillian of size $2n^2 \times 2n^2$,[‡] structured as a 2×2 block matrix in the CT-SC basis:[262]

$$\hat{\hat{\mathcal{L}}} = \begin{pmatrix} \langle \mathrm{CT}|\,\hat{\hat{\mathcal{L}}}\,|\mathrm{CT}\rangle & \langle \mathrm{CT}|\,\hat{\hat{\mathcal{L}}}\,|\mathrm{SC}\rangle \\ \langle \mathrm{SC}|\,\hat{\hat{\mathcal{L}}}\,|\mathrm{CT}\rangle & \langle \mathrm{SC}|\,\hat{\hat{\mathcal{L}}}\,|\mathrm{SC}\rangle \end{pmatrix} \tag{4.30}$$

[‡]Alternatively, one could first construct a combined Hilbert space (of dimension $2n \times 2n$) and then transform to Liouville space. This would yield a larger superoperator of size $4n^2 \times 4n^2$, which is only required if the two subspaces are entangled. The CT state and SCs have no coherences between them, and so the smaller $2n^2 \times 2n^2$ Liouville space suffices.

Except for the kinetic processes that interconvert the CT state and SCs, the two subspaces are completely decoupled. Consequently, the spin dynamics and relaxation superoperators act independently within each subspace and retain a block-diagonal structure in the combined CT-SC basis:

$$\hat{\hat{\mathcal{H}}} = \begin{pmatrix} \hat{\hat{\mathcal{H}}}_{\mathrm{CT}} & 0 \\ 0 & \hat{\hat{\mathcal{H}}}_{\mathrm{SC}} \end{pmatrix} \qquad \hat{\hat{\Gamma}} = \begin{pmatrix} \hat{\hat{\Gamma}}_{\mathrm{CT}} & 0 \\ 0 & \hat{\hat{\Gamma}}_{\mathrm{SC}} \end{pmatrix} \tag{4.31}$$

where $\hat{\hat{\mathcal{H}}}_{\mathrm{SC}}$ is the superoperator for the rotating frame Hamiltonian that describes SCs in the presence of the static magnetic field $\boldsymbol{B}_0$ and the oscillating microwave field $\boldsymbol{B}_1$:

$$\hat{\mathcal{H}}_{\mathrm{SC}} = \hat{\mathcal{H}}_{0,\mathrm{SC}} + \hat{\mathcal{H}}_1 - \omega_{\mathrm{mw}} \hat{S}_z \tag{4.32}$$

with:

$$\hat{\mathcal{H}}_{0,\mathrm{SC}} = \frac{\mu_{\mathrm{B}}}{\hbar} B_0 g_{\mathrm{D}} \hat{S}_{\mathrm{D},z} + \frac{\mu_{\mathrm{B}}}{\hbar} B_0 g_{\mathrm{A}} \hat{S}_{\mathrm{A},z} \tag{4.33}$$

The relaxation behaviour of the SCs is assumed to mirror that of the CT state: $\hat{\hat{\Gamma}}_{\mathrm{SC}} = \hat{\hat{\Gamma}}_{\mathrm{CT}}$. In more advanced treatments, separate superoperators could be introduced to capture distinct relaxation pathways, if the added complexity is justifiable.

The two-state kinetic framework describes the interconversion and decay of CT states and SCs within OPV blends. The relevant processes are summarised in Figure 4.1, with transitions captured by the kinetic superoperator $\hat{\hat{K}}$ shown in blue.

CT states undergo spin-selective recombination to either the singlet ground state (S_0) or lower-lying triplet state (T_1), as described by $\hat{\hat{K}}_{\mathrm{CT}}$ in Equation 4.27. SCs, in contrast, decay to the ground state via a spin-independent pathway with rate constant k_{dec}. Interconversion between the two states occurs through dissociation of the CT state into SCs with rate constant k_{diss}, and re-encounter of SCs to reform a CT state with rate constant k_{enc}. These processes are incorporated in the kinetic superoperator as:

$$\hat{\hat{K}} = \begin{pmatrix} \hat{\hat{K}}_{\mathrm{CT}} + k_{\mathrm{diss}} \hat{\hat{1}} & -k_{\mathrm{enc}} \hat{\hat{1}} \\ -k_{\mathrm{diss}} \hat{\hat{1}} & (k_{\mathrm{dec}} + k_{\mathrm{enc}}) \hat{\hat{1}} \end{pmatrix} \tag{4.34}$$

Not all processes shown in the diagram are explicitly included in $\hat{\hat{K}}$. In particular, the formation of CT states and SCs from S_1, given by rate constants k_{CT} and k_{SC}, is excluded from the kinetic scheme. These rates are not modelled directly, as doing so would require knowledge of the populations of those precursor states. Including them would necessitate expanding the system size further, significantly increasing model complexity.

Instead, these formation steps are assumed to be complete at the onset of the simulation and are implicitly incorporated via the initial density operator, $\hat{\rho}_0$. This operator encodes the relative spin sublevel populations of CT and SC states at $t = 0$, reflecting the net effect of formation pathways without modelling them explicitly.

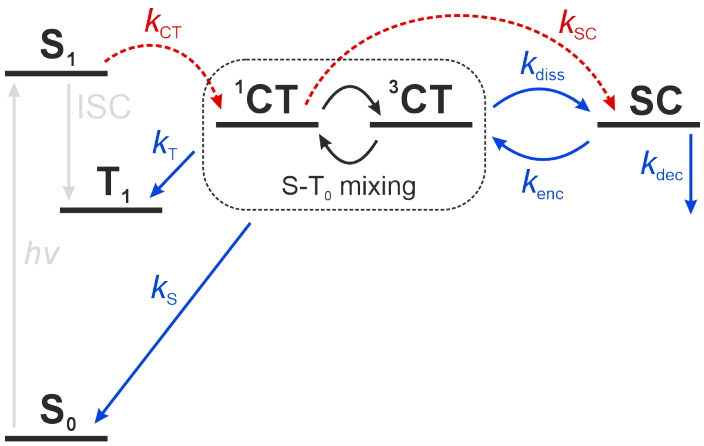

Figure 4.1: Kinetic diagram for the evolution of CT states and SCs in OPV blends, adapted from the photophysical mechanism in Chapter 1 (see Figure 1.8 in Section 1.4). The kinetic processes encompassed in $\hat{\hat{K}}$ are highlighted in blue, while formation processes for the CT state and SCs from S_1 (highlighted in red) are not explicitly included, with their contributions instead affecting the initial density operator $\hat{\rho}_0$.

4.2.4 Initial State of the Spin System

Singlet-Born Charge-Transfer State

When the CT state is formed via dissociation of the singlet exciton (S_1) at the donor:acceptor interface, the resulting spin configuration will reflect its singlet origin. In this case, the initial CT spin density operator, $\hat{\rho}_{0,\mathrm{CT}}$, exhibits coherence and population among eigenstates with singlet character, $|2\rangle$ and $|3\rangle$. As described in Section 2.4.2 of Chapter 2, the initial operator in Hilbert space, in the eigenbasis of the spin Hamiltonian, is:

$$\hat{\rho}_{0,\mathrm{CT}} = \hat{P}_{\mathrm{S}} = \begin{pmatrix} 0 & 0 & 0 & 0 \\ 0 & \sin^2\phi & -\frac{1}{2}\sin 2\phi & 0 \\ 0 & -\frac{1}{2}\sin 2\phi & \cos^2\phi & 0 \\ 0 & 0 & 0 & 0 \end{pmatrix} \tag{4.35}$$

Ultrafast Charge Separation

If the CT state dissociates rapidly into SCs before significant spin evolution occurs, the spin configuration is entirely preserved. Thus, the initial SC density operator $\hat{\rho}_{0,\mathrm{SC}}$ inherits the singlet character of the precursor CT state. For the uncorrelated, uncoupled SCs, $\phi = \frac{\pi}{4}$, and $\hat{\rho}_{0,\mathrm{SC}}$ can be expressed as:

$$\hat{\rho}_{0,\mathrm{SC}} = \hat{P}_{\mathrm{S}} = \begin{pmatrix} 0 & 0 & 0 & 0 \\ 0 & +\frac{1}{2} & -\frac{1}{2} & 0 \\ 0 & -\frac{1}{2} & +\frac{1}{2} & 0 \\ 0 & 0 & 0 & 0 \end{pmatrix} \tag{4.36}$$

Projection operators can then be used to extract the probability of finding a specific spin configuration in one of the individual charged states (e.g. donor or acceptor SCs). For a single-spin basis state $|\psi\rangle$ ($|\alpha_i\rangle$ or $|\beta_i\rangle$), the corresponding probability is obtained by:

$$p_\psi = \mathrm{tr}(\hat{P}_\psi\,\hat{\rho}) = \mathrm{tr}(|\psi\rangle\,\langle\psi|\,\hat{\rho}) \tag{4.37}$$

This trace operation projects the full two-spin density matrix $\hat{\rho}$ onto the chosen state $|\psi\rangle$, returning the total probability of observing that spin configuration.[§]

The projection operators for single-spin states $|\alpha\rangle$ and $|\beta\rangle$ are:

$$\hat{P}_\alpha = |\alpha\rangle\,\langle\alpha| = \begin{pmatrix} 1 & 0 \\ 0 & 0 \end{pmatrix} \qquad \hat{P}_\beta = |\beta\rangle\,\langle\beta| = \begin{pmatrix} 0 & 0 \\ 0 & 1 \end{pmatrix} \tag{4.38}$$

For the two-spin system, the projection operators are expanded by taking Kronecker products:

$$\begin{aligned} \hat{P}_{\alpha_1} &= \hat{P}_\alpha \otimes \hat{1} & \hat{P}_{\alpha_2} &= \hat{1} \otimes \hat{P}_\alpha \\ \hat{P}_{\beta_1} &= \hat{P}_\beta \otimes \hat{1} & \hat{P}_{\beta_2} &= \hat{1} \otimes \hat{P}_\beta \end{aligned} \tag{4.39}$$

Applying these operators to the initial density matrix gives equal probabilities for all spin eigenstates:

$$p_{\alpha_1} = \frac{1}{2} \qquad p_{\beta_1} = \frac{1}{2} \qquad p_{\alpha_2} = \frac{1}{2} \qquad p_{\beta_2} = \frac{1}{2} \tag{4.40}$$

Thus, at $t = 0$, the spin populations are balanced and there is no observable polarisation. This assumes that the spin configuration of $\hat{\rho}_0$ is completely preserved upon CT dissociation, with negligible singlet-triplet mixing prior to charge separation. The validity of this assumption depends on the lifetime of the CT state and the magnitude of the spin interactions determining spin mixing.[142] For radical pairs in photosynthetic reaction centres, no significant spin polarisation was assumed to develop for radical pairs with a lifetime shorter than 200 ps.[142,244]

[§]A classical analogue: projecting a vector $\boldsymbol{v}$ onto a unit vector $\boldsymbol{u}$ using the dot product $\boldsymbol{v} \cdot \boldsymbol{u}$. Just as the dot product gives the component of $\boldsymbol{v}$ along $\hat{\boldsymbol{u}}$, the projection operator isolates the component of the quantum state described by $\hat{\rho}$ that aligns with $|\psi\rangle$.

Non-Geminate Recombination

Over time, uncorrelated SCs may encounter each other and recombine to form a new CT state through a process known as non-geminate recombination. Since these SCs originate from distinct, uncorrelated precursors, the resulting CT state exhibits no spin polarisation.[265,266] Its initial density matrix is diagonal with equal populations across all eigenstates:

$$\hat{\rho}_{0,\mathrm{CT}} = \hat{\rho}_{0,\mathrm{SC}} = \begin{pmatrix} \frac{1}{4} & 0 & 0 & 0 \\ 0 & \frac{1}{4} & 0 & 0 \\ 0 & 0 & \frac{1}{4} & 0 \\ 0 & 0 & 0 & \frac{1}{4} \end{pmatrix} \tag{4.41}$$

Charge Separation after Singlet-Triplet Mixing

If the CT state instead survives long enough for coherent singlet-triplet mixing to occur, the spin polarisation of the SCs will be determined by the density operator of the CT state at the time of separation to SCs. This can be obtained by evolution of the initial density operator $\hat{\rho}_{0,\mathrm{CT}}$ under the static CT state spin Hamiltonian, $\hat{\mathcal{H}}_{0,\mathrm{CT}}$, for a duration t:

$$\hat{\rho}_{0,\mathrm{SC}} = \mathrm{e}^{-\mathrm{i}\,\hat{\mathcal{H}}_{0,\mathrm{CT}}\,t}\,\hat{P}_{\mathrm{S}}\,\mathrm{e}^{+\mathrm{i}\,\hat{\mathcal{H}}_{0,\mathrm{CT}}\,t} \tag{4.42}$$

The spin state probabilities for the separated charges are obtained using the projection operators, as in Equation 4.37:

$$\begin{aligned} p_{\alpha_1} &= \frac{1}{2}\left(1 + 2\sin(2\phi)\cos(2\phi)\,\sin^2(\Omega t)\right) \\ p_{\alpha_2} &= \frac{1}{2}\left(1 - 2\sin(2\phi)\cos(2\phi)\,\sin^2(\Omega t)\right) \\ p_{\beta_1} &= \frac{1}{2}\left(1 - 2\sin(2\phi)\cos(2\phi)\,\sin^2(\Omega t)\right) \\ p_{\beta_2} &= \frac{1}{2}\left(1 + 2\sin(2\phi)\cos(2\phi)\,\sin^2(\Omega t)\right) \end{aligned} \tag{4.43}$$

where

$$\sin(2\phi)\cos(2\phi) = \frac{\delta\omega\,(2J - D)}{\Omega^2} \tag{4.44}$$

with ϕ, Ω and $\delta\omega$ defined as in Section 2.4.2 of Chapter 2. The population differences for the two uncorrelated separated charges are then:

$$\begin{aligned} |\alpha_1\rangle \leftrightarrow |\beta_1\rangle \qquad & \Delta p_1 = +2\sin(2\phi)\cos(2\phi)\sin^2(\Omega t) \\ |\alpha_2\rangle \leftrightarrow |\beta_2\rangle \qquad & \Delta p_2 = -2\sin(2\phi)\cos(2\phi)\sin^2(\Omega t) \end{aligned} \tag{4.45}$$

The transitions for the two spins are therefore oppositely polarised, resulting in an emissive and an absorptive EPR signal, each with a lineshape closely related to that of the individual charged states.

In a powder spectrum averaged over all possible orientations of the dipolar vector with respect to the magnetic field, which one of the two spins gives an emissive or absorptive signal is determined mainly by the sign of the exchange coupling J and the difference in g-values, $(g_\mathrm{D} - g_\mathrm{A})$. In the case of negative J, as in the donor:acceptor OPV blends investigated here, the spectrum of the SC resonant at lower magnetic fields will generally be emissive, while that of the SC resonant at higher magnetic fields will be absorptive. The EPR spectra of SCs obtained following charge separation after a period of spin mixing are therefore expected to exhibit an *ea* signal polarisation.

The magnitude of the spin polarisation will be determined by the time t for which the state evolves under the CT spin Hamiltonian as well as the resonance frequency offset and spin-spin interactions. In the absence of significant singlet-triplet mixing (short t), these populations revert to equal values as in Equation 4.40. Equation 4.45 now provides a way of determining lifetimes that may lead to negligible spin mixing for a given CT state and therefore the absence of an observable polarisation, as discussed in the previous section.

Charge-Transfer States and Separated Charges

To describe the evolution of the time-resolved EPR signals in donor:acceptor OPV blends, contributions from both CT states as well as separated charges need to be considered. A two-state system is therefore defined, with an initial density operator obtained by combining the CT and SC density operators to form an $2n^2 \times 1$ vector $\hat{\rho}_0$:

$$\hat{\rho}_0 = \begin{pmatrix} \hat{\rho}_{0,\mathrm{CT}} \\ \hat{\rho}_{0,\mathrm{SC}} \end{pmatrix} \tag{4.46}$$

$\hat{\rho}_{0,\mathrm{CT}}$ and $\hat{\rho}_{0,\mathrm{SC}}$ are chosen to include the effects of the rates of formation of the CT state (k_CT) and SCs (k_SC) from S_1, as displayed before in Figure 4.1. Formation of the CT state from S_1 gives the initial density operator in Equation 4.35. Direct formation of SCs from S_1 is the ultrafast charge separation process $\mathrm{S}_1 \rightarrow {}^1\mathrm{CT} \rightarrow \mathrm{SC}$, where there is insufficient time for singlet-triplet mixing between the CT eigenstates. This produces uncorrelated SCs with the initial density operator of Equation 4.41:

$$\hat{\rho}_{0,\mathrm{CT}} = \begin{pmatrix} 0 & 0 & 0 & 0 \\ 0 & \sin^2\phi & -\frac{1}{2}\sin 2\phi & 0 \\ 0 & -\frac{1}{2}\sin 2\phi & \cos^2\phi & 0 \\ 0 & 0 & 0 & 0 \end{pmatrix} \qquad \hat{\rho}_{0,\mathrm{SC}} = \begin{pmatrix} \frac{1}{4} & 0 & 0 & 0 \\ 0 & \frac{1}{4} & 0 & 0 \\ 0 & 0 & \frac{1}{4} & 0 \\ 0 & 0 & 0 & \frac{1}{4} \end{pmatrix} \tag{4.47}$$

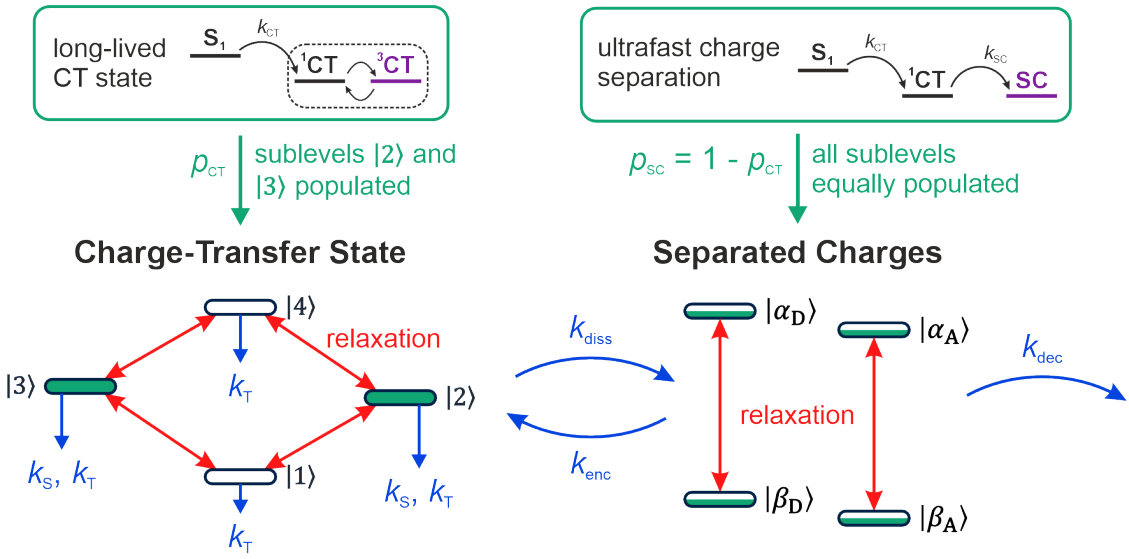

Figure 4.2: Schematic of the dynamic processes in the two-state model comprising the CT state and SCs. Kinetic transitions, shown in blue, describe processes leading to the generation, interconversion and decay of the CT state and SCs. Relaxation processes, in red, drive populations and coherences towards thermal equilibrium. The initial density operator, $\hat{\rho}_0$, includes a spin-polarised CT state formed from a singlet precursor and uncorrelated SCs formed by ultrafast charge separation (Equation 4.47), highlighted in green. The relative contribution of each component is governed by the parameter p_{CT} (Equation 4.46).

The contributions of $\hat{\rho}_{0,\mathrm{CT}}$ and $\hat{\rho}_{0,\mathrm{SC}}$ to the spin system at $t = 0$ will be determined by the relative rates of k_{CT} and k_{SC}. The fraction of photoexcitations that form the long-lived singlet-born CT state is defined as p_{CT}, and the remainder, $1 - p_{\mathrm{CT}}$, corresponds to photoexcitations that yield uncorrelated SCs. The initial density operator is thus expressed as a weighted sum of the two limiting cases:

$$\hat{\rho}_0 = \begin{pmatrix} p_{\mathrm{CT}}\,\hat{\rho}_{\mathrm{CT}} \\ (1 - p_{\mathrm{CT}})\,\hat{\rho}_{\mathrm{SC}} \end{pmatrix} \tag{4.48}$$

The two-state formulation is summarised in Figure 4.2. The parameter p_{CT} defines the relative initial populations of (long-lived) singlet-born CT states and uncorrelated SCs. Their spin sublevel populations, determined by their formation mechanisms, are highlighted in green. As the system evolves, the population and coherences of the CT state and SC are influenced by kinetic (k_{S}, k_{T}, k_{diss}, k_{enc}, and k_{dec}) and spin relaxation (T_1 and T_2) processes. By tuning p_{CT} alongside these kinetic and relaxation parameters, a variety of photophysical processes can be modelled.

4.3 Computational Implementation

Building on the formalism outlined above for propagating the density operator under coherent spin dynamics, kinetics, and relaxation, a computational package, **RADISH** (**RAD**icals **I**n **S**pin **H**amiltonians), was developed to simulate the spin evolution of CT states and SCs in donor:acceptor OPV blends.

While the widely-used, open-source EPR simulation toolbox EasySpin[130] provides powerful capabilities for modelling static EPR spectra, and has recently been extended to include spin polarisation,[267] it lacks the capability to explicitly incorporate the effects of microwave excitation and relaxation explicitly during spin evolution. Moreover, EasySpin does not readily accommodate connections between different spin-polarised states, which is critical for accurately modelling the combined CT and SC kinetics in OPV blends.

RADISH addresses these limitations by enabling explicit, time-resolved simulations of multi-state spin systems, capturing the interplay between CT and SC populations, their coherences, and their evolution during a time-resolved EPR experiment. RADISH is designed for seamless integration with EasySpin, with both written in MATLAB, while utilising identical spin system input formats and sharing key underlying computational routines. This ensures ease of adoption for users familiar with EasySpin, while extending its functionality to incorporate spin dynamics beyond static spectral simulations.

Although RADISH is currently tailored to two-state CT-SC systems relevant to OPV kinetics, its code structure allows straightforward extension to more complex spin systems, including triplets, quartets, or triplet-doublet pairs. The full RADISH code is provided in Appendix D.

4.3.1 Simulation Procedure in RADISH

The time-resolved EPR signal in RADISH is computed through three nested loops corresponding to molecular orientations, magnetic field values, and time points:

- **Orientation** (outermost loop): samples molecular orientations relative to the external magnetic field to perform powder averaging. For each molecular orientation, the effective field-independent spin Hamiltonian terms (spin-spin interactions) are calculated.
- **Magnetic Field** (intermediate loop): sweeps through the external magnetic field values. For each field, the full Hamiltonian is constructed by adding the field-dependent Zeeman terms. The total Liouvillian superoperator is then assembled by combining the Hamiltonian superoperator with the kinetic and

relaxation superoperators, which are precomputed once outside all loops. The propagator $\hat{O}$ is subsequently calculated.

- **Time** (innermost loop): propagates the density matrix forward in time at each time step using the propagator $\hat{\hat{O}}$. At every time point, the elements of the density operator are used to calculate the EPR signal.

The complete time trace is stored for each magnetic field and orientation. After all orientations have been processed, the orientation-dependent signals are weighted and summed to produce the final time-resolved EPR spectrum. Additionally, RADISH can separately track and store the individual CT state and SC contributions, enabling detailed analysis of their spin evolution.

This procedure can be summarised by the following pseudo-code representation, which outlines the main computational steps and loop structure implemented in RADISH:

```
compute KineticSuperoperator
compute RelaxationSuperoperator

for orientation in orientations:
    calculate field-independent Hamiltonian terms

    for B0 in magnetic_fields:
        construct full Hamiltonian with Zeeman terms at B0
        build Liouvillian L = i * HamiltonianSup - KineticSup +
            RelaxationSup
        compute propagator O

        for time_step in time_points:
            propagate density: rho_new = O * rho_old
            detect EPR signal: signal(time_step) = DetectionOp
               * rho_new
            rho_old = rho_new

    weigh signals by orientation probability

sum weighted signals over all orientations to get final time-
   resolved EPR spectrum
```

Propagation of the density operator requires that all matrices and vectors are expressed in a common basis. Consistent with EasySpin, RADISH performs all calculations in the uncoupled basis $\{|\alpha\alpha\rangle, |\alpha\beta\rangle, |\beta\alpha\rangle, |\beta\beta\rangle\}$. The relaxation superoperator $\hat{\hat{\Gamma}}$, however, must first be defined in the eigenbasis of the CT and SC subspaces, as it deals with redistribution of populations and coherences between the eigenstates. It is then transformed into the uncoupled basis via:

$$\hat{\hat{\Gamma}}_{\alpha\beta} = U^{\mathrm{T}} \hat{\hat{\Gamma}}_{\mathrm{eig}} U \tag{4.49}$$

where U is the matrix of eigenvectors of the static Hamiltonian $\hat{\mathcal{H}}_0$ defined in the uncoupled basis and transformed to Liouville space.

A transformation is also applied to the kinetic superoperator, $\hat{\hat{K}}_{\mathrm{CT}}$, which describes singlet- and triplet-selective recombination within the CT subspace. This operator is initially defined in the singlet-triplet coupled basis and must also be converted to the uncoupled basis.

RADISH employs a time-independent effective Hamiltonian $\hat{\mathcal{H}}_{\mathrm{eff}}$ within the rotating frame approximation to simplify the treatment of spin dynamics. Transforming into the rotating frame shifts the reference frame to precess with the spins, rendering many interactions time-independent. However, non-secular terms, which involve spin operators not aligned with the static magnetic field, $\boldsymbol{B}_0$, continue to oscillate rapidly near the Larmor frequency in this frame. These rapidly oscillating terms average out to zero over relevant timescales, especially in the high-field limit where the Zeeman interaction dominates. Neglecting them reduces computational cost and allows larger simulation time steps without significant accuracy loss. In contrast, pseudo-secular terms, present in the dipolar coupling interaction, remain effectively static within the time step and must be retained to accurately model spin-spin interactions.

The resulting $\hat{\mathcal{H}}_{\mathrm{eff}}$ is, therefore, time-independent and captures the dominant static interactions projected along the magnetic field axis. For instance, the effective g-value along $\boldsymbol{B}_0$ is calculated as:

$$g_{\mathrm{eff}} = \boldsymbol{B}_0^{\mathrm{T}} \cdot \boldsymbol{g} \cdot \boldsymbol{B}_0 = \begin{pmatrix} B_x & B_y & B_z \end{pmatrix} \begin{pmatrix} g_{xx} & g_{xy} & g_{xz} \\ g_{yx} & g_{yy} & g_{yz} \\ g_{zx} & g_{zy} & g_{zz} \end{pmatrix} \begin{pmatrix} B_x \\ B_y \\ B_z \end{pmatrix} \tag{4.50}$$

The effective Hamiltonian $\hat{\mathcal{H}}_{\mathrm{eff}}$ in RADISH includes spin-field interactions (electron Zeeman and nuclear Zeeman), spin-spin interactions (dipolar coupling, exchange, and hyperfine), and the microwave Hamiltonian contribution. While hyperfine interactions are often necessary for accurately capturing spin behaviour, their inclusion substantially increases computational cost by enlarging the Liouville space, increasing simulation time.

All interactions in RADISH are defined in the molecular reference frame. Anisotropic interactions ($\boldsymbol{g}$, $\boldsymbol{D}$, $\boldsymbol{A}$) are specified by their principal values and Euler angles α, β, γ, for the transformation from the molecular frame to their principal axis where these tensors are diagonal. The effective value of that interaction along $\boldsymbol{B}_0$ or $\boldsymbol{B}_1$ is calculated using Equation 4.50.

RADISH performs powder averaging by sampling different molecular orientations with respect to the laboratory frame, defined by the orientations of $\boldsymbol{B}_0$ and $\boldsymbol{B}_1$. In the calculations, the molecular frame is fixed, and orientations are defined by rotating

the laboratory frame relative to it. Orientations are generated using EasySpin's *sphgrid* function, which produces a triangular grid over the unit sphere.[130,268] Finer grids, sampling a greater number of orientations, improve spectral accuracy but increase computation time, while undersampling leads to spectral artefacts.

As a benchmark, on a computer with an Intel(R) Core(TM) i5-10500 CPU @ 3.10 GHz, 16.0 GB of RAM, a RADISH simulation with 500 time and field points takes approximately:

- 3 s for a grid size of 5 (41 orientations)
- 22 s for a grid size of 15 (421 orientations)

These performance metrics help guide the choice of grid resolution depending on the desired accuracy and speed.

Once the effective Hamiltonian $\hat{\mathcal{H}}_{\text{eff}}$ is constructed, the full Liouvillian superoperator $\hat{\hat{\mathcal{L}}}$ governing the spin system's dynamics is assembled, incorporating coherent evolution, kinetics, and relaxation. In RADISH, rate constants k are implemented as corresponding time constants τ. The time evolution of the density operator $\hat{\rho}(t)$ is then computed using a fixed time step $\mathrm{d}t$. The choice of $\mathrm{d}t$ sets the maximum oscillation frequency that can be accurately resolved: the Nyquist frequency $1/2\mathrm{d}t$. All spin interactions that give rise to oscillatory dynamics (e.g. dipolar, exchange, hyperfine) must therefore fall below this limit. For example, a time step of 10 ns corresponds to a sampling frequency of 100 MHz, and hence a Nyquist frequency of 50 MHz. Interactions with frequencies above this threshold will be undersampled and incorrectly mapped onto lower frequencies, known as aliasing. At each step, propagation is performed via the time evolution propagator $\hat{\hat{O}}$, as defined in Equation 4.16. To accelerate this step, the matrix exponential $\mathrm{e}^{\hat{\hat{\mathcal{L}}}\mathrm{d}t}$ is evaluated using the efficient *fastExpm* routine.[269,270]

After each propagation step, the EPR signal is detected by projecting the magnetisation along the laboratory-frame y-axis. The density operator is then updated to serve as the initial state for the next time step. Repeating this process over the entire time window generates the full time-resolved EPR signal for a single molecular orientation and magnetic field value. This procedure is repeated across the full range of magnetic field values. Once the time- and field-resolved signals have been computed for all orientations in the sampling grid, each orientation's contribution is weighted according to its relative probability and summed to produce the final powder-averaged time-resolved EPR spectrum.

RADISH supports homogeneous line broadening through convolution of the simulated time-resolved EPR signal with Gaussian or Lorentzian line shapes. Inhomogeneous broadening, such as g-strain, can be incorporated by performing separate RADISH simulations at discrete g-values sampled from the strain distribution and then combining the weighted spectra.

4.3.2 Accounting for Effects on the Transient Signal

Accurate simulation of time-resolved EPR signals requires knowledge of both the microwave magnetic field strength (B_1) and the resonator response, as both significantly influence the shape and appearance of the observed transients.

The microwave field $\boldsymbol{B}_1$ induces precession of the spin magnetisation around the field direction. Under continuous-wave excitation, with sufficiently strong microwave irradiation and slow relaxation, this results in periodic modulations of the detected signal known as Torrey oscillations.[271–273] The frequency of these oscillations is set by the Rabi frequency, ω_1, which is proportional to B_1, while their damping is determined by relaxation processes.[138] These oscillations can appear as distinct features in the time-domain signal, particularly at early times following photoexcitation. As shown in Figure 4.3, increasing B_1 produces faster oscillations in the simulated EPR transient. When such oscillations are clearly visible, B_1 can be treated as a fitting parameter.

Even in the absence of clear oscillations, the influence of B_1 remains significant and still shapes the evolution of the transient signal. If B_1 is underestimated or omitted, its effect can be incorrectly compensated for by fitting increased relaxation or faster decay rates. It is precisely in such cases, when oscillations are not directly observed, that knowledge of the correct B_1 strength becomes most important, to avoid misinterpreting the underlying photophysics.

The limited bandwidth of the resonator introduces an instrumental response function that damps early-time signal features. The damping effect is modelled

p_{CT}	g_D	g_A	J	D	T_1	T_2	B_0
1	2.008	2.000	−6 MHz	[3, 3, −6] MHz	15 µs	1 µs	350 mT

Table 4.1: Parameters for the time-resolved EPR simulations in Figures 4.3 and 4.4.

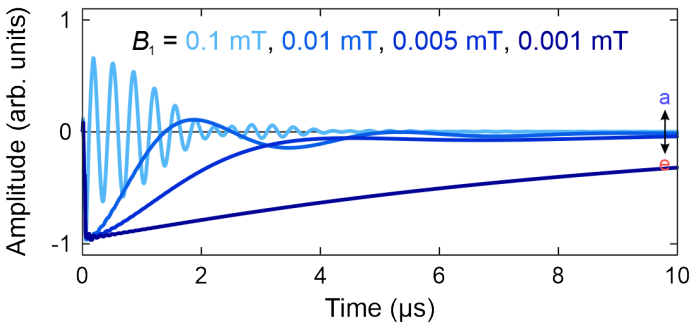

Figure 4.3: Modelled EPR normalised transients for a singlet-born charge-transfer state, for a range of microwave field strengths, B_1, using the spin parameters defined in Table 4.1.

by multiplying each transient with the resonator response function, characterised by the resonator bandwidth $\Delta\nu$, which depends on the quality factor (Q), as detailed in Section 2.5 of Chapter 2:

$$I(t) = I'(t)\left(1 - \mathrm{e}^{-\Delta\nu\, t}\right) \tag{4.51}$$

with $I'(t)$ the ideal EPR transient unaffected by the resonator, and $I(t)$ the observed signal. A higher Q-factor (narrower bandwidth) stores energy for longer in the resonator, delaying response and suppressing fast features at short times.

Quantum Beats

In certain spin systems, particularly isolated CT states in well-ordered environments, $\mathrm{S} - \mathrm{T}_0$ mixing gives rise to long-lived zero-quantum coherence (ZQC). The initial spin state will be a coherent superposition of $|2\rangle$ and $|3\rangle$, resulting in oscillations in the transverse magnetisation. These oscillations, known as quantum beats, are much faster than Torrey oscillations, and are observed in time-resolved EPR spectra if there is sufficient time resolution. These oscillations directly reflect the coherence between the $|2\rangle$ and $|3\rangle$ eigenstates. The frequency and damping of these oscillations depend on the coupling between the two spins (J and $\boldsymbol{D}$) and the rate of dephasing, providing a sensitive probe of local magnetic interactions and decoherence mechanisms.[253,274–276]

Quantum beats of this kind have been experimentally observed in highly ordered, deuterated systems, such as photosynthetic bacterial reaction centres.[275,276] In OPV blends, these oscillations are typically not observed. This absence is attributed to hyperfine coupling to a dense environment of nearby proton spins, that cause fluctuations in the local magnetic field. The zero-quantum coherence rapidly dephases on timescales much shorter than the experimental resolution.[277]

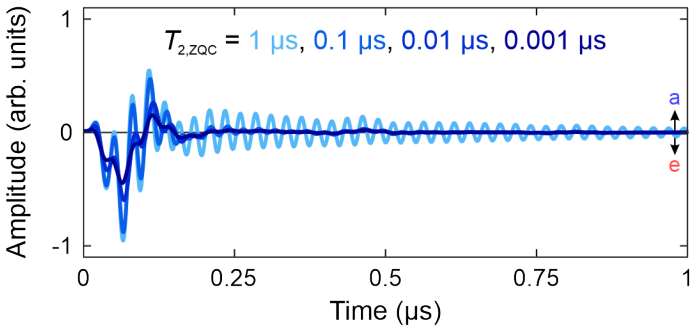

Figure 4.4: Modelled EPR transients for a singlet-born charge-transfer state, for a range of zero quantum decoherence times, using the spin parameters defined in Table 4.1, and $B_1 = 0.005\,\mathrm{mT}$.

Explicitly including many coupled protons in the simulation is computationally prohibitive, as each spin-$\frac{1}{2}$ nucleus increases the Liouville space dimensionality by a factor of 4. Instead, RADISH incorporates this damping phenomenologically. ZQC decay is modelled by assigning a shorter T_2 decoherence time, $T_{2,\mathrm{ZQC}}$, to the off-diagonal elements of the density matrix associated with the $|2\rangle\langle 3|$ and $|3\rangle\langle 2|$ coherences:

$$\langle ij|\,\hat{\hat{\Gamma}}_{\mathrm{CT}}\,|ij\rangle = \frac{1}{T_{2,\mathrm{ZQC}}} \tag{4.52}$$

for $i, j = 2, 3$ and $i \neq j$.

This treatment allows RADISH to account for the rapid dephasing of zero-quantum coherence, without explicitly simulating the full nuclear spin environment. To illustrate the effect of varying $T_{2,\mathrm{ZQC}}$, simulated EPR transients for a CT state with fixed T_2, but varied $T_{2,\mathrm{ZQC}}$, are shown in Figure 4.4. When $T_{2,\mathrm{ZQC}} = T_2$, pronounced quantum beats are visible. As $T_{2,\mathrm{ZQC}}$ is reduced, the beats are increasingly damped, until they disappear entirely for short coherence lifetimes.

4.3.3 Enhancing Computational Efficiency

Significant computational savings can be achieved in RADISH by skipping propagation steps at magnetic field values that are sufficiently far from resonance for a given molecular orientation, where no appreciable EPR signal is expected. To determine whether a given field is near resonance, RADISH first pre-computes all possible spin transition frequencies, both allowed and formally forbidden, by calculating eigenvalue differences of the static Hamiltonian $\hat{\mathcal{H}}_0$. These transition frequencies are then compared to the applied microwave frequency ω_{mw}. If none fall within a user-defined resonance window, typically set to 10 MHz, the simulation omits propagation at that field. This threshold defines the maximum allowed difference $|\omega_i - \omega_{\mathrm{mw}}|$ for any transition frequency ω_i to be considered near-resonant.

Figure 4.5 illustrates the effect of applying such resonance-based masking. For a single molecular orientation, field regions where all transitions lie beyond the chosen threshold are marked in green, these are the skipped field values. The impact on accuracy is quantified in the right panel, which shows the relative root-mean-square deviation (RMSD) between full (unmasked) simulations and simulations run with different threshold values. As the threshold is reduced, fewer field points are propagated, shortening computation time but increasing the spectral deviation. Conversely, a larger threshold includes more off-resonant points, improving spectral fidelity at the cost of longer runtime. Unless otherwise stated, a threshold of 10 MHz is used as a compromise of accuracy and efficiency.

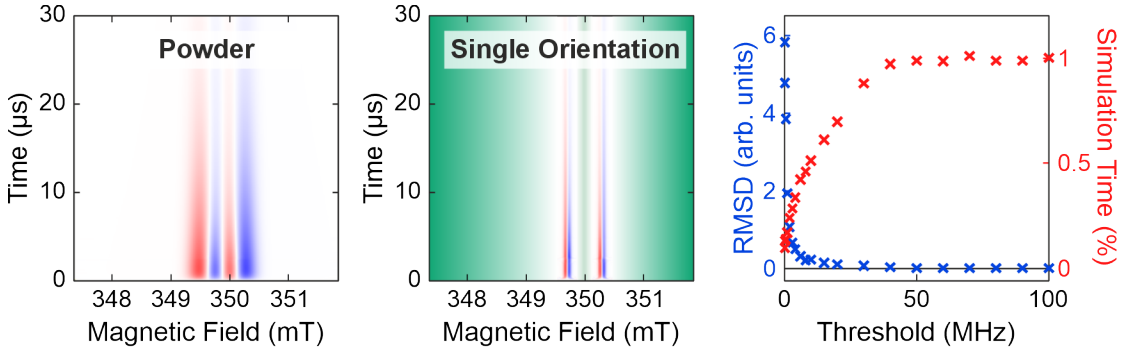

Figure 4.5: Time-resolved EPR spectra for a long-lived charge-transfer state, for a distribution of molecular environments or powder sample (left) and a single molecular orientation (centre). For the single molecular orientation, areas of the plot that are far off-resonance are coloured green. The relative root-mean square deviation (RMSD) is calculated between EPR spectra simulated for a number of different resonance thresholds and the EPR spectrum without the threshold (right). As the threshold is decreased, the simulation time shortens, but the RMSD increases.

4.3.4 Setup of a RADISH Simulation

RADISH simulations are performed by defining a spin system (`Sys`), experimental parameters (`Exp`), and optional settings (`Opt`), mirroring the user inputs in EasySpin. The main function returns three outputs: `x`, containing the magnetic field (in mT) and time (in µs) axes; `spc`, which holds the separate contributions from CT states and SCs that can be summed to yield the full time-resolved EPR spectrum; and `rho`, the time-dependent, vectorised density operator.

The simulation yields a two-dimensional dataset, modelling the experimental time-resolved EPR data, and therefore allows determination of kinetic and relaxation parameters by comparison or fitting. RADISH provides separate signal contributions from CT states and SCs, as well as tracking the time evolution of each of their spin sublevel populations, including occupations of individual eigenstates.

An example script is shown below, generating the time-resolved EPR spectrum of slow separation of the CT state, discussed later in this chapter (Section 4.4.3):

```
% Spin System
Sys.S = [0.5 0.5]; % two S = 1/2 spins
Sys.g = [2.0022 2.0023 2.0033; 2.0002 2.0001 1.9990]; % g
Sys.gFrame = [149 92 145; 0 0 0]*pi/180; % g-frames (radians)
Sys.J = -3.6; % J (MHz)
Sys.dip = [-5.6 2.0 3.6]; % D (MHz)
Sys.eeFrame = [231 29 318]*pi/180; % D-frame (radians)
Sys.lwpp = 0.25; % Gaussian linewidth (mT)
Sys.tauDiss = 10; % 1/k_diss (mus)
Sys.T1 = 50; % T1 (mus)
Sys.T2 = [1 0.0001]; % T2, T2(ZQC) (mus)
```

```
% Experimental Parameters
Exp.mwFreq = 9.8; % microwave frequency (GHz)
Exp.Range = [347 352]; % magnetic field range (mT)
Exp.nPoints = 1001; % field points
Exp.B1 = 0.005; % B1 strength (mT)
Exp.dt = 0.01; % time step (mus)
Exp.tPoints = 1501; % time points
Exp.Temperature = 20; % temperature (K)

% Options
Opt.Threshold = 10; % transition frequency threshold (MHz)
Opt.GridSize = 10; % orientation grid size
Opt.SeparateDetection = true; % separate CT and SC detection

% Run Simulation
[x,spc,rho] = RADISH(Sys,Exp,Opt);
```

4.3.5 Performance Testing and Model Validation

Reliable interpretation of complex time-resolved EPR data critically depends on the accuracy of the underlying simulation framework. To ensure RADISH faithfully captures the essential spin dynamics, relaxation processes, and kinetic pathways of CT states and SCs, a series of benchmark tests were undertaken. These tests are designed to compare RADISH simulation results with those from well-established software packages, alongside experimental data reported in the literature. Such validation is a critical step before applying RADISH to novel experimental datasets.

Although RADISH is primarily designed to simulate full two-dimensional time-resolved EPR signals, its core capability to reproduce static spin-polarised EPR spectra was validated through comparison with EasySpin simulations. In this context, a static spectrum refers to the spin-polarised EPR signal calculated under conditions where spin sublevel populations remain constant over the measurement timescale. EasySpin's *pepper* function constructs the spin Hamiltonian, calculates resonance positions of the EPR transitions, and generates the static spin-polarised spectrum based on defined sublevel populations.[130,267] In RADISH, the full time evolution of the density operator is simulated, including the effects of the microwave field and kinetic and relaxation pathways. To match EasySpin conditions, RADISH simulations were performed with an extremely weak microwave field ($B_1 = 10^{-6}\,\mathrm{mT}$) and negligible relaxation and kinetic rates, so that the spin polarisation remains effectively constant over time. The RADISH signal is averaged between $1 - 2\,\mu\mathrm{s}$, excluding the early-time signal affected by lifetime broadening, to compare directly to the static, spin-polarised EPR spectrum generated by EasySpin. Results of this comparison are shown in Figure 4.6, for four representative spin systems:

a) Singlet-born CT state with isotropic g-values, and exchange and axial dipolar coupling:
   - $g_{\mathrm{D}} = 2.008$, $g_{\mathrm{A}} = 2.000$
   - $J = -6\,\mathrm{MHz}$, $D = [3,\ 3,\ -6]\,\mathrm{MHz}$
   - Gaussian line broadening: $0.4\,\mathrm{mT}$

b) Singlet-born CT state with orthorhombic g-values, and exchange and orthorhombic dipolar coupling:
   - $g_{\mathrm{D}} = [2.003,\ 2.009,\ 2.010]$, g_{D}-frame $= [70°,\ 10°,\ 40°]$
   - $g_{\mathrm{A}} = [1.996,\ 2.000,\ 2.001]$, g_{A}-frame $= [0°,\ 0°,\ 0°]$
   - $J = -2\,\mathrm{MHz}$
   - $D = [2,\ 4,\ -6]\,\mathrm{MHz}$, D-frame $= [5°,\ 30°,\ 150°]$
   - Gaussian line broadening: $0.4\,\mathrm{mT}$

c) Singlet-born CT state as in b) with an additional hyperfine interaction:
   - $A = [4,\ 10,\ 8]\,\mathrm{MHz}$, A-frame $= [30°,\ 45°,\ 15°]$

d) SCs formed from singlet-born CT state that has undergone partial $\mathrm{S} - \mathrm{T}_0$ mixing:
   - $g_{\mathrm{D}} = [2.003,\ 2.009,\ 2.010]$
   - $g_{\mathrm{A}} = [1.996,\ 2.000,\ 2.001]$
   - $J = D = 0\,\mathrm{MHz}$
   - $\left[p_{\mathrm{T}_+}, p_{\mathrm{T}_0}, p_{\mathrm{S}}, p_{\mathrm{T}_-}\right] = \left[0,\ \frac{1}{2},\ \frac{\sqrt{3}}{2},\ 0\right]$
   - Gaussian line broadening: $0.4\,\mathrm{mT}$

As shown in Figure 4.6, RADISH accurately reproduces the spectra generated by EasySpin in all four cases. The first three simulations, all singlet-born CT states, exhibit the expected *eaea* polarisation pattern for distinct g-values. In a), the spectrum is simple and broad due to isotropic g-values and axial dipolar coupling. Cases b) and c) introduce anisotropy in the g-values and dipolar coupling, and in c), a hyperfine interaction, resulting in additional broadening of the same *eaea* pattern. The fourth case, d), models a spin-polarised SC state, derived from a CT state that has undergone partial singlet-triplet mixing. As laid out in Section 4.2.3, the resulting spectrum shows *ea* polarisation: the donor SC of higher g-values is emissive and the acceptor SC of lower g-values is absorptive.

Overall, the excellent agreement between RADISH and EasySpin across these varied test systems confirms that RADISH faithfully captures the spin Hamiltonian physics and is capable of simulating static spin-polarised EPR spectra. To further validate RADISH against established experimental and simulation benchmarks, the spin polarisation evolution of a well-characterised system from the literature

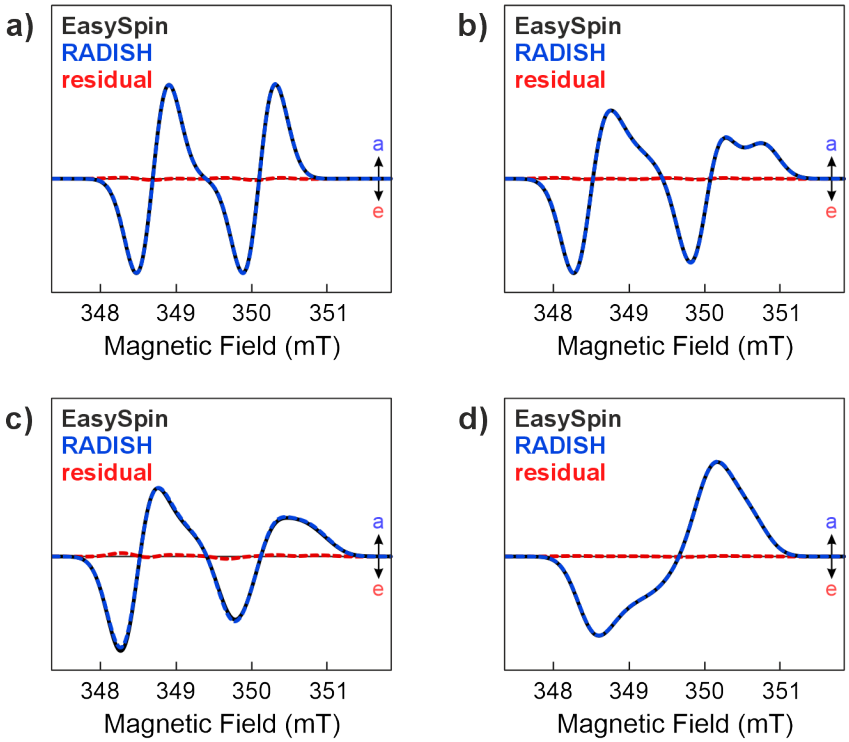

Figure 4.6: X-band RADISH simulations of static spin-polarised EPR spectra compared with corresponding EasySpin simulations. The residual between the two simulations is plotted in red. a) Isotropic g-values, J and axial D-values; b) orthorhombic g-values, J and orthorhombic D-values; c) The same spin system as b) with additional proton hyperfine coupling; d) spin-polarised SCs formed from a CT state that has undergone some singlet-triplet mixing.

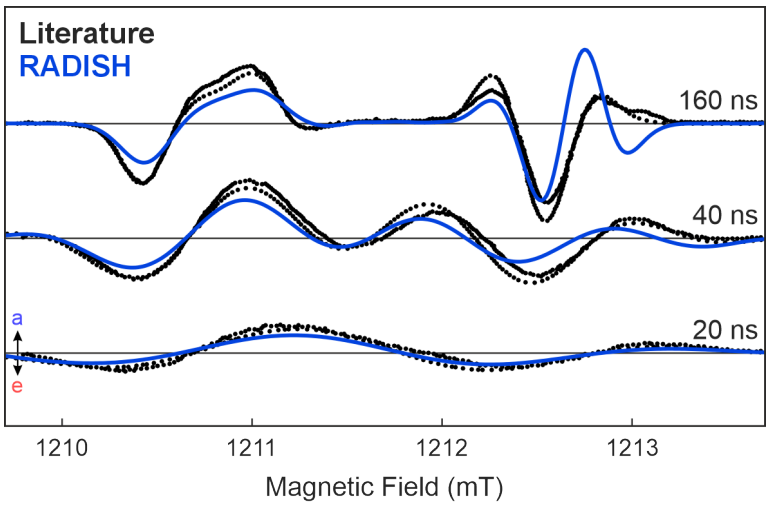

Figure 4.7: Comparison of Q-band RADISH simulations (blue) with experimental time-resolved EPR spectra (black) and literature simulations (dotted) for the photoinduced CT state $P_{700}^{+}A_{1}^{-}$ in Photosystem I.[254] The RADISH simulations were performed with the parameters reported in the literature, excluding hyperfine interactions.

was modelled: the photoinduced charge-transfer state $P_{700}^{+}A_{1}^{-}$ in Photosystem I.[254] Simulation parameters were taken directly from the original study, with hyperfine interactions omitted to reduce computational demand.

As illustrated in Figure 4.7, RADISH accurately reproduces the *eaea* polarisation pattern and its evolution with time. The early-time spectrum at 20 ns exhibits a broad, weakly polarised signal that develops more resolved features at later times, in agreement with both the experimental observations and previously published simulations. Discrepancies between RADISH and the literature simulation likely stem from the omission of twelve hyperfine couplings - eight ^{15}N nuclei and four ^{2}H nuclei in the manuscript. Explicit incorporation of these interactions in a RADISH simulation would dramatically increase the Liouvillian dimensions, making the simulation computationally prohibitive. While these interactions can influence the spectral shape in systems like Photosystem I, their inclusion is less critical for donor:acceptor OPV blends, where hyperfine interactions are typically unresolved and contribute only to the line broadening. In addition, the Q-value of the resonator used was not reported in the original literature.

This close agreement between RADISH and experimental data demonstrates the capability of the framework to reliably capture the spin dynamics of real CT state systems. Validation against benchmark data is critical to ensure confidence in the predictive power of RADISH. The successful reproduction of both experimental and prior simulation results confirms that RADISH effectively encapsulates the fundamental physics of photoinduced spin processes, supporting its application to the quantitative interpretation of complex time-resolved EPR spectra.

4.4 Model Cases of Charge Separation in OPVs

Having validated the RADISH simulation framework through testing and benchmarking against established results and EasySpin simulations, it was next applied to model key kinetic regimes relevant to charge transfer and separation in OPV blends. To illustrate the capabilities of the framework and to establish a conceptual basis for interpreting experimental data, this section introduces four representative model scenarios:

4.4.1 Long-lived charge-transfer state: $S_1 \rightarrow (^1CT \leftrightarrow {}^3CT)$

4.4.2 Ultrafast charge separation: $S_1 \rightarrow {}^1CT \rightarrow SC$

4.4.3 Slow charge separation: $S_1 \rightarrow (^1CT \leftrightarrow {}^3CT) \rightarrow SC$

4.4.4 Equilibrium between the charge-transfer state and separated charges: $S_1 \rightarrow (^1CT \leftrightarrow {}^3CT) \rightleftharpoons SC$

These scenarios span a range of photophysical pathways expected to be possible in OPV blends and are designed to capture the various mechanisms by which excitons evolve at the donor:acceptor interface.[102] Each scenario is defined by specific kinetic rate constants and initial populations, leading to characteristic spin polarisation patterns and evolutions. Simulating the time-resolved EPR data for each case helps identify features diagnostic of the underlying mechanisms.

The insights gained from these model simulations provide a reference for the following chapter, which presents a detailed experimental study of time-resolved EPR in fullerene and non-fullerene acceptor OPV blends. RADISH simulations are used to extract quantitative kinetic parameters and to determine the dominant photophysical mechanisms responsible for charge transfer and separation.

The examples shown use spin parameters for the OPV blend PBDB-T:PCBM. PBDB-T$^{\bullet+}$ and PCBM$^{\bullet-}$ have distinct g-values, determined from multi-frequency pulse EPR experiments reported in the previous chapter (Section 3.3.1), while J- and D-values were estimated from spin-polarised CT state signals that will be described in detail in Chapter 5 (Section 5.3.3). Hyperfine interactions were not included, as they were found to be unresolved in EPR spectra of fullerene acceptor blends:

- $g_{\mathrm{D}} = [2.0022, 2.0023, 2.0033]$, g_{D}-frame $= [149°, 92°, 145°]$
- $g_{\mathrm{A}} = [2.0002, 2.0001, 1.9990]$, g_{A}-frame $= [0°, 0°, 0°]$
- $D = [-5.6, 2.0, 3.6]\,\mathrm{MHz}$, D-frame $= [231°, 29°, 318°]$
- $J = -3.6\,\mathrm{MHz}$
- Linewidth $= 0.25\,\mathrm{mT}$
- $B_1 = 0.005\,\mathrm{mT}$

4.4.1 Charge-Transfer State Formation and Decay

For many molecular donor:acceptor systems, including photosynthetic reaction centres, cryptochromes involved in avian magnetoreception, and molecular triads studied in quantum information science, the CT state is localised and has no possibility to fully separate before decaying.[245,253,278,279] The CT state often retains the polarisation of its precursor state, before recombining to lower-lying singlet or triplet states (e.g. S_0 or T_1 in OPV blends), defined by the time constants τ_{S} and τ_{T}.

Figure 4.8 presents the predicted time-resolved EPR spectrum for a localised CT state in PBDB-T:PCBM. The modelled kinetic diagram is shown at the top of the figure with photoexcited states that have unpaired spins, and therefore observable by EPR, highlighted in purple. Simulated EPR spectra are shown for the total signal, as well as the individual contributions of the CT state and SCs. Static

spectra extracted at early (1 µs) and late (10 µs) times highlight the changes in spin polarisation with time. The evolution of the CT state and SC populations are plotted in red and green, respectively, with the populations of their four eigenstates shown below in blue, providing detailed insight into the evolution of the spin sublevel populations that determine the signal polarisation of the EPR spectrum.

In the case shown in Figure 4.8, the CT state is formed from a singlet precursor ($S_1 \rightarrow CT$) and the CT sublevels $|2\rangle$ and $|3\rangle$ are initially populated. The lifetime of the CT state is determined by the rates of CT recombination. For the case shown, CT state recombination is spin-independent ($\tau_S = \tau_T = 20\,\mu s$). Sublevels $|2\rangle$ and $|3\rangle$ are depopulated, while sublevels $|1\rangle$ and $|4\rangle$ remain unpopulated throughout. This preserves the two absorptive ($|2\rangle, |3\rangle \rightarrow |4\rangle$) and two emissive ($|2\rangle, |3\rangle \rightarrow |1\rangle$) transitions, and thus the characteristic *eaea*-polarised signal shape, that gradually decreases in amplitude as the CT state population diminishes.

Because no population transfers to SCs, there is no SC contribution to the EPR signal. A subtle contraction of the inner spectral features around 4 µs is visible in the time-resolved spectra, attributable to a small contribution from Torrey oscillations induced by the microwave field $\boldsymbol{B}_1$, of strength 0.005 mT.

4.4.2 Ultrafast Charge Separation

At the other extreme, the CT state may instead be able to dissociate into SCs rapidly, illustrated in Figure 4.9. In the example shown, dissociation occurs within a picosecond ($\tau_{diss} = 1\,ps$), leaving insufficient time to build up spin polarisation through spin mixing in the CT state.[142] Formation of the SCs leads to equal populations of all its spin sublevels. Consequently, there is no net spin polarisation at $t = 0$ as described in Section 4.2.4, and thus no EPR signal is observed initially.

Over longer timescales, the SCs undergo longitudinal relaxation, repopulating the spin sublevels in accordance with the Boltzmann distribution. This thermalisation process, governed by the relaxation time T_1, gives rise to a weak, purely absorptive EPR signal. As SCs also decay via a first-order recombination process (characterised by τ_{dec}), the signal gradually builds and then diminishes. In the simulation shown, $T_1 = 50\,\mu s$ and $\tau_{dec} = 10\,\mu s$. The resulting time evolution is dominated by relaxation and recombination dynamics, with no CT state contribution.

This ultrafast dissociation regime can be modelled in RADISH in two equivalent ways. The first explicitly models ultrafast charge separation by initialising the system entirely in the CT state ($p_{CT} = 1$), with a picosecond dissociation time constant ($\tau_{diss} = 1\,ps$). The second assumes that dissociation occurs instantaneously and instead initialises the system as SCs with equal spin sublevel populations ($p_{CT} = 0$). Both approaches produce identical time-resolved EPR spectra.

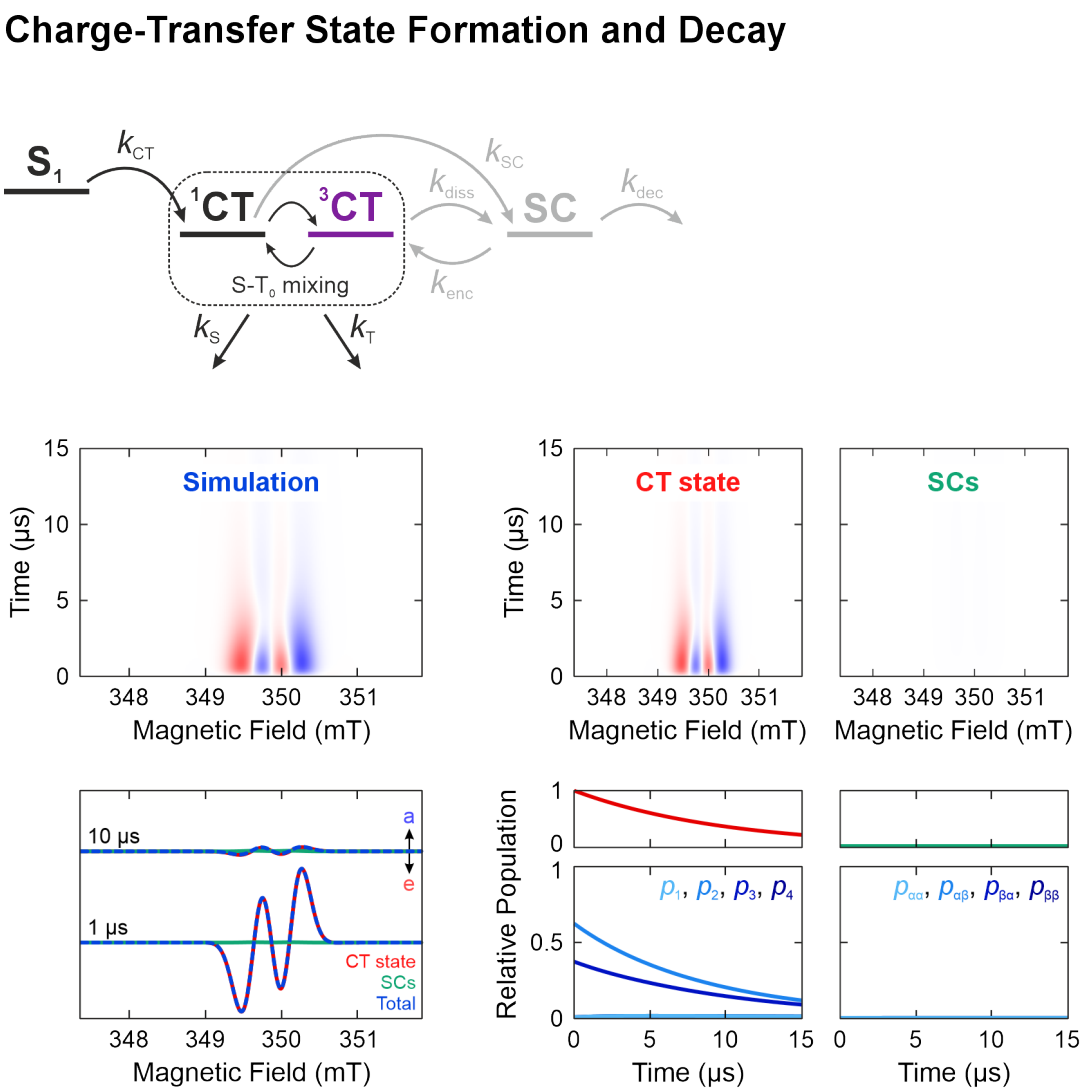

Figure 4.8: Simulation of the time-resolved EPR spectrum for singlet-born charge-transfer state formation and spin-independent recombination, with simulation parameters given in Table 4.2. Simulated EPR spectra are shown for the total signal, as well as the individual contributions of the CT state and SCs. Spectra extracted at short (1 µs) and long (10 µs) times illustrate the evolution of the spin polarisation, while relative populations of the CT state and SCs are displayed in red and green, respectively, and their individual sublevel populations are also shown below. Absorptive features are in blue and emissive features in red in the two-dimensional plots.

$p_{CT} : p_{SC}$	τ_S	τ_T	τ_{diss}	τ_{enc}	τ_{dec}	T_1	T_2
1 : 0	20 µs	20 µs	$\gg$ 100 µs	$\gg$ 100 µs	$\gg$ 100 µs	15 µs	1 µs

Table 4.2: Parameters for the time-resolved EPR simulation in Figure 4.8 of a long-lived charge-transfer state undergoing spin-independent recombination. For rates that do not determine the kinetic pathway, a time constant of $\gg$ 100 µs is given.

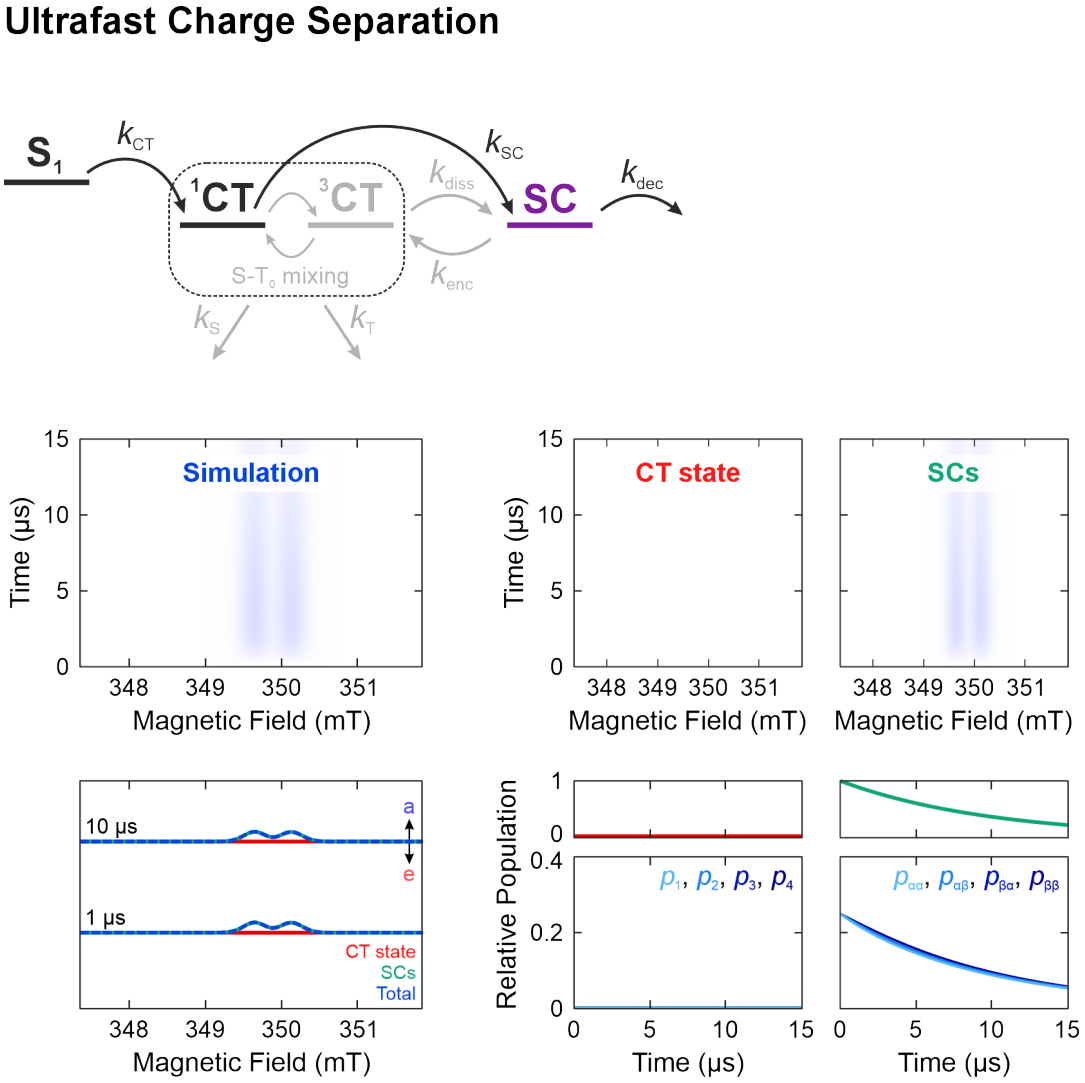

Figure 4.9: Simulation of the time-resolved EPR spectrum for ultrafast formation of separated charges, with simulation parameters given in Table 4.3. Simulated EPR spectra are shown for the total signal, as well as the individual contributions of the CT state and SCs. Spectra extracted at short (1 µs) and long (10 µs) times illustrate the evolution of the spin polarisation, while relative populations of the CT state and SCs are displayed in red and green, respectively, and their individual sublevel populations are also shown below.

$p_{CT} : p_{SC}$	τ_S	τ_T	τ_{diss}	τ_{enc}	τ_{dec}	T_1	T_2
1 : 0	$\gg 100$ µs	$\gg 100$ µs	1 ps	$\gg 100$ µs	10 µs	15 µs	1 µs
0 : 1	$\gg 100$ µs	$\gg 100$ µs	$\gg 100$ µs	$\gg 100$ µs	10 µs	15 µs	1 µs

Table 4.3: Parameters for the time-resolved EPR simulation in Figure 4.9 for ultrafast charge separation. Ultrafast charge separation can either be modelled explicitly (first row), with initially only a CT state ($p_{CT} = 1$) that dissociates in picoseconds, or by defining the initial population as only SCs ($p_{CT} = 0$) that have equal sublevel populations due to ultrafast charge separation (second row).

Within the RADISH model, time constants τ_{CT} and τ_{SC} are not explicitly defined; rather, their influence is incorporated through the relative initial populations (p_{CT} : p_{SC}). Ultrafast charge separation corresponds to the case where $\tau_{CT} \gg \tau_{SC}$, resulting in $p_{CT} = 0$, whereas slow separation is characterised by $\tau_{CT} \ll \tau_{SC}$ and $p_{CT} = 1$.

4.4.3 Charge Separation after Singlet-Triplet Mixing

In donor:acceptor OPV blends, an intermediate regime may arise between the two limiting cases described previously. The CT state is long-lived enough to undergo significant singlet-triplet mixing, but can also dissociate at the donor:acceptor interface to form SCs. This scenario, referred to as slow charge separation, produces the spin polarisation evolution shown in Figure 4.10.

As before, the CT state is initially formed from a singlet precursor, generating the expected *eaea*-polarised EPR signal shape at short times after photoexcitation. If dissociation to SCs outcompetes recombination to the ground state ($\tau_{diss} \ll \tau_S, \tau_T$), then the coupled CT state dissociates and separates into uncorrelated SCs. The resulting SCs inherit the spin polarisation built up in the CT state. In the case of a singlet-born CT state that has undergone singlet-triplet mixing, this produces an *ea*-polarised signal, reflecting a population imbalance between SC sublevels.

The resulting EPR signal, therefore, contains contributions from both CT states and SCs. For the example shown with $\tau_{diss} = 10\,\mu s$, the EPR signal shape at 1 µs is largely dictated by the spin polarisation of the CT state. By 10 µs, the signal is dominated by SCs, with a clear transition in polarisation shape from *eaea* to *ea* as dissociation proceeds.

4.4.4 Equilibrium with Separated Charges

A more complex kinetic scenario is presented in Figure 4.11, where both slow and ultrafast charge separation pathways are active. At $t = 0$, the initial population is distributed between the CT state and SCs ($p_{CT} = 0.3$). The CT state and SCs are in equilibrium[¶] with one another via the forward and backward time constants τ_{diss} and τ_{enc}. In addition, a spin-selective recombination of the CT state occurs predominantly via the singlet channel ($\tau_S \ll \tau_T$).

[¶]The term 'equilibrium' here is somewhat of a misnomer. Strictly speaking, this model scenario does not represent a true thermodynamic equilibrium, since there is a net population loss over time, described by the time constants τ_S, τ_T, and τ_{dec} (see Figure 4.1 of Section 4.2.3). Nonetheless, the OPV literature commonly refers to reversible charge transfer as being in an 'equilibrium' and this convention is followed for consistency.[81,99,280]

At early times ($t = 1\,\mu s$), the EPR spectrum is dominated by the strongly *eaea*-polarised signal of the singlet-born CT state. Although SCs are present from the start due to ultrafast separation, their weaker *ea*-type polarisation, from some CT state dissociation, is largely masked by the stronger CT state contribution.

As time progresses, the CT sublevel populations are shaped by the interplay between spin-selective recombination and reversible interconversion with the SCs. Singlet recombination, characterised by the time constant τ_S, selectively depopulates the $|2\rangle$ and $|3\rangle$ sublevels of the CT manifold. At the same time, SCs undergoing re-encounter (τ_{enc}) repopulate all CT sublevels more uniformly. As a result, the $|1\rangle$ and $|4\rangle$ sublevels become increasingly populated relative to $|2\rangle$ and $|3\rangle$, progressively altering the spin polarisation of the CT state. By $t = 10\,\mu s$, this redistribution leads to a reversal in the CT signal shape, shifting from the initial *eaea* pattern to an *aeae*-type polarisation.

Meanwhile, the SC polarisation also evolves under the influence of longitudinal spin relaxation, governed by T_1. This relaxation drives the sublevel populations of the SCs towards thermal equilibrium, reducing the initial *ea*-type polarisation and giving rise to a predominantly absorptive signal. The same relaxation mechanism also acts on the CT state, subtly amplifying the absorptive components of the evolving *aeae* signal.

At $t = 10\,\mu s$, the CT and SC populations have reached dynamic equilibrium, which is determined by the ratio of the forward and backward rates ($\tau_{enc} : \tau_{diss} = 3 : 1$). Both species contribute to the overall EPR spectrum, and the resulting signal shape depends on their relative weighting. If $\tau_{diss} \gg \tau_{enc}$, the SCs dominate and the long-time spectrum becomes primarily absorptive. Conversely, if $\tau_{diss} \ll \tau_{enc}$, the CT state is the dominant contribution, exhibiting an *aeae*-type polarisation at later times.

The simulation of time-resolved EPR spectra across these four distinct kinetic scenarios demonstrates the powerful insight that can be gained into spin dynamics and charge separation mechanisms in OPV blends. By systematically exploring different photophysical pathways, each modelled EPR spectrum demonstrates how specific kinetic parameters and spin-selection rules influence the evolution of spin polarisation. The RADISH simulation framework enables the disentanglement of overlapping contributions of CT states and SCs, interpretation of time-dependent changes in spectral shape, and tracking of the evolution of sublevel populations. These capabilities allow not only for qualitative mechanistic interpretation, but also for the quantitative extraction of kinetic parameters from experimental time-resolved EPR data.

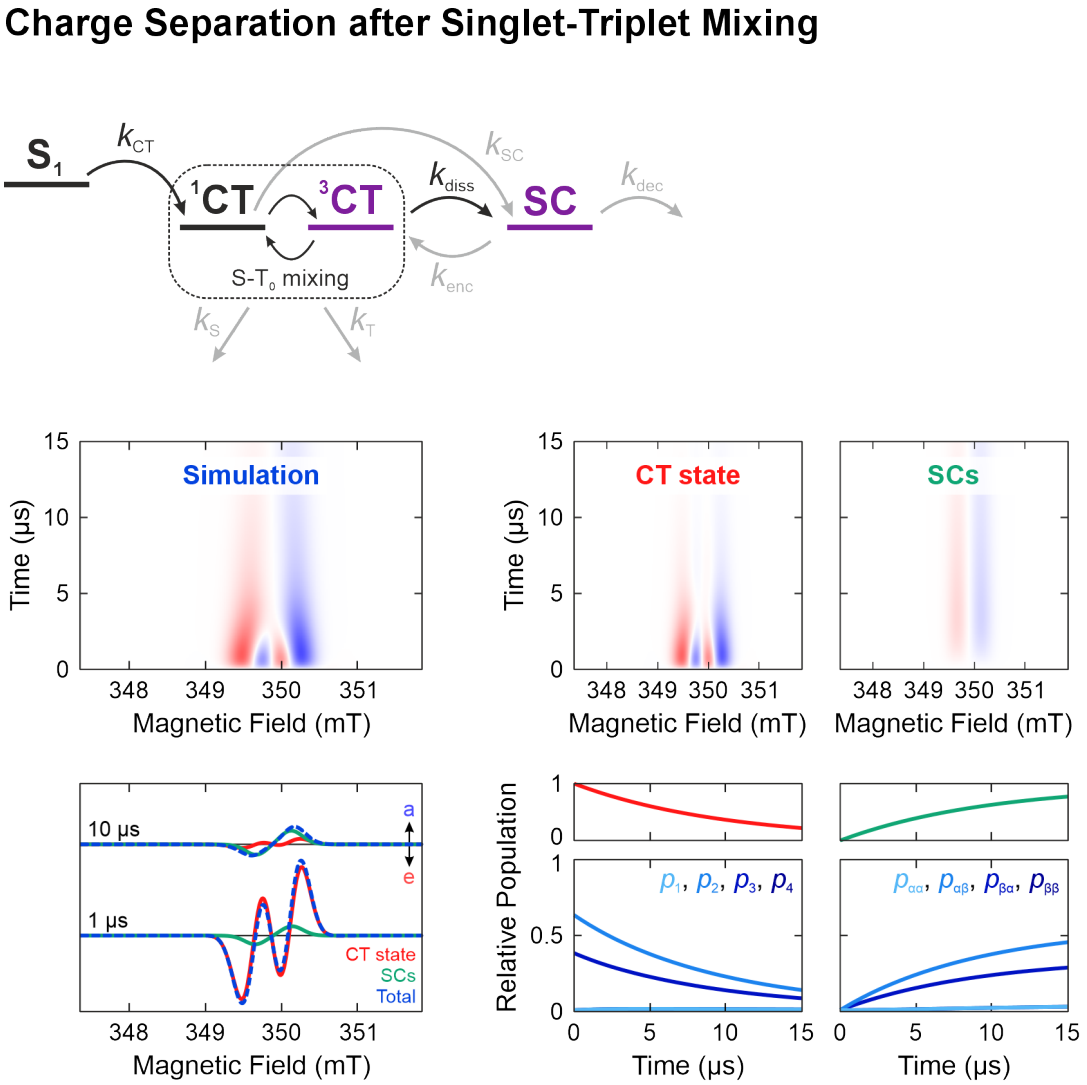

Figure 4.10: Simulation of the time-resolved EPR spectrum for separation of the charge-transfer state to form separated charges on a microsecond timescale, with simulation parameters given in Table 4.4. Simulated EPR spectra are shown for the total signal, as well as the individual contributions of the CT state and SCs. Spectra extracted at short (1 µs) and long (10 µs) times illustrate the evolution of the spin polarisation, while relative populations of the CT state and SCs are displayed in red and green, respectively, and their individual sublevel populations are also shown below.

$p_{CT} : p_{SC}$	τ_S	τ_T	τ_{diss}	τ_{enc}	τ_{dec}	T_1	T_2
1 : 0	$\gg 100$ µs	$\gg 100$ µs	10 µs	$\gg 100$ µs	$\gg 100$ µs	15 µs	1 µs

Table 4.4: Parameters for the time-resolved EPR simulation in Figure 4.10 of slow separation of the charge-transfer state to form separated charges.

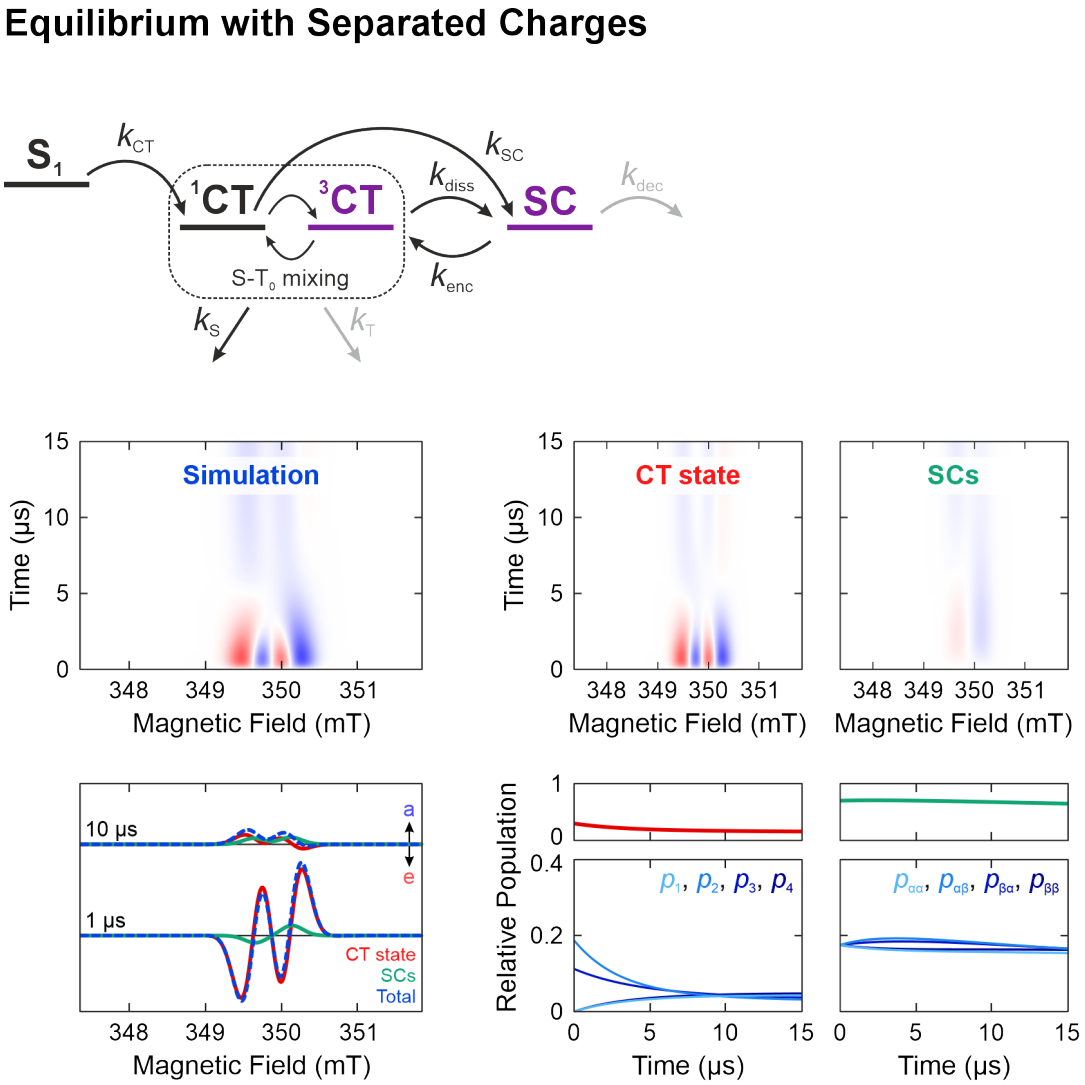

Figure 4.11: Simulation of the time-resolved EPR spectrum for an equilibrium between the charge-transfer state and separated charges formed by ultrafast charge separation, with simulation parameters given in Table 4.5. Simulated EPR spectra are shown for the total signal, as well as the individual contributions of the CT state and SCs. Spectra extracted at short (1 µs) and long (10 µs) times illustrate the evolution of the spin polarisation, while relative populations of the CT state and SCs are displayed in red and green, respectively, and their individual sublevel populations are also shown below.

$p_{CT} : p_{SC}$	τ_S	τ_T	τ_{diss}	τ_{enc}	τ_{dec}	T_1	T_2
0.3 : 0.7	10 µs	$\gg$ 100 µs	10 µs	30 µs	$\gg$ 100 µs	15 µs	1 µs

Table 4.5: Parameters for the time-resolved EPR simulation in Figure 4.11 of an equilibrium between the charge-transfer state and separated charges.

4.5 Conclusions

Accurately simulating spin dynamics in time-resolved EPR spectroscopy is essential for unravelling the complex photophysical processes that govern light-induced spin-polarised systems. From charge-transfer state formation to charge separation and spin-selective recombination, the transient evolution of spin populations provides critical insight into molecular mechanisms. This chapter has shown how the mathematical framework of open quantum systems, utilising the Liouville-von Neumann equation, superoperators, and density matrices, can be implemented in a computationally efficient simulation approach that can be used to disentangle overlapping contributions in experimental signals.

Using the RADISH simulation package, a range of illustrative kinetic scenarios were explored to demonstrate how variations in charge separation, recombination, and re-encounter rates give rise to a distinct evolution of spectral lineshapes and spin polarisation patterns in the EPR spectra. Modelling spin dynamics in this way enables the extraction of detailed, time-resolved information from experimental EPR data, and provides a powerful bridge between theoretical understanding and experimentally observed photophysical behaviour.

The framework developed here provides the foundation for the next chapter, which presents a detailed time-resolved EPR study of donor:acceptor OPV blends. There, the tools and concepts established in this chapter will be used to interpret the spin polarisation patterns of photoexcited CT states and SCs, yielding new insight into the pathways of charge generation in OPVs.

Chapter 5

Charge Separation at the Donor:Acceptor Interface

5.1 Introduction

Despite rapid advances in device performance, the fundamental photophysical mechanisms underlying charge generation in OPVs remain only partially understood.[36,60] At the heart of efficient charge generation lies the behaviour of the interfacial charge-transfer (CT) state. This CT state can either dissociate into separated charges (SCs) that contribute to photocurrent or recombine, leading to efficiency loss. One significant loss pathway involves the formation of triplet excitons (T_1), either via intersystem crossing (ISC) from singlet excitons ($S_1 \rightarrow T_1$) instead of charge transfer, or through recombination of the CT state, either in a geminate (CT $\rightarrow$ T_1) or non-geminate (SC $\rightarrow$ CT $\rightarrow$ T_1) fashion. Additionally, growing evidence suggests that CT states and SCs may exist in a quasi-equilibrium (CT $\rightleftharpoons$ SC), particularly in high-performing non-fullerene acceptor blends,[81,99,100,281,282] challenging the classical view of unidirectional charge

separation.[283,284] These key processes are all summarised in the photophysical diagram in Chapter 1 (Figure 1.8 in Section 1.4). A detailed understanding of CT dynamics is therefore crucial for establishing structure-function relationships and guiding the design of next-generation OPV materials.

Transient absorption and other ultrafast optical techniques have been instrumental in probing short-lived excited states in OPVs.[70,285–288] However, their ability to distinguish between CT states and SCs is limited by overlapping spectral signatures.[289,290] As an alternative, time-resolved EPR spectroscopy offers a complementary approach based on probing their spin properties. The different paramagnetic states in the OPV photophysical mechanism (CT states, SCs and triplets) have distinct spectral signatures and can be clearly distinguished from one another, as outlined in Section 2.4 of Chapter 2. Although EPR probes longer timescales than optical methods, the initial spin polarisation encodes information about the formation mechanisms of photoinduced states. Notably, the spin-selectivity of many photophysical mechanisms provides information on precursor states that are shorter than the EPR time scale (from tens to hundreds of nanoseconds), giving access to ultrafast processes through the spin polarisation they induce.[142] As such, time-resolved EPR provides a powerful spectroscopic handle on the microscopic processes that govern macroscopic device performance in OPVs.

In this chapter, time-resolved EPR was employed to investigate the photoexcited spin states of high-performing non-fullerene acceptor blends PM6:Y6 and PBDB-T:ITIC, along with their fullerene acceptor analogues PM6:PCBM and PBDB-T:PCBM. The EPR measurements reveal two distinct spin-polarised signals: a component spanning a field range up to 100 mT attributed to triplet excitons, and a narrower component (< 5 mT width) arising from CT states and separated charges.

Pronounced triplet signals are observed for the fullerene acceptor blends, whereas the non-fullerene acceptor blends show only very weak triplet features. To identify their origin, measurements were also performed on the pristine donor and acceptor materials. The triplet spin polarisation patterns observed for all blends are characteristic of ISC, with no contribution from triplet formation via geminate recombination of the CT state, suggesting that this pathway is not significant. Measurements performed on a narrower field range confirm the formation of spin-polarised CT states immediately after photoexcitation in all blends, with polarisation patterns indicative of direct formation via S_1 dissociation. These CT signatures persist across temperatures and excitation fluences, underscoring their central role in charge generation. Spectral simulation of the early-time CT state spectra reveals a range of donor:acceptor separations and orientations, with non-fullerene acceptor blends displaying more ordered, tightly-bound CT states.

Modelling of the spin dynamics, kinetics and relaxation processes, using the Liouville-von Neumann formalism outlined in Chapter 4, enabled extraction of charge transfer, recombination, and separation rates. PM6:PCBM exhibited behaviour consistent with rapid, irreversible CT dissociation. In contrast, PM6:Y6, PBDB-T:ITIC, and PBDB-T:PCBM displayed more complex kinetics, involving two distinct charge separation pathways: an ultrafast (picosecond) channel and a slower (microsecond) channel via the CT state. Modelling also required inclusion of a reversible $\mathrm{CT} - \mathrm{SC}$ equilibrium, particularly prominent in the non-fullerene acceptor blends. These findings shed light on the spin dynamics, molecular interactions, and recombination mechanisms that underpin efficiency improvements in OPVs.

5.2 Experimental Methods

5.2.1 Sample Preparation

Inner-wall films of the donor:acceptor blends PBDB-T:PCBM, PM6:PCBM, PBDB-T:ITIC, and PM6:Y6 were prepared using the method described in Section 3.2.1 of Chapter 3, while preparation of inner-wall films of the pristine donor and acceptor materials PBDB-T, PM6, PCBM, ITIC, and Y6 followed the same method, using the $20\,\mathrm{mg\,mL^{-1}}$ stock solutions of each material that were prepared for the blends to produce the films.

Spin-coated films were also prepared, which are characterised by thinner active layer thicknesses that are similar to those used in operating OPV devices, around 100 nm.[33,34] Sample solutions were pipetted onto thin quartz substrates, of dimensions $2.1\,\mathrm{mm} \times 10 - 15\,\mathrm{mm} \times 0.5\,\mathrm{mm}$, and spin-coated to remove the solvent ($30\,\mathrm{s}$, $1500\,\mathrm{rpm}$, $500\,\mathrm{rpm\,s^{-1}}$). Two spin-coated substrates were placed back-to-back within the EPR tube, before flame-sealing in an oxygen-free environment. Sample films showed minimal degradation after a set of EPR measurements.

5.2.2 EPR Experiments

X-band and Q-band time-resolved EPR experiments were performed using the same spectrometer setups as described in Section 3.2.2 of Chapter 3. Measurements at different temperatures in the range from 20 K to 140 K were performed using liquid helium cooling with an Oxford Instruments CF935 cryostat and temperature-control system. Laser excitation at 532 nm was provided by an EKSPLA NT230 diode-pumped Q-switched Nd:YAG laser and optical parametric oscillator (OPO) with 5 ns pulses and a 50 Hz repetition rate, and an approximate beam spot of 5 mm diameter. The laser power was attenuated and adjusted by a $\frac{\lambda}{2}$-waveplate and a

polariser, before being depolarised using an achromatic depolariser. A Stanford Research System digital delay generator (DG645) was used for synchronisation of the laser and EPR spectrometer. The laser energy incident on the sample was estimated based on laser energy measurements within the resonator and cryostat using a ThorLabs TD2X thermal detector placed at the position of the sample (after calibration outside the resonator). The laser power at the sample was around $35 - 40\%$ of the laser power at the source. The source laser power was tuned such that the sample received laser fluences of $20\,\mu J\,cm^{-2}$ or $1\,mJ\,cm^{-2}$. Time-resolved EPR experiments were performed by direct detection with the transient recorder (Video Amplifier III, 1 GHz bandwidth) without lock-in amplification using a microwave power of 0.255 mW ($B_1 = 0.005\,mT$).

A field-calibration was performed with a standard N@C_{60} sample of a known g-value.[150] The off-resonant background signal was removed by two-dimensional baseline correction using low- and high-field off-resonance transients and subtracting the signal prior to laser excitation. For measurements of spin-coated films, samples were rotated with respect to the static magnetic field $\boldsymbol{B}_0$: 0° for the plane of the substrate aligned with $\boldsymbol{B}_0$, and 90° for the substrate plane perpendicular.

5.2.3 Data Analysis

Simulations of time-resolved EPR spectra were carried out using the open-source package EasySpin (version 6.0.5) in the MATLAB environment.[130,267] For the triplet state, time-resolved EPR of the pristine donor and acceptor materials were extracted from 0 to 1 µs after photoexcitation, and fitted as an intersystem crossing triplet. For the spin-coated films, preferential ordering of the molecules in the sample was accounted for by modelling Gaussian distributions about each of the three Euler angles (α, β, γ) that describe the transformation between the molecular frame and the laboratory frame (see Section 2.2.1 in Chapter 2): $G = g(\mu_\alpha, \sigma_\alpha) \times g(\mu_\beta, \sigma_\beta) \times g(\mu_\gamma, \sigma_\gamma)$, with means μ and standard deviations σ.

For simulations of the static singlet-born CT state, time-resolved EPR spectra were extracted at $0.1 - 0.3$ µs after laser excitation at different microwave frequencies (X-band: 9.8 GHz, and Q-band: 33.9 GHz) and laser fluences ($20\,\mu J\,cm^{-2}$ and $1\,mJ\,cm^{-2}$) and globally fitted, considering multiple best-fit solutions, to calculate the donor:acceptor positions and orientations, the electron-electron couplings and the line broadening. g-values were previously determined from steady-state echo-detected EPR spectra in Chapter 3. The fits were performed using a genetic algorithm to avoid local minima solutions, with the simulation procedure described in greater detail later in Section 5.3.3. For the full two-dimensional simulations of the time-resolved EPR spectra at narrow field ranges, the home-built simulation package RADISH, described in Chapter 4, was used to model the evolution of the CT state and the SCs.

5.3 Results and Discussion

Time-resolved EPR spectra were recorded over a broad magnetic field range (270 – 430 mT) for the four donor:acceptor blends: PM6:PCBM, PBDB-T:PCBM, PM6:Y6, and PBDB-T:ITIC. Measurements were carried out at 20 K, X-band microwave frequency and with a laser fluence of 1 mJ cm^{-2}. The resulting spectra are presented in Figure 5.1, with the upper panels displaying the signal averaged over the first microsecond following photoexcitation. Two distinct spectral features are observed:

- A narrow signal centred around 350 mT is detected in each blend and is attributed to spin-polarised CT states and SCs. This feature arises at $g \approx g_e$ and reflects exciton dissociation and separation at the donor:acceptor interface.

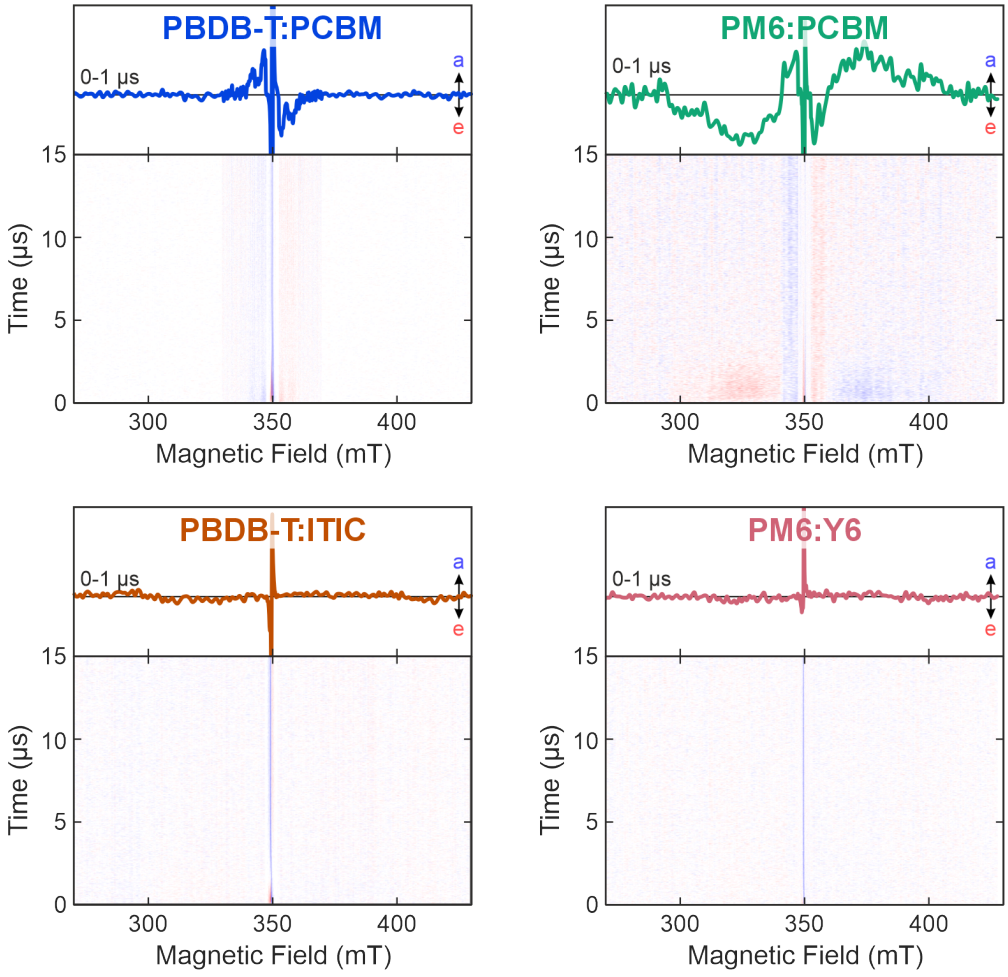

Figure 5.1: Time-resolved EPR X-band spectra of PBDB-T:PCBM, PM6:PCBM, PBDB-T:ITIC, and PM6:Y6 at 20 K, a laser fluence of 1 mJ cm^{-2}, and 532 nm. Absorptive features are in blue and emissive features in red in the two-dimensional plots. In the top panels, spectra are averaged over 0 – 1 µs, with broad signals from triplet excitons, and narrow signals due to charge-transfer states and separated charges.

- A much broader signal is observed in the fullerene acceptor blends (PM6:PCBM and PBDB-T:PCBM), extending up to 100 mT in width. This signal is characteristic of triplet excitons, whose spectral width results from zero-field splitting in the strongly-coupled triplet state. In the non-fullerene acceptor blends, this triplet contribution is substantially weaker, with the spectra dominated by the narrower CT state and SC features.

The presence and relative intensity of these signals indicate qualitative differences in the photophysics of the blends. In particular, enhanced triplet formation is evident in the fullerene acceptor blends, suggesting a more significant contribution from intersystem crossing or triplet-generating recombination processes. Conversely, the suppressed triplet signal in the non-fullerene acceptor blends implies that these loss pathways are less prominent.

In the following sections, the two spectral features are examined in detail. First, the origin and characteristics of the broad triplet signals are analysed, supported by comparative measurements of the pristine donor and acceptor materials. This is followed by a detailed investigation of the narrow-field region, where modelling of the CT and SC signals under varying experimental conditions yields insights into the molecular arrangement at the donor:acceptor interface and the dynamics of charge separation. Together, these time-resolved EPR measurements demonstrate how the evolution of spin polarisation serves as a powerful probe of the charge separation in organic photovoltaics.

5.3.1 Time-Resolved EPR of Triplet States

Triplet states in donor:acceptor OPV blends can be generated through several pathways: intersystem crossing (ISC) from S_1, geminate recombination of the CT state, or non-geminate recombination of SCs via the CT state. To elucidate the origin of the triplet signals observed in the blend spectra shown in Figure 5.1, time-resolved EPR measurements were conducted on the pristine donor and acceptor materials. In these single-component films, triplet formation predominantly occurs through ISC, as CT states are not readily formed without the donor:acceptor interface that facilitates exciton dissociation. By comparing the triplet spectral signatures of the pristine materials with those of the blends, it becomes possible to determine whether the triplet signals in the blends arise mainly from ISC or from recombination processes involving CT states.

Triplet States in Pristine Materials

The triplet EPR spectra of inner-wall films of the donor materials (PBDB-T, PM6) and acceptors (PCBM, ITIC, Y6) were recorded and averaged over the first microsecond (Figure 5.2). Strong spin-polarised signals were observed in all samples. The donor spectra exhibit broad signals of approximately 100 mT width with *eeeaaa* polarisation, while the non-fullerene acceptors (ITIC and Y6) showed similar polarisation but slightly narrower spectral widths of around 90 mT. In contrast, PCBM displayed a considerably narrower signal (20 mT) with inverted *aaaeee* polarisation.

The spectral shapes of triplet EPR signals are primarily governed by two factors: the zero-field splitting (ZFS) parameters and the populations of the zero-field spin sublevels. The zero-field interaction, as described in Section 2.2.3 of Chapter 2, arises from magnetic dipolar coupling between the two unpaired electrons in the triplet state and is characterised by the parameters D and E. The magnitude of D reflects the average spatial separation between the electrons and can be estimated directly from the experimental spectrum, corresponding approximately to half of the total width of the triplet spectrum. The rhombic component E, which accounts for deviations from axial symmetry, influences the positions of the inner turning points in the spectrum.

The relative populations of the zero-field sublevels, p_X, p_Y, and p_Z, determine the absorptive or emissive nature of individual transitions, resulting in the observed spin polarisation pattern. In OPV materials, ISC is primarily driven by spin-vibronic coupling,[107] which is selective to molecular orientation, as discussed in Section 2.4.3 of Chapter 2. As time-resolved EPR probes only population differences, rather than their absolute values, fitting was carried out by setting the lowest sublevel population to zero and normalising the total population to unity.

Simulations of the triplet EPR spectra of the pristine material revealed ISC as the sole formation pathway. These simulations, shown in Figure 5.2, successfully reproduce the experimentally observed spin polarisation patterns: *eeeaaa* for all systems except PCBM, which displays *aaaeee* polarisation. The corresponding ZFS parameters and population distributions are summarised in Table 5.1. Time-resolved EPR provides information on the magnitude, but not the sign, of D and E. A negative D-value has previously been reported for PCBM,[292,293] whereas a positive D-value is assumed for the other materials based on results on similar planar π-conjugated molecules and DFT calculations.[146]

The donor polymers PBDB-T and PM6 exhibit comparable ZFS parameters ($|D| \approx 1500$ MHz, small $|E|$) and similar sublevel populations, consistent with their nearly identical molecular structures. For ITIC and Y6, the D-values were

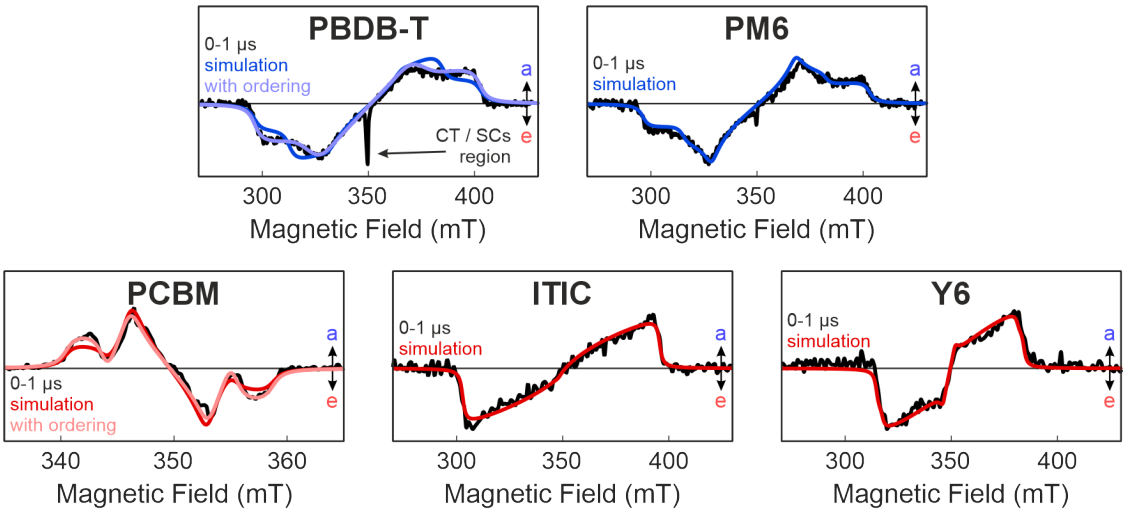

Figure 5.2: Time-resolved EPR spectra of PBDB-T, PM6, PCBM, ITIC and Y6, measured at 20 K and at X-band, integrated over $0 - 1\,\mu s$. Note that PCBM has a narrower triplet signal and is plotted on a different magnetic field axis to the other materials. The samples were photoexcited at 532 nm; ITIC was excited at 650 nm, as it has weak absorbance at 532 nm.[291]

Material	D (MHz)	E (MHz)	Populations $p_X : p_Y : p_Z$	Linewidth (mT)
PBDB-T *	1490	−130	0.52 : 0.48 : 0.00	3.63
PM6	1495	−129	0.44 : 0.56 : 0.00	2.64
PCBM†	−257	23	0.13 : 0.87 : 0.00	0.83
ITIC	1300	−433	0.50 : 0.50 : 0.00	1.27
Y6	970	−270	0.49 : 0.51 : 0.00	1.16

*PBDB-T ordering: $\mu_\alpha = 306°$, $\sigma_\alpha = 203°$, $\mu_\beta = 32°$, $\sigma_\beta = 80°$, $\mu_\gamma = 308°$, $\sigma_\gamma = 31°$
†PCBM ordering: $\mu_\alpha = 143°$, $\sigma_\alpha = 83°$, $\mu_\beta = 68°$, $\sigma_\beta = 235°$, $\mu_\gamma = 168°$, $\sigma_\gamma = 93°$

Table 5.1: Simulation parameters for photoexcited ISC triplet states of PBDB-T, PM6, PCBM, ITIC and Y6. For PBDB-T and PCBM, inclusion of preferential molecular ordering improved the simulation of the experimental spectra. D and E have estimated fitting errors of 5 MHz, while μ and σ have estimated uncertainties of 5° and 15°, respectively.

reduced to 1300 MHz and 970 MHz, respectively, and the observed E-values reflect a greater rhombicity. In the case of ITIC, the zero-field interaction approaches the orthorhombic limit ($E = -\frac{1}{3}D$), resulting in the merging of features and the reduction of well-defined turning points. In contrast, PCBM yields a much narrower spectrum, with a considerably smaller zero-field interaction ($D = -260$ MHz), in agreement with previous studies.[112,148,294–296]

For PBDB-T and PCBM, the relative intensities of the inner spectral features are overestimated if an isotropic powder distribution, in which all molecular orientations are equally represented, is assumed. Improved agreement with experimental data

was obtained by incorporating a modest degree of molecular ordering into the simulations, with ordering parameters detailed in Table 5.1. In an ordered film, certain molecular orientations contribute more strongly to the EPR signal, while others are suppressed. This anisotropic weighting alters the relative intensities of the spectral features. In the ISC triplets of PBDB-T and PCBM, the inner turning points, linked to transitions along the D_X and D_Y ZFS tensor axes, were found to be weaker than predicted under full powder averaging, suggesting that those orientations are under-represented due to partial molecular alignment in the film. Such ordering may arise from molecular aggregation or the development of semi-crystalline domains during film formation. For example, it has been shown that films processed from chlorobenzene exhibit higher crystallinity than those prepared using chloroform, owing to the slower solvent evaporation rate, which allows more time for molecular reorganisation.[36,297]

To better replicate the morphology present in operational OPV devices, measurements were also conducted on spin-coated films with thicknesses comparable to those of typical active layers, using the same procedure reported in the literature for OPV device fabrication.[33,34] These thinner films are expected to exhibit greater molecular ordering than the inner-wall samples previously discussed, owing to their reduced thickness and differing processing conditions. Consequently, it is important to establish whether such ordering influences the intersystem crossing mechanism, altering triplet sublevel populations, or induces changes in the nature of the triplet state, reflected in D and E.

Time-resolved EPR spectra were recorded for films of the polymer donors PBDB-T and PM6 spin-coated on substrates under the same experimental conditions as those applied to the inner-wall films. The triplet EPR spectra, averaged over 0 to 1 µs, are displayed in Figure 5.3 for three different orientations (0°, 45°, and 90°) of the substrate plane relative to the applied magnetic field. The angle between the substrate and the magnetic field is illustrated schematically in the figure. For comparison, the triplet EPR spectra of the donor inner-wall films are also presented, with resonance field positions of the six canonical $X_{\pm}$, $Y_{\pm}$, and $Z_{\pm}$ transitions indicated.

Distinct differences in the EPR spectra were observed for the spin-coated films at different substrate orientations, indicating preferential molecular ordering within these films. When the magnetic field was aligned parallel to the substrate plane (0°), features corresponding to molecules with their X or Y $\boldsymbol{D}$-tensor axis aligned along the magnetic field were preferentially populated. Upon rotation to 90°, where the magnetic field was perpendicular to the substrate plane, spectral features associated with molecules having the Z $\boldsymbol{D}$-tensor axis aligned with the magnetic field became dominant.

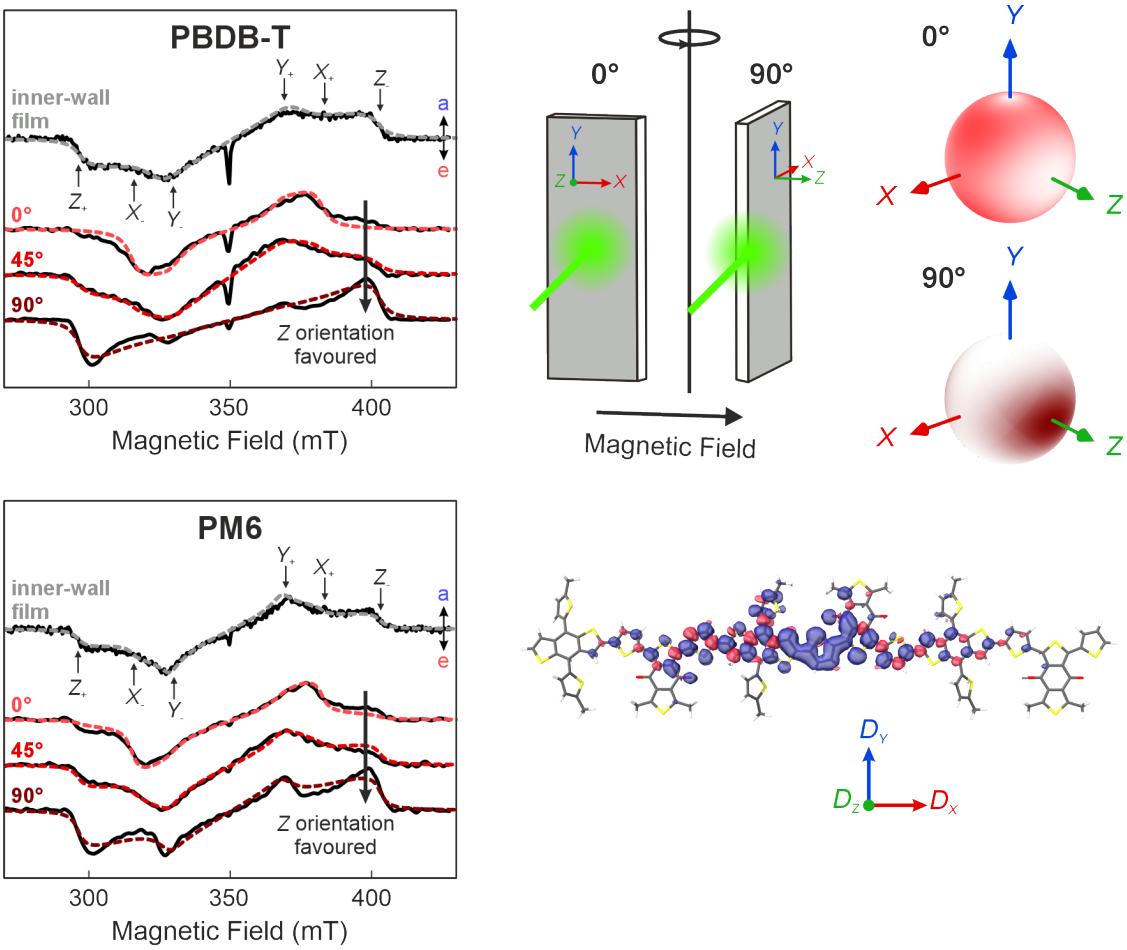

Figure 5.3: (Left) Time-resolved EPR spectra of PBDB-T and PM6 films spin-coated onto substrates, averaged over $0 - 1\,\mu s$, at different substrate plane angles relative to the external magnetic field, compared with spectra from inner-wall films. Dotted lines show simulations for both film types with labelled canonical field positions. (Right) Schematic showing the orientation of the spin-coated film relative to the magnetic field and $\boldsymbol{D}$-tensor. Shaded spheres indicate magnetic field orientations $\boldsymbol{B}_0$ relative to $\boldsymbol{D}$-tensor axes that contribute to the EPR signal at 0° and 90°. The $\boldsymbol{D}$-tensor orientation and spin density, predicted by DFT for a PBDB-T trimer, are shown; PM6 shares the same ordering distribution and tensor orientation.

The triplet EPR spectra at 0°, 45°, and 90° were simultaneously modelled using a single consistent ordering distribution to represent the preferential molecular alignment in the spin-coated films. The simulations, shown in Figure 5.3, closely reproduce the experimental spectra at all three orientations. The same ZFS parameters and sublevel populations as those employed for the inner-wall films (Table 5.1) were used, indicating that the morphology exerts limited influence on the intrinsic nature of the triplet state or its formation mechanism.

The molecular orientations probed at 0° and 90° are illustrated by shaded spheres in Figure 5.3, representing the range of magnetic field vector $\boldsymbol{B}_0$ orientations, relative

to the axis for the principal D-values D_X, D_Y, and D_Z, that contribute to the observed EPR signals. At 90°, the axis for the D_Z principal value and $\boldsymbol{B}_0$ are approximately aligned, meaning only molecules with their $\boldsymbol{D}$ Z-axis oriented along $\boldsymbol{B}_0$ contribute to the signal. The Z axis of the $\boldsymbol{D}$-tensor, therefore, must lie perpendicular to the substrate plane. The extent of ordering was found to be comparable between PBDB-T and PM6.

To relate the tensor orientation to molecular structure, DFT calculations were performed on polymer models comprising three repeat units. The calculations, shown in Figure 5.3, predict that the $\boldsymbol{D}$ Z-axis aligns perpendicular to the molecular plane, while the X- and Y-axes correspond to the long and short in-plane molecular axes, respectively. For planar, aromatic, π-conjugated systems such as PBDB-T and PM6, intersystem crossing is governed by vibrationally-induced spin-orbit coupling, resulting in preferential population of the X and Y in-plane triplet sublevels $(p_x, p_y > p_z)$,[147,298,299] as observed in simulations of the pristine donor spectra.

The orientation-dependent EPR measurements indicate that the Z axis of the $\boldsymbol{D}$-tensor lies perpendicular to the substrate plane, and DFT results place it perpendicular to the molecular plane. From this, it can be inferred that the polymer molecules adopt a face-on orientation relative to the substrate, with stacking parallel to the substrate plane. This arrangement is in agreement with grazing-incidence wide-angle X-ray scattering (GIWAXS) studies reported in the literature.[300] These findings confirm that the spin-coated film preparation method used produces morphologies consistent with those previously documented.

The triplet signal of PBDB-T, and to a lesser extent PM6, shows a pronounced emissive feature near 350 mT, the magnetic field position of the CT state and SCs. This emissive polarisation suggests a non-thermal equilibrium origin. A similar feature has been observed in pristine donor triplet EPR spectra,[112,148] tentatively linked to spin-polarised SC formation. PBDB-T and PM6 are composed of alternating electron-donating and electron-accepting units along their backbone.[36] This architecture may promote intramolecular charge transfer within the polymer domains.[301,302] At the short intramolecular distances involved, strong spin-spin exchange coupling could facilitate mixing of the CT state $|\mathrm{S}\rangle$ and $|\mathrm{T}_+\rangle$ sublevels, generating emissive polarisation upon charge separation.[303,304]

Triplet States in Donor:Acceptor Blends

With the nature and formation mechanisms of ISC triplets in the pristine donor and acceptor materials fully characterised, the triplet signals observed in the time-resolved EPR spectra of the donor:acceptor blends shown in Figure 5.1 can now be analysed. Averaged from 0 to 1 µs, the EPR spectra of inner-wall films of the

four OPV blends are presented in Figure 5.4, recorded under identical conditions to inner-wall films of the pristine materials. The corresponding pristine donor (blue) and acceptor (red) spectra, alongside their simulated ISC triplet signals (Figure 5.2), are displayed for reference. Each blend spectrum was fitted as a weighted sum of the simulated donor and acceptor ISC triplets.

In the PBDB-T:PCBM blend, the EPR spectrum displays a narrow triplet of approximately 20 mT width, closely matching the PCBM ISC triplet; no evidence for PBDB-T ISC triplets is detected. Conversely, PM6:PCBM exhibits contributions from both the PCBM ISC triplet and a broader ISC triplet attributable to PM6, with the best fit yielding a donor-to-acceptor triplet ratio of roughly 0.8 : 0.2. In blends containing non-fullerene acceptors, the triplet signals in the broader field range are weak, and the overlap of the pristine donor and non-fullerene acceptor spectral features complicates precise assignment. However, the observed triplet signal widths are narrower than the donor triplet spectra, suggesting that the triplets predominantly arise from ISC within the acceptors ITIC and Y6.

No signature of triplet formation via geminate recombination was detected in any blend. Such triplet formation would manifest as characteristic *aeeaae* ($D < 0$) or *eaaeea* ($D > 0$) polarisation patterns, with the same width and canonical turning points as the ISC triplets, as outlined in Section 2.4.3 of Chapter 2.[146] The absence of these specific polarisation signatures rules out geminate recombination as a significant triplet formation pathway in these systems. Non-geminate recombination from uncorrelated charges, in contrast, populates all triplet sublevels equally, also explained in the same section in Chapter 2, resulting in no net spin polarisation, remaining invisible to time-resolved EPR. However, transient absorption spectroscopy and photoluminescence-detected magnetic resonance experiments have determined that non-geminate recombination is indeed a significant triplet formation channel for both fullerene and non-fullerene acceptor blends.[106,112,148]

The triplet formation mechanisms are summarised in Table 5.2. All blends exhibit some degree of ISC triplet formation, predominantly within the acceptor domains. Additionally, PM6:PCBM shows triplets resulting from ISC in the PM6 donor domain. Geminate recombination is not observed, and non-geminate recombination remains unseen by time-resolved EPR. Triplet signals are significantly stronger in blends exhibiting poorer photovoltaic performance, suggesting a correlation between increased triplet generation and reduced device efficiency. Although intersystem crossing is formally spin-forbidden, it can effectively compete with charge transfer when donor and acceptor domains are not optimally structured for exciton dissociation, preventing singlet excitons from reaching an interface within their lifetime. Since triplet states act as loss channels that prevent excitons from contributing to photocurrent, these results reinforce the necessity of suppressing triplet formation to achieve high-efficiency OPVs.

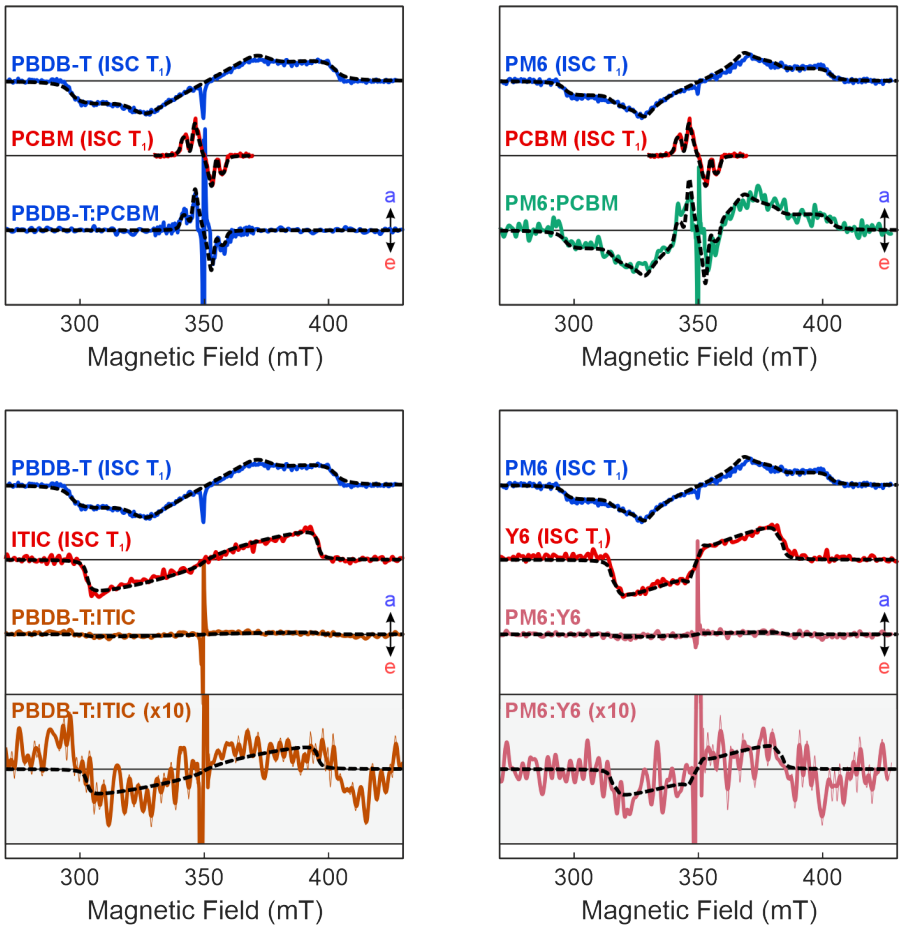

Figure 5.4: Time-resolved EPR X-band spectra of PBDB-T:PCBM, PM6:PCBM, PBDB-T:ITIC, and PM6:Y6 at 20 K, averaged over $0 - 1\,\mu s$. For comparison, the corresponding pure donor (blue) and acceptor (red) spectra from Figure 5.2 are shown. Black dotted lines represent simulated ISC triplets of the donors and acceptors, along with a weighted sum fitted for each blend. The inferred triplet formation mechanisms are summarised in Table 5.2.

Material	Triplet Formation Mechanism			
	Intersystem Crossing		Recombination	
	Donor	Acceptor	Geminate	Non-Geminate
PBDB-T:PCBM	×	✓	×	?
PM6:PCBM	✓	✓	×	?
PBDB-T:ITIC	×	✓(very weak)	×	?
PM6:Y6	×	✓(very weak)	×	?

Table 5.2: Assignment of the formation mechanism of triplet states observed in the EPR spectra of PBDB-T:PCBM, PM6:PCBM, PBDB-T:ITIC, and PM6:Y6, using the results in Figure 5.4 and simulation results from Table 5.1. Non-geminate recombination produces no observable EPR signal, and so cannot be assigned.

5.3.2 Time-Resolved EPR of Charge-Transfer States

Spin-polarised CT states and SCs, observed at field positions near the free-electron g-value, are indicative of efficient exciton dissociation and successful charge transfer at the donor:acceptor interface. In contrast to the triplet excitons arising from intersystem crossing, CT states and SCs are directly involved in photocurrent generation and are therefore associated with enhanced photovoltaic performance. Although CT state signatures are present in the EPR spectra shown in Figure 5.1, greater spectral resolution of the CT state and SC contributions is achieved by measuring time-resolved EPR over a narrower magnetic field range centred around $g = g_e$.

To investigate the spin dynamics of CT states and any SCs in greater detail, time-resolved EPR measurements were performed under a range of experimental conditions:

1. The effect of laser fluence was examined to determine how variations in photogenerated charge concentration influence charge transfer and separation.
2. Spectra recorded at Q-band frequency were compared to those at X-band, in order to improve resolution of overlapping absorptive and emissive features.
3. Temperature-dependent measurements were used to evaluate the influence of thermal energy on spin dynamics.
4. Spectra from spin-coated films were compared with those from inner-wall films to assess the relevance of the observed spin signatures to operational OPV devices.

Together, these experiments provide a comprehensive picture of CT state and SC behaviour and offer valuable insight into the factors that govern efficient charge transfer and separation in organic photovoltaic materials.

Fluence Dependence of Fullerene Acceptor Blends

Figure 5.5 shows time-resolved EPR spectra of the fullerene acceptor blends PBDB-T:PCBM and PM6:PCBM, measured at 20 K and X-band under two different laser fluences: $20\,\mu J\,cm^{-2}$ and $1\,mJ\,cm^{-2}$. For each blend, EPR signal intensity is plotted as a function of magnetic field and time following photoexcitation. The left and centre panels correspond to the lower and higher laser fluence measurements, respectively. To facilitate direct comparison of spectral shapes, the $20\,\mu J\,cm^{-2}$ data have been scaled by amplitude so that the magnitude of the early-time signals match those at high fluence. The right panel displays spectra averaged over short ($0.1 - 0.3\,\mu s$) and long ($20 - 60\,\mu s$) time windows following photoexcitation. The

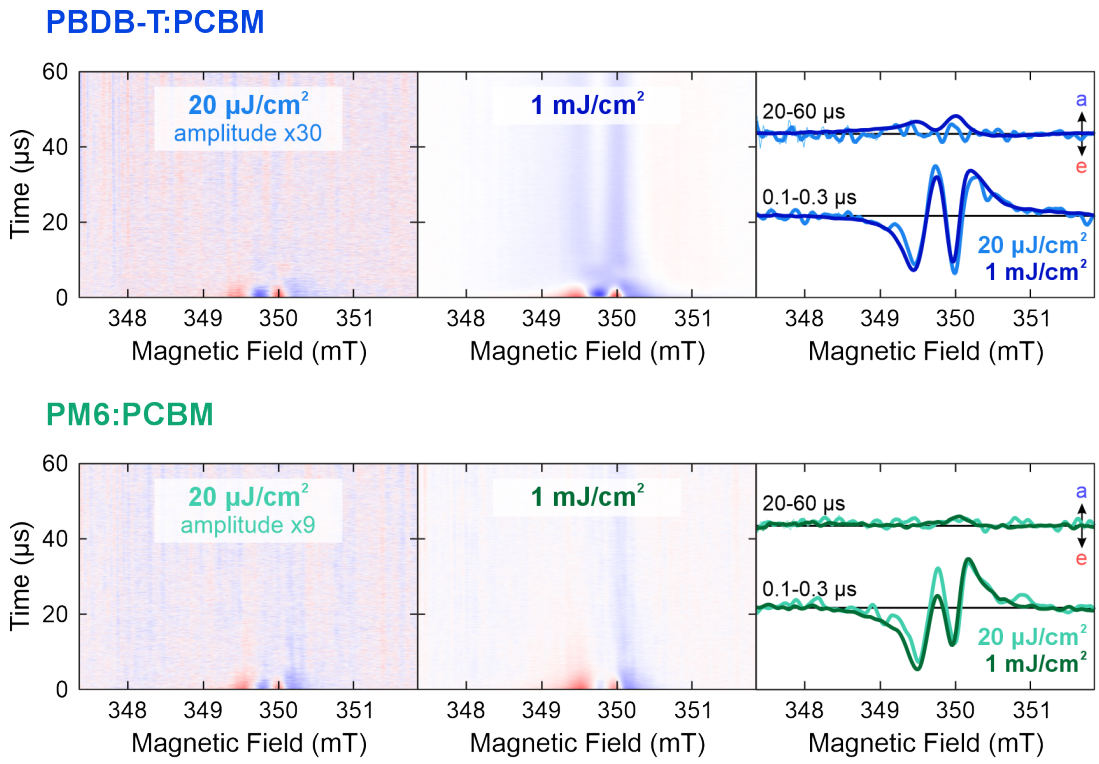

Figure 5.5: Time-resolved EPR spectra of PBDB-T:PCBM and PM6:PCBM, measured at 20 K and at X-band, at two different laser fluences, 20 µJ cm^{-2} and 1 mJ cm^{-2}, with a comparison of averaged spectra at short (0.1 − 0.3 µs) and long (20 − 60 µs) times after photoexcitation. The magnitude of the 20 µJ cm^{-2} data is scaled by the amplitude factor given in the left panel. Absorptive features are in blue and emissive features in red in the two-dimensional plots.

short-time averaging window excludes the earliest delays (before 0.1 µs), where lifetime broadening effects distort the spectral lineshape.[140]

Varying the excitation fluence provides insight into differences in spin dynamics as the concentration of charges changes with the number of incoming photons. The higher fluence (1 mJ cm^{-2}) was chosen to maximise signal intensity while avoiding photoinduced degradation. In contrast, measurements at the lower fluence (20 µJ cm^{-2}), although more experimentally time-consuming due to a reduction in signal-to-noise ratio, more closely approximate solar irradiance conditions and are consistent with the fluence intensities used in transient absorption studies.[83,164,305]

An *eaea*-polarised signal is observed at short times after photoexcitation, at both laser fluences. Comparison of the signals in the averaged EPR spectra at 0.1 − 0.3 µs shows no significant change in shape between laser fluences. The amplitude of the EPR signal is significantly increased upon increasing the laser fluence from 20 µJ cm^{-2} to 1 mJ cm^{-2} (×30 for PBDB-T:PCBM and ×9 for PM6:PCBM), a result of a greater number of photoexcitations increasing the concentration of species that reach the donor:acceptor interface and generate EPR-detectable spin

states. However, the increase is not linear with the 50-fold rise in incident photon flux, indicating that additional mechanisms limit the efficiency of charge generation at high excitation densities.

The observed *eaea* polarisation pattern is a hallmark of singlet-born CT states, as outlined in Chapter 2 (Section 2.4.2), and is consistent with a negative exchange interaction J, where ^{3}CT is lower in energy than ^{1}CT.[141,142] This signature indicates that the CT state arises from dissociation of a singlet exciton at the donor:acceptor interface ($S_1 \rightarrow$ CT).

The characteristic lineshape originates from the overlap of four spin-polarised transitions, divided into two *ea*-pairs. A detailed explanation of this signal polarisation is given in Section 2.4.2. One *ea*-pair is centred at the isotropic g-value of the donor, and the other at that of the acceptor, corresponding to the peak positions of the steady-state SCs observed from echo-detected EPR spectra in Section 3.3.1 of Chapter 3. Within each *ea*-pair, the individual emissive and absorptive components are split by exchange and dipolar coupling between the coupled spins. The central field positions of each *ea* pair, which coincide with the maxima of the SC signals, correspond to regions of near-complete cancellation in the CT signal. Because the *eaea* lineshape arises from significant cancellation between overlapping transitions, the spectral shape is sensitive to small changes in spin parameters.

If the CT state was instead formed via dissociation of a thermalised triplet exciton ($T_1 \rightarrow$ CT), an inverted *aeae* polarisation would be expected, assuming the same sign of J.[143,144] A triplet-born CT state could produce an *eaea* pattern if the exchange interaction were positive ($J > 0$),[138] but in such a case, the formation of the CT state would be accompanied by a corresponding depletion of the triplet exciton population. This is not observed in the time-resolved EPR spectra shown in Figure 5.1, providing further evidence that the detected CT states originate from dissociation of the singlet exciton. ISC to generate T_1 from S_1, prior to CT state formation, is also generally too slow to account for the observation of a CT state signal within 100 ns.[61]

At longer times after photoexcitation, the PBDB-T:PCBM time-resolved EPR signal evolves noticeably away from the initial *eaea* pattern at both laser fluences. For the spectrum measured at $1\,\mathrm{mJ\,cm^{-2}}$, a predominantly absorptive signal begins to emerge at around $5 - 10\,\mu$s and persists well beyond $60\,\mu$s, outlasting the short-lived CT state signature. From time-resolved EPR simulations in Chapter 4 (Section 4.4.4), a long-lived absorptive component arises if the following two conditions are met: rapid charge separation from the singlet exciton ($S_1 \rightarrow {}^1\mathrm{CT} \rightarrow$ SC) and an equilibrium between charge-transfer states and separated charges (CT $\rightleftharpoons$ SC). This long-lived signal is completely absent in the lower fluence measurement

of PBDB-T:PCBM, suggesting that these processes become significant only at higher charge densities.

For PM6:PCBM, the time evolution of the EPR signal is qualitatively similar at both laser fluences: the initial *eaea* signal decays within approximately 5 µs, with no significant long-lived absorptive component developing at later times. This suggests that, unlike PBDB-T:PCBM, PM6:PCBM does not enter a regime where CT − SC equilibrium becomes significant, even at high excitation densities. The only fluence-dependent difference is in the overall signal intensity, reflecting the increased number of photogenerated CT states at higher fluence, with the underlying spin dynamics remaining unchanged.

Fluence Dependence of Non-Fullerene Acceptor Blends

For the non-fullerene acceptor blends PBDB-T:ITIC and PM6:Y6, the time-resolved EPR spectra, shown in Figure 5.6, exhibit an *ea* polarisation pattern at early times after photoexcitation, and comparison of the $0.1 - 0.3$ µs EPR spectrum again shows no significant change between laser fluence. Unlike the fullerene acceptor blends, which show a well-resolved *eaea* pattern due to clear spectral separation between the donor and acceptor signals, the CT state spectrum here appears as a coalesced *ea*-like signal. This is a consequence of the significant overlap between the principal g-values of the polymer donors ($2.0020 - 2.0033$) and the non-fullerene acceptors ($2.0021 - 2.0038$) - see Chapter 3 (Table 3.4). The donor- and acceptor-centred *ea* transition pairs thus overlap, blending the individual features of the *eaea* polarisation into an *ea*-like lineshape in the early-time EPR spectra.

The overall *ea* polarisation pattern remains influenced by the spin interactions of the donor and acceptor species. In Chapter 3, large hyperfine couplings of around 20 MHz were identified in the X-band echo-detected EPR spectra of the donor and acceptor SCs for the non-fullerene acceptor blends, attributed to nuclei on $ITIC^{\bullet-}$ and $Y6^{\bullet-}$ and verified by ENDOR measurements and DFT calculations. Because the isotropic g-values of the non-fullerene acceptors are slightly higher than those of the donors, these hyperfine interactions broaden the *ea*-polarised CT state signals predominantly at lower magnetic fields, producing spectral humps or wings below 349 mT.

In the PBDB-T:ITIC EPR spectrum, recorded at $1\,\mathrm{mJ\,cm^{-2}}$, the singlet-born CT state's *ea* polarisation evolves into a predominantly absorptive signal by around 2 µs, which persists beyond 60 µs. At the lower laser fluence, the long-lived absorptive signal is diminished but still present. The $20 - 60$ µs averaged spectra show this absorptive signal with low field broadening from the non-fullerene acceptor hyperfine interactions, alongside a smaller emissive component at fields above 349.7 mT.

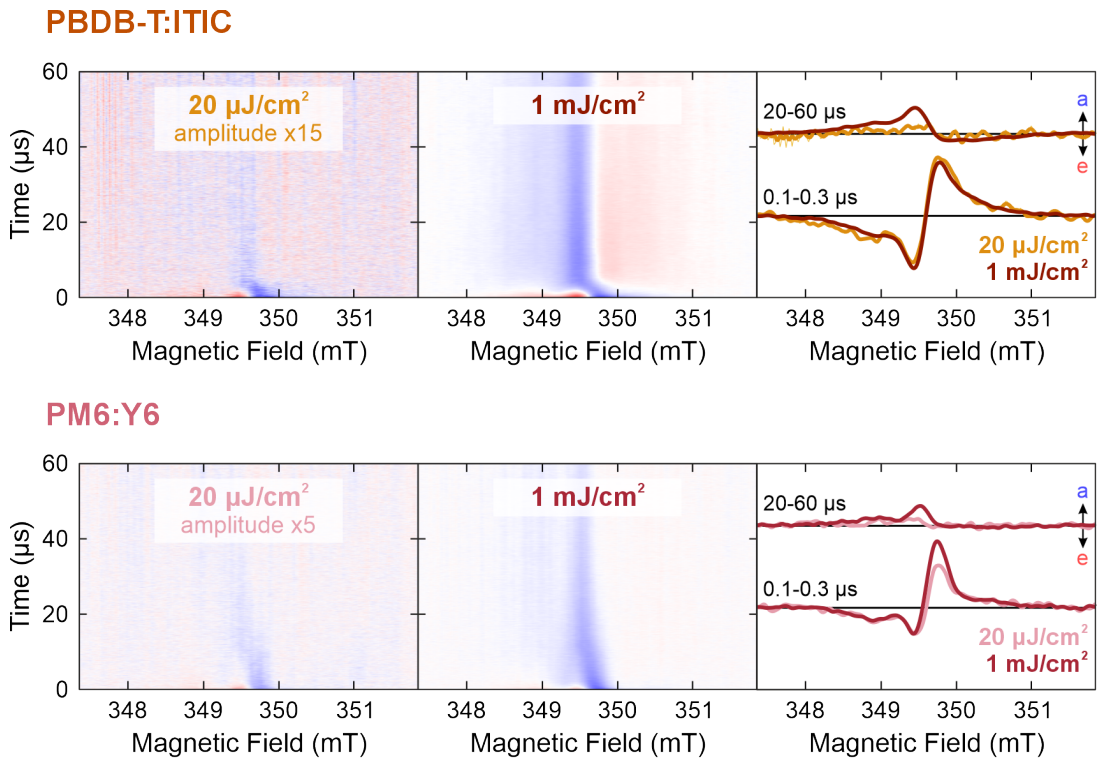

Figure 5.6: Time-resolved EPR spectra of PBDB-T:ITIC and PM6:Y6, measured at 20 K and at X-band, at two different laser fluences, 20 µJ cm^{-2} and 1 mJ cm^{-2}, with a comparison of averaged spectra at short (0.1 – 0.3 µs) and long (20 – 60 µs) times after photoexcitation.

The presence of the small emissive feature at higher fields suggests a partial reversal of the spin polarisation pattern, shifting from *ea* to *ae*. This *ae*-polarised signal would occur if there is an excess population of the CT eigenstates of pure triplet character $|1\rangle$ and $|4\rangle$. Such a situation can arise in the presence of a fast, singlet-selective decay, combined with either a singlet-born CT state with significant relaxation returning the system to equilibrium polarisation with population in the pure triplet levels $|1\rangle$ and $|4\rangle$, while the selective decay removes population from only the $|2\rangle$ and $|3\rangle$ states with singlet character, or with a CT state formed by re-encounter of uncorrelated SCs with initially equal populations of all sublevels. This selective decay effectively inverts the spin polarisation pattern of the CT transitions. For this inverted pattern to remain detectable up to 60 µs, the CT state must also have a sufficiently long lifetime. However, since the spectrum between 20 and 60 µs remains predominantly absorptive, rather than showing a fully inverted or symmetric absorptive-emissive shape, the actual spin population distribution is likely more nuanced than a simple polarisation inversion.

For PM6:Y6, the CT state signal is particularly short-lived, with all emissive polarisation disappearing within 1 µs at both laser fluences. At lower laser fluence, the EPR spectrum at 0.1 – 0.3 µs displays a more balanced *ea* polarisation, showing

a clear presence of the singlet-born CT state. At higher fluence, absorptive features also contribute to the early-time spectrum, before transitioning to a fully absorptive signal after 1 µs. This long-lived absorptive component persists at the lower fluence as well, albeit with reduced intensity compared to the initial *ea*-polarised CT state signal, similar to the behaviour observed in PBDB-T:ITIC.

PM6:Y6 also exhibits a weaker dependence of absolute EPR intensity on laser fluence, showing only a fivefold increase when the photon flux increases fifty times. This contrasts with the larger intensity increases of approximately ×30, ×9, and ×15 for PBDB-T:PCBM, PM6:PCBM, and PBDB-T:ITIC, respectively. A smaller intensity increase may suggest that PM6:Y6 is more efficient under standard solar irradiance conditions (20 µJ cm^{-2}), saturating earlier because it already operates near its maximum charge generation capacity under solar illumination.

Long-time Evolution of the Time-Resolved EPR Spectra

Whilst the time-resolved EPR signals at 20 µJ cm^{-2} decay within 60 µs, at 1 mJ cm^{-2}, the long-time predominantly absorptive signal contribution persists for much longer times. Time-resolved EPR measurements were performed over a longer time range, 0 – 500 µs, with transients extracted at magnetic field positions corresponding to the resonant positions of the donor and acceptor SCs, plotted in Figure 5.7. In all cases, the absorptive signal decays slowly over a timescale of about 500 µs, as the charges recombine non-radiatively to the ground state.

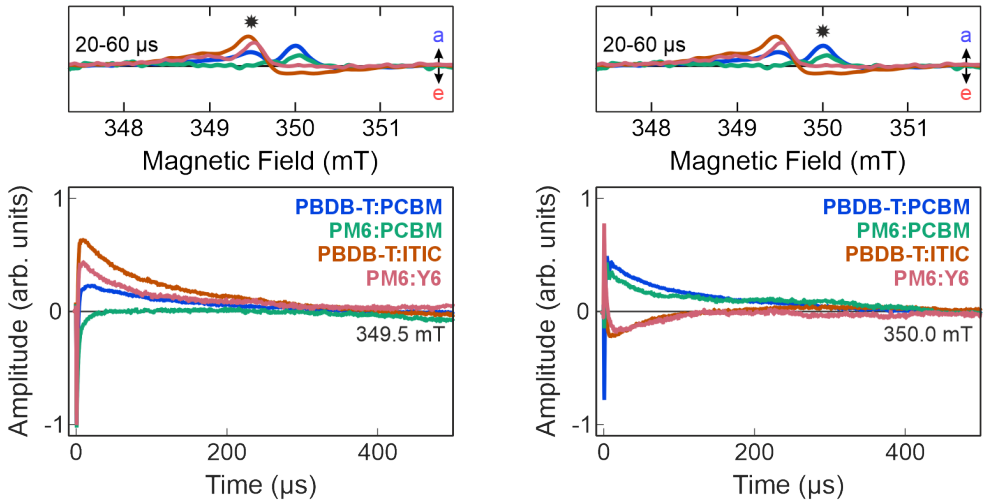

Figure 5.7: Decay traces of the time-resolved EPR signal of PBDB-T:PCBM, PM6:PCBM, PBDB-T:ITIC, and PM6:Y6, at 20 K, 1 mJ cm^{-2} and at X-band. The traces were averaged between 349.45 – 349.55 mT and 349.95 – 350.05 mT, indicated on the spectra shown in the top panel.

The presence of such a long-lived absorptive signal is particularly significant. For other systems with CT states, such as radical pairs in photosynthesis, cryptochromes for avian magnetoreception and molecular triads in quantum information science, a long-time absorptive EPR signal has not been reported.[245,253,278,279] In these systems, primary CT state formation is typically followed by sequential charge transfer to form spatially-separated charges, that remain coupled and spin-correlated. In these cases, the radical pairs typically retain the spin polarisation pattern inherited from the precursor and modified during singlet-triplet mixing in primary and/or secondary CT states.

In contrast, in OPV systems, after dissociation from the initial CT state, electrons and holes may diffuse to large separations such that coupling and spin correlation is lost. This results in approximately equally populated spin sublevels, and subsequent relaxation can drive the system towards thermal equilibrium, yielding a net absorptive EPR signal. These charges may then re-encounter, which can lead to non-geminate recombination, as observed in transient absorption measurements of OPVs.[106,112,148] If the re-encounter does not result in immediate recombination, a CT state is again formed, which will be characterised by an absorptive polarisation. The observation of a persistent long-lived absorptive signal in all blends studied therefore provides compelling evidence for the presence of uncorrelated SCs and/or CT states formed through non-geminate re-encounter.

Q-Band Time-Resolved EPR

To gain improved spectral resolution of the CT state EPR spectra, time-resolved EPR measurements were performed at Q-band (33.9 GHz) under the same conditions as the previous X-band experiments (20 K, 1 mJ cm^{-2}). The higher microwave frequency at Q-band spreads the four CT transitions over a wider magnetic field range, reducing spectral overlap and enabling clearer separation of absorptive and emissive features.[254,306–308] Additionally, hyperfine interactions contribute less to line broadening at Q-band, as they are frequency-independent; instead, spectral shapes are dominated by g-anisotropy, allowing donor and acceptor contributions to be more distinctly resolved.

The time-resolved Q-band spectra are shown in Figure 5.8, measured at 20 K and high laser fluence (1 mJ cm^{-2}). For the fullerene acceptor blends, PBDB-T:PCBM and PM6:PCBM, the spectra exhibit clear *eaea* polarisation shortly after photoexcitation, consistent with the singlet-born CT states previously identified at X-band. At later times, PM6:PCBM shows the emergence of a weak absorptive component. For PBDB-T:PCBM, the signal between 20 and 60 µs reveals a pronounced *aea* polarisation: a central slightly emissive peak flanked by two stronger absorptive

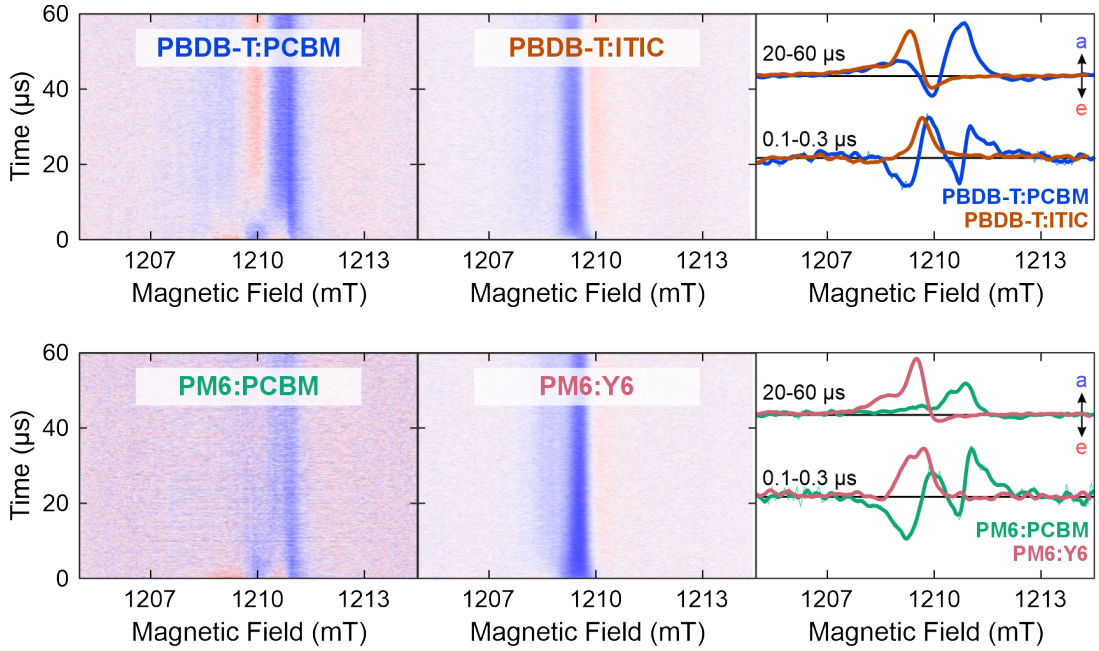

Figure 5.8: Time-resolved EPR Q-band spectra of PBDB-T:PCBM, PBDB-T:ITIC, PM6:PCBM, and PM6:Y6, with averaged spectra at short (0.1 – 0.3 µs) and long (20 – 60 µs). All measurements were done at 20 K and at 1 mJ cm^{-2}.

features. This pattern, not resolved at X-band due to spectral overlap, suggests a partial contribution of an *aeae*-polarised CT state, due to overpopulation of $|1\rangle$ and $|4\rangle$, as previously theorised for PBDB-T:ITIC at X-band.

In the non-fullerene acceptor blends, PM6:Y6 and PBDB-T:ITIC, the early-time *ea*-polarised CT signals seen at X-band are no longer apparent at Q-band. Instead, the spectra are dominated by a long-lived, mostly absorptive signal that persists from 0 to 60 µs, with a weak emissive shoulder appearing above 1210 mT. While this emissive feature was already observed for PBDB-T:ITIC at X-band, its more distinct appearance in PM6:Y6 at Q-band confirms that both non-fullerene acceptor blends also exhibit signs of spin polarisation inversion consistent with a long-lived CT state undergoing singlet-selective decay.

For all blends, the long-lived absorptive contributions are enhanced at Q-band, relative to the early-time signals associated with singlet-born CT states. This enhancement can be partially rationalised by considering the effect of microwave frequency on spin polarisation. Thermalised spin states have populations described by the Boltzmann distribution, where the equilibrium polarisation increases linearly with microwave frequency. Consequently, when transitioning from X-band (9.8 GHz) to Q-band (33.9 GHz), thermal polarisation is expected to increase by a factor of approximately 3.5. This effect would amplify any absorptive contributions arising from spin states that have relaxed towards thermal equilibrium during the measurement window.

The spin polarisation of singlet-born CT states, however, is fixed by their spin-selective formation from singlet excitons and is not governed by thermal equilibrium. Although singlet-triplet mixing within the CT manifold (^{1}CT $\leftrightarrow$ ^{3}CT) is field-dependent, the influence of any differences between X- and Q-band magnetic fields on the EPR spectrum is generally expected to be insignificant. The observed enhanced contribution of the absorptive signal compared to the initially spin-polarised CT state therefore suggests that some thermally-populated spin states contribute to the signal at long times, likely due to longitudinal relaxation of CT states and SCs during the measurement.

However, the relative suppression of early-time signals for PBDB-T:ITIC and PM6:Y6 at Q-band may also stem from instrumental effects. The Q-band resonator used in these measurements has a higher quality factor, resulting in a longer response time to changes in microwave absorption. This slower response diminishes the detection sensitivity to short-lived spin states and may further contribute to the apparent prominence of the long-lived absorptive component at Q-band.

Interpretation of the long-lived absorptive signal in the time-resolved EPR spectra recorded for different blends and at different microwave frequencies and laser fluences in terms of a purely thermally-polarised signal requires careful consideration. In order to generate a thermalised signal of comparable magnitude to the strongly polarised singlet-born CT state by evolution from that CT state within a few microseconds would require an unrealistically short longitudinal relaxation time, T_1, and much lower temperatures than used in the experiments. Only a significantly higher concentration of thermalised spin states compared to the spin-polarised CT states could explain the observed time-dependence and relative intensity of the two contributions. It is therefore likely that a more complex mechanism needs to be considered to fully explain the experimental observations.

Temperature Dependence of the Evolution of Spin Polarisation

To assess whether the spin-dependent processes observed at 20 K remain relevant under conditions closer to those in operational OPV devices, time-resolved EPR measurements were performed at higher temperatures of 80 K and 140 K. These measurements aim to determine whether the dynamics of CT states and SCs remain consistent as thermal energy increases. As temperature rises, increased thermal energy accelerates charge transport by hopping and therefore favours recombination of photoexcited states, resulting in diminished EPR signal intensity and necessitating longer signal averaging. Additionally, the shortened lifetimes of transient states, such as the spin-correlated CT states, at elevated temperatures may lead to their decay occurring within the instrument's response time, preventing

detection. These factors ultimately restricted the practical upper temperature limit of the measurements to around 140 K, beyond which reliable signal acquisition becomes very challenging due to insufficient sensitivity.

The time-resolved X-band EPR spectra recorded for the four donor:acceptor blends at 20 K, 80 K, and 140 K are shown in Figure 5.9, up to 10 µs. Given the reduction in signal intensity with temperature, the spectra at 80 K and 140 K have been scaled for amplitude comparison. For PBDB-T:PCBM, the characteristic polarisation evolution from an *eaea*-polarised singlet-born CT state to a long-lived *aa*-polarised signal is preserved across all temperatures. However, the rate of this polarisation evolution increases with temperature, occurring over approximately 5 µs at 20 K but accelerating to within 0.5 µs at 140 K. A similar trend is observed for PM6:PCBM, with faster polarisation evolution at higher temperatures.

For PBDB-T:ITIC, the *ea*-polarised singlet-born CT state signal remains visible at 140 K, but also exhibits a faster polarisation evolution as temperature increases. The progression to the long-lived absorptive signal is less strongly temperature-dependent compared to the fullerene acceptor blends, however, occurring at roughly 2 µs at 20 K and 0.8 µs at 140 K. In addition, the emissive component of the long-time signal at high field diminishes with increasing temperature, indicating changes in the kinetic processes responsible for this polarisation at low temperature. In contrast, PM6:Y6 exhibits very little dependence on temperature, and there are no significant differences between the time-resolved EPR spectra at 20 K, 80 K, and 140 K. The singlet-born CT state is observed up to 0.5 µs at 140 K, compared to 1 µs at 20 K.

The consistent presence of spin-polarised CT states and long-lived absorptive signals across the temperature range studied, with only the timescale of their evolution varying, indicates that the fundamental photophysical mechanisms driving charge transfer and separation remain operative from 20 K up to at least 140 K. It is therefore reasonable to expect that these mechanisms continue to be relevant up to room temperature.

This expectation is supported by multiple studies in the literature. A study of recombination dynamics in a series of fullerene acceptor blends revealed a strong correlation between the yield of separated charges at 10 K and the yield of free charges at room temperature,[309] suggesting that the processes observed at low temperature reflect those active under device-operating conditions. Moreover, transient absorption investigations have demonstrated that charge generation is not significantly impeded by low temperature,[310–312] which aligns with the observation of the long-lived absorptive signal in the time-resolved EPR spectra at all measured temperatures. This signal further confirms that efficient charge separation persists under cryogenic conditions.

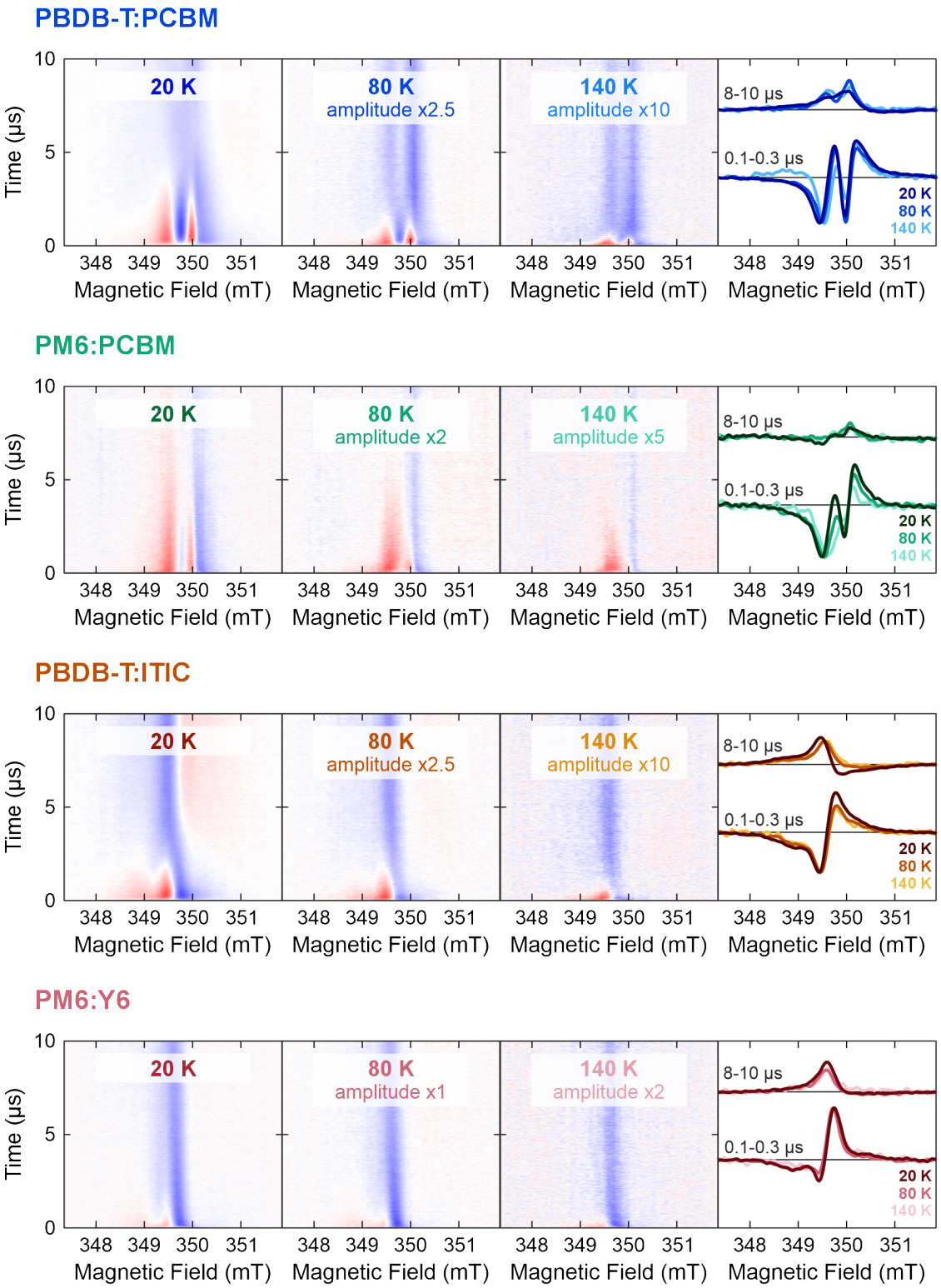

Figure 5.9: Time-resolved X-band EPR spectra of PBDB-T:PCBM, PM6:PCBM, PBDB-T:ITIC, and PM6:Y6, at 1 mJ cm^{-2} and at three different temperatures: 20 K, 80 K, and 140 K, with a comparison of averaged spectra at short (0.1 – 0.3 µs) and intermediate (8 – 10 µs) times after photoexcitation.

Specifically, for PM6:Y6, charge separation has been shown to be independent of thermal activation,[77,82] explaining the minimal spectral changes observed between 20 K and 140 K. Efficient charge generation in PM6:Y6 has been observed down to 10 K,[313] reinforcing the conclusion that the same charge separation mechanism operates across this temperature range. It is thus justifiable to conclude that the CT states, separated charges, and their associated dynamics observed at 20 K are representative of the essential photophysical processes at operating temperatures.

Dependence on Film Morphology

To determine whether the spin-dependent mechanisms observed in thick inner-wall films also apply to more device-relevant morphologies, time-resolved EPR measurements were performed on spin-coated films of donor:acceptor blends. It is important to assess whether morphology influences the charge dynamics, and whether the photophysical behaviour identified in thicker films is preserved. Time-resolved EPR spectra for all four donor:acceptor blends are shown in Figure 5.10,

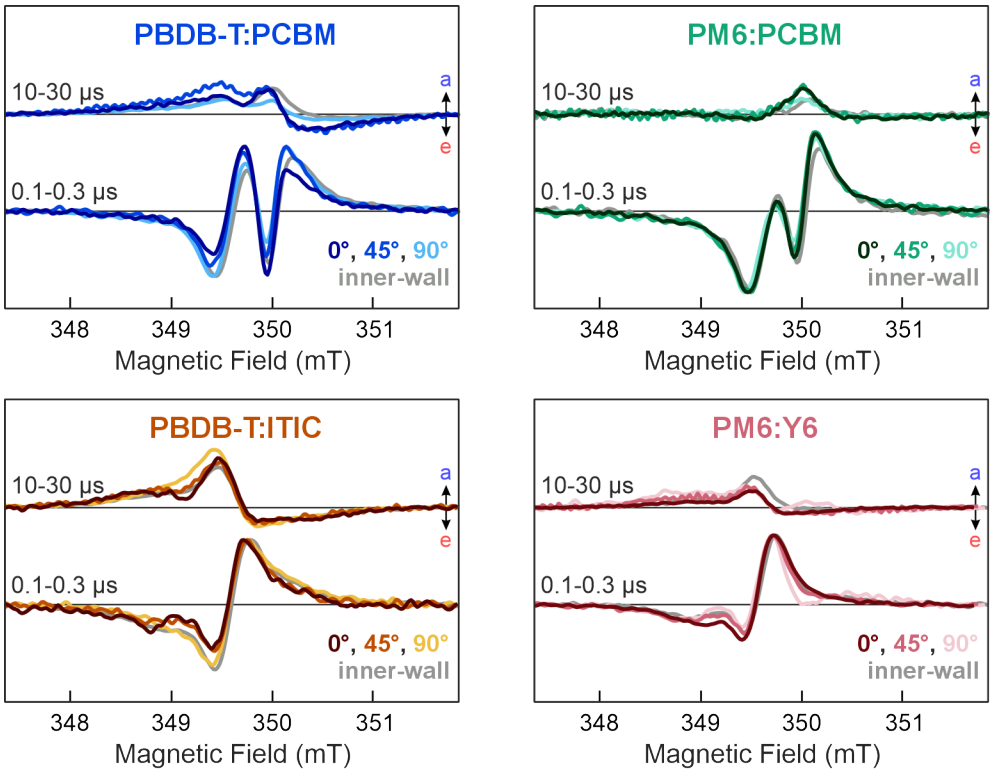

Figure 5.10: Time-resolved EPR X-band spectra of spin-coated films of PBDB-T:PCBM, PBDB-T:ITIC, PM6:PCBM and PM6:Y6, at different angles with respect to the external magnetic field, measured at 20 K and 1 mJ cm^{-2}. The spectra are averaged over short (0.1 – 0.3 µs) and long (10 – 30 µs) times, and compared to the signal of the thicker inner-wall films (grey). The angles refer to the angle of the plane of the substrate relative to the magnetic field direction, as illustrated in Figure 5.3 of Section 5.2.2.

and were recorded at three different angles (0°, 45°, and 90°) of the substrate plane relative to the applied magnetic field. Spectra are shown averaged over early ($0.1 - 0.3\,\mu s$) and late ($10 - 30\,\mu s$) time windows following photoexcitation, and are compared directly to the corresponding spectra recorded for the thicker inner-wall films. Full two-dimensional time-resolved EPR spectra for the spin-coated films are provided in Appendix E.

In all cases, the same spin-polarised signals are observed: a singlet-born CT state exhibiting an *eaea*-like polarisation for fullerene acceptor blends and an *ea*-like pattern for non-fullerene acceptor blends at early times, followed by a predominantly absorptive signal at later times. This consistent evolution of spin polarisation matches that seen in the inner-wall samples, indicating that the charge separation mechanism remains unaffected by differences in film processing and ordering.

Compared to the triplet EPR measurements in Section 5.3.1, where rotation-dependent changes in spectral shape were pronounced due to the strong dependence of triplet spectral features on canonical orientations, the CT state spectra exhibit only minimal changes with sample rotation. The CT state signals arise from a combination of overlapping transitions whose spin polarisation features partially cancel, making subtle changes due to molecular alignment more difficult to resolve and interpret. In addition, the morphology of the pristine materials, used in the triplet measurements of the spin-coated films, has been shown from GIWAXS studies to often change when blended in a donor:acceptor bulk heterojunction.[46,314,315]

Only very minor spectral differences are seen between the different orientations of the spin-coated films and the inner-wall films. The minimal differences between the three orientations of the much thinner spin-coated films support the treatment of the thicker inner-wall films as disordered, powder-like samples, where a uniform distribution of molecular orientations contributes to the EPR signal intensity. The observation of the same spin polarisation signatures and their consistent evolution in both film types demonstrates that the CT state and SC dynamics identified in inner-wall samples are equally present in thinner, spin-coated films. These results confirm that the spin-dependent processes captured in thick films are directly relevant to the morphologies and conditions typical of operational OPV devices.

5.3.3 Characterisation of the Charge-Transfer State

Having established that the early-time *eaea*-polarised features observed in the time-resolved EPR spectra arise from singlet-born CT states generated immediately after photoexcitation, the next step is to gain quantitative insight into the microscopic structure of these states. While the polarisation pattern confirms the presence of spin-polarised CT states, it does not directly reveal the donor:acceptor

separation, the strength of their magnetic interactions, or their relative spatial orientation: factors that are essential for understanding how intermolecular geometry and electronic coupling influence charge separation efficiency.

To access this structural information, the time-resolved EPR spectra, averaged over the $0.1 - 0.3\,\mu s$ time window following photoexcitation, were compared to simulations, performed across multiple experimental conditions - X-band at both low ($20\,\mu J\,cm^{-2}$) and high ($1\,mJ\,cm^{-2}$) excitation fluence, as well as Q-band at high fluence - to ensure consistency of the extracted parameters. The EPR spectra for each condition were globally fitted using a single spin Hamiltonian for each donor:acceptor blend.

These global simulations yield spin Hamiltonian parameters that quantitatively describe the spatial and electronic characteristics of the CT state. Dipolar and exchange interactions encode information on the electronic coupling and distance between the charges. Additionally, the polarisation pattern and spectral shape of the CT state signal are sensitive to the relative orientation of the donor and acceptor molecules, allowing the simulations to provide insight into the local molecular geometry at the donor:acceptor interface.

The spin Hamiltonian of the CT state is governed by three main types of contributions, determined by a set of parameters characteristic of the investigated spin system:

1. **Electron Zeeman interactions**: $\hat{\mathcal{H}}_{eZ} = \frac{\mu_B}{\hbar}\boldsymbol{B}_0\boldsymbol{g}_D\hat{\boldsymbol{S}}_D + \frac{\mu_B}{\hbar}\boldsymbol{B}_0\boldsymbol{g}_A\hat{\boldsymbol{S}}_A$
   - g-values were determined in Chapter 3 from steady-state, echo-detected EPR spectra.
   - The orientations of the donor and acceptor $\boldsymbol{g}$-tensors (g-frames), relative to the molecular frame, are defined by Euler angles (α, β, γ) (see Section 2.2.1 in Chapter 2) and must be fitted during the simulation.
2. **Hyperfine interactions**: $\hat{\mathcal{H}}_{hf} = \sum_{i=1}^{n}\hat{\boldsymbol{S}}_A\boldsymbol{A}_{A,i}\hat{\boldsymbol{I}}_i$
   - Hyperfine interactions were determined in Chapter 3 from DFT predictions that were experimentally verified through comparison to ENDOR spectra.
3. **Electron-electron interactions**: $\hat{\mathcal{H}}_{ee} = J\hat{\boldsymbol{S}}_D\hat{\boldsymbol{S}}_A + \hat{\boldsymbol{S}}_D\boldsymbol{D}\hat{\boldsymbol{S}}_A$
   - The exchange term, J, decreases exponentially with donor:acceptor separation, r: $J = J_0e^{-\beta r}$, where J_0 is the maximum exchange coupling and β controls the distance dependence.[132,316,317]
   - The dipolar coupling tensor $\boldsymbol{D}$ reflects through-space interactions and depends on the spin density distributions of the donor and acceptor and on the inter-spin distance.

- The principal axis of $\boldsymbol{D}$ is assumed to align with the donor:acceptor inter-spin vector $\boldsymbol{r}$, with orientation described by its own set of Euler angles.
- Both the magnitudes and orientations of the electron-electron interactions are unknown and must be determined through fitting during the CT state simulations.

Because the EPR spectrum of the CT state exhibits cancellation of overlapping transitions, it is sensitive to small variations in spin Hamiltonian parameters. This makes the CT spectrum a powerful probe of spin interactions, but nevertheless susceptible to *overfitting*: the risk that too many free parameters allow the simulation to reproduce experimental features without accurately reflecting the true underlying spin system parameters. To ensure that the structural parameters extracted from the spectra are meaningful, it is therefore essential to minimise the number of adjustable variables and constrain the simulation as much as possible with independently-determined quantities.

Many of the spin Hamiltonian parameters were determined in advance through steady-state characterisation in Chapter 3. The g-values of donor and acceptor species were measured with high precision using multi-frequency echo-detected EPR (Section 3.3.1), with additional spectral resolution provided by relaxation-filtered and EDNMR-induced EPR (Sections 3.3.2 and 3.3.3). For PBDB-T$^{\bullet+}$, PM6$^{\bullet+}$, and PCBM$^{\bullet-}$, hyperfine structure is not resolved in the EPR spectra, and these interactions were included as Gaussian line broadening. In contrast, for ITIC$^{\bullet-}$ and Y6$^{\bullet-}$, partially resolved hyperfine couplings are observed at X-band, and so large hyperfine interactions were explicitly included in the simulation.

To further reduce the number of parameters, one of the three orientational frames (donor g-frame, acceptor g-frame, and spin-spin coupling D-frame) was fixed. Because the donor:acceptor blends are disordered (powder) films, all molecular orientations with respect to the magnetic field are sampled equally, and it is only the relative orientation between tensors that determines the spectral shape. Therefore, the absolute orientation of one tensor frame can be arbitrarily chosen as a reference. In this case, the acceptor g-frame was fixed, and the donor g- and D-frames were varied during fitting, reducing the number of Euler angles to fit from nine to six.

The remaining unknown spin parameters required for the CT state simulation are the isotropic exchange interaction J, the dipolar coupling tensor $\boldsymbol{D}$, and the two relative Euler frames. While J is directly included as a free parameter, $\boldsymbol{D}$ is not treated as an independent fitting variable, but instead derived from a physically motivated model. In the simplest case, $\boldsymbol{D}$ can be approximated as a point-dipole interaction, in which each spin is treated as fully localised and $D \propto 1/r^3$, where

r is the donor:acceptor separation. However, this approximation is not valid for the CT states in OPV materials, as DFT calculations and ENDOR spectra show significant spin delocalisation over multiple molecular units. As a result, a more accurate distributed point-dipole model is used: the predicted spin density from DFT is projected onto atomic positions, and the dipolar interaction is calculated as the sum over all pairwise couplings between donor and acceptor atoms, weighted by their spin densities. For each simulation, r and the relative molecular orientation determine the dipolar interaction. Each simulation therefore involves a carefully limited set of free parameters: the exchange interaction J, the donor:acceptor separation r (from which the dipolar coupling $\boldsymbol{D}$ is derived), two sets of Euler angles (donor g- and D-frames), and a Gaussian line broadening parameter for each microwave frequency. To further minimise the number of fit parameters, g-strain contributions to the linewidth were excluded.

To explore this multi-dimensional parameter space while avoiding convergence to local minima, a hybrid fitting strategy was employed, combining a coarse grid search with a global genetic algorithm. The grid search systematically sampled the three Euler angles of the D-frame, covering the full range of possible donor:acceptor relative orientations. At each grid point, a genetic algorithm was used to optimise the remaining parameters: donor g-frame, J, r, and linewidth. This algorithm, as implemented in EasySpin,[130] mimics natural selection: at each iteration, a population of parameter sets is scored by how well it reproduces the experimental spectrum (quantified by the root-mean-square deviation, RMSD). The best-performing parameter sets are retained, new random sets are added and a number of existing sets are 'mutated' by adding random fluctuations, and the process is repeated. Over successive generations, the algorithm evolves towards globally optimal solutions, avoiding the risk of becoming trapped in local minima.

The genetic algorithm was run multiple times for each grid point to further reduce the likelihood of convergence to local minima and ensure the robustness of the resulting fits. After completing the full grid, the collection of best fits was analysed to identify the distribution of parameters that most accurately reproduce the experimental singlet-born CT state spectra.

The simulation algorithm can be summarised as follows:

1. Define a grid over the three Euler angles describing the relative donor:acceptor geometry (D-frame). Loop over each grid point, fixing these Euler angles.
2. For each fixed D-frame, initialise multiple random sets of parameters for the exchange interaction J, donor:acceptor separation r, and donor g-frame.
3. Calculate the dipolar coupling $\boldsymbol{D}$ from r using the distributed point-dipole model based on spin density distributions calculated from DFT and the selected donor:acceptor geometry.

4. Construct the spin Hamiltonian from the current spin parameters, diagonalise it to obtain energy levels, and compute population differences and transition intensities for the four allowed transitions, achieved through the *pepper* function in EasySpin.[130]
5. Simulate the EPR spectra of the singlet-born CT state at all three experimental conditions (X-band with $20\,\mu J\,cm^{-2}$ laser fluence, X-band with $1\,mJ\,cm^{-2}$ laser fluence, and Q-band with $1\,mJ\,cm^{-2}$ laser fluence), from the population differences and transition intensities, as described in Chapter 2 (Section 2.4.2), and calculate the RMSD between the simulated and experimental EPR spectra.
6. Apply a genetic algorithm to iteratively refine J, r, and the donor g-frame parameters.
7. Repeat this genetic optimisation multiple times at each grid point, saving the best-fitting parameters to ensure global convergence and avoid local minima.
8. After repeating this for all grid points, the collected best-fit parameter sets are sorted by their RMSD values. An RMSD cut-off is then applied to select the top N fits, enabling identification of the globally optimal solutions and providing insight into the distribution of parameters that accurately reproduce the experimental spectra.

Following the completion of the simulation procedure, a total of 20,000 best-fit parameter sets were retained for each donor:acceptor blend, filtered by RMSD to select those that most accurately reproduced the experimental data. These results are presented in Figure 5.11, which compares the simulated EPR spectra to the experimental spectra of the early-time, singlet-born CT state for PBDB-T:PCBM, PM6:PCBM, PBDB-T:ITIC, and PM6:Y6. Simulations are shown for the three experimental conditions studied: X-band with $20\,\mu J\,cm^{-2}$ laser fluence, X-band with $1\,mJ\,cm^{-2}$ laser fluence, and Q-band with $1\,mJ\,cm^{-2}$ laser fluence. The distribution of simulated spectra is coloured according to fit quality: the best 100 fits (lowest RMSD) are shown in dark shades, while progressively lighter shades represent the 500, 1000, 5000, and 10,000 best fits, as the match to experiment gets worse. Experimental data are overlaid in black for direct comparison.

At X-band, the primary spectral features - polarisation pattern, relative peak intensities, and overall lineshape - are broadly captured across a wide range of spin parameter combinations. Even fits with relatively high RMSD values reproduce the correct *eaea* polarisation. This insensitivity arises from the limited spectral resolution of X-band measurements, where significant cancellation occurs between overlapping absorptive and emissive transitions. Consequently, for almost any fixed donor:acceptor orientation (as defined by a single grid point), some combination of J, r, and donor g-frame can be found that yields a simulated spectrum in good

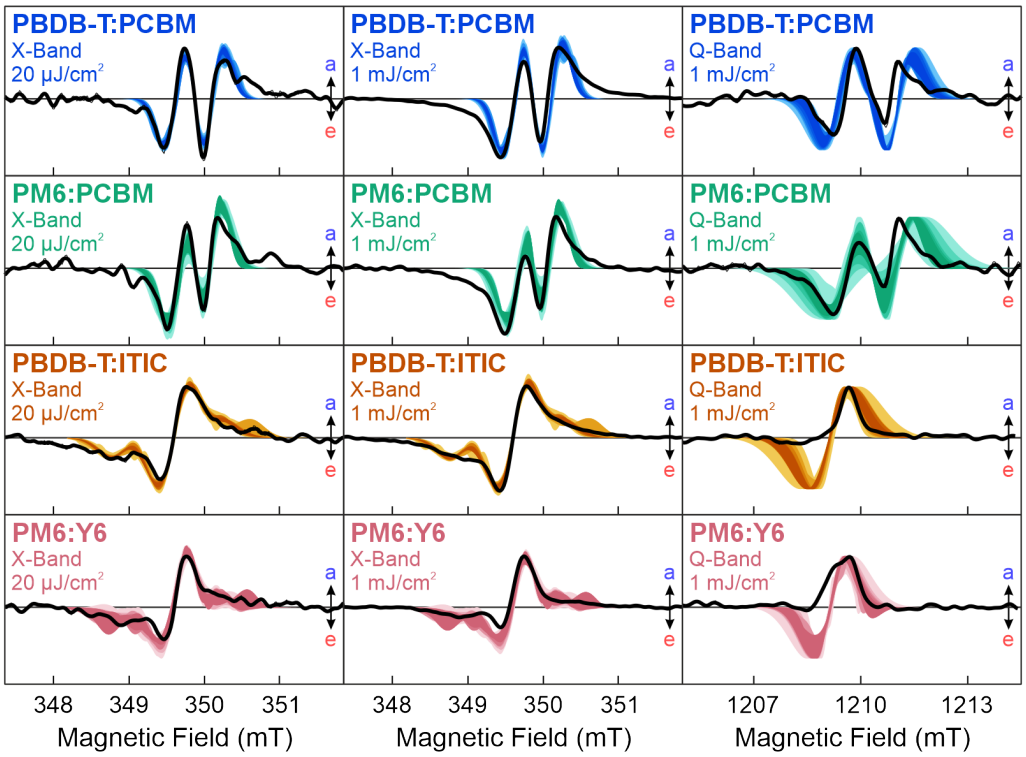

Figure 5.11: Simulated EPR spectra of PBDB-T:PCBM, PM6:PCBM, PBDB-T:ITIC, and PM6:Y6, compared to experimental EPR spectra, extracted at $0.1 - 0.3\,\mu s$, at X- and Q-band, and $20\,\mu J\,cm^{-2}$ and $1\,mJ\,cm^{-2}$. The best 100 fits, sorted by RMSD, are coloured in dark, with worse fits ($N = 500$, 1000, 5000, and 10,000) paler.

agreement with the experiment. Thus, X-band data alone is insufficient to uniquely constrain the spin Hamiltonian parameters.

The inclusion of Q-band spectra provide additional discriminatory power. The higher microwave frequency enhances spectral resolution, making the EPR spectra more sensitive to subtle variations in J and r. This narrows the distribution of acceptable fit parameters and places tighter constraints on the underlying spin interactions. For instance, in the PM6:PCBM blend, only a subset of parameter combinations successfully reproduces the fine structure of the Q-band spectrum, particularly the inner *ea* features of the *eaea*-polarised signal. Simulations with excessively large J and $\boldsymbol{D}$ values result in over-broadened features, failing to match experimental linewidths and relative intensities.

The spin parameter sets extracted from the best-fitting simulated EPR spectra are analysed in Figures 5.12 and 5.13. These figures summarise the distributions of key parameters - donor:acceptor separation r, exchange interaction J, and donor:acceptor spatial orientations - for the parameter sets that best reproduce the experimental spectra. For reference, a secondary axis in the r-distribution plots gives the maximum D-value, D_{max}, under the point-dipole approximation ($D \propto 1/r^3$).

Material	J (MHz)	$D_{\max}$ (MHz)	r (nm)	Linewidth (mT)	
				X-Band	Q-Band
PBDB-T:PCBM	-3.4 ± 1.0	4.7 ± 2.8	2.9 ± 0.6	0.24 ± 0.03	0.61 ± 0.10
PM6:PCBM	-2.1 ± 0.8	5.7 ± 3.4	3.1 ± 0.6	0.24 ± 0.03	0.96 ± 0.13
PBDB-T:ITIC	-4.6 ± 0.7	7.9 ± 2.8	2.7 ± 0.3	0.38 ± 0.02	0.88 ± 0.12
PM6:Y6	-4.6 ± 0.4	11.9 ± 3.7	2.3 ± 0.2	0.25 ± 0.03	0.72 ± 0.14

Table 5.3: Simulation parameters that give the spectral distributions of the best 100 fits shown in Figure 5.11. The error is determined by the standard deviation of each set of parameter values. $D_{\max}$ is determined from the largest principal value of the dipolar interaction, which is calculated from r using the distributed point-dipole model. g-values of the donor and acceptor molecules were determined in Chapter 3 (Tables 3.1 and 3.4 of Section 3.3.1)

For an axial dipolar tensor, $D_{\max}$ corresponds to alignment of the dipolar coupling vector $\boldsymbol{r}$ and the external magnetic field $\boldsymbol{B}_0$ ($\theta = 0°$), and $D = d(1 - 3\cos\theta)$ gives $D = -2d$. The corresponding mean values and standard deviations of the parameters are listed in Table 5.3.

In Figure 5.12, the distributions of r and J values are shown for each blend, with darker colours indicating fits of lower RMSD. A clear distinction emerges between the fullerene acceptor blends (PBDB-T:PCBM and PM6:PCBM) and the non-fullerene acceptor blends (PBDB-T:ITIC and PM6:Y6). The non-fullerene acceptor blends exhibit narrower distributions with shorter donor:acceptor separations and larger exchange interactions, indicative of more strongly bound CT states. In contrast, the fullerene acceptor blends show broader distributions and lower average J, consistent with weaker binding and increased positional disorder.

The average donor:acceptor separation r is approximately 3.0 nm for the fullerene acceptor blends and around 2.5 nm for the non-fullerene acceptor blends. Correspondingly, the magnitude of J increases from around 2 MHz to 5 MHz. These trends reflect enhanced electronic coupling and a more ordered CT state in the non-fullerene acceptor blends. In particular, PM6:Y6 shows sharp peaks in the distributions of both r and J, indicating well-defined CT state geometries.

The relationship between r and J provides further insight into the nature of the CT state. J decays exponentially with r according to $J(r) = J_0 e^{-\beta r}$, where J_0 represents the coupling at vanishing separation and β governs the rate at which the interaction decays with distance.[131,132] Although J_0 and β cannot be extracted from the simulation data, the fitted J and r values can be assessed relative to $J(r)$ decay profiles reported in the literature. For radical pairs in proteins, large values of $J_0 \approx 10^{11}$ MHz and $\beta \approx 14\,\mathrm{nm}^{-1}$ have been reported,[132,317] while organic dyads exhibit smaller values of $J_0 \approx 10^5$ MHz and $\beta \approx 5\,\mathrm{nm}^{-1}$.[316] The values observed in the OPV blends align more closely with the dyad regime, where the exchange

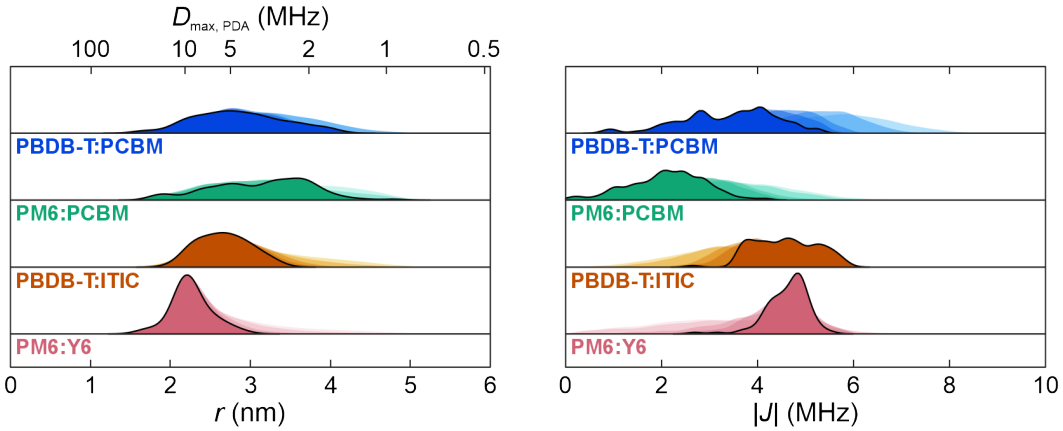

Figure 5.12: Distribution of parameters determining r and J, extracted from the spectral fits in Figure 5.11. The best 100 fits are plotted in dark colours, with worse fits (N = 500, 1000, 5000, and 10,000) in lighter colours. Relative donor:acceptor orientations within the CT state for these distributions of best-fit parameters are displayed in Figure 5.13. Mean and standard deviations of r and J for each blend are summarised in Table 5.3.

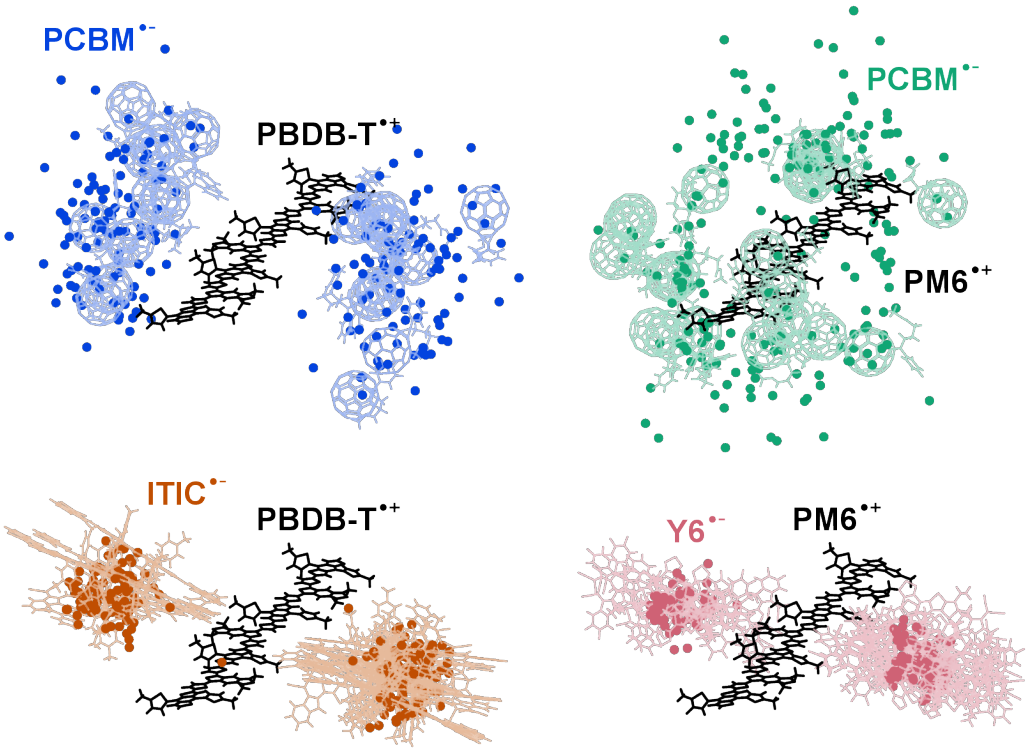

Figure 5.13: Distribution of acceptor positions around the donor for PBDB-T:PCBM, PM6:PCBM, PBDB-T:ITIC, and PM6:Y6. Positions were obtained from the best 100 spectral fits, by RMSD. The truncated trimer structure of the polymer donor is displayed in black, with centres of mass of the acceptors given by the coloured dots; for a subset of spectral fits (best 20), the full structure of the acceptor is also shown.

interaction persists over extended donor:acceptor separations. This behaviour is consistent with substantial wavefunction delocalisation. Time-resolved EPR studies of other OPV blends required exchange couplings of a similar magnitude in order to reproduce the experimental spectra and these were rationalised in terms of extended delocalisation present in organic semiconducting materials.[139]

The donor:acceptor geometries associated with the best-fitting spin parameters are visualised in Figure 5.13. The donor polymer is shown in black, with coloured points indicating the centre of mass of the acceptor molecules from the top 100 parameter sets. Full molecular structures are depicted for the 20 best fits. Importantly, no significant steric clashes or physically unreasonable overlaps between donor and acceptor molecular structures are observed, supporting the physical plausibility of the extracted models. In the fullerene acceptor blends, the acceptor positions are more dispersed and lack strong orientational preference, with only weak side-on bias observed in PBDB-T:PCBM. In contrast, the non-fullerene acceptor blends display more compact and ordered arrangements, with a strong preference for side-on stacking of the acceptor relative to the polymer backbone. Such ordering may be stabilised by intercalation of the acceptor molecules into the side chains of the donor polymer.[318] Stronger ordering, together with the larger exchange couplings and shorter distances observed, points to substantial wavefunction overlap and delocalisation in non-fullerene acceptor blends.

The significance of this delocalisation becomes clear when the donor:acceptor separations are considered in the context of the electrostatic attraction between the two charges. At the distances estimated in Table 5.3, the Coulomb interaction energy between two point charges (assuming a typical dielectric constant of 3 for organic semiconductors)[72] ranges from 210 meV for PM6:Y6 to 150 meV for PM6:PCBM. These values far exceed the available thermal energy of 1.7 meV at 20 K. If charges were confined to localised points, separation would be energetically inaccessible. Delocalisation therefore provides a means to reduce the effective Coulomb interaction and facilitate charge separation, despite the lack of thermal energy.

This functional role of delocalisation is well established in high-efficiency non-fullerene acceptor blends. Delocalisation facilitates hole transport along the polymer backbone and suppresses charge recombination, both of which are crucial for efficient charge separation,[226,319] and therefore delocalisation is widely credited as a key driver of the high efficiencies observed in non-fullerene acceptor blends.[86,87,164,233,320] The simulation results, combined with the characterisation of spin delocalisation in Chapter 3, provide quantitative evidence linking enhanced spin interactions to increased wavefunction delocalisation and spatial ordering in non-fullerene acceptor blends, offering valuable insight into the microscopic origins of their OPV efficiencies.

5.3.4 Modelling the Evolution of Spin Polarisation

Following the characterisation of the early singlet-born CT states, the full time-resolved EPR spectra were modelled in order to understand the subsequent spin dynamics and photophysical pathways in the OPV blends. While the spectral simulations in the previous section provided insight into the static spin-spin interactions and spatial distributions within the bound CT state, the time-resolved EPR spectra contain further information encoded in the evolution of spin polarisation. These dynamics can be used to probe the mechanisms of charge transfer, separation, and recombination - processes central to device performance.

To describe these dynamics, the Liouville-von Neumann formalism implemented within the home-built RADISH simulation framework (Chapter 4) was employed. As in the previous section, the objective was to extract meaningful physical insights while limiting model complexity to prevent overfitting.

The Hamiltonian parameters, describing the static spin interactions, were fixed using the results of earlier characterisation. The g-values and hyperfine couplings of the donor and acceptor charges were taken from steady-state EPR in Chapter 3, while the spin-spin interaction parameters J and $\boldsymbol{D}$, as well as the g- and D-frames, were taken from the simulations of the singlet-born CT state in the preceding section. Mean values from the best-fitting distributions shown in Table 5.3 of the previous section were used for the spin-spin interaction parameters.

The spin dynamics were simulated using the kinetic model described in Chapter 4. The initial population of the system is distributed between the CT state and SCs, defined by p_{CT} and $p_{\mathrm{SC}} = 1 - p_{\mathrm{CT}}$. The CT state is formed from dissociation of singlet excitons ($\mathrm{S}_1 \rightarrow ({}^1\mathrm{CT} \leftrightarrow {}^3\mathrm{CT})$), while SCs present at $t = 0$ are populated via ultrafast charge separation ($\mathrm{S}_1 \rightarrow {}^1\mathrm{CT} \rightarrow \mathrm{SC}$), via a CT state which is too short-lived to undergo significant singlet-triplet mixing.[142]

The decay of the CT state occurs via spin-selective recombination. Eigenstates with singlet character, $|2\rangle$ and $|3\rangle$, recombine at a rate k_{S}, while all eigenstates also decay via triplet recombination at rate k_{T}. However, based on the absence of a triplet recombination signature in the time-resolved EPR spectra recorded over a wide field range (Section 5.3.1), k_{T} was assumed to be negligible. The separated charges decay at rate k_{dec}, although under open-circuit conditions, no external driving force for charge extraction is present. As such, SC decay was also assumed to be negligible on the EPR timescale. The interconversion between the CT state and SCs is described by k_{diss} (CT dissociation) and k_{enc} (SC re-encounter).

The formation rates of CT (k_{CT}) and SC (k_{SC}) populations from S_1 were not explicitly included as time constants. Singlet exciton lifetime is significantly shorter

than the EPR timescale (sub-nanosecond),[321] and so these processes are assumed to be complete at the start of the experiment, with their relative contributions instead absorbed into the initial population parameter p_{CT}.

Relaxation is incorporated via the longitudinal and transverse relaxation times, T_1 and T_2. To minimise free parameters, it was assumed that the CT state and SCs share the same relaxation times. While T_1 and T_{m} were determined experimentally from inversion recovery and echo decay pulse EPR experiments in Chapter 3 (Section 3.3.2), these measurements reflect the relaxation properties of long-lived, trapped charges. In contrast, the CT state and mobile SCs experience higher local charge densities near the donor:acceptor interface, and therefore their relaxation is expected to occur more rapidly. For this reason, relaxation times were treated as free fit parameters.

The appearance of the transient signal is also determined by experimental settings, which must also be taken into account, as these can influence the appearance of the spectra independently of the underlying spin dynamics. In particular, the quality factor (Q) of the resonator and the strength of the applied microwave field (B_1) affect the shape and rise and decay times of the observed EPR response. A Q-value of 4000 for these measurements was determined experimentally from the resonator profile.

Although B_1 cannot be measured directly during the experiment, its amplitude is determined by the applied microwave power P and the resonator bandwidth $\Delta\omega$ through the relationship:

$$B_1 = \frac{C'}{\sqrt{\Delta\omega}}\sqrt{P} \tag{5.1}$$

where C' is a proportionality constant determined primarily by the resonator geometry but also subject to modification by temperature and sample properties.[322] While values may vary slightly across measurements, B_1 can be assumed to be approximately equivalent across the different blend films studied, as all were prepared under similar conditions and measured using the same resonator set-up.

Microwave excitation leads to coherent precession of the spin magnetisation around the $\boldsymbol{B}_1$ field vector, which can give rise to oscillatory behaviour in the time domain. These modulations, known as Torrey oscillations,[271] manifest as periodic features in the transient EPR signal and are governed by the precession frequency ω_1, which is proportional to B_1. When observable, these oscillations provide a direct method for estimating B_1, as ω_1 can be extracted from the signal via Fourier transform and used to calculate the corresponding B_1 strength.

To determine B_1, time-resolved EPR spectra of PBDB-T:PCBM were recorded at X-band and 20 K under a series of applied microwave powers, as shown in

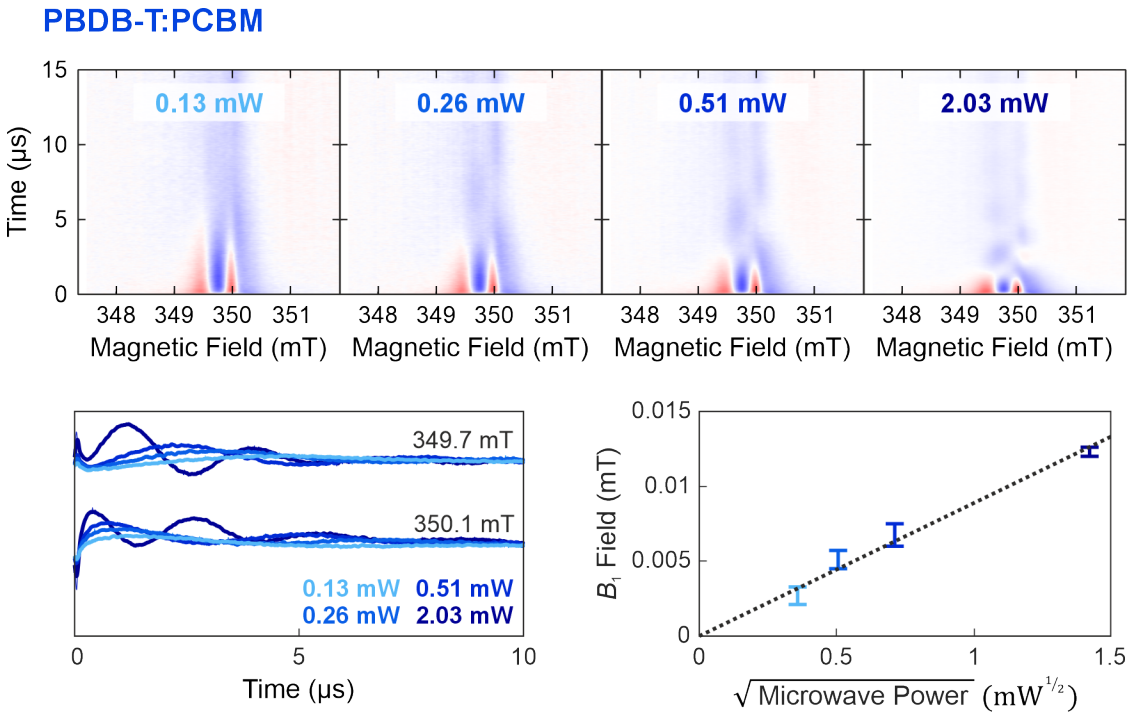

Figure 5.14: Time-resolved EPR spectra of PBDB-T:PCBM, recorded at X-band and 20 K, under varying microwave powers. Transients at 349.7 mT and 350.1 mT reveal Torrey oscillations, whose frequency is proportional to the B_1 field strength. The B_1 amplitude scales linearly with the square root of the applied microwave power.

Figure 5.14. Transients extracted at 349.7 mT and 350.1 mT, corresponding to the PBDB-T$^{\bullet+}$ and PCBM$^{\bullet-}$ resonance positions respectively, display more pronounced oscillations with increasing power. The oscillation frequencies extracted from these transients confirm the expected square root dependence of B_1 on the applied power. Even in cases where Torrey oscillations are not clearly resolved, the influence of B_1 remains significant. If not accounted for properly, these effects may be misinterpreted as accelerated spin relaxation or kinetic decay. Therefore, accurate estimation of the microwave field strength remains essential even when oscillatory features are absent.

To avoid complications from excessive oscillation while maintaining adequate signal intensity, all the time-resolved EPR measurements were conducted at an intermediate microwave power of 0.26 mW. At this power, signal intensity remains sufficient, while distortions due to $\boldsymbol{B}_1$-induced oscillations are minimised. From simulation of the visible modulation frequencies at higher powers and extrapolation to the operating microwave power, the corresponding microwave field strength was estimated to be $B_1 = 0.005$ mT, which was used as an input parameter in the time-resolved EPR simulations.

With prior determination of spin system parameters and experimental contributions accounted for, the overall parameter set required to simulate the full

time-resolved EPR spectrum could be significantly reduced. As a result, only six parameters were varied during simulation: the singlet recombination time, τ_S, the charge separation and recombination time constants, τ_{diss} and τ_{enc}, the initial population ratio of the CT state and SCs, p_{CT}, and the relaxation times, T_1 and T_2. These remaining free parameters were extracted through modelling of the time-resolved EPR spectra.

Given the computational intensity of RADISH simulations, a genetic algorithm fitting approach was not practical. Instead, a staged grid search procedure was performed to systematically explore the parameter space. Coarse grids were first used to locate regions of qualitative agreement between simulated and experimental spectra, which were then refined using successively narrower grids. At each stage, visual inspection of the time-resolved EPR spectra was used to guide the range and resolution of subsequent grids and to assess the quality of the fits.

This approach allows approximate kinetic parameters to be extracted with reasonable confidence. In reality, the experimental spectra are likely to reflect distributions of rates and relaxation times rather than single values. As such, kinetic and relaxation parameters are listed as ranges, outside which key features in the time-resolved EPR spectra are no longer reproduced. Nonetheless, the close match between simulated and observed spectra enables mechanistic conclusions to be drawn. In particular, the dominant pathways of charge transfer, recombination, and separation can be identified, along with characteristic timescales, even where precise parameter values remain uncertain.

To ensure a coherent and consistent interpretation of the underlying photophysical mechanisms, the time-resolved EPR spectra were modelled across a wide set of experimental conditions. This included X-band measurements performed at the different laser fluences and temperatures: 20 K at laser fluences of both $20\,\mu J\,cm^{-2}$ and $1\,mJ\,cm^{-2}$, as well as at higher temperatures of 80 K and 140 K, both at a fluence of $1\,mJ\,cm^{-2}$. By applying the same kinetic model to each dataset, a unified picture of the charge separation and recombination dynamics could be constructed, allowing trends to be identified with greater confidence.

As laser fluence directly influences the photoexcited charge concentration, only those parameters expected to depend on charge density were varied in the fluence-dependent simulations. Accordingly, only the bimolecular re-encounter rate of SCs (k_{enc}) and the relaxation times (T_1 and T_2) were adjusted between fluences. All other parameters were held constant, as they are not expected to change with excitation density. In contrast, for the temperature-dependent measurements, the effect of temperature on spin and kinetic behaviour is less clear and so no assumptions were made: all six parameters were allowed to vary freely.

The discussion of the time-resolved EPR results is divided into two parts, based on the presence or absence of the long-lived absorptive polarisation feature observed in the experimental spectra. The first part focuses on PM6:PCBM, which consistently lacks this feature across all experimental conditions. The second part addresses PBDB-T:PCBM, PBDB-T:ITIC, and PM6:Y6, all of which display a pronounced long-lived absorptive component, indicating more complex charge separation dynamics.

Unidirectional Charge Separation in PM6:PCBM

Simulations of the X-band time-resolved EPR spectra for PM6:PCBM, at the four experimental conditions are displayed in Figure 5.15, alongside the corresponding experimental spectra. Simulated and experimental spectra averaged over short ($0.1 - 0.3\,\mu s$) and long ($10 - 30\,\mu s$) time windows following photoexcitation are also shown. For all conditions, the experimental spectra exhibit a strong, short-lived *eaea* polarisation pattern at early times, that evolves to a very weak signal at longer times. During this evolution, the *eaea* pattern first develops into an *ea*-like polarisation after a few microseconds, with no long-lived absorptive component observed under any of the investigated conditions. All the key spectral features at each condition could be reproduced by the simulated EPR spectra.

The parameters used in these simulations are summarised in Table 5.4, given as ranges over which that parameter can be varied, while still matching the experimental time-resolved EPR spectra. Further details on the individual contributions of the CT state and SC spin polarisations to each simulated spectrum, as well as the time evolution of their overall and spin sublevel populations, are provided in Appendix F. At 20 K, EPR spectra measured at low and high laser fluence could be described by the same parameters, indicating that charge separation and recombination in PM6:PCBM is largely fluence-independent.

PM6:PCBM

Temp. (K)	Fluence ($mJ\,cm^{-2}$)	p_{CT}	τ_S (µs)	τ_{diss} (µs)	T_1 (µs)	T_2 (µs)
20	0.02	1	$20 - 30$	$10 - 30$	> 50	$0.5 - 1.0$
20	1	1	$20 - 30$	$10 - 30$	> 50	$0.5 - 1.0$
80	1	1	> 2	$1 - 2$	$5 - 50$	$0.2 - 0.5$
140	1	1	> 1	$0.2 - 0.5$	$1 - 5$	$0.05 - 0.1$

Table 5.4: Simulation parameters for PM6:PCBM for the time-resolved EPR simulations in Figure 5.15. The rate constants k_T, k_{enc}, and k_{dec} were assumed to be negligible, and so the time constants τ_T, τ_{enc}, and τ_{dec} are set to very large.

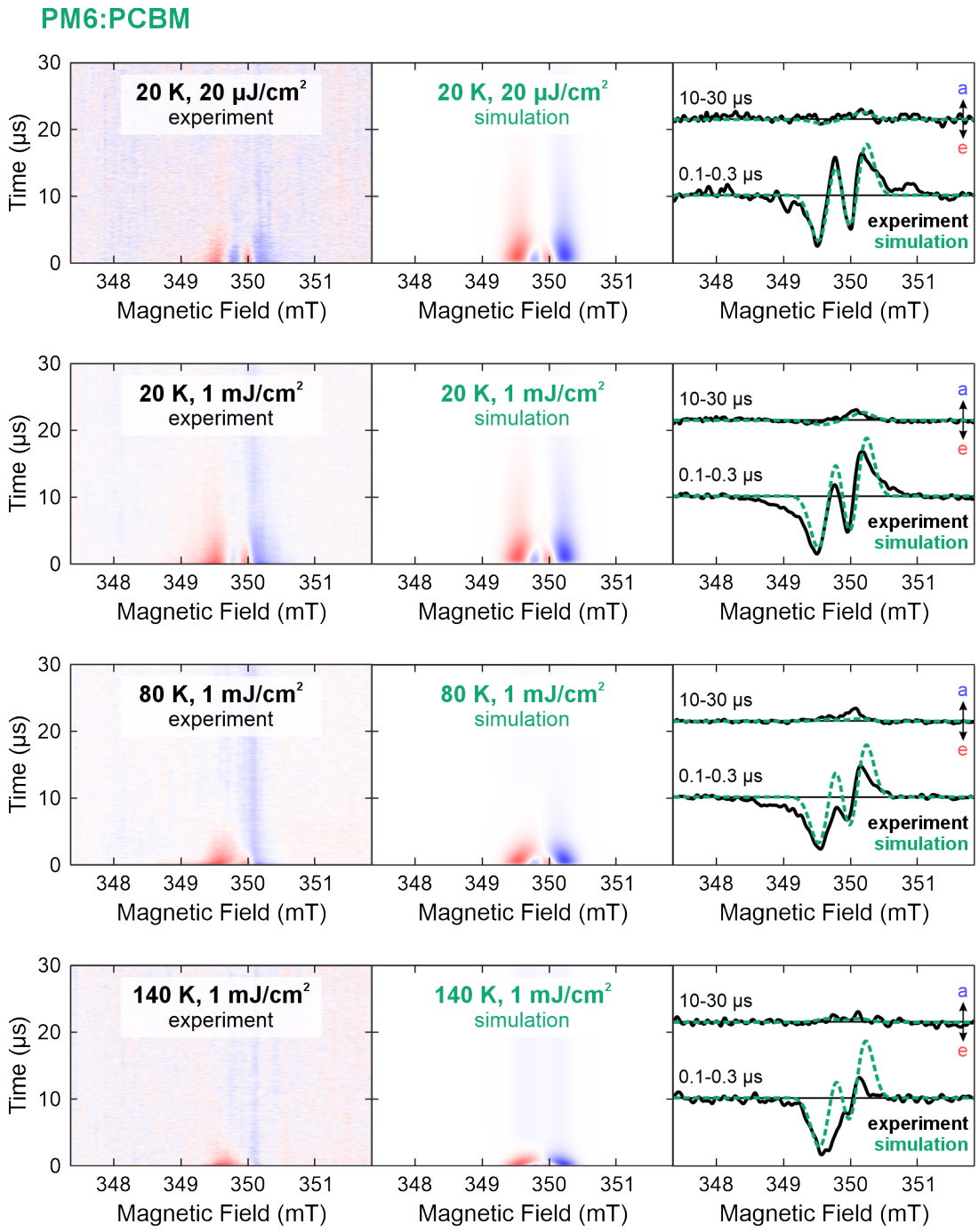

Figure 5.15: Comparison of experimental and simulated time-resolved EPR X-band spectra of PM6:PCBM, for different laser fluences ($20\,\mu J\,cm^{-2}$ and $1\,mJ\,cm^{-2}$) and temperatures (20 K, 80 K, and 140 K). Averaged spectra at short ($0.1 - 0.3\,\mu s$) and long ($10 - 30\,\mu s$) times after photoexcitation are also shown.

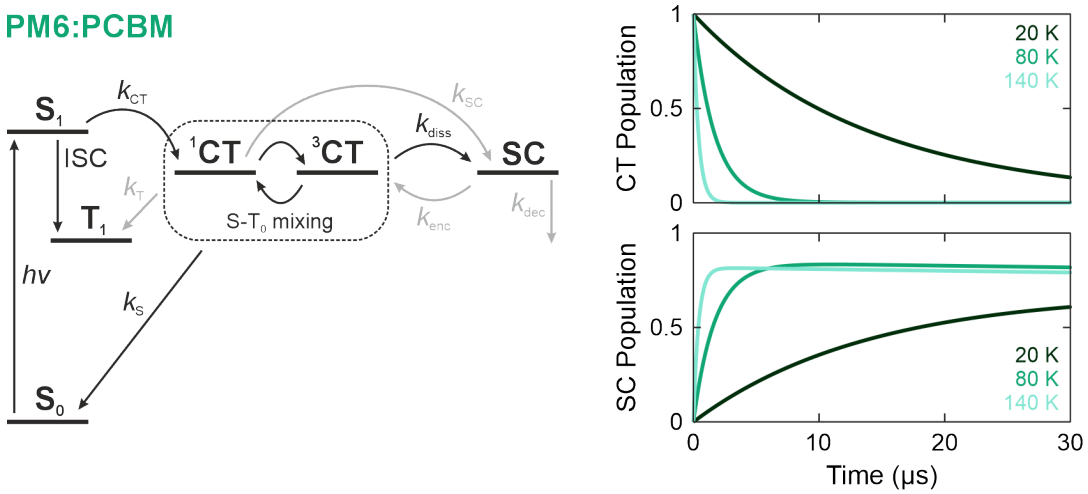

Figure 5.16: (Left) Predicted photophysical mechanism for PM6:PCBM. (Right) Evolution of the populations of the charge-transfer state and separated charges, at 20 K, 80 K, and 140 K.

The photophysical mechanism that best describes PM6:PCBM is illustrated in Figure 5.16, along with the CT state and SC populations extracted from the simulations for each temperature. Following photoexcitation, the singlet exciton dissociates into CT states at the donor:acceptor interface. These CT states either dissociate to form separated charges following spin-mixing (with time constant τ_{diss}) or recombine to the ground state (with time constant τ_{S}). The resulting SCs are long-lived but very weakly-polarised, which accounts for the negligible spectral intensity at later times. As temperature increases, both dissociation and recombination processes speed up, leading to a faster loss of CT state polarisation and earlier SC formation, as observed in the population plots. In addition, the longitudinal relaxation time T_1 decreases, promoting thermal equilibration within the CT state and SC spin sublevels and giving rise to a weak absorptive signal in the long-time spectra.

The initial evolution of the singlet-born CT state *eaea* polarisation to an *ea*-polarised signal indicates transfer of spin polarisation from the CT state to the SCs. For this to occur, the rate of CT state dissociation must outcompete its recombination to the ground state ($\tau_{\mathrm{diss}} < \tau_{\mathrm{S}}$). If singlet-selective recombination was dominant, then the spin polarisation passed on to the SCs would be far less polarised and the *ea* signal would not be as strong. Together, these results support a simple unidirectional charge separation mechanism in PM6:PCBM:

$$\mathrm{S}_1 \rightarrow \mathrm{CT} \rightarrow \mathrm{SC}$$

This kinetic scheme successfully reproduces all the key features observed in the experimental time-resolved EPR spectra. Since each step in the process is monomolecular, the dynamics of spin polarisation remain unaffected by changes in excitation fluence, consistent with the fluence-independent spectral evolution observed experimentally.

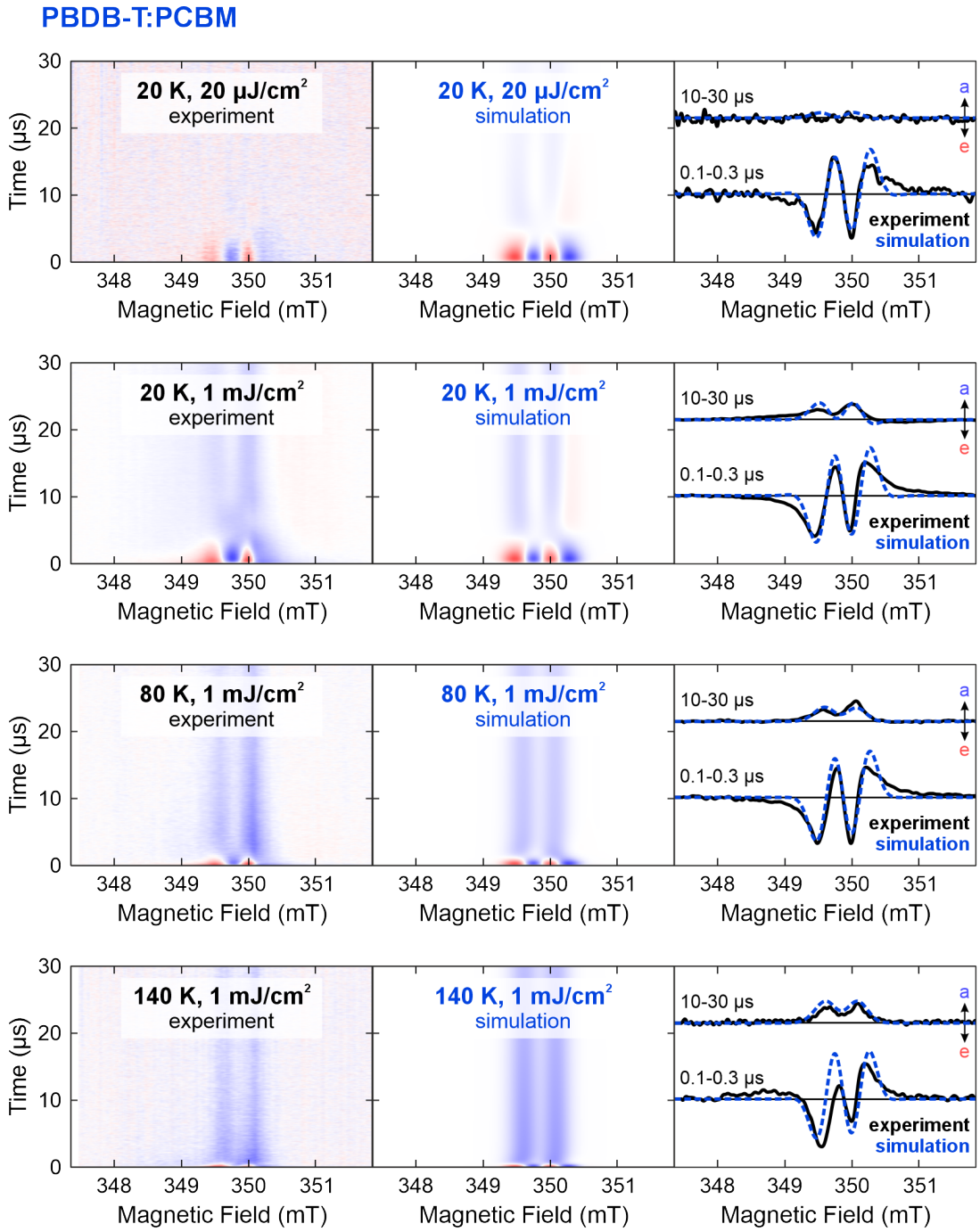

Figure 5.17: Comparison of experimental and simulated time-resolved EPR X-band spectra of PBDB-T:PCBM, for different laser fluences ($20\,\mu J\,cm^{-2}$ and $1\,mJ\,cm^{-2}$) and temperatures (20 K, 80 K, and 140 K). Averaged spectra at short ($0.1 - 0.3\,\mu s$) and long ($10 - 30\,\mu s$) times after photoexcitation are also shown.

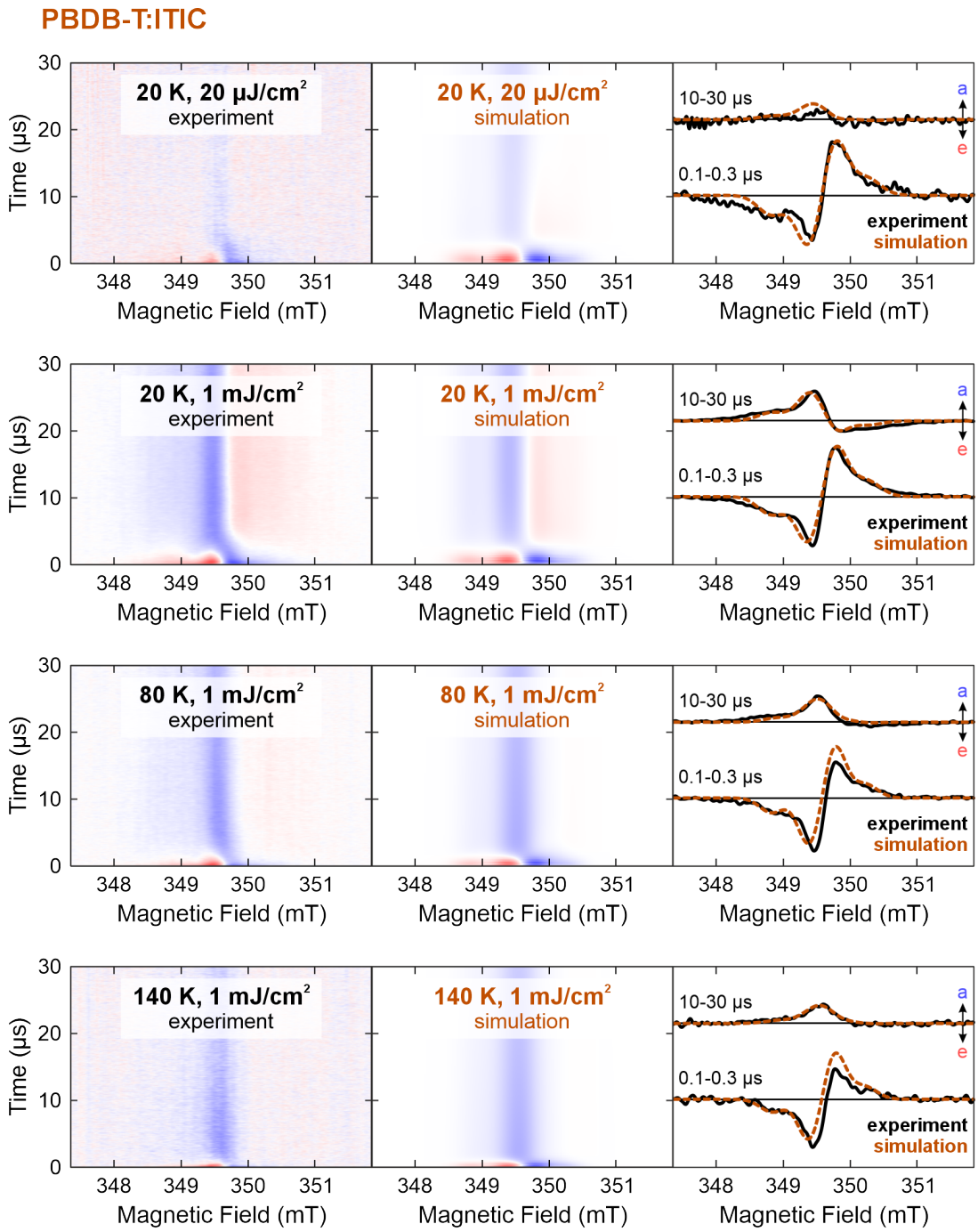

Figure 5.18: Comparison of experimental and simulated time-resolved EPR X-band spectra of PBDB-T:ITIC, for different laser fluences ($20\,\mu J\,cm^{-2}$ and $1\,mJ\,cm^{-2}$) and temperatures (20 K, 80 K, and 140 K). Averaged spectra at short ($0.1 - 0.3\,\mu s$) and long ($10 - 30\,\mu s$) times after photoexcitation are also shown.

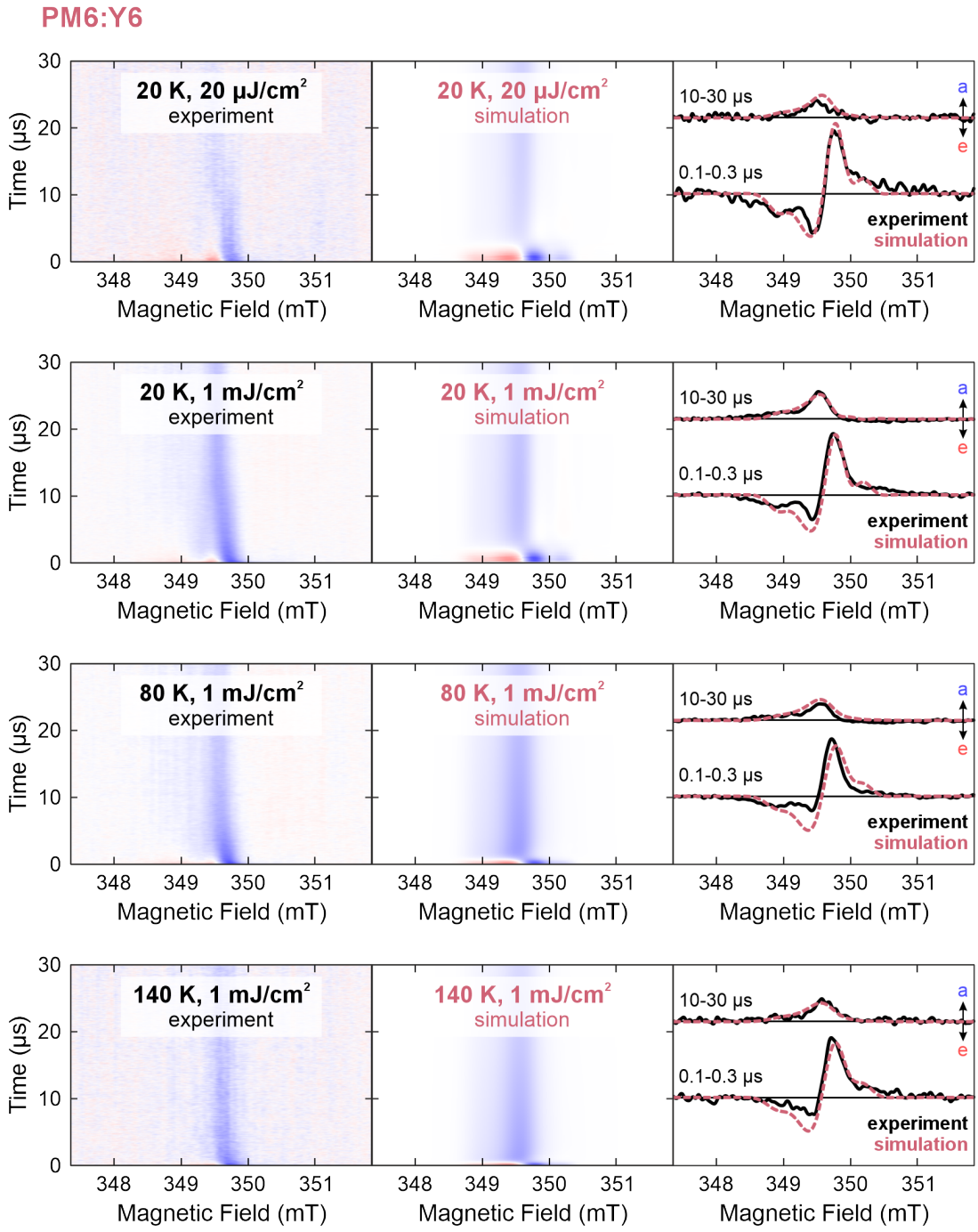

Figure 5.19: Comparison of experimental and simulated time-resolved EPR X-band spectra of PM6:Y6, for different laser fluences ($20\,\mu J\,cm^{-2}$ and $1\,mJ\,cm^{-2}$) and temperatures (20 K, 80 K, and 140 K). Averaged spectra at short ($0.1 - 0.3\,\mu s$) and long ($10 - 30\,\mu s$) times after photoexcitation are also shown.

PM6:PCBM

Temp. (K)	Fluence ($mJ\,cm^{-2}$)	p_{CT}	τ_S (µs)	τ_{diss} (µs)	τ_{enc} (µs)	T_1 (µs)	T_2 (µs)
20	0.02	1	$20-30$	$10-30$	>200	>50	$0.5-1.0$
20	1	1	$20-30$	$10-30$	>200	>50	$0.5-1.0$
80	1	1	>2	$1-2$	>200	$5-50$	$0.2-0.5$
140	1	1	>1	$0.2-0.5$	>200	$1-5$	$0.05-0.1$

PBDB-T:PCBM

Temp. (K)	Fluence ($mJ\,cm^{-2}$)	p_{CT}	τ_S (µs)	τ_{diss} (µs)	τ_{enc} (µs)	T_1 (µs)	T_2 (µs)
20	0.02	$0.25-0.35$	$2-6$	$10-20$	>200	>50	$0.5-1.0$
20	1	$0.25-0.35$	$2-6$	$10-20$	$40-60$	$10-20$	$0.5-1.0$
80	1	$0.2-0.3$	$0.5-2$	$1-5$	$10-30$	$1-5$	$0.1-0.4$
140	1	$0.2-0.25$	$0.2-2$	$0.5-2$	>10	$0.5-2$	$0.05-0.1$

PBDB-T:ITIC

Temp. (K)	Fluence ($mJ\,cm^{-2}$)	p_{CT}	τ_S (µs)	τ_{diss} (µs)	τ_{enc} (µs)	T_1 (µs)	T_2 (µs)
20	0.02	$0.3-0.4$	$0.2-0.8$	$15-30$	>200	$20-100$	$0.5-1.0$
20	1	$0.3-0.4$	$0.2-0.8$	$15-30$	$15-30$	$10-25$	$0.5-1.0$
80	1	$0.15-0.25$	$0.2-0.8$	$1-4$	$10-20$	$2-10$	$0.1-0.5$
140	1	$0.15-0.25$	$0.2-0.8$	$0.5-1$	$10-20$	$0.5-2$	$0.05-0.1$

PM6:Y6

Temp. (K)	Fluence ($mJ\,cm^{-2}$)	p_{CT}	τ_S (µs)	τ_{diss} (µs)	τ_{enc} (µs)	T_1 (µs)	T_2 (µs)
20	0.02	$0.3-0.4$	$0.1-0.5$	$1-10$	$30-50$	$10-25$	$0.5-1.0$
20	1	$0.3-0.4$	$0.1-0.5$	$1-10$	$20-40$	$5-20$	$0.5-1.0$
80	1	$0.15-0.25$	$0.1-0.5$	$0.5-3$	$10-30$	$2-10$	$0.1-0.4$
140	1	$0.15-0.25$	$0.1-0.5$	<1	$10-20$	$1-4$	$0.05-0.2$

Table 5.5: Simulation parameters for PM6:PCBM, PBDB-T:PCBM, PBDB-T:ITIC, and PM6:Y6 for the time-resolved EPR simulations in Figures 5.15 and 5.17 to 5.19. The rate constants k_T, and k_{dec} were assumed to be negligible, and so the time constants τ_T, and τ_{dec} are set to very large.

Ultrafast Charge Separation and Equilibrium with Separated Charges in PBDB-T:PCBM, PBDB-T:ITIC, and PM6:Y6

On the other hand, the time-resolved EPR spectra of PBDB-T:PCBM and the non-fullerene acceptor blends PBDB-T:ITIC and PM6:Y6 require a more complex kinetic model to explain their EPR behaviour. The simulations of the X-band time-resolved EPR spectra for these three blends, under the various experimental conditions, are shown in Figures 5.17 to 5.19, alongside the corresponding experimental spectra. Averaged spectra over short ($0.1 - 0.3\,\mu s$) and long ($10 - 30\,\mu s$) time windows following photoexcitation are also included.

All three blends exhibit a short-lived singlet-born CT state, which evolves into a predominantly absorptive signal at longer delay times. Unlike PM6:PCBM, clear differences in time-resolved EPR spectra emerge under varying laser fluence: the intensity of the long-lived absorptive feature increases with fluence. In some cases, particularly for PBDB-T:ITIC at 20 K and $1\,mJ\,cm^{-2}$, a high-field emissive component is also present at long times. The simulations capture the key features: the initial *eaea* polarisation, its lifetime and evolution, and the shape and relative intensity of the long-lived signal. Simulation parameter ranges for each blend and condition are listed in Table 5.5. Further details, including individual CT and SC contributions to the overall signal, are included in Appendix F.

Compared to PM6:PCBM, the main differences in kinetics for PBDB-T:PCBM, PBDB-T:ITIC, and PM6:Y6 are a proportion of charges undergoing ultrafast charge separation ($p_{SC} = 1 - p_{CT} > 0$) and a non-negligible re-encounter rate of these charges (τ_{enc}). Both are essential to generate the long-lived absorptive feature.

The influence of p_{CT} on the long-time EPR signal ($10 - 30\,\mu s$) is shown in Figure 5.20, where experimental spectra at 20 K and $1\,mJ\,cm^{-2}$ are compared with simulations at varying p_{CT}. A value of $p_{CT} = 0.3$ falls within the range extracted for all three blends (Table 5.5). The early-time spectra ($0.1 - 0.3\,\mu s$) remain unaffected by changes in p_{CT}, as they are dominated by the polarised singlet-born CT state. In contrast, the intensity of the long-lived feature is sensitive to p_{CT}: increasing it to 0.5 reduces ultrafast separation, lowering the SC contribution and thus the long-lived signal intensity, while decreasing p_{CT} to 0.2 enhances ultrafast charge separation, exaggerating the absorptive contribution. This sensitivity constrains the acceptable range of p_{CT} values needed to reproduce experimental spectra.

The spectral shape of the EPR signal at long times ($10 - 30\,\mu s$) is governed by the equilibrium between the charge-transfer state and the separated charges, quantified by the equilibrium constant:

$$K = \frac{k_{diss}}{k_{enc}} = \frac{\tau_{enc}}{\tau_{diss}} \tag{5.2}$$

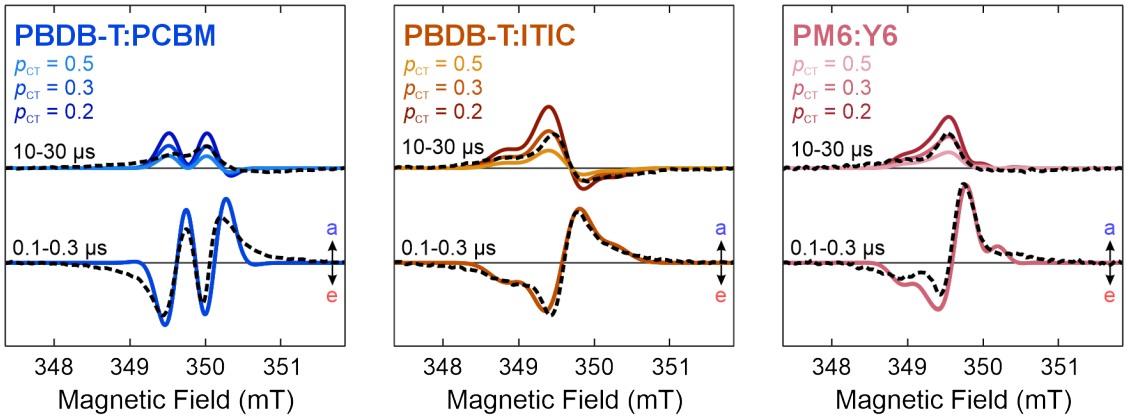

Figure 5.20: Effect of the extent of ultrafast charge separation, relative to formation of singlet-born CT states, as governed by p_{CT}. A smaller p_{CT} corresponds to a greater number of excitons going through the ultrafast charge separation channel. Simulated EPR spectra, at 20 K and 1 mJ cm^{-2}, are compared to experimental spectra at short (0.1 – 0.3 µs) and long (10 – 30 µs) times after photoexcitation, for different p_{CT} values.

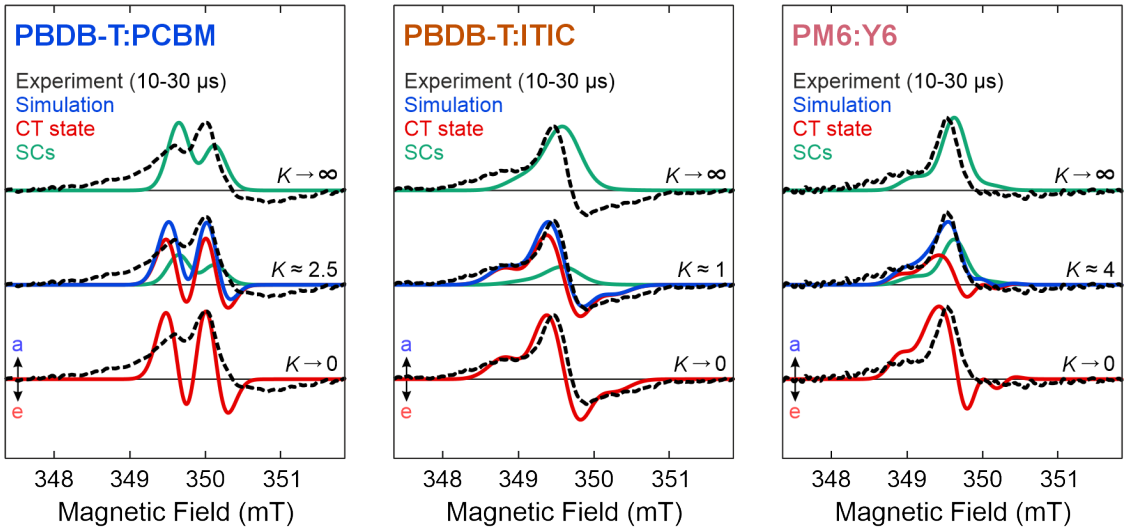

Figure 5.21: Effect of the CT – SC equilibrium constant, governed by τ_{diss} and τ_{enc}, on the spectral shape at long (10 – 30 µs) times after photoexcitation. Simulated EPR spectra are shown, at 20 K and 1 mJ cm^{-2}, for the K used in the time-resolved EPR simulations in Figures 5.17 to 5.19, as well as K values at either extreme: $K \to \infty$ ($\tau_{enc} \gg \tau_{diss}$) and $K \to 0$ ($\tau_{enc} \ll \tau_{diss}$).

The impact of this equilibrium on the long-time EPR spectra is shown in Figure 5.21. Experimental X-band spectra (20 K, 1 mJ cm^{-2}) are compared to simulated spectra using the K values calculated from Table 5.5, alongside simulations for the limiting cases: $K \to \infty$, where charge separation is irreversible, and $K \to 0$, where the CT state is unable to dissociate. In all blends, simulations with $K \to \infty$ fail to reproduce the correct spectral shape, with the absorptive features shifted to higher field positions. This confirms that inclusion of charge re-encounter is a requisite to capture the shape of the experimental EPR spectra.

The relative signal contributions of the CT state and SCs vary with K. When $K \gg 1$ ($\tau_{\text{enc}} \gg \tau_{\text{diss}}$), only SCs are present, and the spectrum resembles the echo-detected EPR spectra of the steady-state charges in Chapter 3 (Section 3.3.1): two absorptive peaks centred at the g-values of the donor and acceptor. When $K \ll 1$ ($\tau_{\text{enc}} \ll \tau_{\text{diss}}$), the CT state polarisation is dominant. Recombination of the CT state is singlet-selective ($\tau_{\text{S}} \ll \tau_{\text{T}}$) for the OPV blends and the CT sublevels $|2\rangle$ and $|3\rangle$ will be selectively depopulated, resulting in a flipped *aeae*-polarised CT state. Therefore, K controls whether the long-time spectrum is predominantly absorptive ($K \gg 1$) or shows residual emissive features from the CT state ($K \leq 1$). Among the studied blends, PBDB-T:ITIC displays the most prominent high-field emissive contribution, consistent with a more CT-like equilibrium ($K \approx 1$), while PM6:Y6 lies further towards SCs ($K \approx 4$).

Beyond the influence of p_{CT} on relative intensity and K on spectral shape, the longitudinal relaxation time T_1 also influences the long-time EPR signal. Simulations required T_1 values of tens of microseconds to reproduce the observed thermal polarisation in the CT state and SCs. These are shorter than the steady-state T_1 values measured by the inversion recovery pulse EPR experiments in Chapter 3 (Section 3.3.2). The values determined in pulse EPR experiments reflect the relaxation behaviour of trapped, long-lived SCs under steady-state conditions, whereas the simulated dynamics involve mobile charges at high local concentrations near the donor:acceptor interface. The higher charge concentration should increase the number of spin-spin interactions, facilitating relaxation towards thermal equilibrium and leading to shorter T_1 values. The qualitative trend of decreasing T_1 with increasing temperature observed in the inversion recovery experiment is also captured in the simulation results, supporting the consistency of trends in relaxation times despite differences in absolute values.

An unexpected observation is the lack of temperature dependence in the singlet CT recombination time, τ_{S}, for the non-fullerene acceptor blends. Singlet CT recombination can proceed to any singlet state, not just S_0. It has been proposed that the small energetic offset between S_1 and CT may facilitate reversible equilibrium or hybridisation between the states.[81,323,324] Thus, τ_{S} may include decay to S_0 and

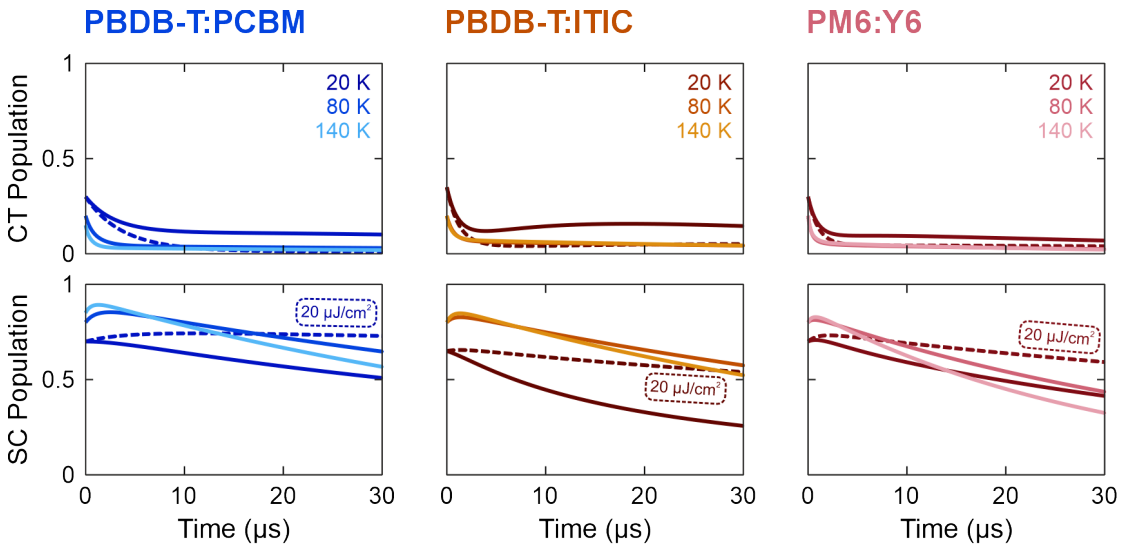

Figure 5.22: Evolution of the populations of the charge-transfer state and separated charges for PBDB-T:PCBM, PBDB-T:ITIC, and PM6:Y6, at 1 mJ cm^{-2}, and 20 K, 80 K, and 140 K. The population evolution for 20 µJ cm^{-2} and 20 K is also shown, as dashed lines.

also reverse electron transfer to S_1, which is inaccessible in fullerene acceptor blends, but accessible in non-fullerene acceptor blends, given the small energetic offset.

The time evolution of CT and SC populations is presented in Figure 5.22, for temperatures of 20 K, 80 K, and 140 K. Simulations corresponding to low-fluence measurements (20 K, 20 µJ cm^{-2}) are shown as dashed lines. All three donor:acceptor blends exhibit similar kinetic behaviour. Immediately after photoexcitation, approximately $60 - 80\%$ of charges are generated via ultrafast charge separation; this can be seen in the figure from the SC population at $t = 0$. These SCs remain in dynamic equilibrium with interfacial CT states, which persist with a small but non-negligible steady-state population over microsecond timescales. At lower excitation fluence, reduced bimolecular recombination and fewer re-encounters lead to a smaller CT steady-state population, as reflected in the decreased signal intensity of the long-time spectral features.

With clear signatures of ultrafast charge separation and an equilibrium between the CT state and SCs, the kinetic mechanism of PBDB-T:PCBM, PBDB-T:ITIC, and PM6:Y6 can be summarised by the kinetic scheme shown in Figure 5.23. Two channels of charge separation are proposed:

1. **Ultrafast charge separation**: $S_1 \rightarrow {}^1\text{CT} \rightarrow \text{SC}$ with k_{CT} and k_{SC}.
2. **Slow charge separation**: $S_1 \rightarrow ({}^1\text{CT} \leftrightarrow {}^3\text{CT}) \rightarrow \text{SC}$ with k_{CT} and k_{diss}.

In the ultrafast channel, the CT state must dissociate before significant spin mixing has had a chance to occur, therefore no significant singlet-born spin

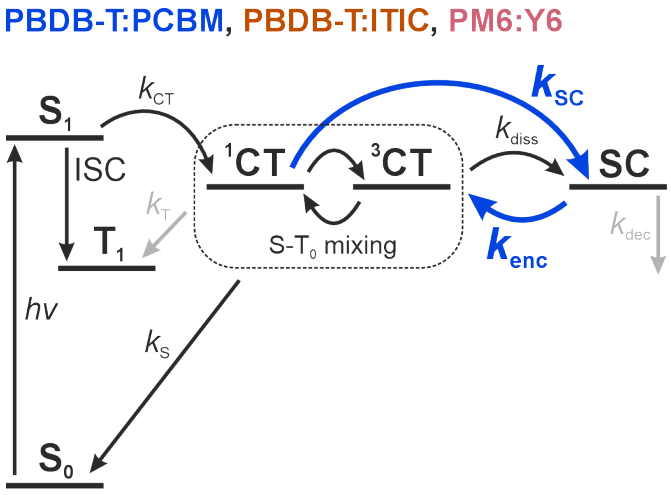

Figure 5.23: Predicted photophysical mechanism for PBDB-T:PCBM, PBDB-T:ITIC, and PM6:Y6. The key differences compared to PM6:PCBM are: ultrafast charge separation (^{1}CT $\rightarrow$ SC with k_{SC}) and re-encounter of separated charges (SC $\rightarrow$ CT with k_{enc}).

polarisation is built up,[142] which would otherwise be detectable by EPR. The slower channel, active on the microsecond timescale at low temperature, involves singlet-triplet mixing in the CT state before eventual charge separation. This dual-pathway mechanism aligns with recent findings by Moore et al., who identified both charge separation channels occurring in a fullerene acceptor OPV blend through optical spectroscopy.[282]

The relative donor:acceptor positions within the CT state, estimated in Section 5.3.3 (see Figure 5.13), can be rationalised within the model of two modes of charge separation. For PBDB-T:PCBM, PBDB-T:ITIC, and PM6:Y6, the CT state *eaea* polarisation could only be recreated for acceptor molecules lying side-on to the polymer π-system. For PM6:PCBM, there was no observed positional preference. The molecular orientations were obtained from modelling of the observable singlet-born CT state EPR signal. As a result, these obtained positions correspond to positions that undergo slow charge separation after spin mixing. Relative donor:acceptor positions that do not produce the *eaea* polarisation may therefore correspond to CT states that undergo ultrafast charge separation. The donor and acceptor molecules in non-fullerene acceptor blends are known to $\pi - \pi$ stack,[46,325] which enables significant wavefunction overlap and enhanced delocalisation, reducing the Coulombic attraction of the CT state that hinders efficient charge separation.[76,86,173,326] For PM6:PCBM, the absence of ultrafast charge separation in the time-resolved EPR data aligns with the random distribution of PCBM$^{\bullet-}$ around PM6$^{\bullet+}$.

Re-encounter of SCs to reform CT states is not an intuitively expected beneficial process in high-performance OPVs, as efficient devices ideally generate charges that

are then extracted at the electrodes. However, this re-encounter of SCs to reform CT states may play an important role in preventing charges from recombining to the ground state. It has been shown that reformation of the CT state from SCs together with fast CT dissociation lowers the steady-state CT density, reducing recombination loss pathways to the ground state or triplet state.[99–101] Fast dissociation of the CT state is observed for the non-fullerene acceptor blends studied, which is a requirement for efficient charge generation,[102] while the most efficient OPV blend PM6:Y6 exhibited the lowest steady-state CT density at equilibrium ($K \approx 4$ at 20 K).

These results provide the first full characterisation of the cause of the long-lived predominantly absorptive feature at long times after photoexcitation for donor:acceptor OPV blends. Whilst the CT state and SCs of the blends studied here have not been characterised before, an older benchmark fullerene acceptor blend, P3HT:PCBM, has been studied by time-resolved EPR before in the literature. An absorptive feature was observed at long times after photoexcitation, with tentative assignment either to thermalised SCs,[175] or very fast relaxation of the CT state.[256] The modelling procedure described in this chapter was successfully applied to time-resolved EPR measurements of P3HT:PCBM, shown in Appendix G. The long-lived absorptive feature, and its fluence- and temperature-dependence were all explainable within the bimodal charge separation model, with a CT − SC equilibrium constant that lies towards the CT state ($K \approx 1$ at 20 K) and preferential acceptor geometry above and below the polymer backbone in a $\pi - \pi$ fashion.

5.4 Conclusions

This chapter provided a comprehensive investigation into the charge transfer and separation dynamics for a series of donor:acceptor OPV blends using time-resolved EPR spectroscopy. By capturing the evolution of spin-polarised states across a range of fluences and temperatures, the dynamic roles of charge-transfer states and separated charges at the donor:acceptor interface were revealed. A central outcome is the unambiguous identification of CT states formed directly from the singlet exciton across all conditions studied due to the distinctive *eaea/ea* spin signature, an assignment that is often difficult to establish using optical methods alone.

Detailed characterisation of the molecular order within the CT state, including donor:acceptor orientations and spatial separations, revealed differences between the highest and lowest performing OPV blends. A more ordered CT state, with significant delocalisation, correlated with increased power conversion efficiency. Through comprehensive modelling of the time-resolved spectra, two distinct charge separation channels were identified: one ultrafast and one occurring on the microsecond timescale. Donor and acceptor molecules stacked in a $\pi - \pi$ formation,

maximising wavefunction overlap, can be linked to the charges that undergo the ultrafast, and not the microsecond, charge separation channel. Promoting $\pi - \pi$ stacking at the donor:acceptor interface, whilst maintaining charge delocalisation within both donor and acceptor molecules, may help optimise this ultrafast pathway.

Beyond their immediate relevance to the systems investigated, these findings have broader implications for the design and interpretation of high-efficiency organic photovoltaic materials. The suppression of intersystem crossing in non-fullerene acceptor blends underlines the importance of reducing triplet exciton formation for efficient charge generation. The discovery of a dynamic equilibrium between CT states and SCs, previously assumed to be unidirectional, reframes recombination as a manageable loss process rather than an unavoidable fate. These results demonstrate the unique strengths of time-resolved EPR in accessing the spin-dependent dynamics that underpin charge generation and recombination, offering a powerful spectroscopic lens for probing processes that are otherwise invisible to conventional methods.

Chapter 6

The Role of Trapped Charges

6.1 Introduction

The previous chapter demonstrated how time-resolved EPR can provide detailed insight into the processes underlying charge separation and recombination in OPV blends. By capturing the evolution of spin-polarised states over microsecond timescales, it was possible to characterise charge-transfer (CT) states, identify distinct separation pathways, and understand the interplay between bound and separated charges (SCs). However, key processes relevant to device efficiency, such as long-lived charge dynamics and trapping, may extend beyond the temporal reach of a time-resolved EPR experiment.[81,327,328]

In particular, the observation of steady-state signals in pulse EPR measurements in Chapter 3 suggests that a significant population of photogenerated charges persists for milliseconds or longer after photoexcitation. Understanding the role of these long-lived species and how they interact with the primary charge separation mechanism is essential for a full picture of OPV photophysics. Therefore, pulse EPR techniques were applied in a time-resolved fashion with the aim to distinguish between transient and long-lived species. Unlike standard continuous-microwave

time-resolved EPR, which suffers from low-frequency noise, laser instability, and baseline drift at delay times beyond tens to hundreds of microseconds,[138] pulse EPR offers a more stable platform for investigating long-lived states. This expanded timescale access allows for the direct tracking of charge populations and their relaxation behaviour over a far longer window, linking early-time photophysics to long-time behaviour and charge trapping.

Through carefully designed pulse EPR experiments, the relative contribution of any long-lived trapped charges can be quantified, and their potential influence on the photophysical processes explored. As shown by time-resolved EPR results in Chapter 5, high-performing OPV blends can exhibit an equilibrium between CT states and free charges. If trapped charges can be thermally reactivated, which depends on the energetic depth of the trap site relative to the available thermal energy, then they may participate in delayed recombination and rejoin the equilibrium. Time-resolved pulse EPR can detect both short- and long-lived species, enabling direct investigation of their interplay and clarifying the extent to which trap-mediated kinetics affect OPV performance.

First, echo-detected EPR was used to characterise the energetic disorder of trap states in PBDB-T:PCBM, PM6:PCBM, PBDB-T:ITIC, and PM6:Y6. At 20 K, a large fraction of donor and acceptor SCs were found to be deeply trapped. These long-lived species contributed a stronger net magnetisation than the transient CT and SC species observed in time-resolved EPR. At higher temperatures, the population of photoinduced trapped charges decreases, suggesting that thermal activation may allow them to participate in the CT − SC equilibrium under operational conditions.

In order to isolate short-lived, spin-polarised species from thermalised trapped charges, two separation strategies were tested. Pulse EPR spectra were recorded as a function of time after laser excitation and difference spectra were calculated by subtraction to reveal additional contributions at long delay times that differ from the states observed by time-resolved EPR in Chapter 5, indicating that the steady-state signal is itself perturbed by the presence of transient species. A second approach employed a microwave pulse preceding laser excitation to suppress the contribution of long-lived states to the echo signal. The transient signal isolated via this method exhibited the same spin polarisation as that observed by time-resolved EPR, confirming that the suppression pulse method reliably separates short-lived transient species. The differences between the results obtained by the subtraction and suppression methods were attributed to charge detrapping via exciton quenching, leading to an additional loss mechanism in which trapped charges interact with nearby excitons, reducing efficiency by preventing interfacial charge transfer for some of the photoinduced excitons.

6.2 Experimental Methods

6.2.1 Sample Preparation

The same film samples of PBDB-T:PCBM, PM6:PCBM, PBDB-T:ITIC, and PM6:Y6 as described in Chapter 3, prepared using the method described in Section 3.2.1, were used.

6.2.2 EPR Experiments

X- and Q-band pulse EPR measurements were performed using the same set-up as for the steady-state EPR measurements in Chapter 3 (Section 3.2.2), with the same laser excitation settings as described in Chapter 5 (Section 5.2.2) for the time-resolved EPR measurements. Synchronisation of the laser, the microwave pulses and the detection was achieved through a Stanford Research System digital delay generator (DG645). Measurements were also performed with the pulsed laser not synchronised with the spectrometer to mimic steady-state conditions, after verifying that this type of illumination returned equivalent echo-detected EPR spectra to measurements performed using continuous white-light illumination with a Schott DCR III 150 W halogen light source. A field calibration using the known N@C_{60} g-value[150] was carried out prior to measurements at all frequency bands. All pulse EPR spectra were recorded as echo-detected field sweeps, using the pulse sequences described in Figure 6.1. All pulses were programmed using an Arbitrary Waveform Generator to minimise distortions of the pulse shapes. The pulse amplitudes were calibrated by recording echo intensities during a linear sweep of the amplitude of one or more of the pulses. The echo intensity was maximised

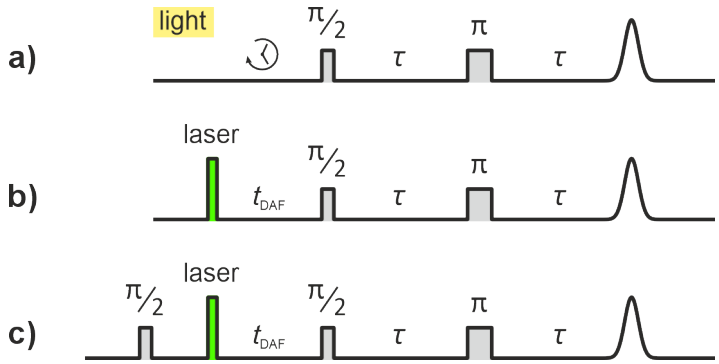

Figure 6.1: Pulse sequences used for the EPR experiments described in this chapter. a) Hahn echo as a function of time after turning off continuous illumination b) Hahn echo as a function of delay-after-flash (DAF) c) Hahn echo with a $\frac{\pi}{2}$-pulse preceding the laser pulse to suppress the contribution of long-lived contributions to the steady-state signal

for the Hahn echo detection sequence. For the pre-flash suppression $\frac{\pi}{2}$-pulse, the pulse amplitude was chosen such that the intensity of the echo attributed to both donor and acceptor peaks of the steady-state echo-detected EPR spectrum was minimised, and the pulse length matched $t_{\pi/2}$ of the Hahn echo pulse sequence. To account for incomplete suppression, a reference measurement was also taken for every delay-after-flash, with the laser not synchronised with the spectrometer, and subtracted from each recorded spectrum. At X-band, $t_{\pi/2} = 50\,\text{ns}$, $t_\pi = 100\,\text{ns}$, and $\tau = 300\,\text{ns}$. At Q-band, $t_{\pi/2} = 100\,\text{ns}$, $t_\pi = 200\,\text{ns}$, and $\tau = 400\,\text{ns}$. A two-step phase cycle on the Hahn echo was used in all cases.

6.3 Results and Discussion

6.3.1 Selective and Non-Selective Excitation

Accurate recording of EPR spectra using echo-detected field sweeps requires careful consideration of microwave pulse selectivity, particularly when probing spin-polarised CT states. The initial density matrix characterising singlet-born spin-correlated CT states is considerably different compared to the Boltzmann equilibrium for uncorrelated coupled spins, as described in Section 4.2 of Chapter 4. This initial state, in particular the presence of *two-spin order*, defined by the two-spin operator $\hat{S}_{1z}\hat{S}_{2z}$, as opposed to pure Zeeman order ($\hat{S}_{1z}$ and $\hat{S}_{2z}$) of spins in Boltzmann equilibrium,[329] has the consequence that selective and non-selective excitation result in different observable pulse EPR signals.

Under selective excitation, where only one spin (either donor or acceptor) is addressed, the initial two-spin order can evolve into detectable single-quantum coherence on the excited spin (xy-magnetisation), and pulse EPR experiments performed under these conditions match the behaviour of uncorrelated spins. In contrast, non-selective excitation of both spins leads to a different flip-angle dependence, with the signal maximised for a flip angle of 45°, and a phase shift of the echo signal, resulting in an out-of-phase echo.[329] As a consequence, pulse EPR field sweeps performed with selective excitation return the spin-polarised spectrum expected for a singlet-born CT state, with the *eaea* or *ea* polarisation patterns for fullerene and non-fullerene acceptor blends, respectively. Non-selective excitation, on the other hand, produces spectra that are qualitatively different.[330]

Non-selective excitation is essential in techniques such as out-of-phase electron spin echo envelope modulation (OOP-ESEEM), where the out-of-phase echo obtained by simultaneous excitation of both donor and acceptor spins is modulated as a function of inter-pulse delay by the dipolar coupling between them, which can therefore be determined.[317,331]

Excitation selectivity also plays a role for any spin system containing coupled nuclear spins, as the echo intensities may also be modulated by hyperfine interactions, leading to distortions in echo-detected field sweeps. These effects are strongest when non-selective pulses are used, as they rely on excitation of both allowed and forbidden transitions.[117] Their influence can be suppressed using selective pulses, which limits the number of coherence pathways accessed during the pulse sequence.

Accurate interpretation of echo-detected EPR spectra therefore requires verification that the applied pulses are appropriately selective for the system under study. The excitation profile of selective pulses must be narrow enough to excite only one of the two spins, while non-selective pulses must excite both donor and acceptor spins simultaneously.

Since the Fourier transform of an echo corresponds to the EPR spectrum within the excitation profile of the pulse, detection of the full echo transient followed by Fourier transform provides an excellent way of verifying pulse selectivity. This approach, combined with summation of the individual echo Fourier transforms to reconstruct the full spectrum, as described by Bowman et al.,[332] leads to increased spectral resolution, as any broadening determined by the combination of pulse excitation profile and integration window is removed.

A comparison of field sweeps measured by standard echo integration and echo transient detection and Fourier transform is shown in Figure 6.2. Standard echo-detected EPR field sweeps with integration of the full echo signal, measured under continuous illumination to probe the long-lived CT states in PBDB-T:PCBM, are shown in black. For both excitation with long selective and short non-selective pulses, the full echo was recorded at selected field positions and Fourier-transformed. In the case of non-selective pulses, the resulting spectra at all field positions contain contributions from both donor and acceptor spins, confirming that excitation is sufficiently non-selective. In contrast, for selective pulses, the Fourier-transformed spectra contain signals from only one spin species at field positions corresponding to either the donor or acceptor, demonstrating that the chosen pulse lengths lead to selective excitation. Summation of the Fourier-transformed spectra reproduces the echo-detected EPR lineshapes closely in both cases, confirming that the spectra recorded by echo integration are faithful representations of the true spectrum and no significant spectral broadening or distortion arises from the selected detection scheme. The following experiments were all performed with selective pulses, so accurately record the spectral signatures of both spin-correlated CT states and long-lived thermalised charged states.

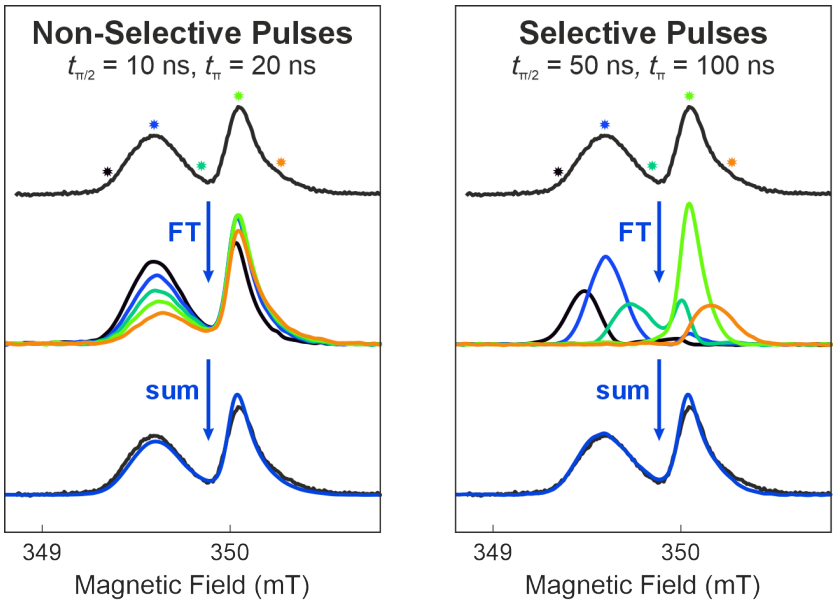

Figure 6.2: Performance verification of non-selective and selective pulsed excitation for the measurement of echo-detected EPR spectra (shown in black) of long-lived charged states in PBDB-T:PCBM. Fourier-transforms of the time-domain echoes, recorded at the marked field positions, illustrate the extent of pulse selectivity. The non-selective pulse excites spins on both donor and acceptor molecules, while the selective pulse mostly results in signals from only one spin species at a time. Summation of the Fourier-transformed spectra reproduces the echo-detected EPR spectra accurately, indicating that no lineshape distortion is introduced by the excitation and echo integration scheme.

6.3.2 Monitoring Charge Detrapping and Recombination

In disordered OPV materials, the presence of trap states is an intrinsic consequence of the heterogeneous microstructure present within the active layer. This disorder is driven by several factors, including irregular molecular packing and the presence of chemical impurities and structural defects.[28,90,91] These variations disrupt the local electronic environment, leading to a broad distribution of energy levels. The resulting energetic disorder gives rise to localised trap states that capture charges and hinder their transport through the material.

A key distinction in evaluating the impact of trap states concerns their energetic depth relative to the transport levels: the LUMO for electrons or the HOMO for holes. Traps situated close in energy to these levels are commonly referred to as **shallow traps**. Charges captured in such states can typically be released via thermal excitation, allowing them to re-enter transport pathways. By contrast, **deep traps** are located significantly farther in energy from the relevant transport levels. Charges occupying these states are effectively immobilised over extended timescales and are unlikely to contribute to photocurrent. Instead, deep traps

will participate in trap-assisted non-radiative recombination processes, thereby contributing to losses in OPV devices.[52,104,105]

Understanding the energetic distribution of trap states - the relative population of shallow versus deep traps - is essential to determining how they affect charge transport and recombination dynamics. The rate at which charges can escape trap sites is temperature-dependent and follows Arrhenius-like behaviour:

$$k_{\text{detrap}} \propto \mathrm{e}^{-\frac{\Delta E}{k_{\mathrm{B}}T}} \tag{6.1}$$

where ΔE is the energy difference between the trap level and the average transport level. A trap that is shallow at room temperature may behave as a deep trap under cryogenic conditions.[104,105] Therefore, low-temperature measurements provide an upper bound on the population of deep traps in a material domain.

To probe the distribution of trap states, the donor:acceptor blends were measured under continuous illumination to establish a steady-state population of trapped charges. During illumination, both shallow and deep trap sites are populated, with continuous trapping and detrapping of photogenerated charges in shallow traps, whereas charges in deep traps are effectively isolated from the pool of mobile charges. After reaching the steady-state, the illumination was turned off, and the field-swept echo-detected EPR spectrum was recorded as a function of time over long timescales (up to an hour). The decay of the signal intensity over this timescale reflects the loss of charges thermally-detrapped from shallow trap sites which, once mobile, will recombine faster. As recombination eliminates unpaired spins, the decline in EPR signal intensity is directly linked to the depopulation of shallow traps. While in an operating OPV device, mobile charges would typically be extracted at the electrodes, under the open-circuit conditions of the EPR experiment, recombination is the only available pathway. Deeply-trapped charges remain immobilised and persist as a long-lived signal.

The decay of the echo-detected EPR signal was measured at both X- and Q-band, at 20 K, and additionally at Q-band at 80 K, as shown in Figure 6.3. These measurements are not equivalent to the conventional echo decay experiment, performed in Section 3.3.2 of Chapter 3, which is determined by the phase-memory time T_{m}. Instead, the far slower decay of the EPR signal due to recombination of detrapped charges is tracked. Spectra were recorded at regular intervals over a period of up to an hour, with signal intensities at each time point compared to the normalised value at $t = 0$, which corresponds to the steady-state intensity under continuous illumination.

The decay curves shown in the figure correspond to selected magnetic field positions in the steady-state EPR spectra (shown in the inset). In the fullerene

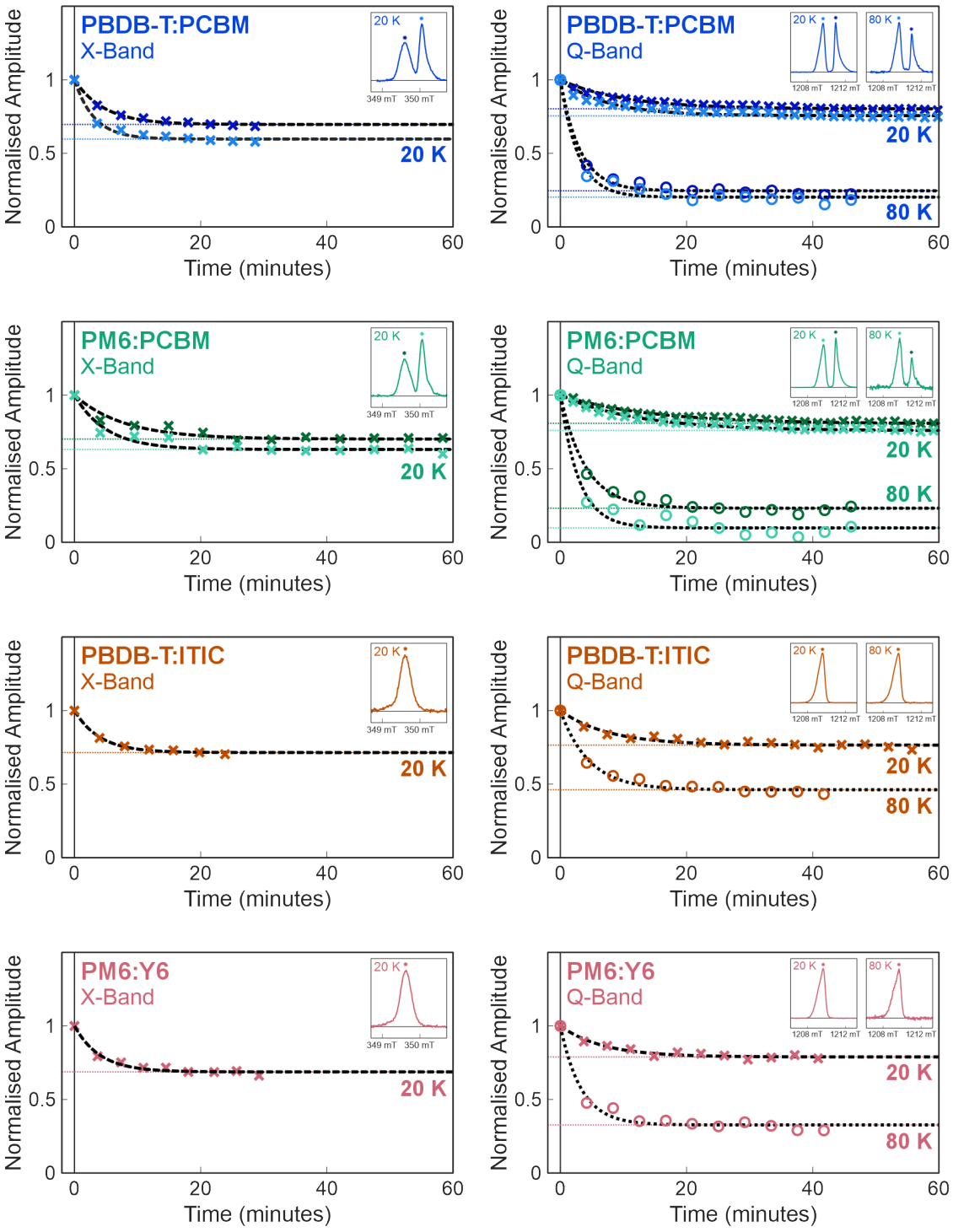

Figure 6.3: Decay of the echo-detected EPR signal as a function of time after continuous illumination for PBDB-T:PCBM, PM6:PCBM, PBDB-T:ITIC, and PM6:Y6. The signal decays were measured at 20 K, at X-band and Q-band. The decay traces (dashed lines) were modelled by exponentials, with fit parameters displayed in Table 6.1.

Material	Charge	I_∞/I_0			τ_{decay} (min)		
		X	Q		X	Q	
		20 K	20 K	80 K	20 K	20 K	80 K
PBDB-T:PCBM	PBDB-T$^{\bullet+}$	0.70	0.80	0.25	4.7	10.0	3.1
	PCBM$^{\bullet-}$	0.60	0.76	0.20	3.1	7.4	2.8
PM6:PCBM	PM6$^{\bullet+}$	0.70	0.81	0.23	7.9	14.1	4.0
	PCBM$^{\bullet-}$	0.63	0.76	0.10	5.1	12.3	2.9
PBDB-T:ITIC		0.71	0.77	0.46	4.0	7.6	4.5
PM6:Y6		0.69	0.79	0.33	4.0	6.8	3.3

Table 6.1: Proportion of deeply trapped charges (I_∞/I_0) and decay time constants (τ_{decay}), extracted from exponential fits to echo decay curves shown in Figure 6.3. Estimated fitting errors are 0.01 for I_∞/I_0, and 1.5, 1.0, and 0.5 min for τ_{decay} at 20 K, X-band, 20 K, Q-band, and 80 K, Q-band, respectively.

acceptor blends, the lower-field spectral feature arises from charges on the polymer donor (PBDB-T$^{\bullet+}$ or PM6$^{\bullet+}$), while the higher-field feature originates from charges on the fullerene acceptor (PCBM$^{\bullet-}$). In the non-fullerene blends, overlap of donor and acceptor g-values prevents spectral separation, so only the total decay of the overall trapped charge population can be followed. For all donor:acceptor blends studied, a reduction in EPR signal intensity is observed over time after the light is turned off. At 20 K, the signal decreases gradually and reaches an approximately constant level after around 30 min, with similar behaviour seen for the decays at the field positions of the donor and acceptor SCs. At 80 K, the decay proceeds more rapidly, and the relative magnitude of the signal at long times compared to the one at steady-state is reduced relative to the lower-temperature measurements.

The signal decays were fitted using a simple exponential decay:

$$I(t) = I_0 \mathrm{e}^{\frac{-t}{\tau_{\text{decay}}}} + I_\infty \tag{6.2}$$

where $I(t)$ is the EPR signal at time t after turning off the light, I_0 the steady-state signal under continuous illumination, I_∞ the residual signal from charges trapped in deep trap sites, and τ_{decay} the characteristic decay time of detrapped charges, reflecting the combined timescale of detrapping ($1/k_{\text{detrap}}$ from Equation 6.1) and subsequent recombination. The ratio I_∞/I_0 provides a measure of the proportion of charges in deep trap sites at a given temperature. The fitted parameters are summarised in Table 6.1.

At 20 K, thermal energy ($k_{\text{B}}T = 1.7$ meV) is insufficient to release most trapped charges. This is reflected in high I_∞/I_0 values, between $60 - 80\%$ across all blends, indicating a majority of traps are effectively deep at this temperature. Raising the temperature to 80 K ($k_{\text{B}}T = 6.9$ meV) enables significant detrapping. For all blends, I_∞/I_0 decreases considerably, with only $10 - 50\%$ of charges now trapped

at this temperature. This observed trend implies that under typical OPV operating conditions (room temperature), a far larger fraction of charges may be thermally detrapped. Decay time constants τ_{decay} also decrease with temperature, consistent with faster detrapping and/or recombination. Since recombination in these systems is driven by the availability of free charges, the temperature dependence of τ_{decay} is largely governed by thermally-activated detrapping.

The origin of the differences between X-band and Q-band measurements is not fully understood. The slightly higher I_∞/I_0 values at Q-band may stem from differences in illumination, as the Q-band resonator's smaller active height and optical window may lead to reduced overall laser excitation, leading to more localised light exposure. This could increase local charge density, enhance recombination, and reduce the steady-state trap density I_0, potentially explaining the variation in relative deep-trap fractions. Differences in τ_{decay} may also result from the shorter measurement window at X-band (up to 30 min), which appears to truncate the decay, leading to underestimation of lifetimes based on an exponential fit of the available data points.

Warming the samples to room temperature and then cooling them back down to cryogenic temperatures without illumination results in negligible spectral intensity, as shown by the minimal signals in the echo-detected EPR spectra measured without illumination in Chapter 3 (Section 3.3.1). This indicates that the deeply trapped charges detected at low temperatures are completely released at operating temperatures and do not represent permanent defects. Although trapped charges are typically regarded as a loss pathway via recombination, their thermal activation allows for the possibility of charge re-encounter and the reformation of the CT state. This would allow participation in the reversible equilibrium between the CT state and mobile SCs observed in the time-resolved EPR spectra of Chapter 5, potentially enabling subsequent attempts at successful charge separation.

6.3.3 Time-Resolved Pulse EPR of Photoinduced States

To assess the relevance of these traps to the photovoltaic mechanism, it becomes important to distinguish their contribution relative to the photoactive species observed in time-resolved EPR, namely, CT states and mobile SCs. Time-resolved EPR selectively probes the transient magnetisation following photoexcitation, but is blind to any magnetisation from long-lived spin populations that persist between laser pulses. In contrast, pulse EPR detects all spin states, short- or long-lived, present in the sample at any given time, provided they have a long enough T_2 such that the spins do not decohere during the pulse sequence. If the contributions of transient and trapped species can be disentangled, their relative roles in the spin dynamics, and by extension, the photovoltaic mechanism, can be rationalised.

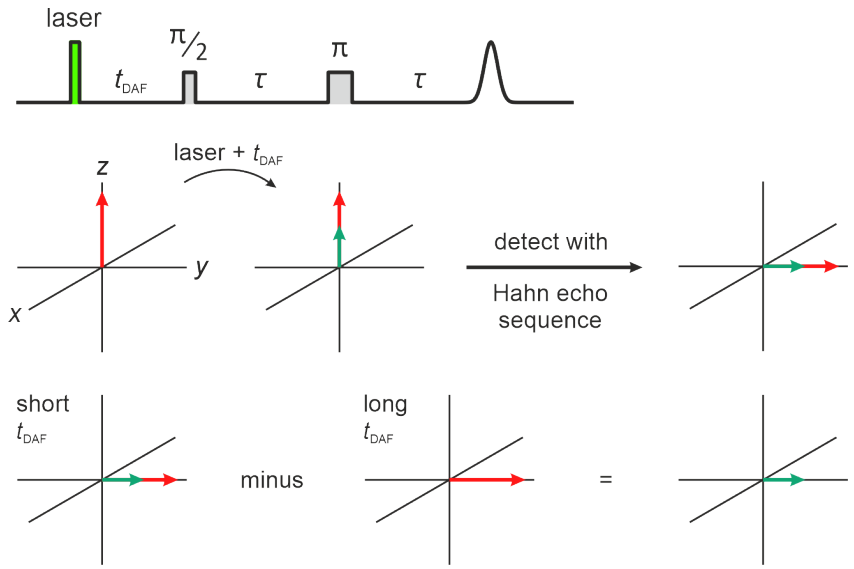

Figure 6.4: Isolation of the short-lived contributions to the EPR signal using the Hahn echo sequence for different delays-after-flash (DAF). The magnetisation induced by the laser flash (green) for a given DAF can be obtained by subtracting the long-time signal that corresponds to the steady-state magnetisation (red).

Subtraction of the Steady-State Signal

The most direct method to achieve this separation is to record the echo-detected EPR signal as a function of time after the laser pulse, referred to as delay-after-flash (DAF), using a Hahn echo sequence, as illustrated in Figure 6.4. Each spectrum includes contributions from both the long-lived trapped states and the short-lived photoinduced species. The echo obtained at long delays ($t_{\mathrm{DAF}} = 20\,\mathrm{ms}$) matches the echo recorded under steady-state conditions, when laser excitation is not synchronised with detection. By subtracting this echo obtained at long DAF, where only steady-state species persist, from the signal obtained at earlier times, the contribution from transient species may be estimated. These spectra isolated by subtraction as a function of DAF (and labelled as **subtraction** spectra), along with the full spectra, are shown in Figure 6.5 for PBDB-T:PCBM, PM6:PCBM, PBDB-T:ITIC, and PM6:Y6, measured at 20 K and at X- and Q-band. To facilitate comparison between X- and Q-band results, the subtraction spectra at Q-band have been scaled by the ratio of the microwave frequencies ($33.9/9.8 \approx 3.5$). This reflects the linear dependence of Boltzmann polarisation with microwave frequency for thermally-populated states, such as trapped charges. Spin-polarised species show no such scaling, since their sublevel populations are set by precursor spin configurations, not thermal equilibrium.

Across all samples, it is observed that, at 20 K, the change in echo-detected EPR signal as a function of DAF is a small contribution relative to the steady-state signal, indicating that most of the magnetisation detected by pulse EPR

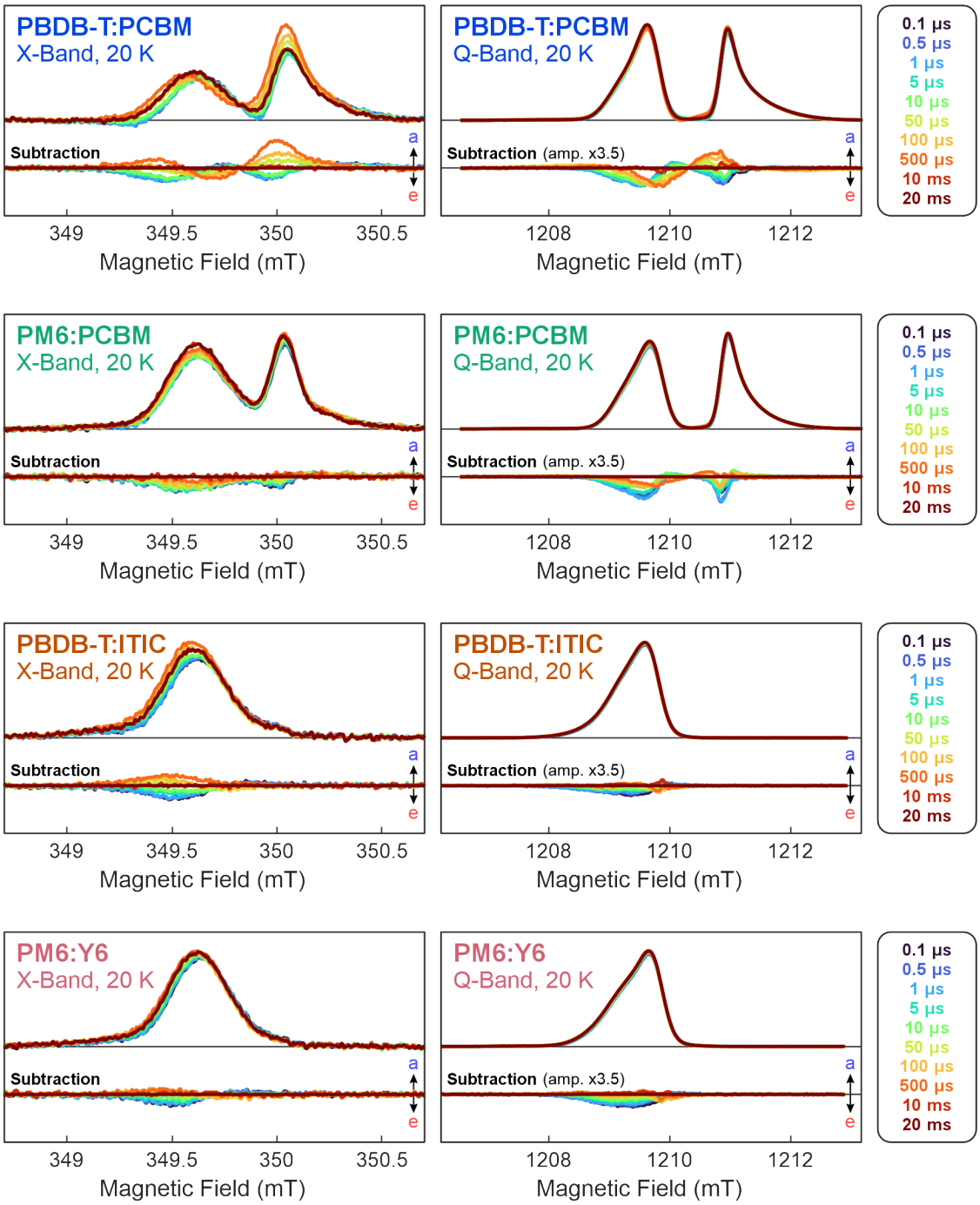

Figure 6.5: Echo-detected EPR X- and Q-band spectra of PBDB-T:PCBM, PM6:PCBM, PBDB-T:ITIC, and PM6:Y6 as a function of delay-after-flash, at 20 K. The change in echo-detected EPR spectra is also displayed, calculated by subtracting the $t_{\mathrm{DAF}} = 20\,\mathrm{ms}$ spectrum from each of the spectra recorded at different t_{DAF}. At Q-band, this contribution is displayed with a magnification of $\times 3.5$, corresponding to the ratio of the Q- and X-band microwave frequencies.

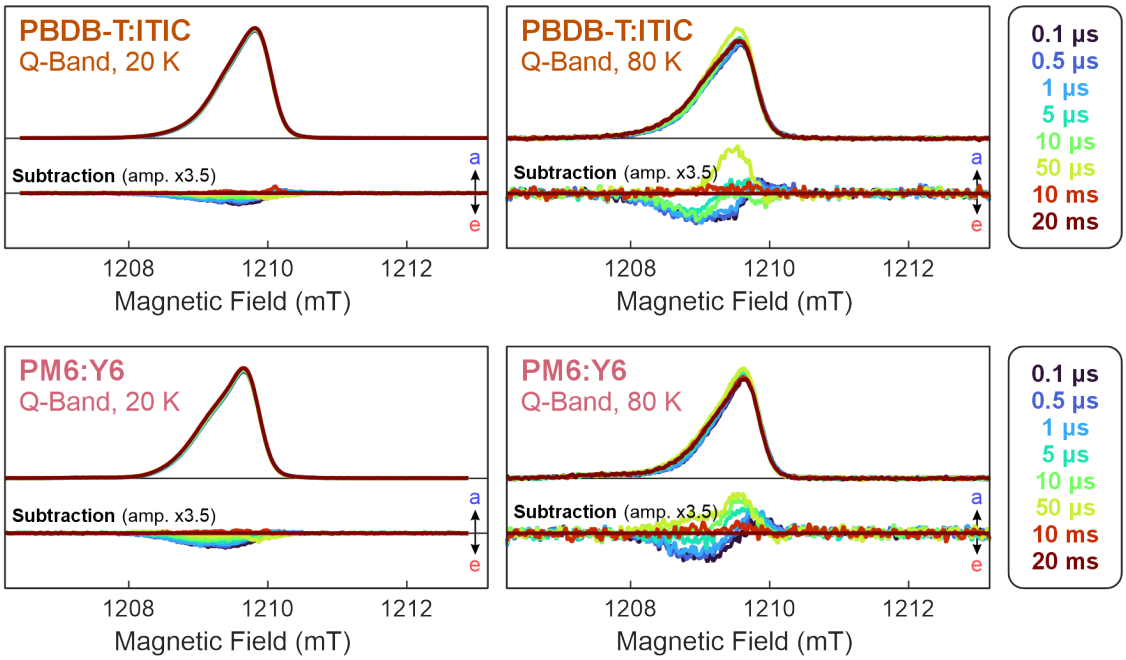

Figure 6.6: Echo-detected EPR Q-band spectra of PBDB-T:ITIC and PM6:Y6 as a function of delay-after-flash, comparing 20 K and 80 K data. The change in echo-detected EPR spectra is also displayed, calculated by subtracting the $t_{\mathrm{DAF}} = 20\,\mathrm{ms}$ spectrum from each of the spectra recorded for different t_{DAF}.

experiments arises from trapped charges that are unable to detrap within the 20 ms experiment repetition time. The subtraction spectra reveal clear signatures of spin-polarised species with emissive and absorptive signal contributions that decay within the 20 ms repetition window.

Temperature-dependent measurements provide additional insight. As shown in Figure 6.6, echo-detected EPR spectra of PBDB-T:ITIC and PM6:Y6 measured at Q-band show a marked increase in the magnitude of the subtraction spectra when the temperature is raised from 20 K to 80 K. This observation is consistent with the notion of thermally-activated detrapping: at elevated temperatures, a larger fraction of the trapped charges is able to escape and recombine, thereby reducing the steady-state intensity and enhancing the relative contribution from transient species.

The evolution of the isolated short-lived states with DAF obtained through the subtraction method is compared to time-resolved EPR spectra measured at early (0.5 µs) and late (10 µs) times after photoexcitation. These comparisons are shown in Figure 6.7. The time-resolved EPR measurements revealed two distinct regimes, discussed in detail in Chapter 5. Immediately following photoexcitation, an *eaea*-polarised (or *ea*-polarised in non-fullerene acceptor blends) signal is observed, attributed to a singlet-born CT state. Over a few microseconds, this evolves into a longer-lived, mostly absorptive signal, which was attributed to spin polarisation

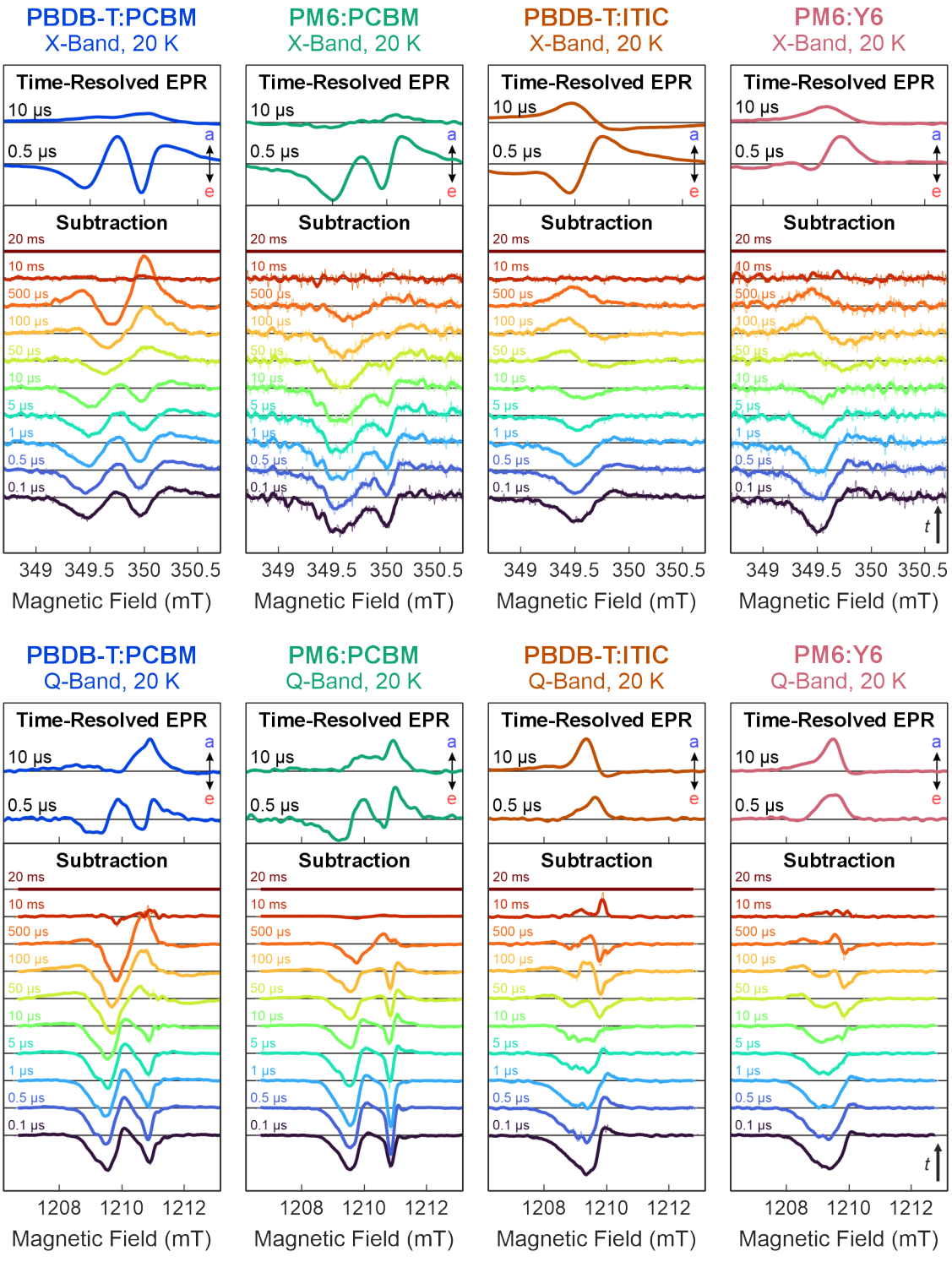

Figure 6.7: Change in echo-detected EPR spectra observed with the subtraction method (subtraction of the $t_{DAF} = 20\,ms$ spectrum from spectra recorded as a function of delay-after-flash), at 20 K and at X-band and Q-band. Time-resolved EPR spectra at short and long times after photoexcitation, from Chapter 5 (Section 5.3.2), are shown in the panel above.

arising from an equilibrium between CT states and mobile SCs. For PM6:PCBM no long-lived absorption signal was observed, instead one-directional charge separation gave a very weak *ea*-polarised signal.

At X-band, the early-time subtraction spectra (0.1 µs to 1 µs) share features with the time-resolved EPR spectra assigned to the singlet-born CT state at 0.5 µs. In particular, the positions of the turning points match the expected polarisation pattern. However, the relative amplitudes of the emissive and absorptive components differ: the subtraction signals are predominantly emissive overall, compared to an almost negligible net polarisation of the early-time spectra recorded by time-resolved EPR.

By 10 ms, the pulse EPR signal has completely disappeared, confirming that all light-induced transient species have lifetimes shorter than the repetition time of the experiment and validating the assumption that subtraction of the $t_{\mathrm{DAF}} = 20\,\mathrm{ms}$ will leave behind only species that were directly induced by the laser flash.

The mismatch in signal shape between the subtraction and time-resolved EPR spectra is even more pronounced at Q-band. At early DAFs, the subtraction spectra are almost entirely emissive for all blends and the characteristic polarisation features of the singlet-born CT state are no longer clearly visible. Although the subtraction spectra become progressively less emissive at later DAFs, they do not reach the fully absorptive shape observed at long times by time-resolved EPR. This discrepancy suggests the presence of an additional emissive contribution that does not appear in the time-resolved EPR spectra.

The increased prominence of the emissive contribution and its close match to the shape of the steady-state EPR signal at Q-band, where Boltzmann polarisation is significantly enhanced, points towards a thermally-populated origin. Isolation of the transient species by the subtraction method relies on the assumption that the long-lived magnetisation associated with the trapped charges remains constant over the timescale of the measurement window. Differences between the subtraction spectra and the spectra from time-resolved EPR indicate that this assumption does not fully hold and that the steady-state population is transiently affected by light excitation.

Suppression of the Steady-State Signal

To separate the short-lived species from this emissive contribution, an alternative method that suppresses the steady-state magnetisation prior to photoexcitation was employed, ensuring that any detected signal originates solely from transient photogenerated species. This was achieved by applying an additional microwave pulse before the laser flash. As shown schematically in Figure 6.8, a $\frac{\pi}{2}$-pulse applied

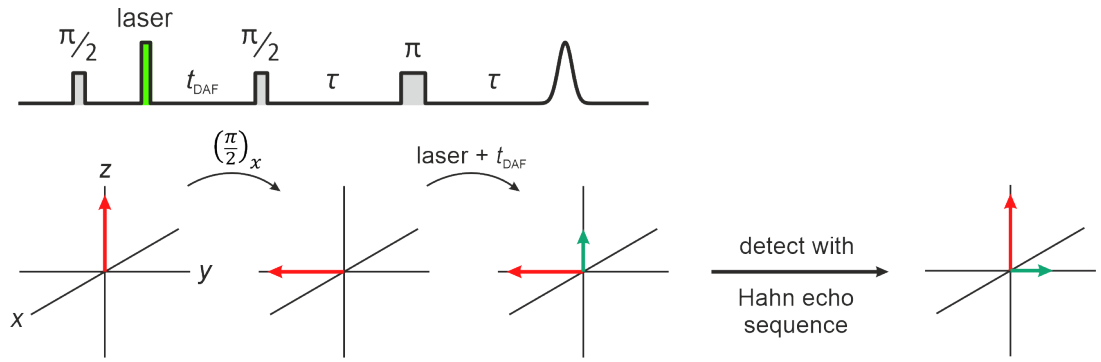

Figure 6.8: Suppression of the steady-state signal contribution by introducing a $\frac{\pi}{2}$-pulse prior to laser excitation. At the time of detection with the Hahn echo sequence, the steady-state magnetisation is along $+z$, and so does not contribute to the detected echo signal.

before the laser flash rotates the magnetisation of the steady-state trapped charges, shown in red, from the $+z$-axis to the $-y$-axis. During the subsequent Hahn echo detection sequence, this magnetisation is moved to the $+z$-axis, eliminating its transverse component and thereby suppressing its contribution to the detected echo. In contrast, magnetisation generated by the laser flash is unaffected by the pre-flash pulse and remains detectable. This **suppression** method therefore allows selective observation of short-lived photoinduced species, even in the presence of changes to the magnetisation of the trapped charges.

The suppression becomes less effective at longer t_{DAF} due to longitudinal relaxation during this delay. For the trapped charges, T_1 ranges from 3 ms to 11 ms at 20 K (determined from inversion recovery experiments in Section 3.3.2 in Chapter 3), enabling reliable suppression over several milliseconds. However, at 80 K, where T_1 drops to $100 - 200$ µs, suppression becomes challenging beyond short delays due to partial recovery of the magnetisation along $+z$ during t_{DAF}. EPR measurements using the suppression pulse were performed up to 500 µs at X-band, and up to 100 µs at Q-band, where achieving uniform suppression across the spectrum was more challenging. Beyond these times, relaxation effects begin to compromise the effectiveness of the suppression method.

To effectively cancel signal contributions from long-lived species already present before the laser pulse at the time of the echo, the suppression pulse must achieve a precise $\frac{\pi}{2}$ rotation of the steady-state magnetisation. The flip angle depends on the microwave field strength ω_1, which itself varies with the g-value: $\omega_1 = \frac{g\mu_{\mathrm{B}}B_1}{\hbar}$. This relationship reduces suppression efficiency when donor and acceptor resonance positions are well-separated, as a single pulse may not uniformly suppress both components. To correct for incomplete suppression, a reference measurement is taken at the same t_{DAF} but with the laser unsynchronised from the pulse sequence.

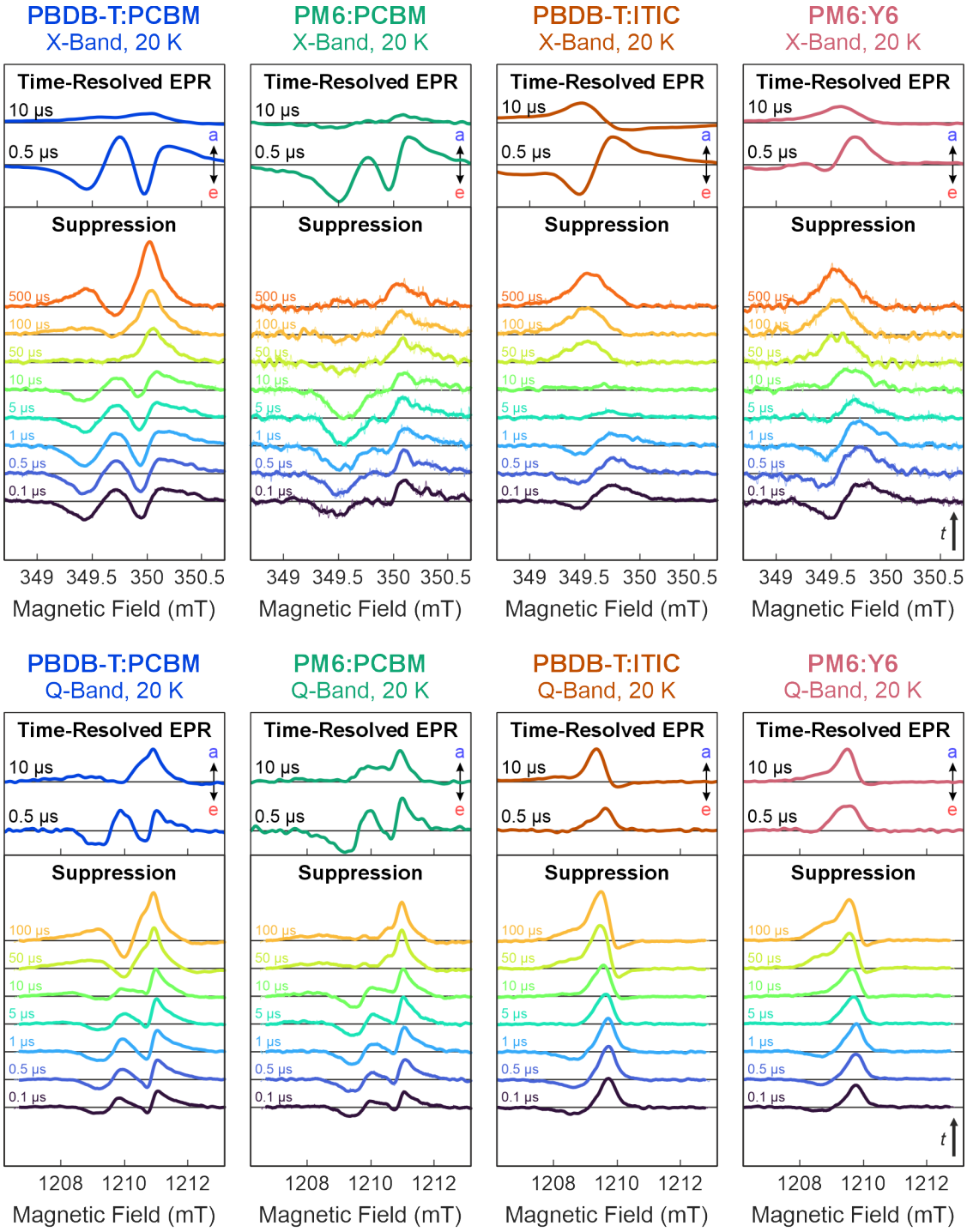

Figure 6.9: Echo-detected EPR spectra, using a $\frac{\pi}{2}$-pulse preceding the laser pulse to suppress contributions from long-lived trapped charges, of PBDB-T:PCBM, PM6:PCBM, PBDB-T:ITIC, and PM6:Y6 as a function of delay-after-flash, at 20 K and X-band and Q-band. Time-resolved EPR spectra at short and long times after photoexcitation, from Figures 5.5, 5.6 and 5.8, are shown in the panel above.

This randomises the timing of the photoexcitation over the 20 ms repetition period. Since the evolution of the short-lived species occurs on much shorter timescales, the reference spectrum, averaged over many repetitions, reflects only the unsuppressed steady-state contributions, which are then subtracted from the spectra recorded with synchronisation to the laser pulse. The resulting signals are shown in Figure 6.9, measured at 20 K and at X- and Q-band, and compared to the same time-resolved EPR spectra at 0.5 µs and 10 µs. The signal shapes obtained using the suppression method now resemble the time-resolved EPR spectra far more closely, both at X- and Q-band. At short t_{DAF} ($0.1 - 1$ µs), the characteristic polarisation patterns associated with the singlet-born CT state, *eaea* in fullerene acceptor blends and *ea* in non-fullerene acceptor blends, become clearly resolved.

This improved agreement confirms that the suppression method probes the same spin-polarised states as time-resolved EPR. However, comparison across delay times, shown for PBDB-T:PCBM at X-band in Figure 6.10, reveals differences in the evolution of spin polarisation between the two techniques. While the spectra from both approaches trend towards increasingly absorptive lineshapes with longer delay, the polarisation in the suppression data evolves more gradually. In addition, immediately after photoexcitation ($t_{\mathrm{DAF}} = 0.1$ µs), the time-resolved EPR shows stronger damping, due to the slower resonator rise time when critically-coupled.

This discrepancy can be partially explained by fundamental differences between the two types of experiments. Time-resolved EPR applies a continuous B_1 field, which damps the signal over time, as predicted from modelled transients shown in Chapter 4 (Figure 4.3 of Section 4.3). The suppression method, by contrast, uses short pulses, which do not induce the same damping effect. However, this alone does not fully account for the slower polarisation evolution observed.

Remaining discrepancies may arise from the selectivity of pulse EPR to species with sufficiently long phase memory times (T_{m}), to maintain coherence during the

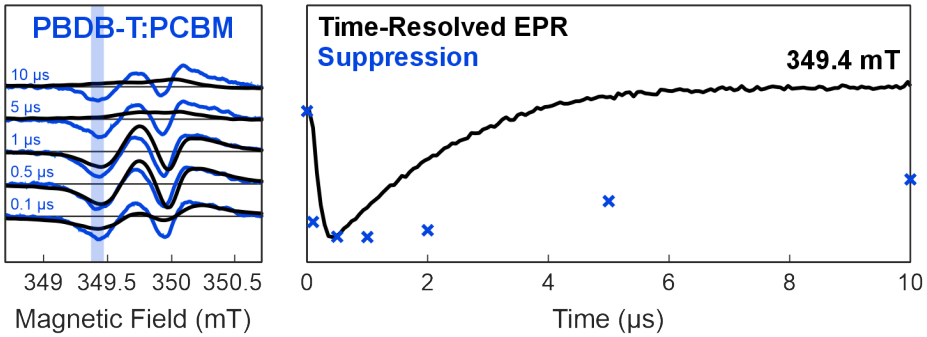

Figure 6.10: Signal evolution for the echo-detected EPR spectrum with the additional suppression pulse (blue) in comparison to time-resolved EPR (black), shown here for PBDB-T:PCBM at 349.4 mT, at 20 K and X-band.

interpulse delay τ of the Hahn echo detection sequence. Transverse relaxation times determined for photoinduced states from simulations of the time-resolved EPR data (see Tables 5.4 and 5.5 in Section 5.3.4 of Chapter 5) are comparable to the τ values of $300-400$ ns used in the suppression pulse experiments, suggesting that states with short T_2 contribute less to the pulse EPR echo. Under the assumption that longer T_2 correlates with lower local spin concentration, these selectively observed states experience slower bimolecular processes such as SC re-encounter and longitudinal (T_1) relaxation, potentially explaining differences in the decay behaviour. This interpretation is consistent with time-resolved EPR measurements at low laser fluence ($20\,\mu J\,cm^{-2}$), where reduced charge density led to slowed kinetics.

Despite the slower polarisation evolution, the presence of early-time *eaea* / *ea* polarisation and longer-time mostly absorptive polarisation patterns indicates that the fundamental mechanisms of charge separation and CT−SC equilibrium described in Chapter 5 also explain the pulse EPR data. This confirms that the suppression method probes the same essential photophysical processes as time-resolved EPR. Having successfully isolated the short-lived, transient species from the steady-state magnetisation, the origin of additional emissive contribution observed in the results of the subtraction method can then be investigated.

Charge Detrapping by Exciton Quenching

A direct comparison between the subtraction (darker colours) and suppression (lighter colours) methods for isolating the transient species is presented in Figure 6.11 for X- and Q-band measurements at 20 K. For each blend, EPR spectra from both approaches are shown across the full range of delays-after-flash, along with their difference spectra, denoted as Δ_{method} (black). In the upper panel, the Δ_{method} spectra are averaged over all t_{DAF} and compared to the inverted steady-state spectra (recorded at $t_{\text{DAF}} = 20$ ms), corresponding to the signatures of the trapped charges, and the $t_{\text{DAF}} = 0.1$ µs spectra obtained with the subtraction method, which correspond to the singlet-born CT state.

Across all blends studied, the Δ_{method} spectra are purely emissive and show excellent spectral agreement with the inverted steady-state signal. Both donor and acceptor resonance positions appear with similar relative intensities, indicating an equal contribution from each species. The magnitude of the emissive signal extracted with the Δ_{method} correlates with the intensity of the steady-state signal, which is increased at Q-band and at lower temperatures. This is evident from the comparison of the subtraction and suppression methods at 80 K in Figure 6.12, showing a reduction in emissive signal intensity compared to 20 K measurements. This emissive component remains essentially constant across the full time window

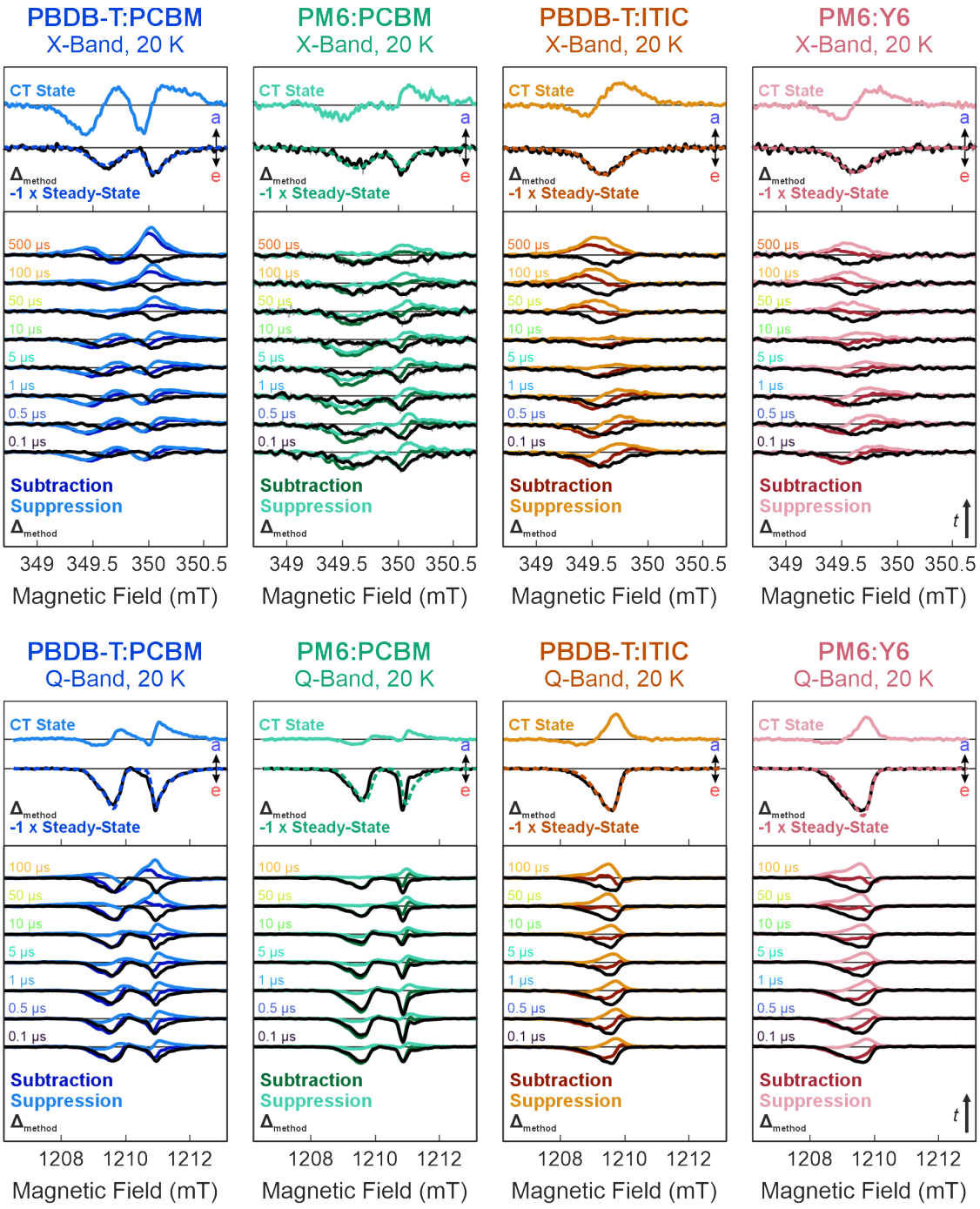

Figure 6.11: Comparison of EPR spectra obtained with the subtraction and suppression methods for isolating the transient species for PBDB-T:PCBM, PM6:PCBM, PBDB-T:ITIC, and PM6:Y6, at 20 K and X-band and Q-band. EPR spectra obtained with the subtraction method are shown in darker colours, spectra obtained with the suppression method are in lighter colours, and the differences in spectra (Δ_{method}) are in black. Top panel: average difference spectrum across all t_{DAF} compared to the inverted steady-state signal ($t_{\text{DAF}} = 20\,\text{ms}$) and the singlet-born CT state ($t_{\text{DAF}} = 0.1\,\mu\text{s}$, with suppression pulse).

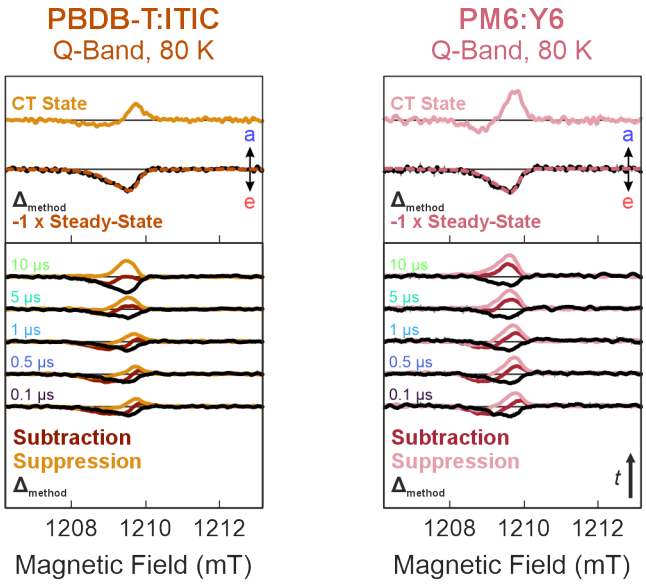

Figure 6.12: Comparison of the spectra obtained with the subtraction and suppression methods for isolating the transient species for PBDB-T:ITIC and PM6:Y6, at 80 K and Q-band. EPR spectra obtained with the subtraction method are shown in darker colours, spectra obtained with the suppression method are in lighter colours, and the difference spectra (Δ_{method}) are in black. Top panel: average difference spectrum across all t_{DAF} compared to the inverted steady-state signal ($t_{\text{DAF}} = 20\,\text{ms}$) and the singlet-born CT state ($t_{\text{DAF}} = 0.1\,\mu\text{s}$, with suppression pulse).

studied (up to 500 µs at X-band), appearing almost instantaneously following laser excitation and decaying completely only on longer time scales that could not directly be probed using this method.

These observations suggest the presence of a fast, light-induced process that depletes a subset of the long-lived trapped charge population immediately following photoexcitation. The spectral similarity and 1 : 1 donor-to-acceptor ratio strongly imply that both species are depleted simultaneously, consistent with a charge recombination process involving pairs of trapped charges. The fact that the emissive signal does not evolve with t_{DAF} indicates that the depletion occurs faster than the time resolution of the experiment (within 0.1 µs), and that the recovery of magnetisation occurs on a much longer timescale.

This behaviour is consistent with exciton quenching by trapped charges, a mechanism previously proposed to explain a reduction in the population of steady-state species in OPV blends upon photoexcitation.[333–335] In this process, singlet excitons (S_1) are generated throughout the donor and acceptor domains. If a trapped charge (TC) is nearby, the exciton can interact with it: energy is transferred from the exciton to the trapped charge, promoting the charge to the transport level where it becomes a mobile, free charge (FC), while the exciton itself is quenched,

relaxing to the ground state (S_0). This process effectively liberates the trapped charge at the expense of the exciton, and can be summarised as:

$$S_1 + TC \rightarrow S_0 + FC$$

If the resulting free charge undergoes rapid recombination, the unpaired spin of the original trapped charge is lost, leading to a reduction in the steady-state EPR signal. Since the subtraction method detects changes relative to the steady-state, this loss of spin magnetisation appears as an emissive contribution in the spectra.

The absence of this emissive feature in time-resolved EPR may be attributed to the nature of detection. Time-resolved EPR measures differential changes following photoexcitation and is inherently insensitive to static signals or signals that vary very slowly. If the emissive component appears within 0.1 µs and then remains approximately constant, and recovers only slowly over tens of milliseconds, it will be unavoidably filtered out in time-resolved EPR detection. This explains why the feature is not visible in time-resolved EPR, but appears clearly in the subtraction method.

In order for this emissive signal to remain constant across all delays-after-flash, the entire process, exciton quenching and charge recombination, must occur faster than the experimental time resolution of 0.1 µs. That is, trapped charges must be liberated and fully recombine before the first measurement point, so that their loss appears instantaneous and without a clear time-dependence observable on the timescales probed with the suppression method. Photoluminescence quenching measurements have shown that singlet exciton lifetimes are shorter than 1 ns in all four OPV blends at room temperature.[321] Temperature-dependent studies report minimal variation in exciton dynamics,[68,336] indicating that similarly short lifetimes are maintained at 20 K and 80 K. This rapid exciton decay is further supported by the immediate appearance ($t \approx 0$) of CT states and ISC triplets in time-resolved EPR spectra in Chapter 5, confirming that singlet excitons decay well within the sub-microsecond regime. Charge carrier lifetimes under open-circuit conditions range from picoseconds to microseconds,[337–340] consistent with recombination of the higher energy liberated charges occurring within the 0.1 µs resolution of the pulse EPR experiment.

Two mechanisms are proposed for exciton-induced charge detrapping,[334] illustrated in Figure 6.13, that are then followed by rapid recombination:

- **Direct charge transfer**: A singlet exciton formed on an acceptor molecule adjacent to a trapped charged state (also on an acceptor) can accept the trapped electron into its HOMO.[43] This transfer neutralises the original trap site (which returns to the ground state, S_0) and converts the exciton into a

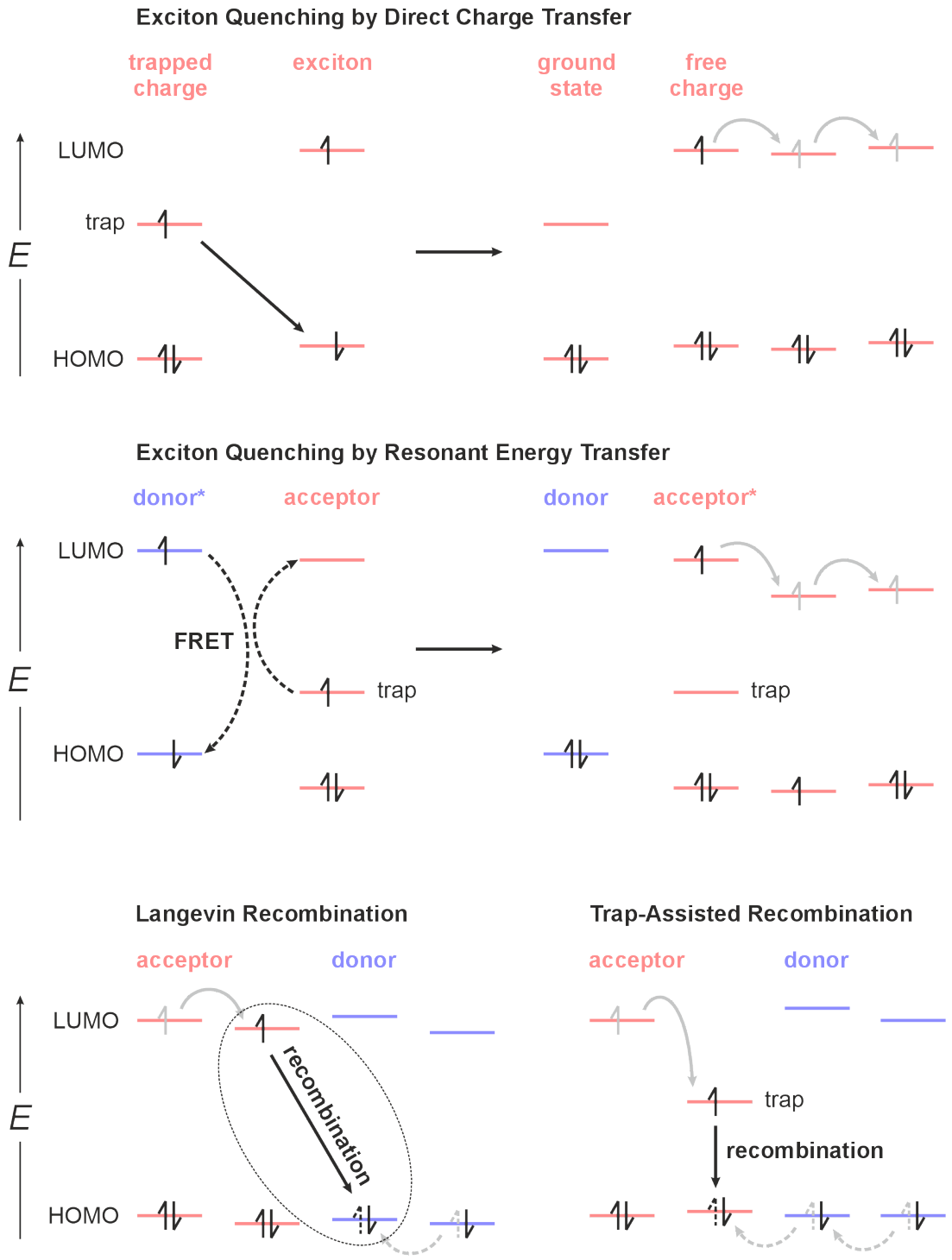

Figure 6.13: Detrapping of trapped charges by exciton quenching, either through direct charge transfer or via resonant energy transfer. In both cases, a trapped charge is liberated, while a singlet exciton is quenched and relaxes to the ground state. These newly-mobile charges can subsequently recombine, either by bimolecular Langevin recombination or monomolecular trap-assisted recombination, removing their contribution to the steady-state EPR signal.

free, mobile charged state, with the electron now located in the LUMO of the exciton host molecule. This process effectively frees the trapped charge at the cost of an exciton, which is quenched in the process. An equivalent process is possible with hole transfer across two donor molecules.

- **Resonant energy transfer (FRET-like)**: If the exciton is located within 10 nm of a trapped charge,[64,65] resonant energy transfer can also occur. For example, an exciton on a donor molecule can transfer its energy to a trapped charged state on an adjacent acceptor. This happens when the donor HOMO-LUMO energy gap ($S_1 \rightarrow S_0$ transition) closely matches the gap between the trap level and the acceptor LUMO. In a state picture of this process, the singlet exciton S_1 state relaxes down to a vibrationally excited level of the ground state, while the trap state is simultaneously promoted to a higher vibrational level, followed by rapid relaxation to their respective lowest vibrational levels, resulting in a ground state donor molecule and a mobile charged state on an acceptor molecule.

In both cases, the exciton is quenched and the trap site is emptied, creating a free charge. This mobile charge can then recombine either monomolecularly by encountering a hole trap (trap-assisted recombination),[52,104,105] or bimolecularly via Langevin recombination with a free hole.[39,97,98]

Exciton quenching is a well-established non-radiative loss mechanism in OPVs, even at room temperature, reducing the yield of separated charges by depleting singlet excitons.[341,342] Although the concentration of charges in trap sites (and therefore the extent of exciton quenching) decreases with increasing temperature, the behaviour of short-lived species observed via time-resolved EPR remains largely unchanged with temperature. Measurements from 20 to 140 K (Chapter 5, Section 5.3.2) have shown that efficient charge separation and an equilibrium between the CT state and SCs still occurs at high temperature. If the charges involved in the equilibrium were detrapped charges, there should be a reduction in the long-lived absorptive signal that is caused by this equilibrium at higher temperatures. Thus, recombination of detrapped charges appears to be favoured with other trapped charges, rather than with mobile ones, suggesting that trap-assisted recombination may be the dominant recombination pathway. This highlights the importance of minimising trap densities in device fabrication: even when present at reduced concentrations compared with low temperature, traps provide a pathway for exciton quenching and charge loss that directly limits photovoltaic performance.

6.4 Conclusions

The results of this chapter bridge the behaviour of long-lived trapped charges observed in steady-state EPR measurements (Chapter 3) and the fast charge transfer and separation dynamics revealed by time-resolved EPR (Chapter 5). Through the use of subtraction and suppression methods for distinguishing short- and long-lived species, connections between CT states and mobile SCs involved in efficient charge generation and charge detrapping processes were drawn. A rapid, photoinduced decrease in the echo intensity of the steady-state trapped charge signal was consistently observed, occurring within 0.1 µs after photoexcitation. This decrease was attributed to a fast exciton quenching process, whereby singlet excitons interact with trapped charges, generating mobile charges that then recombine quickly. Analysis of the energetic distribution of trap states indicated that this quenching mechanism is most pronounced at low temperatures, where the trapped charge density is greatest. These findings identify trapped charges not merely as passive loss sites but also as actively contributing to additional loss mechanisms by quenching photoexcited states, indicating that trap density should be minimised for efficient charge generation, even at OPV operating temperatures.

The successful application of the suppression method to isolate the CT state at early delays-after-flash opens new avenues for probing the CT state microscopic structure. Building on this foundation, advanced pulse EPR techniques, such as out-of-phase electron spin echo envelope modulation (OOP-ESEEM), could be applied at time points where the CT state signal is strongest. This would allow direct measurement of spin-spin couplings and distances, providing experimental validation of the modelled CT state interactions from the time-resolved EPR results in Chapter 5. Furthermore, tracking the spin-spin coupling as a function of delay-after-flash could offer additional insights into the charge separation process following CT state formation.

Chapter 7

Conclusions and Future Work

This thesis has explored the fundamental photophysical processes that drive charge generation in OPV materials from the perspective of electron spins. A variety of EPR spectroscopic techniques have been used to characterise the different paramagnetic states involved in the photovoltaic mechanism: photo-induced CT states, separated charges, and triplet excitons. The investigation extended across a series of donor:acceptor blends spanning three generations of acceptor molecules, the fullerene acceptor blends PM6:PCBM and PBDB-T:PCBM and the high-performing non-fullerene acceptor blends PBDB-T:ITIC and PM6:Y6.

The conversion of light to electricity in OPV blends is fundamentally governed by charged states initially generated by charge transfer at the donor:acceptor interface, and then further separated and transported through the molecular domains towards the electrodes. These photoinduced charged states on donor and acceptor molecules were initially characterised under steady-state conditions using pulse EPR, revealing characteristic spectroscopic signatures and the g-values that determine them. For fullerene acceptor blends, these values were readily extracted by simulation of multi-frequency pulse EPR experiments. However, non-fullerene acceptor blends presented overlapping spectral contributions, which required a more nuanced approach. By either using EDNMR to selectively detect electron spins coupled to ^{14}N nuclei in the non-fullerene acceptor or applying relaxation-based spectral filtering, the individual signals from donor and acceptor species were successfully disentangled. The extracted g-values were rationalised based on DFT-predicted spin density distributions, which were additionally validated by orientation-selective ^{1}H ENDOR.

Charge generation must proceed through successful transfer and separation of charge at the interface by dissociation of the initial photoexcited exciton. A combined experimental and theoretical approach was required to analyse the complex kinetics describing charge separation at the interface, involving spin-correlated CT states and separated charges. A purpose-built simulation package was developed to

rationalise the complicated evolution of spin polarisation resulting from the relative interplay of spin dynamics, kinetics and relaxation for both coupled and separated charges. Inclusion of all of these contributions within the developed simulation framework allowed for rigorous modelling and interpretation of experimental time-resolved EPR results, explaining spin polarisation patterns across different laser intensities, temperatures, and film morphologies with a consistent model.

At early-times, a characteristic polarisation for a singlet-born CT state was observed across all studied blends, unambiguously confirming its central role in the charge generation mechanism. A detailed analysis and simulation of the spin-polarised CT state EPR spectra enabled extraction of the spin-spin couplings and spatial arrangements of the donor and acceptor molecules in the interfacial CT states, revealing a clear trend: non-fullerene acceptor blends form more strongly bound and spatially-ordered CT states. Stronger exchange interactions and reduced spatial separation suggest greater wavefunction overlap and enhanced spin delocalisation, which are favourable for efficient charge separation. The modelled spin density distributions, guided by the experimentally-obtained g-values and hyperfine couplings measured by ENDOR, confirm significant spin delocalisation across the non-fullerene acceptor.

The evolution of the spin-polarised CT state signal, with emissive and absorptive features, into a predominantly absorptive spectrum in time-resolved EPR data, and the change in intensity of this signal with laser fluence and temperature, could be explained within the applied simulation framework. Two channels for charge separation were determined: slow unidirectional charge separation, and for the most efficient blends, ultrafast charge separation, supporting a recent proposal of such a mechanism in a fullerene acceptor blend.[282] These results provide the first direct correlation of the presence of this channel with the high performance of non-fullerene acceptor blends. Furthermore, the simulations revealed the presence of a reversible equilibrium between the CT state and SCs, challenging the classical view of unidirectional charge separation.

Time-resolved EPR was also utilised to investigate the role of triplet exciton formation as a loss pathway; triplets were found to form solely from intersystem crossing, and were less prominent for the more efficient OPV blends, in accordance with the faster rate of charge transfer at the interface observed in these blends.

The steady-state picture of charged states from pulse EPR under constant illumination and the detailed information on short-lived transient CT states extracted from time-resolved EPR data were reconciled through time-resolved pulse EPR. A significant proportion of charges were found to be trapped at 20 K, with thermal activation at higher temperatures increasing the free charge concentration. Through

separation of the spectral signatures of the short-lived and long-lived states by tuning pulse sequences, their interdependence was determined. The different nature of detection in continuous-wave and pulse time-resolved EPR revealed additional signal contributions in the latter, which could be interpreted in terms of exciton quenching by trapped charges and their participation in trap-assisted recombination processes, reducing the charge separation and charge transport efficiencies, respectively. The successful isolation of the transient signals, attributed to the short-lived CT state, with pulse EPR, opens up avenues for more direct measurement of the spin-spin couplings, potentially even as a function of time after photoexcitation, to verify the modelled results from time-resolved EPR and provide additional details on the charge separation process.

The work presented in this thesis establishes a proven model for the analysis and interpretation of EPR spectroscopic data in terms of the photophysical mechanisms governing OPVs from an electron spin perspective. The spin-selective nature of EPR spectroscopy enabled identification of previously unobserved pathways of charge separation and clarified the roles of key intermediates, emphasising the importance of strong electronic coupling, spatial ordering, and low trap densities in supporting ultrafast and efficient charge generation.

Several experimental avenues could be pursued to build on these findings. Extending EPR measurements to higher microwave frequencies (time-resolved EPR at W-band and beyond) would provide an even clearer visualisation of the spin polarisation pattern, allowing a more precise characterisation of the evolution of charge-transfer states and separated charges and narrowing down the uncertainties in the donor:acceptor geometries and separations. In addition, combining EPR with optical spectroscopic methods under identical conditions could reveal processes inaccessible to EPR alone, such as exciton dissociation ($S_1 \rightarrow CT$) and non-geminate recombination ($SC \rightarrow CT \rightarrow T_1$).

While the focus of the work in this thesis was on active-layer films, studies are ongoing in the research group to extend these methodologies to fully-fabricated devices using techniques such as electrically detected magnetic resonance (EDMR) and optically detected magnetic resonance (ODMR).[343,344] Unlike conventional EPR, which probes unpaired spins in isolated films, EDMR and ODMR interrogate spin-dependent processes during device operation. EDMR monitors spin-dependent changes in electrical current, providing greater insight into the fate of charges following charge separation, including recombination and trapping processes. ODMR probes spin-dependent photoluminescence, distinguishing between radiative and non-radiative recombination pathways. In the most efficient OPV blends, both the stability of the $CT - SC$ equilibrium and the balance between radiative and non-radiative recombination are governed by the underlying energy-level alignment;

alignments that favour radiative recombination at the interface are also associated with more favourable CT − SC equilibria.[280]

Charge delocalisation was observed to have a critical role in promoting charge separation from the interface. The polymer donor molecules exhibited delocalisation across at least four monomer sub-units, while the CT state geometries that corresponded to maximal wavefunction overlap ($\pi-\pi$ stacking) promoted ultrafast charge separation. The absence of ultrafast charge separation in PM6:PCBM, combined with the lack of preferential molecular orientations, reinforces the importance of order and stacking at the interface. Systematic studies of materials with varying degrees of $\pi - \pi$ stacking, both between donor and acceptor molecules or between two acceptor molecules, achieved, for example, through controlled annealing or targeted side-chain engineering,[46,345] could provide valuable design rules to optimise interfacial ordering and promote the ultrafast charge separation channel.

The experimental and computational tools developed in this thesis provide a versatile platform for investigating more complex OPV architectures, such as ternary blends and tandem devices. Beyond elucidating fundamental mechanisms, this combined approach of experiment and simulation offers a powerful screening tool for new materials, enabling joint synthetic-spectroscopic efforts where molecular design is directly informed by spectroscopy-guided structure-function relationships. These insights can guide the rational design and synthesis of next-generation, high-performance OPV materials, including more sustainable, 'greener' alternatives,[19,20] rooted in a detailed understanding of charge transfer and separation. Collectively, this work establishes a framework for spectroscopy-informed materials discovery and a pathway towards more efficient and sustainable photovoltaic technologies.

Appendices

Appendix A

Field Calibration

Calibration is performed using a paramagnetic sample with a known and precisely measured g-value. An ideal calibration standard produces a strong, symmetric, and isotropic EPR signal with minimal line width. A nitrogen atom encapsulated within a fullerene cage satisfies these criteria and is commonly used for this purpose. In $N@C_{60}$, a nitrogen atom is trapped inside a C_{60} cage, forming a stable complex. The unpaired electron of the nitrogen atom $\left(S = \frac{3}{2}\right)$ is coupled to the ^{14}N nucleus $(I = 1)$, giving three sets of three EPR lines of equal intensity, each set split by the hyperfine interaction a. Due to the degeneracy of the M_S transitions, the three sets all occur at the same field positions, giving the appearance of a single set of three EPR lines.

The experimental spectrum of $N@C_{60}$ is compared with a simulated spectrum generated using literature values of the g-factor and hyperfine coupling constant A.[150] By shifting the magnetic field axis of the simulated spectrum to best overlay with the experimental data (Figure A.1), the field offset can be precisely determined. This offset is then applied as a correction to all subsequent experimental spectra.

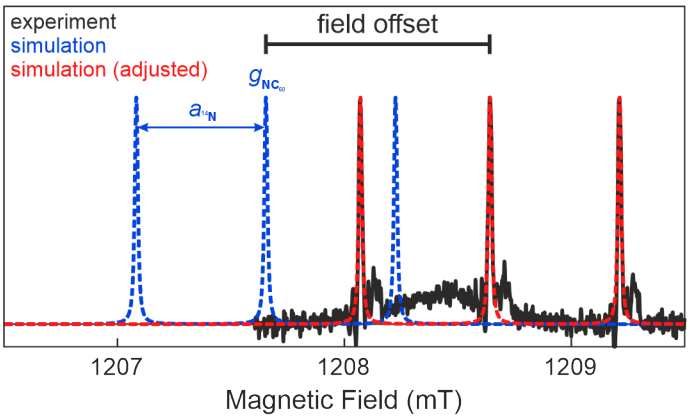

Figure A.1: Field calibration using the EPR spectrum of $N@C_{60}$, shown here at Q-band.

Appendix B

Additional Measurements of Relaxation Times

Material	Charge	Position	T_1 (ms) X 20 K	X 80 K	Q 20 K	W 20 K
PBDB-T:PCBM	PBDB-T$^{\bullet+}$	far-left				13.2
	PBDB-T$^{\bullet+}$	left				11.8
	PBDB-T$^{\bullet+}$	centre	3.5	0.1	4.6	10.5
	PCBM$^{\bullet-}$		4.4	0.1	7.6	11.1
PM6:PCBM	PM6$^{\bullet+}$	far-left				14.4
	PM6$^{\bullet+}$	left				13.1
	PM6$^{\bullet+}$	centre	5.0	0.2	5.8	11.6
	PCBM$^{\bullet-}$		5.6	0.2	6.9	11.8
PBDB-T:ITIC		far-left			11.0	39.4
		left			7.2	20.5
		centre	5.0	0.2	5.0	10.3
PM6:Y6		far-left			8.0	42.2
		left			5.8	31.3
		centre	3.1	0.1	4.9	15.0

Table B.1: T_1 parameters obtained from simulation of inversion recovery curves in Figures B.1, B.3, B.5 and B.7 at a range of temperatures and frequencies. Far-left, left and centre refer to low- to high-field positions of the polymer and fullerene acceptor peaks. Estimated fitting errors are 0.1, 0.03, 0.1, and 0.5 ms for the four respective conditions.

Material	Charge	Position	T_m (µs) X 20 K	X 80 K	Q 20 K	W 20 K	d X 20 K	X 80 K	Q 20 K	W 20 K
PBDB-T:PCBM	PBDB-T$^{\bullet+}$	far-left				5.8				1.6
	PBDB-T$^{\bullet+}$	left				6.0				1.8
	PBDB-T$^{\bullet+}$	centre	3.7	3.2	4.9	6.1	1.3	1.2	1.6	1.8
	PCBM$^{\bullet-}$		3.7	2.9	4.8	6.3	1.2	1.0	1.2	1.5
PM6:PCBM	PM6$^{\bullet+}$	far-left				6.1				1.7
	PM6$^{\bullet+}$	left				6.3				1.9
	PM6$^{\bullet+}$	centre	3.3	3.8	5.8	6.6	1.1	1.4	1.7	1.9
	PCBM$^{\bullet-}$		3.5	3.6	6.9	7.0	0.8	1.0	1.5	1.6
PBDB-T:ITIC		far-left			4.9	4.6			1.6	1.4
		left			5.0	4.6			1.6	1.5
		centre	2.8	3.3	5.4	5.3	1.2	1.2	1.7	1.7
PM6:Y6		far-left			4.5	3.7			1.7	1.1
		left			4.5	4.6			1.6	1.4
		centre	2.8	3.4	4.8	5.8	1.2	1.4	1.6	1.6

Table B.2: T_m and d parameters obtained from simulation of echo decays in Figures B.2, B.4, B.6 and B.8 at a range of temperatures and frequencies. Estimated fitting errors are 0.1 µs at 20 K and 0.5 µs at 80 K for T_m and 0.1 for d.

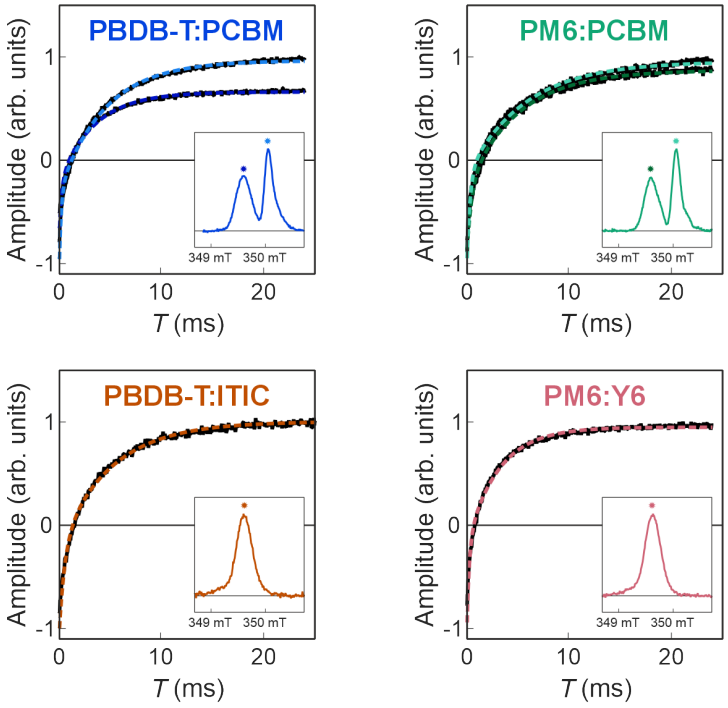

Figure B.1: Inversion recovery curves for PBDB-T:PCBM, PM6:PCBM, PBDB-T:ITIC, and PM6:Y6, measured at 20 K and X-band. Simulation parameters are in Table B.1.

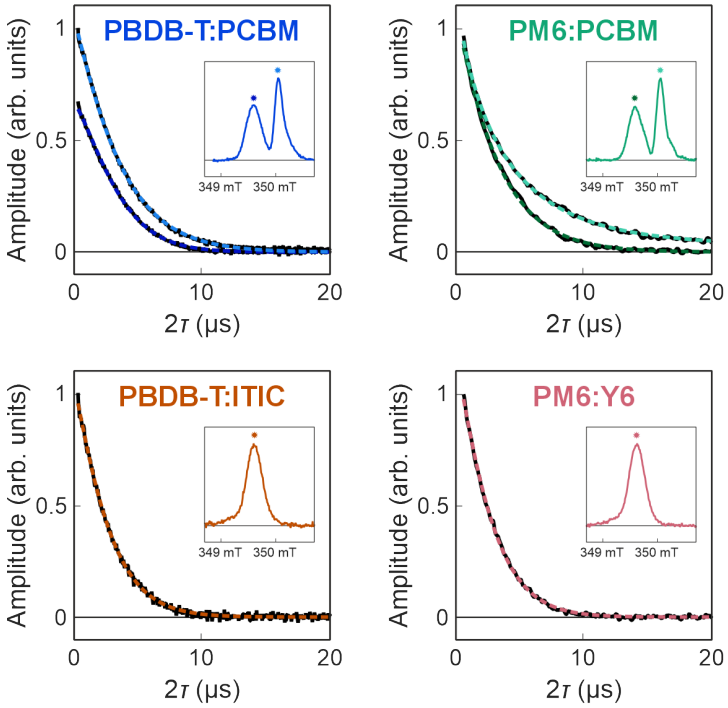

Figure B.2: Decay of the echo-detected EPR signal for PBDB-T:PCBM, PM6:PCBM, PBDB-T:ITIC, and PM6:Y6, measured at 20 K and X-band. Simulation parameters are in Table B.2.

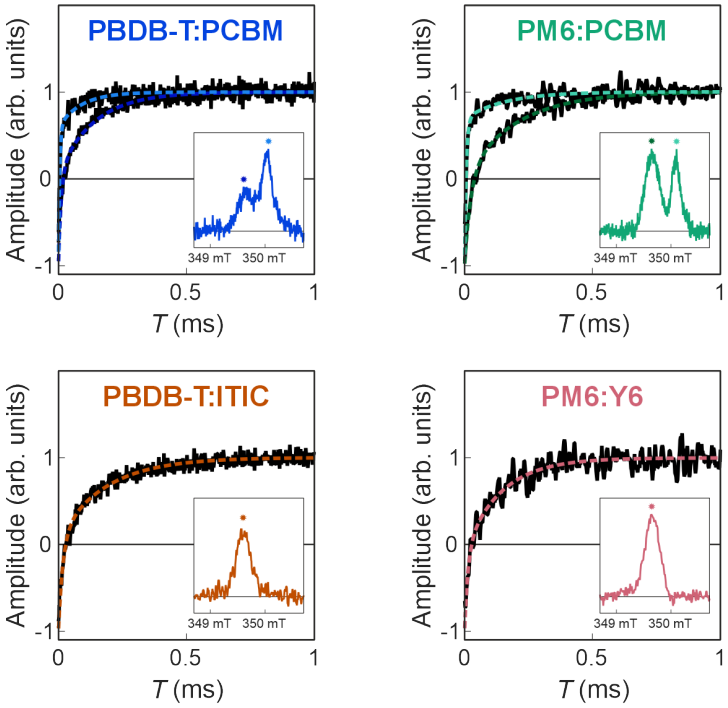

Figure B.3: Inversion recovery curves for PBDB-T:PCBM, PM6:PCBM, PBDB-T:ITIC, and PM6:Y6, measured at 80 K and X-band. Simulation parameters are in Table B.1.

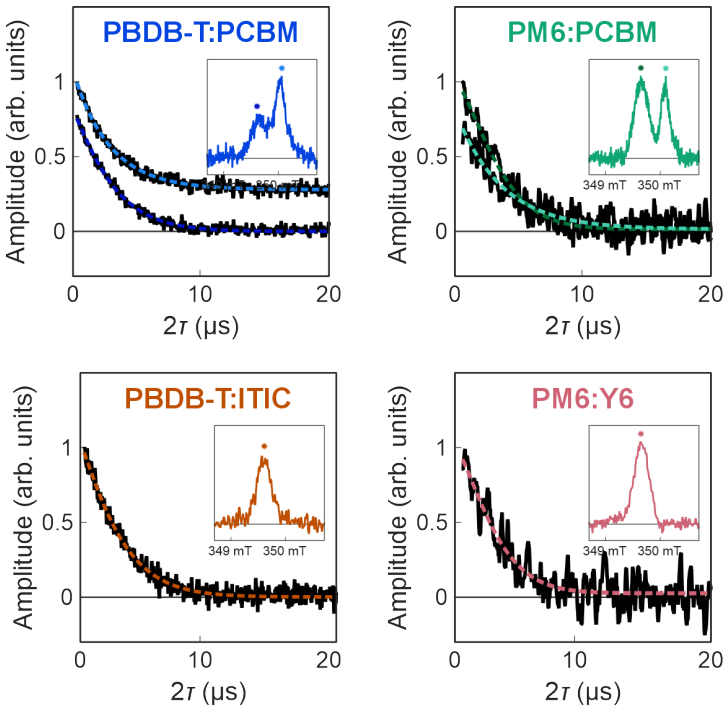

Figure B.4: Decay of the echo-detected EPR signal for PBDB-T:PCBM, PM6:PCBM, PBDB-T:ITIC, and PM6:Y6, measured at 80 K and X-band. Simulation parameters are in Table B.2.

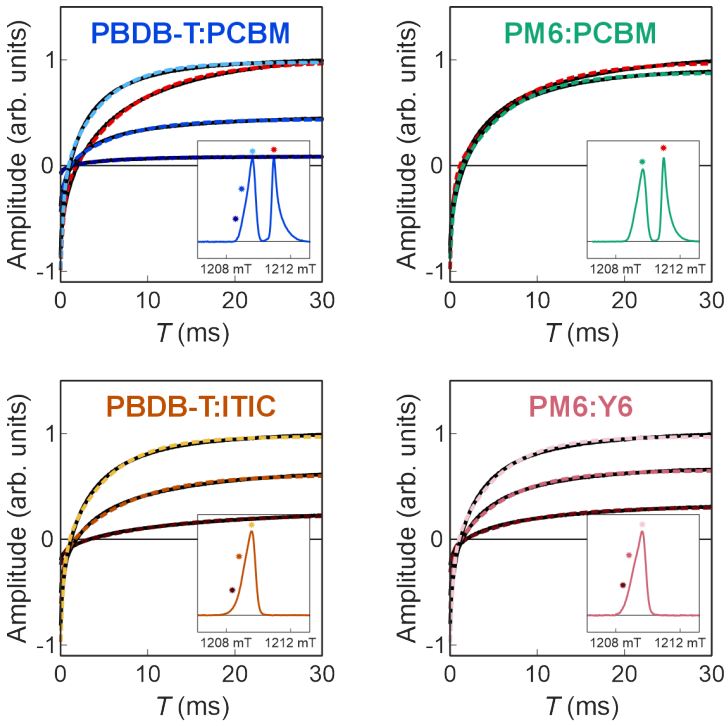

Figure B.5: Inversion recovery curves for PBDB-T:PCBM, PM6:PCBM, PBDB-T:ITIC, and PM6:Y6, measured at 20 K and Q-band. Simulation parameters are in Table B.1.

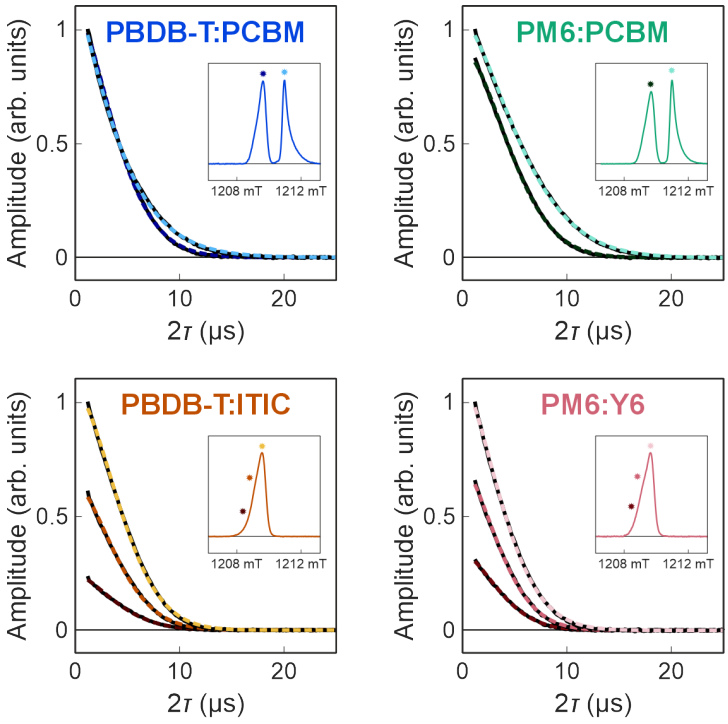

Figure B.6: Decay of the echo-detected EPR signal for PBDB-T:PCBM, PM6:PCBM, PBDB-T:ITIC, and PM6:Y6, measured at 20 K and Q-band. Simulation parameters are in Table B.2.

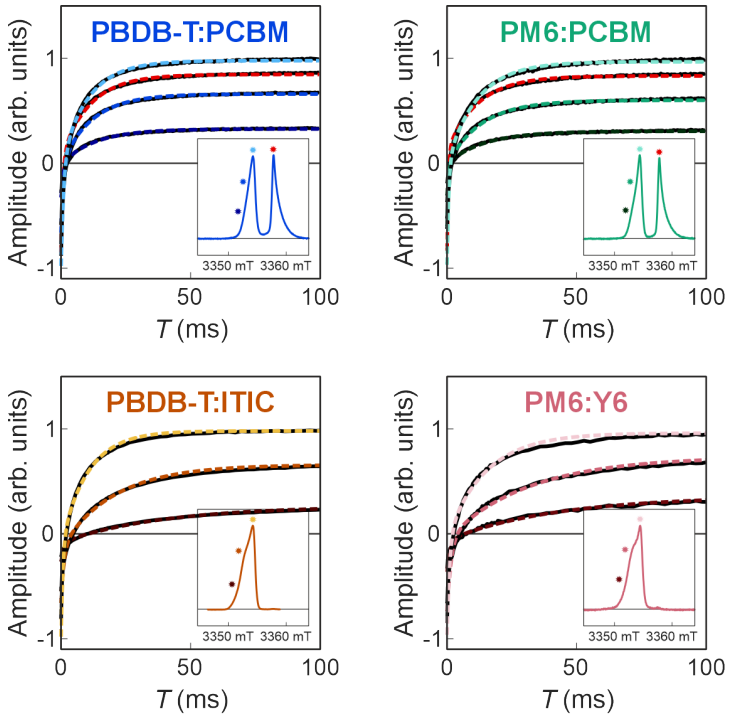

Figure B.7: Inversion recovery curves for PBDB-T:PCBM, PM6:PCBM, PBDB-T:ITIC, and PM6:Y6, measured at 20 K and W-band. Simulation parameters are in Table B.1.

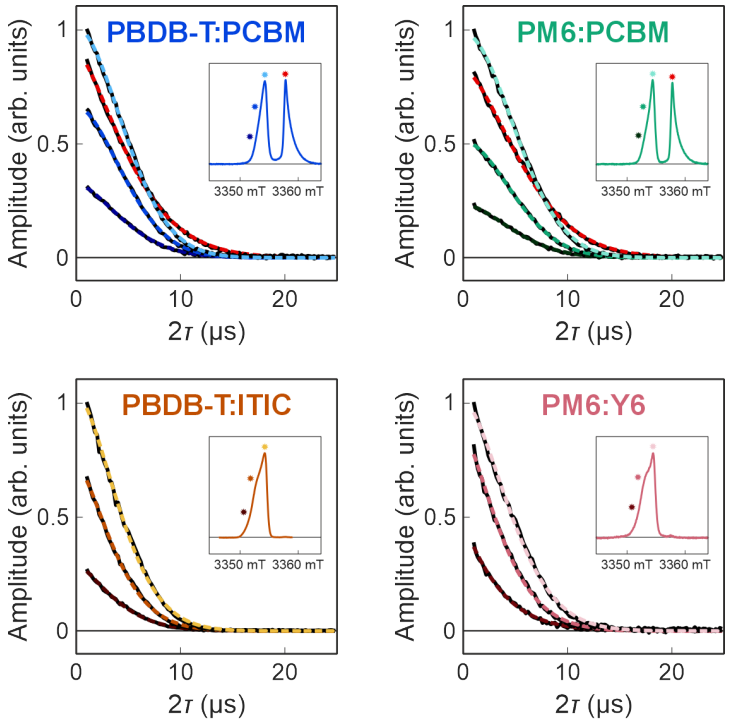

Figure B.8: Decay of the echo-detected EPR signal for PBDB-T:PCBM, PM6:PCBM, PBDB-T:ITIC, and PM6:Y6, measured at 20 K and W-band. Simulation parameters are in Table B.2.

Appendix C

Derivations for Simulations of Spin Dynamics

Time-Step Propagator

The general solution of the master equation for a time-independent Liouvillian $\hat{\hat{\mathcal{L}}}$ is given by:

$$\hat{\rho}(t) = \hat{\rho}_{\mathrm{ss}} + \mathrm{e}^{\hat{\hat{\mathcal{L}}}t}\,(\hat{\rho}_0 - \hat{\rho}_{\mathrm{ss}}) \tag{C.1}$$

where $\hat{\rho}_{\mathrm{ss}}$ is the steady-state solution and $\hat{\hat{\mathcal{L}}} = -i\hat{\hat{\mathcal{H}}} - \hat{\hat{K}} - \hat{\hat{\Gamma}}$ is the Liouvillian superoperator governing the dynamics.

This solution assumes that $\hat{\hat{\mathcal{L}}}$ is time-independent. If some terms in $\hat{\hat{\mathcal{L}}}$ are time-dependent, then the propagation can split into short discrete time steps $\mathrm{d}t$, within which the Liouvillian can be treated as approximately time-independent.

The evolution over one time step $\mathrm{d}t$ is:

$$\hat{\rho}(t + \mathrm{d}t) = \hat{\rho}_{\mathrm{ss}} + \mathrm{e}^{\hat{\hat{\mathcal{L}}}\mathrm{d}t}\,(\hat{\rho}(t) - \hat{\rho}_{\mathrm{ss}}) \tag{C.2}$$

In order to improve computational efficiency, particularly when the time evolution must be applied iteratively in a loop, it is advantageous to recast the evolution as a linear operation:

$$\hat{\rho}(t + \mathrm{d}t) = \hat{\hat{O}}\,\hat{\rho}(t) \tag{C.3}$$

where $\hat{\hat{O}}$ is a superoperator that can be precomputed once and applied at each time step.

Using the expression for the density operator at $t + \mathrm{d}t$, $\hat{\hat{O}}$ can be expressed as;

$$\begin{aligned}
\hat{\hat{O}}\,\hat{\rho}(t) &= \hat{\rho}(t + \mathrm{d}t) \\
&= \hat{\rho}_{\mathrm{ss}} + \mathrm{e}^{\hat{\hat{\mathcal{L}}}\mathrm{d}t}\,(\hat{\rho}(t) - \hat{\rho}_{\mathrm{ss}}) \\
&= \left(\hat{\hat{O}}_{\mathrm{ss}} + \mathrm{e}^{\hat{\hat{\mathcal{L}}}\mathrm{d}t}\left(\hat{\hat{1}} - \hat{\hat{O}}_{\mathrm{ss}}\right)\right)\hat{\rho}(t)
\end{aligned} \tag{C.4}$$

where $\hat{\hat{O}}_{\text{ss}}$ is a projection superoperator in Liouville space, and maps any density operator $\hat{\rho}(t)$ to the steady-state, so that $\hat{\hat{O}}_{\text{ss}}\,\hat{\rho}(t) = \hat{\rho}_{\text{ss}}$ for all normalised states $\hat{\rho}(t)$. This allows the full expression to remain linear in $\hat{\rho}(t)$, enabling pre-computation of the propagator:

$$\hat{\hat{O}} = \hat{\hat{O}}_{\text{ss}} + \mathrm{e}^{\hat{\hat{\mathcal{L}}}\mathrm{d}t}\left(\hat{\hat{1}} - \hat{\hat{O}}_{\text{ss}}\right) \tag{C.5}$$

which is equivalent to the definition in Equation 4.16.

Rotating Frame Transformation

The evolution of the quantum state $|\psi(t)\rangle$ in the lab frame is governed by the time-dependent Schrödinger equation:

$$\frac{\mathrm{d}}{\mathrm{d}t}\,|\psi(t)\rangle_{\text{lab}} = -\mathrm{i}\hat{\mathcal{H}}_{\text{lab}}(t)\,|\psi(t)\rangle_{\text{lab}} \tag{C.6}$$

where $\hat{\mathcal{H}}_{\text{lab}}(t)$ is the Hamiltonian expressed in the lab frame, time-dependent due to an external oscillating field.

To simplify this time dependence, a transformation to a rotating frame is introduced. This is achieved by applying a unitary operator:

$$\hat{U}(t) = \mathrm{e}^{-\mathrm{i}\omega_{\text{mw}}t\hat{S}_z} \tag{C.7}$$

This operator is chosen to represent a rotation about the z-axis at angular frequency ω_{mw}. The state in the rotating frame is defined by:

$$|\psi(t)\rangle_{\text{lab}} = \hat{U}(t)\,|\psi(t)\rangle_{\text{rot}} \tag{C.8}$$

and this rotating frame has the same angular frequency as the oscillating field.

To determine the dynamics in the rotating frame, the time derivative of each side is taken:

$$\frac{\mathrm{d}}{\mathrm{d}t}\,|\psi\rangle_{\text{lab}} = \frac{\mathrm{d}\hat{U}}{\mathrm{d}t}\,|\psi\rangle_{\text{rot}} + \hat{U}\frac{\mathrm{d}}{\mathrm{d}t}\,|\psi\rangle_{\text{rot}} \tag{C.9}$$

The left-hand side, using Equations C.6 and C.8 can be expressed as:

$$\frac{\mathrm{d}}{\mathrm{d}t}\,|\psi\rangle_{\text{lab}} = -\mathrm{i}\hat{\mathcal{H}}_{\text{lab}}\hat{U}\,|\psi\rangle_{\text{rot}} \tag{C.10}$$

simplifying Equation C.9 to:

$$-\mathrm{i}\hat{\mathcal{H}}_{\text{lab}}\hat{U}\,|\psi\rangle_{\text{rot}} = \frac{\mathrm{d}\hat{U}}{\mathrm{d}t}\,|\psi\rangle_{\text{rot}} + \hat{U}\frac{\mathrm{d}}{\mathrm{d}t}\,|\psi\rangle_{\text{rot}} \tag{C.11}$$

After premultiplication by $\hat{U}^\dagger(t)$, the result becomes:

$$\begin{aligned}\frac{\mathrm{d}}{\mathrm{d}t}\left|\psi\right\rangle_{\mathrm{rot}} &= -\mathrm{i}\hat{U}^\dagger\hat{\mathcal{H}}_{\mathrm{lab}}\hat{U}\left|\psi\right\rangle_{\mathrm{rot}} - \hat{U}^\dagger\frac{\mathrm{d}\hat{U}}{\mathrm{d}t}\left|\psi\right\rangle_{\mathrm{rot}} \\ &= -\mathrm{i}\left(\hat{U}^\dagger\hat{\mathcal{H}}_{\mathrm{lab}}\hat{U} - \mathrm{i}\hat{U}^\dagger\frac{\mathrm{d}\hat{U}}{\mathrm{d}t}\right)\left|\psi\right\rangle_{\mathrm{rot}}\end{aligned} \tag{C.12}$$

This expression is rewritten in Schrödinger form:

$$\frac{\mathrm{d}}{\mathrm{d}t}\left|\psi\right\rangle_{\mathrm{rot}} = -\mathrm{i}\hat{\mathcal{H}}_{\mathrm{rot}}\left|\psi(t)\right\rangle_{\mathrm{rot}} \tag{C.13}$$

from which the rotating-frame Hamiltonian is identified as:

$$\hat{\mathcal{H}}_{\mathrm{rot}} = \hat{U}^\dagger(t)\hat{\mathcal{H}}_{\mathrm{lab}}\hat{U}(t) - \mathrm{i}\hat{U}^\dagger(t)\frac{\mathrm{d}\hat{U}}{\mathrm{d}t} \tag{C.14}$$

For spins in a static magnetic field $\boldsymbol{B}_0$ along z, and an oscillating field along x, the lab-frame Hamiltonian is:

$$\hat{\mathcal{H}}_{\mathrm{lab}}(t) = \hat{\mathcal{H}}_0 + \hat{\mathcal{H}}_1(t) \tag{C.15}$$

where $\hat{\mathcal{H}}_0$ defines the static spin interactions and $\hat{\mathcal{H}}_1(t)$, the time-dependent part, is given by:

$$\hat{\mathcal{H}}_1(t) = \frac{g\mu_{\mathrm{B}}}{\hbar}B_1(t)\hat{S}_x = \frac{g\mu_{\mathrm{B}}}{\hbar}B_1\cos(\omega_{\mathrm{mw}}t)\hat{S}_x \tag{C.16}$$

The transformation of the components of the Hamiltonian is carried out using:

$$\begin{aligned}\hat{U}^\dagger\hat{S}_z\hat{U} &= \hat{S}_z \\ \hat{U}^\dagger\hat{S}_x\hat{U} &= \cos(\omega_{\mathrm{mw}}t)\hat{S}_x + \sin(\omega_{\mathrm{mw}}t)\hat{S}_y\end{aligned} \tag{C.17}$$

If non-secular terms are omitted from the static spin Hamiltonian $\mathcal{H}_0$, then, as an approximation, only terms that commute with the electron Zeeman spin Hamiltonian ($\hat{S}_z$) remain in $\mathcal{H}_0$:

$$\hat{\mathcal{H}}_0 = \omega_{\mathrm{eff}}\hat{S}_z \tag{C.18}$$

where ω_{eff} is some effective spin precession frequency. The secular approximation, for a CT state, is valid in the weak coupling regime, when the difference in spin precession frequencies is large compared to the spin-spin coupling, or the system is observed on timescales longer than the period of oscillation of the non-secular terms.

Under these conditions, $\hat{\mathcal{H}}_0$ is unaffected by the transformation:

$$\hat{U}^\dagger\hat{\mathcal{H}}_0\hat{U} = \omega_{\mathrm{eff}}\hat{U}^\dagger\hat{S}_z\hat{U} = \omega_{\mathrm{eff}}\hat{S}_z = \hat{\mathcal{H}}_0 \tag{C.19}$$

For the transformation of the time-dependent spin Hamiltonian $\mathcal{H}_1$:

$$\begin{aligned}\hat{U}^\dagger\hat{\mathcal{H}}_1\hat{U} &= \frac{g\mu_\mathrm{B}}{\hbar}B_1\cos(\omega_\mathrm{mw}t)\,\hat{U}^\dagger\hat{S}_x\hat{U} \\ &= \frac{g\mu_\mathrm{B}}{\hbar}B_1\cos(\omega_\mathrm{mw}t)\,\left(\cos(\omega_\mathrm{mw}t)\hat{S}_x + \sin(\omega_\mathrm{mw}t)\hat{S}_y\right) \\ &= \frac{g\mu_\mathrm{B}}{2\hbar}B_1\left(\hat{S}_x + \cos(2\omega_\mathrm{mw}t)\hat{S}_x + \sin(2\omega_\mathrm{mw}t)\hat{S}_y\right)\end{aligned} \tag{C.20}$$

where the last step makes use of trigonometric identities of $\sin 2x$ and $\cos 2x$.

Finally, the time derivative $\frac{\mathrm{d}\hat{U}}{\mathrm{d}t}$ is calculated:

$$\begin{aligned}\frac{\mathrm{d}\hat{U}}{\mathrm{d}t} &= \frac{\mathrm{d}}{\mathrm{d}t}\mathrm{e}^{-\mathrm{i}\omega_\mathrm{mw}t\hat{S}_z} \\ &= -\mathrm{i}\omega_\mathrm{mw}\hat{S}_z\,\mathrm{e}^{-\mathrm{i}\omega_\mathrm{mw}t\hat{S}_z} \\ &= -\mathrm{i}\omega_\mathrm{mw}\hat{S}_z\hat{U}\end{aligned} \tag{C.21}$$

and so the derivative component of Equation C.14 is:

$$\begin{aligned}-\mathrm{i}\hat{U}^\dagger\frac{\mathrm{d}\hat{U}}{\mathrm{d}t} &= \mathrm{i}\hat{U}^\dagger\,\mathrm{i}\omega_\mathrm{mw}\hat{S}_z\hat{U} \\ &= -\omega_\mathrm{mw}\hat{U}^\dagger\hat{S}_z\hat{U} \\ &= -\omega_\mathrm{mw}\hat{S}_z\end{aligned} \tag{C.22}$$

The overall rotating frame Hamiltonian is thus:

$$\hat{\mathcal{H}}_\mathrm{rot} = \hat{\mathcal{H}}_0 + \frac{g\mu_\mathrm{B}}{2\hbar}B_1\left(\hat{S}_x + \cos(2\omega_\mathrm{mw}t)\hat{S}_x + \sin(2\omega_\mathrm{mw}t)\hat{S}_y\right) - \omega_\mathrm{mw}\hat{S}_z \tag{C.23}$$

This Hamiltonian is still time-dependent, but terms that oscillate at angular frequency of $2\omega_\mathrm{mw}$ can be neglected, as they average out to zero over the timescales of interest:

$$\langle\cos(2\omega_\mathrm{mw}t)\rangle \approx 0, \qquad \langle\sin(2\omega_\mathrm{mw}t)\rangle \approx 0 \tag{C.24}$$

This rotating wave approximation is valid when the amplitude of $\boldsymbol{B}_1$, and thus the frequency ω_1 is much smaller than ω_mw; the system cannot respond to these very fast oscillations, and so they do not contribute. The rotating frame Hamiltonian then becomes time-independent, returning the result in Equation 4.20:

$$\begin{aligned}\hat{\mathcal{H}}_\mathrm{rot} &= \hat{\mathcal{H}}_0 + \frac{g\mu_\mathrm{B}}{2\hbar}B_1\hat{S}_x - \omega_\mathrm{mw}\hat{S}_z \\ &= \hat{\mathcal{H}}_0 + \hat{\mathcal{H}}_1 - \omega_\mathrm{mw}\hat{S}_z\end{aligned} \tag{C.25}$$

where $\hat{\mathcal{H}}_1$ no longer is a function of time. $-\omega_\mathrm{mw}\hat{S}_z$ corresponds to the effective shift in the Hamiltonian in the rotating frame. Physically, it accounts for moving into a frame rotating at angular frequency ω_mw about the z-axis, effectively subtracting this rotation frequency from the Hamiltonian.

Appendix D

MATLAB Script for RADISH Simulations

```
% RADISH  Computation of 1- and 2-spin transient EPR spectra
%
%   RADISH(Sys,Exp)
%   RADISH(Sys,Exp,Opt)
%
%   Calculates 1- and 2-spin transient EPR spectra
%
%   The package EasySpin is a requirement for RADISH to run
%   (version 6.0.0 or later). Download at https://easyspin.org.
%
%   Input:
%    Sys: parameters of the paramagnetic system
%      S, g, Nucs, A, dip, J
%      gFrame, AFrame, eeFrame
%      lw, lwpp
%      initState
%      T1, T2, tauS, tauT
%      tauDiss, tauEnc, tauDec, StatePops (Two-State Model)
%    Exp: experimental parameter settings
%      mwFreq              microwave frequency, in GHz
%      B1                  strength of B1 field, in mT
%      Range               field  range, [Bmin Bmax], in mT
%      nPoints             number of points in the field
   dimension
%      dt                  time step, in mus
%      tPoints             number of points in the time
   dimension
%      Temperature         temperature, in K
%      Qvalue
%    Opt: computational options
%      GridSize            grid size;  N1, [N1 Ninterp]
%      Boltzmann           true (relaxation to Boltzmann),
   false (to equal)
%      Threshold           skip field points where a given
   orientation is
```

```
%                              over X MHz from any resonance
    transition
%
%    Output:
%      x        cell containing time axis (in mus) and field axis
    (in mT)
%      spc      spectrum
%      rho      density matrix elements

function [x,spc,rho] = RADISH(Sys,Exp,Opt)

if nargin==0, help(mfilename); return; end

% Check for EasySpin
if exist('easyspin','file') == 0
  error('EasySpin must be installed for RADISH to run (6.0.0-
     dev.45 or later). Please install at https://easyspin.org')
else
  version = easyspin().Version; % '$ReleaseID$' for Github
     version
  if str2double(version(1)) < 6 || (contains(version,'dev') &&
     str2double(version(end-1:end)) < 45)
    error('Please install EasySpin 6.0.0-dev.45 or later)')
  end
end

% Guard against wrong number of input or output arguments.
if nargin<1, error('Please supply a spin system as first
    parameter.'); end
if nargin<2, error('Please supply experimental parameters as
    second input argument.'); end
if nargin>3, error('Too many input arguments.'); end

if nargout>3, error('Too many output arguments.'); end

% Initialize options structure to zero if not given.
if nargin<3, Opt = struct; end
if isempty(Opt), Opt = struct; end

if ~isstruct(Sys) && ~iscell(Sys)
  error('Sys must be a structure or a cell array of structures!
     ');
end
if ~isstruct(Exp)
  error('Exp must be a structure!');
end
if ~isstruct(Opt)
  error('Opt must be a structure!');
end

% Determine if J and dip specified as a function of r or
    independently
% ----------------------------------------
if isfield(Sys,'r') && ~isempty(Sys.r)
  if isfield(Sys,'J') || isfield(Sys,'dip')
```

```
    error('Both Sys.r and (Sys.J, Sys.dip) are given - use one
       or the other!')
  end
  if ~isfield(Sys,'J0') || ~isfield(Sys,'beta')
    error('Sys.r specified, but J terms missing (J0 and beta)!'
       )
  end
  fJ = @(r) Sys.J0*exp(-Sys.beta*r);
  fdip = @(r) (mu0/4/pi)*(r*1e-9).^-3*(bmagn*gfree)^2/planck/1
     e6;
  Sys.J = fJ(Sys.r);
  Sys.dip = fdip(Sys.r);
end

% Shortcut for specifying singlet (overwrites Sys.initState)
if isfield(Sys,'Psinglet')
  Ptriplet = (1-Sys.Psinglet)/3;
  Sys.initState = {[Ptriplet Ptriplet Ptriplet Sys.Psinglet],'
     coupled'};
end

% Validation of Opt structure
% ---------------------------------------
DefaultOpt.GridSymmetry ='Ci';
[~,DefaultOpt.GridFrame] = hamsymm(Sys);
DefaultOpt.Transitions = [];
DefaultOpt.Sites = [];
DefaultOpt.GridSize = 10;
DefaultOpt.Threshold = []; % MHz
DefaultOpt.Boltzmann = true;
DefaultOpt.Verbosity = false;
DefaultOpt.SeparateDetection = false; % detect radical pair and
    separated radicals separately

Opt = runprivate('adddefaults',Opt,DefaultOpt);

% ---------------------------------------
% ---------------------------------------
% Calculation setup
% ---------------------------------------
% ---------------------------------------

% Spin system validation and setup
if Opt.Verbosity
  fprintf('Spin system validation ...\n');
end
[Sys,err] = runprivate('validatespinsys',Sys);
error(err);

DefaultSys.HStrain = [0 0 0];

Sys = runprivate('adddefaults',Sys,DefaultSys);

computeStrain = any(Sys.HStrain(:));
```

```
% Check if T1, T2 are provided or switch off/set to a very
    large value
if ~isfield(Sys,'T1'), Sys.T1 = (Exp.tPoints-1)*Exp.dt*1e3; end
    % 1e3x larger than last time point
if ~isfield(Sys,'T2'), Sys.T2 = (Exp.tPoints-1)*Exp.dt*1e3; end
    % 1e3x larger than last time point
if any([Sys.T1(:); Sys.T2(:)]<0) || any(~isreal([Sys.T1(:); Sys
    .T2(:)]))
  error('T1 and T2 in Sys.T1 and Sys.T2 must be positive and in
      microseconds.');
end
if min(Sys.T1(Sys.T1~=0),[],'all') < max(Sys.T2(Sys.T2~=0),[],'
    all'), error('T1 must be larger than or equal to T2.'); end
if isvector(Sys.T1) && numel(Sys.T1)>3 || isvector(Sys.T2) &&
    numel(Sys.T2)>3
  error('If specifying T1 and T2 in Sys.T1 and Sys.T2 as
     vectors, they must be 1-element (all coherences equal), 2-
     element ([SQC ZQC/DQC]) or 3-element([SQC ZQC DQC])
     vectors')
end
if ~isvector(Sys.T1) && all(size(Sys.T1)~=Sys.nStates) || ~
    isvector(Sys.T2) &&  all(size(Sys.T2)~=Sys.nStates)
  error('Sizes of Sys.T1 and/or Sys.T2 matrices are incorrect.'
     )
end

% Convert kinetic lifetimes into rate constants
if isfield(Sys,'tauS'), kS = 1/Sys.tauS; else, kS = 0; end %
    set rate constant to 0 if not specified
if isfield(Sys,'tauT'), kT = 1/Sys.tauT; else, kT = 0; end %
    set rate constant to 0 if not specified
if any([kS kT]<0) || any(~isreal([kS kT]))
  error('tauS and tauT in Sys.tauS and Sys.tauT must be
     positive and in microseconds.');
end

% Additional kinetics if considering two radical pairs
TwoStateModel = false;
StatePops = [];
if any(isfield(Sys,{'tauDiss','tauEnc','tauDec','StatePops'}))
  if isfield(Sys,'tauDiss'),  kDiss = 1/Sys.tauDiss; else,
     kDiss = 0; end
  if isfield(Sys,'tauEnc'), kEnc = 1/Sys.tauEnc; else, kEnc =
     0; end
  if isfield(Sys,'tauDec'), kDec = 1/Sys.tauDec; else, kDec =
     0; end
  if any([kDiss kEnc kDec]<0) || any(~isreal([kDiss kEnc kDec])
     ) || any(isinf([kDiss kEnc kDec]))
    error('tauDiss, tauEnc and tauDec in Sys.tauDiss, Sys.
       tauEnc and Sys.tauDec must be positive and in
       microseconds.');
  end
  if ~isfield(Sys,'StatePops'), Sys.StatePops = [1 0]; end  %
     no starting population in separated radicals (default)
  StatePops = Sys.StatePops;
  if numel(StatePops) == 1, StatePops = [StatePops 0]; end
```

```
  if any(StatePops<0) || any(~isreal(StatePops)) || any(isinf(
      StatePops)) || numel(StatePops) ~= 2 || all(StatePops ==
      0)
    error('Populations of the radical pair and separated
       radicals must be non-negative and specified as such: Sys
       .StatePops = [Pair Rads]')
  end
  TwoStateModel = true;
end

% Validation of Exp structure
% ---------------------------------------
DefaultExp.mwFreq = NaN;
DefaultExp.B1 = NaN;
DefaultExp.Range = NaN;
DefaultExp.nPoints = NaN;
DefaultExp.dt = NaN;
DefaultExp.tPoints = 101;
DefaultExp.Temperature = 293; % K, room temperature
DefaultExp.mwMode = '';

DefaultExp.Ordering = [];
DefaultExp.SampleFrame = [0 0 0];
DefaultExp.CrystalSymmetry = '';
DefaultExp.MolFrame = [];
DefaultExp.SampleRotation = [];

Exp = runprivate('adddefaults',Exp,DefaultExp);

Exp.PowderSimulation = ~isempty(Exp.Ordering) ||(isempty(Exp.
   MolFrame) && isempty(Exp.CrystalSymmetry));

if isnan(Exp.mwFreq), error('Exp.mwFreq is missing! Please
   specify in GHz.'); end

if isnan(Exp.B1), error('Exp.B1 is missing! Please specify in
   mT.'); end

if isnan(Exp.Range), error('Exp.Range is missing! Please
   specify in mT.'); end
if any(diff(Exp.Range)<=0) || any(~isfinite(Exp.Range)) || ~
   isreal(Exp.Range)
  error('Exp.Range is not valid!');
end
if any(Exp.Range<0)
  error('Negative magnetic fields in Exp.Range are not possible
     .');
end

if isnan(Exp.dt), error('Exp.dt is missing! Please specify in
   microseconds.'); end
if ~isfinite(Exp.dt) || ~isreal(Exp.dt) || Exp.dt<0
  error('Exp.dt is not valid!')
end
% Time axis
time = (0:(Exp.tPoints-1))*Exp.dt;
```

```
% Default field points based off sampling artefacts
NyquistdB = 0.05/max(time); % largest field step before alias
    sampling noise affects spectrum
if isnan(Exp.nPoints) && numel(Exp.Range) == 2
  Exp.nPoints = ceil(diff(Exp.Range)/NyquistdB) + 1;
end

% Field axis
if numel(Exp.Range) == 2
  Field = linspace(Exp.Range(1),Exp.Range(2),Exp.nPoints); % mT
else
  if numel(Exp.Range) == Exp.nPoints
    Field = Exp.Range; % mT
  else
    error('Please select the same number of nPoints as Exp.
       Range.')
  end
end

% Transient Artefact Test
if mean(diff(Field)) >= NyquistdB
  rangeB = max(Field) - min(Field);
  NyquistPoints = ceil(rangeB/NyquistdB) + 1;
  % warning('Exp.nPoints specified is too small and may cause
     transient artefacts! Please use at least %i points.',
     NyquistPoints)
end


% Setup of orientational grid
% ----------------------------------------
[Exp,Opt] = runprivate('p_sampletype',Exp,Opt);

% Symmetry determination and orientational grid.
if Opt.Verbosity
  fprintf('Set up orientational grid...\n');
end
[Exp,Opt] = runprivate('p_gridsetup',Sys,Exp,Opt);

% Process crystal orientations, crystal symmetry, and frame
    transforms
% This sets Orientations, nOrientations, nSites and
    AverageOverChi
[Orientations,nOrientations,~,~] = runprivate('
    p_crystalorientations',Exp,Opt);
if Opt.Verbosity
  fprintf('Looping over %i orientations...\n',nOrientations);
end

% Setup spin operators, initial and equilibrium states and
    relaxation and
% kinetics operators
% ----------------------------------------

% Electron Spin Operators (S)
```

```
nElectrons = Sys.nElectrons;
nStates = Sys.nStates;
nStatesL = nStates^2;
if TwoStateModel, nStatesL = nStatesL*2; end

totSpinOpsS = cell(1,3);
SpinOpsS = cell(nElectrons,3);
for i = 1:3
  totSpinOpsS{i} = zeros(nStates);
  for iSpin = 1:nElectrons
    SpinOpsS{iSpin,i} = sop(Sys.Spins,[iSpin,i]);
    totSpinOpsS{i} = totSpinOpsS{i} + sop(Sys.Spins,[iSpin,i]);
  end
end

% Nuclear Spin Operators (I)
nNuclei = Sys.nNuclei;
SpinOpsN = cell(nNuclei,3);
for i = 1:3
  for iSpin = 1:nNuclei
    SpinOpsN{iSpin,i} = sop(Sys.Spins,[nElectrons + iSpin,i]);
  end
end

% S1S2
% insert error if you have 2 spins, check Sys.S at beginning
   with only 2
% elements
S1S2 = zeros(nStates);
for i = 1:3
  S1S2 = S1S2 + SpinOpsS{1,i}*SpinOpsS{2,i};
end

% also do check for 2 spins
% States in ST basis defined as linear combination of states in
    uncoupled basis
STbasis = cgmatrix(Sys.S(1),Sys.S(2));
Tp = STbasis(1,:)';
T0 = STbasis(2,:)';
Tm = STbasis(3,:)';
S = STbasis(4,:)';

% Singlet and triplet projection operators
PS = S*S';
PT = T0*T0' + Tp*Tp' + Tm*Tm';

% Account for any nuclei
nElStates = prod(2*Sys.S+1);
nNucStates = nStates/nElStates;
PS = kron(PS,eye(nNucStates))/nNucStates;
PT = kron(PT,eye(nNucStates))/nNucStates;

% Zeeman Interaction prefactors
preE = bmagn/1e3/planck/1e6; % MHz/mT
preN = -nmagn/1e3/planck/1e6; % MHz/mT (opposite charge to
   electron)
```

```
% Initial density matrix
% ----------------------------------------
computeNonEquiPops = ~isempty(Sys.initState);
if computeNonEquiPops
  Sys = validateinitState(Sys);
  Sigma0L = reshape(Sys.initState{1},[],1);
  if TwoStateModel % separated charges have equal starting
     populations of all levels
    Sigma0L = [Sigma0L*StatePops(1); reshape(eye(nStates)/sum(
       nStates)*StatePops(2),[],1)];
  end
  initStateBasis = Sys.initState{2};
else
  Sigma0L = [];
  initStateBasis = [];
  fprintf('Initial state not specified - Boltzmann populations
     assumed\n')
end

% Chemical kinetics superoperator (Haberkorn) & Singlet-triplet
    dephasing term (Jones-Hore)
% ----------------------------------------
PSL = kron(eye(nStates),PS) + kron(PS.',eye(nStates));
PTL = kron(eye(nStates),PT) + kron(PT.',eye(nStates)); %
   transform density operators into Liouville space
KinOp = 0.5*(kS*PSL + kT*PTL);
STdephaseOp = 0.5*(kS + kT)*(kron(PS,PT) + kron(PT,PS)); %
   Jones-Hore

if TwoStateModel
  KinOpPair = KinOp + kDiss*eye(nStates^2);
  KinOpRad = (kEnc + kDec)*eye(nStates^2);
  KinOpRad2Pair = -kEnc*eye(nStates^2);
  KinOpPair2Rad = -kDiss*eye(nStates^2);
  KinOp = [KinOpPair KinOpRad2Pair; KinOpPair2Rad KinOpRad];
  STdephaseOp = blkdiag(STdephaseOp,STdephaseOp);
end


% Set up relaxation superoperator
% ----------------------------------------
idxQC = nElStates:nElStates-1:nElStates^2-1; % anti-diagonal:
   ZQC, DQC indices
lgcQC = zeros(nElStates);
lgcQC(idxQC) = true;

idxDQC = idxQC([1 4]); % DQC indices
lgcDQC = zeros(nElStates);
lgcDQC(idxDQC) = true;

idxZQC = idxQC([2 3]); % ZQC indices
lgcZQC = zeros(nElStates);
lgcZQC(idxZQC) = true;

lgcQC = logical(kron(lgcQC,eye(nNucStates)));
```

```
lgcZQC = logical(kron(lgcZQC,eye(nNucStates)));
lgcDQC = logical(kron(lgcDQC,eye(nNucStates)));

T1 = ones(nStates)*Sys.T1(1);
if numel(Sys.T1) == 2
  T1(lgcQC) = Sys.T1(2); % specify different Z/DQC relaxation
end
if numel(Sys.T1) == 3
  T1(lgcZQC) = Sys.T1(2); % specify ZQC relaxation
  T1(lgcDQC) = Sys.T1(3); % specify DQC relaxation
end
T1 = triu(T1,1);

T2 = ones(nStates)*Sys.T2(1);
if numel(Sys.T2) == 2
  T2(lgcQC) = Sys.T2(2); % specify different Z/DQC relaxation
end
if numel(Sys.T2) == 3
  T2(lgcZQC) = Sys.T2(2); % specify ZQC relaxation
  T2(lgcDQC) = Sys.T2(3); % specify DQC relaxation
end
T2 = triu(T2,1) + triu(T2,1)';

% Assigns default values or Inf to all T1 relaxation paths
   which are zero.
T1(T1==0) = 1e10;
T2(T2==0) = 1e10;

RelaxOp0 = zeros(nStates^2);
kk = 1;
jj = 2;

% calculates the positions of longitudinal relaxation
for k1 = 1:nStates+1:nStates^2
  for k2 = k1+nStates+1 : nStates+1 : nStates^2
    RelaxOp0(k1,k2) = -1/T1(kk,jj);
    RelaxOp0(k2,k1) = -1/T1(kk,jj);
    RelaxOp0(k1,k1) = RelaxOp0(k1,k1) + 1/T1(kk,jj);
    RelaxOp0(k2,k2) = RelaxOp0(k2,k2) + 1/T1(kk,jj);
    jj = jj+1;
  end
  kk = kk+1;
  jj = kk+1;
end
RelaxOp0 = RelaxOp0/nStates;

% populates positions of transverse relaxation elements
n = 1;
% rewrites T2 matrix into a vector, to allow effective
   processing
T2vec = reshape(T2,[],1);
for k = 2:nStates^2-1
  if k ~= n+1+n*nStates
    RelaxOp0(k,k) = 1/T2vec(k);
  else
    n = n+1;
```

```
  end
end
% see EasySpin/spidyan for more information

if TwoStateModel, RelaxOp0 = blkdiag(RelaxOp0,RelaxOp0); end

% ----------------------------------------
% Calculate transient EPR signal
% ----------------------------------------
% Initialise signal (required for parallelization)

Sx = totSpinOpsS{1};

dt = Exp.dt;
B1 = Exp.B1;
mwFreq = Exp.mwFreq;
nTimePoints = Exp.tPoints;
nBPoints = Exp.nPoints;
OriWeights = Exp.OriWeights;
Temperature = Exp.Temperature;

Boltzmann = Opt.Boltzmann; % logical
Threshold = Opt.Threshold; % MHz
SeparateDetection = Opt.SeparateDetection; % logical

[spc,spc_Pair,spc_Rad] = deal(zeros(nTimePoints,nBPoints));
rho = zeros(nStatesL,nTimePoints);

idxDiag = false(nStates,1);
idxDiag(1:nStates+1:nStates^2) = true; % index for diagonal
   elements
idxPair = [true(nStates^2,1); false(nStates^2,1)];
idxRad = [false(nStates^2,1); true(nStates^2,1)];
if TwoStateModel, idxDiag = [idxDiag; idxDiag]; end

nArg = nargout;

% Rotating frame adjustment independent of time or orientation
Ham0_rt = -Exp.mwFreq*1e3*totSpinOpsS{3};

% Detection operator
DetOp = totSpinOpsS{2}; % detection along y
DetL = reshape(DetOp.',1,nStates^2);
if TwoStateModel && ~SeparateDetection
  DetL = [DetL DetL];
end

% Apply tensor frame adjustment
% 2-spin check (error)
rotatetensor = @(x,y) erot(y).'*diag(x)*erot(y); % apply frame
   transformation to molecular frame

% Electron-Zeeman Factors
g = zeros(3,3,nElectrons);
for eSpin = 1:nElectrons
```

```
  g(:,:,eSpin) = rotatetensor(Sys.g(eSpin,:),Sys.gFrame(eSpin
      ,:));
end

% Nuclear-Zeeman Factors
sigma = zeros(3,3,nNuclei);
for nSpin = 1:nNuclei
  sigma(:,:,nSpin) = rotatetensor(Sys.sigma(nSpin,:),Sys.
      sigmaFrame(nSpin,:));
end

% Electron-Electron Factors
J = Sys.J;
D = rotatetensor(Sys.dip,Sys.eeFrame);

% Hyperfine Factor
A = zeros(nNuclei,nElectrons);
for eSpin = 1:nElectrons
  eI = (eSpin-1)*3 + (1:3);
  for nSpin = 1:nNuclei
    nI = (nSpin-1)*3 + (1:3);
    A(nI,eI) = rotatetensor(Sys.A(nSpin,eI),Sys.AFrame(nSpin,eI
        ));
  end
end

% HStrain
HStrain = Sys.HStrain;


% Loop over orientations
% ----------------------------------------
parfor iOri = 1:nOrientations

  [signaliOri,signaliOri_Pair,signaliOri_Rad] = deal(zeros(
      nTimePoints,nBPoints));
  rhoiOri = zeros(nStatesL,nTimePoints);
  U_Rad = zeros(nStates^2);

  % Effective Spin Hamiltonian in Molecular Frame (Field-
      Independent Terms)
% ----------------------------------------
  [B1vecOri,~,B0vecOri] = erot(Orientations(iOri,:),'rows'); %
      B0 and B1: lab --> molecular frame (Schweiger-Jeschke -
      Appendix B.53)

  % Electron Zeeman Interaction
  gSz = zeros(nStates);
  for eSpin = 1:nElectrons
    geff0 = B0vecOri.'*g(:,:,eSpin)*B0vecOri; % effective g in
        mol frame
    gSz = gSz + geff0*SpinOpsS{eSpin,3}; % sum of g.Sz
  end
  Ham0_ez = preE*gSz;

  % Nuclear Zeeman Interaction
```

```
    sigmaSz = zeros(nStates);
    for nSpin = 1:nNuclei
      sigmaeff0 = B0vecOri.'*sigma(:,:,nSpin)*B0vecOri; %
         effective sigma in mol frame
      sigmaSz = sigmaSz + sigmaeff0*SpinOpsN{nSpin,3}; % sum of
         sigma.Sz
    end
    Ham0_nz = preN*sigmaSz;

    % Electron-Electron Interaction
    Deff = B0vecOri.'*D*B0vecOri;
    Ham0_ee = J*S1S2 + Deff*(3/2*SpinOpsS{1,3}*SpinOpsS{2,3} -
       1/2*S1S2); % pseudo-secular approximation

    % Hyperfine Interaction
    Ham0_hf = zeros(nStates);
    for eSpin = 1:nElectrons
      eI = (eSpin-1)*3 + (1:3);
      for nSpin = 1:nNuclei
        nI = (nSpin-1)*3 + (1:3);
        Aeff = B0vecOri.'*A(nI,eI)*B0vecOri;
        Ham0_hf = Ham0_hf + Aeff*(SpinOpsS{eSpin,3}*SpinOpsN{
           nSpin,3}); % secular approximation
      end
    end

    % Total Microwave Hamiltonian
    geff1 = zeros(nElectrons,1);
    for eSpin = 1:nElectrons
      geff1(eSpin) = B1vecOri.'*g(:,:,eSpin)*B1vecOri; %
         effective g in mol frame
    end
    Ham1 = preE*mean(geff1)*B1*Sx; % different effective g along
       B1

    % Loop over magnetic field
    % ----------------------------------------
    for iB = 1:nBPoints

      rhoiB = zeros(nStatesL,nTimePoints);

      % Total Static Hamiltonian
      Ham0 = (Ham0_ez + Ham0_nz) * Field(iB) + Ham0_ee + Ham0_hf;
      Htot = 2*pi*(Ham0 + Ham0_rt + Ham1);
      Hsup = kron(eye(nStates),Htot) - kron(Htot.',eye(nStates));

      % Eigenvectors and Eigenvalues
      [U,E] = eig(Ham0);
      Ediff = diag(E)-diag(E)'; % all possible transition
         energies
      UL = kron(transpose(U),(U'));

      % Equilibrium Density
      SigmaEq = sigeq(Ham0,Temperature); % requires hamiltonian w
         /o rotating frame adjustment
      SigmaEqL = reshape(SigmaEq,[],1);
```

```
if TwoStateModel

  % Two State Total Static Hamiltonian
  Ham0_Rad = (Ham0_ez + Ham0_nz) * Field(iB) + Ham0_hf;
  Htot_Rad = 2*pi*(Ham0_Rad + Ham0_rt + Ham1);
  Hsup_Rad = kron(eye(nStates),Htot_Rad) - kron(Htot_Rad.',
     eye(nStates));
  Hsup = blkdiag(Hsup,Hsup_Rad);

  % Two State Eigenvectors and Eigenvalues
  [U_Rad,E_Rad] = eig(Ham0_Rad);
  Ediff_Rad = diag(E_Rad)-diag(E_Rad)';
  Ediff = [Ediff Ediff_Rad];
  UL_Rad = kron(transpose(U_Rad),(U_Rad'));
  UL = blkdiag(UL,UL_Rad);

  % Two State Equilibrium Density
  SigmaEq_Rad = sigeq(Ham0_Rad,Temperature);
  SigmaEqL_Rad = reshape(SigmaEq_Rad,[],1);
  SigmaEqL = [SigmaEqL; SigmaEqL_Rad];
end

% Transform relaxation superoperator into uncoupled basis
RelaxOp = UL'*RelaxOp0*UL; % eigenbasis --> uncoupled basis

nearRes = min(abs(Ediff(:)-mwFreq*1e3)) <= Threshold;
if ~isempty(Threshold) && ~nearRes
  continue
end % skip steps if outside threshold

% Set up equilibrium state (required for relaxation)
RelaxEq = RelaxOp*SigmaEqL;

% Hamiltonian superoperator and Liouvillean
L = -1i*Hsup - RelaxOp - KinOp - STdephaseOp;
pssEq = -L\RelaxEq; % equilibrium density
pss = pssEq*idxDiag.';
if TwoStateModel
  pss = pssEq(1:nStates^2)*idxDiag(1:nStates^2).';
  pss_Rad = pssEq(nStates^2+1:end)*idxDiag(nStates^2+1:end)
     .';
  pss = blkdiag(pss,pss_Rad);
end

% Propagator
dtProp = fastExpm(L*dt); % faster than expm for larger
   matrices
if Boltzmann % relax to Boltzmann populations
  dtProp = pss + dtProp*(eye(numel(pssEq)) - pss);
end

% Set up initial density
Sigma0L_ = Sigma0L;
if strcmp(initStateBasis,'eigen')
  if TwoStateModel
```

```
        Sigma0L_Pair = Sigma0L_(1:nStates^2);
        Sigma0L_Pair = reshape(U'*reshape(Sigma0L_Pair,nStates,
            nStates)*U,[],1);
        Sigma0L_Rad = Sigma0L(nStates^2+1:end);
        Sigma0L_Rad = reshape(U_Rad'*reshape(Sigma0L_Rad,
            nStates,nStates)*U_Rad,[],1);
        Sigma0L_ = [Sigma0L_Pair; Sigma0L_Rad];
      else
        Sigma0L_ = reshape(U'*reshape(Sigma0L_,nStates,nStates)
            *U,[],1); % eigenbasis --> uncoupled basis
      end
    end
    if computeNonEquiPops
      density = Sigma0L_;
    else
      density = SigmaEqL; % equilibrium density
    end

    % Loop over time axis
    for itime = 1:numel(time)
      % Signal detection
      if TwoStateModel && SeparateDetection
        signali0ri_Pair(itime,iB) = DetL*density(idxPair);
        signali0ri_Rad(itime,iB) = DetL*density(idxRad);
      else
        signali0ri(itime,iB) = DetL*density;
      end
      if nArg >= 3
        if TwoStateModel
          densityH1 = reshape(density(1:nStates^2),nStates,
              nStates); % radical pair
          densityEig1 = U*densityH1*U'; % uncoupled basis -->
              eigenbasis
          densityH2 = reshape(density(nStates^2+1:end),nStates,
              nStates); % separated charges
          densityEig2 = U*densityH2*U'; % uncoupled basis -->
              eigenbasis
          densityEig = [densityEig1(:) densityEig2(:)];
        else
          densityH = reshape(density,nStates,nStates);
          densityEig = U*densityH*U'; % uncoupled basis -->
              eigenbasis
        end
        rhoiB(:,itime) = densityEig(:); % Hilbert --> Liouville
      end
      % Time evolution of the density matrix
      density = dtProp*density;
    end

    if nArg >= 3
      rhoi0ri = rhoi0ri + rhoiB;
    end

  end % iB

  if computeStrain % HStrain
```

```
    gmean = mean(geff1);
    HStrainEff = B0vecOri.'*diag(HStrain)*B0vecOri; % effective
        HStrain
    HStrainWid = unitconvert(HStrainEff,'MHz->mT',gmean);
    if TwoStateModel && SeparateDetection
      signaliOri_Pair = convspec(signaliOri_Pair,[0 mean(diff(
          Field))],[0 HStrainWid],0,1); % Gaussian broadening
      signaliOri_Rad = convspec(signaliOri_Rad,[0 mean(diff(
          Field))],[0 HStrainWid],0,1); % Gaussian broadening
    else
      signaliOri = convspec(signaliOri,[0 mean(diff(Field))],[0
          HStrainWid],0,1); % Gaussian broadening
    end
  end

  weight = OriWeights(iOri);
  if TwoStateModel && SeparateDetection
    spc_Pair = spc_Pair + weight*real(signaliOri_Pair);
    spc_Rad = spc_Rad + weight*real(signaliOri_Rad);
  else
    spc = spc + weight*real(signaliOri);
  end

  if nArg >= 3
    rho = rho + weight*real(rhoiOri);
  end

end % iOri


% Linebroadening
if TwoStateModel && SeparateDetection
  % Add Gaussian linebroadening
  spc_Pair = convspec(spc_Pair,[0 mean(diff(Field))],[0 Sys.lw
      (1)],0,1);
  spc_Rad = convspec(spc_Rad,[0 mean(diff(Field))],[0 Sys.lw(1)
      ],0,1);
  % Add Lorentzian linebroadening
  spc_Pair = convspec(spc_Pair,[0 mean(diff(Field))],[0 Sys.lw
      (2)],0,0);
  spc_Rad = convspec(spc_Rad,[0 mean(diff(Field))],[0 Sys.lw(2)
      ],0,0);
else
  % Add Gaussian linebroadening
  spc = convspec(spc,[0 mean(diff(Field))],[0 Sys.lw(1)],0,1);
  % Add Lorentzian linebroadening
  spc = convspec(spc,[0 mean(diff(Field))],[0 Sys.lw(2)],0,0);
end

% Normalise density matrix
if nArg >= 3
  sumDiag = sum(rho(idxDiag,1));
  rho = rho./sumDiag;
end

% Account for resonator response function
```

```
if isfield(Exp,'Qvalue')
  BW = Exp.mwFreq*1e3/Exp.Qvalue; % MHz
  tresponse = 1/BW; % us
  response = (1-exp(-time/tresponse)).';
  if TwoStateModel && SeparateDetection
    spc_Pair = spc_Pair.*response;
    spc_Rad = spc_Rad.*response;
    spc = {spc_Pair,spc_Rad};
  else
    spc = spc.*response;
  end
end

if Exp.nPoints==1
  x = time;
else
  x{1} = time;
  x{2} = Field;
end

end
```

Appendix E

Additional Time-Resolved EPR Measurements

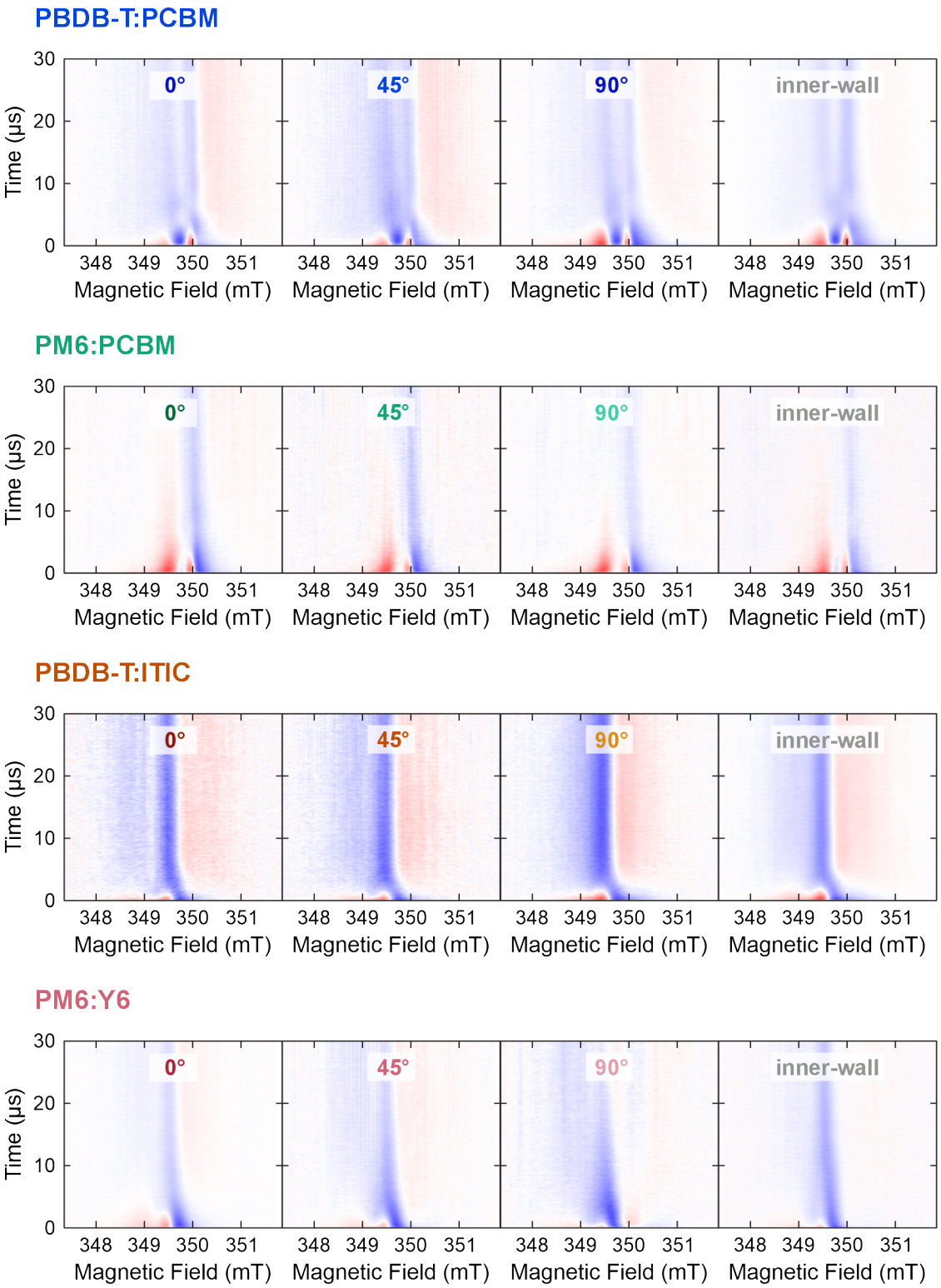

Figure E.1: Time-resolved EPR X-band spectra of spin-coated films of PBDB-T:PCBM, PBDB-T:ITIC, PM6:PCBM and PM6:Y6, with different angles with respect to the external magnetic field, measured at 20 K, 1 mJ cm^{-2}. Time-resolved EPR spectra of the thicker inner-wall films are shown for comparison.

Appendix F

Additional Details of Time-Resolved EPR Simulations

Additional details for the time-resolved EPR simulations of PBDB-T:PCBM, PM6:PCBM, PBDB-T:ITIC, and PM6:Y6 shown in Figures 5.15 and 5.17 to 5.19 of Chapter 5, at temperatures of 20 K, 80 K, and 140 K, and laser fluences of 20 µJ cm^{-2} and 1 mJ cm^{-2}. Kinetic and relaxation parameters are summarised in Table F.1. The time-resolved EPR simulations made use of g-values determined from steady-state pulse EPR in Chapter 3 (Tables 3.1 and 3.4 in Section 3.3.1) and g-frames, J, D, and D-frames from simulation of the singlet-born CT state signal from time-resolved EPR averaged over $0.1 - 0.3$ µs in Chapter 5 (Table 5.3 of Section 5.3.3).

For each figure, simulated EPR spectra are shown for the total signal, as well as the individual contributions of the CT state and SCs. Static spectra extracted at early ($0.1 - 0.3$ µs) and late ($10 - 30$ µs) times highlight the changes in spin polarisation with time. The evolution of the CT state and SC populations are plotted in red and green, respectively, with the populations of their four eigenstates shown below in blue, providing detailed insight into the evolution of the spin sublevel populations that determine the signal polarisation of the EPR spectrum. For the non-fullerene acceptor blends, two orthorhombic proton hyperfine interactions were also included in the time-resolved EPR simulations, both with maximum principal A-values of 20 MHz, and so the populations of each sublevel are determined from averages over the four sublevels of each electron spin state split by the hyperfine interactions.

PBDB-T:PCBM

Temp. (K)	Fluence ($\mathrm{mJ\,cm^{-2}}$)	p_{CT}	τ_{S} (µs)	τ_{diss} (µs)	τ_{enc} (µs)	T_1 (µs)	T_2 (µs)
20	0.02	$0.25-0.35$	$2-6$	$10-20$	>200	>50	$0.5-1.0$
20	1	$0.25-0.35$	$2-6$	$10-20$	$40-60$	$10-20$	$0.5-1.0$
80	1	$0.2-0.3$	$0.5-2$	$1-5$	$10-30$	$1-5$	$0.1-0.4$
140	1	$0.2-0.25$	$0.2-2$	$0.5-2$	>10	$0.5-2$	$0.05-0.1$

PM6:PCBM

Temp. (K)	Fluence ($\mathrm{mJ\,cm^{-2}}$)	p_{CT}	τ_{S} (µs)	τ_{diss} (µs)	τ_{enc} (µs)	T_1 (µs)	T_2 (µs)
20	0.02	1	$20-30$	$10-30$	>200	>50	$0.5-1.0$
20	1	1	$20-30$	$10-30$	>200	>50	$0.5-1.0$
80	1	1	>2	$1-2$	>200	$5-50$	$0.2-0.5$
140	1	1	>1	$0.2-0.5$	>200	$1-5$	$0.05-0.1$

PBDB-T:ITIC

Temp. (K)	Fluence ($\mathrm{mJ\,cm^{-2}}$)	p_{CT}	τ_{S} (µs)	τ_{diss} (µs)	τ_{enc} (µs)	T_1 (µs)	T_2 (µs)
20	0.02	$0.3-0.4$	$0.2-0.8$	$15-30$	>200	$20-100$	$0.5-1.0$
20	1	$0.3-0.4$	$0.2-0.8$	$15-30$	$15-30$	$10-25$	$0.5-1.0$
80	1	$0.15-0.25$	$0.2-0.8$	$1-4$	$10-20$	$2-10$	$0.1-0.5$
140	1	$0.15-0.25$	$0.2-0.8$	$0.5-1$	$10-20$	$0.5-2$	$0.05-0.1$

PM6:Y6

Temp. (K)	Fluence ($\mathrm{mJ\,cm^{-2}}$)	p_{CT}	τ_{S} (µs)	τ_{diss} (µs)	τ_{enc} (µs)	T_1 (µs)	T_2 (µs)
20	0.02	$0.3-0.4$	$0.1-0.5$	$1-10$	$30-50$	$10-25$	$0.5-1.0$
20	1	$0.3-0.4$	$0.1-0.5$	$1-10$	$20-40$	$5-20$	$0.5-1.0$
80	1	$0.15-0.25$	$0.1-0.5$	$0.5-3$	$10-30$	$2-10$	$0.1-0.4$
140	1	$0.15-0.25$	$0.1-0.5$	<1	$10-20$	$1-4$	$0.05-0.2$

Table F.1: Simulation parameters for PBDB-T:PCBM, PM6:PCBM, PBDB-T:ITIC, and PM6:Y6 for the time-resolved EPR simulations in Figures F.1 to F.16. The rate constants k_{T}, and k_{dec} were assumed to be negligible, and so the time constants τ_{T}, and τ_{dec} are set to very large.

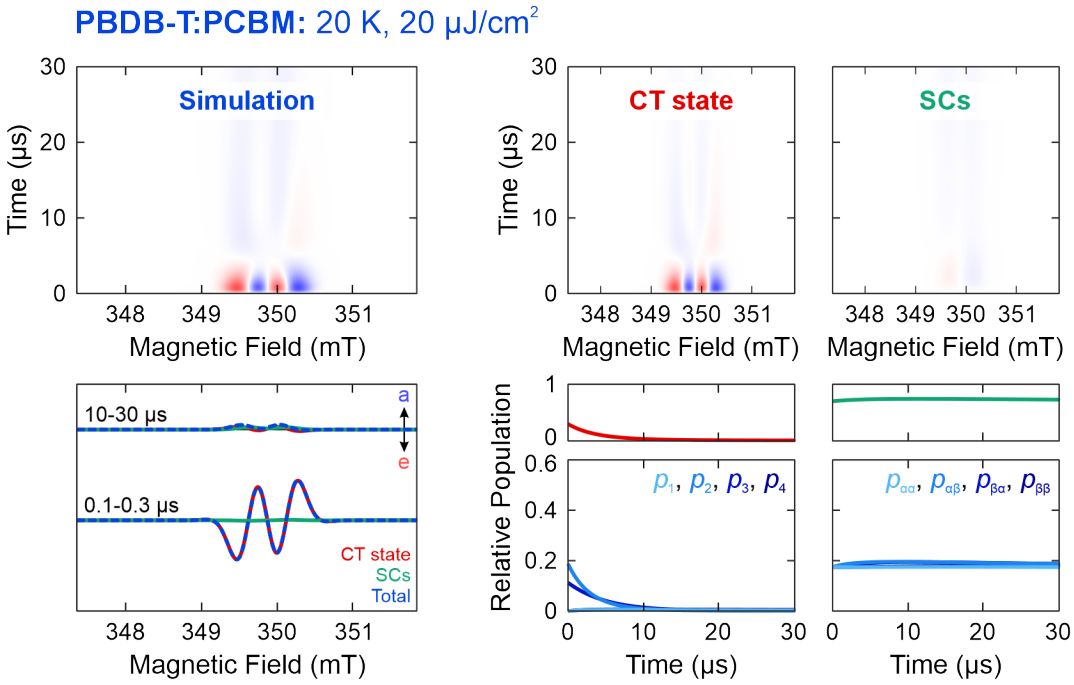

Figure F.1: Additional detail of the time-resolved EPR simulation, as described in the text, of PBDB-T:PCBM from Figure 5.17, at X-band, 20 K, and 20 µJ cm^{-2}.

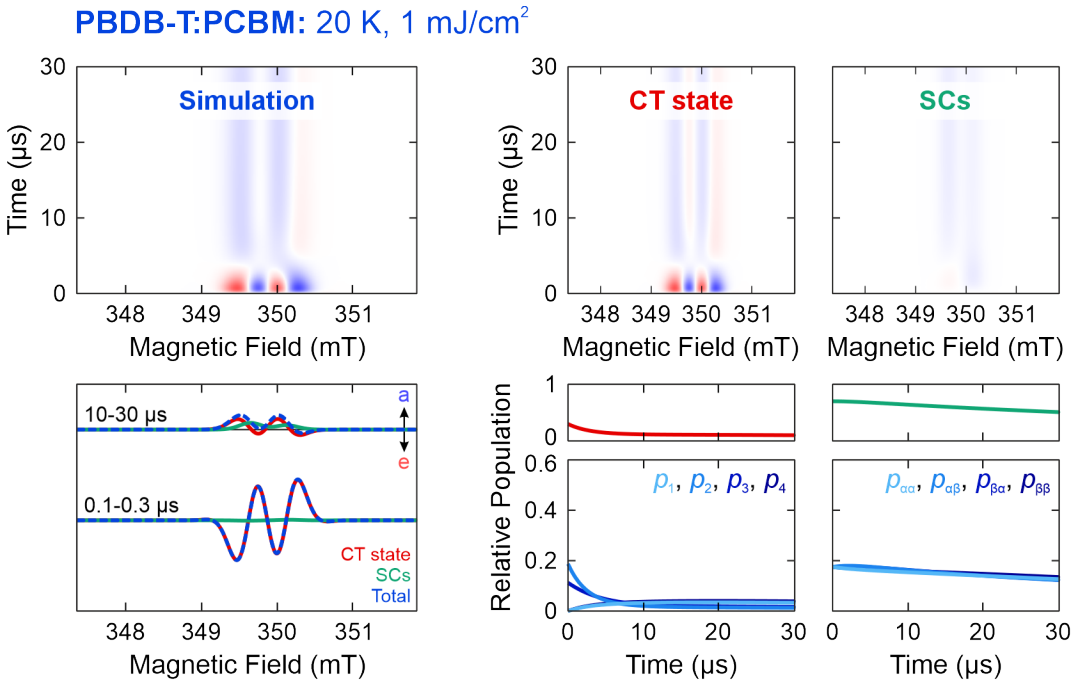

Figure F.2: Additional detail of the time-resolved EPR simulation, as described in the text, of PBDB-T:PCBM from Figure 5.17, at X-band, 20 K, and 1 mJ cm^{-2}.

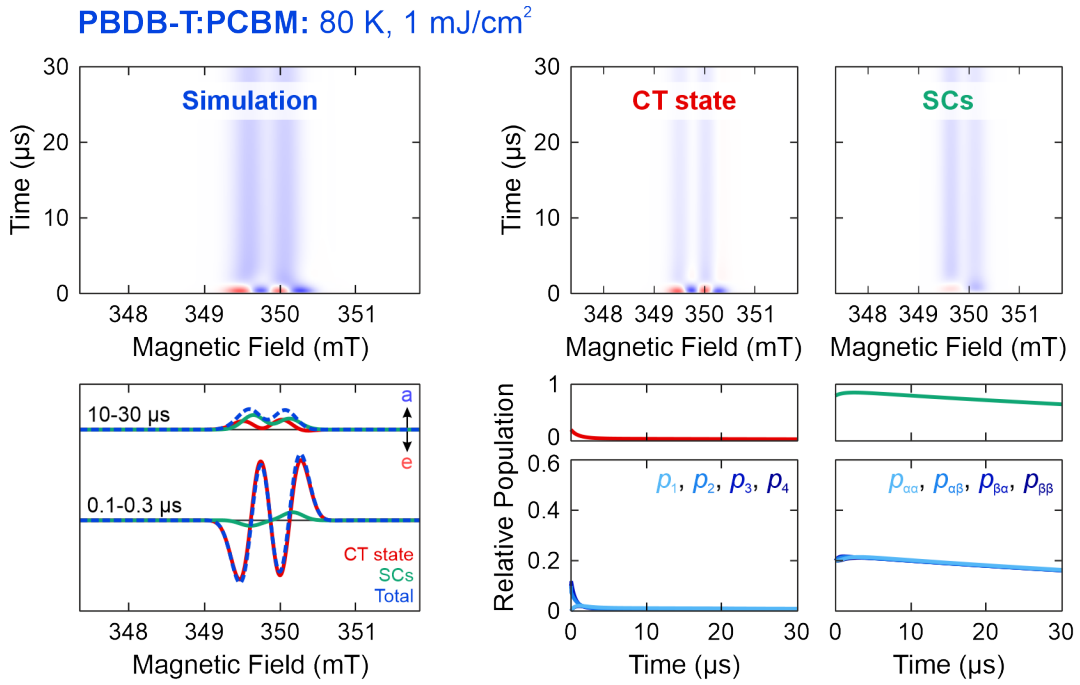

Figure F.3: Additional detail of the time-resolved EPR simulation, as described in the text, of PBDB-T:PCBM from Figure 5.17, at X-band, 80 K, and 1 mJ cm^{-2}.

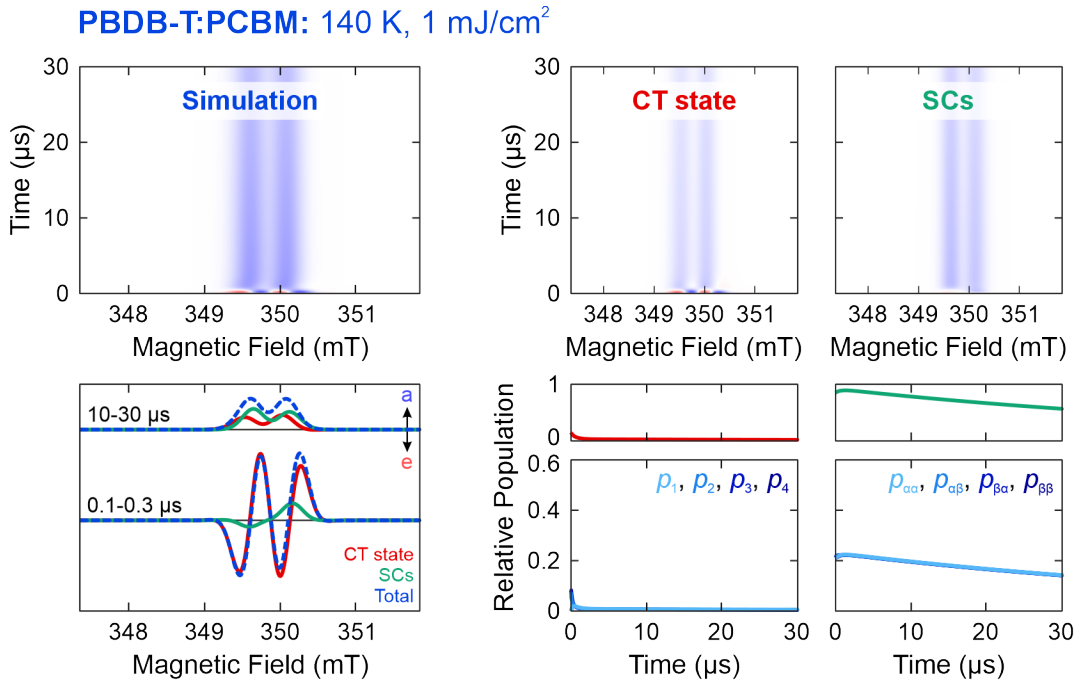

Figure F.4: Additional detail of the time-resolved EPR simulation, as described in the text, of PBDB-T:PCBM from Figure 5.17, at X-band, 140 K, and 1 mJ cm^{-2}.

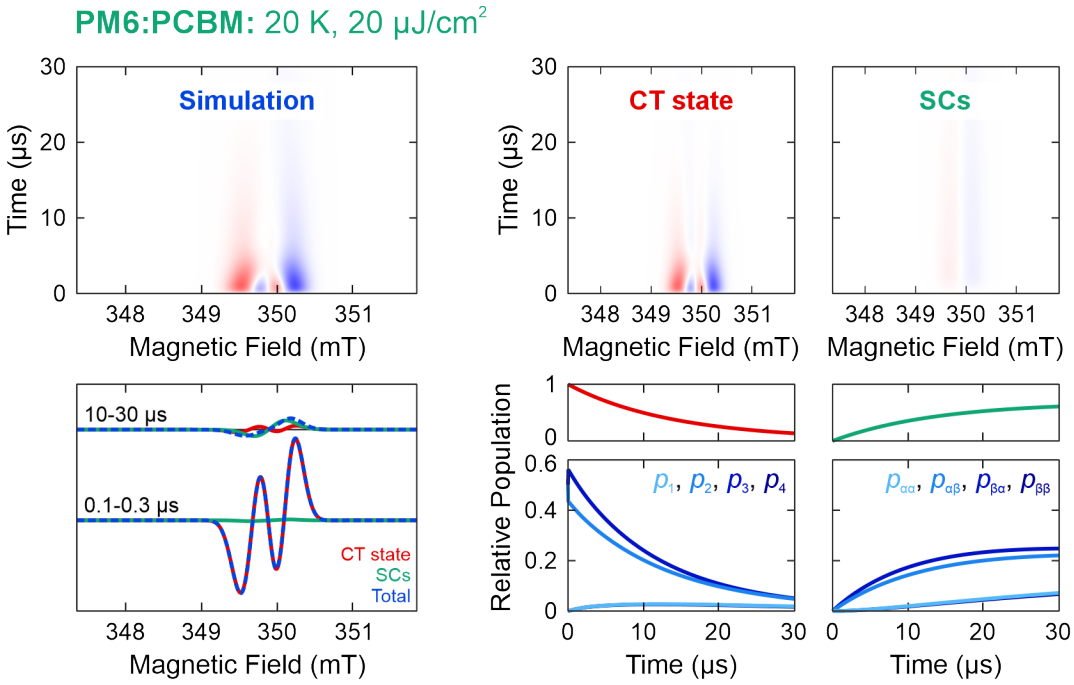

Figure F.5: Additional detail of the time-resolved EPR simulation, as described in the text, of PM6:PCBM from Figure 5.15, at X-band, 20 K, and 20 µJ cm^{-2}.

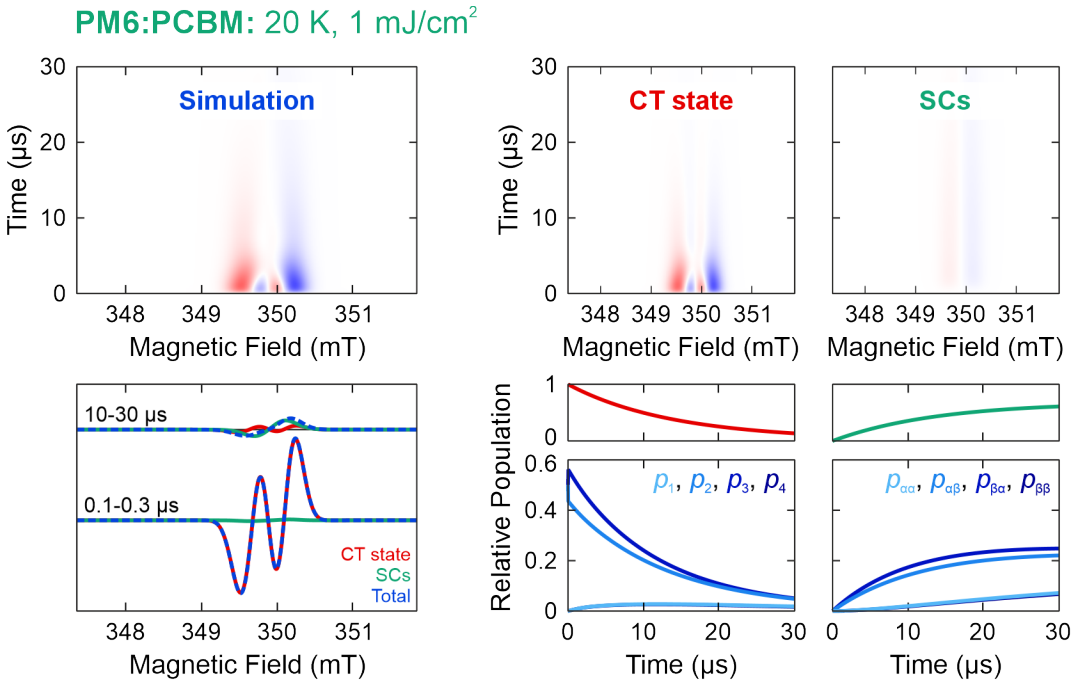

Figure F.6: Additional detail of the time-resolved EPR simulation, as described in the text, of PM6:PCBM from Figure 5.15, at X-band, 20 K, and 1 mJ cm^{-2}.

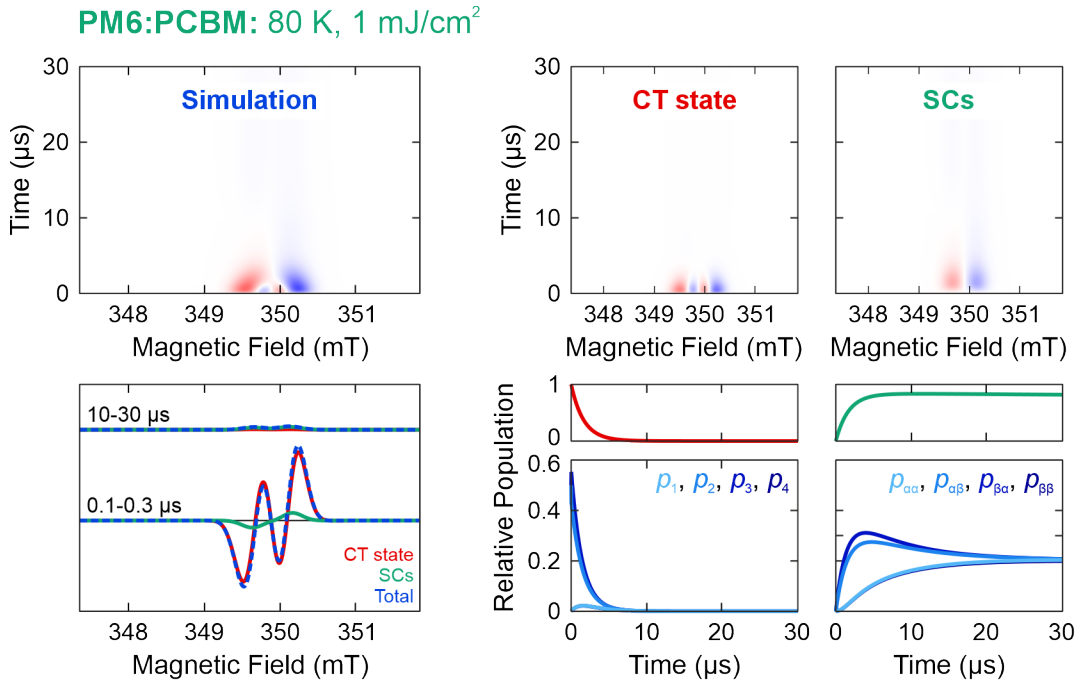

Figure F.7: Additional detail of the time-resolved EPR simulation, as described in the text, of PM6:PCBM from Figure 5.15, at X-band, 80 K, and 1 mJ cm^{-2}.

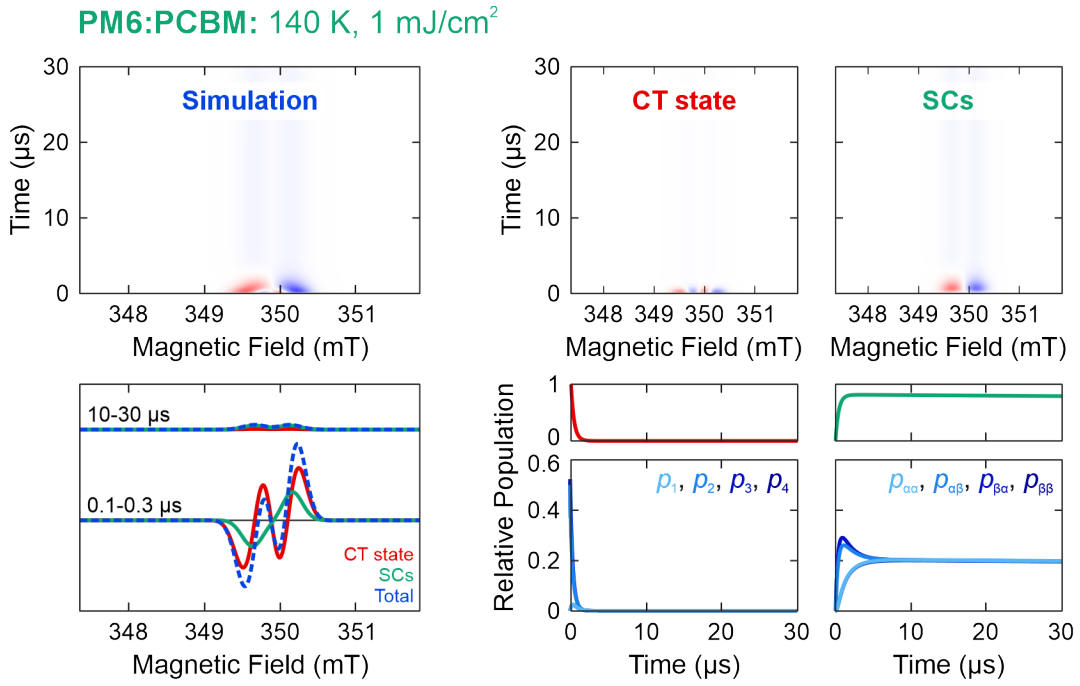

Figure F.8: Additional detail of the time-resolved EPR simulation, as described in the text, of PM6:PCBM from Figure 5.15, at X-band, 140 K, and 1 mJ cm^{-2}.

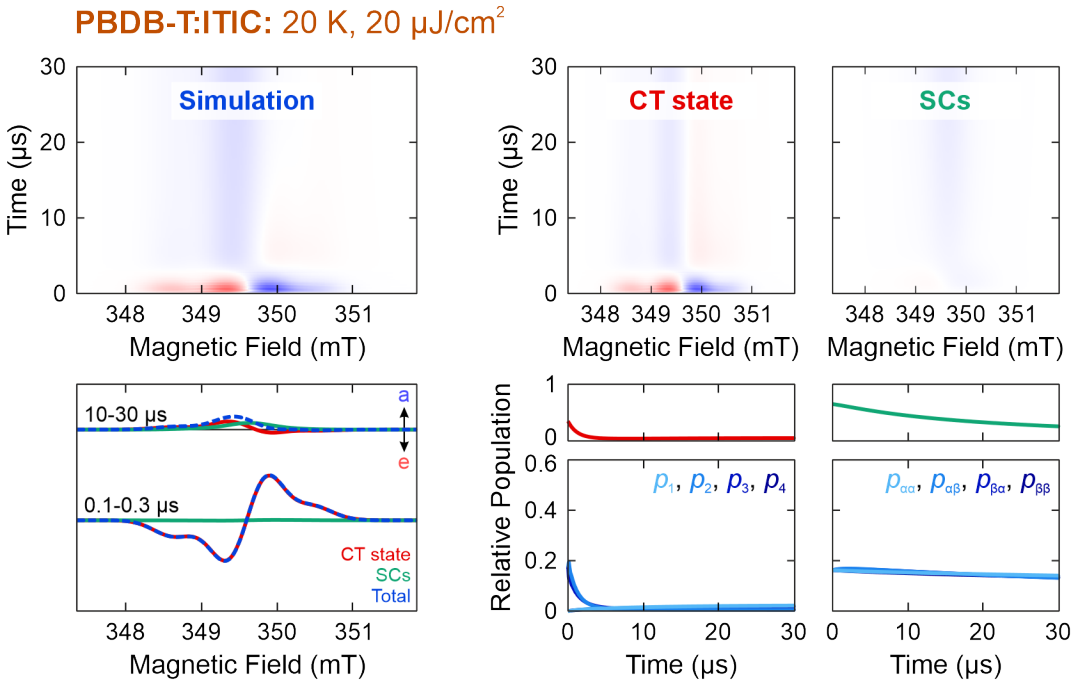

Figure F.9: Additional detail of the time-resolved EPR simulation, as described in the text, of PBDB-T:ITIC from Figure 5.18, at X-band, 20 K, and 20 µJ cm^{-2}.

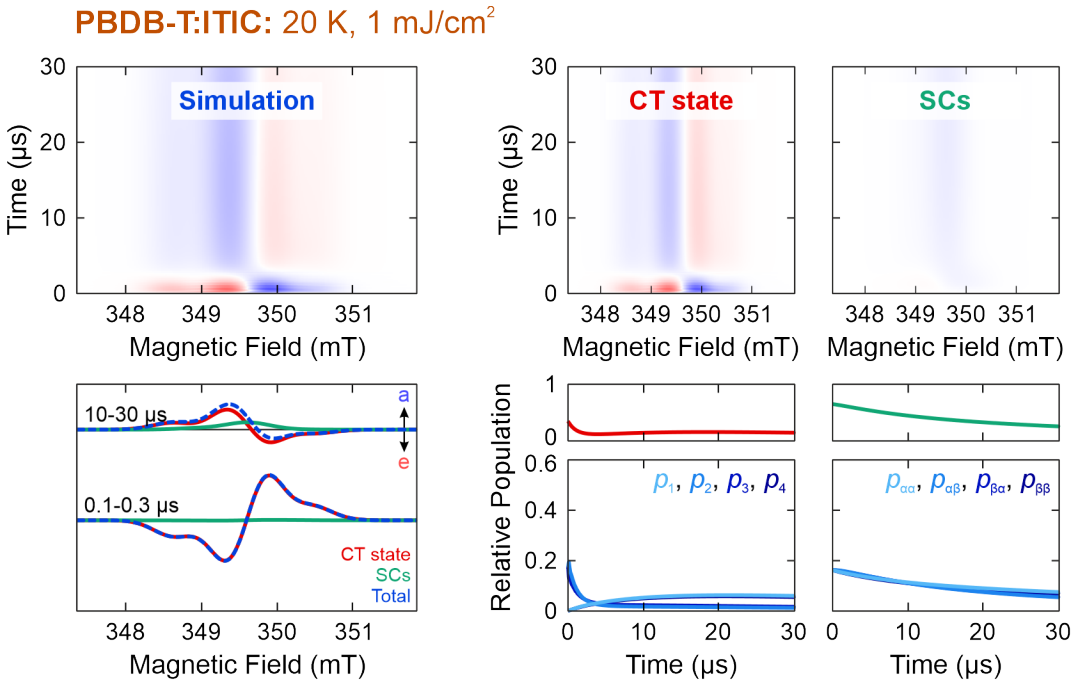

Figure F.10: Additional detail of the time-resolved EPR simulation, as described in the text, of PBDB-T:ITIC from Figure 5.18, at X-band, 20 K, and 1 mJ cm^{-2}.

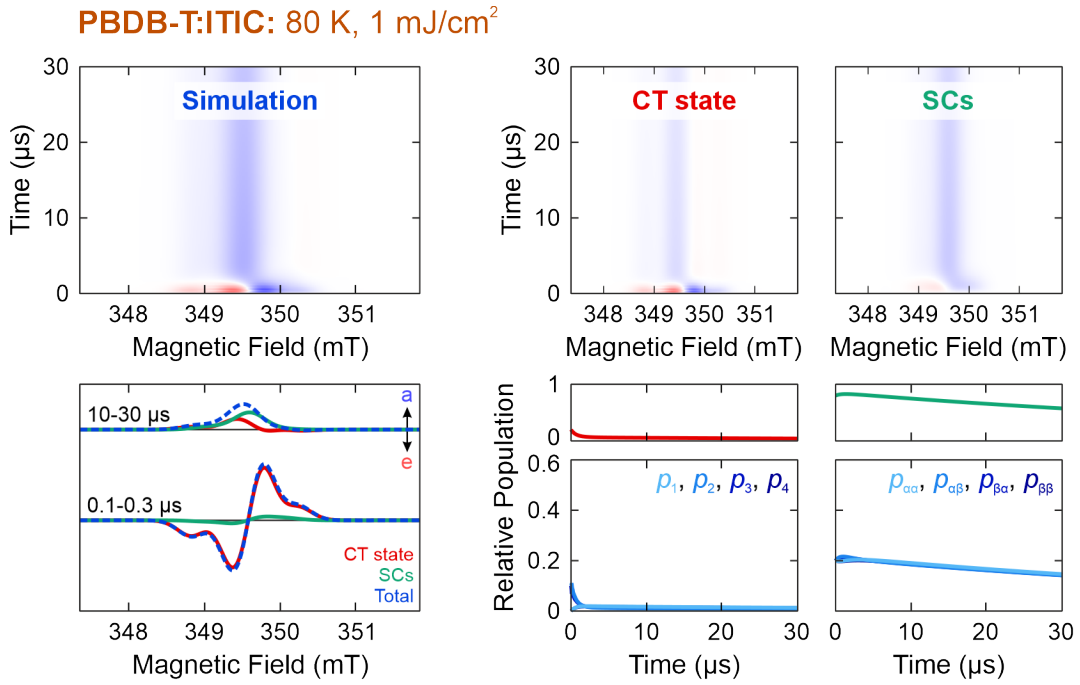

Figure F.11: Additional detail of the time-resolved EPR simulation, as described in the text, of PBDB-T:ITIC from Figure 5.18, at X-band, 80 K, and 1 mJ cm^{-2}.

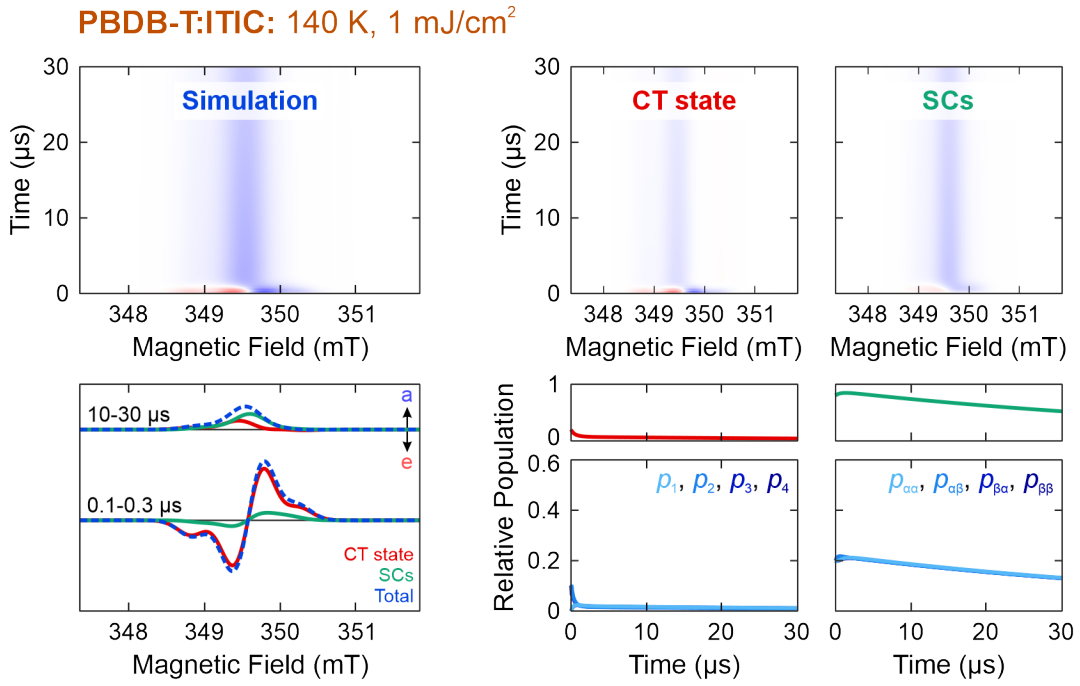

Figure F.12: Additional detail of the time-resolved EPR simulation, as described in the text, of PBDB-T:ITIC from Figure 5.18, at X-band, 140 K, and 1 mJ cm^{-2}.

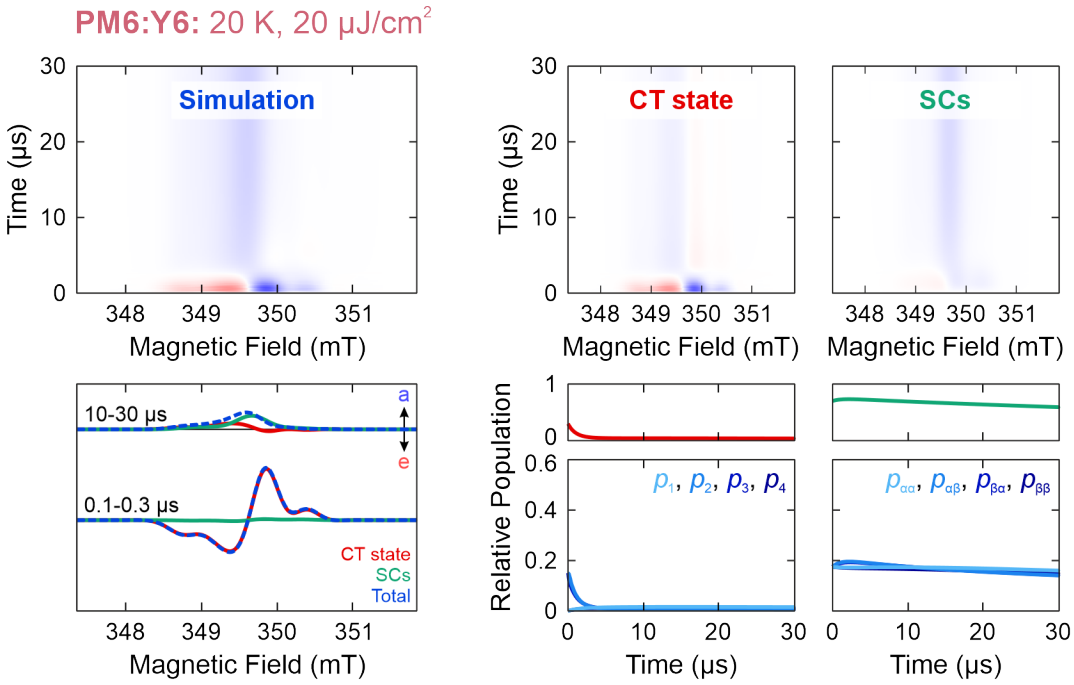

Figure F.13: Additional detail of the time-resolved EPR simulation, as described in the text, of PM6:Y6 from Figure 5.19, at X-band, 20 K, and 20 µJ cm^{-2}.

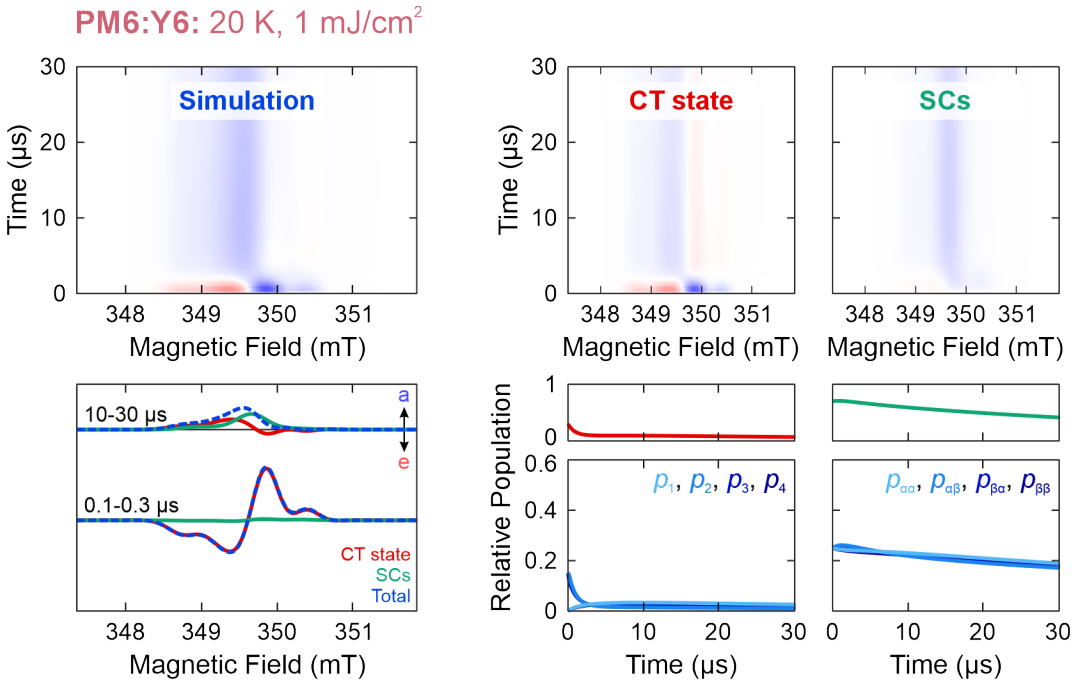

Figure F.14: Additional detail of the time-resolved EPR simulation, as described in the text, of PM6:Y6 from Figure 5.19, at X-band, 20 K, and 1 mJ cm^{-2}.

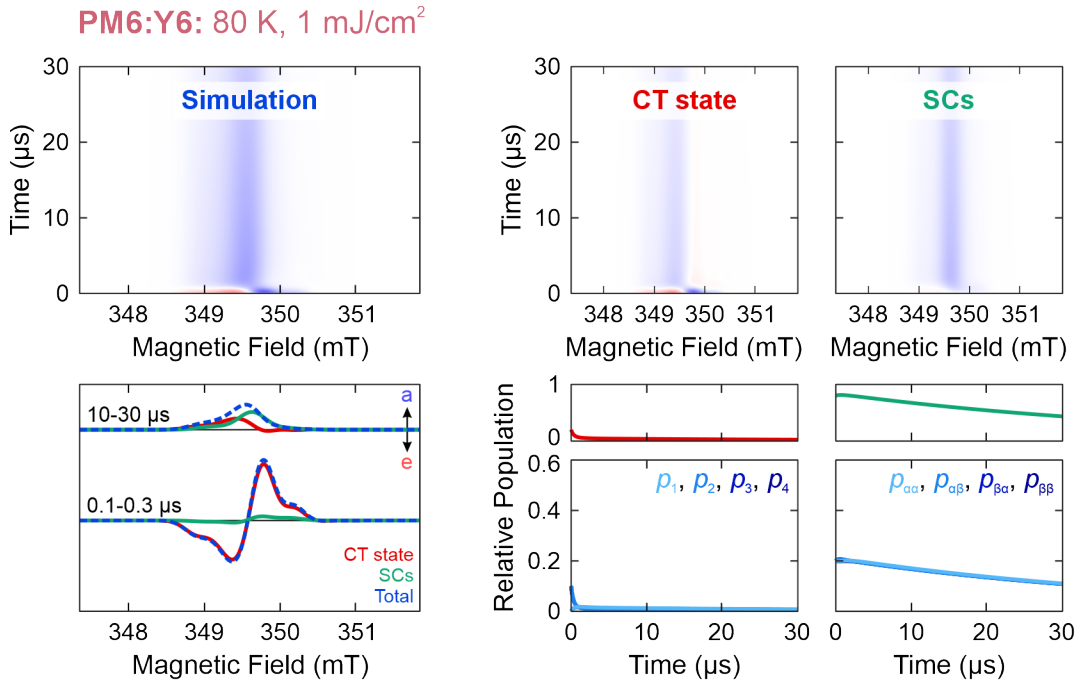

Figure F.15: Additional detail of the time-resolved EPR simulation, as described in the text, of PM6:Y6 from Figure 5.19, at X-band, 80 K, and 1 mJ cm^{-2}.

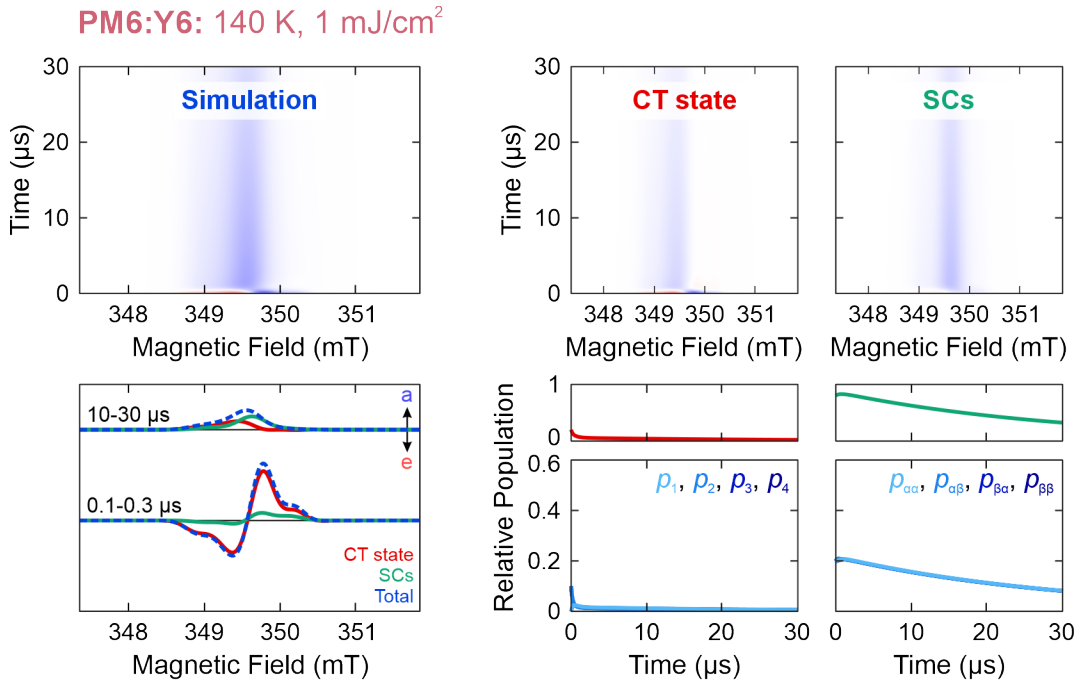

Figure F.16: Additional detail of the time-resolved EPR simulation, as described in the text, of PM6:Y6 from Figure 5.19, at X-band, 140 K, and 1 mJ cm^{-2}.

Appendix G

Charge Transfer and Separation in P3HT:PCBM

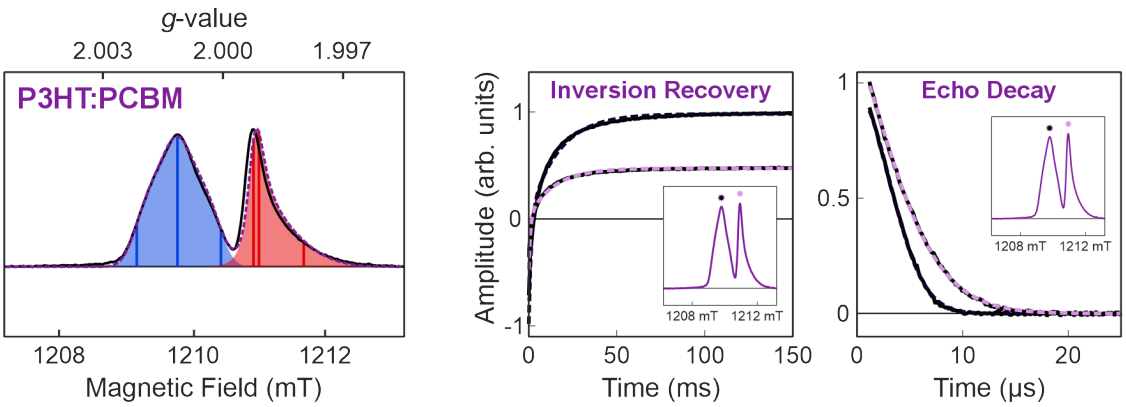

Figure G.1: Left) Simulation of the light-induced EPR spectra of P3HT:PCBM at 20 K and at Q-band. Right) Inversion recovery curves and echo decays of P3HT:PCBM at 20 K and at Q-band. Simulation parameters can be found in Table G.1.

Material	g-value			g-strain	Linewidth (mT)	
	g_x	g_y	g_z	z	X	Q
$P3HT^{\bullet+}$	2.0010	2.0021	2.0031	-	0.23[139]	0.34
$PCBM^{\bullet-}$	2.0002	2.0001	1.9990	0.0019	0.10	0.16

Table G.1: Simulation parameters of the light-induced echo-detected EPR spectrum for $P3HT^{\bullet+}$ and $PCBM^{\bullet-}$ at Q-band, from Figure G.1. The donor:acceptor weight was 1 : 0.61. Estimated fitting errors are 0.0001 for g-values and g-strains, and 0.02 mT for linewidths.

Material	Charge	T_1 (ms)	T_m (µs)	d
P3HT:PCBM	$P3HT^{\bullet+}$	16.41	4.44	1.9
	$PCBM^{\bullet-}$	14.44	5.48	1.4

Table G.2: T_1, T_m and d parameters of P3HT:PCBM obtained from simulation of inversion recovery curves and echo decays in Figure G.1, at 20 K and at Q-band. The estimated fitting error is 0.1 ms for T_1, 0.1 µs for T_m, and 0.1 for d.

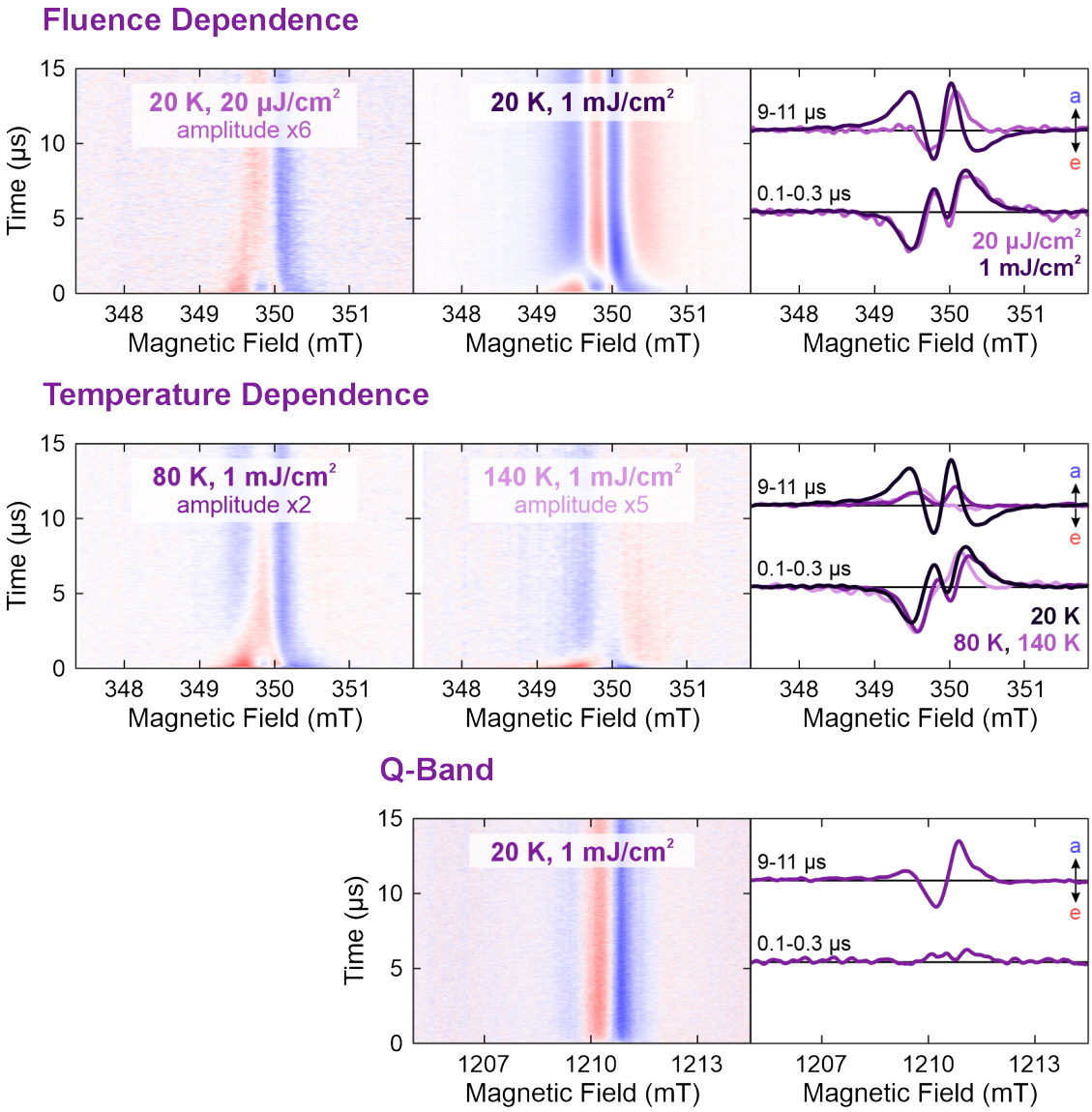

Figure G.2: Time-resolved EPR spectra of P3HT:PCBM, measured at X- and Q-band, at 20 K, 80 K, and 140 K, and at 20 µJ cm^{-2} and 1 mJ cm^{-2}. Averaged spectra at short (0.1 − 0.3 µs) and intermediate (9 − 11 µs) times after photoexcitation are shown for comparison. Absorptive features are in blue and emissive features in red in the two-dimensional plots.

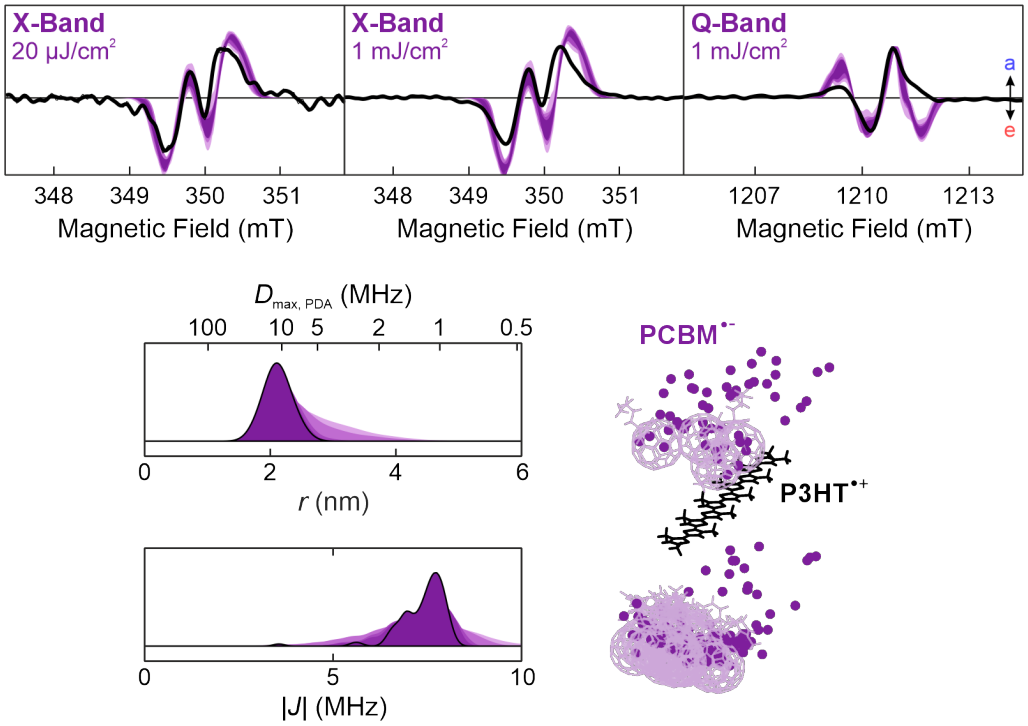

Figure G.3: Top) Simulated EPR spectra of P3HT:PCBM, compared to experimental EPR spectra, extracted at $0.1 - 0.3\,\mu s$, at X- and Q-band, and $20\,\mu J\,cm^{-2}$ and $1\,mJ\,cm^{-2}$. At Q-band, no singlet-born CT state is observed at any time, and so the experimental EPR spectra was extracted from $5 - 15\,\mu s$, assuming full inversion of the spin polarisation (i.e. thermalised triplet). The best 100 fits, sorted by RMSD, are coloured in dark, with worse fits ($N = 500$, 1000, 5000, and 10,000) paler. Bottom) Distribution of parameters determining r and J and $P3HT^{\bullet+}$ positions around $PCBM^{\bullet-}$ obtained from the spectral fits. Mean and standard deviations of r and J for each blend are summarised in Table G.3. The truncated trimer structure of the polymer donor is displayed in black, with centres of mass of the acceptors given by the coloured dots; for a subset of spectral fits (best 20), the full structure of the donor is also shown.

Material	J (MHz)	D_{max} (MHz)	r (nm)	Linewidth (mT)	
				X-Band	Q-Band
P3HT:PCBM	-7.4 ± 0.6	11.2 ± 1.3	2.1 ± 0.2	0.21 ± 0.03	0.30 ± 0.04

Table G.3: Simulation parameters that give the spectral distributions of the best 100 fits shown in Figure G.3. The error is determined by the standard deviation of each set of parameter values. D_{max} is determined from the largest principal value of the dipolar coupling interaction, which is calculated from r using the distributed point-dipole model. g-values of the donor and acceptor molecules were determined from Figure G.1 and given in Table G.1.

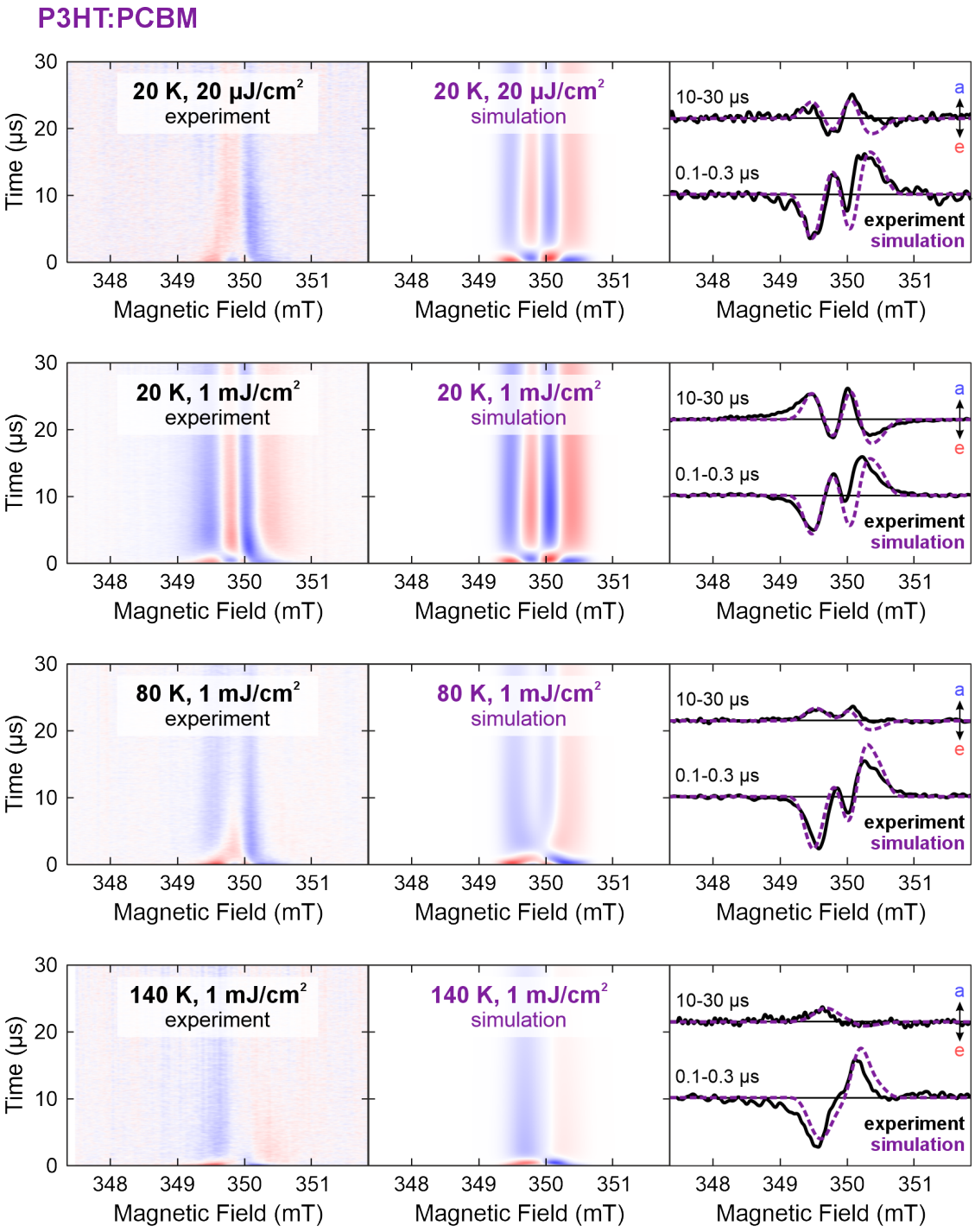

Figure G.4: Comparison of experimental and simulated time-resolved EPR X-band spectra of P3HT:PCBM, for different laser fluences ($20\,\mu J\,cm^{-2}$ and $1\,mJ\,cm^{-2}$) and temperatures (20 K, 80 K, and 140 K). Averaged spectra at short ($0.1 - 0.3\,\mu s$) and long ($10 - 30\,\mu s$) times after photoexcitation are also shown.

P3HT:PCBM

Temp. (K)	Fluence ($\mathrm{mJ\,cm^{-2}}$)	p_{CT}	τ_{S} (µs)	τ_{diss} (µs)	τ_{enc} (µs)	T_1 (µs)	T_2 (µs)
20	0.02	$0.35-0.5$	$0.5-2$	$4-8$	$8-12$	>80	$0.5-1.0$
20	1	$0.35-0.5$	$0.5-2$	$4-8$	$4-6$	$40-80$	$0.5-1.0$
80	1	$0.25-0.35$	$0.5-2$	$0.4-1.5$	$4-6$	$5-10$	$0.2-0.4$
140	1	$0.15-0.25$	$0.5-2$	$0.1-0.5$	$3-5$	$1-5$	$0.05-0.1$

Table G.4: Simulation parameters for P3HT:PCBM for the time-resolved EPR simulations in Figure G.4. The rate constants k_{T}, and k_{dec} were assumed to be negligible, and so the time constants τ_{T}, and τ_{dec} are set to very large.

Abbreviations

a . . . . . absorption

A . . . . . Acceptor

BHJ . . . . . Bulk Heterojunction

CT . . . . . Charge-Transfer State

D . . . . . Donor

DAF . . . . . Delay-after-flash

DFT . . . . . Density Functional Theory

dip . . . . . dipolar interaction

e . . . . . emission

EDMR . . . . . Electrically-detected Magnetic Resonance

EDNMR . . . . . ELDOR-detected NMR

ee . . . . . electron-electron interaction

ELDOR . . . . . Electron Double Resonance

ENDOR . . . . . Electron-Nuclear Double Resonance

EPR . . . . . Electron Paramagnetic Resonance

ex . . . . . exchange interaction

eZ . . . . . electron Zeeman interaction

FC . . . . . Free Charge

FRET . . . . . Förster Resonance Energy Transfer

GIWAXS . . . . . Grazing-Incidence Wide-Angle X-Ray Scattering

hf . . . . . electron-nuclear hyperfine interaction

HOMO . . . . . Highest Occupied Molecular Orbital

HTA . . . . . High Turning Angle

ID . . . . . Inner Diameter

ISC . . . . . Intersystem Crossing

ITIC . . . . . a non-fullerene acceptor molecule

LUMO . . . . . Lowest Unoccupied Molecular Orbital

NMR . . . . . Nuclear Magnetic Resonance

nn . . . . . nuclear-nuclear interaction

nq . . . . . nuclear quadrupole interaction

nZ . . . . . nuclear Zeeman interaction

OD . . . . . Outer Diameter

ODMR . . . . . Optically-detected Magnetic Resonance

OOP-ESEEM . . . Out-of-phase Electron Spin Echo Envelope Modulation

OPV . . . . . Organic Photovoltaic

P3HT . . . . . a polymer donor molecule

PBDB-T . . . . . a polymer donor molecule

PCBM . . . . . a fullerene acceptor molecule

PCE . . . . . Power Conversion Efficiency

PM6 . . . . . a polymer donor molecule

Q . . . . . Quality Factor

RMSD . . . . . Root-Mean-Square Deviation

$\mathbf{S_0}$ . . . . . Ground State

$\mathbf{S_1}$ . . . . . Singlet Exciton

SC . . . . . Separated Charge

SOC . . . . . Spin-Orbit Coupling

SRT . . . . . Shot Repetition Time

$\mathbf{T_1}$ . . . . . Triplet Exciton

TC . . . . . Trapped Charge

TWT . . . . . Travelling-Wave Tube

Y6 . . . . . a non-fullerene acceptor molecule

zf . . . . . zero-field interaction

ZFS . . . . . Zero Field Splitting

ZQC . . . . . Zero Quantum Coherence

Bibliography

(1) Gielen, D.; Boshell, F.; Saygin, D.; Bazilian, M. D.; Wagner, N.; Gorini, R. *Energy Strategy Rev.* **2019**, *24*, 38–50.

(2) Ritchie, H.; Roser, M.; Rosado, P. - Renewable Energy, https://ourworldindata.org/renewable-energy, 2020.

(3) Energy Institute - Statistical Review of World Energy 2024, https://www.energyinst.org/statistical-review, 2024.

(4) International Energy Agency - Global Energy Review 2025, https://www.iea.org/reports/global-energy-review-2025, 2025.

(5) Kannan, N.; Vakeesan, D. *Renewable Sustainable Energy Rev.* **2016**, *62*, 1092–1105.

(6) Kabir, E.; Kumar, P.; Kumar, S.; Adelodun, A. A.; Kim, K. H. *Renewable Sustainable Energy Rev.* **2018**, *82*, 894–900.

(7) Victoria, M.; Haegel, N.; Peters, I. M.; Sinton, R.; Jäger-Waldau, A.; del Cañizo, C.; Breyer, C.; Stocks, M.; Blakers, A.; Kaizuka, I.; Komoto, K.; Smets, A. *Joule* **2021**, *5*, 1041–1056.

(8) Yoshikawa, K.; Kawasaki, H.; Yoshida, W.; Irie, T.; Konishi, K.; Nakano, K.; Uto, T.; Adachi, D.; Kanematsu, M.; Uzu, H.; Yamamoto, K. *Nat. Energy* **2017**, *2*, 17032.

(9) Shockley, W.; Queisser, H. J. *J. Appl. Phys.* **1961**, *32*, 510–519.

(10) Tao, M.; Chen, T.; Click, N.; Adcock, R. *Curr. Opin. Green Sustainable Chem.* **2023**, *44*, 100863.

(11) National Renewable Energy Laboratory - Best Research-Cell Efficiencies, https://www.nrel.gov/pv/cell-efficiency, 2025.

(12) Rehman, F.; Syed, I. H.; Khanam, S.; Ijaz, S.; Mehmood, H.; Zubair, M.; Massoud, Y.; Mehmood, M. Q. *Energy Adv.* **2023**, *2*, 1239–1262.

(13) Green, M. A.; Dunlop, E. D.; Yoshita, M.; Kopidakis, N.; Bothe, K.; Siefer, G.; Hao, X.; Jiang, J. Y. *Prog. Photovoltaics Res. Appl.* **2025**, *33*, 795–810.

(14) Riede, M.; Spoltore, D.; Leo, K. *Adv. Energy Mater.* **2021**, *11*, 2002653.

(15) Solak, E. K.; Irmak, E. *RSC Adv.* **2023**, *13*, 12244–12269.

(16) Yi, J.; Zhang, G.; Yu, H.; Yan, H. *Nat. Rev. Mater.* **2024**, *9*, 46–62.

(17) Green, M. A.; Keevers, M. J. *Prog. Photovoltaics Res. Appl.* **1995**, *3*, 189–192.

(18) Vezie, M. S.; Few, S.; Meager, I.; Pieridou, G.; Dörling, B.; Ashraf, R. S.; Goñi, A. R.; Bronstein, H.; McCulloch, I.; Hayes, S. C.; Campoy-Quiles, M.; Nelson, J. *Nat. Mater.* **2016**, *15*, 746–753.

(19) Baran, D. *Nat. Mater.* **2025**, *24*, 324–325.

(20) Zhang, S.; Xue, Z.; He, Z.; Wei, Q.; Yang, N.; Wu, X.; Chen, C. C.; Sun, C.; Zhong, H. *Chem. Eng. J.* **2024**, *481*, 148728.

(21) Wu, J.; Gao, M.; Chai, Y.; Liu, P.; Zhang, B.; Liu, J.; Ye, L. *Mater. Rep.: Energy* **2021**, *1*, 100062.

(22) Li, C.; Song, J.; Lai, H.; Zhang, H.; Zhou, R.; Xu, J.; Huang, H.; Liu, L.; Gao, J.; Li, Y.; Jee, M. H.; Zheng, Z.; Liu, S.; Yan, J.; Chen, X. K.; Tang, Z.; Zhang, C.; Woo, H. Y.; He, F.; Gao, F.; Yan, H.; Sun, Y. *Nat. Mater.* **2025**, *24*, 433–443.

(23) Dunlap, W. C.; Watters, R. L. *Phys. Rev.* **1953**, *92*, 1396–1397.

(24) Green, M. A. *AIP Adv.* **2013**, *3*, 112104.

(25) Tsutsumi, J.; Matsuzaki, H.; Kanai, N.; Yamada, T.; Hasegawa, T. *J. Phys. Chem. C* **2013**, *117*, 16769–16773.

(26) Zhu, Y.; Zhao, F.; Wang, W.; Li, Y.; Zhang, S.; Lin, Y. *Adv. Energy Sustainability Res.* **2022**, *3*, 2100184.

(27) Zhu, L.; Wei, Z.; Yi, Y. *J. Phys. Chem. C* **2022**, *126*, 14–21.

(28) Köhler, A.; Bässler, H., *Electronic Processes in Organic Semiconductors*; Wiley: 2015.

(29) Tang, C. W. *Appl. Phys. Lett.* **1986**, *48*, 183–185.

(30) Menke, S. M.; Holmes, R. J. *Energy Environ. Sci.* **2014**, *7*, 499–512.

(31) Firdaus, Y.; Corre, V. M. L.; Karuthedath, S.; Liu, W.; Markina, A.; Huang, W.; Chattopadhyay, S.; Nahid, M. M.; Nugraha, M. I.; Lin, Y.; Seitkhan, A.; Basu, A.; Zhang, W.; McCulloch, I.; Ade, H.; Labram, J.; Laquai, F.; Andrienko, D.; Koster, L. J. A.; Anthopoulos, T. D. *Nat. Commun.* **2020**, *11*, 5220.

(32) Tokmoldin, N.; Hosseini, S. M.; Raoufi, M.; Phuong, L. Q.; Sandberg, O. J.; Guan, H.; Zou, Y.; Neher, D.; Shoaee, S. *J. Mater. Chem. A* **2020**, *8*, 7854–7860.

(33) Vollbrecht, J.; Tokmoldin, N.; Sun, B.; Brus, V. V.; Shoaee, S.; Neher, D. *J. Appl. Phys.* **2022**, *131*, 221101.

(34) Perdigón-Toro, L.; Phuong, L. Q.; Eller, F.; Freychet, G.; Saglamkaya, E.; Khan, J. I.; Wei, Q.; Zeiske, S.; Kroh, D.; Wedler, S.; Köhler, A.; Armin, A.; Laquai, F.; Herzig, E. M.; Zou, Y.; Shoaee, S.; Neher, D. *Adv. Energy Mater.* **2022**, *12*, 2103422.

(35) Zhao, F.; Wang, C.; Zhan, X. *Adv. Energy Mater.* **2018**, *8*, 1703147.

(36) Shoaee, S.; Luong, H. M.; Song, J.; Zou, Y.; Nguyen, T. Q.; Neher, D. *Adv. Mater.* **2023**, *36*, 2302005.

(37) Xu, X.; Li, Y.; Peng, Q. *Adv. Mater.* **2022**, *34*, 2107476.

(38) Bi, S.; Ouyang, Z.; Shaik, S.; Li, D. *Sci. Rep.* **2018**, *8*, 9574.

(39) Armin, A.; Li, W.; Sandberg, O. J.; Xiao, Z.; Ding, L.; Nelson, J.; Neher, D.; Vandewal, K.; Shoaee, S.; Wang, T.; Ade, H.; Heumüller, T.; Brabec, C.; Meredith, P. *Adv. Energy Mater.* **2021**, *11*, 20003570.

(40) Zhang, G.; Lin, F. R.; Qi, F.; Heumüller, T.; Distler, A.; Egelhaaf, H. J.; Li, N.; Chow, P. C.; Brabec, C. J.; Jen, A. K.; Yip, H. L. *Chem. Rev.* **2022**, *122*, 14180–14274.

(41) Zhang, S.; Qin, Y.; Zhu, J.; Hou, J. *Adv. Mater.* **2018**, *30*, 1800868.

(42) Liu, T.; Huo, L.; Chandrabose, S.; Chen, K.; Han, G.; Qi, F.; Meng, X.; Xie, D.; Ma, W.; Yi, Y.; Hodgkiss, J. M.; Liu, F.; Wang, J.; Yang, C.; Sun, Y. *Adv. Mater.* **2018**, *30*, 1707353.

(43) Nelson, J. *Mater. Today* **2011**, *14*, 462–470.

(44) Zeng, R.; Zhu, L.; Zhang, M.; Zhong, W.; Zhou, G.; Zhuang, J.; Hao, T.; Zhou, Z.; Zhou, L.; Hartmann, N.; Xue, X.; Jing, H.; Han, F.; Bai, Y.; Wu, H.; Tang, Z.; Zou, Y.; Zhu, H.; Chen, C. C.; Zhang, Y.; Liu, F. *Nat. Commun.* **2023**, *14*, 4148.

(45) Gao, W.; Ma, R.; Peña, T. A. D.; Yan, C.; Li, H.; Li, M.; Wu, J.; Cheng, P.; Zhong, C.; Wei, Z.; Jen, A. K.; Li, G. *Nat. Commun.* **2024**, *15*, 1946.

(46) Yuan, J.; Zhang, Y.; Zhou, L.; Zhang, G.; Yip, H. L.; Lau, T. K.; Lu, X.; Zhu, C.; Peng, H.; Johnson, P. A.; Leclerc, M.; Cao, Y.; Ulanski, J.; Li, Y.; Zou, Y. *Joule* **2019**, *3*, 1140–1151.

(47) Bartelt, J. A.; Beiley, Z. M.; Hoke, E. T.; Mateker, W. R.; Douglas, J. D.; Collins, B. A.; Tumbleston, J. R.; Graham, K. R.; Amassian, A.; Ade, H.; Fréchet, J. M.; Toney, M. F.; Mcgehee, M. D. *Adv. Energy Mater.* **2013**, *3*, 364–374.

(48) Doumon, N. Y.; Wang, G.; Chiechi, R. C.; Koster, L. J. A. *J. Mater. Chem. C* **2017**, *5*, 6611–6619.

(49) Lin, Y.; Wang, J.; Zhang, Z. G.; Bai, H.; Li, Y.; Zhu, D.; Zhan, X. *Adv. Mater.* **2015**, *27*, 1170–1174.

(50) Li, C. Z.; Yip, H. L.; Jen, A. K. *J. Mater. Chem.* **2012**, *22*, 4161–4177.

(51) Bronstein, H.; Nielsen, C. B.; Schroeder, B. C.; McCulloch, I. *Nat. Rev. Chem.* **2020**, *4*, 66–77.

(52) Karki, A.; Gillett, A. J.; Friend, R. H.; Nguyen, T. Q. *Adv. Energy Mater.* **2021**, *11*, 2003441.

(53) Zhang, F.; Inganäs, O.; Zhou, Y.; Vandewal, K. *Natl. Sci. Rev.* **2016**, *3*, 222–239.

(54) Gueymard, C. A. *Sol. Energy* **2004**, *76*, 423–453.

(55) Cheng, P.; Li, G.; Zhan, X.; Yang, Y. *Nat. Photonics* **2018**, *12*, 131–142.

(56) Chang, L.; Lademann, H. W.; Bonekamp, J. B.; Meerholz, K.; Moulé, A. J. *Adv. Funct. Mater.* **2011**, *21*, 1779–1787.

(57) Xin, Y.; Wang, Z.; Xu, L.; Xu, X.; Liu, Y.; Zhang, F. *J. Nanomater.* **2013**, *2013*, 104825.

(58) Liu, W.; Li, W.; Yao, J.; Zhan, C. *Chin. Chem. Lett.* **2018**, *29*, 381–384.

(59) Deibel, C.; Dyakonov, V. *Rep. Prog. Phys* **2010**, *73*, 096401.

(60) Wang, J.; Xie, Y.; Chen, K.; Wu, H.; Hodgkiss, J. M.; Zhan, X. *Nat. Rev. Phys.* **2024**, *6*, 365–381.

(61) Zhang, K. N.; Hao, X. T. *J. Phys. Chem. Lett.* **2023**, *14*, 6051–6060.

(62) Riley, D. B.; Sandberg, O. J.; Zarrabi, N.; Kim, Y. R.; Meredith, P.; Armin, A. *Adv. Mater.* **2023**, *35*, 2211174.

(63) Menke, S. M.; Ran, N. A.; Bazan, G. C.; Friend, R. H. *Joule* **2018**, *2*, 25–35.

(64) Gautam, B. R.; Younts, R.; Carpenter, J.; Ade, H.; Gundogdu, K. *J. Phys. Chem. A* **2018**, *122*, 3764–3771.

(65) Zhou, M.; Zhang, K.; Li, X.; Ge, Y.; Zhang, W.; Lu, P.; Hao, X. *Sol. RRL* **2024**, *8*, 2400136.

(66) Park, S. Y.; Chandrabose, S.; Price, M. B.; Ryu, H. S.; Lee, T. H.; Shin, Y. S.; Wu, Z.; Lee, W.; Chen, K.; Dai, S.; Zhu, J.; Xue, P.; Zhan, X.; Woo, H. Y.; Kim, J. Y.; Hodgkiss, J. M. *Nano Energy* **2021**, *84*, 105924.

(67) Lin, Y.; Zhao, F.; Prasad, S. K.; Chen, J. D.; Cai, W.; Zhang, Q.; Chen, K.; Wu, Y.; Ma, W.; Gao, F.; Tang, J. X.; Wang, C.; You, W.; Hodgkiss, J. M.; Zhan, X. *Adv. Mater.* **2018**, *30*, 1706363.

(68) Karuthedath, S.; Gorenflot, J.; Firdaus, Y.; Chaturvedi, N.; Castro, C. S. D.; Harrison, G. T.; Khan, J. I.; Markina, A.; Balawi, A. H.; Peña, T. A. D.; Liu, W.; Liang, R. Z.; Sharma, A.; Paleti, S. H.; Zhang, W.; Lin, Y.; Alarousu, E.; Anjum, D. H.; Beaujuge, P. M.; Wolf, S. D.; McCulloch, I.; Anthopoulos, T. D.; Baran, D.; Andrienko, D.; Laquai, F. *Nat. Mater.* **2021**, *20*, 378–384.

(69) Chen, Z.; He, C.; Ran, P.; Chen, X.; Zhang, Y.; Zhang, C.; Lai, R.; Yang, Y.; Chen, H.; Zhu, H. *Energy Environ. Sci.* **2023**, *16*, 3373–3380.

(70) Gélinas, S.; Rao, A.; Kumar, A.; Smith, S. L.; Chin, A. W.; Clark, J.; Poll, T. S. V. D.; Bazan, G. C.; Friend, R. H. *Science* **2014**, *343*, 512–516.

(71) Coropceanu, V.; Chen, X. K.; Wang, T.; Zheng, Z.; Brédas, J. L. *Nat. Rev. Mater.* **2019**, *4*, 689–707.

(72) Torabi, S.; Jahani, F.; Severen, I. V.; Kanimozhi, C.; Patil, S.; Havenith, R. W.; Chiechi, R. C.; Lutsen, L.; Vanderzande, D. J.; Cleij, T. J.; Hummelen, J. C.; Koster, L. J. A. *Adv. Funct. Mater.* **2015**, *25*, 150–157.

(73) Wilken, S., *Charge Recombination in Organic Solar Cells*; AIP Publishing LLC: 2020, pp 5-1-5–32.

(74) Vandewal, K.; Albrecht, S.; Hoke, E. T.; Graham, K. R.; Widmer, J.; Douglas, J. D.; Schubert, M.; Mateker, W. R.; Bloking, J. T.; Burkhard, G. F.; Sellinger, A.; Fréchet, J. M.; Amassian, A.; Riede, M. K.; McGehee, M. D.; Neher, D.; Salleo, A. *Nat. Mater.* **2014**, *13*, 63–68.

(75) Causa', M.; Jonghe-Risse, J. D.; Scarongella, M.; Brauer, J. C.; Buchaca-Domingo, E.; Moser, J. E.; Stingelin, N.; Banerji, N. *Nat. Commun.* **2016**, *7*, 12556.

(76) Kroh, D.; Athanasopoulos, S.; Nádaždy, V.; Kahle, F. J.; Bässler, H.; Köhler, A. *Adv. Funct. Mater.* **2023**, *34*, 2302520.

(77) Perdigón-Toro, L.; Zhang, H.; Markina, A.; Yuan, J.; Hosseini, S. M.; Wolff, C. M.; Zuo, G.; Stolterfoht, M.; Zou, Y.; Gao, F.; Andrienko, D.; Shoaee, S.; Neher, D. *Adv. Mater.* **2020**, *32*, 1906763.

(78) Schwarze, M.; Schellhammer, K. S.; Ortstein, K.; Benduhn, J.; Gaul, C.; Hinderhofer, A.; Toro, L. P.; Scholz, R.; Kublitski, J.; Roland, S.; Lau, M.; Poelking, C.; Andrienko, D.; Cuniberti, G.; Schreiber, F.; Neher, D.; Vandewal, K.; Ortmann, F.; Leo, K. *Nat. Commun.* **2019**, *10*, 2466.

(79) Fu, Y.; Lee, T. H.; Chin, Y. C.; Pacalaj, R. A.; Labanti, C.; Park, S. Y.; Dong, Y.; Cho, H. W.; Kim, J. Y.; Minami, D.; Durrant, J. R.; Kim, J. S. *Nat. Commun.* **2023**, *14*, 1870.

(80) Pananusorn, P.; Sotome, H.; Uratani, H.; Ishiwari, F.; Phomphrai, K.; Saeki, A. *J. Chem. Phys.* **2024**, *161*, 184710.

(81) Hinrichsen, T. F.; Chan, C. C. S.; Ma, C.; Paleček, D.; Gillett, A.; Chen, S.; Zou, X.; Zhang, G.; Yip, H.-L.; Wong, K. S.; Friend, R. H.; Yan, H.; Rao, A.; Chow, P. C. Y. *Nat. Commun.* **2020**, *11*, 5617.

(82) Rijal, K.; Fuller, N.; Rudayni, F.; Zhang, N.; Zuo, X.; Berrie, C. L.; Yip, H. L.; Chan, W. L. *Adv. Mater.* **2024**, *36*, 2400578.

(83) Clarke, T.; Ballantyne, A.; Jamieson, F.; Brabec, C.; Nelson, J.; Durrant, J. *Chem. Commun.* **2009**, *9*, 89–91.

(84) Rao, A.; Chow, P. C.; Gélinas, S.; Schlenker, C. W.; Li, C. Z.; Yip, H. L.; Jen, A. K.; Ginger, D. S.; Friend, R. H. *Nature* **2013**, *500*, 435–439.

(85) Heitzer, H. M.; Savoie, B. M.; Marks, T. J.; Ratner, M. A. *Angew. Chem. Int. Ed.* **2014**, *53*, 7456–7460.

(86) Zhang, G.; Chen, X.-K.; Xiao, J.; Chow, P. C. Y.; Ren, M.; Kupgan, G.; Jiao, X.; Chan, C. C. S.; Du, X.; Xia, R.; Chen, Z.; Yuan, J.; Zhang, Y.; Zhang, S.; Liu, Y.; Zou, Y.; Yan, H.; Wong, K. S.; Coropceanu, V.; Li, N.; Brabec, C. J.; Bredas, J.-L.; Yip, H.-L.; Cao, Y. *Nat. Commun.* **2020**, *11*, 3943.

(87) Balzer, D.; Kassal, I. *Sci. Adv.* **2022**, *8*, 9692.

(88) Niklas, J.; Zheng, T.; Neshchadin, A.; Mardis, K. L.; Yu, L.; Poluektov, O. G. *J. Am. Chem. Soc.* **2020**, *142*, 1359–1366.

(89) Liu, C.; Huang, K.; Park, W. T.; Li, M.; Yang, T.; Liu, X.; Liang, L.; Minari, T.; Noh, Y. Y. *Mater. Horiz.* **2017**, *4*, 608–618.

(90) Zhu, X.; Wang, K.; He, J.; Zhang, L.; Yu, H.; He, D.; Hu, B. *J. Phys. Chem. C* **2019**, *123*, 20691–20697.

(91) Wu, J.; Lee, J.; Chin, Y. C.; Yao, H.; Cha, H.; Luke, J.; Hou, J.; Kim, J. S.; Durrant, J. R. *Energy Environ. Sci.* **2020**, *13*, 2422–2430.

(92) Giannini, S.; Blumberger, J. *Acc. Chem. Res.* **2022**, *55*, 819–830.

(93) Son, S. Y.; Kim, J. H.; Song, E.; Choi, K.; Lee, J.; Cho, K.; Kim, T. S.; Park, T. *Macromolecules* **2018**, *51*, 2572–2579.

(94) Carr, J. A.; Chaudhary, S. *Energy Environ. Sci.* **2013**, *6*, 3414–3438.

(95) Mukherjee, S.; Proctor, C. M.; Tumbleston, J. R.; Bazan, G. C.; Nguyen, T. Q.; Ade, H. *Adv. Mater.* **2015**, *27*, 1105–1111.

(96) Göhler, C.; Wagenpfahl, A.; Deibel, C. *Adv. Electron. Mater.* **2018**, *4*, 1700505.

(97) Fukuhara, T.; Tamai, Y.; Ohkita, H. *Sustainable Energy Fuels* **2020**, *4*, 4321–4351.

(98) Wilken, S.; Scheunemann, D.; Dahlström, S.; Nyman, M.; Parisi, J.; Österbacka, R. *Adv. Electron. Mater.* **2021**, *7*, 2001056.

(99) Burke, T. M.; Sweetnam, S.; Vandewal, K.; McGehee, M. D. *Adv. Energy Mater.* **2015**, *5*, 1500123.

(100) Armin, A.; Subbiah, J.; Stolterfoht, M.; Shoaee, S.; Xiao, Z.; Lu, S.; Jones, D. J.; Meredith, P. *Adv. Energy Mater.* **2016**, *6*, 1600939.

(101) Armin, A.; Durrant, J. R.; Shoaee, S. *J. Phys. Chem. C* **2017**, *121*, 13969–13976.

(102) Shoaee, S.; Armin, A.; Stolterfoht, M.; Hosseini, S. M.; Kurpiers, J.; Neher, D. *Sol. RRL* **2019**, *3*, 1900184.

(103) Wu, Y.; Li, Y.; van der Zee, B.; Liu, W.; Markina, A.; Fan, H.; Yang, H.; Cui, C.; Li, Y.; Blom, P. W.; Andrienko, D.; Wetzelaer, G. J. A. *Sci. Rep.* **2023**, *13*, 4717.

(104) Rauh, D.; Deibel, C.; Dyakonov, V. *Adv. Funct. Mater.* **2012**, *22*, 3371–3377.

(105) Zhang, X.; Zuo, X.; Xie, S.; Yuan, J.; Zhou, H.; Zhang, Y. *J. Mater. Chem. A* **2017**, *5*, 17230–17239.

(106) Grüne, J.; Londi, G.; Gillett, A. J.; Stähly, B.; Lulei, S.; Kotova, M.; Olivier, Y.; Dyakonov, V.; Sperlich, A. *Adv. Funct. Mater.* **2023**, 2212640.

(107) Penfold, T. J.; Gindensperger, E.; Daniel, C.; Marian, C. M. *Chem. Rev.* **2018**, *118*, 6975–7025.

(108) Chow, P. C.; Albert-Seifried, S.; Gélinas, S.; Friend, R. H. *Adv. Mater.* **2014**, *26*, 4851–4854.

(109) Chen, Z.; Chen, X.; Jia, Z.; Zhou, G.; Xu, J.; Wu, Y.; Xia, X.; Li, X.; Zhang, X.; Deng, C.; Zhang, Y.; Lu, X.; Liu, W.; Zhang, C.; Yang, Y.; Zhu, H. *Joule* **2021**, *5*, 1832–1844.

(110) Li, C.; Yao, G.; Gu, X.; Lv, J.; Hou, Y.; Lin, Q.; Yu, N.; Abbasi, M. S.; Zhang, X.; Zhang, J.; Tang, Z.; Peng, Q.; Zhang, C.; Cai, Y.; Huang, H. *Nat. Commun.* **2024**, *15*, 8872.

(111) Zhou, R.; Gao, X.; Chen, H.; Gao, J.; Liu, Z. *J. Mater. Chem. A* **2025**, *13*, 15554–15573.

(112) Gillett, A. J.; Privitera, A.; Dilmurat, R.; Karki, A.; Qian, D.; Pershin, A.; Londi, G.; Myers, W. K.; Lee, J.; Yuan, J.; Ko, S. J.; Riede, M. K.; Gao, F.; Bazan, G. C.; Rao, A.; Nguyen, T. Q.; Beljonne, D.; Friend, R. H. *Nature* **2021**, *597*, 666–671.

(113) Biskup, T. *Front. Chem.* **2019**, *7*, 10.

(114) Roessler, M. M.; Salvadori, E. *Chem. Soc. Rev.* **2018**, *47*, 2534–2553.

(115) Mohr, P. J.; Newell, D. B.; Taylor, B. N.; Tiesinga, E. *Rev. Mod. Phys.* **2025**, *97*, 025002.

(116) Atherton, N. M., *Principles of electron spin resonance*; PTR Prentice Hall: 1993; Vol. 33, pp 698–698.

(117) Schweiger, A.; Jeschke, G., *Principles of Pulse Electron Paramagnetic Resonance*; Oxford University Press, Oxford: 2001.

(118) Weil, J. A.; Bolton, J. R., *Electron Paramagnetic Resonance*; Wiley: 2006.

(119) Stoll, S.; Goldfarb, D., *EPR Spectroscopy - Fundamentals and Methods*; John Wiley and Sons Ltd.: 2018.

(120) Pilbrow, J. R., *Transition Ion Electron Paramagnetic Resonance*; Oxford University Press: 1990, p 717.

(121) Goldstein, H., *Classical Mechanics*; Addison-Wesley: 1950.

(122) Gast, P.; Groenen, E. J. *eMagRes* **2016**, *5*, 1435–1444.

(123) Willer, M.; Schweiger, A. *Chem. Phys. Lett.* **1997**, *264*, 1–8.

(124) Zhang, P.; Perfetti, M.; Kern, M.; Hallmen, P. P.; Ungur, L.; Lenz, S.; Ringenberg, M. R.; Frey, W.; Stoll, H.; Rauhut, G.; Slageren, J. V. *Chem. Sci.* **2018**, *9*, 1221–1230.

(125) Poole, C. P.; Farach, H. A.; Jackson, W. K. *J. Chem. Phys.* **1974**, *61*, 2220–2221.

(126) Telser, J. *eMagRes* **2017**, *6*, 207–234.

(127) Slichter, C. P., *Principles of Magnetic Resonance*; Springer Berlin Heidelberg: 1990.

(128) Bencini, A.; Gatteschi, D., *Electron Paramagnetic Resonance of Exchange Coupled Systems*; Springer Berlin Heidelberg: 1990.

(129) Dreuw, A.; Hoffmann, M. *Front. Chem.* **2023**, *11*, 1239604.

(130) Stoll, S.; Schweiger, A. *J. Magn. Reson.* **2006**, *178*, 42–55.

(131) Pedersen, J. B.; Freed, J. H. *J. Chem. Phys.* **1973**, *58*, 2746–2762.

(132) Efimova, O.; Hore, P. J. *Biophys. J.* **2008**, *94*, 1565–1574.

(133) Stoll, S.; Goldfarb, D. *eMagRes* **2017**, *6*, 495–510.

(134) Harmer, J. R. *eMagRes* **2016**, *5*, 1493–1514.

(135) Goldfarb, D. *eMagRes* **2017**, *6*, 101–114.

(136) Van der Est, A. *Photosynth. Res* **2009**, *102*, 335–347.

(137) Forbes, M. D.; Jarocha, L. E.; Sim, S.; Tarasov, V. F. *Adv. Phys. Org. Chem.* **2013**, *47*, 1–83.

(138) Weber, S. *eMagRes* **2017**, *6*, 255–270.

(139) Kraffert, F.; Behrends, J. *Mol. Phys.* **2017**, *115*, 2373–2386.

(140) Mi, Q.; Ratner, M. A.; Wasielewski, M. R. *J. Phys. Chem. A* **2010**, *114*, 162–171.

(141) Rao, A.; Gillett, A. J.; Friend, R. H. *Nat. Mater.* **2022**, *21*, 976–978.

(142) Hore, P. J., *Advanced EPR: Applications in Biology and Biochemistry*; Elsevier: 1989, pp 405–440.

(143) Kobori, Y.; Fuki, M.; Murai, H. *J. Phys. Chem. B* **2010**, *114*, 14621–14630.

(144) Carmieli, R.; Smeigh, A. L.; Conron, S. M. M.; Thazhathveetil, A. K.; Fuki, M.; Kobori, Y.; Lewis, F. D.; Wasielewski, M. R. *J. Am. Chem. Soc.* **2012**, *134*, 11251–11260.

(145) Stevenson, R. *J. Magn. Reson.* **1984**, *57*, 24–42.

(146) Richert, S.; Tait, C. E.; Timmel, C. R. *J. Magn. Reson.* **2017**, *280*, 103–116.

(147) Antheunis, D. A.; Schmidt, J.; Waals, J. H. V. D. *Mol. Phys.* **1974**, *27*, 1521–1541.

(148) Privitera, A.; Grüne, J.; Karki, A.; Myers, W. K.; Dyakonov, V.; Nguyen, T. Q.; Riede, M. K.; Friend, R. H.; Sperlich, A.; Gillett, A. J. *Adv. Energy Mater.* **2022**, *12*, 2103944.

(149) Hemminga, M. A., *ESR Spectroscopy in Membrane Biophysics*; Springer US: 2007; Vol. 27, pp 17–47.

(150) Wittmann, J. J.; Can, T. V.; Eckardt, M.; Harneit, W.; Griffin, R. G.; Corzilius, B. *J. Magn. Reson.* **2018**, *290*, 12–17.

(151) Bloch, F. *Phys. Rev.* **1946**, *70*, 460–474.

(152) Hahn, E. L. *Phys. Rev.* **1950**, *80*, 580–594.

(153) Carr, H. Y.; Purcell, E. M. *Phys. Rev.* **1954**, *94*, 630–638.

(154) Stoll, S. *eMagRes* **2017**, *6*, 23–37.

(155) Eaton, S. S.; Eaton, G. R., *Biological Magnetic Resonance*; Kluwer Academic: 2000.

(156) Eaton, S. S.; Eaton, G. R., *Relaxation Times of Organic Radicals and Transition Metal Ions*, 2002, pp 29–154.

(157) Eaton, S. S.; Eaton, G. R., *Relaxation Mechanisms*; John Wiley and Sons, Ltd: 2016, pp 1543–1556.

(158) Canarie, E. R.; Jahn, S. M.; Stoll, S. *J. Phys. Chem. Lett.* **2020**, *11*, 3396–3400.

(159) Zecevic, A.; Eaton, G. R.; Eaton, S. S.; Lindgren, M. *Mol. Phys.* **1998**, *95*, 1255–1263.

(160) Graham, M. J.; Zadrozny, J. M.; Shiddiq, M.; Anderson, J. S.; Fataftah, M. S.; Hill, S.; Freedman, D. E. *J. Am. Chem. Soc.* **2014**, *136*, 7623–7626.

(161) Kevan, L.; Schwartz, R. N., *Time Domain Electron Spin Resonance*; Wiley: 1979, p 414.

(162) Fan, C.; Doan, P. E.; Davoust, C. E.; Hoffman, B. M. *J. Magn. Reson.* **1992**, *98*, 62–72.

(163) Doan, P. E.; Lees, N. S.; Shanmugam, M.; Hoffman, B. M. *Appl. Magn. Reson.* **2010**, *37*, 763–779.

(164) Tamai, Y.; Fan, Y.; Kim, V. O.; Ziabrev, K.; Rao, A.; Barlow, S.; Marder, S. R.; Friend, R. H.; Menke, S. M. *ACS Nano* **2017**, *11*, 12473–12481.

(165) Liu, J.; Shi, Y.; Dong, J.; Nugraha, M. I.; Qiu, X.; Su, M.; Chiechi, R. C.; Baran, D.; Portale, G.; Guo, X.; Koster, L. J. A. *ACS Energy Lett.* **2019**, *4*, 1556–1564.

(166) Markina, A.; Lin, K.-H.; Liu, W.; Poelking, C.; Firdaus, Y.; Villalva, D. R.; Khan, J. I.; Paleti, S. H. K.; Harrison, G. T.; Gorenflot, J.; Zhang, W.; Wolf, S. D.; McCulloch, I.; Anthopoulos, T. D.; Baran, D.; Laquai, F.; Andrienko, D. *Adv. Energy Mater.* **2021**, *11*, 2102363.

(167) Lüer, L.; Wang, R.; Liu, C.; Dube, H.; Heumüller, T.; Hauch, J.; Brabec, C. J. *Adv. Sci.* **2024**, *11*, 2305948.

(168) Niklas, J.; Mardis, K. L.; Banks, B. P.; Grooms, G. M.; Sperlich, A.; Dyakonov, V.; Beaupré, S.; Leclerc, M.; Xu, T.; Yu, L.; Poluektov, O. G. *Phys. Chem. Chem. Phys.* **2013**, *15*, 9562–9574.

(169) Bakulin, A. A.; Rao, A.; Pavelyev, V. G.; van Loosdrecht, P. H. M.; Pshenichnikov, M. S.; Niedzialek, D.; Cornil, J.; Beljonne, D. *Science* **2012**, *335*, 1336–1340.

(170) Casalegno, M.; Pastore, R.; Idé, J.; Po, R.; Raos, G. *J. Phys. Chem. C* **2017**, *121*, 16693–16701.

(171) Athanasopoulos, S.; Bässler, H.; Köhler, A. *J. Phys. Chem. Lett.* **2019**, 7107–7112.

(172) Balzer, D.; Smolders, T. J.; Blyth, D.; Hood, S. N.; Kassal, I. *Chem. Sci.* **2021**, *12*, 2276–2285.

(173) Jia, X.; Soprani, L.; Londi, G.; Hosseini, S. M.; Talnack, F.; Mannsfeld, S.; Shoaee, S.; Neher, D.; Reineke, S.; Muccioli, L.; D'Avino, G.; Vandewal, K.; Beljonne, D.; Spoltore, D. *Mater. Horiz.* **2023**, *11*, 173–183.

(174) Balzer, D.; Kassal, I. *Chem. Sci.* **2024**, *15*, 4779–4789.

(175) Behrends, J.; Sperlich, A.; Schnegg, A.; Biskup, T.; Teutloff, C.; Lips, K.; Dyakonov, V.; Bittl, R. *Phys. Rev. B* **2012**, *85*, 125206.

(176) Niklas, J.; Beaupré, S.; Leclerc, M.; Xu, T.; Yu, L.; Sperlich, A.; Dyakonov, V.; Poluektov, O. G. *J. Phys. Chem. B* **2015**, *119*, 7407–7416.

(177) Thomson, S. A.; Niklas, J.; Mardis, K. L.; Mallares, C.; Samuel, I. D.; Poluektov, O. G. *J. Phys. Chem. C* **2017**, *121*, 22707–22719.

(178) Landeghem, M. V.; Maes, W.; Goovaerts, E.; Doorslaer, S. V. *J. Magn. Reson.* **2018**, *288*, 1–10.

(179) Maly, T.; Prisner, T. F. *J. Magn. Reson.* **2004**, *170*, 88–96.

(180) Maly, T.; MacMillan, F.; Zwicker, K.; Kashani-Poor, N.; Brandt, U.; Prisner, T. F. *Biochemistry* **2004**, *43*, 3969–3978.

(181) Landeghem, M. V.; Kudrjasova, J.; Maes, W.; Goovaerts, E.; Doorslaer, S. V. *Appl. Magn. Reson.* **2019**, *50*, 1253–1265.

(182) Aguirre, A.; Gast, P.; Orlinskii, S.; Akimoto, I.; Groenen, E. J.; Mkami, H. E.; Goovaerts, E.; Doorslaer, S. V. *Phys. Chem. Chem. Phys.* **2008**, *10*, 7129–7138.

(183) Steyrleuthner, R.; Zhang, Y.; Zhang, L.; Kraffert, F.; Cherniawski, B. P.; Bittl, R.; Briseno, A. L.; Bredas, J. L.; Behrends, J. *Phys. Chem. Chem. Phys.* **2017**, *19*, 3627–3639.

(184) Arvind, M.; Tait, C. E.; Guerrini, M.; Krumland, J.; Valencia, A. M.; Cocchi, C.; Mansour, A. E.; Koch, N.; Barlow, S.; Marder, S. R.; Behrends, J.; Neher, D. *J. Phys. Chem. B* **2020**, *124*, 7694–7708.

(185) Tait, C. E.; Reckwitz, A.; Arvind, M.; Neher, D.; Bittl, R.; Behrends, J. *Phys. Chem. Chem. Phys.* **2021**, *23*, 13827–13841.

(186) Zhao, W.; Qian, D.; Zhang, S.; Li, S.; Inganäs, O.; Gao, F.; Hou, J. *Adv. Mater.* **2016**, *28*, 4734–4739.

(187) Zhang, M.; Guo, X.; Ma, W.; Ade, H.; Hou, J. *Adv. Mater.* **2015**, *27*, 4655–4660.

(188) Reijerse, E.; Lendzian, F.; Isaacson, R.; Lubitz, W. *J. Magn. Reson.* **2012**, *214*, 237–243.

(189) Neese, F. *J. Comput. Chem.* **2003**, *24*, 1740–1747.

(190) Neese, F.; Wennmohs, F.; Hansen, A.; Becker, U. *Chem. Phys.* **2009**, *356*, 98–109.

(191) Neese, F. *WIREs Comput. Mol. Sci.* **2012**, *2*, 73–78.

(192) Helmich-Paris, B.; de Souza, B.; Neese, F.; Izsák, R. *J. Chem. Phys.* **2021**, *155*, 104109.

(193) Neese, F. *WIREs Comput. Mol. Sci.* **2022**, *12*, 1606.

(194) Neese, F. *J. Comput. Chem.* **2023**, *44*, 381–396.

(195) Mardirossian, N.; Head-Gordon, M. *Phys. Chem. Chem. Phys.* **2014**, *16*, 9904–9924.

(196) Najibi, A.; Goerigk, L. *J. Comput. Chem.* **2020**, *41*, 2562–2572.

(197) Weigend, F.; Ahlrichs, R. *Phys. Chem. Chem. Phys.* **2005**, *7*, 3297–3305.

(198) Weigend, F. *Phys. Chem. Chem. Phys.* **2006**, *8*, 1057–1065.

(199) Grimme, S.; Antony, J.; Ehrlich, S.; Krieg, H. *J. Chem. Phys.* **2010**, *132*, 154104.

(200) Grimme, S.; Ehrlich, S.; Goerigk, L. *J. Comput. Chem.* **2011**, *32*, 1456–1465.

(201) Caldeweyher, E.; Bannwarth, C.; Grimme, S. *J. Chem. Phys.* **2017**, *147*, 034112.

(202) Caldeweyher, E.; Ehlert, S.; Hansen, A.; Neugebauer, H.; Spicher, S.; Bannwarth, C.; Grimme, S. *J. Chem. Phys.* **2019**, *150*, 154122.

(203) Caldeweyher, E.; Mewes, J. M.; Ehlert, S.; Grimme, S. *Phys. Chem. Chem. Phys.* **2020**, *22*, 8499–8512.

(204) Stein, T.; Kronik, L.; Baer, R. *J. Am. Chem. Soc.* **2009**, *131*, 2818–2820.

(205) Baer, R.; Livshits, E.; Salzner, U. *Annu. Rev. Phys. Chem.* **2010**, *61*, 85–109.

(206) Anderson, L. N.; Oviedo, M. B.; Wong, B. M. *J. Chem. Theory Comput.* **2017**, *13*, 1656–1666.

(207) Thorley, K. J. *J. Phys. Chem. B* **2023**, *127*, 5102–5114.

(208) Scharber, M. C.; Sariciftci, N. S. *Prog. Polym. Sci.* **2013**, *38*, 1929–1940.

(209) Neese, F. *J. Phys. Chem. A* **2001**, *105*, 4290–4299.

(210) Neese, F. *J. Chem. Phys.* **2001**, *115*, 11080–11096.

(211) Neese, F. *J. Chem. Phys.* **2005**, *122*, 034107.

(212) Neese, F., *Quantum Chemistry and EPR Parameters*; John Wiley and Sons, Ltd: 2017, pp 1–22.

(213) Huzinaga, S. *J. Chem. Phys.* **1965**, *42*, 1293–1302.

(214) Kutzelnigg, W.; Fleischer, U.; Schindler, M., *NMR Basic Principles and Progress*; Springer Berlin Heidelberg: 1972; Vol. 23, p 165.

(215) Barone, V., *Recent Advances in Density Functional Methods*; World Scientific: 1995; Vol. 1, pp 287–334.

(216) Rega, N.; Cossi, M.; Barone, V. *J. Chem. Phys.* **1996**, *105*, 11060–11067.

(217) Ceuster, J. D.; Goovaerts, E.; Bouwen, A.; Hummelen, J. C.; Dyakonov, V. *Phys. Rev. B* **2001**, *64*, 1952061–1952066.

(218) Poluektov, O. G.; Filippone, S.; Martín, N.; Sperlich, A.; Deibel, C.; Dyakonov, V. *J. Phys. Chem. B* **2010**, *114*, 14426–14429.

(219) Konkin, A.; Ritter, U.; Scharff, P.; Roth, H. K.; Aganov, A.; Sariciftci, N. S.; Egbe, D. A. *Synth. Met.* **2010**, *160*, 485–489.

(220) Sperlich, A.; Liedtke, M.; Kern, J.; Kraus, H.; Deibel, C.; Filippone, S.; Delgado, J. L.; Martín, N.; Dyakonov, V. *Phys. Status Solidi RRL* **2011**, *5*, 128–130.

(221) Kraffert, F.; Steyrleuthner, R.; Albrecht, S.; Neher, D.; Scharber, M. C.; Bittl, R.; Behrends, J. *J. Phys. Chem. C* **2014**, *118*, 28482–28493.

(222) Poluektov, O. G.; Niklas, J.; Mardis, K. L.; Beaupré, S.; Leclerc, M.; Villegas, C.; Erten-Ela, S.; Delgado, J. L.; Martín, N.; Sperlich, A.; Dyakonov, V. *Adv. Energy Mater.* **2014**, *4*, 1301517.

(223) Konkin, A.; Ritter, U.; Scharff, P.; Mamin, G.; Aganov, A.; Orlinskii, S.; Krinichnyi, V.; Egbe, D. A.; Ecke, G.; Romanus, H. *Carbon* **2014**, *77*, 11–17.

(224) Mardis, K. L.; Webb, J. N.; Holloway, T.; Niklas, J.; Poluektov, O. G. *J. Phys. Chem. Lett.* **2015**, *6*, 4730–4735.

(225) Niklas, J.; Mardis, K. L.; Poluektov, O. G. *J. Phys. Chem. Lett.* **2018**, *9*, 3915–3921.

(226) Krinichnyi, V. I.; Yudanova, E. I.; Denisov, N. N.; Konkin, A. A.; Ritter, U.; Bogatyrenko, V. R.; Konkin, A. L. *J. Phys. Chem. B* **2021**, *125*, 12224–12240.

(227) Lu, Q.; Qiu, M.; Zhao, M.; Li, Z.; Li, Y. *Polymers* **2019**, *11*, 958.

(228) Zou, X.; Wen, G.; Hu, R.; Dong, G.; Zhang, C.; Zhang, W.; Huang, H.; Dang, W. *Molecules* **2020**, *25*, 4118.

(229) Liu, W.; Liu, Q.; Xiang, C.; Zhou, H.; Jiang, L.; Zou, Y. *Surf. Interfaces* **2021**, *26*, 101385.

(230) Huang, S. Q.; Wang, L. L.; Pan, Q. Q.; Zhao, Z. W.; Gao, Y.; Su, Z. M. *Molecules* **2023**, *28*, 6968.

(231) Haider, M. D. S.; Hussain, R.; Kanwal, N.; Hussain, A.; Yawer, A.; Haider, M. I. S.; Ayub, K.; Fawy, K. F. *Surf. Interfaces* **2024**, *55*, 105434.

(232) Speller, E. M.; Clarke, A. J.; Luke, J.; Lee, H. K. H.; Durrant, J. R.; Li, N.; Wang, T.; Wong, H. C.; Kim, J. S.; Tsoi, W. C.; Li, Z. *J. Mater. Chem. A* **2019**, *7*, 23361–23377.

(233) Price, M. B.; Hume, P. A.; Ilina, A.; Wagner, I.; Tamming, R. R.; Thorn, K. E.; Jiao, W.; Goldingay, A.; Conaghan, P. J.; Lakhwani, G.; Davis, N. J.; Wang, Y.; Xue, P.; Lu, H.; Chen, K.; Zhan, X.; Hodgkiss, J. M. *Nat. Commun.* **2022**, *13*, 2827.

(234) Yan, Y.; Zhao, S.; Zhang, Y.; Wang, T.; Shi, Y.; Qiu, D.; Zhang, J.; Zhu, L.; Wang, M.; Qiao, J.; Hao, X.; Zhang, X.; Wei, Z. *Sol. RRL* **2023**, *7*, 2300342.

(235) Kumar, A.; Hudson, R. J.; Shumilov, N. A.; Lin, C. Y.; Smith, T. A.; Davis, N. J.; Ru, E. C. L.; Price, M. B.; Hume, P. A.; Hodgkiss, J. M. *J. Phys. Chem. Lett.* **2025**, 1367–1375.

(236) Kveder, M.; Merunka, D.; Jokić, M.; Makarević, J.; Rakvin, B. *Phys. Rev. B* **2009**, *80*, 052201.

(237) Stone, A. J. *Mol. Phys.* **1964**, *7*, 311–316.

(238) Krinichnyi, V. I.; Troshin, P. A.; Denisov, N. N. *J. Chem. Phys.* **2008**, *128*, 164715.

(239) Doan, P. E.; Hoffman, B. M. *Chem. Phys. Lett.* **1997**, *269*, 208–214.

(240) Morton, J. J.; Lees, N. S.; Hoffman, B. M.; Stoll, S. *J. Magn. Reson.* **2008**, *191*, 315–321.

(241) Epel, B.; Pöppl, A.; Manikandan, P.; Vega, S.; Goldfarb, D. *J. Magn. Reson.* **2001**, *148*, 388–397.

(242) Kehl, A.; Hiller, M.; Hecker, F.; Tkach, I.; Dechert, S.; Bennati, M.; Meyer, A. *J. Magn. Reson.* **2021**, *333*, 107091.

(243) Niklas, J.; Poluektov, O. G. *Adv. Energy Mater.* **2017**, *7*, 1602226.

(244) Hore, P.; Hunter, D.; McKie, C.; Hoff, A. *Chem. Phys. Lett.* **1987**, *137*, 495–500.

(245) Bittl, R.; Weber, S. *Biochim. Biophys. Acta, Bioenerg.* **2005**, *1707*, 117–126.

(246) Weber, S.; Biskup, T.; Okafuji, A.; Marino, A. R.; Berthold, T.; Link, G.; Hitomi, K.; Getzoff, E. D.; Schleicher, E.; Norris, J. R. *J. Phys. Chem. B.* **2010**, *114*, 14745–14754.

(247) Van der Est, A.; Poddutoori, P. K., *Photosynthesis: Structures, Mechanisms, and Applications*; Springer International Publishing: 2017, pp 359–387.

(248) Xu, J.; Jarocha, L. E.; Zollitsch, T.; Konowalczyk, M.; Henbest, K. B.; Richert, S.; Golesworthy, M. J.; Schmidt, J.; Déjean, V.; Sowood, D. J.; Bassetto, M.; Luo, J.; Walton, J. R.; Fleming, J.; Wei, Y.; Pitcher, T. L.; Moise, G.; Herrmann, M.; Yin, H.; Wu, H.; Bartölke, R.; Käsehagen, S. J.; Horst, S.; Dautaj, G.; Murton, P. D.; Gehrckens, A. S.; Chelliah, Y.; Takahashi, J. S.; Koch, K. W.; Weber, S.; Solov'yov, I. A.; Xie, C.; Mackenzie, S. R.; Timmel, C. R.; Mouritsen, H.; Hore, P. J. *Nature* **2021**, *594*, 535–540.

(249) Weiss, L. R.; Bayliss, S. L.; Kraffert, F.; Thorley, K. J.; Anthony, J. E.; Bittl, R.; Friend, R. H.; Rao, A.; Greenham, N. C.; Behrends, J. *Nat. Phys.* **2017**, *13*, 176–181.

(250) Drummond, B. H.; Aizawa, N.; Zhang, Y.; Myers, W. K.; Xiong, Y.; Cooper, M. W.; Barlow, S.; Gu, Q.; Weiss, L. R.; Gillett, A. J.; Credgington, D.; Pu, Y. J.; Marder, S. R.; Evans, E. W. *Nat. Commun.* **2021**, *12*, 4532.

(251) Bayliss, S. L.; Laorenza, D. W.; Mintun, P. J.; Kovos, B. D.; Freedman, D. E.; Awschalom, D. D. *Science* **2020**, *370*, 1309–1312.

(252) Mayländer, M.; Chen, S.; Lorenzo, E. R.; Wasielewski, M. R.; Richert, S. *J. Am. Chem. Soc.* **2021**, *143*, 7050–7058.

(253) Kothe, G.; Weber, S.; Ohmes, E.; Thurnauer, M. C.; Norris, J. R. *J. Phys. Chem* **1994**, *98*, 2706–2712.

(254) Link, G.; Berthold, T.; Bechtold, M.; Weidner, J. U.; Ohmes, E.; Tang, J.; Poluektov, O.; Utschig, L.; Schlesselman, S. L.; Thurnauer, M. C.; Kothe, G. *J. Am. Chem. Soc.* **2001**, *123*, 4211–4222.

(255) Salikhov, K. M.; Pushkar, Y. N.; Golbeck, J. H.; Stehlik, D. *Appl. Magn. Reson* **2003**, *24*, 467–482.

(256) Miura, T.; Aikawa, M.; Kobori, Y. *J. Phys. Chem. Lett.* **2014**, *5*, 30–35.

(257) Haberkorn, R. *Mol. Phys.* **1976**, *32*, 1491–1493.

(258) Jones, J. A.; Hore, P. J. *Chem. Phys. Lett.* **2010**, *488*, 90–93.

(259) Jones, J. A.; Maeda, K.; Hore, P. J. *Chem. Phys. Lett.* **2011**, *507*, 269–273.

(260) Kuprov, I., *Spin: From Basic Symmetries to Quantum Optimal Control*; Springer International Publishing: 2023, pp 223–289.

(261) Quintes, T.; Weber, S.; Richert, S. *J. Phys. Chem. A* **2025**, *129*, 3375–3388.

(262) Ernst, R. R.; Bodenhausen, G.; Wokaun, A., *Principles of Nuclear Magnetic Resonance in One and Two Dimensions*; Oxford University Press: 1990.

(263) Pribitzer, S.; Doll, A.; Jeschke, G. *J. Magn. Reson.* **2016**, *263*, 45–54.

(264) Shushin, A. *Chem. Phys. Lett.* **1991**, *183*, 321–326.

(265) McLauchlan, K. A., *Advanced EPR: Applications in Biology and Biochemistry*; Elsevier: 1989, pp 345–369.

(266) Batchelor, S. N.; Heikkila, H.; Kay, C. W. M.; McLauchlan, K. A.; Shkrob, I. A. *Chem. Phys.* **1992**, *162*, 29–45.

(267) Tait, C. E.; Krzyaniak, M. D.; Stoll, S. *J. Magn. Reson.* **2023**, *349*, 107410.

(268) Wang, D.; Hanson, G. R. *Appl. Magn. Reson.* **1996**, *11*, 401–415.

(269) Hogben, H. J.; Krzystyniak, M.; Charnock, G. T.; Hore, P. J.; Kuprov, I. *J. Magn. Reson.* **2011**, *208*, 179–194.

(270) Kuprov, I. *J. Magn. Reson.* **2011**, *209*, 31–38.

(271) Torrey, H. C. *Phys. Rev.* **1949**, *76*, 1059–1068.

(272) Furrer, R.; Fujara, F.; Lange, C.; Stehlik, D.; Vieth, H. M.; Vollmann, W. *Chem. Phys. Lett.* **1980**, *75*, 332–339.

(273) Stehlik, D.; Bock, C. H.; Thurnauer, M., *Advanced EPR: Applications in Biology and Biochemistry*; Elsevier: 1989, pp 371–403.

(274) Kothe, G.; Weber, S.; Bittl, R.; Ohmes, E.; Thurnauer, M. C.; Norris, J. R. *Chem. Phys. Lett.* **1991**, *186*, 474–480.

(275) Kothe, G.; Weber, S.; Ohmes, E.; Thurnauer, M. C.; Norris, J. R. *J. Am. Chem. Soc* **1994**, *116*, 7729–7734.

(276) Bittl, R.; van der Est, A.; Kamlowski, A.; Lubitz, W.; Stehlik, D. *Chem. Phys. Lett.* **1994**, *226*, 349–358.

(277) Laukenmann, K.; Weber, S.; Kothe, G.; Oesterle, C.; Angerhofer, A.; Wasielewski, M. R.; Svec, W. A.; Norris, J. R. *J. Phys. Chem* **1995**, *99*, 4324–4329.

(278) Heinen, U.; Berthold, T.; Kothe, G.; Stavitski, E.; Galili, T.; Levanon, H.; Wiederrecht, G.; Wasielewski, M. R. *J. Phys. Chem. A* **2002**, *106*, 1933–1937.

(279) Biskup, T.; Hitomi, K.; Getzoff, E. D.; Krapf, S.; Koslowski, T.; Schleicher, E.; Weber, S. *Angew. Chem. Int. Ed.* **2011**, *50*, 12647–12651.

(280) Sandberg, O. J.; Armin, A. *J. Phys. Chem. C* **2021**, *125*, 15590–15598.

(281) Ullbrich, S.; Benduhn, J.; Jia, X.; Nikolis, V. C.; Tvingstedt, K.; Piersimoni, F.; Roland, S.; Liu, Y.; Wu, J.; Fischer, A.; Neher, D.; Reineke, S.; Spoltore, D.; Vandewal, K. *Nat. Mater.* **2019**, *18*, 459–464.

(282) Moore, G. J.; Günther, F.; Yallum, K. M.; Causa', M.; Jungbluth, A.; Réhault, J.; Riede, M.; Ortmann, F.; Banerji, N. *Nat. Commun.* **2024**, *15*, 9851.

(283) Howard, I. A.; Mauer, R.; Meister, M.; Laquai, F. *J. Am. Chem. Soc.* **2010**, *132*, 14866–14876.

(284) Bakulin, A. A.; Dimitrov, S. D.; Rao, A.; Chow, P. C.; Nielsen, C. B.; Schroeder, B. C.; McCulloch, I.; Bakker, H. J.; Durrant, J. R.; Friend, R. H. *J. Phys. Chem. Lett.* **2013**, *4*, 209–215.

(285) Clarke, T. M.; Durrant, J. R. *Chem. Rev.* **2010**, *110*, 6736–6767.

(286) Gao, F.; Inganäs, O. *Phys. Chem. Chem. Phys.* **2014**, *16*, 20291–20304.

(287) Zheng, Z.; Awartani, O. M.; Gautam, B.; Liu, D.; Qin, Y.; Li, W.; Bataller, A.; Gundogdu, K.; Ade, H.; Hou, J. *Adv. Mater.* **2017**, *29*, 1604241.

(288) Tamai, Y.; Murata, Y.; Natsuda, S.; Sakamoto, Y. *Adv. Energy Mater.* **2024**, *14*, 2301890.

(289) Vandewal, K.; Tvingstedt, K.; Gadisa, A.; Inganäs, O.; Manca, J. V. *Phys. Rev. B* **2010**, *81*, 125204.

(290) Giannini, S.; Sowood, D. J. C.; Cerda, J.; Frederix, S.; Grune, J.; Londi, G.; Marsh, T.; Ghosh, P.; Duchemin, I.; Greenham, N. C.; Vandewal, K.; D'Avino, G.; Gillett, A. J.; Beljonne, D. *Mater. Today* **2023**, 308–326.

(291) Mahadevan, S.; Liu, T.; Pratik, S. M.; Li, Y.; Ho, H. Y.; Ouyang, S.; Lu, X.; Yip, H. L.; Chow, P. C.; Brédas, J. L.; Coropceanu, V.; So, S. K.; Tsang, S. W. *Nat. Commun.* **2024**, *15*, 2393.

(292) Dauw, X. L.; van den Berg, G. J.; van den Heuvel, D. J.; Poluektov, O. G.; Groenen, E. J. *J. Chem. Phys.* **2000**, *112*, 7102–7110.

(293) Gastel, M. V. *J. Phys. Chem. A* **2010**, *114*, 10864–10870.

(294) Ceola, S.; Corvaja, C.; Franco, L. *Mol. Cryst. Liq. Cryst.* **2003**, *394*, 31–43.

(295) Franco, L.; Toffoletti, A.; Ruzzi, M.; Montanari, L.; Carati, C.; Bonoldi, L.; Po', R. *J. Phys. Chem. C* **2013**, *117*, 1554–1560.

(296) Kurganskii, I. V.; Ivanov, M. Y.; Fedin, M. V. *J. Phys. Chem. B* **2018**, *122*, 6815–6822.

(297) Grott, S.; Kotobi, A.; Reb, L. K.; Weindl, C. L.; Guo, R.; Yin, S.; Wienhold, K. S.; Chen, W.; Ameri, T.; Schwartzkopf, M.; Roth, S. V.; Müller-Buschbaum, P. *Sol. RRL* **2022**, *6*, 2101084.

(298) Clarke, R. H.; Frank, H. A. *J. Chem. Phys.* **1976**, *65*, 39–47.

(299) Beljonne, D.; Shuai, Z.; Pourtois, G.; Bredas, J. L. *J. Phys. Chem. A* **2001**, *105*, 3899–3907.

(300) Zhang, M.; Zhu, L.; Qiu, C.; Hao, T.; Jiang, Y.; Leng, S.; Chen, J.; Zhou, G.; Zhou, Z.; Zou, Y.; Su, X.; Shi, Z.; Zhu, H.; Zhang, Y.; Russell, T. P.; Zhu, X.; Liu, F. *Small Sci.* **2022**, *2*, 2100092.

(301) He, Y.; Li, N.; Heumüller, T.; Wortmann, J.; Hanisch, B.; Aubele, A.; Lucas, S.; Feng, G.; Jiang, X.; Li, W.; Bäuerle, P.; Brabec, C. J. *Joule* **2022**, *6*, 1160–1171.

(302) Theunissen, D.; Smeets, S.; Maes, W. *Front. Chem.* **2023**, *11*, 1326131.

(303) Buckley, C.; Hunter, D.; Hore, P.; McLauchlan, K. *Chem. Phys. Lett.* **1987**, *135*, 307–312.

(304) Osintsev, A.; Popov, A.; Fuhs, M.; Möbius, K. *Appl. Magn. Reson.* **2001**, *20*, 111–135.

(305) Lee, T. H.; Dong, Y.; Pacalaj, R. A.; Park, S. Y.; Xu, W.; Kim, J. S.; Durrant, J. R. *Adv. Funct. Mater.* **2022**, *32*, 2208001.

(306) Hulsebosch, R. J.; Borovykh, I. V.; Paschenko, S. V.; Gast, P.; Hoff, A. J. *J. Phys. Chem. B* **1999**, *103*, 6815–6823.

(307) Link, G.; Heinen, U.; Berthold, T.; Ohmes, E.; Weidner, J.-U.; Kothe, G. *Z. Phys. Chem.* **2004**, *218*, 171–191.

(308) Thurnauer, M. C.; Poluektov, O. G.; Kothe, G., *Time-Resolved High-Frequency and Multifrequency EPR Studies of Spin-Correlated Radical Pairs in Photosynthetic Reaction Center Proteins*; Springer Science and Business Media: 2004, pp 165–206.

(309) Barker, A. J.; Chen, K.; Hodgkiss, J. M. *J. Am. Chem. Soc.* **2014**, *136*, 12018–12026.

(310) Mikhnenko, O. V.; Cordella, F.; Sieval, A. B.; Hummelen, J. C.; Blom, P. W.; Loi, M. A. *J. Phys. Chem. B* **2008**, *112*, 11601–11604.

(311) Grzegorczyk, W. J.; Savenije, T. J.; Dykstra, T. E.; Piris, J.; Schins, J. M.; Siebbeles, L. D. *J. Phys. Chem. C* **2010**, *114*, 5182–5186.

(312) Chen, K.; Barker, A. J.; Reish, M. E.; Gordon, K. C.; Hodgkiss, J. M. *J. Am. Chem. Soc.* **2013**, *135*, 18502–18512.

(313) Chan, C. C.; Ma, C.; Zou, X.; Xing, Z.; Zhang, G.; Yip, H. L.; Taylor, R. A.; He, Y.; Wong, K. S.; Chow, P. C. *Adv. Funct. Mater.* **2021**, *31*, 2107157.

(314) Zhang, Q.; Yuan, X.; Feng, Y.; Larson, B. W.; Su, G. M.; Maung, Y. M.; Rujisamphan, N.; Li, Y.; Yuan, J.; Ma, W. *Sol. RRL* **2020**, *4*, 1900524.

(315) Rodríguez-Martínez, X.; Marina, S.; Harillo-Baños, A.; Campoy-Quiles, M.; Martin, J. *J. Mater. Chem. C* **2025**, 13776–13786.

(316) Lukas, A. S.; Bushard, P. J.; Weiss, E. A.; Wasielewski, M. R. *J. Am. Chem. Soc.* **2003**, *125*, 3921–3930.

(317) Al Said, T.; Weber, S.; Schleicher, E. *Front. Mol. Biosci.* **2022**, *9*, 890826.

(318) Cates, N.; Cho, E.; Gysel, R.; Risko, C.; Coropceanu, V.; Miller, C. E.; Sweetnam, S.; Sellinger, A.; Heeney, M.; McCulloch, I.; Brédas, J.-L.; Toney, M. F.; McGehee, M. D. *Adv. Energy Mater.* **2012**, *2*, 1208–1217.

(319) Krinichnyi, V. I.; Yudanova, E. I.; Denisov, N. N.; Konkin, A. A.; Ritter, U.; Wessling, B.; Konkin, A. L.; Bogatyrenko, V. R. *J. Phys. Chem. C* **2020**, *124*, 10852–10869.

(320) Jiang, K.; Westbrook, R. J. E.; Xia, T.; Zhong, C.; Lu, J.; Khasbaatar, A.; Liu, K.; Lin, F. R.; Jang, S.-H.; Zhang, J.; Li, Y.; Diao, Y.; Wei, Z.; Yip, H.-L.; Ginger, D. S.; Jen, A. K.-Y. *Nat. Commun.* **2025**, *16*, 3176.

(321) Suthar, R.; Abhijith, T.; Dahiya, H.; Singh, A. K.; Sharma, G. D.; Karak, S. *ACS Appl. Mater. Interfaces* **2022**, *15*, 3214–3223.

(322) Eaton, G. R.; Eaton, S. S.; Barr, D. P.; Weber, R. T., *Quantitative EPR*; Springer Vienna: 2010, pp 79–87.

(323) Chen, X. K.; Coropceanu, V.; Brédas, J. L. *Nat. Commun.* **2018**, *9*, 5295.

(324) Eisner, F. D.; Azzouzi, M.; Fei, Z.; Hou, X.; Anthopoulos, T. D.; Dennis, T. J. S.; Heeney, M.; Nelson, J. *J. Am. Chem. Soc.* **2019**, *141*, 6362–6374.

(325) Xiang, C.; Zhao, Q.; Liu, W.; Cao, J.; Zou, Y.; Zhou, H. *J. Mater. Chem. A* **2022**, *10*, 25611–25619.

(326) Kroh, D.; Eller, F.; Schötz, K.; Wedler, S.; Perdigón-Toro, L.; Freychet, G.; Wei, Q.; Dörr, M.; Jones, D.; Zou, Y.; Herzig, E. M.; Neher, D.; Köhler, A. *Adv. Funct. Mater.* **2022**, *32*, 2205711.

(327) Stolterfoht, M.; Armin, A.; Shoaee, S.; Kassal, I.; Burn, P.; Meredith, P. *Nat. Commun.* **2016**, *7*, 11944.

(328) Ziffer, M. E.; Jo, S. B.; Zhong, H.; Ye, L.; Liu, H.; Lin, F.; Zhang, J.; Li, X.; Ade, H. W.; Jen, A. K.; Ginger, D. S. *J. Am. Chem. Soc.* **2018**, *140*, 9996–10008.

(329) Timmel, C. R.; Fursman, C. E.; Hoff, A. J.; Hore, P. J. *Chem. Phys.* **1998**, *226*, 271–283.

(330) Panariti, D.; Conron, S. M.; Zhang, J.; Wasielewski, M. R.; Valentin, M. D.; Tait, C. E. *Phys. Chem. Chem. Phys.* **2023**, *26*, 3842–3856.

(331) Lukina, E. A.; Popov, A. A.; Uvarov, M. N.; Suturina, E. A.; Reijerse, E. J.; Kulik, L. V. *Phys. Chem. Chem. Phys.* **2016**, *18*, 28585–28593.

(332) Bowman, M. K.; Krzyaniak, M. D.; Cruce, A. A.; Weber, R. T. *J. Magn. Reson.* **2013**, *231*, 117–125.

(333) Hodgkiss, J. M.; Albert-Seifried, S.; Rao, A.; Barker, A. J.; Campbell, A. R.; Marsh, R. A.; Friend, R. H. *Adv. Funct. Mater.* **2012**, *22*, 1567–1577.

(334) Van Reenen, S.; Vitorino, M. V.; Meskers, S. C.; Janssen, R. A.; Kemerink, M. *Phys. Rev. B* **2014**, *89*, 205206.

(335) Lukina, E. A.; Suturina, E.; Reijerse, E.; Lubitz, W.; Kulik, L. V. *Phys. Chem. Chem. Phys.* **2017**, *19*, 22141–22152.

(336) Chandrabose, S.; Chen, K.; Barker, A. J.; Sutton, J. J.; Prasad, S. K.; Zhu, J.; Zhou, J.; Gordon, K. C.; Xie, Z.; Zhan, X.; Hodgkiss, J. M. *J. Am. Chem. Soc.* **2019**, *141*, 6922–6929.

(337) Shuttle, C. G.; Hamilton, R.; O'Regan, B. C.; Nelson, J.; Durrant, J. R. *PNAS* **2010**, *107*, 16448–16452.

(338) Etzold, F.; Howard, I. A.; Mauer, R.; Meister, M.; Kim, T. D.; Lee, K. S.; Baek, N. S.; Laquai, F. *J. Am. Chem. Soc.* **2011**, *133*, 9469–9479.

(339) Proctor, C. M.; Kim, C.; Neher, D.; Nguyen, T. Q. *Adv. Funct. Mater.* **2013**, *23*, 3584–3594.

(340) Proctor, C. M.; Kuik, M.; Nguyen, T. Q. *Prog. Polym. Sci.* **2013**, *38*, 1941–1960.

(341) Zarrabi, N.; Yazmaciyan, A.; Meredith, P.; Kassal, I.; Armin, A. *J. Phys. Chem. Lett.* **2018**, *9*, 6144–6148.

(342) Sun, B.; Tokmoldin, N.; Alqahtani, O.; Patterson, A.; Castro, C. S. D.; Riley, D. B.; Pranav, M.; Armin, A.; Laquai, F.; Collins, B. A.; Neher, D.; Shoaee, S. *Adv. Energy Mater.* **2023**, *13*, 2300980.

(343) Kraffert, F.; Steyrleuthner, R.; Meier, C.; Bittl, R.; Behrends, J. *Appl. Phys. Lett.* **2015**, *107*, 043302.

(344) Grüne, J.; Dyakonov, V.; Sperlich, A. *Mater. Horiz.* **2021**, *8*, 2569–2575.

(345) Verploegen, E.; Mondal, R.; Bettinger, C. J.; Sok, S.; Toney, M. F.; Bao, Z. *Adv. Funct. Mater.* **2010**, *20*, 3519–3529.